MECHANICAL PERFORMANCE AND SUSTAINABILITY ASSESSMENT OF REINFORCED SOIL WALLS

IVAN PUIG DAMIANS

A dissertation submitted to
Universitat Politècnica de Catalunya (UPC-BarcelonaTech)
in partial fulfillment of the requirements
for the Degree of

Doctor of Philosophy
in
Geotechnical Engineering and Geo-Sciences

Thesis advisors:

Prof. ALEJANDRO JOSA / **Prof.** ANTONIO LLORET / **Prof.** RICHARD J. BATHURST

MECHANICAL PERFORMANCE AND SUSTAINABILITY ASSESSMENT OF REINFORCED SOIL WALLS

IVAN PUIG DAMIANS

A dissertation submitted to
Universitat Politècnica de Catalunya (UPC-BarcelonaTech)
in partial fulfillment of the requirements
for the Degree of

Doctor of Philosophy
in
Geotechnical Engineering and Geo-Sciences

Thesis advisors:

Prof. ALEJANDRO JOSA / **Prof.** ANTONIO LLORET / **Prof.** RICHARD J. BATHURST

Barcelona, June 2016

Universitat Politècnica de Catalunya (UPC-BarcelonaTech)
School of Civil Engineering (ETSECCPB)
Department of Civil Engineering and Environmental Engineering (DECA)

ABSTRACT

Soil reinforced retaining wall structures are materially more efficient than competing construction solutions such as gravity and cantilever walls. Nevertheless, the behaviour and interactions between the component materials are complex and not fully understood. Current design methods are typically limited to simple cases with respect to material properties, geometry, and boundary conditions. Advanced numerical models using finite element and/or finite difference methods offer the possibility to extend the understanding of these systems and to predict wall performance under operational conditions.

In this Thesis, numerical models were developed and shown to give satisfactory predictions of wall behavior when compared with results of instrumented physical structures. The verified models were useful for sensitivity analyses using a range of wall geometries and boundary conditions, material parameters and different constitutive models. As examples of the obtained results, the compressibility of the precast panel bearing pads significantly modified the axial vertical facing load but has no significant effect on the tension developed in the soil reinforcement layers. Also, the stiffness of the foundation soil has greater effect on the tension developed in soil steel reinforcing elements than for polymeric reinforcement layers. It has been possible to perform sensitivity analysis using parameters that define soil-structure interactions. Such interactions have been analyzed using different commercial software programs and by defining them with elements from the continuum media using 2D and 3D models. Laboratory reinforcement pullout tests using steel ladder and polymeric strips were performed as part of the Thesis. Those parameters that have the greatest influence on soil-reinforcement interaction are identified, quantified, and compared to default-design values and a range of values used to calibrate numerical models. From the results of 2D and 3D numerical models suitable correlations have been obtained to allow 2D models to be used in plane strain reinforced soil walls with discontinuous soil reinforcement elements in the running wall length of these structures.

With a proper sustainability assessment it has been possible to make quantitative comparisons between reinforced soil wall structures and other alternatives performing the same function (such as gravity and cantilever walls) constructed to different heights. Using a model based on the multi-attribute utility theory and value analysis decision-making, the best solutions with least negative impact were identified in an example set of alternative earth retaining wall options from a sustainable perspective. The results include possible scenarios based on the relative importance of the three pillars of sustainability (i.e., environmental, economic, and

social/functional) as judged by different stakeholders. Reinforced soil walls turned out to be the best choice in most cases analyzed, based on a quantitative end score.

The models and analysis methodologies developed as part of this Thesis work have improved understanding of the behavior of these structures, and offered possibilities to improve and optimize designs in the future.

RESUM

Els murs de contenció amb sòl reforçat són estructures materialment més eficients que altres solucions constructives alternatives, com ara els murs de gravetat o en voladís. No obstant això, el seu comportament i les interaccions entre els materials que componen aquestes estructures són complexos i no entesos completament. Els mètodes de disseny actuals solen estar limitats a casos senzills respecte a les propietats dels materials, la geometria i les condicions de contorn. Models numèrics avançats utilitzant elements finits i/o diferències finites ofereixen la possibilitat d'ampliar la comprensió d'aquests sistemes estructurals i de predir el comportament de l'estructura en condicions de servei.

En aquesta Tesi s'han desenvolupat models numèrics que han demostrat donar prediccions satisfactòries del comportament d'aquest tipus de murs quan es comparen amb resultats obtinguts d'estructures físiques instrumentades. Aquests models verificats han estat útils per a poder fer anàlisis de sensibilitat segons diferents geometries del parament i condicions de contorn, paràmetres dels materials i diferents models constitutius. Com a exemple dels resultats obtinguts, s'ha determinat que la capacitat de compressió de les peces de recolzament dels panells prefabricats modifica de manera significativa la càrrega desenvolupada vertical axial en el parament, però no té un efecte significatiu en la tensió desenvolupada a les capes de reforç del sòl. O també, que la rigidesa del sòl de fonamentació té un efecte més gran sobre la tensió desenvolupada en elements de reforç metàl·lics que en polimèrics. Ha estat possible dur a terme anàlisis de sensibilitat utilitzant els paràmetres que defineixen les interaccions sòl-estructura. Aquestes interaccions han estat analitzades utilitzant diferents programes comercials numèrics i definint-les amb elements del medi continu tant en models 2D com en 3D. Com a part de la Tesi, s'han de dut a terme assaigs de laboratori d'extracció de reforços tipus malla metàl·lica i banda polimèrica. Els paràmetres que tenen una influència principal en la interacció sòl-reforç han sigut identificats, quantificats i comparats tant amb els valors per defecte de disseny com amb valors reportats a la literatura utilitzats per a calibrar models analítics, permetent el calibratge dels models numèrics generats. Dels resultats dels models 2D i 3D s'han obtingut correlacions que permeten concloure que els models 2D en deformació plana són adequats per a representar el

funcionament de les estructures de sòl reforçat amb elements de reforç discontinus a la direcció del parament.

Mitjançant una avaluació adequada de la sostenibilitat ha estat possible fer comparacions quantitatives entre estructures de sòl reforçat i altres alternatives constructives que compleixen la mateixa funció (com els murs de gravetat o en voladís) construïdes a diferents altures. Mitjançant un model basat en la teoria de la utilitat multiatribut i d'anàlisi de valor per a la presa de decisions, es van identificar els processos més representatius i de major impacte des d'un punt de vista sostenible. Els resultats obtinguts inclouen un ajust basat en possibles escenaris de presa de decisió per la importància relativa dels tres pilars de la sostenibilitat (ambiental, econòmic, i social/funcional). L'alternativa de sòl reforçat va resultar ser la millor, obtenint una puntuació més alta en gran part dels escenaris de presa de decisió considerats. En base a una puntuació quantitativa final, els murs de sòl reforçat van resultar ser la millor opció en la majoria dels casos analitzats.

Els models i metodologies d'anàlisi desenvolupades com a part de aquest treball de Tesi han millorat la comprensió del comportament d'aquestes estructures, i ofereixen possibilitats per a millorar i optimitzar els seus dissenys en el futur.

RESUMEN

Los muros de contención con suelo reforzado son estructuras materialmente más eficientes que otras soluciones constructivas alternativas, tales como los muros de gravedad o en voladizo. Sin embargo, su comportamiento y las interacciones entre los materiales que componen estas estructuras son complejos y no completamente comprendidos. Los métodos de diseño actuales suelen estar limitados a casos sencillos con respecto a las propiedades de los materiales, la geometría y las condiciones de contorno. Modelos numéricos avanzados utilizando elementos finitos y/o diferencias finitas ofrecen la posibilidad de ampliar la comprensión de estos sistemas y de predecir el comportamiento de la estructura en condiciones de servicio.

En esta Tesis se han desarrollado modelos numéricos que han demostrado dar predicciones satisfactorias del comportamiento de este tipo de muros cuando se comparan con resultados obtenidos de estructuras físicas instrumentadas. Estos modelos verificados han sido útiles para análisis de sensibilidad según diferentes geometrías del paramento y condiciones de contorno, parámetros de los materiales y diferentes modelos constitutivos. Como ejemplo de los resultados obtenidos, la capacidad de compresión de las piezas de apoyo de los paneles prefabricados modifica de manera significativa la carga vertical axial desarrollada en el

paramento, pero no tiene un efecto significativo en la tensión desarrollada en las capas de refuerzo del suelo. O también, que la rigidez del suelo de cimentación tiene un mayor efecto sobre la tensión desarrollada en elementos de refuerzo metálicos que en poliméricos. Ha sido posible llevar a cabo análisis de sensibilidad utilizando los parámetros que definen las interacciones suelo-estructura. Tales interacciones han sido analizadas utilizando diferentes programas numéricos comerciales y definiéndolas con elementos del medio continuo tanto en modelos 2D como 3D. Como parte de la Tesis, se han llevado a cabo ensayos de laboratorio de extracción de refuerzos tipo malla metálica y banda polimérica. Los parámetros que tienen una mayor influencia en la interacción suelo-refuerzo han sido identificados, cuantificados y comparados tanto con los valores por defecto de diseño como con valores reportados en la literatura usados para calibrar modelos analíticos, permitiendo la calibración numérica de los modelos generados. De los resultados de los modelos 2D y 3D se han obtenido correlaciones que permiten concluir que los modelos 2D en deformación plana son adecuados para representar el funcionamiento de las estructuras de suelo reforzado con elementos de refuerzo discontinuos en la dirección del paramento.

Con una evaluación adecuada sostenibilidad ha sido posible hacer comparaciones cuantitativas entre estructuras de suelo reforzado y otras alternativas constructivas que cumplen la misma función (tales como los muros de gravedad o en voladizo) construidas a diferentes alturas. Mediante un modelo basado en la teoría de la utilidad multiatributo y análisis de valor para la toma de decisiones, se identificaron los procesos más representativos y de mayor impacto desde un punto de vista sostenible. Los resultados obtenidos incluyen un ajuste basado en posibles escenarios de toma de decisión por la importancia relativa de los tres pilares de la sostenibilidad (ambiental, económico, y social/funcional). La alternativa de suelo reforzado resultó ser la mejor, obteniendo una mayor puntuación en gran parte de los escenarios de toma de decisión considerados. En base a una puntuación final cuantitativa, los muros de suelo reforzado resultaron ser la mejor opción en la mayoría de los casos analizados.

Los modelos y metodologías de análisis desarrolladas como parte de este trabajo de Tesis han mejorado la comprensión del comportamiento de estas estructuras, y ofrecen posibilidades para mejorar y optimizar sus diseños en el futuro.

ACKNOWLEDGMENTS

It is said about gratitude that, being a virtue, it is more related to miserable people than to fortunate people. Therefore and luckily, I must be a very unfortunate person.

First, I would like to acknowledge the support provided by the Universitat Politècnica de Catalunya (UPC-BarcelonaTech).

I'm specially and sincerely grateful to my supervisors and mentors: Alejandro Josa, Antonio Lloret, and Richard J. Bathurst.

Sr.Josa impressed me a lot from the very beginning when I was undergraduate student: his teaching courses were so good that I wanted to take them again the following year (I partially failed at first attempt), but also the following one (I started feeling comfortable with the undrained shear strength concept and I clearly needed more). His righteous personality, sense of humor, and perfectionism sensitivity made me become a better person in many aspects. He encouraged me to continue into the academic world with the Master and Ph.D. enrolment, and gave me the opportunity to start teaching some of his courses. Nowadays (8 years later) I feel very fortunate checking my perfect watch to make sure not to be late and to continue helping him the best I can.

Toni has always been open to solve my multiple and jumbled questions: he has provided me constant encouragement throughout my Thesis analysis, huge patience, and has helped me a lot with his always wise and prudent advice. I am really fortunate to have met him.

Having been to Canada has been one of my best decisions in my life. Most of my Thesis trend has been shaped and focused to clear and better purposes thanks to Dr.Bathurst. Sometimes, you could have problems to bring his thoughts into something understandable (even for very closer and well-known people in life), if the explanations are in a foreign language (English in my case), all this may become catastrophic: Dr.Bathurst always has a friendly and Jobian patience trying to understand what I wanted to say. I am also very thankful to him for his review, suggestions, writing, and for his constant support during the course of this research work. I sincerely hope that he was geographically closer to me; I really miss our dry Pale Ale pint-time after non-stop 12-hours-a-day working non-stop in RMC.

I would like to extend my sincere gratitude to Juan Lima (VSL): he gave me the opportunity to be into the professional world and I hope to continue working and sharing knowledge with him much longer. I learn a lot from him daily with his always kind guidance; he is a clear example of how smart, meticulous, and scientific feeling can be an essentially practical engineer being officially away from the academic world. His support, patience, constant encouragement, and friendship throughout the pursuit of my Doctorate degree are sincerely appreciated.

I would like to also extend my sincere appreciation and gratitude to Sebastià Olivella for his always available time to solve Code_Bright issues. Special acknowledge also to my university workmate and friend José Luis Zornoza, and to Josep Suriol for his always friendly attitude and interesting discussions about any humanistic concern. I really hope to continue being in contact with all of them for many years.

I would also like to thank Yoshihisha Miyata and Neil Dixon for serving in the external referee process and, also Vicente Navarro, for serving in my examination committee. I'd like to thank Cristina Jommi and Jean Vaunat too, for their availability to serve as board members reserve.

I would like to also extend my sincere appreciation and gratitude to Anna and Alba (UPC colleagues); Ignasi and Cristian (UPC office mates); to my friend Hu Wei (or 无为? B-power!), Fawzy, Yazan, and Sina (RMC colleagues), with special acknowledge to Yan Yu (I really appreciate all his help and availability and hope we will continue working together); to Gerard and Agnés (Catalan-Canadian friends which made me feel closer to my home when I was actually far away); to Markeller, Andrew, and the other RiT liver-gym mates (strongly required daily IPA times after long working days); to Paulo Albuquerque; to Eduard Adroguer for his sustainable contribution; to Francesc Sanchís; to my escaped cousin Lluís; to Aleix, Andoni, Aristotelian Aldo, Judit, and of course also a huge gratitude to my historical friends Sali, Jaime, Uri, Javi, Karl Carlus Greixac Hungus (37 Sullivan members), and Nerea, without them, even though possible, the traveled path up to where I am would have been extremely gray.

There are few words that can express my gratitude to my family with special reference to those who are no longer with us and will never be forgotten. To my parents, brother, and my relatives in Gironella, thank you all for your support and encouragement through my life and for understanding how important this educational goal was to me. Finally, to my loving life-mate Bàrbara: I owe you a special debt of gratitude for your support and sacrifice during my studies.

June, 2016

TABLE OF CONTENTS

INTRODUCTION

i) BACKGROUND AND PRELIMINARY STATEMENT OF THE THESIS

A brief background, understood as the State of the Question, preceding the study and development of the tasks that are expected to reach the objectives of this Doctoral Thesis, is included in this Section. The order followed in this Section is, first, a brief description of the beginnings and origin of the construction technique of containment structures using reinforced soil with a description of the general concept that refers to this structural typology. Components and main construction elements of these structures are explained, and a brief explanation of global and particular behaviour inherent in reinforced soil structures is provided. An example of poor performance under working stress conditions is briefly introduced and explained, linked to the first analyzed case in the Thesis, and a brief introduction to the concept of sustainability assessment is given, which corresponds to the last part of the Thesis.

i.a) General

Since its inception in the 70's with the "Terre Armée" patent in 1963 (Vidal 1966), with first constructions in France in 1968 and with the creation of specialized companies in this regard in 1970 in Canada and in Australia and first practical application in the United States in 1977 (Berthoneet 2003), the retained earth reinforced soil walls have adapted to many construction solutions, improving and optimizing the performance of its components and growing in their applicability against other structural options (Anderson and Brabant 2006). It is understood that the reinforced soil system is comprised of compacted backfill material with suitable properties, and a passive reinforcement placed therein. The construction procedure for a reinforced soil wall structure develops with progressive placement of the panels of the facing, suitably located and assembled on another panel above compressible bearing pad pieces, gradually emplaced in height as the backfilling and compaction by tiers progresses and the soil reinforcing elements are installed at different heights and connected to the facing panels. Thus, in earth retaining reinforced soil, the retaining material is a major structural component of the structure.

i.b) Reinforced soil structures

The main components of reinforced soil structures (see Figure i.1) are listed below:

- **Panels** are responsible for the balance of tensions in the facing boundary of the soil mass. Usually they are precast concrete panels assembled without contact, i.e., keeping open joints between (horizontal and vertical) with the consequent effect of drainage. The geometry of these panels can vary according to the system and company, but typically have double symmetry and square proportions, with an area from 2 to 5 m^2 and about 10 to 20 cm thick. In all panel joints, geotextiles sheets must be installed in inward panel side to prevent erosion of the fill material in drainage processes.

- **Reinforcements** are generally linear elements (bars, strips, plates, meshes, grids, sheets, etc.), with little or no resistance to bending, but assuring enough friction by shear and pullout strength with soil interaction, with additional passive strength in case of ribbed or gridded reinforcement shapes. Depending on their material nature (steel or polymeric) reinforcements can be considered rigid or flexible in terms of their extensibility against tensile loads and relative to soil strains. Different analytical methodologies and criteria are used in order to calculate the construction project with regard to the reinforcement type and consistent with its ultimate strength resistance (both tensile material capacity and soil-reinforcement shear strength). Reinforcements must ensure good durability and corrosion resistance by any chemical and biological attack coming from the fill material.

- **Backfill** material has to satisfy strength, density, gradation and plasticity requirements, which may be related to the reinforcement type assumed. Backfill material shall be installed properly and compacted according to the technical requirements of the project and particle size, reaching the appropriate maximum density under optimal water content. Backfill shall satisfy sieve gradation requirements to provide enough internal drainage, and also chemical composition, suitable to ensure good system performance and minimal corrosion of reinforcements.

It should be noted that the particular mechanical properties of the backfill material and the reinforcing elements must be matched to give an optimal performance in soil-reinforcement friction effect. Thus, both the backfill gradation and confinement degree, and reinforcement roughness usually come together to ensure that sufficient friction strength is developed in this interaction.

There are also other components (other than the geotextiles joint sheets already mentioned), which may be less important in terms of the final structural stability, but no less important for correct assembly of the structure and behaviour under working stress -operational- conditions. These are listed as follows:

- The **bearing pads** are compressible pieces installed at all horizontal facing panel joints whose function is to ensure the facing flexibility, minimizing the differential settlements which may arise between the backfill and the facing (further explanations

within the Thesis). Although clearly softer than the concrete panels, bearing pads may have enough compression strength to withstand the vertical forces originating from the facing and to avoid concrete-concrete contact. Typically, bearing pads are manufactured from polymeric material (rubber, neoprene, polyethylene, etc.) and with appropriate hardness and strength.

- The facing **leveling pad** is usually provided with a running footing under the first line of panels. Leveling pad is not a foundation so its function is not to bear the structure according to criteria of bearing load capacity, but to properly align the first level of panels during construction. According to this, the leveling pad must have small geometry dimensions (about 15 cm depth and 30 cm wide). The location depth of the leveling pad (i.e., facing embedment) is related to practical considerations ensuring a good structural confinement at the facing toe. For retaining structures in regular flat conditions with no evidence of additional ground soil instability risks, this embedment depth is about 10-15% of the wall facing height.

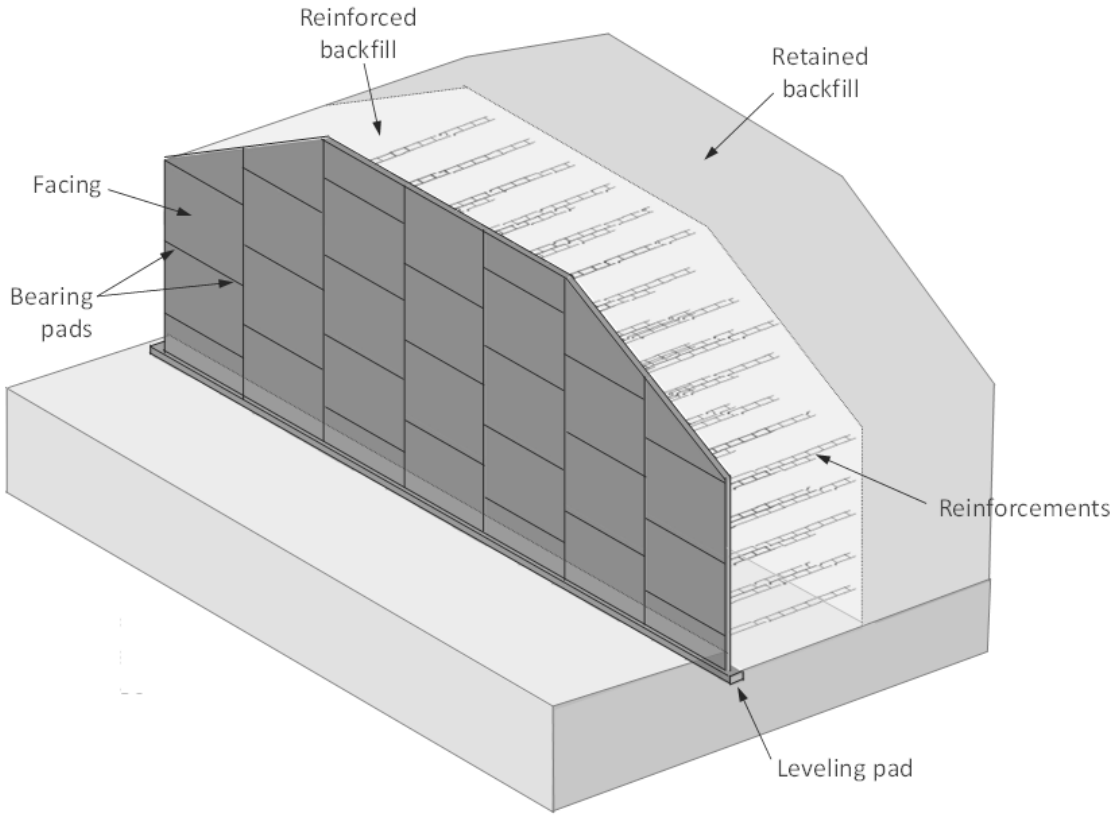

Figure i.1. General composition of a reinforced soil wall structure.

Reinforced soil structures are most often used as retaining earth solutions and bridge abutments. Reinforced soil solutions tend to be cheaper compared to other containment systems and construction is much faster due to the precast facing panels. The main issue of

these structures is the construction process, which should be very methodical, with proper compaction of the fill material, and with special care in compliance with the technical requirements (especially those for the same fill, to ensure a balance between adequate strength and corrosion of reinforcement). The reinforced soil structures, despite the particular backfill requirements, behave as a soil mass volume, both solid and flexible (both inside and on the facing), which allows a significant tolerance to differential settlement compared to other types of containment structures (providing higher safety factors against external stability requirements as overturning, sliding and overall failures).

i.c) Reinforced soil design: main basis

Historically, there have been several calculation methodologies for the design of retaining earth reinforced soil structures. It is important to identify the modes of failure so thsy optimized design can be carried out. In mechanical stabilized earth retaining wall structures, the typical modes of failure can be grouped related to external and internal stability. External loading verifications are directly related to lateral earth pressure conditions analyzed. By this manner, to verify external stability of a reinforced soil structure the entire reinforced soil mass with external (outsider) loading conditions shall be analyzed. Overturning or eccentricity, sliding at base plane, foundation bearing capacity (settlement), and global stability are the common external stability verifications to be performed.

Internal stability failure modes include soil reinforcement rupture (strength limit state), and excessive reinforcement elongation under the design load (service limit state). Main instabilities within the reinforced soil body are: reinforcing element failure (reinforcement strength lower than the actual loading generated), reinforcement-to-facing connection failure, and pullout failure (inadequate soil-reinforcement interaction shear strength). Each of these failure mechanisms has particular verifications to be properly satisfied. Reinforcement failure shall be avoided for any maximum tensile load carried by the reinforcing elements, factorized, and developed at any reinforcement layer at any time during the design life. A main concept in internal stability verification of MSE walls is the location of this maximum tensile load (see Figure i.2). This geometric line location defines and provides a conceptual boundary between the active zone (soil providing active earth pressure against the wall facing) and the resistant zone (zone where reinforcement is providing strength due to the soil-reinforcement shear interaction). Whereas internal and connection mechanical reinforcement ruptures are related to reinforcing material strength, typically solved with enough material amount (cross-section) and/or higher strength components, pullout failure is related to reinforcing material length in the resistant zone L_e (reinforcement in-soil anchorage), and/or soil-reinforcement contact roughness (which can be defined by the related interaction friction angle). On the other hand, the pullout resistance must be equal to the shear stresses developed at the whole contact area between the reinforcement and the fill soil. According to this, the pullout resistance (in total force units) can be understood theoretically as the sum of the shear stresses along the resistance length of the reinforcement (L_e) at a certain location.

The soil reinforcement extensibility and material type are major factors in determining reinforcement loads location within the reinforcement body. Inextensible reinforcement materials reach their peak strength at strains lower than the strain required for the soil to reach its peak strength, whereas extensible reinforcements reach their peak strength at strains greater than the strain required for soil to reach its peak strength.

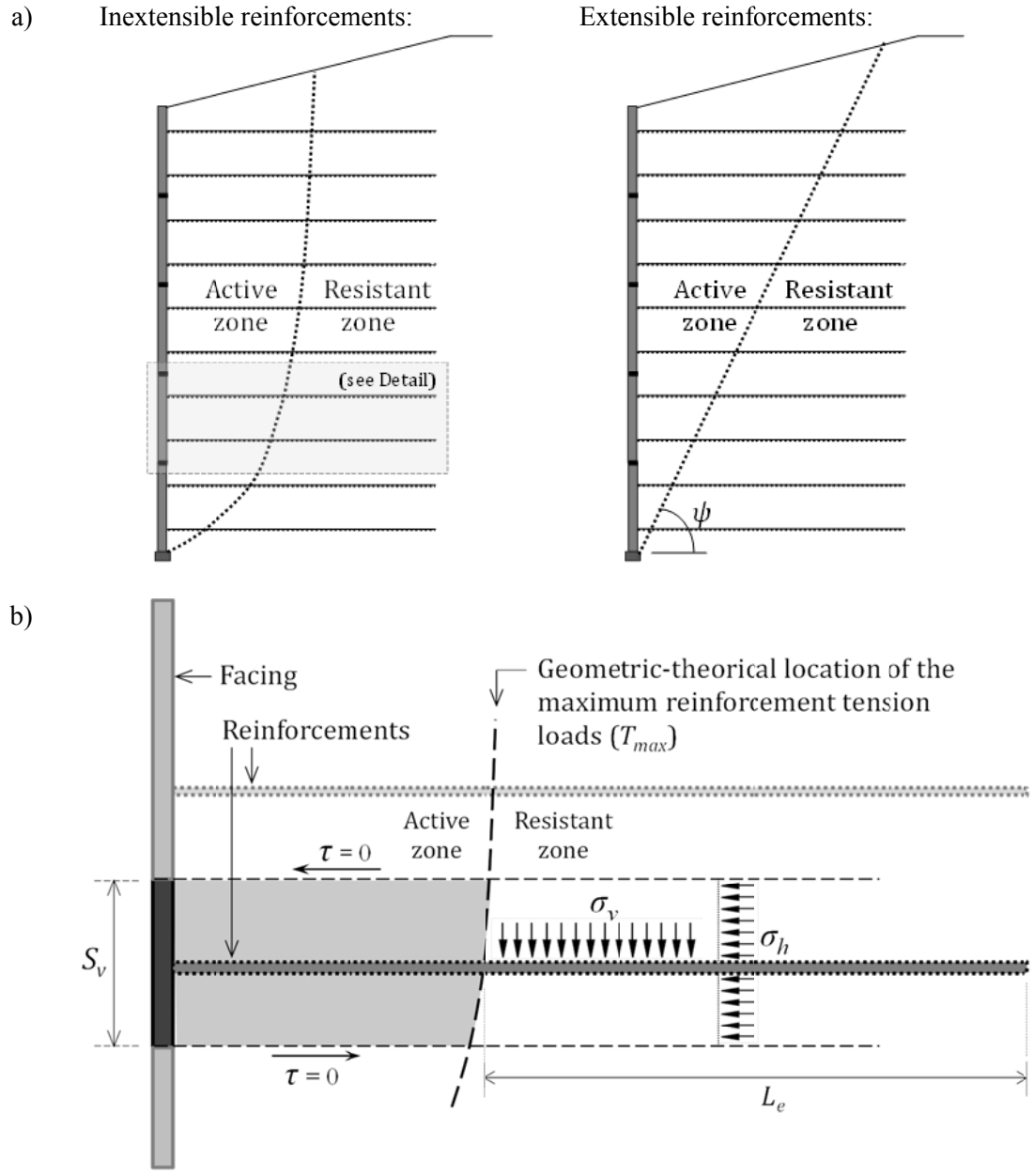

Figure i.2: Location of the maximum tensile loads (T_{max}) with regards to reinforcement extensibility (a) and loads acting in reinforcements: resistance length concept (b).

In general, inextensible reinforcements correspond to metallic strips, bar mats, steel ladders, or welded wire mats, where soil deformation is several times greater than reinforcement strains. Extensible reinforcements consist of geotextiles or geogrids, where the reinforcement

strains are accordingly with the soil strains, with somehow accompanied deformations. Not a clear extensibility statement can be directly said about polymeric strips reinforcement, as this kind of reinforcing element, unless having greater extensibility than steel elements under tensile loading behaviour, the strains are not adequately greater (accordingly to the soil deformation) and they could be identified as inextensible reinforcement type for many loading conditions.

As commented, since part of the backfill, even reinforced, is consequently originating from earth pressure (thrust) on the facing, consequent shear load distributions are generated along the reinforcements, with a localized maximum value between the facing and the tail-end of the reinforcements (expected to have no tension if no back-anchorage is provided). This maximum tensile load location may vary with respect to reinforcement extensibility (see Figure i.2), and divides the reinforced backfill zone into active state zone (from the facing up to the maximum tensile location zone) and resistance zone (from the maximum up to the tail-end of reinforcements). Conceptually, the flexible nature of the reinforced soil system allows the tolerance of strains originated during the construction process, in which the earth pressure increases due to the backfill soil confinement from a certain layer wall height (e.g., from active to at-rest states; although may be different according to the reinforcement type). Thus, if stiffer reinforcement elements are considered (e.g., steel strips or steel ladders), due to their intrinsic inextensible behaviour, the area of backfill in active state is significantly reduced than for the case of extensible reinforcement elements (e.g., polymeric grids).

i.d) Reinforced soil concept

There are many ways to improve the mechanical behaviour of a soil: soil densification, injections to ground, additions and thermic methods, etc. (soil stabilization). Whereas other techniques provide strength in a general manner (as cemented floor, with soil matrix modification) or just in one direction (as ground piles, with strength improvement just for vertical compression), soil reinforcement provides strength in all directions without affecting the soil matrix. From a conceptual standpoint, reinforcement elements inserted within the soil modifies the deformability of the matrix soil (lower deformability compared to a material without reinforcement) under both triaxial and oedometric compression. The simple inclusion of linear or planar elements, properly layered in the soil, provides added strength to the matrix material, as the material reaches a new state of "cohesion". As it can be observed from tested samples in triaxial tests these inclusions not only modify the net-total value of the strength but also the failure planes developed in ultimate limit condition state. If general behaviour of cohesionless soil is considered, how the soil density and/or confinement degree affects the soil can be explained in terms of the volumetric strains and strength under shear loading (Figure i.3). There is a significant increasing of volume due to shear at low confining pressure for high density sandy soils, which leads to a strength increase (ϕ_{peak}) with regard to the high confining pressure state or low density soil scenario (where the maximum strength corresponds to the soil behaviour at constant volume shear loading, ϕ_{cv}). This behaviour of increasing volume (and strength) it is understood as soil dilatancy, which is inherent to granular-cohesionless materials.

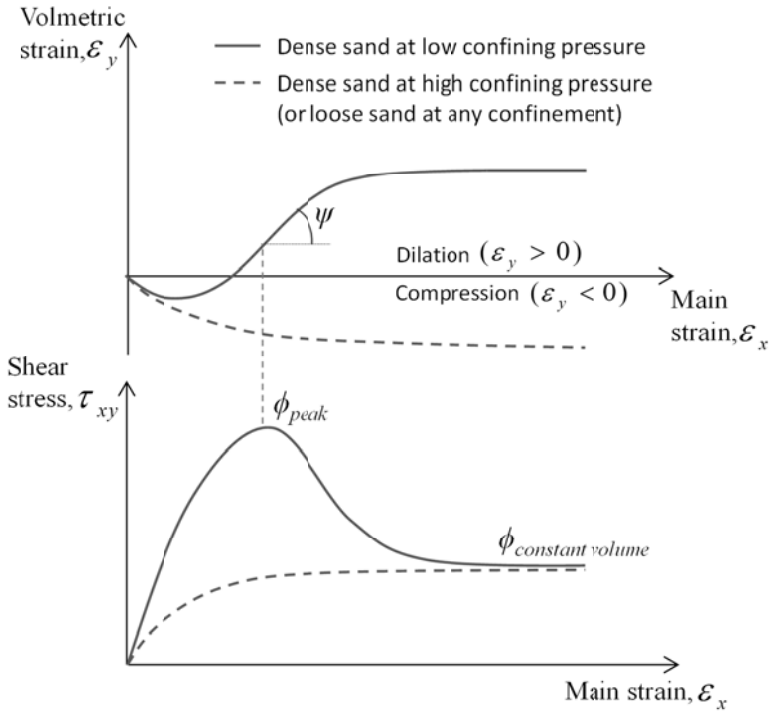

Figure i.3: Load-deformation curves for sandy soil.

In case of reinforcement presence, the mechanical behaviour of the resulting reinforced soil mass can be deduced from the mechanical behaviour of the soil matrix itself. Considering the mentioned dilatancy effect (Figure i.3), in case of reinforcement placed horizontally in a portion of soil (see Figure i.4), if vertical loading is then applied, lateral pressure is developed and consequent shear stresses are developed through the soil-reinforcement, different in case of non-reinforcement presence ($\sigma_{h,unreinforced} \neq \sigma_{h,reinforced}$). Due to the shear behaviour, the soil dilatancy is activated (volume increase generated around reinforcement) with a consequent increase in the internal vertical stress above and below the reinforcement elements (σ^*_v), and increasing of strength is finally derived (with an apparent cohesion; c^*). The effect can be then explained also as, in case of fixed and constant vertical loading scenario ($\sigma_{v,u} = \sigma_{v,r}$)., the horizontal stress generated is reduced within the reinforced soil with regard to the non-reinforced soil case ($\sigma_{h,u} > \sigma_{h,r}$; see details in Figure i.4) as the reinforcement elements are absorbing by shear part of the lateral stresses generated. Consequently, as it can be observed using Mohr's circle representation (Figure i.5), assuming granular cohesionless soil, an increase in soil friction angle is generated at low confining pressure states, whereas the same friction angle of the soil matrix is reached at high confining pressure states. According to this, as vertical pressures are generally assumed equal to the self-weight of soil in retaining structures design (i.e., σ_v = soil density × depth), the actual lateral coefficient of earth pressure in reinforced soil cases with low confining pressures and rough-surface reinforcements (K_r) is typically assumed to be higher than the typical active-state one in retaining wall systems ($K_r > K_a$, i.e., $K_r / K_a > 1$). The actual value of K_r is usually not linear

in these cases, with proper values related to reinforcement types obtained from empirical knowledge.

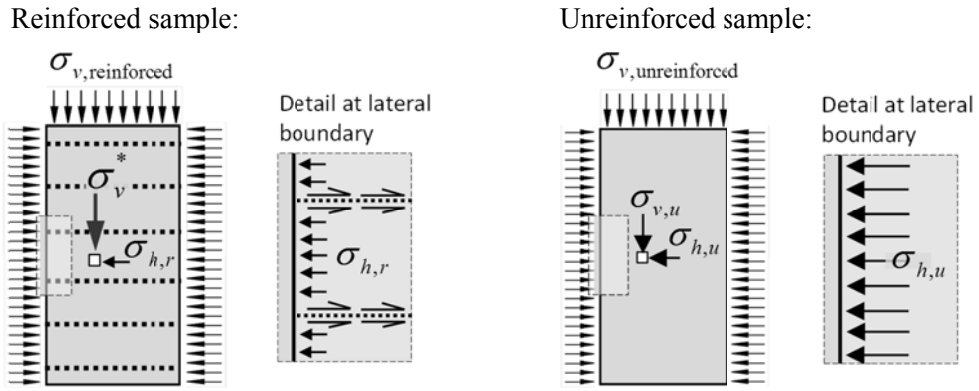

Figure i.4: Example of reinforced and unreinforced soil samples under surcharge.

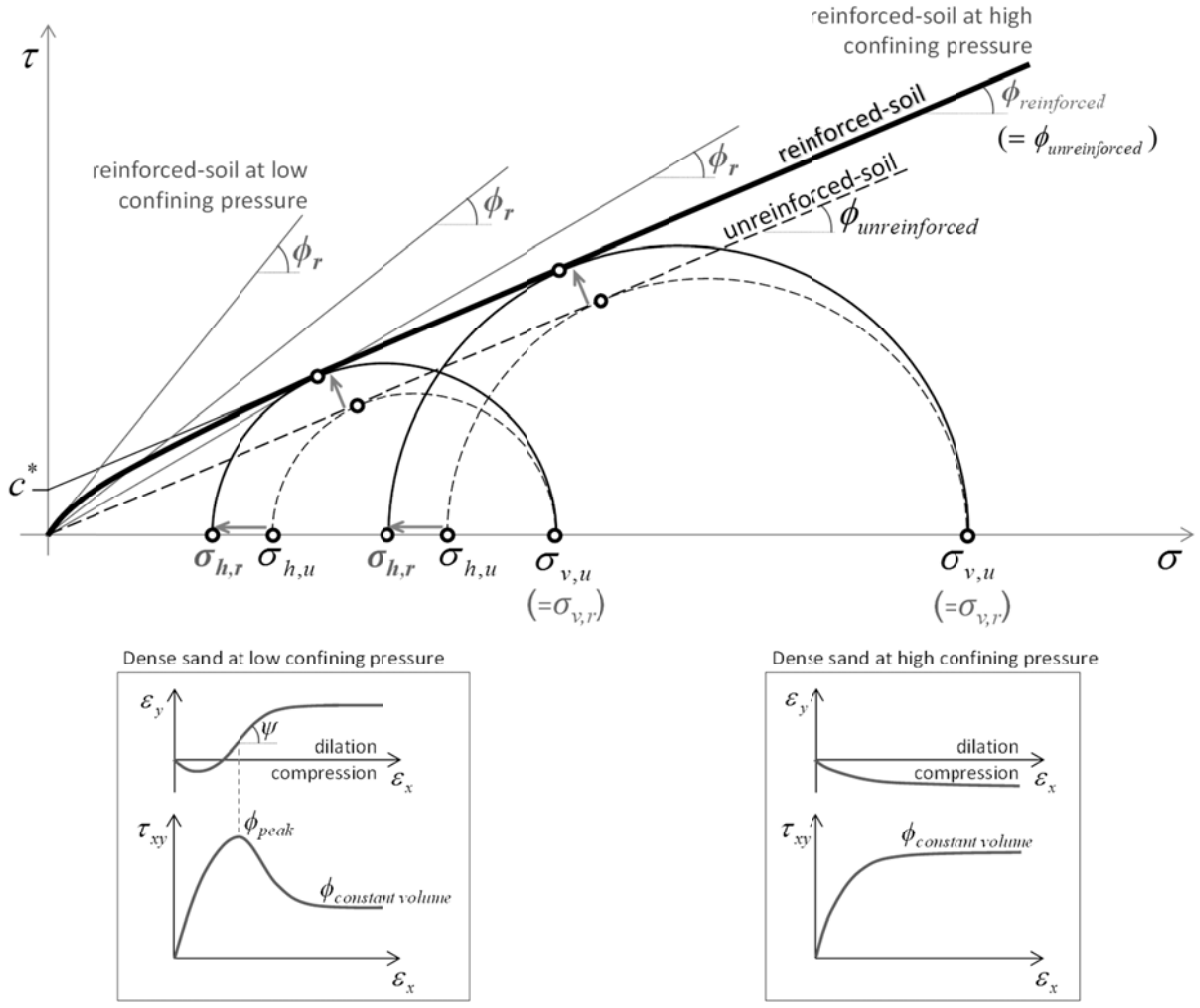

Figure i.5: Mohr-Coulomb failure criterion in case of soil reinforcement.

i.e) Working stress condition examples

Calculation methods (standards, technical specifications, analytical and semi-analytical, etc.) tend to respond to structural compliance under assumptions of ultimate stability, with the final consideration of the safety factors required. From the point of view of the working stress –operational- conditions, such structures can lead to some problems (far from ultimate stability requirements) both due to poor construction practice or excessive relative settlements between the facing and the backfill. Particularly relevant in this Thesis, it should be noted the failure of panels due to spalling as a result of bearing pad crushing and concrete-to-concrete contact (Neely 2005). However, bearing pads are required to resist from 2 to 3 times the self-weight of the panels (Berg et al., 2009), so this may lead to unpredicted facing loads. Spalling usually appears after wall construction, and is commonly located at panel corners in the bottom regions of the wall facing. As introduced, this behaviour deficiency is closely linked to the compressible behaviour of the bearing pads, placed on purpose, precisely between panels, to avoid direct contact between concrete, as well as the facing deformability (tilt and rotation). As commented, the key aspect of the behaviour of the panels is the relative movements between panels themselves, and between the backfill. This last one is the relative movement which controls the amount of mobilized shear loads developed at the inward side of the facing, and also the down-drag tensile load generated at reinforcement-to-panel connections due to backfill settlement. The friction can be analytically developed through tensional equilibrium (see development in Figure i.6, adapted from Neely 2005) of a soil portion in contact with the facing and limited to the area of lower compaction effort applied during construction (typically between 1 to 1.5 meters of the facing).

As obtained from this analytical development (Neely 2005), the stresses caused by friction between the backfill and the backfill of the facing are not negligible, and its evolution with depth that increases up to a constant value when the depth tends to infinity, fits other shear stress analytical developments reported in literature (e.g., Kerisel 1961, Brinch Hansen 1968). Results for specific cases and with numerical model developments have been found to be in reasonably agreement. However, the real problem may include more complexity than mobilized shear stresses between the backfill and the facing panels, and numerical models may be required to provide clearer idea about the bearing pad crushing phenomena.

As a result of the work done, a significant progress in understanding this stress-strain behaviour example was achieved. The work carried out suggests that the behaviour of the wall under operational conditions can be analyzed reasonably well based on the numerical methods (e.g., PLAXIS, FLAC, and CODE_ BRIGHT), while it is difficult to draw conclusions based on traditional analyzes based on ultimate limit states. In particular, it appears that, along with the internal differential deformation of the facing itself, the crushing of the bearing pads depends on the backfill and foundation stiffness combination, as well as the bearing pad stiffness (and intrinsic stress-strain law) which in many cases seems to exceed the limit compression strength.

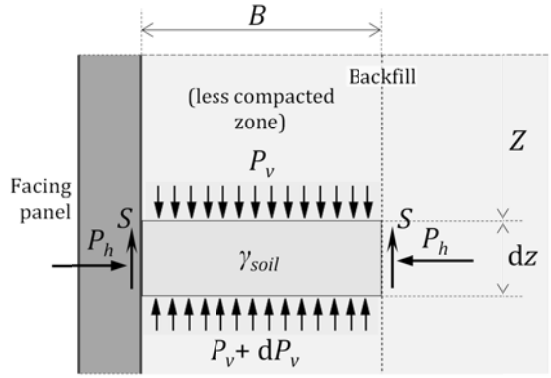

By equilibrium:

Weight = vertical loads $\rightarrow \gamma B dz = B(P_v + dP_v - P_v) + 2sdz$

$$\gamma B dz = BdP_v + 2sdz = BdP_v + 2\left(P_h \tan\delta\right)dz = BdP_v + 2\overbrace{\left(KP_v \tan\delta\right)}^{s}dz$$

$$BdP_v = \left(\gamma B - 2KP_v \tan\delta\right)dz \rightarrow \frac{BdP_v}{\gamma B - 2KP_v \tan\delta} = dz$$

Integrating the last expression:

$$\frac{-B}{2K\tan\delta}\ln\left(\gamma B - 2KP_v \tan\delta\right) = Z + C$$

$$\ln\left(\gamma B - 2KP_v \tan\delta\right) = \frac{-2K\tan\delta}{B}\left(Z + C\right)$$

Assuming $C^* = C\left(\frac{-2K\tan\delta}{B}\right)$, results:

$$\gamma B - 2KP_v \tan\delta = \exp\left(\frac{-2KZ\tan\delta}{B} + C^*\right) = \exp\left(\frac{-2KZ(\gamma)\tan\delta}{B(\gamma)} + C^*\right)$$

$$1 - \frac{P_v}{\left(\frac{\gamma B}{2K\tan\delta}\right)} = \left(\frac{1}{\gamma B}\right)\exp\left(\frac{-2KZ(\gamma)\tan\delta}{B(\gamma)}\right)\exp\left(C^*\right)$$

Defining $P_v(\text{máx}) = \frac{\gamma B}{2K\tan\delta}$, results:

$$1 - \frac{P_v}{P_v(\max)} = \left(\frac{1}{\gamma B}\right)\exp\left(\frac{-\gamma Z}{P_v(\max)}\right)\exp\left(C^*\right)$$

Imposing that for $Z = 0 \rightarrow P_v = 0$, the constant C^* reaches de value $C^* = \ln(\gamma B)$, and results the following expression:

$$P_v = P_v(\max)\left[1 - \exp\left(-\frac{\gamma Z}{P_v(\max)}\right)\right]$$

From initial equilibrium equation, replacing the reached values and including (dP_v) from the latest equation, the following shear stresses (s) equation is obtained:

$$s = s(\max)\left[1 - \exp\left(-\frac{\gamma Z}{P_v(\max)}\right)\right]$$

the following relation can be then deduced:

$$s = P_v\frac{s(\max)}{P_v(\max)}$$

Resulting the following maximum shear stress in depth:

$$s(\max) = \gamma B / 2$$

Figure i.6: Graphical representation of a portion of the backfill soil in contact with the facing (Neely 2005) and analytical development of force equilibrium to find the required frictional force.

The results of finite element analysis have shown a significant vertical force component generated due to the relative settlement between the facing panels and the backfill soil, accompanying also the final reinforcement tilt at connections and generating consequent down-drag loads (see Figures i.7 and i.8). This down-drag load was found to dramatically increase vertical facing load up to several times the self-weight of the facing panels. This effect has already been assessed and quantified in multiple instrumented reinforced soil walls of different structural heights, panel geometries and also reinforcement types (Bastick et al., 1993, Chida and Nakagaki 1979, Christopher et al., 1994, Runser et al., 2001) with different explanation of the phenomena with no mention about the multiple facing load or bearing pad compression behaviour. In traditional reinforced soil walls design this effect on increasing vertical load on the facing (relative to the weight of concrete panels) is usually not taken into account, however, may be important in some cases. Chapter 1 of the Thesis starts with this issue and goes deeper into explaining the consequential spalling phenomenon.

In addition to the mechanical performance of reinforced soil structures, other methodologies are currently available to better understand the functionality of geotechnical engineering structures based on a sustainability assessment. Sustainability is a new consideration for many stakeholders in retaining wall projects. This is possibly due to the (still currently) innovative concept of the term, traditionally linked to unrealistic and idyllic concept only related to the environment green movements. Speculative and without effective quantification, sustainability is commonly sadly related to a concept not linked to practical

aspects. However, the term 'sustainability' refers to the quality of sustainable, and something 'sustainable' (said of a process, for example) refers to “capable of being maintained”. From a more objective point of view, it can be deduced that sustainability is not only related to environmental considerations, but also economic and social/functional aspects. Thus 'sustainable development' may be defined as the “development that meets the needs of the present without compromising the ability of future generations to meet their own needs” (Brundtland et al., 1987).

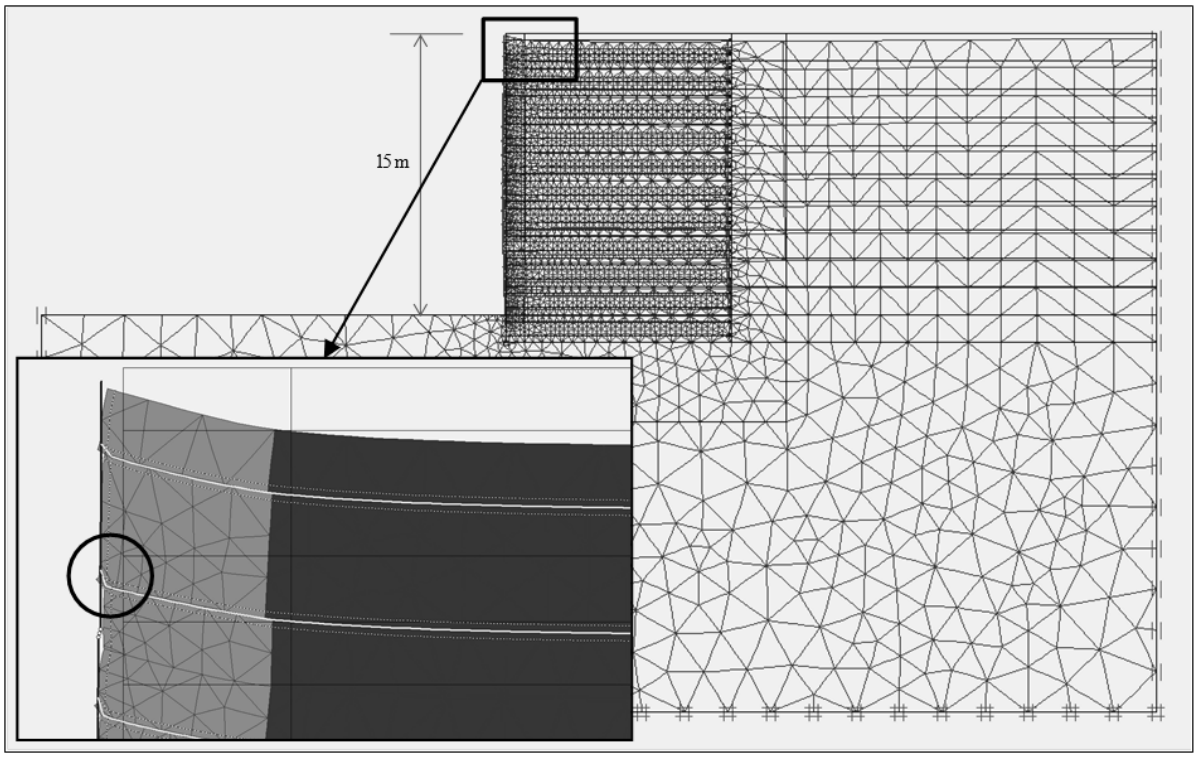

Figure i.7: Graphic representation of the vertical reinforcement down-drag contribution: Mesh deformation for a numerical model created with PLAXIS 2D program.

Quantification of sustainability in structures is something relatively new, but is expected to be increasingly established in specific and comprehensive international regulations, solving the current limitations that exist today and allowing the performance of value models of sustainability for the whole building, construction and civil engineering fields (materials optimization of structures, increasingly sustainable solutions, etc.). The MIVES (Value Integrated Model for Sustainable Evaluations) methodology uses a value analysis and decision-making support by assessing different alternatives with the purpose of assessing them under objective criteria and full quantification and weighting of indicators affecting the case studies. The sustainability analysis of a work process or any particular structure use to satisfy various criteria such as, for example, the use of the energy used both in the production and construction states, the use of renewable resources, the use of recycled products, the development of the work execution, and minimization of impacts on environment as a result

of the execution of the work. Through comparisons between alternatives satisfying the same functional unit, it can be determined whether an activity, structure or work is more, less or equally sustainable than another. These comparisons should be made globally. **Chapters 10** and **11** provide further explanation of the sustainability assessment concept and methodology by analyzing different earth retaining structure alternatives.

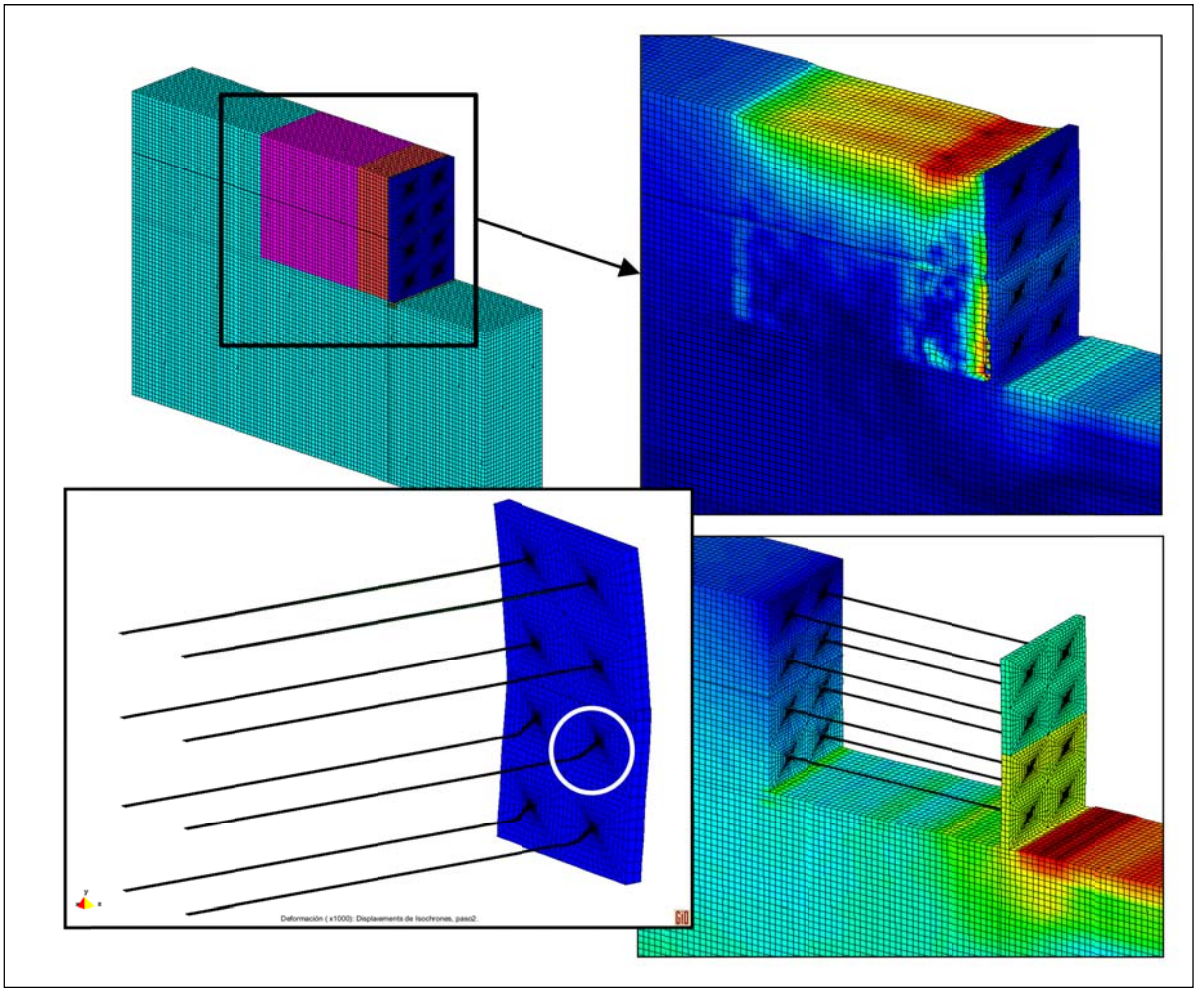

Figure i.8: Graphic representation of the vertical reinforcement down-drag contribution: the deformed mesh with backfill settlement detail, facing panels rotation and reinforcement tilt in a 3D numerical model created with CODE_BRIGHT program.

ii) SCOPE, JUSTIFICATION AND THESIS METHODOLOGY

The ultimate goal of this Ph.D. Thesis is the increased understanding of the stress-strain mechanical behaviour of retained earth structures constructed with the reinforced soil technique, and further comprehension of these structures from a sustainable perspective within an engineering framework. Specific objectives can be highlighted:

- Development, calibration and validation of numerical models (2D and 3D) to provide maximum reliability on numerical responses of reinforced soil structure behaviour.
- Obtaining detailed study about sustainability of reinforced soil structures by comparative life-cycle assessment and sustainability evaluation of these structures with comparison to similar solutions performing the same function.

The origin of the first Thesis developments arose with the realization of a technical report on bearing pads optimization, commissioned by VSL Construction Systems (VSL International Ltd. - Bouygues Construction's Specialist Civil Works division), which is a company specialized in this type of earth reinforced soil structures in civil engineering works in general. From the first analyzes done, it was decided to go deeper into the same subject, gaining more knowledge about the reinforced soil topic, and finding several sources on which it could further expand the investigation of reinforced soil structures. In particular and from a first approach, it was possible to give a direct contribution about analyzing the compressibility and geometry of the bearing pads (horizontal joints) in the behaviour of the structural assembly of these types of structure. The literature search resulted in a more precise approach towards the mechanical stress-strain behaviour of these structures. Because the more accurate calculations currently correspond to numerical calculation methodologies (finite element and finite difference methods), it seems reasonable to focus on a proper handling of these numerical methodologies and to improve current knowledge in the application of numerical methods of analysis.).

From the developments carried out and results achieved, it seems that the approach to the Thesis problem may be particularly and reasonable justified. Having in mind that multiple problems under working stress conditions are still appearing in these structures, and also by the fact that several university research teams worldwide are still developing studies and accurate analysis regarding these retaining earth methodologies, the presented Thesis may be considered to be fully justified. Furthermore, instrumentation of actual reinforced soil structures in addition to stability and endurance full-scale models are still being developed both by private sector companies and by public institutions through university agreements.

It is irresponsible for any construction engineering study which could result in a significant modification of the environment without any thorough and in depth sustainability analysis. That is why it was decided also to extend the initial scope of this Thesis to achieve a practical and useful application of certain existing tools of life-cycle assessment (LCA) to then perform proper sustainability assessment of retaining earth reinforced soil structures.

The Thesis has been developed following a publishing methodology of each relevant aspect achieved from the research carried out. This has allowed the author to improve the researching skills from the very beginning point, and to be updated with other at-same-time researching developments within the related topic, which allowed to further advance.

iii) THEORETICAL AND PRACTICAL FRAMEWORK OF THE THESIS

The Thesis development has included theoretical and numerical aspects related to soil mechanics, geotechnical engineering and foundation structures fields. The most applied theoretical aspects required for the research done mainly relate to the development and use of both analytical and numerical methods of calculation. Analytical calculation methods have been based on empirical results in the past. These are reflected in the multiple international design standards for retaining earth reinforced soil structures. In these Codes, results from research case studies and calculation works performed use to be continuously compared with data obtained from field instrumentation and consequently updated.

With regard to the practical aspects, during the Thesis development it has been possible to design, build and perform laboratory reinforcement pullout tests. It has been possible also to participate in actual soil reinforcement structures at both design and construction stages, and to assess several real reinforced wall structures both due to particular site conditions and due to in-site issues that emerged during construction.

iv) SCIENTIFIC PRODUCTION OBTAINED FROM THE STUDY

The journal papers published and conference papers and lectures presented over the course of (and related to) the Thesis study are listed below:

Journal papers:

A. Damians, I.P., Bathurst, R.J., Josa, A., Lloret, A. and Albuquerque, P.J.R., 2013. Vertical facing loads in steel reinforced soil walls. ASCE Journal of Geotechnical and Geoenvironmental Engineering 139(9), 1419-1432.

B. Damians, I.P. Bathurst, R.J., Josa, A. and Lloret, A., 2014. Numerical study of the influence of foundation compressibility and reinforcement stiffness on the behaviour of reinforced soil walls. International Journal of Geotechnical Engineering 8(3), 247-259.

C. Damians, I.P., Bathurst, R.J., Josa, A. and Lloret, A., 2015. Numerical analysis of an instrumented steel reinforced soil wall. ASCE International Journal of Geomechanics 15(1), 04014037.

D. Yu, Y., Damians, I.P., Bathurst, R.J., 2015. Influence of choice of FLAC and PLAXIS interface models on reinforced soil-structure interactions. Computers and Geotechnics 65, 164-174.

E. Damians, I.P., Bathurst, R.J., Josa, A. and Lloret, A., 2015. Vertical facing panel-joint gap analysis for steel-reinforced soil walls. ASCE International Journal of Geomechanics, 10.1061/(ASCE)GM.1943-5622.0000632, 04015103.

F. Damians, I.P., Bathurst, R.J Adroguer E., Josa, A., and Lloret, A., 2016. Environmental assessment of earth retaining wall structures. ICE Environmental Geotechnics. 10.1680/jenge.15.00040.

G. Damians, I.P., Bathurst, R.J Adroguer E., Josa, A., and Lloret, A., 2016. Sustainability assessment of earth retaining wall structures. ICE Environmental Geotechnics. (in-press)

Conference papers and lectures:

a. Damians, I.P., Josa, A., Albuquerque, P.J.R., Lloret, A., Ledesma, A., and de Santos, C., 2011. Análisis numérico de los esfuerzos verticales en el paramento de un muro de tierra reforzada en suelo diabásico (translation into English: Numerical analyses of vertical forces in the facing of a reinforced soil wall on diabasic soil). Joint CGS/Pan-Am Conference, Toronto, Canada, October 2011, 8p.

b. Bathurst, R.J., Damians, I.P, Josa, A., and Lloret, A., 2012. Influence of foundation compressibility on reinforcement loads in geosynthetic reinforced soil walls. Proceedings of the 5th European Geosynthetics Congress, Vol.5, pp.43-47, Valencia, Spain. September 2012.

c. Damians, I.P., Bathurst, R.J., Josa, A., and Lloret, A., 2013. Influence of facing vertical stiffness on reinforced soil wall design. Proceedings of the 18th International Conference on Soil Mechanics and Geotechnical Engineering, Paris, France. 2nd – 6th September 2013, Vol.3, pp.1959-1962.

d. Damians, I.P., Bathurst, R.J., Josa, A., and Lloret, A., 2013. Comparison of finite element and finite difference modelling results with measured performance of a reinforced soil wall. Proceedings of GéoMontréal 2013. 66th Canadian Geotechnical Conference and 11th Joint CGS/IAH-CNC Groundwater Conference. Montréal, Quebec, Canada, 29th September – 3rd October 2013, 7p.

e. Yu, Y., Damians, I.P., Bathurst, R.J., Lloret, A., and Josa, A., 2014. Equivalent interface properties for FLAC and PLAXIS models to simulate soil-strucutre interactions in MSE walls. Proceedings of the GeoRegina 2014. 67th Canadian Geotechnical Conference, Regina, Saskatchewan, Canada. 28th September – 1st October, 2014, 8p.

f. Damians, I.P., Bathurst, R.J., Lima J., Lloret, A., and Josa, A., 2015. Numerical study of the use of actively-tensioned polymeric strips for reinforced soil walls. Proceedings of the XVI European Conference on Soil Mechanics and Geotechnical Engineering (ECSMGE), Edinburgh, Scotland. 13th – 17th September 2015. Vol.7, pp.3833-3838.

g. Adroguer, E., Damians, I.P., Josa, A., Lloret, A., and Bathurst, R.J., 2015. Sustainability assessment of earth retaining wall structures: preliminary model and simplified application. XVI European Conference on Soil Mechanics and Geotechnical Engineering (ECSMGE 2015), Edinburgh, Scotland. 13th – 17th September 2015. Vol.5, pp.2463-2468.

h. Damians, I.P., Yu, Y., Lloret, A., Bathurst, R.J., and Josa, A., 2015. Equivalent interface properties to model soil-facing interactions with zero-thickness and continnum element methodologies. XV Pan-American Conference on Soil Mechanics and Geotechnical Engineering (XV PCSMGE). Buenos Aires, Argentina 15th – 18th November 2015, 8p.

Other complementary reports have also been generated over the time of this Thesis but are not linked to the Thesis scope (so are not listed nor referenced in this document). However, in addition to the official and accessible papers previously reported, other documents have been developed during the Thesis that are related to its subject of study. This work is mainly comprised of internal reports and handbook documentation (not open access) derived from the author's (at date) work position as Geotechnical Engineer with VSL International Ltd (part of Bouygues Construction's Specialist Civil Works Division).

v) STRUCTURE OF THE THESIS

The Thesis is largely structured with chapters that generally correspond to particular published papers, and roughly follow the sequence of publication dates which in turn follow logical lines of investigation. Table v.1 presents the Thesis organization and structure. Whereas some chapters reproduce the reviewed and published content of the related papers, some others have been substantially extended from the original versions and report the results of additional complementary calculation case studies. The published paper versions were in some cases reduced from original source versions due to publication space limitations.

Table v.1. Thesis organization and structure:

Part	Software used	Related chapter	Related paper(s)
A. 2D - Numerical analysis	PLAXIS	1. Vertical facing loads	A, D, a
		2. Numerical model calibration	C
		3. Panel joint gap	E
		4. Facing stiffness and strip tensioning	c, f
	PLAXIS & FLAC	5. RMC wall comparison	d
	FLAC	6. Foundation compressibility	B, b
B. 3D - Numerical analysis	CODE_BRIGHT	7. Soil-Facing interaction	D, e, h
		8. Soil-Reinforcement interaction. Pullout tests	-
		9. Full-height MSE wall	-
C. Sustainability assessment	SIMAPRO & MIVES	10. LCA	F
		11. Sustainability	G, g
Conclusions			

vi) THESIS SUMMARY BY CHAPTERS

PART A: **2D – Numerical analysis of mechanically stabilized reinforced soil walls**

The first chapter (**Chapter 1**) investigates the influence of backfill soil, foundation soil and horizontal joint vertical compressibility on the magnitude of vertical loads developed in steel reinforced soil concrete panel retaining walls at the end of construction. Measurements of toe loads recorded from instrumented field walls were reviewed and demonstrate that vertical toe loads can be much larger than the self-weight of the facing. In extreme cases, these loads can result in panel to panel contact leading to concrete spalling at the front of the wall. Vertical loads in excess of panel self-weight have been ascribed to relative movement between the backfill soil and the panels that can develop panel-soil interface shear and down-drag loads at the connections between the panels and the steel reinforcement elements. A 2D finite element PLAXIS model was developed to systematically investigate the influence of backfill soil, foundation soil and bearing pad stiffness, and panel-soil interaction on vertical loads in the panel facing. The results showed that an appropriately selected number and type of compressible bearing pads can be effective in reducing vertical compression loads in these structures and at the same time ensure an acceptable vertical gap between concrete panels. The parametric analyses were restricted to a single wall height (16.7 m) and embedment depth of 1.5 m matching a well-documented field case. However, the observations reported are applicable to other similar structures.

Chapter 2 describes the results and lessons learned using a PLAXIS finite element method (FEM) model to simulate quantitative performance features of the Minnow Creek steel strip reinforced soil wall structure located in the USA. The Minnow Creek Wall structure was constructed and instrumented in 1999. It was a unique case study (at Thesis time) because of the comprehensive measurements that were taken to record a wide range of wall performance features. Two different constitutive models for the soil were used (linear-elastic Mohr-Coulomb and Hardening Soil model with Mohr-Coulomb failure criterion) and numerical outcomes compared with physical measurements. The numerical results were shown to be sensitive to boundary conditions assumed at the toe of the wall. The generally encouraging agreement between physical and numerically predicted results gives confidence that commercial FEM software packages can be useful for the analysis and design of these types of structures provided that care is taken in the selection of input parameters.

Chapter 3 reports the results of a numerical parametric PLAXIS model study focused on the prediction of vertical load distribution and vertical gap compression between precast concrete facing panel units in steel reinforced soil walls ranging in height from 6 m to 24 m. The vertical compression is generally accommodated by polymeric bearing pads placed at the horizontal joints between panels during construction. The study demonstrates how gap compression and magnitude of vertical load transmitted between horizontal joints are influenced by joint location along the height of the wall, joint compressibility, and backfill and foundation soil stiffness. The summary plots in this study can be used to estimate the

number and type (stiffness) of the bearing pads to ensure a target minimum gap thickness at the end of construction, demonstrate the relative influence of wall height and different material component properties on vertical load levels and gap compression, or used as a benchmark to test numerical models used for project-specific design. The study also demonstrates that while the load factor (ratio of vertical load at a horizontal joint to weight of panels above the joint) and joint compression are relatively insensitive to foundation stiffness, the total settlement resulting at the top of the wall facing was very sensitive to foundation stiffness. The study examines the quantitative consequences of using a simple linear compressive stress-strain model for the bearing pads versus a multi-linear model which is better able to capture the response of bearing pads taken to greater compression. The study demonstrates that qualitative trends in vertical load factor are preserved when a more advanced stress-dependent stiffness soil hardening model is used for the backfill soil compared to the simpler linear-elastic Mohr-Coulomb model. While there are differences in vertical loads and gap compression using both soil models for the backfill, the differences are small and not of practical concern. The general numerical approach can be used by engineers to optimize the design of the bearing pads for similar steel reinforced soil wall structures using available commercial finite element model packages together with simple constitutive models.

Current design practices for reinforced soil walls typically ignore the influence of facing type and foundation compressibility on the magnitude and distribution of reinforcement loads in steel reinforced soil walls under operational conditions. In **Chapter 4**, the effect of the facing vertical stiffness (due to elastomeric bearing pads placed in the horizontal joints between panels) on load capacity of steel reinforced soil walls is examined in a systematic manner using a numerical modelling approach. Numerical modelling was carried out using the commercial finite element program PLAXIS. The numerical model was verified against measurements recorded for an instrumented 6 m-high wall reinforced with steel strips. The influence of the facing stiffness and backfill-foundation stiffness combinations on the vertical load through the facing and on the magnitude and distribution of the reinforcement loads was examined. For walls subjected to operational (working stress) conditions at end of construction, the numerical results confirm that the vertical stiffness of the facing and soil-stiffness combinations can have a great effect on the vertical facing loads and on the magnitude and distribution of the load mobilized in the soil reinforcement layers. Also the effect of the strip tension in polymeric strip reinforcement was also analysed in **Chapter 4.** Polymeric strip reinforced soil walls require a practical method to fix the reinforcement tail-ends in the soil backfill during construction to ensure adequate anchorage and to avoid any slack along the linear reinforcement elements. A number of different techniques are currently used depending on the reinforcement type, arrangement and the contractor. This chapter reports the results of a series of numerical simulations that were carried out on an idealized 6 m-high wall with precast partial height facing panels. A different reinforcement pre-tension load was applied to the layers in each simulation case. The results of numerical simulations include the reinforcement axial load distribution, vertical facing load and end-of-construction facing alignment plotted as a function of the reinforcement layer depth location and applied pre-tension load. The results demonstrate that the magnitude of pre-tensioning has a

significant effect on wall performance for walls subjected to operational (working stress) conditions at end of construction.

The performance of a metallic reinforced soil segmental retaining wall is examined in a systematic manner using two numerical modelling approaches. Finite element modelling was carried out using the commercial program PLAXIS and finite difference modelling using the commercial program FLAC. Numerical model results using both approaches were compared against measurements recorded for a well-instrumented full-scale 3.6-m high wall constructed with a sand backfill, modular-block facing, and steel reinforcement (welded wire mesh). **Chapter 5** presents measured and predicted toe loads, facing displacements, and reinforcement connection loads at end of construction and during subsequent staged surcharge loading approaching failure. Both numerical models have been verified against recorded measurements. The sensitivity of the assigned backfill soil friction angle on the magnitude and distribution of reinforcement connection loads is also examined. The chapter concludes with a summary of lessons learned to achieve satisfactory agreement between predicted performance and wall measurements using both modelling approaches.

Most geosynthetic and metallic reinforced soil walls are designed assuming that the wall foundation is rigid and/or does not influence the magnitude and distribution of reinforcement loads under operational conditions. This assumption may not apply to walls constructed over compliant (compressible) foundations. **Chapter 6** describes the results of a series of numerical FLAC model simulations that were carried out on idealized 3.6, 6 and 9 m-high modular block walls seated on foundations having four different compressibility values (foundation both under the facing toe and under the backfill soil mass). The walls were constructed with two reinforcement materials having very different stiffness values but the same tensile strength. So, for each foundation condition, the influence of reinforcement material stiffness was also investigated. The results of simulations show that as foundation stiffness decreases, reinforcement loads increase. However, for the two reinforcement materials in this study, the influence of axial stiffness of the reinforcement had a greater effect on wall performance than the foundation stiffness for walls subjected to operational (working stress) conditions at end of construction. Additionally, differential soil-facing settlement due to foundation compressibility discontinuity under the structure was also analyzed considering a particular scenario of toe fixity for a 6 m wall height case (e.g., vertical facing displacement restrained due to special foundation case). Finally, elastic plastic Mohr-Coulomb and Lade single-hardening constitutive models for sand were both considered in the numerical 6 m wall height case to detect any prediction differences that result from choice of soil model.

PART B: **3D – Numerical analysis of mechanically stabilized reinforced soil walls**

This part addresses two issues, the modelling of soil-structure mechanical interaction assuming a certain thickness of material defined using continuum elements (in a non-default numerical model software modes), and the implementation of this methodology in 3D

numerical models (performing soil-facing interaction, soil-reinforcement interaction pullout tests, and full-height reinforced soil walls).

The numerical modelling of earth retaining structures requires the use of interface boundaries between the dissimilar materials to simulate the discontinuity and transfer of normal and shear stresses from the soil to the facing component. Numerical software programs generally have interface models to simulate soil-structure interactions using zero-thickness interface elements. These programs give similar numerical outcomes of normal and shear stresses at the interfaces between the soil and structures. However, in some software packages neither zero-thickness interface models nor other similar special interface models are available. Thus the use of continuum elements at the interfaces between the soil and structural components is the only option to numerically examine soil-structure interactions. Up to this Thesis stage (and commonly in most of the numerical analysis of reinforced soil walls), the numerical models have been developed under 2D conditions. By now, the 2D methodologies have been demonstrated to reach good results with regard to real/instrumented data. The simplification from actual 3D to 2D plane strain is possible by the transformation of the structural components width dimensions and the actual amount per width of any discrete component (basically, bearing pads and linear reinforcements, if required) to equivalent 1 m-width components (which become an equivalent sheet in case of reinforcement inclusions). As the main (or weak) stress-strain directions of these kinds of structure is localized due to the slice symmetry assumed along the running direction of the wall, the transformation to a plane-strain continuum-slice is assumed to be, in general, representative. As reported in previous chapters, this methodology is a satisfactory alternative approach and avoids more complex 3D modelling representation. However, in some cases the 2D approach lead to loss of important information (e.g., earth pressure or soil-soil settlement between reinforcement elements). In these cases 3D numerical models may be necessary.

Soil-facing mechanical interactions play an important role in the behaviour of earth retaining walls. Generally, numerical analysis of earth retaining structures requires the use of interface elements between dissimilar component materials to model soil-structure interactions and to capture the transfer of normal and shear stresses through these discontinuities. In finite element method software programs, soil-structure interactions can be modelled using special interface tools as “zero-thickness” interface elements between the soil and structural components. These elements use a strength/stiffness reduction factor that is applied to the soil adjacent to the interface. In this study, because the software program used (CODE_BRIGHT) has no specific tool to model interfaces, continuum elements were used to model soil-structure and soil-reinforcement interactions. The continuum element approach could allow for more control of the interface features (i.e., material strength and stiffness properties) as well as the element sizes and shapes at the interfaces. A methodology and proposed parameter values for continuum elements defining soil-facing interactions are presented in **Chapter 7**. These provide similar numerical outcomes as those using zero-thickness elements in already calibrated 2D models.

In **Chapter 8**, results from series of pullout tests performed to determined strength properties of polymeric strips and steel ladders are presented. These tests are required to determine the soil-reinforcement interaction under different confinement conditions and are particularly useful to quantify interface stiffness and strength. These parameters allow reinforcement design optimization to be carried out and/or to determine an adequate number of reinforcement elements to ensure safety in project-specific reinforced soil earth retaining walls. A methodology to carry out steel ladder and polymeric strips pullout testing is described in this Chapter. Obtained results were compared to results using international Codes default values. With the same continuum elements interface described in previous **Chapter 7**, a 3D model was also generated to model soil-reinforcement interactions under pullout conditions. Model calibration was carried out for two reported pullout tests corresponding to steel and polymeric reinforcement types. Next, a series of sensitivity analyses were performed to achieve further understanding of the problem.

Numerical 2D models to perform mechanically stabilized earth (MSE) retaining wall full-height structures have been extensively used in the literature and presented in previous **Chapters 1** through **6**. As demonstrated, proper calibration has been possible even for non-planar reinforcement cases (i.e., strips or bars; see **Chapters 2** and **4**). The main 2D model limitations appear when linear-dimensional reinforcement is performed (as strips, bars, ladders, etc.). The problem is typically solved by transforming the real 3D case to a 2D model with equivalent "sheet" properties. However, in cases where linear reinforcement (i.e., strips, bars, ladders, etc.) are used, it could be interesting and maybe necessary to have a more complete understanding of the system behaviour. Under this scenario, it may be necessary to identify differences in results which can appear between locations in the running wall direction. These variations have been already identified in previous **Chapter 8** in the context of the pullout test performance. In those cases, variability in computed vertical pressures through the width direction of the pullout box (i.e., on the horizontal and opposite to the reinforcement displacement direction) was observed due to actual soil-soil vertical transfer of the shear stresses. Nevertheless, some preliminary three-dimensional numerical models with limited scope can be found in the geotechnical engineering literature. Due to the multiple components and mechanical complexity of the reinforced soil wall problem, accurate numerical modelling is a challenge. However, after the previous methodology, results achieved, and lessons learned regarding the modelling of the soil-facing (**Chapter 7**) and soil-reinforcement (**Chapter 8**) interaction problems, interface modelling was improved and implemented in a 3D finite element model with CODE_BRIGHT software program to analyze an equivalent 6 m-high mechanically stabilized earth strip-reinforcement retaining wall structure (**Chapter 9**). The purpose of this model is to achieve more accurate results that are not achievable with two-dimensional models.

PART C: **Sustainability assessment of mechanically stabilized reinforced soil walls**

Life cycle assessment (LCA) is recognized as a powerful technique to determine the environmental impact component of sustainability assessments of structures in civil engineering projects at the time of design. **Chapter 10** explains the principal parts and stages

in a LCA methodology and demonstrates the approach using the examples of two conventional retaining wall types (gravity and cantilever type) and two MSE wall solutions using steel and polymeric soil reinforcement. The analyses include structures built to four different heights. The LCA methodology was able to quantitatively distinguish between the component environmental impacts of different wall solutions and thus provide a practical numerical score-based tool for designers to choose between candidate solutions. The MSE wall solutions resulted in lower environmental impacts than gravity and cantilever wall solutions as measured by global warming potential, cumulative energy demand, six major midpoint environmental indicator categories, three endpoint damage categories and in terms of overall endpoint scores. The target audiences for this study are geotechnical and structural engineers engaged in the design of earth retaining wall structures but are less familiar with recent developments in LCA and how LCA can be linked to the design of these systems.

Retaining earth (ER) structures have been used for centuries. Even though new technologies and innovations in materials are emerging, early solutions are still being projected and in use. Given this context, a proper sustainability assessment should be applied when selecting alternative ER structures. **Chapter 11** offers a benchmark on which to improve the sustainability assess of ER structures, with criteria based on technical, environmental, economic and social factors. Although a wide range of materials and constructive solutions are available for ER systems, this study focuses on specific most common wall types: gravity, cantilever and mechanically stabilized earth (MSE) walls (both geosynthetic and metallic reinforcement considered). The methodology used is explained and a sustainability model is applied to 3, 5, 10 and 15 m-high ER structures. Sensitivity analyses were performed to detect the most relevant factors affecting the impact on environmental and economic pillars of sustainability assessment. From the obtained results, the mechanically stabilized earth wall (MSEW) alternatives with polymeric reinforcement were more competitive from a sustainability point of view.

vii) KEYWORDS OF THE THESIS

PARTS A and B: Reinforced soil walls; Steel reinforcement; Reinforcement stiffness; Vertical loads; Facing panels; Bearing pads; Precast concrete facing panels; Foundation compressibility; 2D modelling, Finite element modeling; PLAXIS; Finite difference modeling; FLAC; Soil-structure interaction; interfaces; Zero-thickness elements; Continuum elements; 3D modelling; CODE_BRIGHT.

PART C: Environmental assessment; Life cycle assessment (LCA); LCA inventory; Sustainable development; Earth retaining walls; Gravity walls; Cantilever walls; Mechanically stabilized earth (MSE) walls; Steel soil reinforcement; Polymeric reinforcement; Geosynthetics.

CHAPTER 1

VERTICAL FACING LOADS IN STEEL REINFORCED SOIL WALLS [1]

1.1. INTRODUCTION

1.1.1. General approach

Mechanically stabilized earth (MSE) walls constructed with steel strip or steel grid (bar mat and steel ladder) soil reinforcement elements are now a mature technology with a long history of successful performance both in the USA and worldwide. An example of a recent 46-m high tiered steel strip reinforced soil wall has been described by Stuedlein et al. (2010, 2012). Design methodologies for internal and external stability of these systems can be found in government design guidance documents (e.g., AASHTO 2010, Berg et al., 2009, BSI 2010). The majority of these structures are constructed with steel reinforced concrete panels that are placed in a staggered pattern. The panels are placed incrementally in concert with placement and compaction of backfill soil layers and the reinforcement elements (Figure 1.1). The reinforcement elements are affixed to the back of the panels at regular vertical and horizontal spacing using a pair of steel connection tabs and a bolt or similar arrangement. A key structural feature of these panel systems is the placement of compressible bearing pads at the horizontal joint between panels (Figure 1.2). These pads provide a flexible joint opening that can accommodate differential settlement while at the same time allowing vertical in-plane loading to be carried through the height of the wall face to the footing at the base of the wall. If the bearing pads are too compressible and/or there are not enough pads at a horizontal joint location, then concrete-to-concrete contact can occur between panel units leading to concrete spalling (Neely 2005, Neely and Tan 2010). Examples of panel spalling are illustrated in the photographs of Figure 1.3. The primary mechanism leading to compression of the bearing pads is down-drag force mobilized at the back of the panel units. This down-drag force occurs when the backfill soil settles more than the vertical wall facing due to compaction of the backfill soil, compression of the backfill soil under self-weight, outward movement of the wall face and possible settlement of the foundation soil below the structure. The down-drag

[1] Chapter based on Damians, I.P., Bathurst, R.J., Josa, A., Lloret, A. and Albuquerque, P.J.R.; 2013. Vertical facing loads in steel reinforced soil walls. ASCE Journal of Geotechnical and Geoenvironmental Engineering 139(9), 1419-1432.

forces are transmitted through soil-panel interface shear, and hanging-up of the backfill soil on the connections between the panel units and the reinforcement elements (Christopher et al., 1994). A schematic illustrating how panel-soil interface shear and down-drag forces contribute to wall panel vertical load is shown in Figure 1.4. Unfortunately, it is difficult to predict the magnitude of these down-drag forces within a conventional limit equilibrium-based design framework because these loads are due to relative movement between the wall face and backfill soil and complex interactions at the reinforcement-panel connections as noted above.

a) Steel strips: b) Bar mats:

Figure 1.1: Metallic reinforced soil wall systems: a) steel strip reinforcement (Choufani et al., 2011), b) bar mat reinforcement (Berg et al., 2009) (Connection details from Berg et al., 2009).

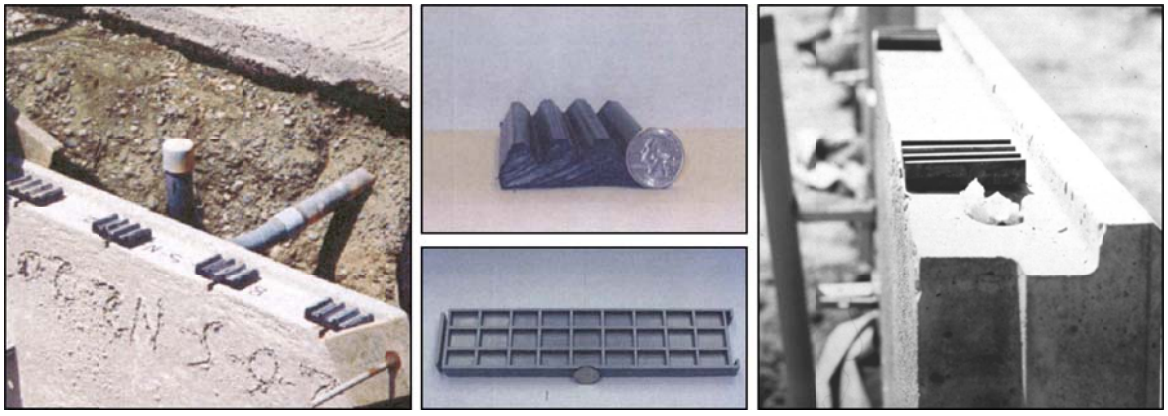

Figure 1.2: Example bearing pads (Neely 2005, Berg et al., 2009).

a) b)

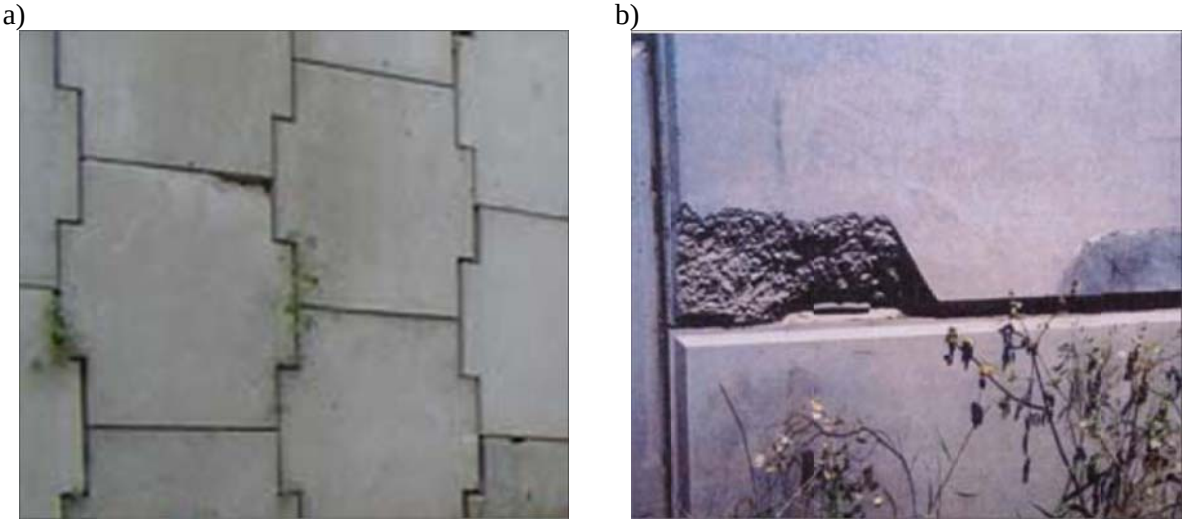

Figure 1.3: Spalling of concrete panel facing units: a) Thome and Janke (2005), b) Neely (2005). Note: panel widths are 1.5 and 2.25 m in a) and b), respectively.

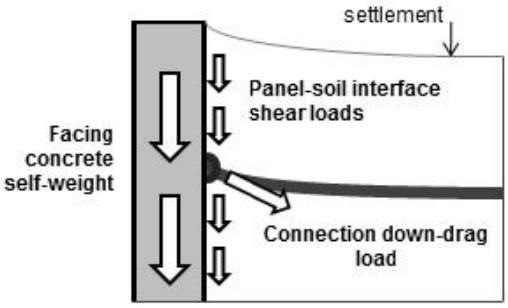

Figure 1.4: Contributions to vertical axial loads in concrete facing panels.

In this chapter it is first demonstrated that significant down-drag forces are possible in these structures based on field measurements reported in the literature. The properties of typical bearing pads are reviewed and then a 2D finite element model is developed to investigate the combined influence of vertical joint compressibility, backfill soil stiffness, foundation soil compressibility and panel-soil interface shear on vertical load through the wall face. This study demonstrates how numerical parametric analysis can be used by design engineers to optimize the number and selection of the bearing pads to be located at the horizontal joint between concrete panels to satisfy a target compression of the bearing pads and avoid panel to panel contact.

1.1.2. Vertical wall loads from monitored structures

The internal stability design of steel reinforced soil walls is currently based on a semi-empirical approach which has been calibrated against reinforcement loads recorded in monitored structures. Useful summaries of these monitored structures including geometry, steel reinforcement and soil properties have been reported by Allen et al. (2001, 2004), Bathurst et al. (2008a, 2009, 2011), Huang et al. (2012) and Miyata and Bathurst (2012a). These earlier papers also demonstrate that current design methods are reasonably accurate at predicting reinforcement loads under operational (working stress) conditions. However, only a few structures in these databases have included measured vertical load transmitted to the wall footing from the wall facing. Some details of these walls are summarized in Table 1.1. Calculated vertical loads recorded at the base of the wall facings using load cell measurements are shown in Figure 1.5a. Also shown in the figure are the vertical toe loads based on self-weight of the facing panels. There are small differences in the slope of the self-weight plots as a result of differences in panel thickness. In all the case studies, the recorded vertical toe loads are greater than the self-weight of the facing units. It is convenient to introduce a vertical load factor defined as the ratio of total vertical load to column self-weight. For the three steel strip wall case studies, the load factor at end of construction is in the range of 1.8 to 2.8 (Figure 1.5b and Table 1.1.1). For the steel bar mat wall, the load factor at end of construction is 4.7. Christopher et al. (1994) mentioned that this large value is likely due to down-drag loads at the connections. Berg et al. (2009) recommends that the type and number of bearing pads be selected assuming a vertical load factor of 2 to 3 at the location of the horizontal joint.

It should be noted that the case studies identified in Table 1.1 are restricted to steel reinforced soil walls. However, there are similar data for an instrumented full-scale 6-m high geosynthetic-reinforced soil wall with incremental concrete panels constructed in the laboratory (Tariji et al., 1996). The computed vertical load factor for this wall was 2.2.

Table 1.1. Case studies with measured vertical footing loads:

Case study number	Reinforcement type	Wall height (m)	Soil unit weight (kN/m^3)	Soil friction angle (degrees)	Vertical load factor [(a)]	Reference
1	Steel strip	6.0	17.7	38	2.1	Chida & Nakagaki (1979)
2	Steel strip	10.5	16.8	36 – 37	2.5	Bastick et al. (1993)
3	Steel strip	16.9	20.8	38	1.8 to 2.8	Runser (1999), Runser et al. (2001)
4	Bar mat	6.1	20.4	35	4.7	Christopher et al. (1994)

Note: [(a)] Ratio of total vertical load at base of facing panels units to self-weight of the panels.

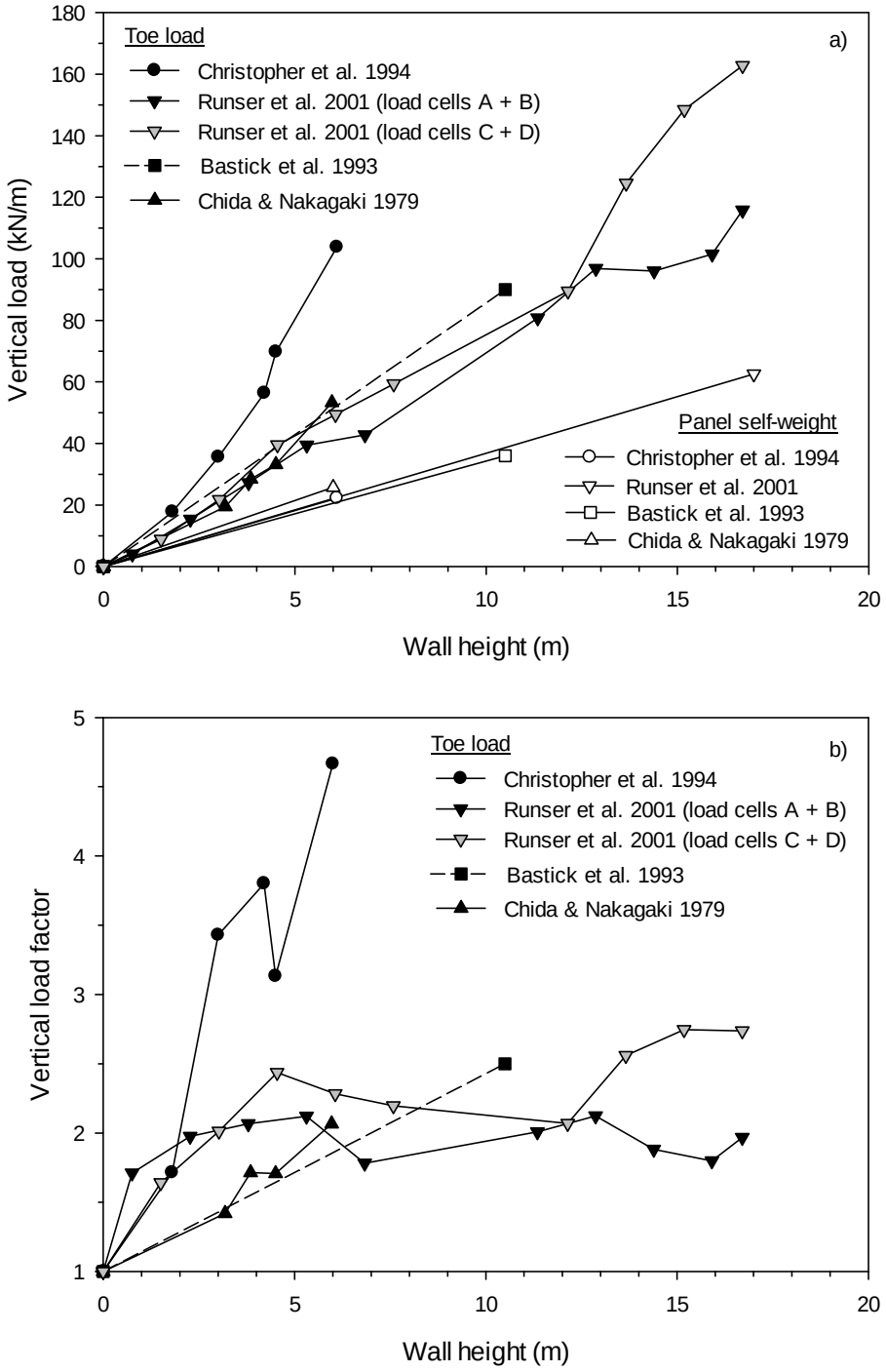

Figure 1.5: Vertical toe load response from instrumented field walls: a) measured vertical toe load versus wall height; b) vertical load factor versus wall height where load factor is the ratio of measured vertical toe load to wall panel self-weight.

1.1.3. Bearing pads

Steel reinforced soil walls constructed with incremental concrete panels include provision for vertical deformation, differential settlement and rotation by incorporating polymeric bearing pads placed at the horizontal joints between the concrete panels. These pads are needed to reduce down-drag forces, prevent concrete to concrete panel contact, and to ensure a minimum gap between panels (Berg et al., 2009). The most common materials are ethylene propylene diene monomer (EPDM), high density polyethylene (HDPE), and neoprene (Neely and Tan 2010). For example, the instrumented wall reported by Runser et al. (2001) used two neoprene pads per joint. However, material properties and dimensions of the pads used in their study are not reported. The mechanical stiffness of the pads used with concrete facing panels is influenced by the contact area due to cavities or grooves (voids) formed in the pads (e.g., waffle-type bearing pads). These treatments can result in 20% to 30% reduction in contact area. The nominal thickness of the pads is typically 20 mm. However, 25-mm thick pads have also been used for high walls and (or) for walls where large down-drag forces due to high backfill surface loads can be expected (Choufani et al., 2011). The enclosed plan area for individual bearing pads used in practice can vary between products. For instance, Neely and Tan (2010) give examples of pads with perimeter plan dimensions from 0.007 m^2 (EPDM) to 0.018 m^2 (HDPE). Example vertical stress-strain curves from laboratory compression tests are shown in Figure 1.6.

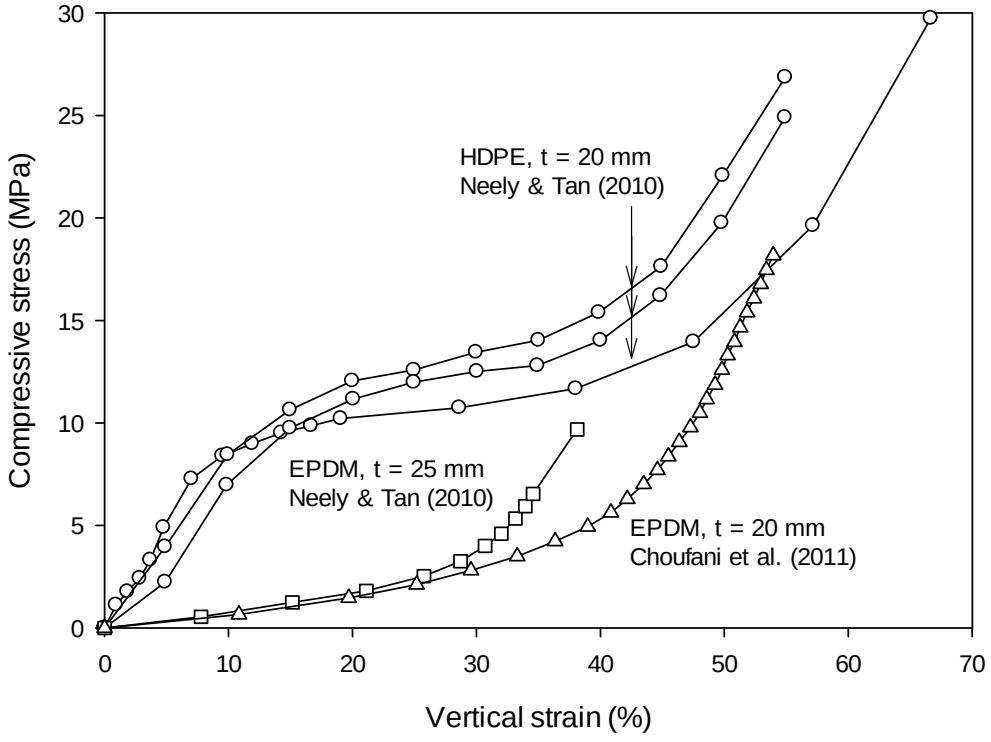

Figure 1.6: Compression behaviour of HDPE and EPDM bearing pad materials.

The initial elastic modulus (E_{pad}) can be computed using the secant slope passing through the elastic strain limit and is about 15 to 75 MPa depending on the constituent material type and voids. For 20-mm thick pads, the elastic limit corresponds to about 2 to 9 mm of compression (10% to 50% vertical strain). In the case study by Choufani et al. (2011), they report that the wall performed well with the 25-mm thick bearing pads compressing up to 80%. This means that the horizontal gap between panels at end of construction was about 5 mm. This is the same value reported for the reference instrumented wall (Runser 1999) at end of construction.

1.2. NUMERICAL MODELLING

1.2.1. General

Parametric analyses using a 2D finite element model (FEM) were carried out to investigate the influence of joint compressibility, backfill soil stiffness, foundation stiffness and panel-soil interface shear on vertical panel facing loads. Program PLAXIS (2008) was used to carry out the numerical simulations. The numerical model is shown in Figure 1.7. The height of the panel wall (H = 16.7 m) and depth of toe embedment (D = 1.5 m) were chosen to be close to the height of the instrumented field wall (H = 16.9 m) reported by Runser et al. (2001) and to match the embedment depth of this structure. The width of the numerical model was selected to concurrently optimize computation time and minimize the influence of problem boundaries. The length of the steel reinforcement elements was taken as $L = 0.7H$ which is a typical recommended minimum value in design codes (e.g., AASHTO 2010, Berg et al., 2009). The wall facing was modelled as discrete panels of 1.5 m height with a horizontal joint thickness of 20 mm. The panels and joints (bearing pads) were modeled using linear-elastic beam elements. The beam elements were connected through hinge contacts with zero rotational stiffness. Hence, vertical and horizontal loads can be transmitted at the contact between each bearing pad and adjoining concrete panels but not moment. This approach allows for vertical compression of the panels joints (bearing pads) and rotation at each joint. Only numerical results in which there was a positive gap are presented. No attempt was made to simulate the concrete-to-concrete contact condition, which in practice should be avoided. The soil zones were modelled as elastic-plastic Mohr-Coulomb materials. Two horizontal rows of reinforcement elements were attached to each panel unit which matches the typical arrangement for steel reinforced soil walls (vertical spacing = 0.75 m) (e.g., Runser et al., 2001). Each connection provided full rotational freedom at these locations. The facing column was seated on a concrete levelling pad that was 0.3 m wide and 0.15 m thick (Berg et al., 2009). For simplicity, the soil in front of the wall was taken as the foundation soil. The numerical wall was built incrementally from the bottom up to simulate construction in the field.

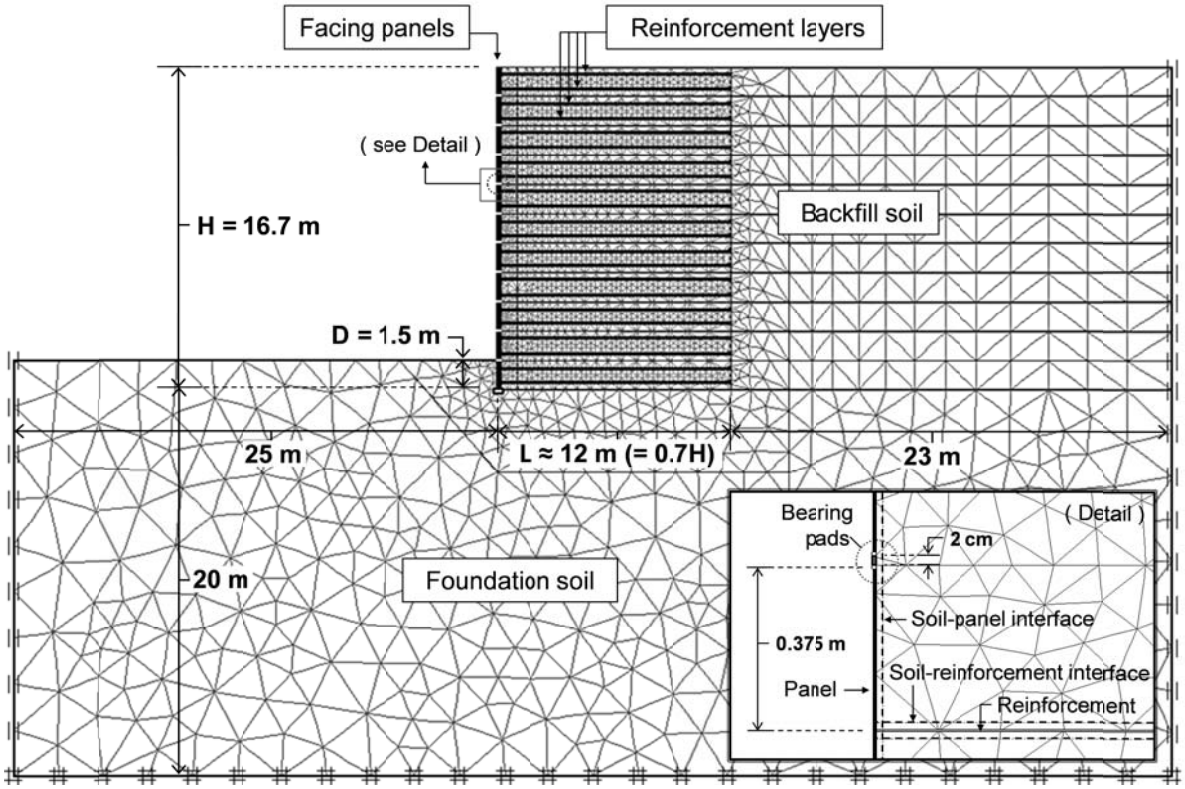

Figure 1.7: 2D finite element model geometry.

1.2.2. Material properties

Material properties for the concrete facing panels and horizontal joints are summarized in Table 1.2. The material type, dimensions and number of bearing pads can vary between projects. PLAXIS "beam" elements were used for the concrete panels and bearing pad joints. The equivalent axial stiffness for the joints with polymeric pads was computed as:

$$(EA)_{joint} = E_{pad} A_{pad} \frac{n_{pad}}{L_p} \tag{1.1}$$

Where: E_{pad} is the elastic modulus of the pad, A_{pad} is the perimeter (enclosed) plan area of a single bearing pad, n_{pad} is the number of pads per joint and L_p is the width of the panels (minus any overlap) along the running length of the wall face. The values in Table 1.2 are representative for each material and most common panel width (about 1.5 to 2.5 m measured at the front face). Panel widths vary in practice depending on the type of steel reinforced soil system. The elastic modulus (E_{pad}) for EPDM and HDPE pads was taken at 40 - 50% and 10 - 20% strain, respectively, using the data in Figure 1.6. To keep the numerical modeling simple, potential strain hardening that can occur at larger compressive strains was not considered in this study. The axial stiffness values given in Table 1.2 represent typical

minimum values for incremental concrete panel reinforced soil walls (i.e., two bearing pads per joint for EPDM and HDPE cases). A third configuration with no polymeric pads was examined by assuming that the entire horizontal joint was concrete. In the numerical model the same beam element representing the equivalent continuous bearing pad is used as before, but the axial stiffness of this element is assigned a very high value. This configuration allows the panels to rotate at the location of the horizontal joints as is the case for the polymeric bearing pads. Finally it should be noted that the influence of a wide range of possible panel joint stiffness was examined in this investigation by considering different numbers of bearing pads and/or bearing pad elastic modulus (i.e., EPDM or HDPE). The concrete pad scenario is a hypothetical case only and is used to provide a maximum limit on joint vertical stiffness for the parametric study.

Table 1.2. Concrete panel and joint beam properties:

Material	Parameter	Values		
Concrete precast panels	Elastic modulus (GPa)		35	
	Axial stiffness, *EA* (GN/m)		6.0	
	Bending stiffness, *EI* (MNm^2/m)		11	
	Poisson's ratio		0.15	
Bearing pads		EPDM	HDPE	Concrete [(a)]
	Elastic modulus, E_{pad} [(b)] (MPa)	15 - 25	45 - 74	~ 35000
	Axial stiffness, $(EA)_{joint}$ (MN/m)	0.13	1.1	6000
	Bending stiffness, *EI* (kNm^2/m)	0.25	2.10	11000
	Poisson's ratio	0.5	0.4	0.15

Note: [(a)] Simulates the idealized case of no polymeric bearing pads between panels.

[(b)] Equivalent elastic modulus (E_{pad}) based on total (perimeter) plan area of individual pads. The range of values depends on the elastic strain limit used to back-calculate the modulus in Figure 1.6.

The soil zones were modelled as linear elastic material with Mohr-Coulomb failure criterion. Material properties for the soil zones are summarized in Table 1.3. Five different backfill soils and two different foundation soils were considered in this investigation. The range of elastic modulus values for the backfill soil correspond to the range of elastic secant modulus values computed at 50% of the failure deviatoric stress for three different soils compacted to different densities (Boscardin et al., 1990). The range of backfill soil modulus values also matches values of silty sand to dense sand or loose gravel reported by Bowles (1996). Single elastic modulus estimates for soils are well known to be an imperfect mechanical characteristic of soil stiffness due to the sensitivity of soil stiffness to confining pressure. However, the focus of the current study is to investigate the influence of relative stiffness of the backfill and foundation soil on wall vertical face loading under working stress conditions. Hence, the Boscardin et al., data were used as a guide to select a range of compacted soil stiffness values in order to investigate a wide range of relative vertical loading response. The lowest value used for the backfill soil (type 5) in this study does not imply that poorly

compacted soils (or very compressible soils) should be used in the construction of these types of structures.

The combinations of soil type shown in Table 1.3 allow ten different cases to be examined with respect to relative stiffness of the backfill soil and foundation stiffness. For the backfill soil zone, a column of soil 1 m wide was assumed in the numerical models to account for reduced stiffness of the soil due to the use of lighter compaction equipment which is recommended practice close to the facing panel (Berg et al., 2009). In order to keep the numerical modelling as simple as possible, no attempt was made to simulate compaction effects by applying a transient surcharge pressure at each soil layer during construction (e.g., Huang et al., 2009). Finally, it can be noted that the numerical simulation results were sensibly independent of the magnitude of cohesive strength assigned to the soil in the numerical models. This is because the simulations were restricted to working stress conditions and not taken to soil failure.

Table 1.3. Soil properties:

Material	Parameter		Values	
Backfill	Unit weight (kN/m^3)		19	
	Cohesion (kPa)		5 [(a)]	
	Friction angle (degrees)		36	
	Dilatancy angle (degrees)		6	
			> 1.0 m from face	< 1.0 m from face
	Elastic modulus (MPa)	Soil backfill type 1	100	50
		Soil backfill type 2	70	35
		Soil backfill type 3	50	25
		Soil backfill type 4	30	15
		Soil backfill type 5	10	5
	Poisson's ratio		0.3	
Foundation	Unit weight (kN/m^3)		18	
	Cohesion (kPa)		50	
	Friction angle (degrees)		30	
	Elastic modulus (MPa)	Foundation soil type 1	1000	
		Foundation soil type 2	10	
	Poisson's ratio		0.3	

Note: [(a)] Soil assumed as a no-tension material.

Material properties for the reinforcement are listed in Table 1.4. The PLAXIS “geogrid” element was used to model the reinforcement elements as continuous sheets that have only axial stiffness and can transmit load to the surrounding soil through interface shear. The choice of the word “geogrid” in the PLAXIS program to describe this generic element type is

unfortunate since the reinforcement in the current investigation is metallic and not polymeric. The equivalent linear-elastic axial stiffness of the geogrid element for each layer of reinforcement elements is computed using Equation 1.1 but with reinforcement elastic modulus, cross-sectional area and number of reinforcement elements per panel row. For steel strips, the area is the rectangular cross-section of each steel strap; for steel grid systems this parameter is the circular cross-section area of each longitudinal member. The axial stiffness values summarized in Table 1.4 vary with depth because the number of steel strip elements in a row may vary with depth (e.g., Runser et al., 2001) or the cross-section area of the elements changes with depth as is the case for some steel ladder walls. Both approaches are used in design practice to account for increasing horizontal earth pressure with depth below the wall crest. Finally, it can be noted that the magnitude of axial stiffness values falls within the range of values found in databases for instrumented steel strip walls and steel grid (bar mat) walls summarized by Bathurst et al. (2011) and Huang et al. (2012).

Table 1.4. Reinforcement properties:

Height above toe of wall (m)	Linear-elastic stiffness $(EA)_{reinforcement}$ (MN/m)
0 to 2.3	88
2.3 to 6.1	73
6.1 to 9.9	59
9.9 to 16	44
> 16	73

1.2.3. Interfaces

PLAXIS “interface” elements were used to model strength and stiffness between soil and reinforcement elements, and between the soil and concrete facing panels. These elements include an interface reduction factor (R) which is the ratio of interface shear strength to shear strength of the surrounding soil (called the interface friction coefficient hereafter). The reader is referred to the PLAXIS (2008) reference manual for further details on interface modelling. The concrete panel-soil interface was assigned a value of $R = (\tan\delta / \tan\phi) = 0.3$ (where ϕ is the peak friction angle of the soil (36^o) and δ is the concrete soil interface friction angle (12^o)) and zero dilatancy angle. The ratio of $R = 0.3$ falls between values back-calculated from horizontal loads computed from strain gages mounted on the reinforcement layers close to the panel connections and embedded pressure cells at the back of the facing panels, and vertical loads at the base of the wall (Runser 1999, Runser et al., 2001). These values were computed at the end of construction so it is possible that the back-calculated interface friction angle is the mobilized value and not the peak available interface friction angle. For this reason, simulations were also carried out using $R = 0.45$ and 0.6 corresponding to $\delta = 18^o$ and 24^o, respectively. These higher values match values reported in the literature (NFEC 1986). The reinforcement elements were assumed to be perfectly bonded to the surrounding soil by assigning $R = 1$ (i.e., $\delta = \phi$). This approach is consistent with the very high pullout resistance

that has been documented for steel strip and steel grid reinforcement materials (Schlosser and Elias 1978, Miyata and Bathurst 2012b, Bathurst et al., 2011). It should be noted that interface shear was also assumed to be mobilized between the front of the wall facing and the foundation soil over the embedment depth D = 1.5 m.

1.3. RESULTS

1.3.1. General

Global deformation response for combinations of backfill soil and foundation soil are illustrated in Figure 1.8 for the base case of interface shear coefficient R = 0.3 and two HDPE bearing pads between panel units. It should be noted that even for the largest deformation case (Figure 1.8a) the wall remains at working stress condition because: a) the strains in the reinforcement layers were less than yield; b) shear stresses between the soil reinforcement elements and the soil were well below the interface shear strength, and; c) there were no contiguous failure surfaces in the reinforced soil zone, retained soil zone or foundation.

The deformations in this figure are exaggerated by a factor of five to help identify differences in deformation trends and magnitudes that result from the four combinations of soil stiffness shown. For example, the largest (bulk) deformations occur for the case with both soil zones assigned (low) E = 10 MPa (Figure 1.8a) and the smallest deformations when the highest values of E are used for both the backfill soil (100 MPa) and the foundation (1000 MPa) (Figure 1.8d). As expected, the settlement at the base of the wall is proportional to and largely controlled by the stiffness of the foundation soil. For example, the settlement at the toe is approximately 300 mm for the most compressible foundation cases (Figures 1.8a and 1.8c) and approximately 3 mm for the stiffest foundation cases (Figures 1.8b and 1.8d). It is interesting to note that average toe settlement for the steel reinforced soil wall reported by Runser et al. (2001) was 32 mm. This value is close to the predicted settlement at the wall toe of 27 mm using a foundation elastic modulus of 100 MPa in the current study. This gives confidence that the range of foundation stiffness values in this numerical study captures the toe settlement in the field case study reported by Runser et al. (2001). Figure 1.8c shows that the reinforced soil mass rotates backward when the foundation soil is 10 times less stiff than the backfill soil. The potential for negative rotation of a steel reinforced soil wall mass when seated on a relatively soft (yielding) foundation has been noted by Jones and Edwards (1980).

As mentioned, the focus of this parametric study is on the influence of relative soil stiffness and vertical joint stiffness on the development of vertical wall facing loads. Hence, assessment of reinforcement load predictions is not an objective. Nevertheless, it is interesting to note that the magnitude of peak reinforcement loads generated for the case with $E_{(backfill)}$ = 100 MPa and $E_{(foundation)}$ = 10 and 1000 MPa (Figures 1.8c-d) was in the range of 60 to 65 kN/m which compares to 64 kN/m reported by Runser et al. (2001). For the same combination of soils, the magnitude of peak connection reinforcement load was in the range

of 33 to 55 kN/m which compares to 41 kN/m reported in the same study. This gives confidence that the magnitudes of numerical results are reasonable. The range in magnitude of reinforcement loads from all simulations was not practically influenced by the type of bearing pads (and joint axial stiffness values) shown in Table 1.2 (i.e., within ±3% of the base case with the stiffest soils). However, for each combination of soil type with the same interface friction coefficient value there were local changes in the distribution of loads that can be ascribed to the influence of joint compressibility.

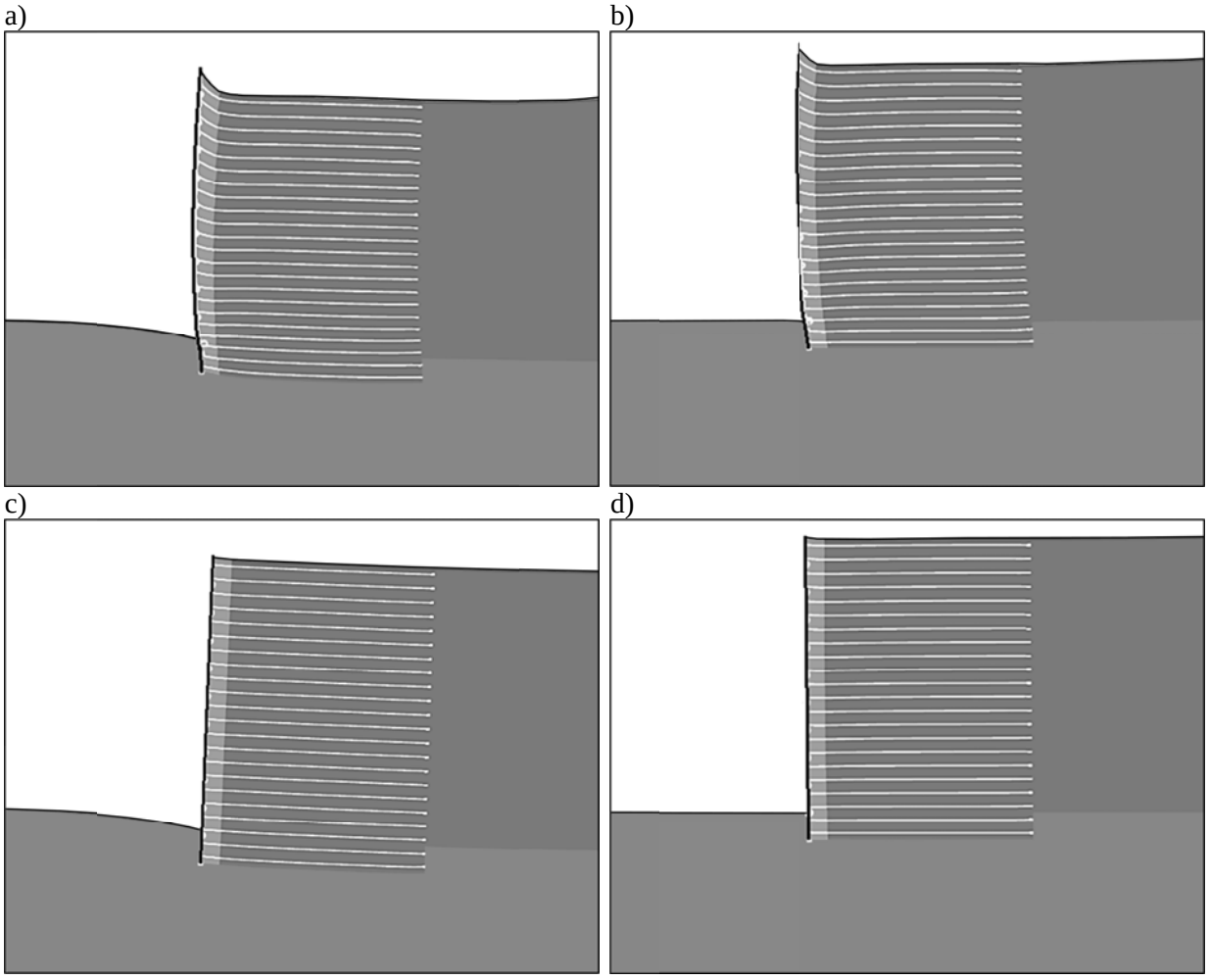

Figure 1.8: Global soil wall deformations illustrating influence of relative stiffness of the backfill and foundation soils. Note: displacements have been increased by a factor of five: a) $E_{(backfill)} = E_{(foundation)} =$ 10 MPa; b) $E_{(backfill)} = 10$ MPa, $E_{(foundation)} = 1000$ MPa; c) $E_{(backfill)} = 100$ MPa, $E_{(foundation)} = 10$ MPa; d) $E_{(backfill)} = 100$ MPa, $E_{(foundation)} = 1000$ MPa.

The numerical simulations were carried out to investigate wall response under operational (working stress) conditions. This criterion was satisfied by noting that all steel reinforcement strains were less than the yield strain of the steel (0.19% axial strain).

1.3.2. Influence of joint stiffness and soil stiffness on vertical facing panel loads

Figures 1.9 (R = tan δ / tan ϕ = 0.3), 1.10 (R = 0.45), and 1.11 (R = 0.6) provide a summary of the total vertical loads through the height of the concrete panel walls and component contributions due to down-drag and panel-soil interface shear for two combinations of backfill and foundation soil. The two cases shown are the extreme combinations for foundation stiffness (i.e., $E_{(backfill)}$ = 100 MPa with $E_{(foundation)}$ = 10 and 1000 MPa). For both cases the total vertical load at each panel joint location increases in the order of increasing joint axial stiffness material (i.e., EPDM, HDPE and concrete). The contribution of the panel self-weight to total vertical load is shown by the linearly increasing line in these two figures. The total vertical load values for all soil and panel joint stiffness cases are greater than the panel self-weight at each joint elevation and at the base of the wall due to connection down-drag loads and mobilized panel-soil interface shear.

The total vertical loads for each case increase with depth below the wall crest until the top of the bottom embedded panel. The largest total vertical loads are recorded at the top of the bottom panel and then decrease to the base of the wall. This pattern is due to the development of interface shear at the front of the bottom embedded panel which generates some vertical load capacity. In fact for the EPDM case in Figure 1.9c, the net soil-panel friction force acts upward. This is because the panel joints are very compressible and the backfill and foundation soil are very stiff. This minimizes relative displacement between the back of the concrete panels and the backfill soil. The reinforced soil mass acts as a block with upward frictional force generated over the front embedded depth.

An important observation from Figures 1.9, 1.10, and 1.11 is that for the same bearing pad case and same backfill stiffness the total vertical load is greater for the foundation with the smaller stiffness. For example, in Figure 1.9, the maximum total vertical load (top of bottom panel) for the relatively stiff foundation soil case (Figure 1.9c) is 250, 215 and 90 kN/m for the concrete, HPDE and EPDM cases, respectively, versus 280, 255 and 160 kN/m for the relatively compressible foundation soil case (Figure 1.9a). It is interesting to compare these vertical loads with values computed using classical Coulomb active earth theory for a cohesive-frictional soil in contact with a vertical wall of the same height. For the case of R = 0.3 the total vertical load (due to interface friction and self-weight) is about 170 kN/m. Hence, Coulomb theory underestimates the total vertical load for concrete and HDPE horizontal joint stiffness cases, but overestimates the total vertical load for the relatively compressible (EPDM) horizontal joint stiffness case. These differences are expected because the walls in our simulations are: a) assumed to be at working stress conditions (not at limit equilibrium); b) deformation and compressibility of the backfill and foundation soils are not considered in classical earth pressure theory, and; c) there are additional load effects due to reinforcement-wall connection down-drag.

Panel-soil interface friction coefficient $R = \tan\delta / \tan\phi = 0.3$.

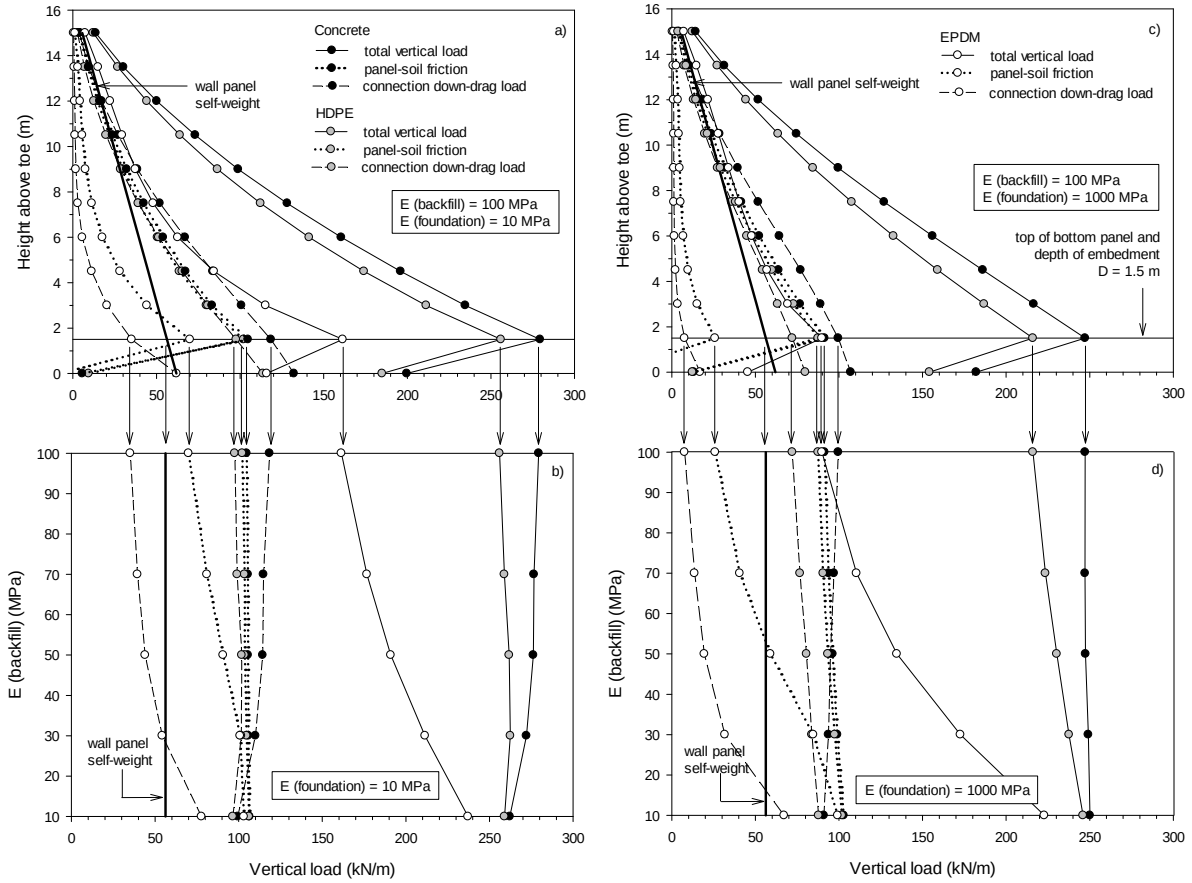

Figure 1.9: Influence of joint stiffness material on total and contributing vertical facing panel loads: a) stiff backfill soil in combination with lower stiffness foundation soil; b) influence of backfill soil stiffness and lower stiffness foundation soil on vertical load at top of bottom panel; c) stiff backfill soil in combination with higher stiffness foundation soil; d) influence of backfill soil stiffness and higher stiffness foundation soil on vertical load at top of bottom panel. Note: panel-soil interface friction coefficient $R = \tan\delta / \tan\phi = 0.3$.

Figures 1.9, 1.10, and 1.11 show the influence of backfill soil stiffness on the maximum vertical load and the contribution of down-drag and interface shear components on loads predicted at the critical panel location (i.e., top of bottom embedded panel). For the case of the most compressible joint material (two EPDM bearing pads) there is a trend of increasing load values with decreasing backfill soil stiffness. However, the data plots in these two figures for this case are truncated corresponding to numerical outcomes indicating panel to panel contact. For the relatively stiffer concrete and HDPE joint material cases, the influence of backfill soil stiffness is relatively little.

Panel-soil interface friction coefficient $R = \tan\delta / \tan\phi = 0.45$.

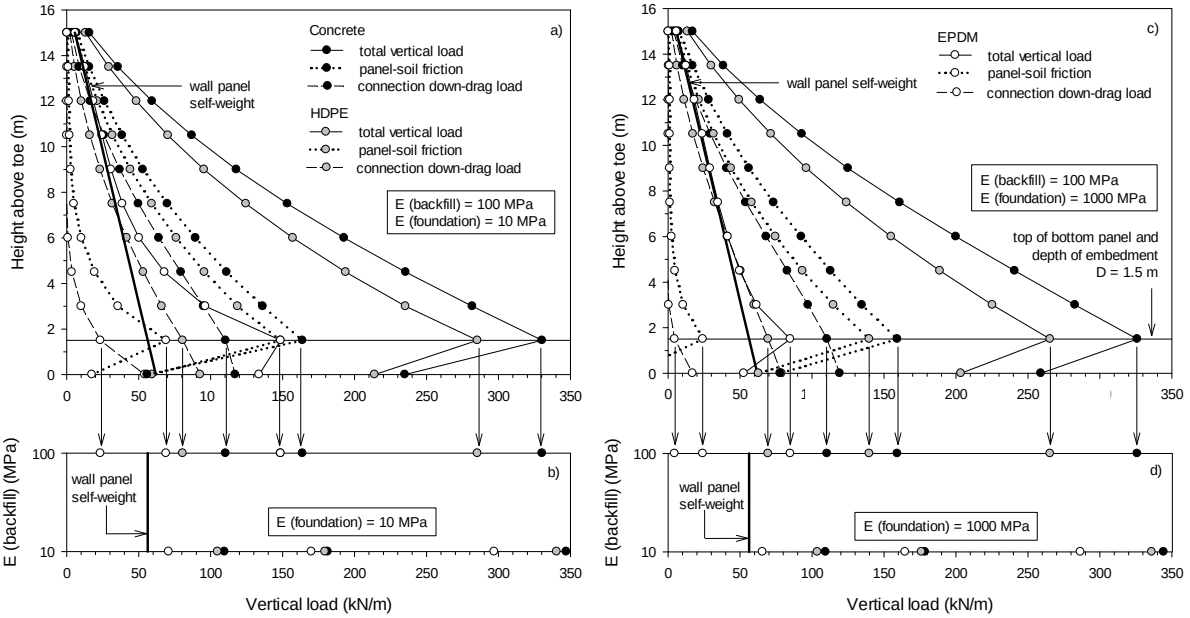

Figure 1.10: Influence of joint stiffness material on total and contributing vertical facing panel loads: a) stiff backfill soil in combination with lower stiffness foundation soil; b) influence of backfill soil stiffness and lower stiffness foundation soil on vertical load at top of bottom panel; c) stiff backfill soil in combination with higher stiffness foundation soil; d) influence of backfill soil stiffness and higher stiffness foundation soil on vertical load at top of bottom panel. Note: panel-soil interface friction coefficient $R = \tan\delta / \tan\phi = 0.45$.

Figure 1.12 shows the fraction of total vertical load due to panel self-weight, connection down-drag and concrete panel-soil interface shear force at the top of the bottom panel as a function of panel-soil interface shear coefficient for walls with $E_{(backfill)}$ = 100 MPa. For the most compressible joint case (Figure 1.12a) and the stiffest foundation soil the increasing fraction of toe load is in the order of down-drag load, panel-soil friction and panel self-weight (open symbols). For the matching conditions but with the most compressible foundation soil case, the increasing fraction of toe load is in the order of down-drag load, panel self-weight and panel-soil friction (solid symbols). The influence of panel-soil interface shear magnitude on relative load contributions is negligible. For the same cases but a stiffer HDPE joint material (Figure 1.12b), the relative contribution of panel-soil friction increases with increasing panel-soil friction coefficient. However, the relative contributions to total vertical load are judged to be negligible based on foundation stiffness (compare solid and open symbol pairs).

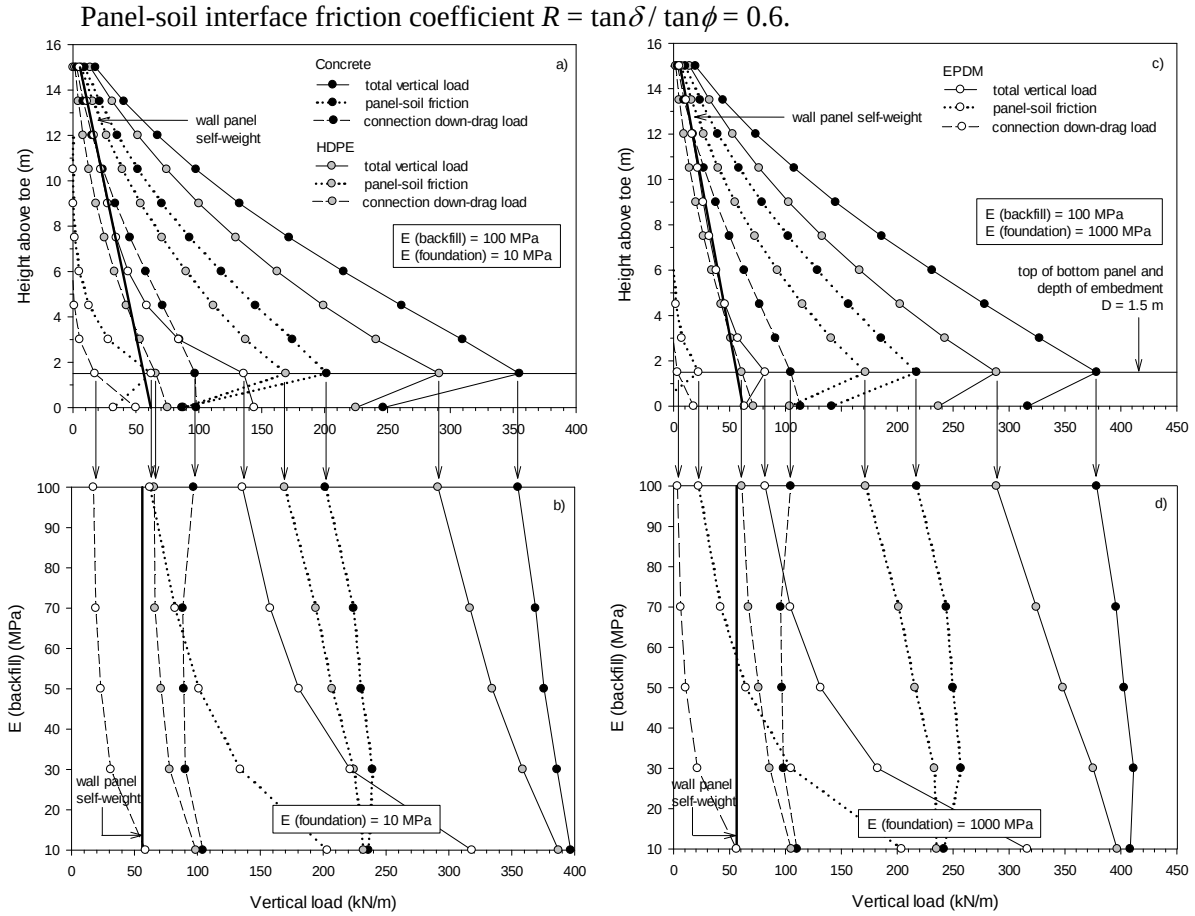

Figure 1.11: Influence of joint stiffness material on total and contributing vertical facing panel loads: a) stiff backfill soil in combination with lower stiffness foundation soil; b) influence of backfill soil stiffness and lower stiffness foundation soil on vertical load at top of bottom panel; c) stiff backfill soil in combination with higher stiffness foundation soil; d) influence of backfill soil stiffness and higher stiffness foundation soil on vertical load at top of bottom panel. Note: panel-soil interface friction coefficient $R = \tan\delta / \tan\phi = 0.6$.

Figure 1.13 examines the influence of panel-soil interface friction on the total load developed at the top of the bottom panel. For the relatively stiff concrete and HDPE joint cases the total vertical load increases with increasing interface friction angle (i.e., increasing friction coefficient R). This trend is expected from classical notions of rigid wall-soil interaction. Rowe and Ho (1997) showed a similar trend of increasing vertical facing load with increasing interface friction angle from results of 2D FEM simulations of continuous panel walls but reinforced with more extensible geosynthetic reinforcement layers. However, in the current study, this trend decreases with decreasing stiffness of the panel joint material and in fact is slightly reversed for the weakest (EPDM) case. A qualitative explanation is that the wall vertical stiffness for the EPDM cases is similar to the equivalent vertical stiffness of the soil behind the wall. Superimposed on the plots is the range of total vertical toe loads for the 16.7-m high steel strip reinforced soil wall reported by Runser et al. (2001). The range of toe loads

falls between the cases for two HDPE and two EPDM bearing pads and the stiffest foundation soil case in this study ($E_{(foundation)}$ = 1000 MPa, Figure 1.13b). In fact, the measured range of toe loads is in agreement with an interpolated value of foundation stiffness of 100 MPa between the two figures and assuming two EPDM bearing pads.

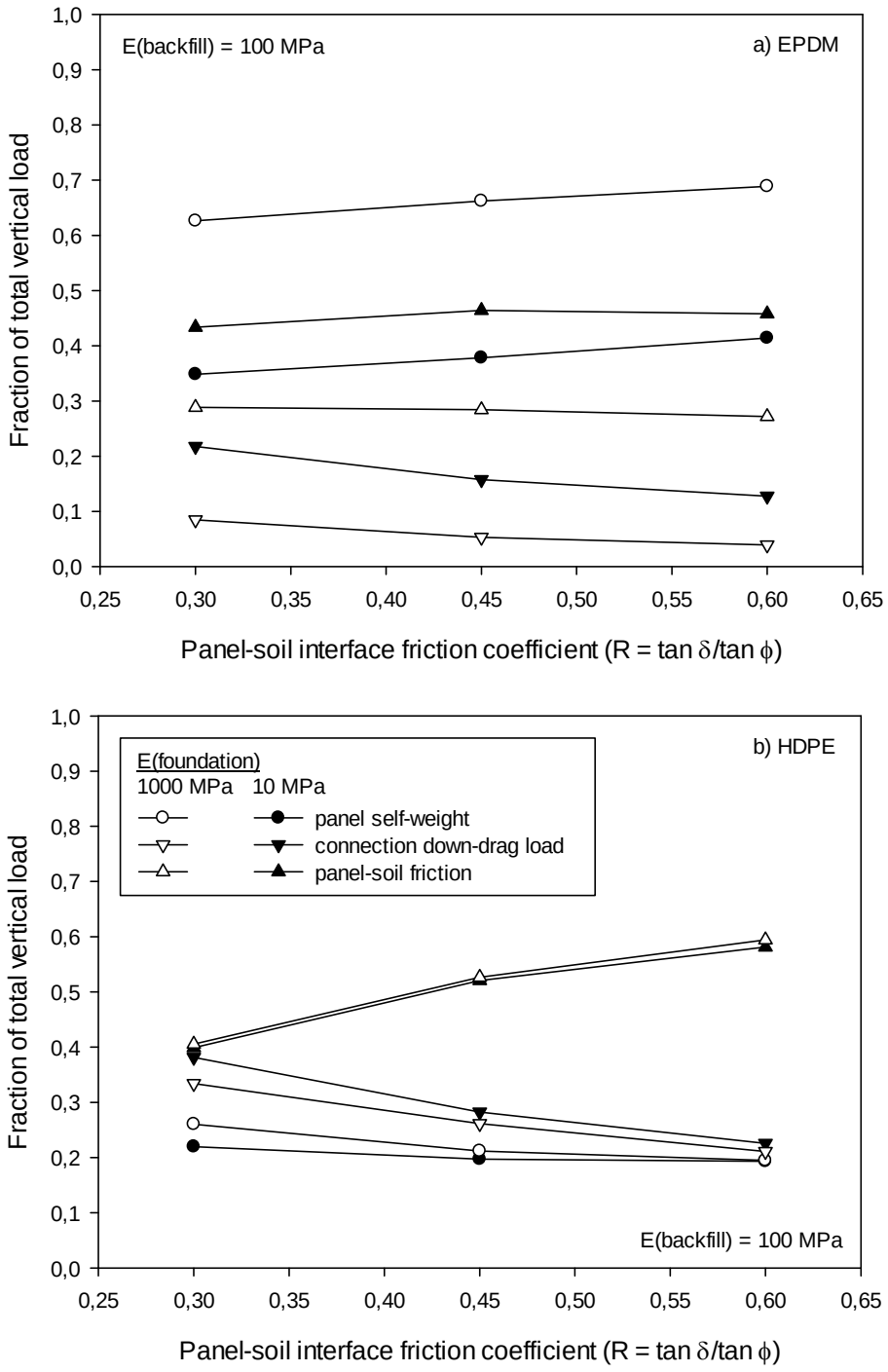

Figure 1.12: Fraction of total vertical panel base load versus panel-soil friction coefficient (*R*).

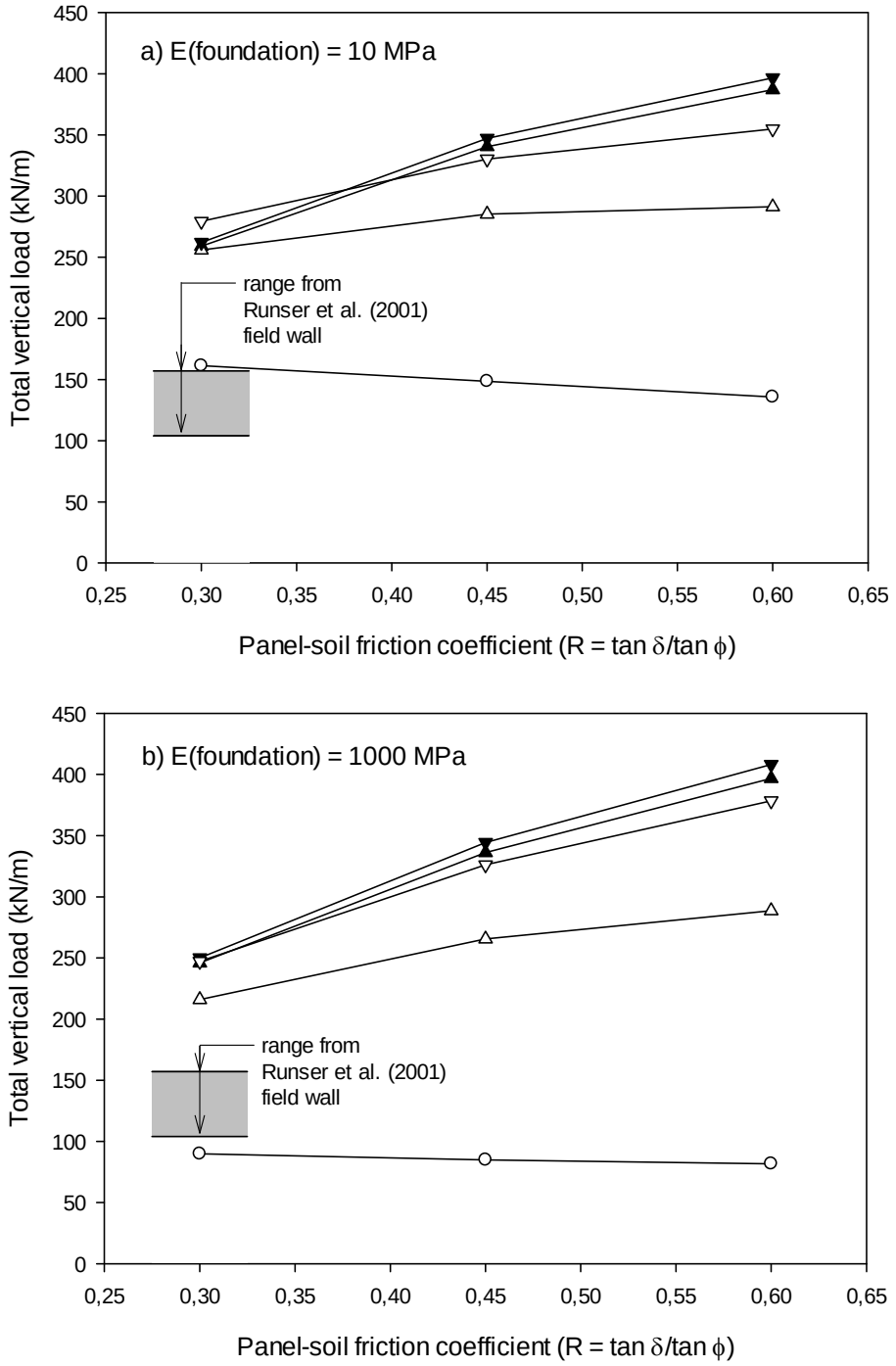

Figure 1.13: Influence of panel-soil friction coefficient (R) on total vertical load at top of bottom panel. Note: EPDM with backfill soil E = 10 MPa not included because panel contact occurred.

Figure 1.14 shows the computed axial strains at panel joint locations along the facing at the end of wall construction using bearing pads with initial thickness of 20 mm, with panel-soil interface friction coefficient $R = \tan\delta / \tan\phi = 0.3$. EPDM bearing pad generated larger joint gap closure in soft backfill cases (full gap closure and expected panel contact for joint facing at depths below 6 m from top of facing). However, as commented, single-initial bearing pad

stiffness were assumed in both bearing pad cases. Actual stress-strain bearing pad behaviour would reduce gap closure in case of EPDM (stiffer after 40-50% strain), and increase it in case of HDPE (soft-flat stress-strain curve between 10 and 40% strain). Further analysis about panel-joint gap are provided in Chapter 3.

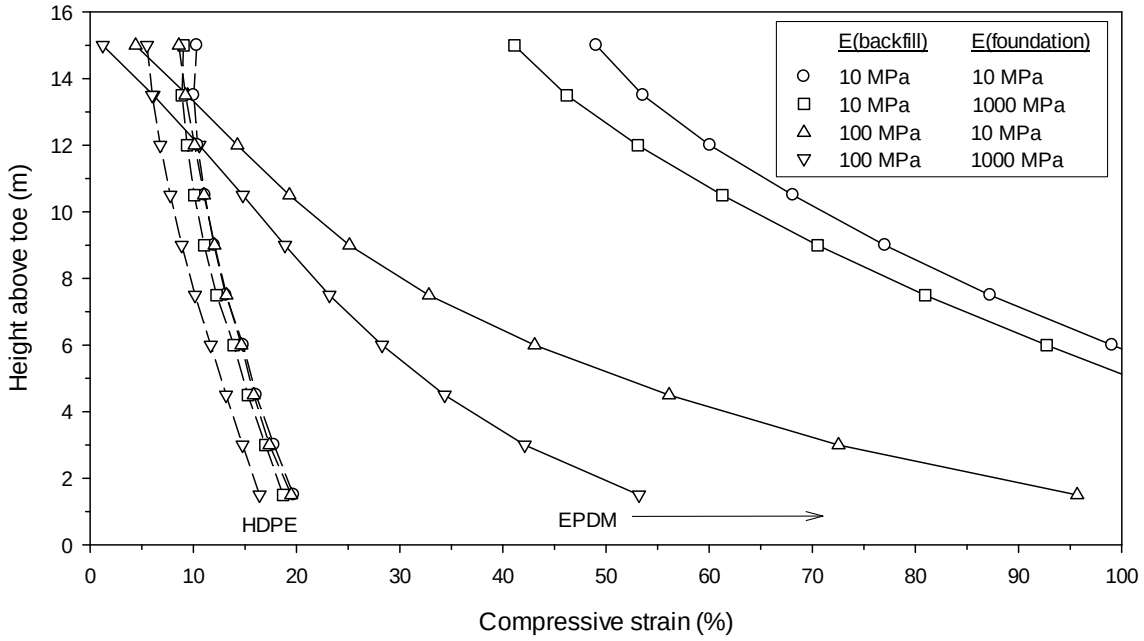

Figure 1.14: Computed axial strains at panel joint locations along the facing at end of wall construction using bearing pads with initial thickness of 20 mm. Note: panel-soil interface friction coefficient $R = \tan\delta / \tan\phi = 0.3$.

Figure 1.15 shows the maximum compressive strain and gap size at the critical panel joint location as a function of axial stiffness of the joint for the 16.7-m high wall that is the base case in the current study. As expected, joint compressive strains decrease with increasing joint axial stiffness (*EA*). However, the practical influence of magnitude of backfill soil stiffness and foundation stiffness also decreases with increasing joint stiffness. Hence, the choice of joint stiffness in steel reinforced soil walls becomes more important as the backfill soil stiffness decreases relative to foundation soil stiffness and/or as the foundation stiffness decreases. Examples of the type and number of 20-mm thick bearing pads to match the joint axial stiffness values on the horizontal axis are shown in the figure. The data show that it is possible to select a sufficient number of EPDM bearing pads to keep the vertical gap between panel units to less than 5 mm for the range of soil stiffness values investigated.

Figure 1.16 shows the computed maximum vertical load factor for all combinations of input parameters in the current investigation and $R = 0.3$ and $R = 0.6$. The vertical load factor has been computed at the critical joint elevation which is at the top of the bottom panel. The independent parameter in this figure is the joint axial stiffness (Table 1.2) normalized against the product of the backfill elastic modulus and thickness of the uncompressed joint (i.e., t =

0.02 m). Only data points corresponding to positive gap values are plotted. The data plots show that above a ratio of one the load factor approaches a value of 4 to 5 for cases with R = 0.3. Below this value the load factor decreases rapidly with decreasing log value of the normalized joint stiffness. For numerical simulation results using R = 0.6 (i.e., large mobilized panel-soil interface shear resistance) the load factors approach a value of 6 to 7 beyond a normalized joint stiffness of about 10. The numerical data and field data show that compressible joint materials can be effective in reducing vertical compression loads in these structures.

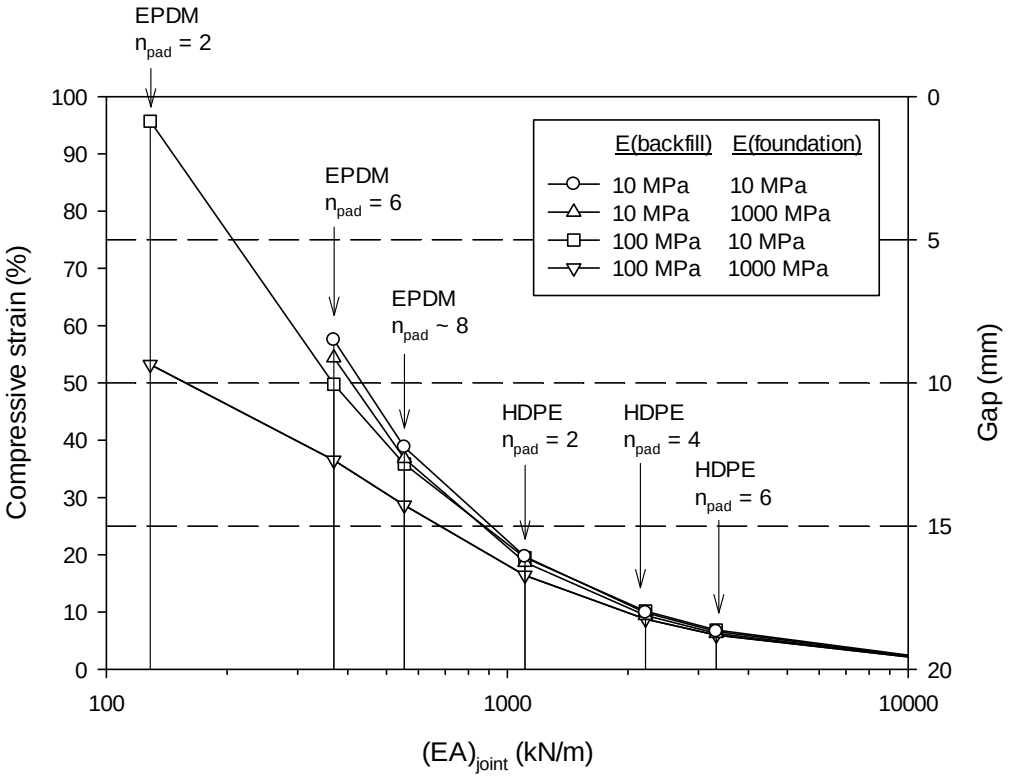

Figure 1.15: Computed axial strains and joint gap thickness at top of bottom panel at end of wall construction using bearing pads with initial thickness of 20 mm. Note: panel-soil interface friction coefficient $R = \tan\delta / \tan\phi = 0.3$.

1.4. DISCUSSION AND CONCLUSIONS

The investigation described in this chapter is focused on steel reinforced soil wall systems with precast concrete panels. The numerical simulations are limited to a single wall height and embedment depth. For simplicity, the analyses in this investigation have used a linear-elastic constitutive model for the soil together with a Mohr-Coulomb failure criterion. Design engineers routinely use simple constitutive models in practice even for substantial reinforced steel wall structures (e.g., Linquist 2008).

In the current investigation, the loads in the reinforcement and shear stresses in the reinforced soil zone are consistent with working stress conditions. Despite the simplicity of the soil model, the measured reinforcement loads at the end of construction are in the range recorded for an instrumented field wall of similar dimensions reported in the literature (Runser et al., 2001). More importantly, the magnitudes of predicted total vertical load include the range reported by Runser et al., and the vertical load factors reported in the current study are in the range reported for instrumented steel strip walls.

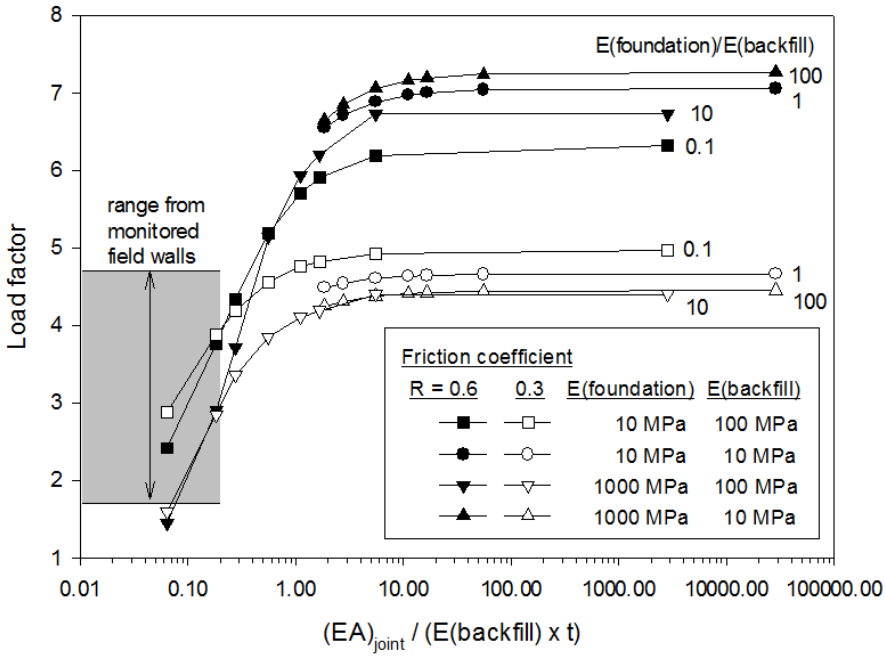

Figure 1.16: Influence of relative soil stiffness and ratio of joint stiffness to local backfill stiffness on maximum vertical facing load factor. Note: $R = \tan\delta / \tan\phi = 0.3$ and 0.6.

More complex constitutive soil models are available in the literature but these models require input properties that are seldom available to design engineers. Furthermore, improved accuracy of numerical predictions using more advanced models may not be assured (Ling 2003). In practical terms, numerical models need only be as accurate as the measurements against which the predictions can be compared. As an example, Huang et al. (2009) demonstrated this point when they compared numerical predictions for a steel wire mesh reinforced soil wall against measured values for reinforcement strains and toe loads. In one simulation they used a linear-elastic Mohr-Coulomb soil model and in the second a more sophisticated single hardening model (Lade 2005). At the end of construction (working stress conditions) there was no practical difference between computed toe loads or reinforcement loads using the simpler soil model and the range of measured values.

The numerical investigation in this chapter has used the example of a 16.7-m high steel reinforced soil wall constructed with a range of reinforced backfill soil, foundation soil and

horizontal joint stiffness to examine the development of vertical facing load at end of construction. The following major conclusions can be made:

1. Vertical toe loads are greater than panel self-weight due to shear forces mobilized between the back of the concrete panels and the backfill soil, and down-drag forces generated at the connections between the steel reinforcement elements and the concrete facing panels.

2. The magnitude of the vertical load at the bottom of the facing panels cannot be predicted accurately using conventional limit-equilibrium models because of the complex effects of deformation and compressibility of the backfill and foundation soils, horizontal joint stiffness and additional load due to reinforcement-wall connection down-drag.

3. Numerical results show that when the backfill soil is relatively soft, the compressibility of the horizontal joint has relatively little influence on the vertical load factor (where vertical load factor is the ratio of total vertical load in the panel wall divided by the self-weight of the panel wall).

4. This chapter shows that an appropriately selected number and type of compressible bearing pads can be effective in reducing vertical compression loads in these structures and at the same time ensure an acceptable vertical gap between concrete panels.

While the current study has been limited to a single wall geometry and range of soil properties, the general conclusions are expected to apply to other steel reinforced soil wall geometries. An important contribution of this study is that it provides a strategy for design engineers to investigate the influence of soil stiffness and panel joint stiffness using available commercial finite element model packages together with simple constitutive models. This approach allows the engineer to optimize the selection of bearing pads for similar steel reinforced soil wall structures.

CHAPTER 2

NUMERICAL ANALYSIS OF AN INSTRUMENTED STEEL REINFORCED SOIL WALL [1]

2.1. INTRODUCTION

2.1.1. General approach

Mechanically stabilized earth (MSE) walls constructed with steel strip soil reinforcement are now a mature technology. These structures are found worldwide and in the vast majority of cases have performed well. The development of this technology as reported in the western literature can be traced to papers by Schlosser (1978) and Schlosser et al. (1979). A similar survey of the development of these walls in Japan can be found in the paper by Miyata and Bathurst (2012a). These prior works demonstrate that reinforcement loads for internal stability limit states design use equations that are largely empirical in nature with parameters back-fitted to measured loads from a relatively small number of instrumented structures. Allen et al. (2001) and Miyata and Bathurst (2012a) compiled a database of instrumented steel strip reinforced walls from published and unpublished sources. The measurements from these monitored walls have been used to assess the accuracy of limit-equilibrium based design methods found in current design guidelines (e.g., AASHTO 2012; Berg et al., 2009; BSI 2010; CFEM 2006; PWRC 2003). Examples of prior work of this type are the papers by Bathurst et al. (2008a, 2009). Load measurements from these databases have been used to develop new or improved empirical-based working stress design methods that more accurately predict reinforcement loads under operational conditions (Allen et al., 2004) and to propose more accurate pullout capacity models (Miyata and Bathurst 2012b). More recently, the value of physical data from instrumented wall case studies has increased since they are needed for rigorous reliability theory-based calibration of load and resistance factor design (LRFD) methods (e.g., Huang et al., 2012; Kim and Salgado 2012; Bathurst et al., 2013).

[1] Chapter based on Damians, I.P., Bathurst, R.J., Josa, A., and Lloret, A., 2015. Numerical analysis of an instrumented steel-reinforced soil wall. ASCE International Journal of Geomechanics, 15(1): 04014037.

The motivation for the research described in this Chapter is the observation that, while the need for high-quality measurements is necessary for further refinement of calibrated LRFD design methods, the number of single-tier steel strip MSE wall case studies is only 23 according to Bathurst et al. (2009) and Bathurst and Miyata (2012a). A strategy to improve the deficit in physical measurements of reinforcement loads in steel strip reinforced soil walls is to use results from numerical models that have been verified against physical measurements. Results from verified numerical models can then be used to fill the gaps that exist in the physical databases noted earlier. The Minnow Creek steel strip reinforced soil wall project reported by Runser (1999) and Runser et al. (2001) stands out as the most comprehensive instrumented field case study available today to compare numerical model predictions of a typical steel strip reinforced soil wall to measured performance at the end of construction. This wall has been used as a reference structure for a parametric numerical investigation of factors influencing vertical facing loads in steel reinforced soil walls in previous Chapter 1 (as in Damians et al., 2013a).

The current study first gives a brief summary of the Minnow Creek Wall project and instrumentation details. A 2D finite element (FE) model (PLAXIS 2008) is then developed to predict reinforcement loads, vertical toe loads, panel-joint compression and earth pressures. The study describes how input parameters for constituent soil and structural elements were selected and verified against independent measurements. Numerical predictions are compared against physical measurements and, for the cases where predictions are judged to be poor, reasons are given. The influence of constituent soil model type (Mohr-Coulomb and Hardening Soil model) and wall toe embedment condition on numerical outcomes is demonstrated. The study is a valuable reference for engineers who are tasked with making Class A predictions of steel strip reinforced soil walls, or to carry out sensitivity analyses (e.g., Kibria et al., 2013; Hatami and Bathurst 2001) using commercially available software packages together with simple constitutive models for the component materials.

2.1.2. Minnow Creek Wall

The project wall is a 16.9 m-high steel strip reinforced soil structure that was used to support one abutment of a bridge crossing Minnow Creek in Indiana, USA (Runser 1999; Runser et al., 2001). The wall was constructed for the Indiana Department of Transportation (INDoT) and was completed in 1999. Schematic views of the wall and instrumentation are shown in Figure 2.1. The instrumented section was located about 10 m from the bridge deck to avoid the influence of the support pilings. The wall facing comprised cruciform precast concrete panels (1.5 m x 1.5 m × 140 mm-thick) with a concrete coping at the wall crest. The bottom row of panels was seated on a concrete leveling pad 300 mm-wide by 150 mm-thick. Elastomeric bearing pads were placed along the horizontal joints between the concrete facing panels to ensure a minimum gap between panels. The panels were connected to ribbed steel strips (50 mm-wide by 4 mm-thick) extending from 12 to 15.5 m behind the facing into the reinforced soil zone. The number of reinforcement strips at each panel varied with elevation.

The wall was seated on a competent foundation (standard penetration test blow count N_{SPT} > 50) comprised mainly of layers of medium to dense sand and sandy loam. A summary of the structural elements in the wall is given in Table 2.1. Shortly after the placement of the first panel, a rip-rap toe slope was placed at the base of the wall. The reinforced soil zone was comprised of gravely sand and the retained soil was sand. Basic soil properties are summarized in Table 2.2. Based on piezometer data, the water table remained constant at about 2 m above the toe of the wall after the third panel row was installed.

Table 2.1. Minnow Creek Wall structural elements:

Structural elements	Type & material	Dimensions
Reinforcement	Ribbed steel strips (galvanized Grade 65 steel, $E_{steel} = 200 \times 10^3$ MPa)	Length: 15.54 m in the five bottom layers, 11.89 m in the other up layers. Section: 50 × 4 mm (width × thickness)
Panels	Precast concrete panels. 7.3 kN weight/panel	1.5 × 1.5 × 0.14 m (high × width × thickness)
Bearing pads	Elastomeric EPDM (ethylene propylene diene monomer)	Plan area: 100 mm × 85 mm Thickness: 20 mm

Table 2.2. Minnow Creek Wall basic soil properties:

Soil materials	Soil Classification (Unified [a] / AASHTO [b])	Dry unit weight (kN/m^3)	Saturated unit weight (kN/m^3)	Unsaturated unit weight (kN/m^3)	Friction angle, ϕ (degrees) [c]	Cohesion (kPa)
Reinforced soil (B-Borrow)	SP (A-1-a)	20.8	22.5	21.8	38	0 (w ~ 4%)
Retained fill	SW-SM (A-1-b)	19.7	21.8	20.8	35.3	0 (w ~ 5%)
Foundation	N_{SPT} > 50			18.85		

Notes: [a] ASTM D2487 (2011); [b] AASHTO M145. 2004; [c] Triaxial peak friction angle (ϕ_{tx}).

2.1.3. Instrumentation and monitoring

The instrumentation (Figure 2.1) included strain gages attached along the length of five steel strips and 11 rows of steel strips with one set of strain gages each to monitor only connection loads. Additional instrumentation included earth pressure cells placed at the base of the reinforced soil mass and embedded at the back of selected concrete panel units, and load cells at the base of the wall facing. Lateral wall facing deformations were monitored using an

inclinometer tube attached to the back of the concrete facing. Gap measurements were recorded during construction at the horizontal joint between the second and third concrete panels at the instrumented section. The wall was monitored during and up to end of construction. Where data are available, measurements were constant for practical purposes for an additional one month after which monitoring was discontinued (Runser 1999).

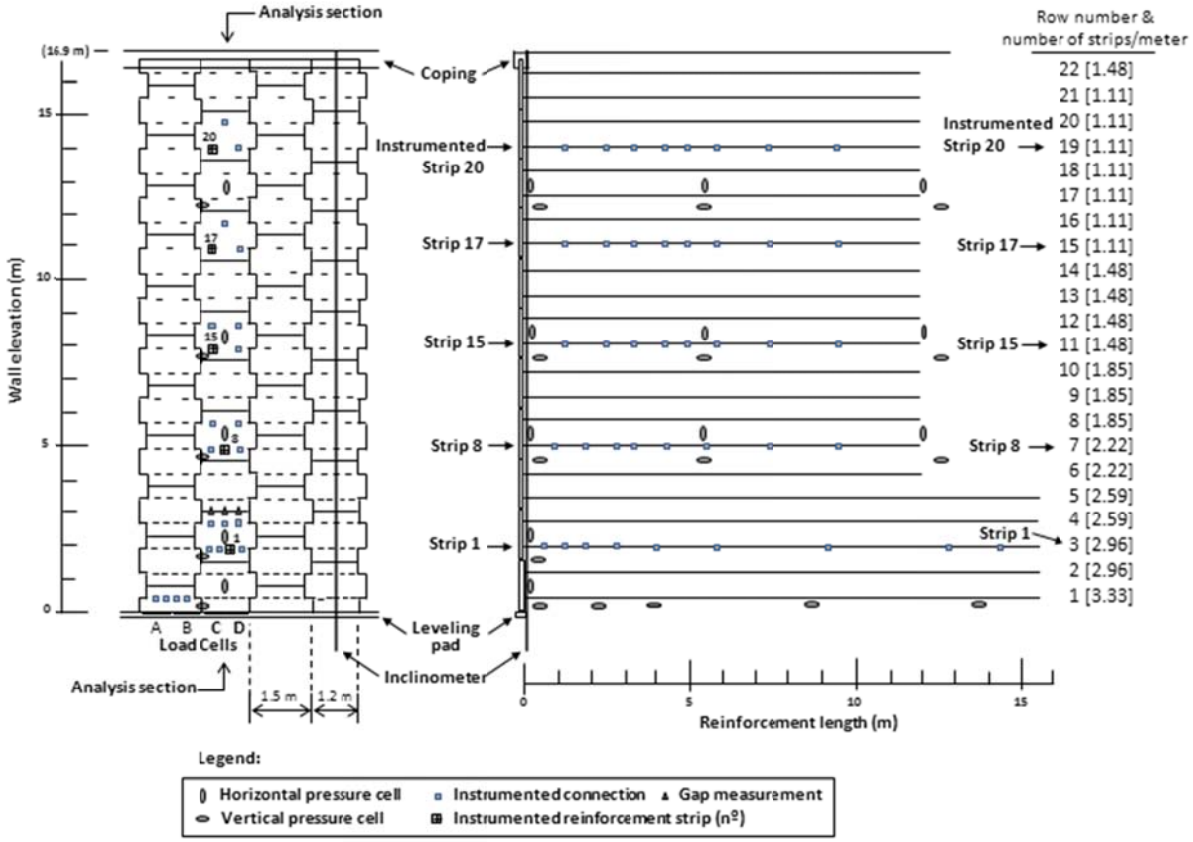

Figure 2.1: Elevation and cross-section views of instrumented wall (after Runser et al., 2001).

2.2. NUMERICAL MODELLING

2.2.1. General

The 2D PLAXIS (2008) finite element program was used to simulate the construction of the wall. The numerical finite element mesh is shown in Figure 2.2.

The wall facing was modeled as discrete panels of 1.5 m height. The panels and joints (bearing pads) were simulated using linear-elastic beam elements. The horizontal joint

thickness was 20 mm. The beam elements were connected through hinge contacts with zero rotational stiffness. This approach means that vertical and horizontal loads can be transmitted at the contact between each bearing pad and adjoining concrete panels but not bending moment. Hence, vertical compression of the panel joints (bearing pads) and rotation at each joint can occur.

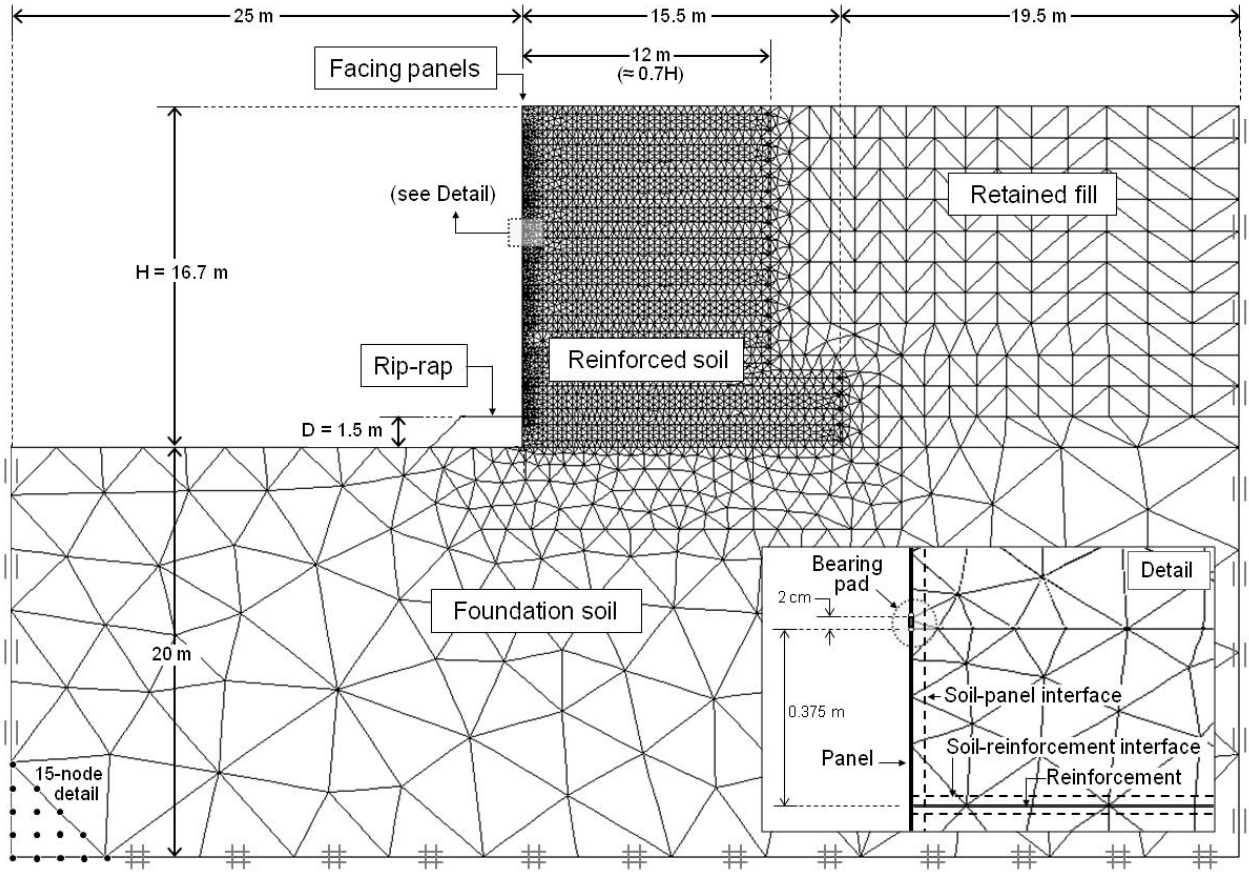

Figure 2.2: Numerical model and mesh details for 2D finite element model simulations of Minnow Creek Wall.

The soil zones were modeled using 15-noded triangular elements (total of 65155 nodes and 6854 elements). The element areas were reduced to 0.02 m^2 at facing-soil and soil-reinforcement interfaces and to 0.001 m^2 adjacent to the panel joints. For clarity, mesh refinement is not shown in the rip-rap fore slope. The mesh was constructed in 0.75 m-high lifts. Thinner lift heights were shown not to influence numerical outcomes. Properties of the compacted soil were inferred from conventional laboratory triaxial compression tests on compacted soil exhumed after the wall was completed and the soil specimens reconstituted to field density and moisture content. No further attempt was made to capture compaction effects such as using a transient uniform surface pressure at the top of each lift (e.g., Hatami

and Bathurst 2005, 2006; Huang et al., 2009). The influence of toe embedment on numerical predictions was examined by carrying out simulations with and without the rip-rap fore slope.

2.2.2. Material constitutive models and properties

The reinforcement strip layers in the wall were modeled as continuous sheet elements called "geogrid" elements in the PLAXIS manual. These elements were assigned a constant axial stiffness (*EA*) based on elastic modulus of the steel, strip cross-section area and number of strips per running length of wall (Figure 2.1 and Table 2.1). Hence, the layer stiffness for the 22 rows of steel strips varied from 44 to 133 MN/m in the simulations depending on the layer elevation. A very soft soil zone with dimensions of 15 cm by 15 cm and centered on the free end of each reinforcement element was included in the numerical mesh to ensure a zero axial load prediction at the ends of all reinforcement layers.

The material properties assumed for the precast concrete facing panels and the elastomeric bearing pads placed at horizontal joints between panels are shown in Table 2.3. The pads are used to prevent concrete-to-concrete contact by ensuring a minimum gap between panels as vertical load is transferred through the wall facing and to accommodate potential differential settlement and panel rotation.

Table 2.3. Facing panels and bearing pad properties:

Parameters	Panels		EPDM bearing pads [(a)]	
			$0 < \varepsilon < \varepsilon_{cr}$ [(b)]	$\varepsilon_{cr} < \varepsilon < 1$
Elastic modulus (MPa)	40000		6.4	96
Axial stiffness (MN/m)	5600		0.08	1.21
Bending stiffness (kNm^2/m)	9150		0.13	1.98
Poisson's ratio	0.15		0.45	
Linear weight (kN/m/m)	regular panel:	3.4	0.1	
	embedded panel:	0.2		
	coping panel:	9.9		

Notes: [(a)] EPDM = ethylene propylene diene monomer material (Neely 2005, Neely and Tan 2005, Choufani et al., 2011) with a plan area equal to 0.0085 m^2.
[(b)] ε_{cr} = from 0.45 to 0.55 (see Figure 2.3).

Laboratory compression data reported by Choufani et al. (2011) are plotted in Figure 2.3 assuming two pads per panel joint. The right-hand plot is the compression response deduced from gap measurements recorded during wall construction between the second and third panels. The stresses for the field case are due to self-weight of the panels plus down drag forces at the connections between the panels and steel reinforcement layers and interface shear between the panels and backfill soil. The stresses were estimated from the

measurements recorded by load cells (C + D) at the base of the wall (Figure 2.1) less the stress recorded after the first two panels located below the monitored gap were installed and the soil placed and compacted. This calculation is approximate and as a result the critical (break point) strain (ε_{cr}) may be over-estimated (i.e., stress values for the steep portion of the bi-linear approximation may be greater than shown). Based on available data the critical strain is judged to lie between 0.45 and 0.55. An average value of ε_{cr} = 0.5 was used in the numerical simulations.

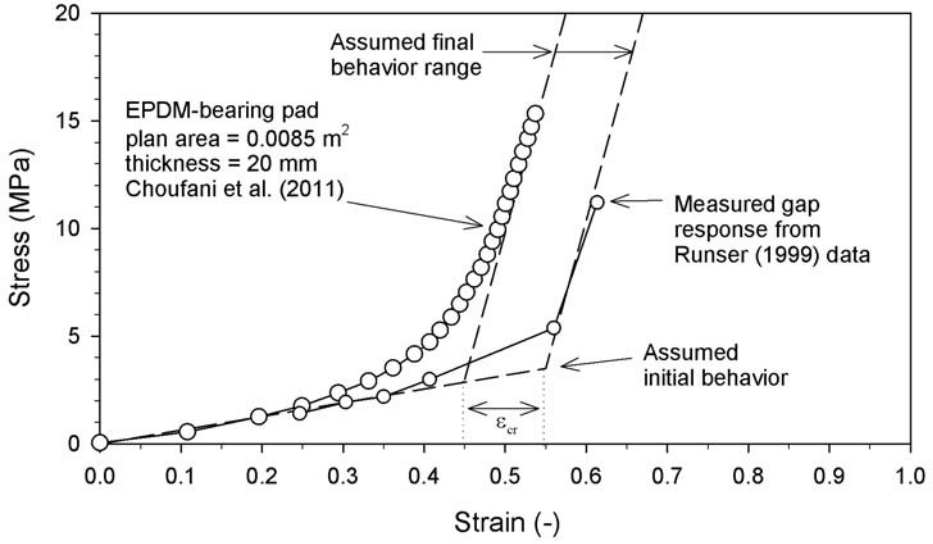

Figure 2.3: Stress-strain behavior of the bearing pads.

The reinforced soil and retained soil zones were modeled firstly as isotropic linear-elastic perfectly-plastic materials with the Mohr-Coulomb failure criterion (M-C model) and secondly using the non-linear hardening soil (HS) model available with the PLAXIS (2008) software package. The hardening model includes the Mohr-Coulomb failure criterion. The same M-C and HS models used in the current investigation and implemented in the PLAXIS software package have been used in a benchmark tied back excavation problem exercise with other FEM software packages (Carter et al., 2000). The stress-dependent stiffness of the soil in the HS model is described by a power law (parameter m) and parameter (R_f) that is the ratio of the asymptotic value of the shear strength and the ultimate deviatoric stress at failure. Other stiffness moduli are required ($E_{50}^{(ref)}$, $E_{oed}^{(ref)}$ and $E_{ur}^{(ref)}$). For brevity they are not described here and the reader is directed to the PLAXIS software manual for details (PLAXIS 2012). To simplify analyses the foundation soils were treated as a homogenous isotropic 20 m-deep layer with linear-elastic Mohr-Coulomb properties. Results of triaxial testing mentioned earlier are shown in Figure 2.4. Model parameters inferred from these tests are summarized in Table 2.4.

a) Reinforced soil:

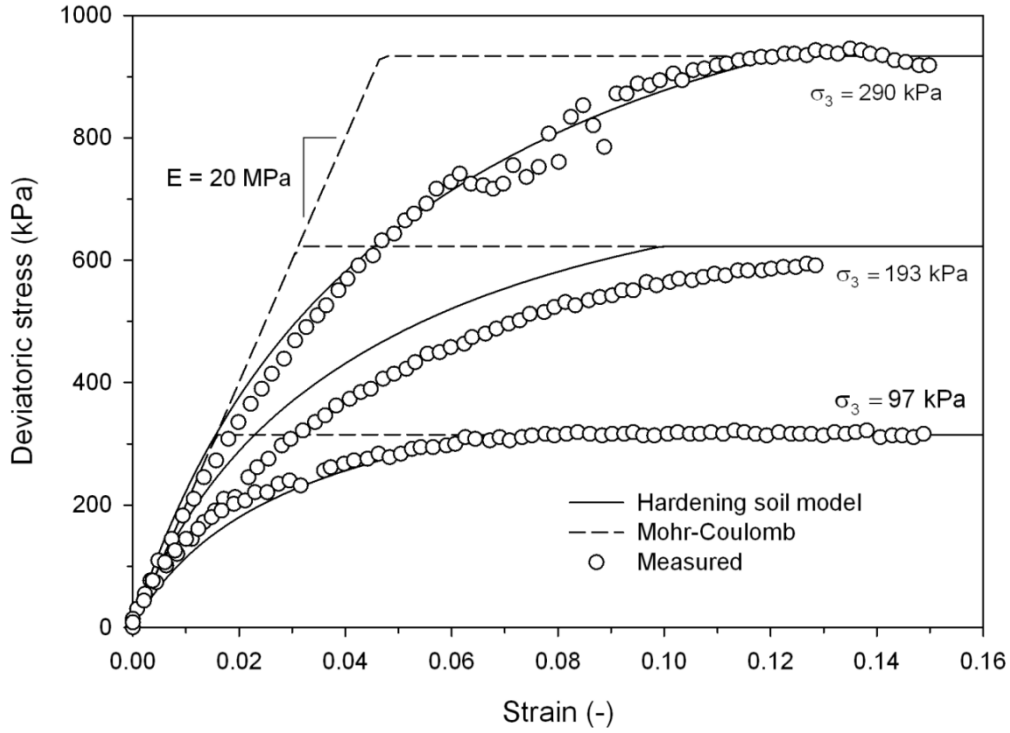

b) Retained soil:

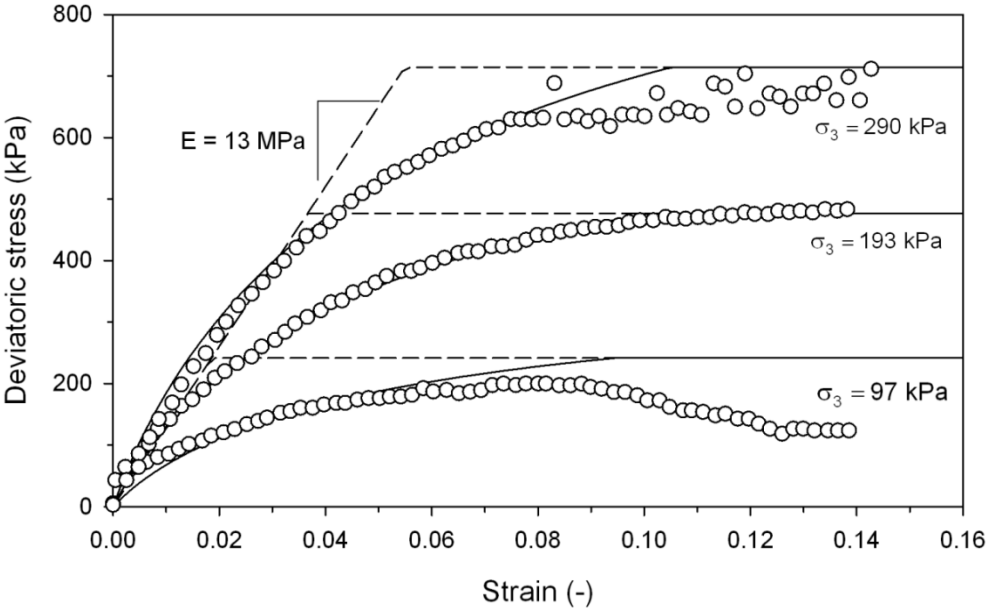

Figure 2.4: Measured and predicted stress-strain results from triaxial testing.

Table 2.4. Model soil properties:

Parameters	Reinforced soil ("B-Borrow")		Retained fill	Foundation
Unit weight, saturated (kN/m^3)	22.5		21.8	22.8
Unit weight, unsaturated (kN/m^3)	21.8		20.8	18.85
Cohesion (kPa)	1 [(a)]		1[(a)]	50
Plane strain peak friction angle, ϕ (degrees) [(b)]	44		41	45
Dilatancy angle, ψ (degrees) [(c)]	14		11	15
Mohr-Coulomb	< 1.0 m from facing [(d)]	> 1.0 m from facing		
Elastic modulus (MPa)	10	20	13	110
Poisson's ratio (-)	0.3		0.3	0.3
Hardening soil model	(m = 0.5 and R_f = 0.75)		(m = 0.9 and R_f = 0.9)	
E_{50}^{ref} (MPa)	3	10	5.5	n/a
E_{oed}^{ref} (MPa)	3	10	5.5	n/a
E_{ur}^{ref} (MPa)	9.2	30	16.6	n/a
Initial stiffness, E_i (MPa) [(e)]	4.8	20.8	18.1	n/a
Poisson's ratio (-)	0.2		0.2	n/a

Notes: [(a)] Non-zero cohesion value has been assumed for the numerical model to ensure numerical stability at very low confining pressure. The soil is assumed as a no-tension material (tension cut-off).

[(b)] The relationship between the friction angles from triaxial and plane strain testing (usually ϕ_{ps} from about 1.12 to 1.2 times ϕ_{tx}) can be found in references (e.g., Kulhawy and Mayne 1990).

[(c)] Assumed as $\psi = \phi - 30^o$.

[(d)] Area where less compaction energy was applied (Runser 1999). The elastic stiffness modulus varies from 0.5 to 0.31 times (α-ratio) the elastic stiffness modulus of the well-compacted soil for the Mohr-Coulomb and Hardening model cases, respectively.

[(e)] The initial stiffness is calculated as $E_i = 2E_{50} / (2 - R_f)$, (PLAXIS 2012) where E_{50} = 13 MPa (reinforced soil) and E_{50} = 10 MPa (retained fill) are the average of the secant modulus values at 50% of the height of the deviatoric stress at failure using the three stress-strain curves in Figure 2.4a and 2.4b. For the less stiff backfill zone at < 1.0 m from the facing there are no triaxial test data. E_i was calculated using the same equation and assuming $E_{50} = E_{50}^{ref}$ = 3 MPa.

The selection of a single-value elastic modulus for the linear-elastic Mohr-Coulomb model is problematic for granular soils that have stress-dependent stiffness. Not only does confining pressure vary with depth below the backfill surface, but there is possible attenuation of confining pressure close to the back of the wall facing due to the use of less compaction

energy immediately behind the facing and outward wall facing deformations. Hence, the choice of a single value of modulus for each soil type was based on a combination of fitting to the initial portion of the stress-strain curves in Figure 2.4 and ensuring that the selected values resulted in what was judged to be reasonably good agreement with predicted wall performance measures. The value of E was reduced by 50% for the soil zone located within 1 m of the back of the facing using the Mohr-Coulomb model in the FE parametric analyses. This assumption follows the approach adopted in previous Chapter 1 (as reported by Damians et al., 2013a) to capture the influence of reduced compaction energy close to the structure face using a walk-behind vibratory plate compactor (Runser 1999). The influence of magnitude of stiffness reduction of the reinforced soil zone within 1 m of the back of the wall face is explored quantitatively in the next section.

The approximations to the stress-strain curves from triaxial testing using both models are shown in Figure 2.4. The Mohr-Coulomb model with friction angle determined from axisymmetric loading is used to cap the hardening soil model curves. In numerical simulations, the triaxial friction angle was converted to a (larger) plane strain peak friction angle using $\phi_{ps} = 1.2\phi_{tx}$ (Kulhawy and Mayne 1990) to better reflect field boundary conditions.

Back-calculated coefficients of lateral earth pressures from earth pressure cells embedded in the reinforced soil gave values ranging from 0.2 to 3 with the highest values closest to the back of the facing (Runser et al., 2001). A single value of $K_o = 0.3$ was assumed in the numerical model during simulation of each lift placement. This value is in close agreement with the classical Jaky equation using the peak friction angles of the reinforced and retained soil zones. The elastic modulus of the foundation soil (E = 110 MPa) was selected by trial and error to match predicted toe settlement with measured values at the end of construction (i.e., 27 to 34 mm). The elastic modulus value falls within the range for dense sands and gravel reported by Bowles (1996).

PLAXIS "interface" elements were used to model strength and stiffness between the soil and concrete facing panels and between soil and the reinforcement strips. These elements include an interface reduction factor (R) which is the ratio of interface shear strength to shear strength of the surrounding soil (hereafter called the interface friction coefficient). The value of R for the concrete-soil interface can be calculated from measured facing loads as:

$$R = \frac{\sum \mathrm{F_v} / \sum F_h}{\tan \phi} \tag{2.1}$$

where: ΣF_v is the total vertical footing load measured at the bottom of the instrumented section minus the facing self-weight, ΣF_h is the total horizontal force against the back of the instrumented panels and, $\phi = \phi_{ps}$ is the peak plane strain friction angle of the soil. Back-calculated R values from data reported by Runser (1999) give values in the range 0.25 to 0.5. However, measured vertical forces at the wall toe include down drag forces developed at the

reinforcement strip connections and at the backfill-panel interface which means that these R values are too large. A reasonable assumption based on data reported in previous Chapter 1 is that down drag forces may account for about 40% of the footing vertical load not including self-weight of the panels. Hence, a reasonable range for *R* based on interface friction alone is 0.2 to 0.4. This range of values was used as a starting point in the FE analyses to follow.

Soil-reinforcement interaction was modeled using a value of $R = 0.3$ for the first meter of reinforcement length immediately behind the wall facing and assuming a perfect bond behavior (i.e., $R = 1$) over the remaining length. This latter value is consistent with measured pullout test data for ribbed steel strips and well compacted granular soils reported in the literature (Schlosser and Elias 1978; Miyata and Bathurst 2012b; Bathurst et al., 2011).

2.3. INITIAL MODEL CALIBRATION AND VERIFICATION

Quantitative numerical predictions of major performance features such as reinforcement loads and wall displacements can be expected to vary with choice of soil model and model input parameters as well as assumed problem geometry. As examples, wall behavior can be expected to be influenced by embedment depth at the toe of the wall, the value of soil-panel interface friction coefficient (R) and the ratio (α) of elastic modulus of the soil located within 1 m of the wall facing to that of the reinforced soil zone located at greater distance. The influence of ratio α on numerical outcomes is different depending on what soil model is used (i.e., Mohr-Coulomb or hardening soil model). To make fair comparisons regarding the effect of soil-panel interaction on predicted wall behavior, some equivalencies in the selection of parameters must be respected as described next.

If the Mohr-Coulomb model is used in the PLAXIS software, then the elastic shear modulus (G_i) of any interface varies with elastic shear modulus of the soil (G_{soil}) as:

$$G_i = R^2 G_{soil} \tag{2.2}$$

For the hardening soil model the equivalent interface shear stiffness is also a function of the elastic unload-reload modulus E_{ur}^{ref} and Poisson's ratio ν_u:

$$G_i^{(ref)} = R^2 G_{soil}^{(ref)} = R^2 \left(\frac{E_{ur}^{(ref)}}{2(1+\nu_u)} \right) \tag{2.3}$$

Assuming a default value of $\nu_u = 0.2$ leads to the following relationships:

$$\begin{cases} \text{if } R = 0.4 \rightarrow E_{ur}^{(ref)} = 15G_i \\ \text{if } R = 0.3 \rightarrow E_{ur}^{(ref)} = 27G_i \\ \text{if } R = 0.2 \rightarrow E_{ur}^{(ref)} = 60G_i \end{cases} \tag{2.4}$$

Reducing the elastic modulus of the reinforced soil by 50% (α = 0.5) using the Mohr-Coulomb model is equivalent to α = 0.31 using the hardening soil model if both methods are to give the same vertical toe load. Once E_{ur} is fixed, the default values for the other elastic modulus values (e.g., Table 2.4) can be calculated as:

$$E_{50}^{(ref)} \approx E_{oed}^{(ref)} \approx \frac{1}{3} E_{ur}^{(ref)} \tag{2.5}$$

The selected hardening soil model parameters can be seen to give a generally good fit to the triaxial compression curves in Figure 2.4. In addition, the initial small strain stiffness of the curves is similar for both models. Figure 2.5 shows the results of sensitivity analyses using a range of soil and interface input parameter values. The simulations identified as the reference base cases can be seen to closely match the measured vertical toe force with R = 0.25. These simulations were carried out using the soil parameters in Table 2.4. The figure shows that ignoring the 1.5 m-depth of toe embedment over-estimated the measured toe load. The additional cases can be seen to give reasonable agreement with measured toe load but these simulations required reinforced soil modulus values that were judged to be excessively low (i.e., E = 5 MPa and $E_{ur}^{(ref)}$ = 4.6 MPa). Based on these results the following parameters were used hereafter: R = 0.25, α = 0.5 and 0.31 using the Mohr-Coulomb and hardening soil models, respectively.

In this study, a desk top computer with an Intel Core 2 Duo Pa8600 (2.40 GHz) central processor unit was used. The computer solved a typical problem in about 20 minutes for the Mohr-Coulomb cases, and 70 minutes for the hardening soil model cases.

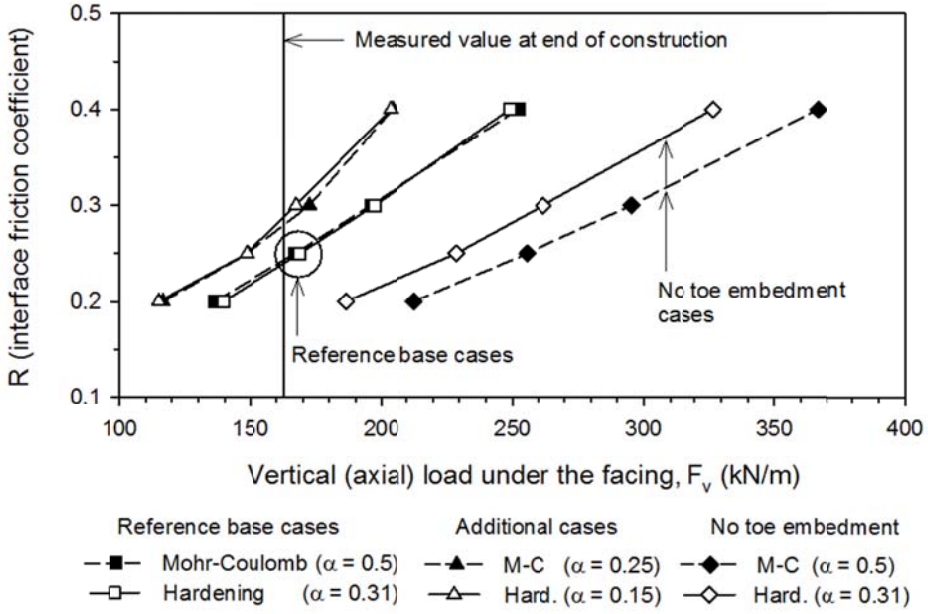

Figure 2.5: Influence of stiffness reduction parameter (α), interface friction coefficient (R), soil model type and toe embedment condition on predicted vertical toe load (F_v).

2.4. RESULTS OF NUMERICAL SIMULATIONS

In this section predictions of major performance features of the Minnow Creek Wall are compared to measured results. Figure 2.6 shows that predicted vertical toe loads increase non-linearly with height of wall construction. Previously selected values of α and R together with the 1.5 m-depth of toe embedment case (first row of panels embedded) can be seen to give the overall best agreement with measured values. The plot shows that the measured and predicted values are greater than the self-weight of the facing column consistent with the development of down drag forces described earlier. The predicted and measured vertical load factor (total vertical toe load/facing column self-weight) at the end of construction is about 2.8 regardless of the choice of soil model. This value falls in the range of previously reported values for steel strip reinforced soil walls reported in Chapter 1 (Damians et al., 2013a).

Figure 2.7 shows measured and predicted gap measurements in the wall facing during construction. The bilinear gap compression model used to model the bearing pads can be seen to capture the bilinear gap response at the monitored location between panels. As expected because the gap location is above the depth of toe embedment, the simulations with and without toe embedment give similar results for the same soil model type. There is a detectable difference in predicted gap values depending on soil model type up to a wall height of 8 m with visually better agreement using the M-C model. However, from a practical point of view the differences are judged to be negligible.

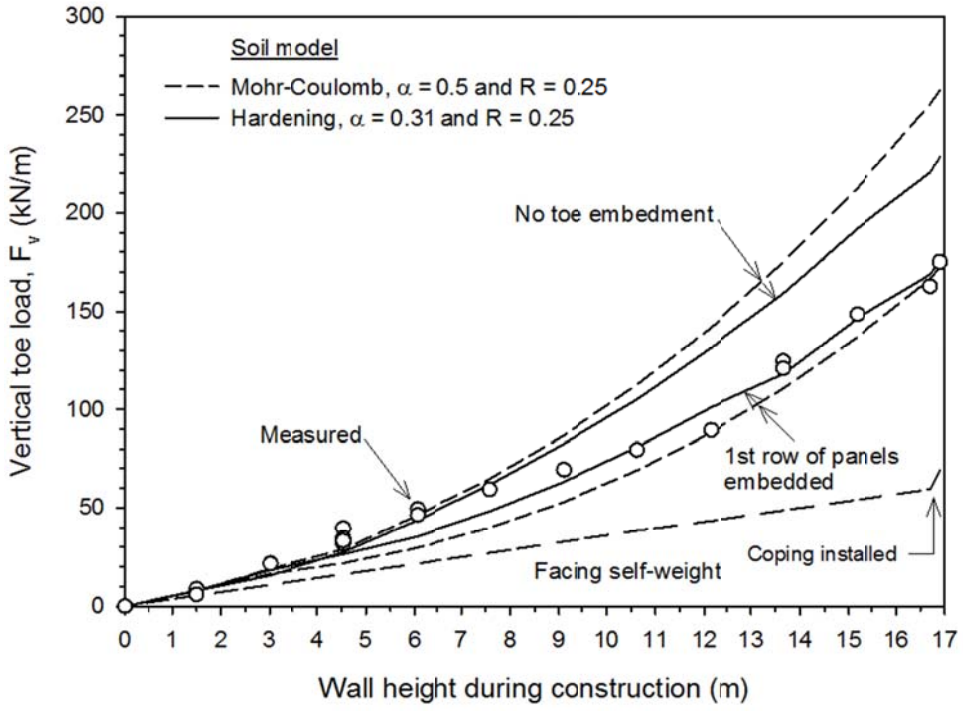

Figure 2.6: Measured and predicted vertical toe loads during wall construction.

The development of tensile load in the connections for panel 6 is shown in Figure 2.8. Both soil model approaches capture the trend of increasing connection loads with construction height. The Mohr-Coulomb model is most accurate at end of construction case for the bottom layer and the hardening soil model is most accurate for the top layer of reinforcement strips. However, it is likely that actual loads are sensitive to field construction technique and level of care exercised in placing the panels, and placement and compaction of the soil behind the panels.

Figure 2.9 shows predicted and measured steel strip tensile loads at the connections and maximum loads located within the reinforced soil zone at the end of construction. The predicted results are judged to be in good agreement with measured results regardless of soil model type. The predicted maximum load in the bottommost instrumented steel strip is more accurate using the embedment case. Comparison of the numerical predictions for embedded and non-embedded cases shows that the influence of embedment on maximum tensile loads is restricted to an elevation of about 3 m above the toe which is twice the embedment depth of 1.5 m.

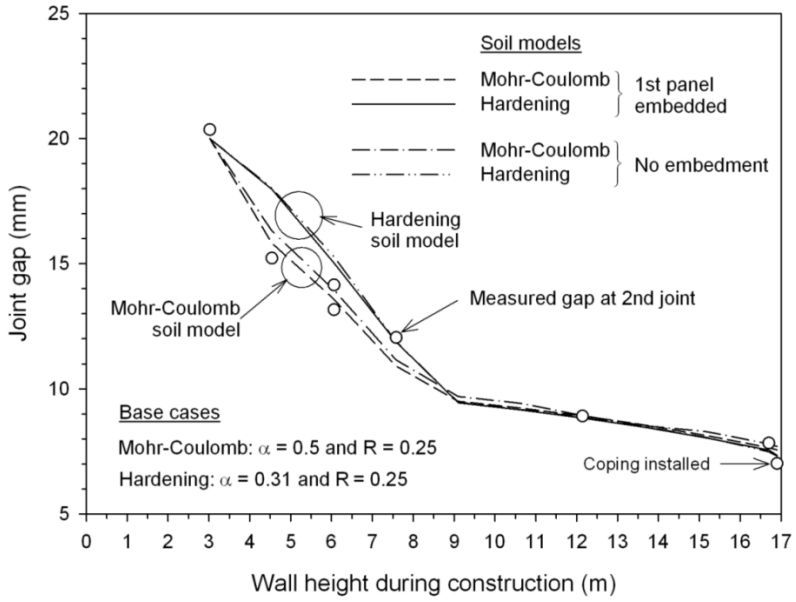

Figure 2.7: Measured and predicted gap measurement between second and third concrete facing panels.

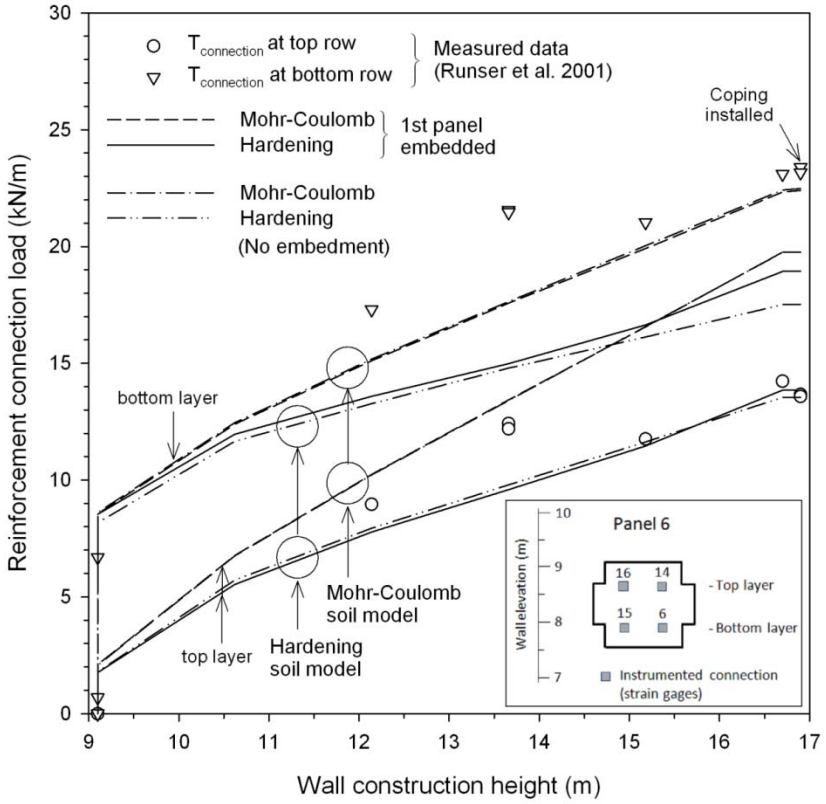

Figure 2.8: Measured and predicted connection loads in panel 6 during construction.

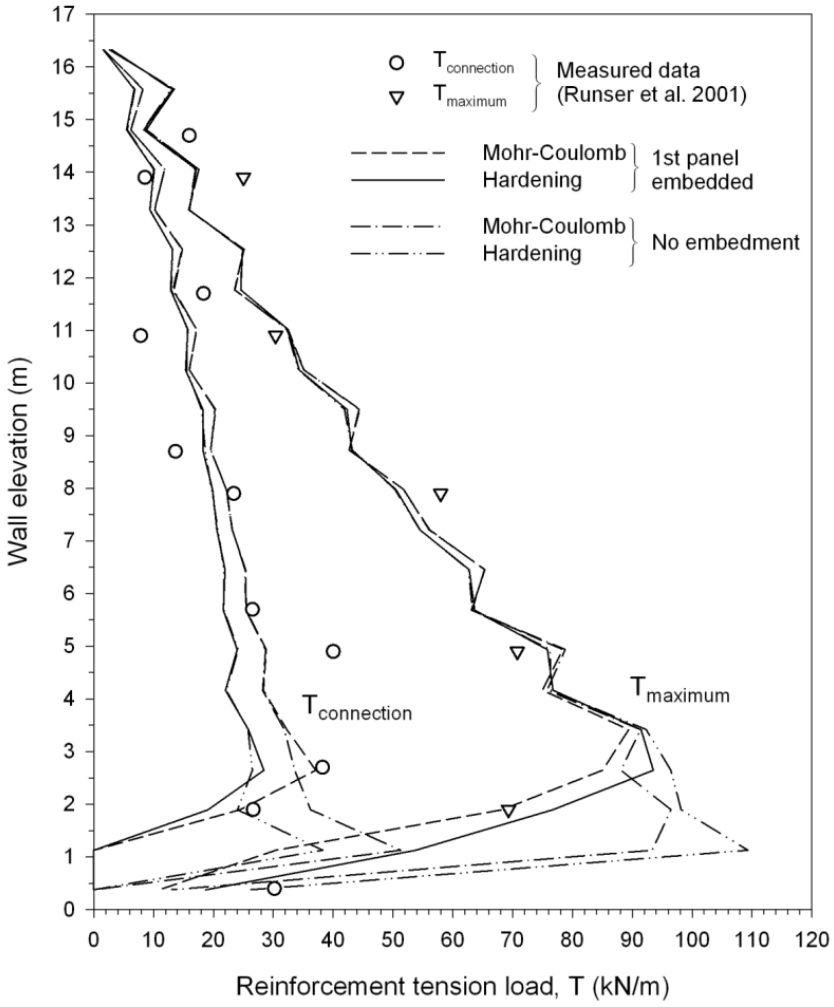

Figure 2.9: Measure and predicted steel strip tensile loads at the connections and maximum loads located within the reinforced soil zone at the end of construction.

The magnitude and distribution of measured tensile loads along selected instrumented strips in the wall are plotted in Figure 2.10. The plots show that predicted numerical loads are generally larger using the Mohr-Coulomb soil model but both models predict decreasing tensile load toward the free end of the strip commencing at about 2 m from the facing consistent with the trend in the measured data. The visual impression is that the hardening soil model does better capturing the magnitude and distribution of measured reinforcement loads for the two lowest strips in the figure. Similar to the observations made for the previous figure, both models give more accurate estimates of measured loads in the bottommost instrumented strip when simulations are carried out assuming a 1.5 m-depth of wall embedment.

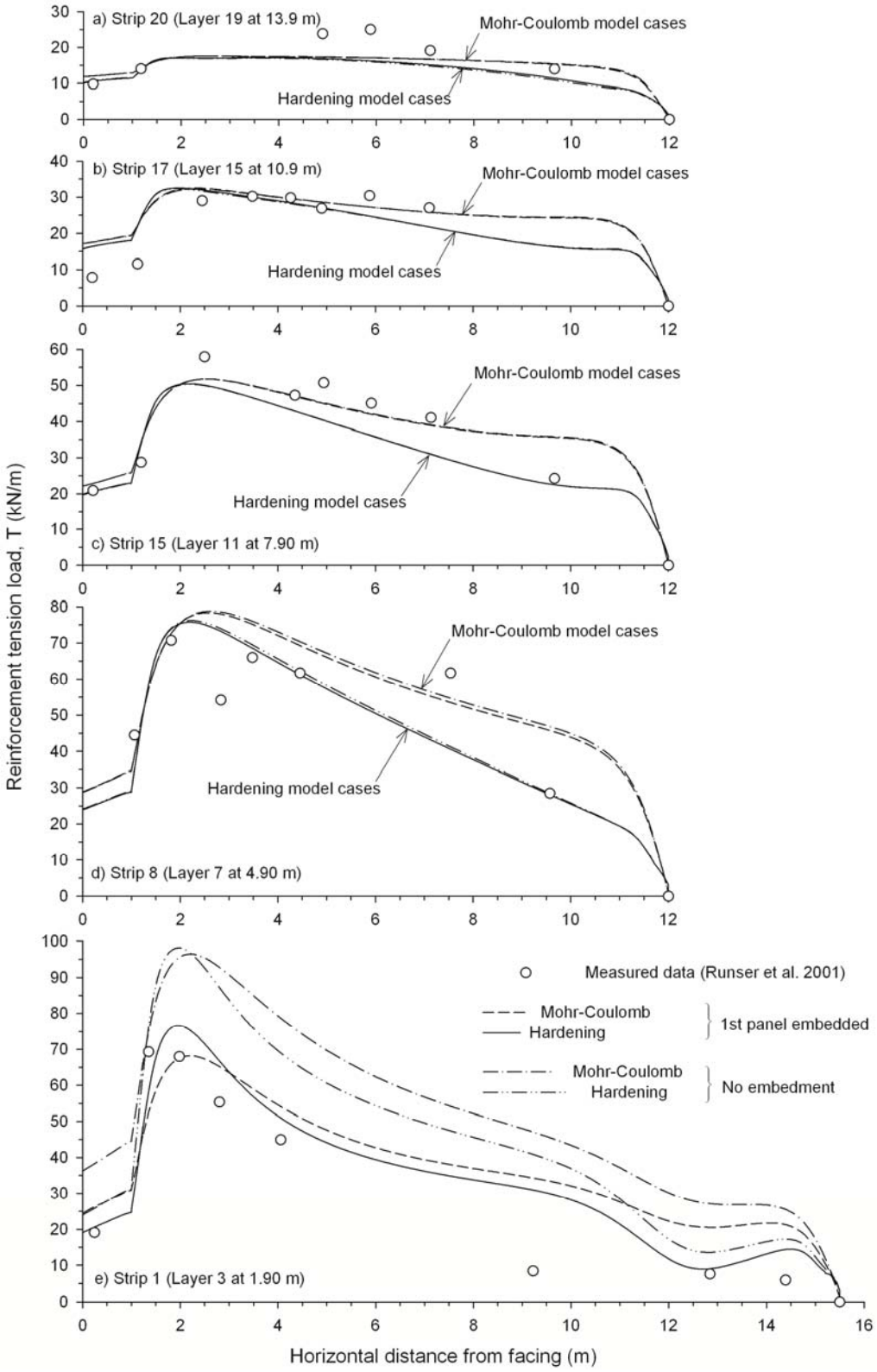

Figure 2.10: Measured and predicted tensile loads in instrumented steel strips at end of construction.

Predicted (numerical) results for horizontal pressures acting against the facing panels are plotted in Figure 2.11. The measured results are taken from earth pressure cells embedded in

the back of the panels and inferred from connection loads. Runser et al. (2001) reported that the values deduced from the connection loads were more reliable. Numerical results for the embedded toe case give larger pressures against the back of the wall for each soil model case which may be expected if the toe is constrained by the fore slope. In general, it appears that the hardening model is better able to capture the pressure distribution at the bottom of the wall for the embedded bottom panel case. Between elevations of 5 m and 10 m it can be argued that the Mohr-Coulomb model does better.

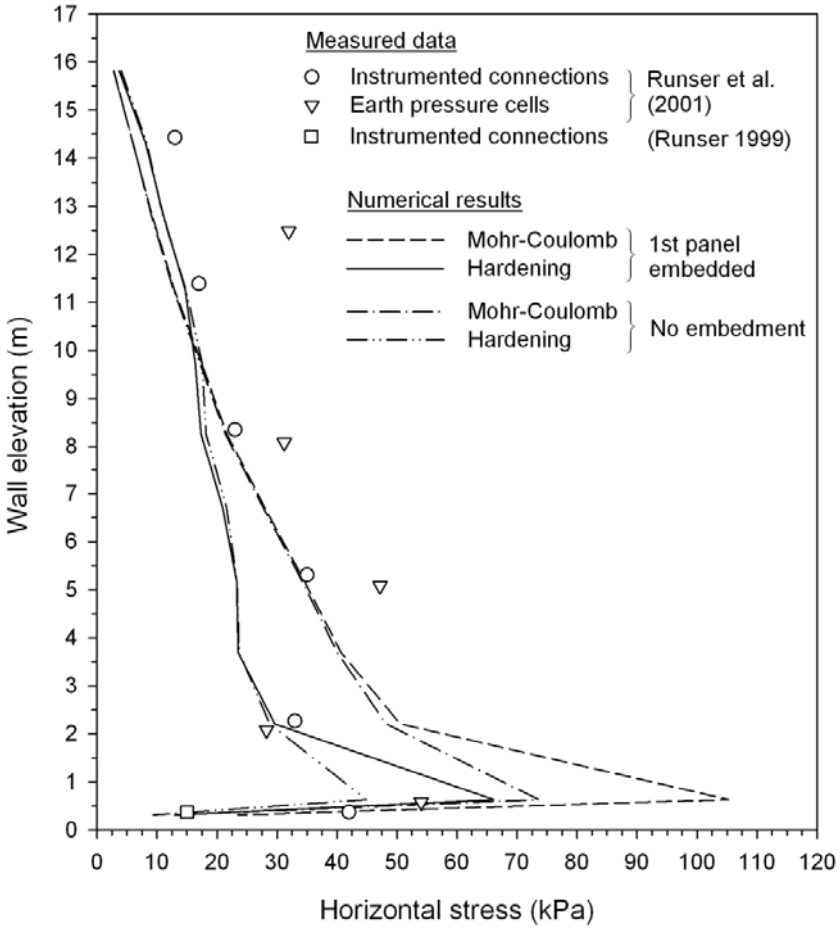

Figure 2.11: Horizontal earth pressures acting against the back of the wall facing.

Figure 2.12 shows measured and predicted horizontal earth pressures within the soil backfill. The differences in numerical results are largest at the base of the wall consistent with comments made regarding the data in Figure 2.11. Over most of the wall height there is no practical difference in horizontal earth pressure predictions based on soil model type or wall toe condition. There is a visually detectable increase in over-prediction of horizontal earth pressures with depth in Figure 2.12a. Excluding the measurement outlier in Figure 2.12b, the

numerical results in this figure are seen to be in very good agreement with measured values where these measured data are available.

a) within reinforced soil zone:

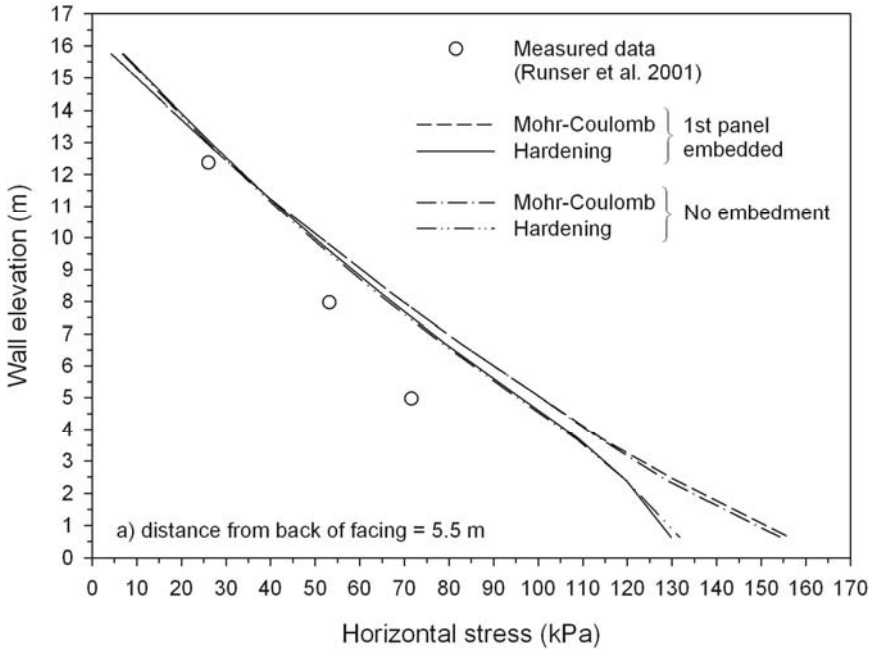

b) at back of reinforced soil zone:

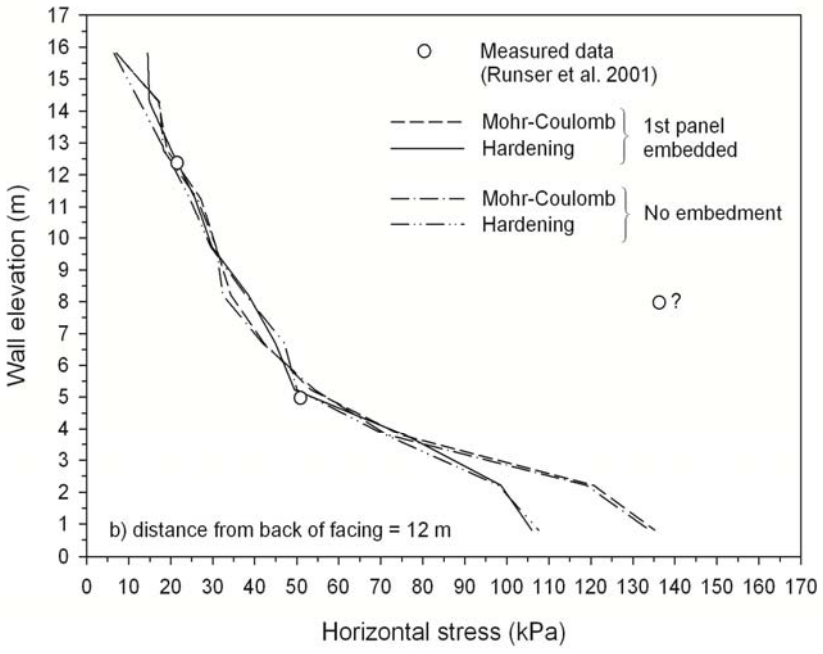

Figure 2.12: Horizontal pressures acting within and at back of reinforced soil zone.

The distributions of measured vertical earth pressure at four different elevations in the wall are shown in Figure 2.13. In each plot there is a reference pressure computed as the product of soil unit weight and depth below the backfill surface ($\sigma_v = \gamma z$). The measured data show a consistent reduction in vertical earth pressure immediately behind the facing column. This is consistent with the notion of hanging up of the soil at the reinforcement connections and wall panel-soil interface shear transfer leading to down drag loads on the facing panels as discussed earlier. In the bottommost plot where the number of earth pressure cells is greater, there is a local increase in measured earth pressure at a distance of 2 m from the back of the facing. This may be due to local arching between the soil and the facing panels. A similar pattern of reduced vertical earth pressure behind the facing followed by a local increase in pressure has been recorded for instrumented hard-faced reinforced soil walls built on competent (rigid) foundations (Bathurst and Benjamin 1990; Tajiri et al., 1996; Huang et al., 2009). The plots in Figure 2.13 show that, regardless of soil constitutive model and toe condition adopted in the numerical simulations, all numerical results are qualitatively and quantitatively similar. Most importantly, the models captured the relatively large and rapid changes in earth pressure in the vicinity of the back of the wall face.

The target alignment of the finished wall face was vertical (Runser 1999) and this is the datum for the final surveyed wall face profile plotted in Figure 2.14. The as-built profile shows that the maximum outward displacement is about 170 mm but there are obvious bulges in the final alignment. These out-of-alignment deformations are the result of the contractor attempting to correct for construction-related misalignment and replacement of some panels during construction (Runser 1999). Clearly, it is not possible to predict in advance misalignments of this type and the consequential effects on the final wall alignment. The numerical simulation predictions superimposed on Figure 2.14 are the result of idealized vertical placement of each panel on top of the underlying unit. The numerical results which are independent of construction-related deformations show that the top-most panels will rotate inward at the top of the wall as a result of net outward wall deformations that occur at lower elevations. Perhaps, if the contractor had not readjusted the wall facing alignment during construction, the final wall profile would have been smoother similar to the trend in the numerical results shown in the figure. Regardless of which soil model is used the influence of wall embedment on end-of-construction wall profile disappears above the bottom-most panel but the hardening model gives about a factor of three times the maximum out-of alignment as the Mohr-Coulomb soil model. The reason for this can be ascribed to the non-linear stress-strain curve in the hardening model which results in a softer soil response.

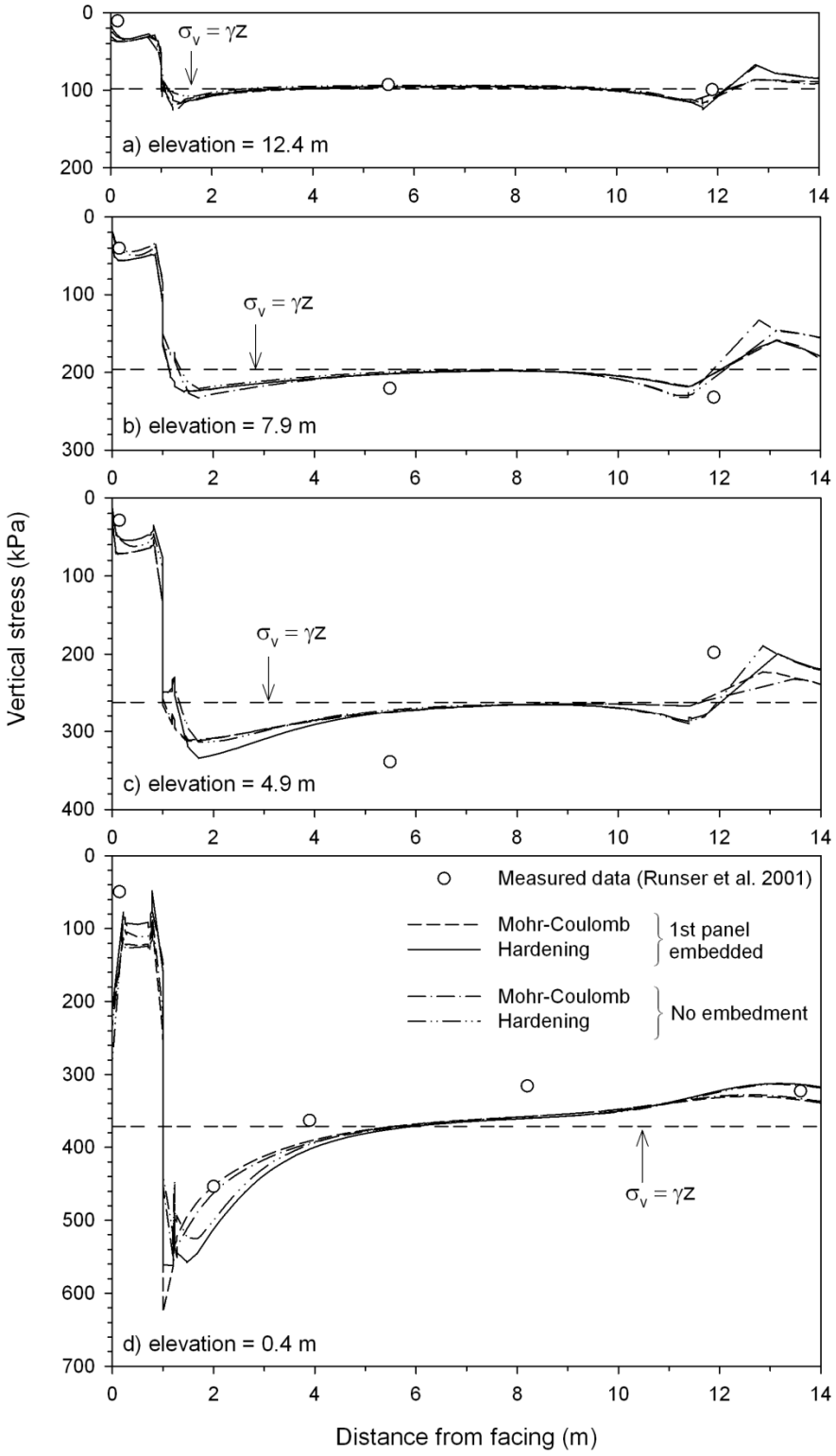

Figure 2.13: Vertical earth pressures at different elevations and distances from the back of the wall facing.

2.5. ADDITIONAL RESULTS

While not shown here, numerical results revealed that soil plasticity using both soil models was not achieved in the reinforced soil zone with the exception of the small soft zone introduced at the end of the reinforcement layers to artificially ensure that the reinforcement loads were zero at these locations, and at the interface between the wall facing panels and the reinforced soil. This is consistent with the expectation of the wall designers who designed the wall for working stress conditions.

The numerical results presented thus far have been compared to measured data. The simulation results are encouraging in this regard and give confidence that the numerical model developed for this study can be used to investigate other performance features for which physical measurements are not available.

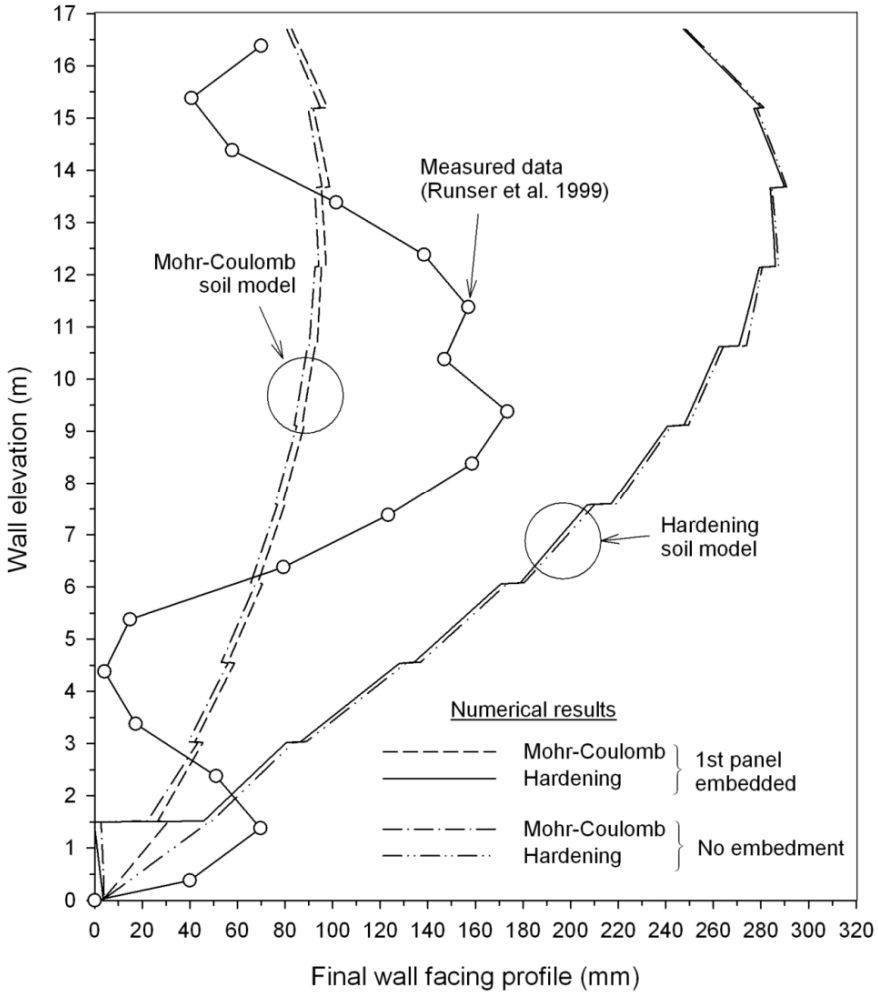

Figure 2.14: Final wall profile from vertical.

2.5.1. Vertical loads contribution under facing

The heavy dashed line in Figure 2.15 shows vertical panel load due to self-weight starting at the top of the wall. This plot is easily computed knowing the panel thickness and unit weight. The other three groups of data are the total vertical load along the height of the wall plus the contributions to vertical load from panel-soil interface friction and connection down drag loads. Recall that the total measured load at the bottom of the wall shown in Figure 2.15 was used to calibrate model interface friction parameters (e.g., Figure 2.5). Figure 2.15 illustrates that the vertical loads acting through the height of the wall are always greater than the self-weight of the panels due to panel-soil interface friction and connection down drag forces. In these simulations the contribution of connection down drag loads was greater than the contribution due to panel-soil friction. From a practical point of view the choice of soil model is judged not to have large influence on the distribution of total and component load contributions. However, the effect of lower panel embedment does have a large influence on the toe load as shown in Figure 2.15 and discussed earlier in the Chapter. Plots of the type shown in this figure can be used to select the size, number and compressibility of the bearing pads that are placed between the panels to ensure that a minimum gap is preserved at the horizontal joint between panels (see Damians et al., 2013a).

2.5.2. Effect of the bearing pad stiffness

The effect of the bearing pad stiffness is analyzed with assuming two HDPE bearing pad pieces installed at facing panel joints. The equivalent material properties for HDPE are shown in Table 2.5, with parameter values fitting the stress-strain curve already previously shown in previous Chapter (see Figure 1.6). As shown, different stiffness were assumed with regards to the strain compression degree, simplifying the bearing pad compression curve with three different trends roughly approximated by a critical strain of about 10-15% (first to second stiffness division) and about 40-50% (second to third-last stiffness division). Deeper explanation of this trilinear behaviour simplification is furtherly explained in next Chapter 3.

This new HDPE comparison case was only considered within Mohr-Coulomb soil model cases assuming first toe-panel embedment. Figure 2.16 presents the gap evolution during wall height construction. As expected, different panel joint behaviour was obtained due to the third different stiffness. Greater joint gap opening was reached during wall construction due to the higher stiffness assumed. A sudden loss of gap opening was obtained due to the second lower stiffness. The final gap at the end of construction was greater in HDPE than in EPDM bearing pads case.

Most of other results including reinforcement tensile loads were found to be very similar between previous EPDM and current HDPE bearing pads case. Figure 2.17 shows results of related to horizontal facing displacements and vertical facing loads generated between both panel joint stiffness cases. As observed, minor differences were obtained in both results (slightly lower facing displacement and vertical facing load results in HDPE cases).

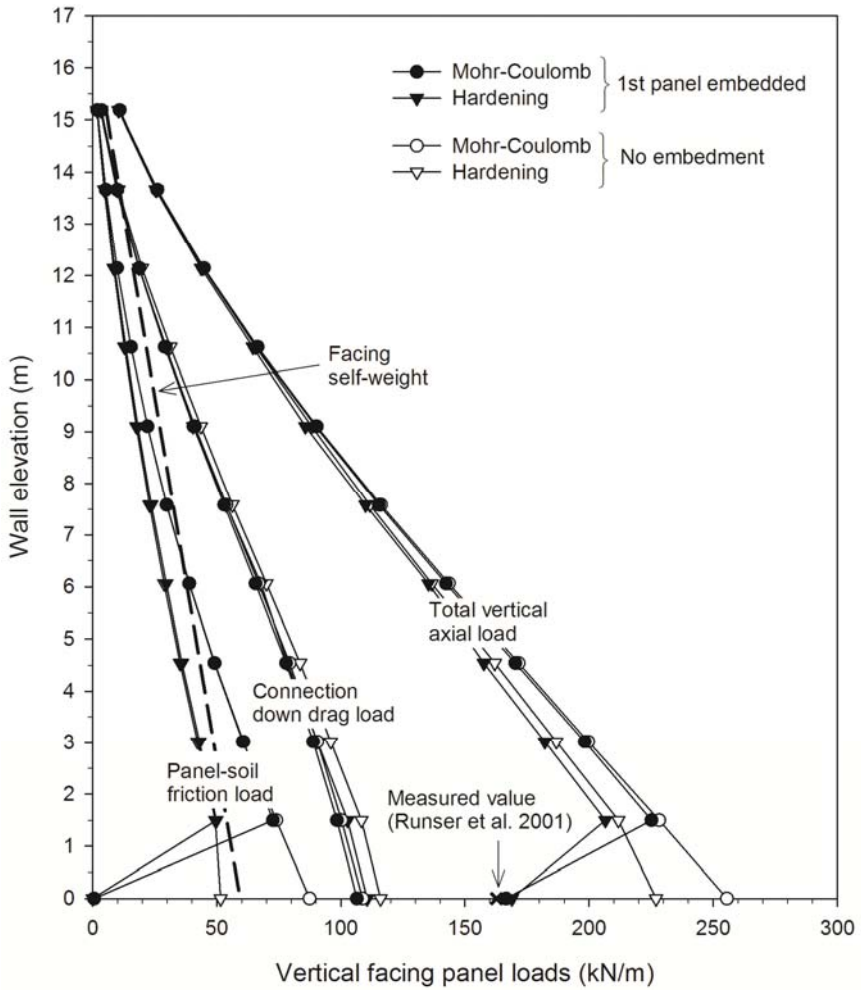

Figure 2.15: Total and component contributions to vertical load in concrete panel facing at end of construction.

Table 2.5. HDPE bearing pad properties:

Parameters	HDPE bearing pads [a]		
	$0 < \varepsilon < \varepsilon_{cr,1}$ [b]	$\varepsilon_{cr,1} < \varepsilon < \varepsilon_{cr,2}$ [c]	$\varepsilon_{cr,2} < \varepsilon < 1$
Elastic modulus (MPa)	85	6.4	85
Axial stiffness (MN/m)	1.21	0.08	1.21
Bending stiffness (kNm^2/m)	1.98	0.13	1.98
Poisson's ratio		0.40	
Linear weight (kN/m/m)		0.1	

Notes: [a] HDPE = high-density polyethylene with a plan area equal to 0.0085 m^2 and 20 mm-thick.

[b] $\varepsilon_{cr,1}$ correspond to the first stress-strain slope change point, from about 10% to 15% strain rate (see Figure 1.6).

[c] $\varepsilon_{cr,2}$ correspond to the second stress-strain slope change point, from about 40% to 50% strain (see Figure 1.6).

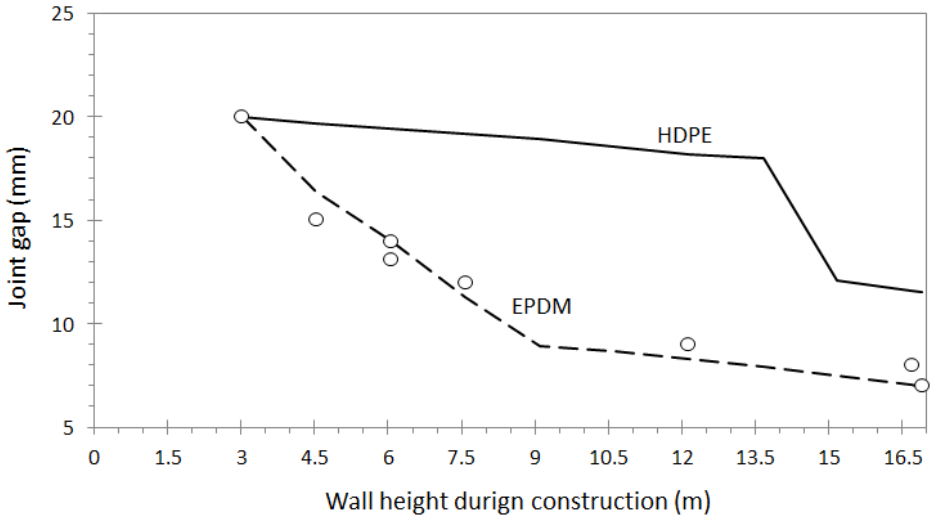

Figure 2.16: Measured and predicted gap measurement between second and third concrete facing panels. comparison between EDPM and HDPE bearing pads model results. Note: Mohr-Coulomb soil model and wall toe embedment condition cases.

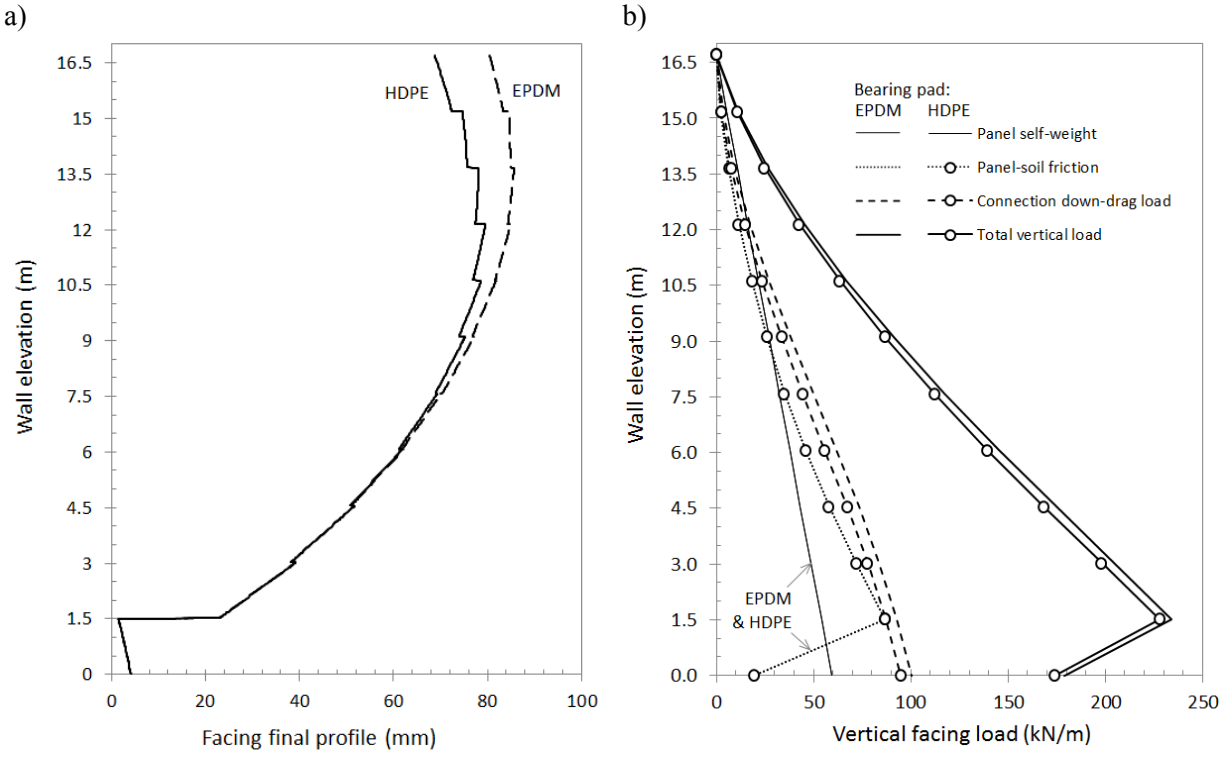

Figure 2.17: Final wall profile (a) and to vertical load in concrete panel facing at end of construction (b): comparison between EDPM and HDPE bearing pads model results. Note: Mohr-Coulomb soil model and wall toe embedment condition cases.

2.5.3. Reinforcement loads comparison with respect to the current design methods

Figures 2.18.a-b compare the normalized coefficient of earth pressure (the ratio between the coefficients of earth pressure of the reinforced soil mass and the active one of the soil, K_r / K_a), which are obtained from the reported data and the numerical models, to the ones obtained by current design methods: Simplified Method (from AASTHO 2010) if steel strips are assumed, and Coherent Gravity Method (from BS-8006, BSI 2010) if steel reinforcement is assumed (no distinction is made between metallic reinforcement material types in BS-8006). The K_r / K_a ratio allows, first, to fix the coefficient of earth pressure of the reinforced soil mass (K_r), and then, to obtain the maximum tensile load in the reinforcements (T_{max}) in units of force per unit running length of wall using the equation as follows:

$$T_{max} = S_v(K_r\sigma_v) \tag{2.6}$$

Where: S_v is the reinforcement spacing and σ_v is the vertical earth pressure acting at the reinforcement layer located at a determined depth (note that $K_r\sigma_v$ corresponds to the equivalent horizontal earth pressure, which is acting at the same reinforcement layer). The coefficient of earth pressure K_r is expected to vary linearly with depth below the top of the wall. This variation is different according to the used standard design:

- If Simplified Method (AASTHO 2010) is assumed, for metal strip reinforcements (the same reinforcement type of the report case analyzed in this Chapter), K_r varies from 1.7 to 1.2K_a at the top of the wall to a depth of 6 m, and remains constant thereafter (K_r / K_a = 1.2).

- If Coherent Gravity Method (BS-8006, BSI 2010) is assumed, for steel reinforcement (there is no distinction between steel reinforcement types) K_r varies from K_0 (coefficient of earth pressure at rest: $K_0 = 1 - \sin\phi$, which is equal to 1.68 if $\phi = 38º = \phi_{tx}$, and 1.71 if $\phi = 44º = \phi_{ps}$ in the reinforced soil) at the top of the wall, to K_a value at a depth of 6 m, and then, the ratio K_r / K_a results constant (equal to 1).

The K_r / K_a relation obtained from the instrumentation data can have a significant variation if the friction angle of the soil is assumed under triaxial (ϕ_{tx} = 38º) or plane-strain (ϕ_{ps} = 44º) conditions, so both assumptions are shown using different markers. About this, already noted from Figure 2.9, the numerical model has good responses according to the reported data when ϕ_{ps} is assumed, and the results are generally coincident in both soil models. The embedment seems to have no significant effect in these results, with an exception at the low part of the wall (but with not relevant divergence).

From the obtained results can be observed that the predicted values from the standard design methodologies are, in general, significantly lower if T_{max} is analyzed, but quite accurate if T_{con} is analyzed. Current standard design methods (Simplified and Coherent Gravity methods)

assume that both tensile loads have the same value ($T_{max} = T_{con}$). This assumption seems not to be in agreement with respect to the obtained results from the instrumentation neither from the numerical analysis (Figure 2.9). Both current design methods considered have similar resulting value if depths greater than 6 meters (1.2 and 1.0, respectively). If the T_{con} data is analyzed (Figure 2.18.b), the resulting values from the standards design seem to predict fine the K_r / K_a reported and numerically-obtained values, but there is a largest increasing tendency of the normalized coefficient of earth pressure at the top zone. This means underestimated tensile loads values from the current design methods: a maximum value of about $2.5K_a$ from the numerical model when both standard design curves specify a maximum value of about $1.7K_a$ at the top (assuming $\phi_{soil} = \phi_{ps} = 44º$ in the Coherent Gravity Method). This also can be noted with even more divergence of results if T_{max} is analyzed (Figure 2.18.a). This incremental values of the K_r/K_a ratio at the upper zone has been also noted and reported by Allen et al., 2004; Bathurst et al., 2008b, 2009 and 2011, and Huang et al., 2012. According to that and after back-calculations of many instrumented steel strip reinforced soil walls, a modification of the design curves proposed by Huang et al. (2012) and Bathurst et al. (2009) for steel strips reinforcement were also considered to complement the comparison. Then, if T_{con} is analyzed, can be noted how the design curve proposed in Huang et al. (2012) is in a good agreement with respect to the reported and numerically-obtained results. If T_{max} data is now observed, the design curve proposed in Bathurst et al. (2009) gives a good response for depths less than 6 meters, and this proposed curve is the most accurate according the instrumented values, but for depths greater than 6 meters all of them are out of the design curves (the two standards and both proposed modifications) anyway.

2.5.4. Safety factor analysis: Toe embedment and rip-rap effect comparisons

After the comparison done over the exposed results, and appreciating the good response of the numerical model developed, safety analyses will be exposed. Safety analyzes in PLAXIS are based on the method of "ϕ-c reduction", resulting in a state of failure (PLAXIS 2008). Basically, the "ϕ-c reduction" is a type of calculation that reduce successively the strength parameters tanϕ and c (cohesion) of the soils and interfaces which conform the model until failure occurs. These analyzes allow, first, to determine how expected far of failure is the structure studied, and second, to predict the localization of the greatest displacements which generate the instability (deformed mesh), and consequent and more probable failure surface. This information can be used to develop better and accurate structural elements and materials, in terms of optimization, and also, for example, to take care about the constructions procedures trying to not promote actions that can derive to increase the instability.

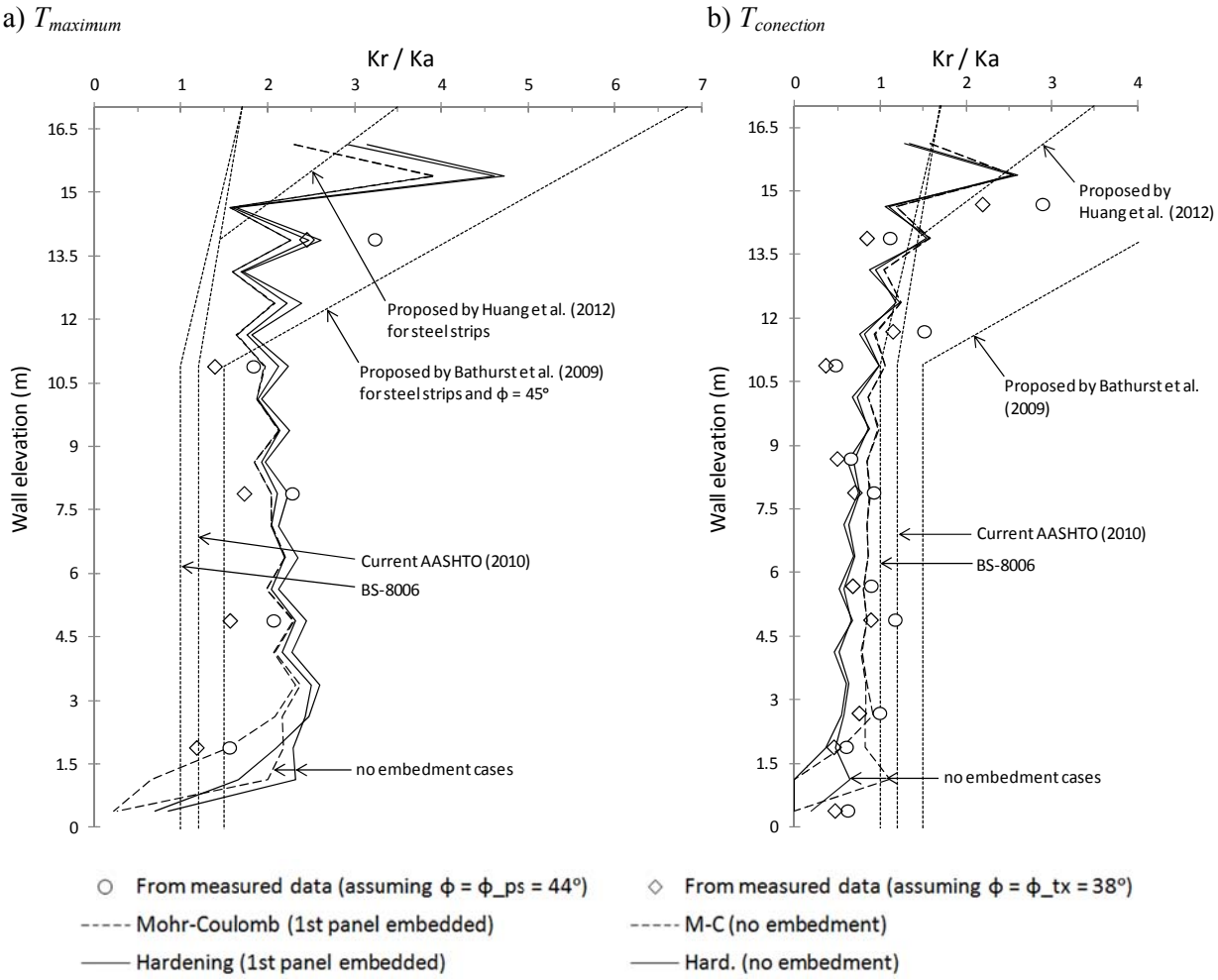

Figure 2.18: Reinforcement loads comparison with design criteria: T_{max} (a) and T_{con} (b).

Figures 2.19 and 2.20 present the results of the "ϕ-c reduction" analyses for the three geometry assumptions available, which are: with no-embedment; with the first panel embedded, and also assuming the rip-rap installation over the embedment. As it has been already explained, a rip-rap covering 4.5 m of wall face was installed after wall construction and instrumentation reported data of the Minow Creek wall. The figures show the shear shadings of the incremental deviatoric strains resulting from the "ϕ-c reduction" analyses. The shear shadings representation illustrates the locations of the failure surfaces generation of the model (related to the failure surfaces generation into the soil of the cases performed). Two ranges of strains are shown do to make clear the resulting zones where more shear strains concentration occur, that are, from 0 to 10 %-deformation (or greater, but limiting the black hue at 0.1 strain values), and from 0 to 1 %-deformation. As a result to this, can be shown more clearly the areas of higher concentration of relative shear stresses, which corresponds to the zones where failure is more probable to take place. It can be observed three zones where the accumulation of shear strains is greater and higher: the generation of a vertical failure surface between the reinforced soil and the retained fill, caused by the different settlements of

both soil types. The shear strains developed into the retained fill from the end of the reinforcements, with a failure surface slope caused by the active earth pressure area of the retained fill. Finally, a clear base-failure at the toe of the structure, which connects to the end of the first layer of reinforcement and the previous failure shape mentioned (active pressure into the retaining fill). All the failure shapes decrease of intensity (black hue) if there is a presence of material at the toe of the face (first panel embedded and rip-rap installation assumptions). As can be noted from the figures, both models (Mohr-Coulomb and Hardening) have similar responses of the shear shadings generation, and similar resulting values of the safe factor for each case analyzed. The rip-rap has the practical function to provide protection and more structural stability. As can be noted from the safe factor resulting values exposed in Figures 2.19 and 2.20, this is a good assumption about the functionality of the rip-rap: the safe factor increases about 8-9.5 % with respect to the no-embedment case, and about 5-6 % with respect to the first panel embedded case. These results are according to the external stability (overturning and sliding) expected to be developed when there is material at the toe of the structure and in front of the wall (area susceptible to develop passive earth pressure), and also the global stability if there is an increase of the weight at the same location.

2.6. DISCUSSION AND CONCLUSIONS

The Minnow Creek Wall structure is a unique instrumented steel strip reinforced soil wall case study because of the comprehensive measurements that were taken to record a wide range of wall performance features (Runser et al., 2001). To the best of the author' knowledge, the current study reports the first attempt to compare measured wall responses to the results of finite element method (FEM) simulation of this structure. The finite element modeling was carried out using a commercially available and widely distributed software package (PLAXIS) and simple constitutive models for the soil and material interfaces.

An advantage of the Minnow Creek case study is that there are project-specific data available such as vertical gap measurements at the panel joints and vertical toe load measurements that were used to refine the choice of parameters used in the horizontal panel joint and wall-soil interface models. For example, without this data it would not have been possible to detect and fit a model to the bilinear stress-strain behavior at the horizontal joint between panels. The availability of wall settlement measurements was valuable because it allowed the author to back-calculate an equivalent single-value elastic modulus for the stiff foundation zone in the finite element mesh.

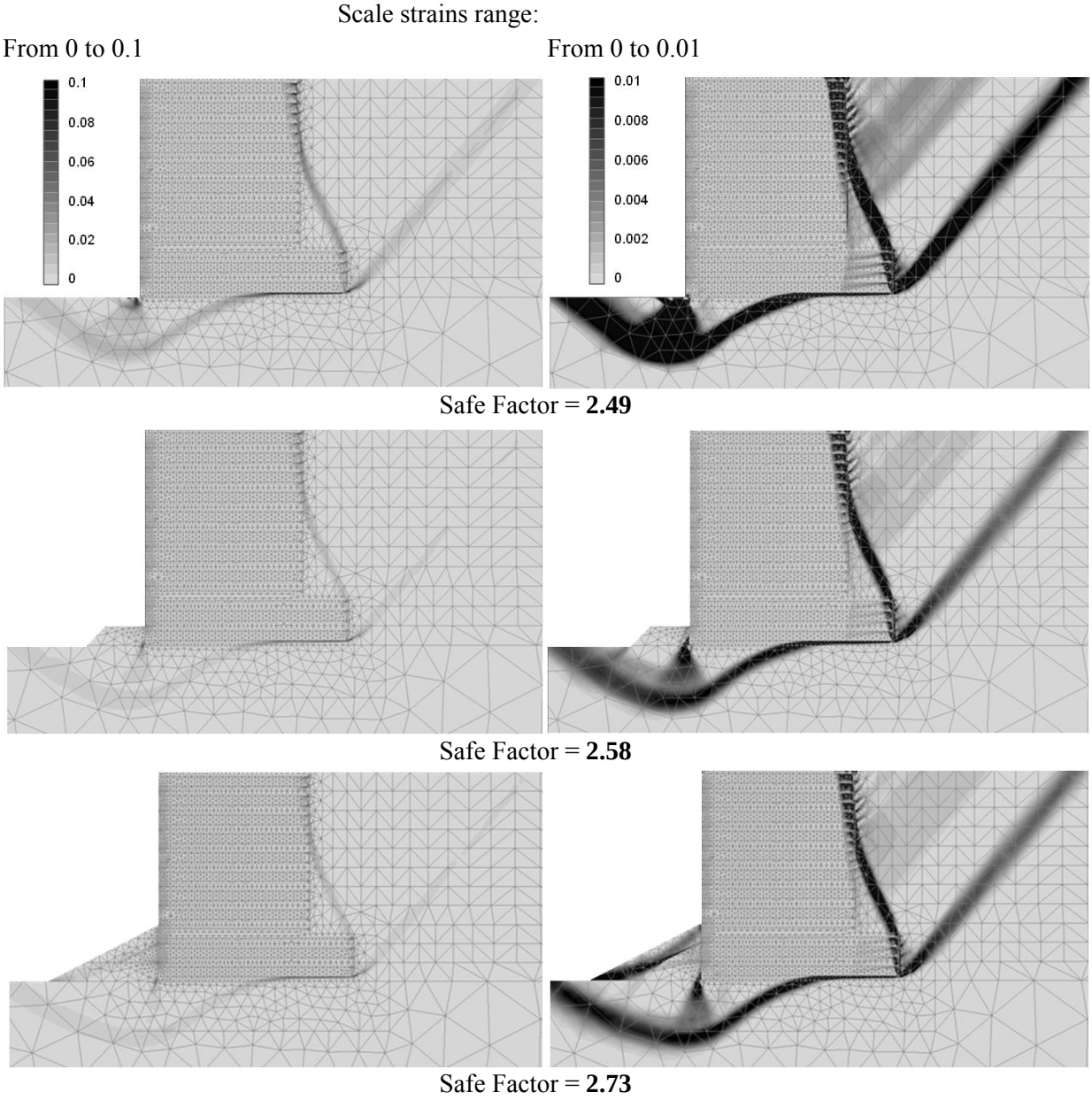

Figure 2.19: Shear shadings of the incremental deviatoric strains of Mohr-Coulomb cases: no-embedment (top), first panel embedded (central), and rip-rap installation (bottom).

While there are detectable differences in numerical outcomes in most cases using the linear-elastic plastic Mohr-Coulomb (M-C) soil model and the hardening soil (HS) model in the PLAXIS software, there is often encouraging satisfactory agreement between physical and numerically predicted results using either soil model. Exceptions are predictions of wall lateral facing deformations and connection loads at the end of construction which were very sensitive to the type of soil model adopted.

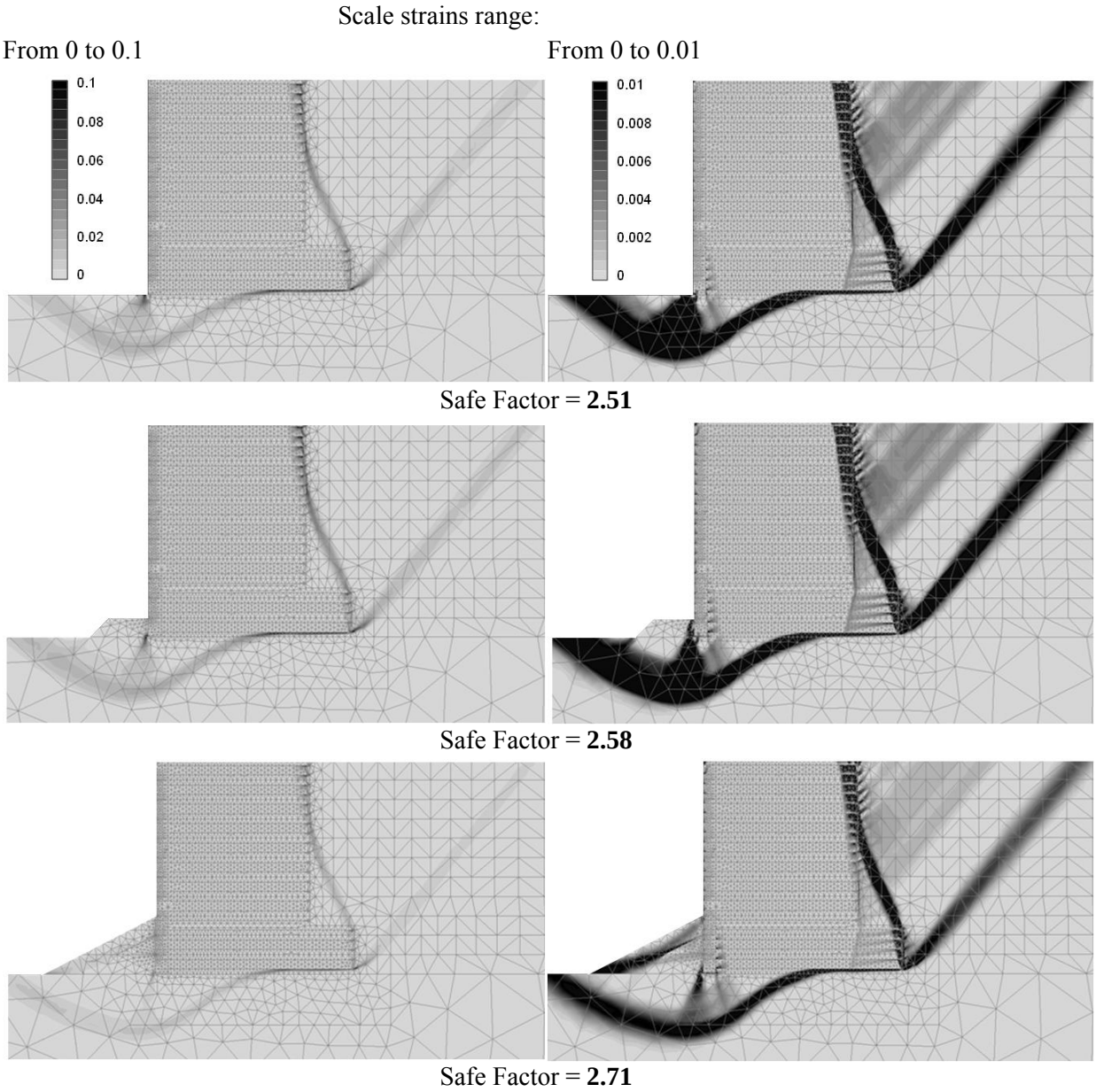

Figure 2.20: Shear shadings of the incremental deviatoric strains of Hardening model cases: no-embedment (top), first panel embedded (central), and rip-rap installation (bottom).

The choice of 1.5 m-depth of toe embedment or no embedment was seen to influence wall responses at or close to the bottom of the wall. In most cases numerical simulation of wall embedment improved the agreement between predicted responses and measured values but only in the vicinity of the embedded wall toe. A necessary requirement to achieve numerical outcomes that were judged to be in satisfactory agreement with measured results was the use of a less stiff column of soil extending 1 m behind the facing. This approach is consistent with the use of smaller compaction equipment within 1 m of the back of the Minnow Creek

Wall. This is recommended construction practice in the field for these types of structures (Berg et al., 2009).

A disadvantage of the HS model was that numerical simulations took 2 to 5 times longer to execute compared to the M-C model. Numerical stability and convergence were also more sensitive to level of mesh discretization. A disadvantage of the M-C model is that the selection of a single-value for elastic modulus of the foundation soil would have been problematic had wall settlement data not been available to back-calculate a suitable value.

The lessons learned above and generally satisfactory agreement between numerical and measured results give confidence that commercial FEM software packages can be a useful analysis and design tool for steel reinforced soil wall structures provided that care is taken in the selection of input parameters. Examples of recent FEM and finite difference modeling of more complex project-specific tiered steel strip walls have been reported by Linquist (2008) and Studlein et al. (2010), respectively.

In addition to being a valuable tool to optimize future project-specific designs, the FEM models developed as part of this investigation can be used to carry out parametric analyses to investigate in a systematic manner the influence of a wider range of input parameters on wall performance (e.g., other soil backfill materials, foundation compressibility, metallic reinforcement types and arrangement, and wall heights). An example is the work presented in previous Chapter (Damians et al., 2013a). Numerical results can also be used to fill-in the data gaps in the instrumented field wall literature. The combined physical and numerical data can then be used to verify current or recently proposed closed-form (analytical) solutions for the prediction of reinforcement load and pullout resistance for metallic reinforced soil walls under operational (working stress) conditions (e.g., Bathurst et al., 2008a; Allen et al., 2004; Miyata and Bathurst 2012a,b).

CHAPTER 3

VERTICAL FACING PANEL-JOINT GAP ANALYSIS FOR STEEL-REINFORCED SOIL WALLS [1]

3.1. INTRODUCTION

3.1.1. General approach

Steel reinforced soil walls constructed with steel strips, bar mats or steel ladders that are attached to steel-reinforced concrete panels are a mature technology. The design focus in guidance documents used by geotechnical engineers is most often on the internal and external stability of the gravity mass formed by the facing panels and reinforced soil zone (e.g., AASHTO 2014). However, the facing column is an important structural component of these systems. It must be designed to carry vertical loads that are greater than the self-weight of the panels. As presented in Chapter 1, Damians et al. (2013a) collected data from instrumented steel reinforced soil walls and found that the ratio of measured vertical load to panel self-weight (load factor) ranged from about 2 to 5. These additional vertical loads are the result of downdrag forces generated by backfill soil-panel interface shear due to relative settlement of the backfill plus parasitic downward loads generated at the connections between the steel soil reinforcement elements and the back of the facing (Figure 1). The relative stiffness of the backfill soil and the horizontal joint (bearing pad) stiffness will influence the magnitude of downdrag loads acting at the wall face and connections. If vertical downdrag loads are excessive and/or joint stiffness is too low, then the panels can come into contact leading to spalling and/or failure of the concrete panels. Documented examples of these types of failures are given in the Chapter 1. While panel facing damage due to loss of gap space is visually detectable it does not typically threaten the overall stability of the structure. For this reason when it does occur, it is ranked as moderately significant based on a post-construction inspection and performance assessment protocol developed in the USA (Gerber 2012) even though wall appearance may be unsatisfactory to the observer.

[1] Chapter based on Damians, I.P., Bathurst, R.J., Josa, A. and Lloret, A.; 2015. Vertical facing panel-joint gap analysis for steel-reinforced soil walls. ASCE International Journal of Geomechanics. 10.1061/(ASCE)GM.1943-5622.0000632, 04015103.

In the earlier related study (Chapter 1), numerical parametric analysis were carried out to investigate the influence of joint compressibility, reinforced soil stiffness and foundation stiffness on vertical panel loads and gap compression using the case of a single wall of height H=16.7 m (Damians et al., 2013a). The parameters varied were joint axial stiffness (compressibility due to the number and type (stiffness) of the bearing pads), backfill soil and foundation stiffness. The numerical modelling was carried out using the program PLAXIS (2008) together with simple linear elastic-plastic constitutive models for the component materials. The same finite element modeling package with the same constitutive models for the component materials and interfaces has been used to satisfactorily reproduce the behavior of an instrumented 16.7 m-high steel strip reinforced soil wall (see Chapter 2, as Damians et al., 2015). Lessons learned regarding the use of program PLAXIS to model reinforced soil walls with discontinuous reinforcement layers can be found in the papers by Yu et al. (2015a, b).

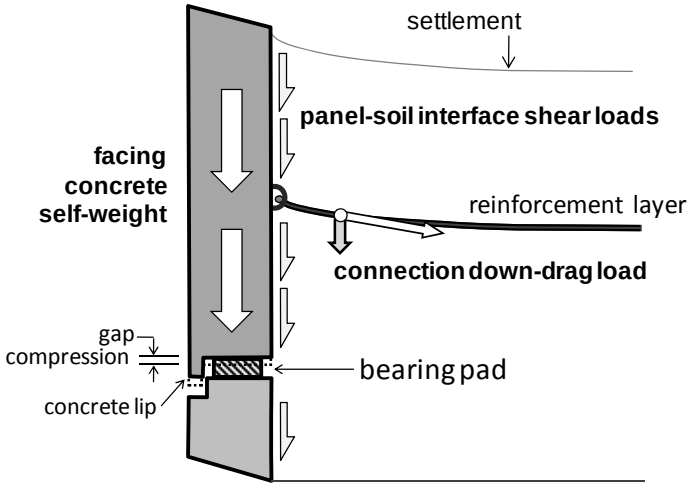

Figure 3.1: Vertical load in concrete panel wall face and gap compression. Note: Some panel systems have a lip at the back and front of the panel joint.

The numerical simulation results reported in Chapter 1 (Damians et al., 2013a) also confirmed physical measurements mentioned earlier that the magnitude of the vertical load between panels was always greater than the panel self-weight above the joint. The ratio of vertical load to panel self-weight (load factor) ranged from about 2 to 7 depending on the relative joint stiffness and the relative stiffness of the backfill soil and the foundation soil in their numerical simulations. The numerical simulation results for H = 16.7 m and interface friction coefficient R = 0.3 were shown to be consistent with computed load factors from field measurements in the range of about 2 to 5 for joint stiffness values of about 0.1 to 1.1 MPa/m.

Chapter 1 is an important start to identify issues related to joint compressibility and design, and to demonstrate the influence of wall joint compressibility and stiffness of the backfill soil

and foundation on vertical loads developed in the concrete panel facing units of steel reinforced soil walls. However, this earlier work was limited to a single wall height and simple constitutive models and assumptions for the component materials (e.g. linear elastic models with Mohr Coulomb failure criterion for the soil and linear elastic reinforcement). Furthermore, numerical outcomes were restricted to the bottom (most critical) joint without reporting the behavior of the horizontal joints along the entire height of the wall. Questions remain regarding possible differences in the quantitative results and qualitative trends reported in this earlier study with respect to other wall heights. To answer these questions, numerical simulation of walls with height H = 6, 12, 18 and 24 m were carried out and their performance summarized. In addition, the influence of constitutive model type for the backfill soil and load-compression behavior of the bearing pads is also explored in more detail.

3.1.2. Bearing pads

A detailed explanation of the role of the polymeric bearing pads that are placed at the horizontal joints between the concrete panels in steel reinforced soil walls can be found in the Chapter 1 (Damians et al., 2013a). A brief summary of the important points is repeated here for completeness.

The primary functions of bearing pads are to act as spacers to: 1) transfer vertical load between the concrete facing panels; 2) accommodate possible differential settlements between the backfill and the facing; and, 3) prevent contact between the panels. In the USA a minimum gap of thickness of 12 mm is recommended after the wall is constructed (Berg et al., 2009). In the UK the recommended minimum gap thickness is 1/150 of the panel height (BSI BS8006 2010). Hence, for a panel height of 1.5 m (the case in this study) the minimum gap thickness at end of construction is 10 mm. Clearly, to meet these performance criteria the number of bearing pads (typically a minimum of two), stiffness (compressibility) and thickness of the bearing pads (typically 20 – 25 mm) are of primary importance. The most common bearing pad materials are EPDM (ethylene propylene diene monomer) and HDPE (high density polyethylene). Measurements of gap closure have been reported in the literature. Finlay (1978) reported a maximum closure of 10 mm for a 6.3 m-high section of wall and Choufani et al. (2011) reported 20 mm of gap closure for a 20 m-high wall constructed with 25 mm-thick bearing pads.

As semi-flexible facing structure, reinforced soil walls using partial height precast concrete facing panels require compressible bearing devices in the horizontal joints between vertically-contiguous panels. The bearing pads serve as a spacer during the assembly of the structure. With ensuring a certain joint gap during wall life, bearing pads allows to ease the water drainage and avoid hydrostatical loads from backfill against the facing. From a structural point of view, the main functions of bearing pads are to transfer the vertical loads on the facing and to accommodate possible differential settlements between the backfill and the facing (becoming semi-flexible), with avoiding contact between panels.

Bearing pads have compressibility behaviour under loading and allow movement between panels during compression and settlement of the reinforced backfill. Their compressibility needs therefore to be consistent and in correspondence with the compressibility of the retained backfill (which can depend also to the foundation compressibility). The stiffness of the bearing pads should be such that, once the soil settlement has occurred and the structure is already under working stress conditions, the deformed pad geometry leaves an opened gap of at least 5 mm to prevent the contact between panels (Berg et al., 2009).

The material and particular shape of the bearing pads can vary according to the reinforced-soil structure company or particular system requirements. The most common materials used as bearing pad are EPDM (ethylene propylene diene monomer) and HDPE (high density polyethylene). Typically, the bearing pad pieces have a nominal thickness of about 20 – 25 mm, which defines the initial joint-gap between facing panels and may be increased for tall walls at bottom joint locations (Choufani et al., 2011). Their contact area will depend of the particular piece's shape used (i.e., massive, but also waffle or grooved to optimize reaching the appropriate stress-strain behavior). At least two pieces of pads are installed under each panel, but the actual number (or sizing area) depends on the wall height and soil quality (i.e., backfill/foundation particular compressibility scenario which can derive to a huge relative displacement between backfill and facing). The number of bearing pad pieces placed per panel joint should be increased with regards to the depth location (referenced to the top of wall). Alternatively, a fixed amount of two pieces can be assumed to all facing heights, but with using bearing pads with increased length at deeper locations.

3.1.3. Relative soil-facing displacements

As explained in previous numerical analysis presented in Damians et al. (2013a and 2014), the relative displacement between the backfill and the facing (which mainly controls the shear facing loads) is a function of the backfill, foundation, and bearing pad stiffness. This displacement can be generated because the backfill settles due to its compressibility (caused, for example, by poor compaction procedures during construction or the presence of too many fines and consolidation processes, as habitual options), because the foundation settles and generates a vertical displacement of the entire backfill soil mass, or both. During construction, each top-surface backfill-settlement does not appear because each step settle is absorbed by the next step with backfilling to the required layer level (i.e., reinforcements installed horizontally). Thus, accumulated settlement is generated inside the backfill with larger values reached at the middle backfill height in stiffer foundation case (see Figure 3.2a), or at the bottom of backfill in soft foundation case and very stiffer backfill (i.e., moving similarly as a solid-rigid body). In intermediate cases in soft foundation cases, the location of the maximum vertical displacements in the backfill occurs from the bottom to the middle height locations, according to the relative stiffness between the backfill and foundation (see Figure 3.2b).

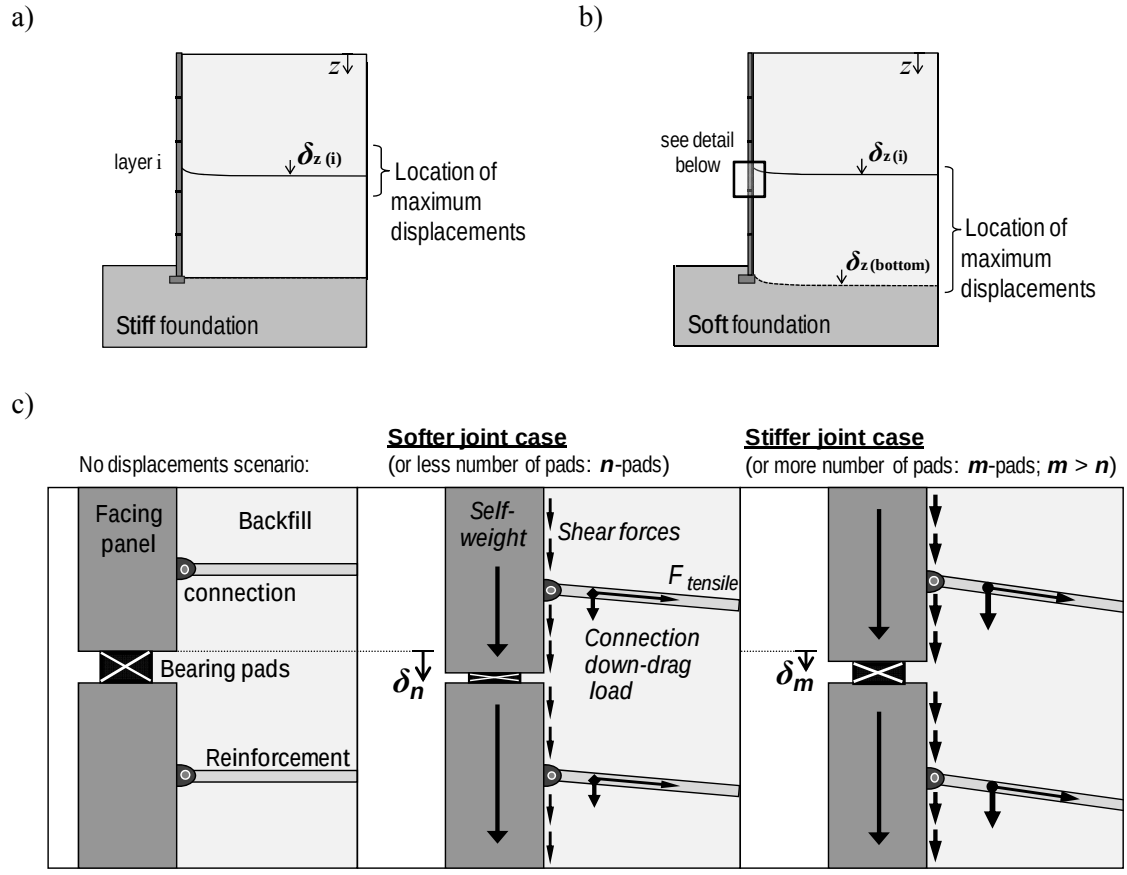

Figure 3.2: Schema of the backfill settlement effect with regards to foundation compressibility (stiff (a) and soft (b) foundation cases) and related bearing pad deformation according to the pad material/shape compressibility and down-drag generation (c).

There is also a tension load of the reinforcements at the connections with a significant vertical contribution (down-drag loads) controlled by the vertical displacement of the backfill with respect to the facing (displacement which tend to generate reinforcement displacements down with respect to their original position; see Figure 3.2c). As previously specified, the bearing pad elements allow the vertical displacements of the facing elements in order to accommodate the backfill settlements and reduce the down drag-loads at the connections (see Figure 3.2c; with assuming the same backfill settlement in both cases). Thus, greater vertical contribution loads (down-drag and shear forces) appear if greater is also the bearing pads stiffness (i.e., less deformation and consequently greater relative displacements between the backfill and the facing).

From this previous explanation can be derived how important is to select the appropriate number of pads (or appropriate pad's shape/material relation) to allow the enough compression to well accommodate the relative displacements, without losing the strength enough to their flattening and consequent panel-to-panel contact. Also derived from Figure 3.2, it is important to remark that the leveling pad under the facing panels must not have shallow foundation properties, so large sizing leveling pad must not be installed to not

generate bearing capacity in this element, with allowing the facing to move down according to the backfill settlement (i.e., reducing the relative displacements generation).

3.2. NUMERICAL MODEL DETAILS

3.2.1. General

The 2D finite element method (FEM) program PLAXIS (2008) was used to carry out the numerical simulations in this study. Figure 3.3 shows the finite element mesh (15-node triangle elements) and geometry adopted in the analyses. Four wall heights were considered corresponding to H = 6, 12, 18 and 24 m. The foundation depth was kept constant at D = 25 m. In a related study, the author investigated the influence of relative foundation compressibility on performance of reinforced walls having a range of backfill and reinforcement stiffness (Damians et al., 2014). In this previous study, the foundation was treated as equivalent linear Winkler springs with stiffness computed as $k = E/D$ (where E is the Young's modulus of the foundation soil). In addition, the foundation stiffness varied from k = 4 MPa/m to rigid corresponding to medium loose sand to intact rock (Bowles 1996). In the current study, k = 0.4 to 400 MPa/m corresponding to clay to weathered rock. The lower limit was purposely selected to capture trends in numerical outcomes corresponding to the low end of foundation stiffness. The reinforcement length (L) was taken as 0.7 times the wall height in all cases, and the embedment depth was $0.1 \times H$. These values satisfy minimum criteria in the USA for the wall heights and geometry in this study (Berg et al., 2009).

The vertical domain boundaries were fixed in the horizontal direction. The bottom boundary was fixed in both horizontal and vertical directions. The model domain (depth and width) and numerical mesh element refinement were selected to jointly optimize computation time and minimize the influence of problem boundaries. Smaller numerical mesh elements were generated in the soil zone immediately in front of the wall toe and in zones adjacent to all reinforced-soil interfaces and horizontal panel joints. Each numerical wall was built incrementally from the bottom up to simulate construction in the field.

In the sections to follow, the properties of the component materials and their implementation within the PLAXIS program are the same as those reported in Chapter 1 (Damians et al., 2013a), unless noted otherwise. Hence, some details in the sections to follow are omitted for brevity.

3.2.2. Material Properties and Interfaces

Material properties for the soil zones (backfill and foundation) are summarized in Table 3.1. The soil materials in the majority of simulations are modeled as elastic-plastic materials using the Mohr-Coulomb failure criterion. For simplicity, no attempt has been made to simulate

compaction effects during placement of soil layers. The ratio of soil elastic modulus for different soil material zones (e.g., backfill soil and foundation) has been kept constant between matching simulations that vary only with respect to wall height. In this study, the backfill stiffness $E_{(backfill)}$ refers to the soil at 1 m and greater from the back of the concrete panels. At closer distances the soil stiffness is reduced by 50% (Table 3.1). This was done to capture the effect of less compaction energy on soil stiffness using lighter compaction equipment which is recommended practice immediately behind the wall face to minimize additional compaction-induced loads on the concrete facing panels (Berg et al., 2009). The focus of this Chapter is on the influence of relative compressibility of the joint inclusions, backfill soil zone and foundation soil on wall facing behavior. Hence, a large cohesive strength component (50 kPa) for the foundation soil was adopted to ensure that deformations originating in the foundation soil were within the elastic range of the soil (i.e., working stress conditions) and thereby simplify the interpretation of results.

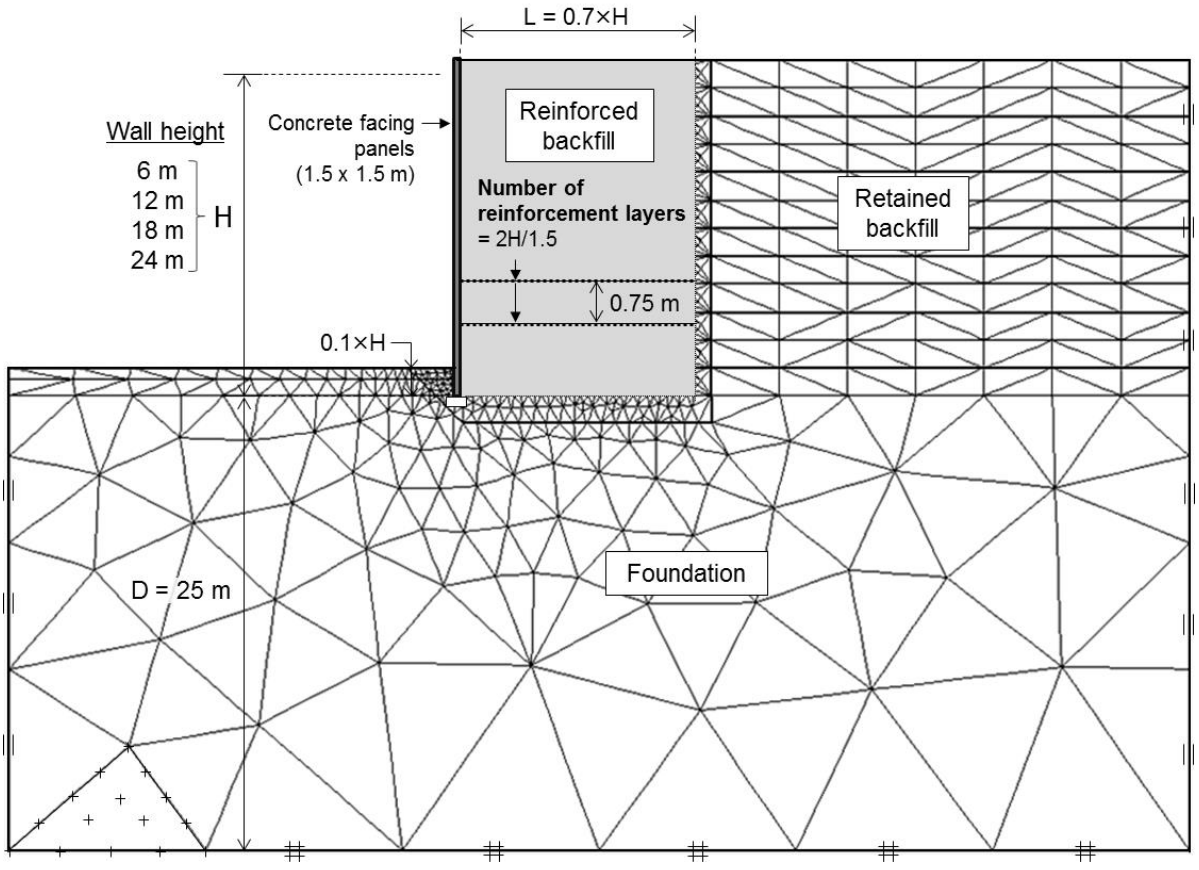

Figure 3.3: Finite element model geometry: Notes: *L* is length of reinforcement; *D* is foundation depth from facing toe.

Table 3.1. Soil properties:

Parameters	Backfill		Foundation
Unit weight (kN/m^3)	19		18
Cohesion (kPa) [1]	5 [2]		50
Friction angle, ϕ (degrees)	36[3]		30
Dilatancy angle, ψ (degrees) [4]	6		0
Elastic Mohr-Coulomb soil model:	< 1.0 m from facing [5]	> 1.0 m from facing	
Elastic modulus (MPa)	- soft case: 5 - stiff case: 50	- soft case: 10 - stiff case: 100	- soft case: 10 - stiff case: 1000
Poisson's ratio (-)	0.3		0.3
Hardening soil model: [6]	(m = 0.5 and R_f = 0.9) [7]		
E_{50}^{ref} (MPa) [8]	- soft case: 5 - stiff case: 50	- soft case: 10 - stiff case: 100	n/a
Poisson's ratio (-)	0.2		n/a

Notes: [1] Soils are assumed as no-tension materials (tension cut-off).

[2] Non-zero cohesion value has been assumed for the numerical model to ensure numerical stability at very low confining pressure.

[3] Peak plane strain friction angle of granular soil is greater than the corresponding triaxial or direct shear test values. Hence, value of ϕ = 36 degrees used in simulations is in agreement with conventional triaxial compression or direct shear peak friction angles of (say) 30 to 34 degrees. The latter are minimum recommended friction angles for select granular fills in North American practice (Berg et al., 2009).

[4] Assumed as $\psi = \phi - 30^o$.

[5] Area where less compaction energy is used during construction to minimize lateral loads on facing panels. The elastic stiffness modulus was assumed to be 50% of the elastic stiffness modulus of the well-compacted soil for both linear elastic Mohr-Coulomb and hardening soil model cases.

[6] Dilatancy and dilation angle are included in hardening model.

[7] m = 0.5 is the power term for stress-level dependency of soil stiffness and the value used here is typical for sand soils. R_f corresponds to the failure ratio between the ultimate deviatoric stress and the asymptotic value of the shear strength.

[8] E_{50}^{ref} corresponds to the reference confining stress-dependent stiffness modulus for primary triaxial loading, corresponding to the secant stiffness at a deviatoric stress level equal to half the failure stress. Reference confining stress = 100 kPa. The unloading and reloading stiffness modulus (E_{ur}^{ref}) was assumed to be 3 times higher than E_{50}^{ref} which is the default assumption in the PLAXIS manual. The tangent stiffness for primary oedometer loading (E_{oed}^{ref}) was assumed to be equal to E_{50}^{ref}.

Huang et al. (2009) and Damians et al. (2014) demonstrated that the use of more complex non-linear multi-parameter soil constitutive models does not guarantee improved numerical accuracy with measured wall performance. Nevertheless, a number of wall cases were repeated using the hardening soil model that is available in PLAXIS in order examine the sensitivity of numerical outcomes to choice of soil constitutive model for the backfill soil. Hardening model parameters are given in Table 3.1. Details of the model can be found in the PLAXIS software manual (PLAXIS 2012). The E_{50}^{ref} value for the hardening soil model was selected to match the elastic modulus of the soil in the corresponding elastic analyses and the same M-C failure criterion was also adopted. The default value of R_f = 0.9 in program PLAXIS was used in this study. For project-specific design a lower value may be appropriate (e.g., R_f = 0.75) based on fitting to triaxial compression testing of site-specific soils as demonstrated by Damians et al. (2014). However, in the current study the numerical outcomes were found not to be sensitive to the choice of R_f in the range of 0.75 to 0.9 which is likely because the soils remained largely in the working stress (elastic) range. It should be noted that minor soil yielding occurred in a very thin column at the back of the facing, at the foundation toe and at the back of the reinforced soil zone in some simulations with both M-C and hardening soil models. However, large and contiguous soil failure zones in the reinforced soil mass consistent with conventional notions of reinforced soil wall failure did not occur in any simulations.

The material properties assumed for the precast concrete facing panels and the polymeric bearing pads (horizontal joints) are shown in Table 3.2. The joint axial stiffness was computed based on plan area of each pad, pad modulus and the number of pads per 1.5 m-long panel joint. These calculations result in an initial linear compression response of the joints as a result of the compressive stress-strain behavior of the individual pads (Figure 3.4). The assumption of linear joint stiffness also simplifies parametric analyses to isolate the influence of the compressibility of the horizontal joints between facing panels, wall height and reinforcement layer location on vertical loads transmitted through the wall facing. For walls with a large number of very stiff bearing pads, the assumption of linear compression is reasonable for in-service (operational) conditions. For walls with more compressible joints, the assumption of linear compression is satisfactory if compression is restricted to (say) 10% for HDPE pads and (say) 40% for EPDM pads based on published data (Neely and Tan 2010; Choufani et al., 2011). In the simulations to follow, the bearing pads were assumed to have an initial thickness of t = 20 mm (Table 3.2). The minimum available gap space is taken as 20 mm by assuming that the gap at the concrete panel lip(s) is at least equal to 20 mm (Figure 3.1).

Table 3.2. Concrete panel and bearing pad (joint) properties:

		Bearing pads [a]					
		EPDM [b]			HDPE [c]		
		number of pads per panel joint					
Parameters	Panels	2	4	6	2	4	6
Axial stiffness, $J = EA$ (kN/m)	5600×10^3	130	260	390	1100	2200	3300
Bending stiffness, EI (kNm^2/m)	9150	0.25	0.50	0.75	2.10	4.20	6.20
Poisson's ratio	0.15		0.49			0.40	

Notes: [a] assuming a pad plan dimension area of 0.008 m^2 for both material cases, and a panel width 1.5 m in the running length direction of the wall and pad thickness of t = 20 mm.

[b] EPDM = ethylene propylene diene monomer.

[c] HDPE = high-density polyethylene.

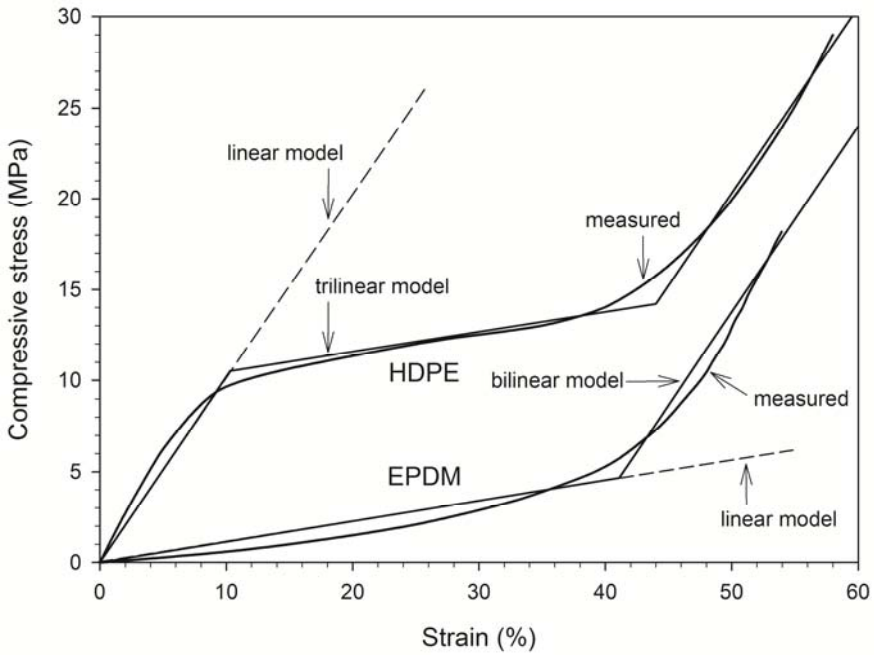

Figure 3.4: Horizontal joint compressive stress-strain behavior of EPDM and HDPE pad materials. Note: EPDM = ethylene propylene diene monomer; HDPE = high-density polyethylene.

The reinforcement layers were placed at uniform vertical spacing of 0.75 m in each wall and each layer was assigned a constant axial stiffness (J; see Table 3.3). The axial stiffness was increased with depth below the top of the wall to capture the increase in number of reinforcing strips in a layer which is common practice for steel strip walls, and/or to capture

the increase in total cross-section area per unit running length of wall that is used in some steel ladder wall systems constructed with circular bars. The axial stiffness values vary from about J = 30 MN/m to 100 MN/m for wall heights of H = 6 to 24 m, respectively. These values are consistent with the range of values reported by Bathurst et al. (2011) for steel grid reinforced soil walls and Huang et al. (2012) for steel strip reinforced soil walls.

Table 3.3: Reinforcement layer stiffness:

Wall height, H (m)	Reinforcement layer location, depth from top of wall, z (m)	Linear-elastic stiffness, $J_{(reinforcement)} = (EA)_{reinforcement}$ (MN/m) [(a)]
6	0.4 to 5.3	28.1
12	0.4 to 6.4	28.1
	7.1 to 8.6	37.5
	9.4 to 10.9	46.9
	11.6	56.3
18	0.4 to 7.1	29.3
	7.9 to 11.6	44.0
	12.4 to 14.6	58.6
	15.4 to 17.6	73.3
24	0.4 to 7.1	29.3
	7.9 to 11.6	44.0
	12.4 to 15.4	58.6
	16.1 to 19.1	73.3
	19.9 to 22.9	87.9
	23.6	102.6

Note: [(a)] E = elastic modulus of steel = 200 GPa, and A = cross-section area of steel strip or bars.

In the earlier preliminary study by Damians et al. (2013a), a sensitivity analysis was carried out using a range of interface friction coefficient R = tan δ / tan ϕ (where δ is soil-concrete panel interface friction angle and ϕ is the friction angle of the backfill soil). The best value was determined to be R = 0.3 based on comparison of predicted vertical toe loads with measured results from an instrumented field wall (Runser et al., 2001; Damians et al., 2014), and thus is the value used in the current study. The soil-reinforcement interaction was modeled assuming a perfect bond behavior (i.e., R = 1). This value is consistent with measured pullout test data for ribbed steel strips and well compacted granular soils reported in the literature (Schlosser and Elias 1978; Miyata and Bathurst 2012b; Bathurst et al., 2011).

3.3. RESULTS OF ANALYSES

3.3.1. Influence of joint stiffness and soil stiffness on vertical facing panel loads

Numerical results using linear axial (compressive) joint stiffness are reported first. Figure 3.5 shows load factor (ratio of measured vertical toe load to sum of panel self-weights) plotted against depth of joint below the top of the wall for four different wall heights, two joint materials, and four different combinations of backfill and foundation stiffness. The soil constitutive models are linear elastic with M-C failure criterion in all cases. For reference purposes, the data for cases with H = 18 m are quantitatively similar to previously reported results in Chapter 1 (earlier related Damians et al., 2013a). Only numerical results in which there was a positive gap are presented. No attempt was made to simulate the concrete-to-concrete contact condition, which in practice should be avoided. The plots also show the load factor at which 10% and 40% compression of the joint is exceeded. These values correspond to the first break point in the compressive stress-strain plots for the HDPE and EPDM bearing pads shown in Figure 3.4. Hence, the plots in Figure 3.5 assume that the initial linear elastic behavior of the bearing pads persist at all compressive strains. The grey symbols in the figure identify numerical outcomes where the compression of the bearing pads has extended beyond the initial linear stress-strain region in Figure 3.4 but the panels are not in contact.

The influence of the above parameters on load factor magnitude and vertical distribution is complex. The following observations can be made from Figure 3.5:

1. In general, for the same foundation stiffness condition, decreasing the stiffness of the joint material (EPDM versus HDPE in these examples) and/or increasing the stiffness of the backfill soil leads to reduced load factor at similar depths below the top of the wall (compare Figure 3.5a with 3.5c, and Figure 3.5b with 3.5d).

2. For the case of a relatively less stiff backfill soil ($E_{(backfill)}$ = 10 MPa) (Figure 3.5a and 5b) there is generally steadily increasing load factor with depth below the wall regardless of joint material.

3. For the relatively stiff backfill condition ($E_{(backfill)}$ = 100 MPa) the vertical load factor is less for the stiffer foundation soil case at similar depths (compare Figure 3.5c with 3.5d).

4. For walls with the more compressible joints (EPDM) the vertical load factor becomes more uniform with depth for increasing backfill soil stiffness and the stiff foundation condition with $E_{(foundation)}$ = 1000 MPa (compare Figure 3.5b with Figure 3.5d). The explanation is that the joint stiffness for the EPDM cases in this parametric study is similar in magnitude to the backfill soil. Hence, relative downward movement of the wall facing and backfill soil is less for the case with $E_{(backfill)}$ = 100 MPa.

5. For the case of HDPE joint material and $E_{(backfill)}$ = 100 MPa and $E_{(foundation)}$ = 10 MPa, there is relatively little influence of wall height on the magnitude of load factor (Figure 3.5c).

6. For many cases the linear-elastic region for the HDPE bearing pads is exceeded. The elastic strain limit of the EPDM pads is greater and it is for this reason that numerical outcomes where the elastic limit of the material has not been exceeded are more easily visible in the figure (e.g., Figures 3.5c and 3.5d).

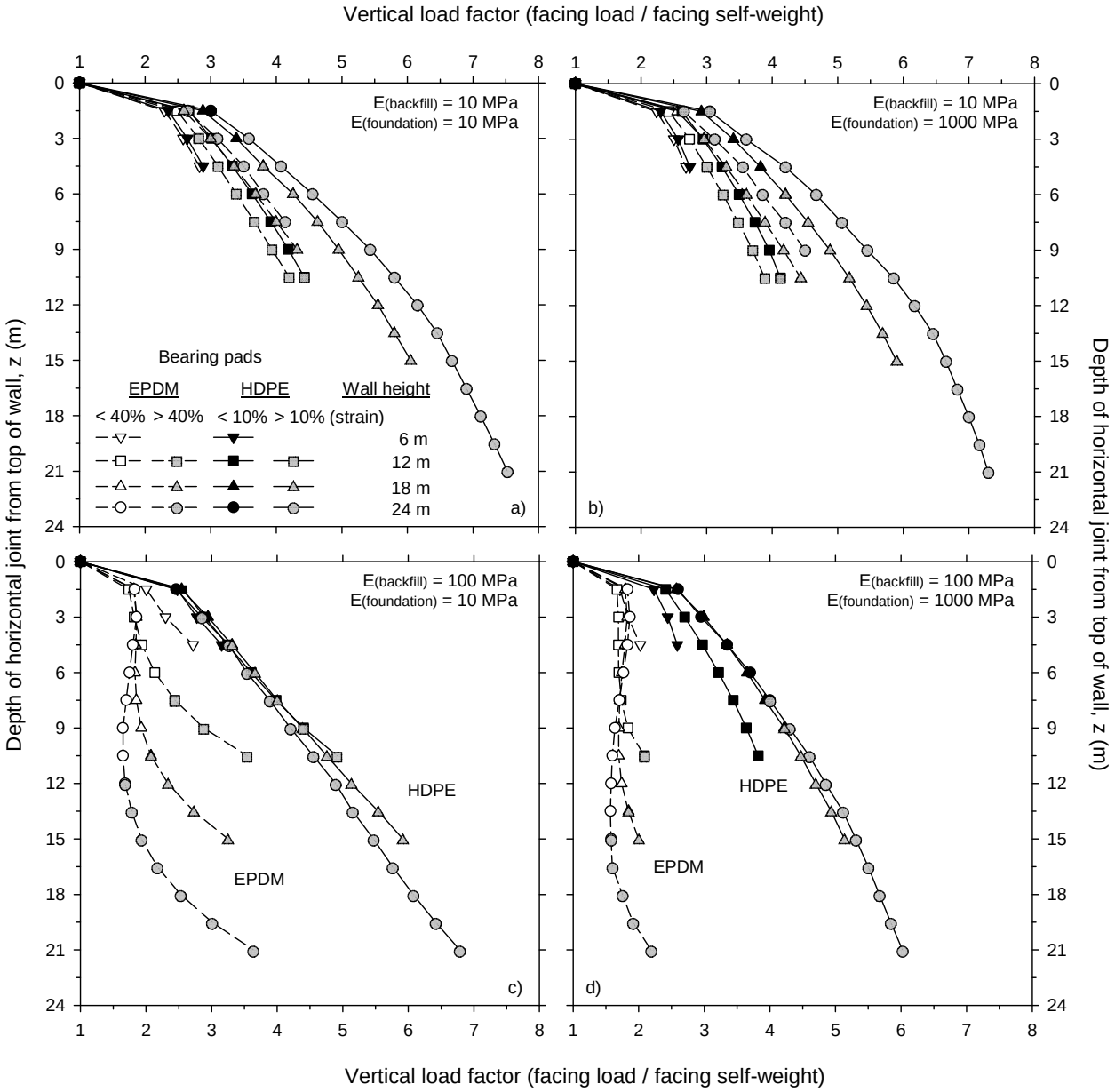

Figure 3.5: Vertical load factor versus joint depth for different wall height (H) and backfill-foundation stiffness combinations, and assuming two 20 mm-thick bearing pads (EPDM or HDPE) per 1.5 m-long joint with linear axial (compressive) stiffness. Note: Numerical results using linear elastic M-C soil model.

Two walls cases with linear elastic HDPE and EPDM bearing pads were repeated using the hardening soil model in PLAXIS for the backfill soil only. This soil model captures non-linear stress-dependent stiffness behavior of frictional soil materials. The results of simulations using both soil models are compared in Figure 3.6.

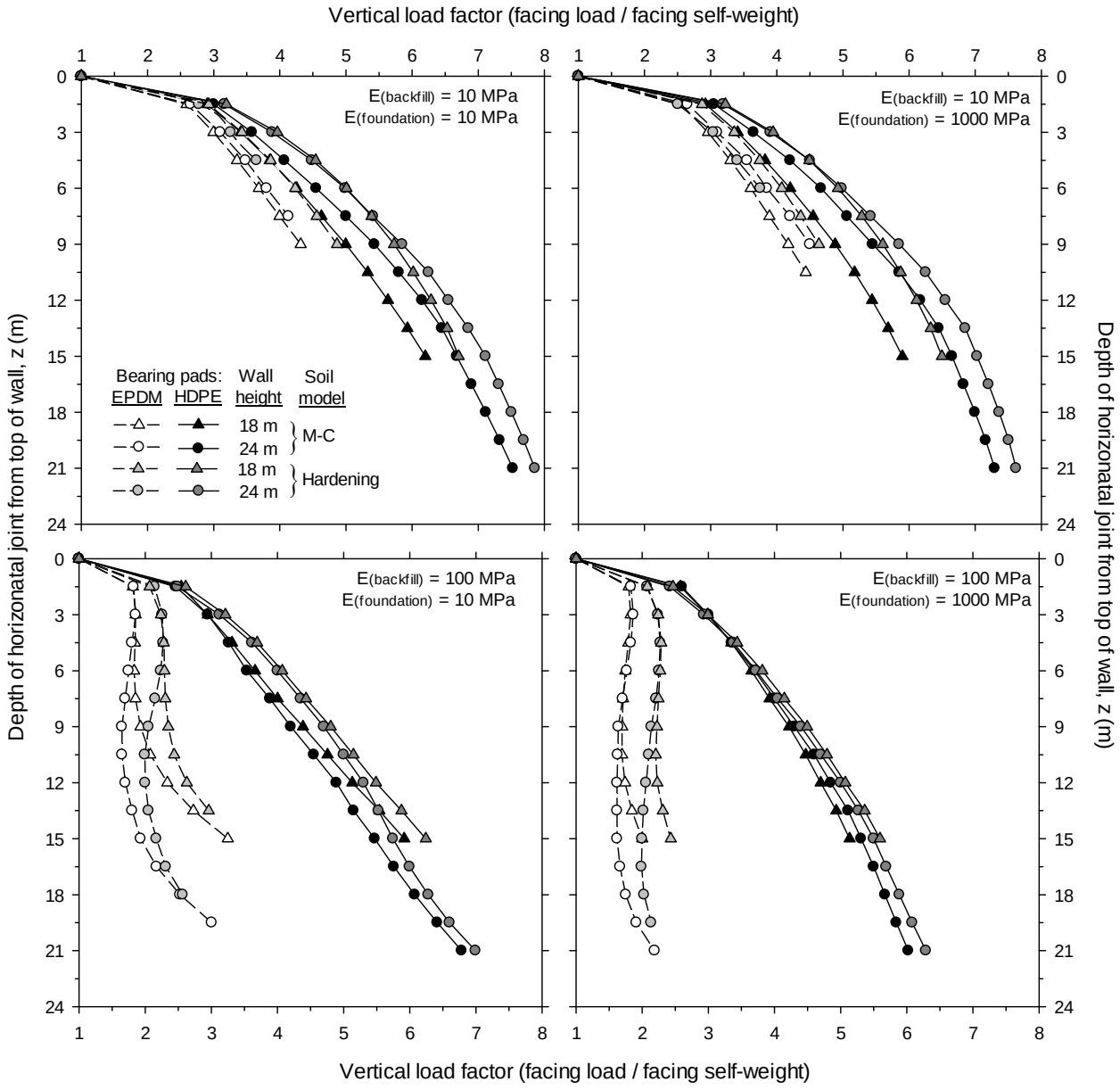

Figure 3.6: Comparison of numerical results using PLAXIS hardening soil model and linear elastic M-C soil model for backfill soil. Vertical load factor versus joint depth for different wall height (*H*) and backfill-foundation stiffness combinations, and assuming two 20 mm-thick bearing pads (EPDM or HDPE) per 1.5 m-long joint with linear axial (compressive) stiffness.

To minimize visual clutter, numerical outcomes with strains greater than the initial elastic limit are not identified. In general, the load factor response curves are similar to those in Figure 3.5 but are shifted to the right indicating that qualitative features in Figure 3.5 are preserved in Figure 3.6. Hence, the PLAXIS soil hardening model predicts greater vertical load transferred through the facing column than the simpler linear-elastic plastic model. Since the focus of the study is largely on the relative performance of the walls using a range of assumed wall component material properties and wall heights, the quantitative differences in the response curves in Figure 3.6 are judged not to be a practical concern from a performance point of view.

However, it is worth noting that the run times were up to six times longer for numerical simulations using the hardening soil model compared to matching cases using the simpler soil model. For example, using a desk top computer with an Intel© Core 2 Duo Pa8600 (2.40 GHz) (Intel, Santa Clara, California) central processor, the computer solved wall models with H = 24 m in approximately 20 min for elastic M-C soil model cases and 120 min for the hardening soil model cases. The numerical results presented hereafter are for simulations carried out using linear elastic M-C soil models.

3.3.2. Influence of joint stiffness and soil stiffness on panel-joint gap

Figure 3.7 shows the vertical load factor generated at selected joint locations (depth z) for each wall height (H) case versus relative joint stiffness. Relative joint stiffness is calculated as the ratio of the product of the pad elastic modulus, pad area and number of pads per joint, to the product of backfill soil stiffness and joint (pad) thickness. In this study t = 20 mm which is a typical thickness for these pads (Damians et al., 2013). As a useful reference, the relative joint stiffness data points in Figure 3.7 are matched to the number of bearing pads manufactured from HDPE and EPDM materials per 1.5 m-long joint. The plots show that the load factor tends to one as the stiffness ratio goes to zero (e.g., as axial bearing pad stiffness goes to zero). For relative joint stiffness values greater than about one the load factor is reasonably constant at each depth location. A load factor of one is possible (i.e., no downdrag forces) if the compressibility of the horizontal joint is sufficient to allow the concrete panels to settle with the backfill soil.

Figure 3.8 shows the computed joint gap thickness (at the location of the bearing pads) and axial (compressive) strain at three normalized depth locations. Three different numbers of EPDM and HDPE pads per panel joint (2, 4 and 6) were assumed in these calculations. The plots show that the magnitude of backfill stiffness plays a major role in joint compression. For the same fixed relative joint stiffness value, the gap compression is less for the stiffer backfill soil condition and gap closure increases with depth below the top of the wall. The influence of foundation stiffness is less for cases with relative joint stiffness of (say) 0.5 or greater. Some additional numerical results are shown for the case of an intermediate value of backfill stiffness ($E_{(backfill)}$ = 50 MPa).

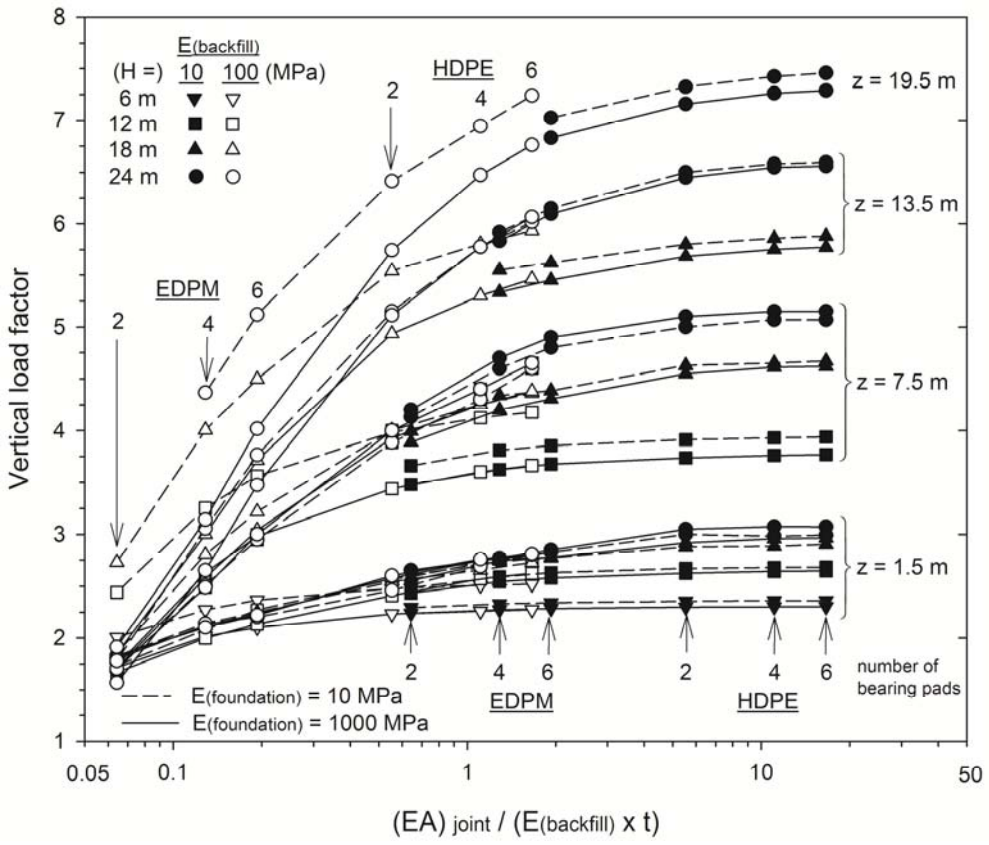

Figure 3.7: Load factor versus relative joint stiffness. Note: Parameter *z* is depth of horizontal joint from top of wall.

Figure 3.9 presents the computed joint aperture (gap) with respect to the computed load factor. Results are presented according to the backfill stiffness case, and for a certain joint depth location cases. As can be observed, in softer backfill cases (figure above), for a fixed joint depth, the load factor hardly varies according to the pad's stiffness and wall height case. Furthermore, in stiffer backfill cases (figure below), the load factor decreases in a significant manner with regards to the pad's stiffness and the gap-value. The influence of the foundation stiffness is not relevant except for taller wall case and stiffer backfill.

An alternative presentation of the results of parametric analyses is given in Figures 3.10, 3.11, and 3.12: Isolines of equal gap thickness are plotted for each wall height scenario and different combinations of backfill and foundation stiffness, and different numbers of EPDM and HDPE bearing pads. These plots can be used for design to select the minimum number of 20 mm-thick pads at each horizontal joint location to not exceed a specified minimum gap thickness. The 12 mm- and 5 mm-gap isolines in the figure may be taken as the range of minimum acceptable post-construction values based on recommendations by Berg et al. (2009) and BSI BS8006 (2010), respectively, and observations by Choufani et al. (2011).

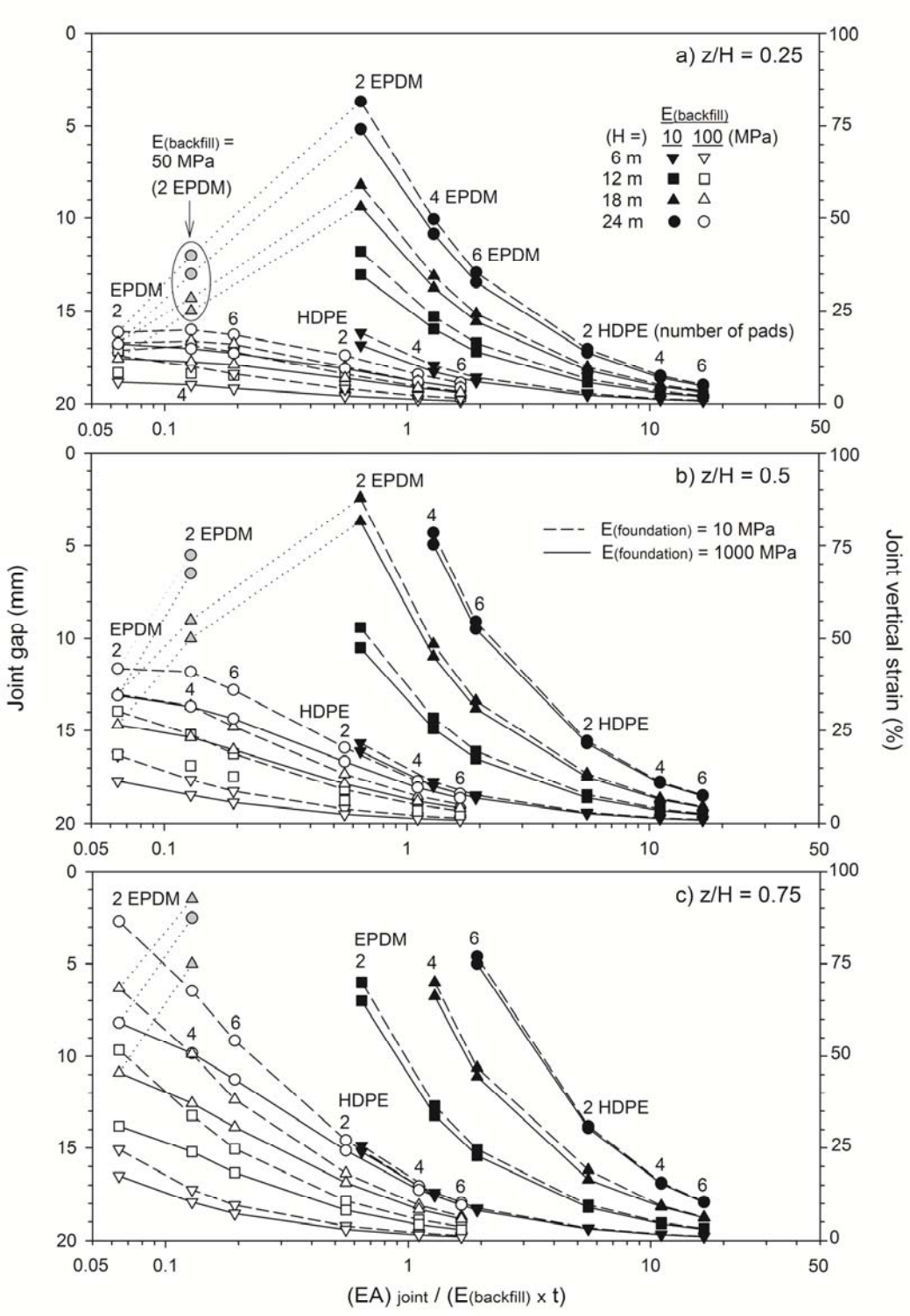

Figure 3.8: Joint gap thickness and compression (at location of bearing pads) versus relative joint stiffness for different normalized depths of joint below top of wall (z/H) using linear bearing pad compressive stress-strain models.

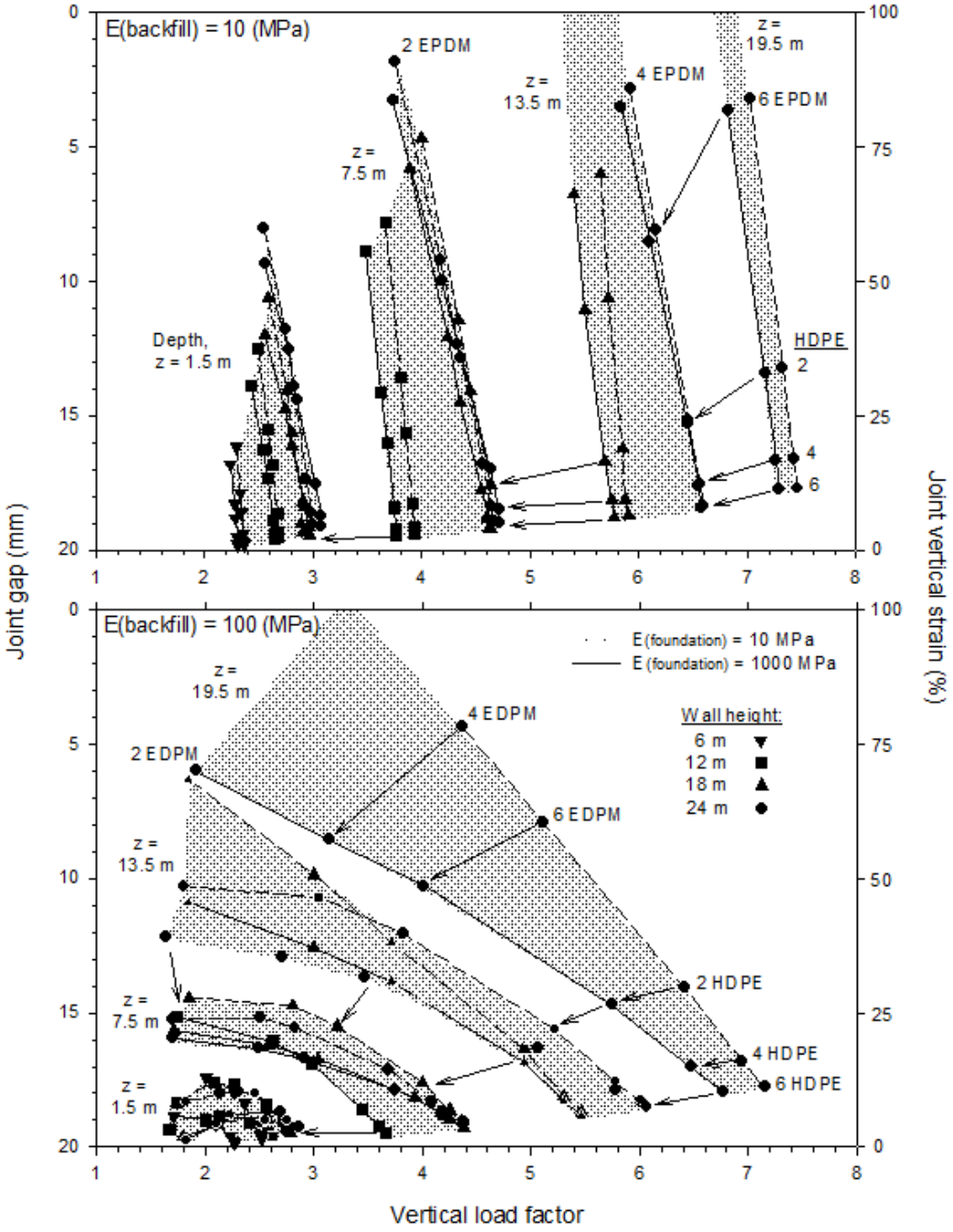

Figure 3.9: Joint gap (at location of bearing pads) versus load factor for different wall heights, backfill and foundation soil stiffness, and bearing pad number and type.

a) H = 6 m

b) H = 12 m

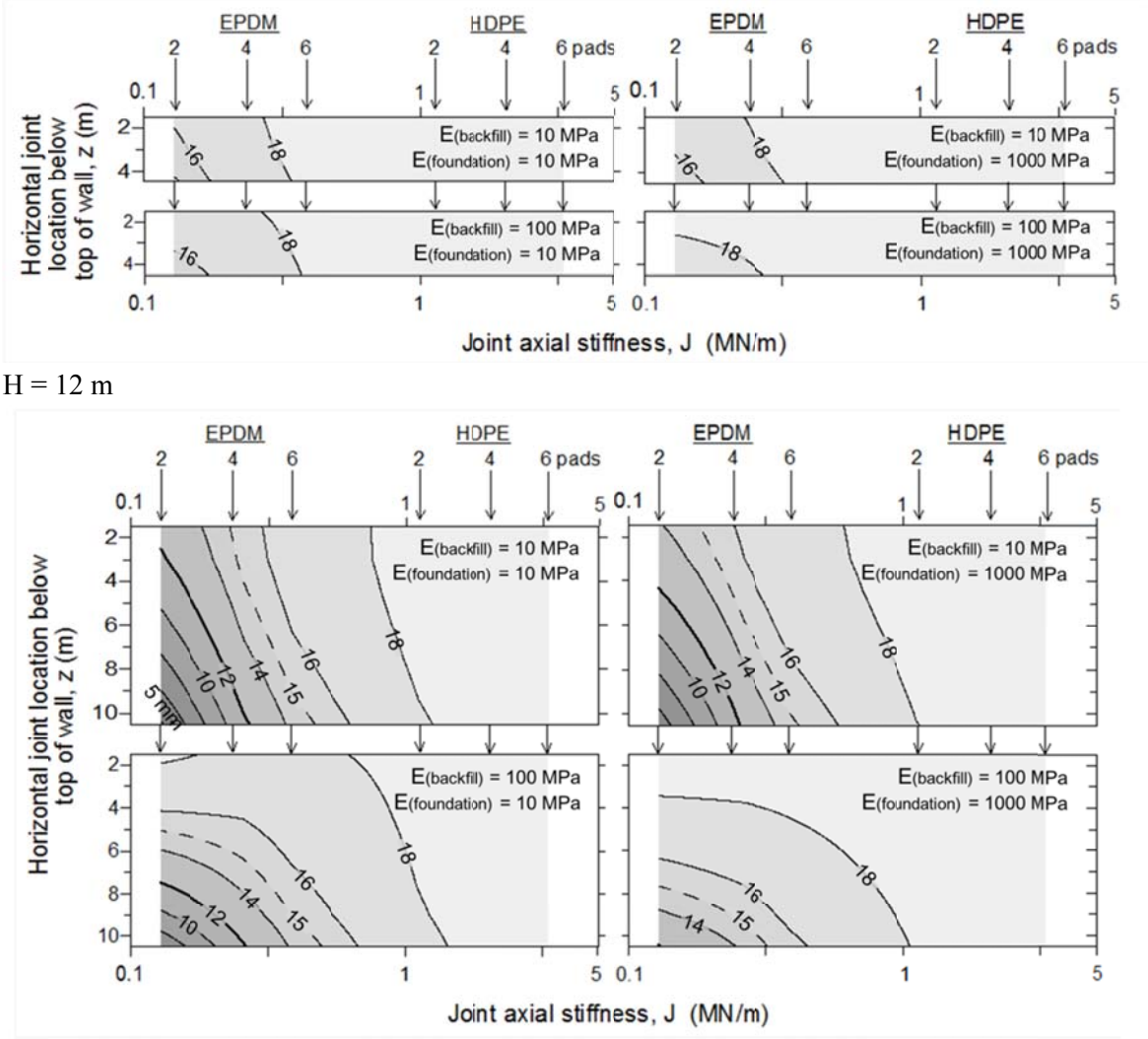

Figure 3.10: Isolines of joint vertical gap thickness for different wall height *H*, joint stiffness (different numbers of bearing pads per joint), and different backfill soil and foundation stiffness conditions. Wall heights: *H* = 6 m (a) and *H* = 12 m (b).

3.3.3. Influence of joint stiffness and soil stiffness on vertical facing settlement

Figure 3.13 shows computed settlements at the top of the concrete facing for different wall heights and combinations of other parameter values. Previous figures demonstrate that the magnitude of load factor is sensitive to joint compressibility and relatively less sensitive to foundation stiffness. However, the plots in Figure 3.13 show that foundation compressibility is much more important than joint compressibility when settlement of the wall facing (or backfill) is a concern. Examples when wall settlements are important are where the wall supports or adjoins other structures.

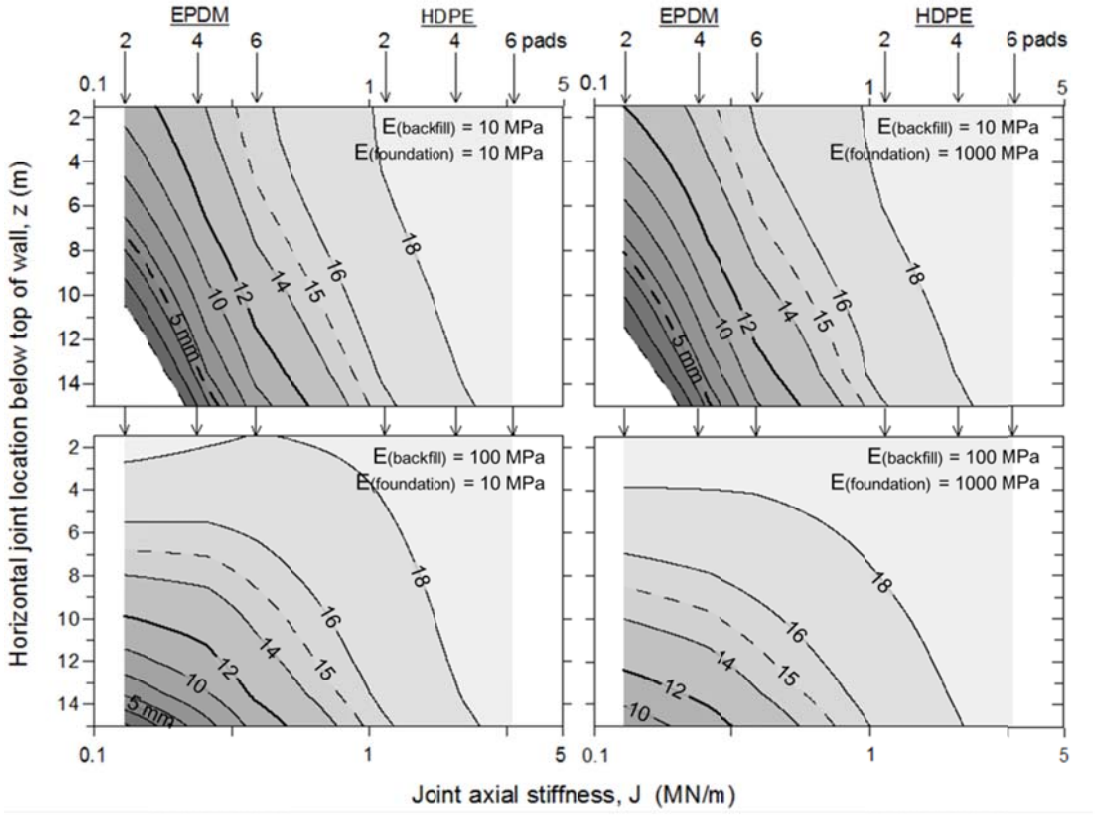

Figure 3.11: Isolines of joint vertical gap thickness for different wall height H, joint stiffness (different numbers of bearing pads per joint), and different backfill soil and foundation stiffness conditions. Wall heights: H = 18 m.

3.3.4. Influence of bearing pad constitutive model on gap thickness prediction

A linear compression law for the joint bearing pads has been adopted in the current study and in the earlier related Chapter 1 (Damians et al., 2013). A linear model has the advantage of simplicity which facilitates comparison and understanding of the contribution of the many factors that influence vertical load transmission and horizontal panel joint compression in steel reinforced soil walls. Linear models are satisfactory for very stiff horizontal joints (e.g., large numbers of bearing pads are used at each joint) and/or the strains are kept within elastic limits (about 10% for HDPE and 40% for EPDM type). However, the actual compression behavior of individual HPDE bearing pads of typical thickness (t = 20 mm) taken to large strains is sigmoidal shaped. For 20 mm-thick bearing pads manufactured from EPDM, the compression behavior at large strains is better captured by a bilinear stress-strain hardening model (Figure 3.4).

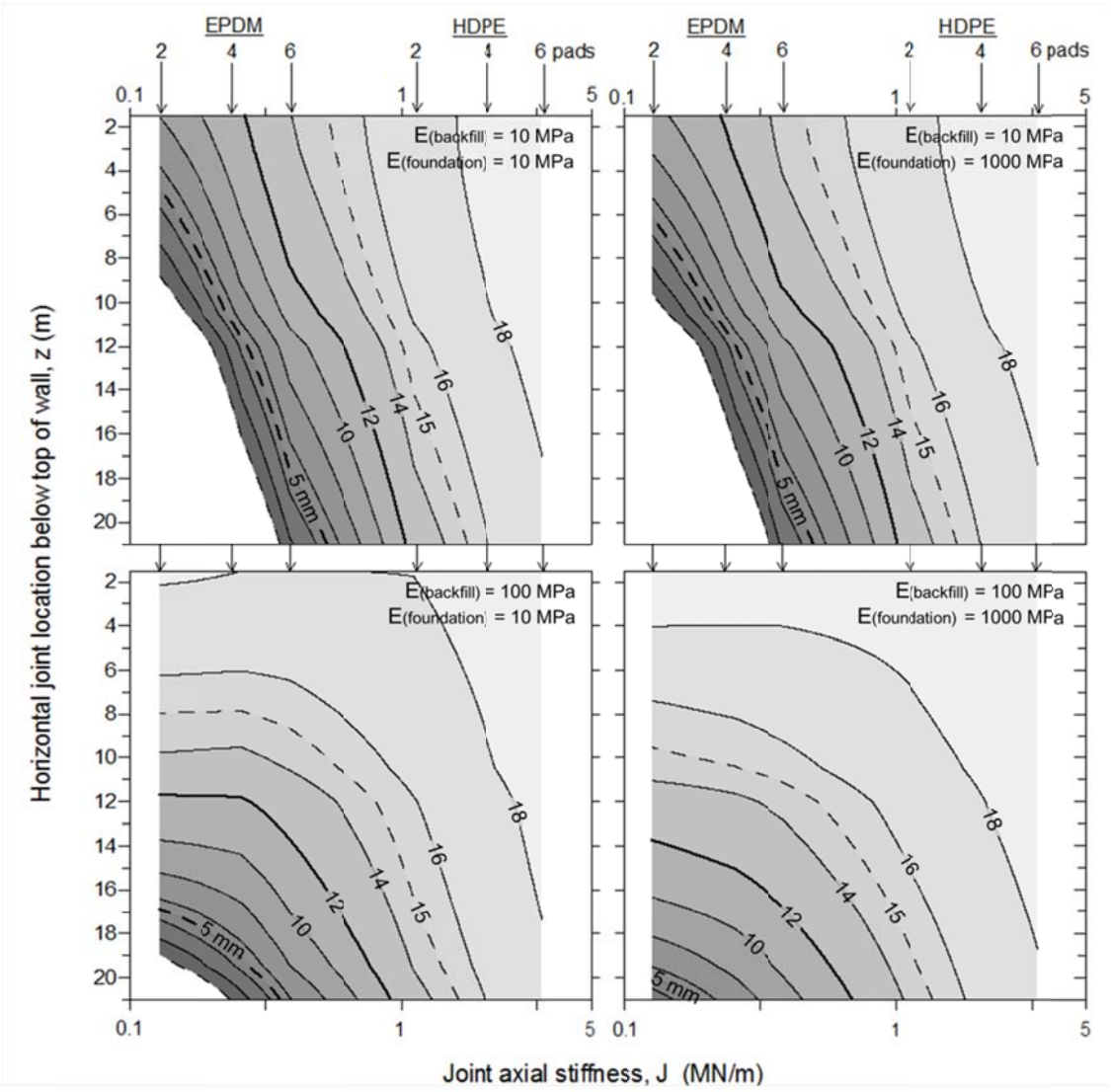

Figure 3.12: Isolines of joint vertical gap thickness for different wall height *H*, joint stiffness (different numbers of bearing pads per joint), and different backfill soil and foundation stiffness conditions. Wall heights: *H* = 24 m.

Figure 3.14 reproduces results of numerical calculations similar to those in Figure 3.8 but adopting the bilinear (EPDM) and trilinear (HDPE) compressive stress-strain approximations to the measured data in Figure 3.4. Comparison of Figure 3.14 with Figure 3.8 shows that in many cases the gap thicknesses using the linear compressive stress-strain model are similar or smaller. Hence, using the simpler linear model will give similar or more conservative (safer) design outcomes. The exceptions are some scenarios with 2 or 4 HDPE bearing pads in combination with relative joint stiffness values greater than about 0.5 and 5, and relatively stiff and soft backfill soil cases, respectively. However, for these cases simply increasing the

number of HDPE pads per joint to 6 pieces will return the joint compression response to the initial linear behavior and thus the two figures will give the same predictions.

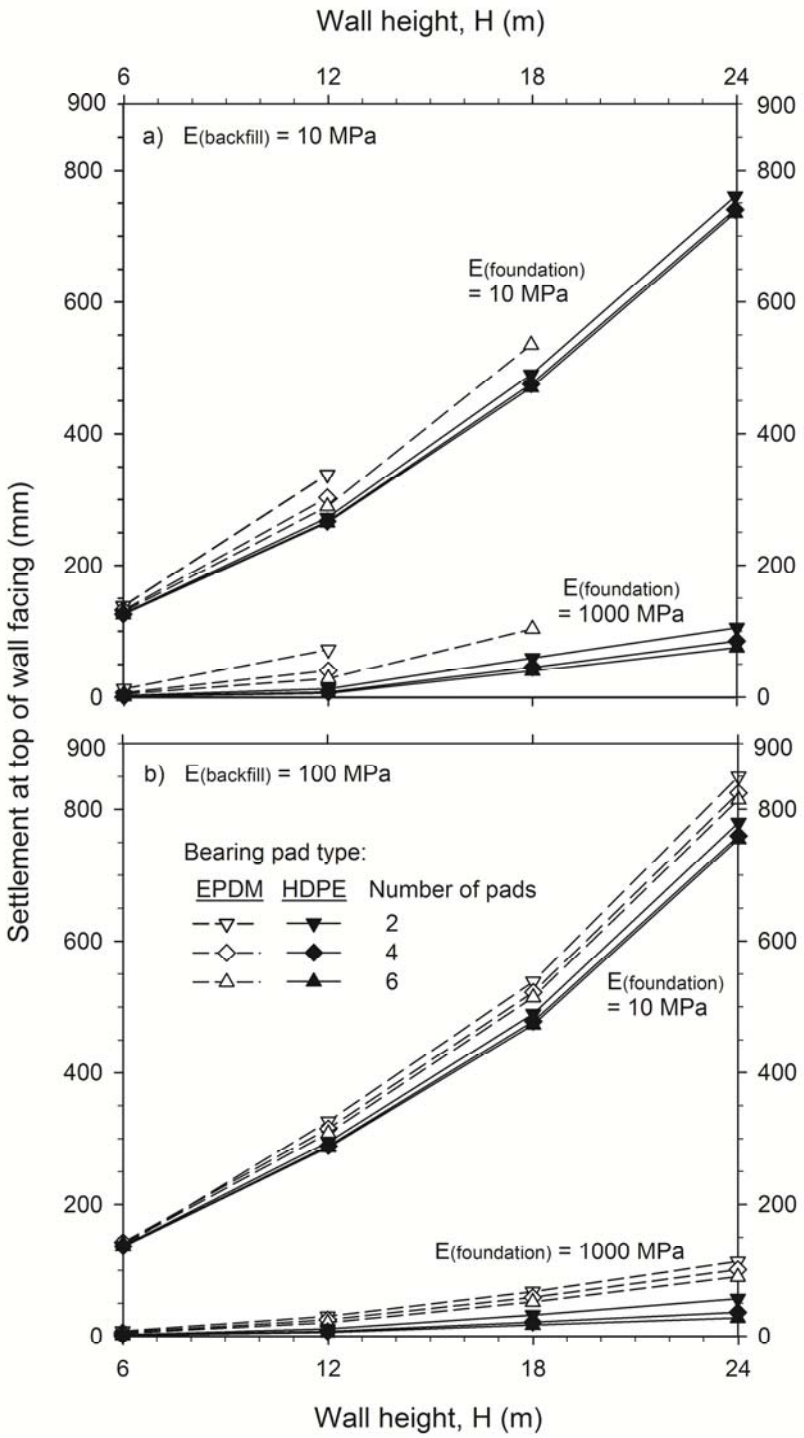

Figure 3.13: Influence of wall height, soil backfill and foundation stiffness, bearing pad type and number on settlement at the top of the concrete panel facing.

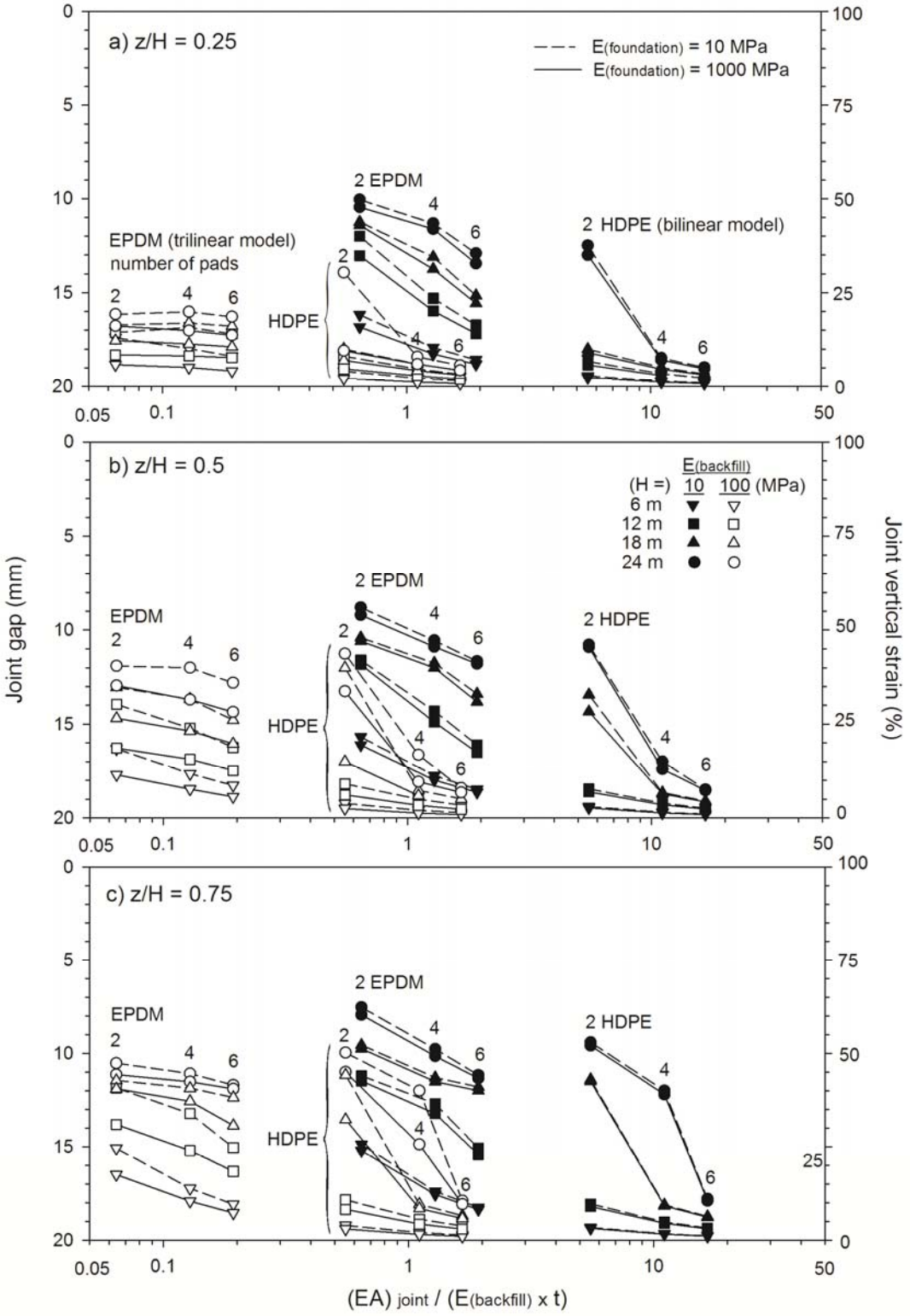

Figure 3.14: Joint gap thickness and compression versus relative joint stiffness for different normalized depths of joint below top of wall (z/H) using bilinear (EPDM) and trilinear (HDPE) bearing pad compressive stress-strain models.

3.4 DISCUSSION AND CONCLUSIONS

The concrete panels that form the facing of steel reinforced soil walls must carry loads that are greater than the self-weight of the panels. The vertical load carried by the facing will result in compression of the horizontal joints between adjoining panels. Excessive vertical loads and/or excessively compliant bearing pads can lead to panel to panel contact which can cause the concrete panels to crack or spall.

This Chapter extends the work of Chapter 1 (Damians et al., 2013) by quantitatively investigating the influence of wall height, backfill soil constitutive model and bearing pad compression model on numerical predictions of vertical panel loads and gap compression. Rather than attempt to associate a particular value of elastic modulus with a particular soil type, which is problematic for frictional soils, a wide range of soil stiffness values spanning two orders of magnitude was used to capture the possible influence of foundation modulus on wall facing response. The numerical results show that the backfill soil stiffness, foundation compressibility and horizontal joint stiffness all influence the magnitude and distribution of vertical load through the height of the wall and bearing pad compression. The current study demonstrates that qualitative trends in vertical load factor are preserved when a more advanced stress-dependent stiffness soil hardening model is used for the backfill soil compared to the simpler linear-elastic Mohr-Coulomb model. There are detectable higher vertical loads through the concrete facing panels and more gap compression in some cases using the advanced backfill soil model, but the differences are small and thus judged not to be of practical concern.

Despite the influence of many factors on the magnitude of vertical facing load and joint compression, a set of design charts was developed that can be used to select the number and type of bearing pads placed at the horizontal joints between the concrete panels so that gap closure is restricted to tolerable amounts and vertical loads transmitted through the concrete panels are not excessive. Additional analysis results are presented as design charts that can be used to estimate the settlement at the top of the concrete facing units. These charts demonstrate that settlement of the concrete facing is most sensitive to the compressibility of the foundation soil.

An important caveat to the results presented here is that only vertical facing loads and uniform joint compression are considered. In actual walls there is also the possibility of differential settlements along horizontal joints and panel tilting. These deformations can also lead to panel contact and subsequent cracking and spalling. Numerical modelling of the type used in this investigation is not a practical approach to investigate these potential but infrequent modes of failure. Rather, these types of problems are best prevented through good construction quality control including careful initial alignment of the bottom row of panels on a level and well-supported footing.

CHAPTER 4

NUMERICAL STUDY OF THE INFLUENCE OF FACING VERTICAL STIFFNESS ON STEEL REINFORCED SOIL WALL DESIGN [1] AND THE USE OF ACTIVELY-TENSIONED POLYMERIC STRIPS [2]

4.1. VERTICAL STIFFNESS ON STEEL REINFORCED SOIL WALL DESIGN

4.1.1. Introduction and General approach

The mechanical behaviour of reinforced soil walls is complicated due to the mechanical complexity of the component materials (including soil type/arrangement), their interactions, wall geometry, and the influence of method of construction. Most reinforced soil walls are designed assuming that the wall foundation is rigid and/or does not influence the magnitude and distribution of reinforcement loads under operational conditions. This assumption may not apply to walls constructed over compressible foundations. This section describes the results of a series of numerical simulations that were carried out on a 6 m-high wall with precast concrete panels with metallically reinforced soil and constructed with backfill (reinforced soil and retained fill) and foundation soils having different stiffness, and different number of horizontal joints (i.e., different height of the panel units) along the facing elevation.

The program PLAXIS (PLAXIS 2008) was used to carry out the numerical simulations. The reference case for model calibration is the instrumented 6 m-high precast panel facing wall reinforced with steel strips reported by Chida and Nakagaki (1979). All the results in the

[1] Chapter section based on Damians, I.P., Bathurst, R.J., Josa, A., and Lloret, A.; 2013. Influence of facing vertical stiffness on reinforced soil wall design. Proceedings of the 18th International Conference on Soil Mechanics and Geotechnical Engineering, Paris, France. 2nd–6th September 2013, Vol.3, pp.1959-1962.

[2] Chapter section based on Damians, I.P., Bathurst, R.J., Lima J., Lloret, A., and Josa, A.; 2015. Numerical study of the use of actively-tensioned polymeric strips for reinforced soil walls. Proceedings of the XVI European Conference on Soil Mechanics and Geotechnical Engineering (XVI ECSMGE), Geotechnical Engineering for Infrastructure and Development. Edinburgh, Scotland. 13th–17th September 2015. Vol.7, pp.3833-3838.

present study correspond to operational (working stress) conditions at the end of the construction.

4.1.2. Numerical model

The PLAXIS global geometry, structural components, and the numerical mesh to simulate the performance of the reference instrumented case are illustrated in Figure 4.1.

Material properties for the soil zones (backfill and foundation) are summarized in Table 4.1. Two different stiffness of the backfill were considered to represent different scenarios due to the effects of compaction. The more compressible soil case (with assumed $E_{backfill}$ = 10 MPa) does not imply that poorly compacted soils should be used in the construction of these types of structures, but was used to ensure detectable differences between simulation outcomes. Moreover, the first meter of reinforced soil in contact with the facing is commonly constructed with less compaction energy and hence was assumed to have one half the stiffness of the fully compacted soil. Two other cases were assumed for the foundation soil; nevertheless, the actual foundation stiffness for the reference wall case was not reported by Chida and Nakagaki. The stiffness combinations in Table 4.1 result in four boundary cases to be examined.

Plane-strain boundary conditions were considered for the selection of the internal friction angle of the soils. The soil material properties also define the strength and stiffness of the interfaces between the soil and the structural elements (panels and reinforcement) using a reduction factor (R_i), which is the ratio of interface shear strength to shear strength of the surrounding soil. The values chosen for this factor in each case (soil-facing and soil-reinforcement) are based on reported data and actual mechanical behavior of these interactions.

Reinforcement elements were modelled using the "geogrid" PLAXIS elements as continuous sheets that have only axial stiffness and can transmit load to the surrounding soil through interface shear (R_i parameter). The equivalent linear-elastic axial stiffness of the geogrid element for each layer of reinforcement elements is computed as follows:

$$(EA)_{\text{geogrid}} = E_{\text{reinforcement}} A_{\text{reinforcement}} \frac{n_{\text{reinforcements}}}{L_{\text{panel}}} \tag{4.1}$$

where: $E_{reinforcement}$ is the stiffness modulus of the reinforcement layers (200 GPa for steel); A_{strip} is the cross-sectional area of one strip (100 × 2.3 mm); n_{strips} is the number of strips along one panel (two strip-units), and L_{panel} is the panel width assumed as 1.5 m. The resulting axial stiffness of the geogrid element is about 60 MPa/m. Other analyses considering different axial stiffness modulus equivalent to other steel reinforced types (e.g., bar mats with axial stiffness about 40 MPa/m) do not generate significant variations from the results presented in this study

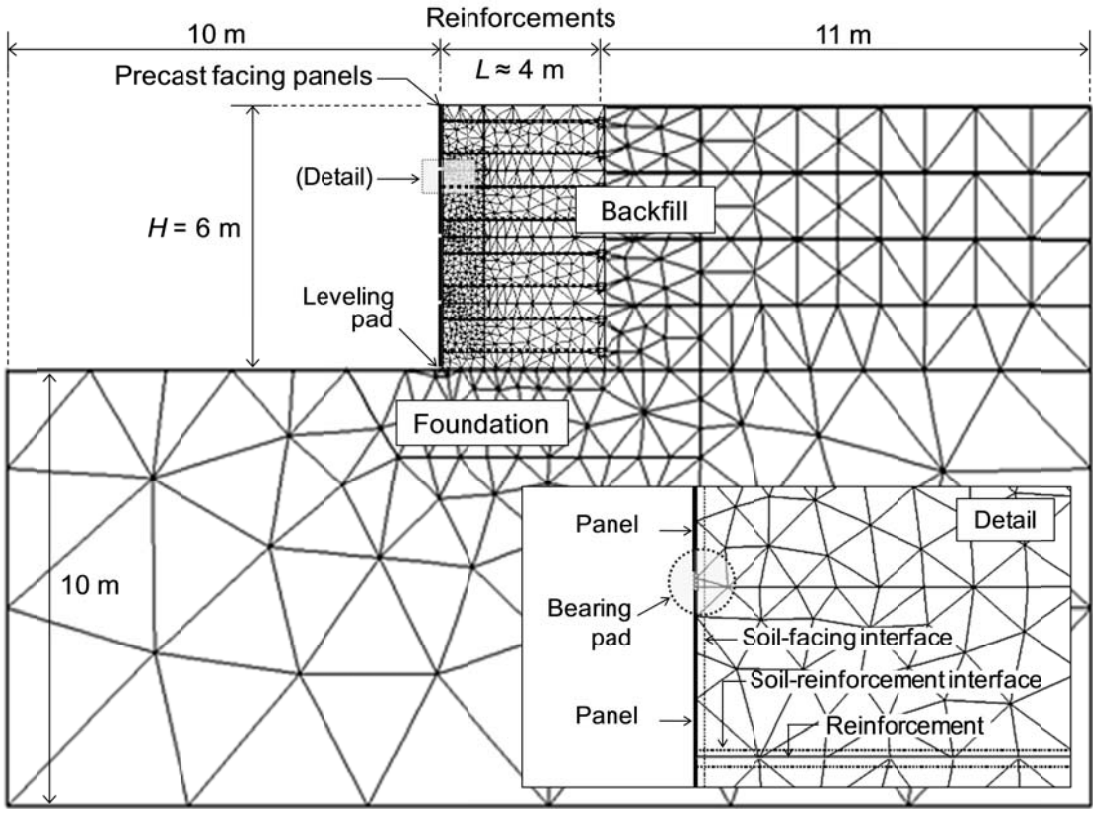

Figure 4.1: PLAXIS numerical model for facing stiffness analysis.

Table 4.1: Model properties of the soil materials.

Parameters	Foundation	Backfill > 1.0 m from face	< 1.0 m from face
Unit weight (kN/m^3)	20	18	18
Cohesion (kPa)	1	1	1
Friction angle (deg)	36	44	44
Dilatancy angle (deg)	6	14	14
Elastic modulus (MPa)	10 – 1000	10 & 100	5 & 50
Poisson's ratio	0.3	0.3	0.3
Interface reduction factor	1	1	0.3 & 0.6

The facing was defined by PLAXIS "beam" elements, and is comprised of the panels and the elastomeric bearing pads. The bearing pads are installed in the horizontal joints between contiguous vertical panels and are used in practice to prevent concrete-to-concrete panel contact.

Material properties for the concrete facing panels and horizontal joints are summarized in Table 4.2. The material type, dimensions and number of bearing pads can vary between projects (Neely and Tan 2010). The same Equation 1 can be used to obtain the parametrical values of the bearing pad elements (Chapter 1 - Damians et al., 2013a). In the present analyses, two EPDM (ethylene propylene diene monomer (M-class) rubber) bearing pads were assumed in each horizontal joint between per panel width.

Table 4.2. Model properties of the beam elements:

Parameters	Panels	Bearing pads (EPDM)
Axial stiffness (MN/m)	6.0	0.1
Bending stiffness (kNm^2/m)	11	0.3
Weight (kN/m/m)	4.5	0.2
Poisson's ratio	0.15	0.49

4.1.3. Vertical stiffness results

Numerical predicted vertical loads at the base of the facing panels and the reinforcement loads were compared to values reported by Chida and Nakagaki (1979) during calibration of the numerical model.

4.1.3.1. Vertical loads under facing

In Chapter 1 (Damians et al., 2013a) it has been shown, from a review of instrumented case studies, that the vertical load at the base of a precast facing wall with steel reinforced soil elements is greater than the self-weight of the panels. The vertical load under facing is a combination of facing self-weight, soil-panel shear and reinforcement down-drag loads, which generate reported load factors from 1.8 to 4.7 times the self-weight of the panels in steel reinforced soil walls (a value of 2.1 is computed for the reference wall reported by Chida and Nakagaki). It should be noted that the studied cases are restricted to steel reinforced soil walls. However, there are similar data for an instrumented full-scale 6-m high geosynthetic-reinforced soil wall with incremental concrete panels constructed in the laboratory (Tariji et al., 1996); the computed vertical load factor is 2.2 for this structure.

Figure 4.2 summarizes results that take into account the effect of the backfill and foundation stiffness scenarios and the backfill-facing interface shear strength (R_i value of 0.3 and 0.6).

The data show that the larger R_i-value assumed results in a range of total vertical facing loads that vary from the reported value of 53.3 kN/m for the reference case. Assuming a value of R_i = 0.3 generates four stiffness scenarios that include the measured case study value more accurately (modifying the $E_{backfill}$ from 100 to 10 MPa when $E_{foundation}$ is 1000 MPa, or modifying $E_{foundation}$ from 1000 to 10 MPa when $E_{backfill}$ is constant at 100 MPa).

Typically, the recommended interface shear strength factor values are about 0.6 times the shear strength of the surrounding soil. However, analysis of a wall reported by Runser et al. (2001) showed that a value of R_i = 0.3 was gave more accurate predictions (Chapter 1 - Damians et al., 2013a). This value was adopted in the current study.

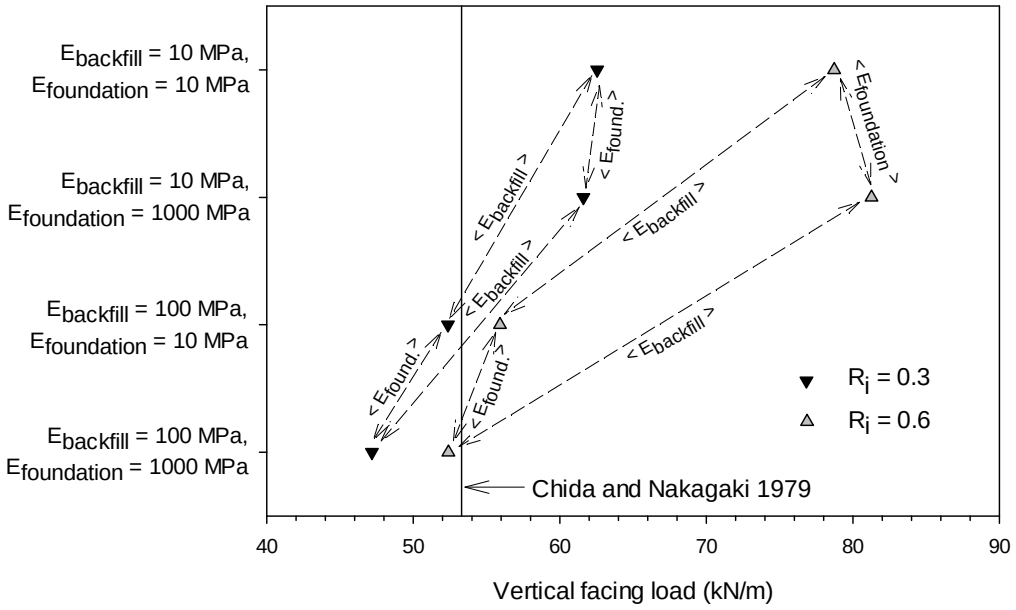

Figure 4.2: Total vertical loads under the facing assuming soil-facing interface reduction factor R_i = 0.3, and R_i = 0.6.

4.1.3.2. Reinforcement loads

In Figure 4.3 are shown the results of the reinforcement tensile loads obtained from numerical modelling and comparison with measured data for selected strips at different elevations. The reinforcement length considered in this study is 0.6 – 0.7 times the total wall height. Steel strips with lengths from 4.0 to 5.0 m were used in the reference case study, so all locations along any reinforcement layer are normalized with the respect to the layer length.

The presented results show good agreement between the numerical model results and measured data. The backfill-foundation stiffness combination results give different tensile-load distributions in the reinforcement layers. The effect of the less-compacted soil near the facing can be clearly detected with the discontinuity at a normalized distance from 0 to 0.25.

Figure 4.4 presents the comparison of the maximum reinforcement tensile-loads and their location with regards to the normalized distance (i.e., distance to the facing of a stress x-point / total length of reinforcement). Values from Chida and Nakagaki (1979) were also included. As shown, their maximum reinforcement tensile loads are quite well fitted with the values

obtained by numerical models assuming low stiffness backfill material. However, the location of the maximums reported is better fitted under opposite cases with stiffer backfill.

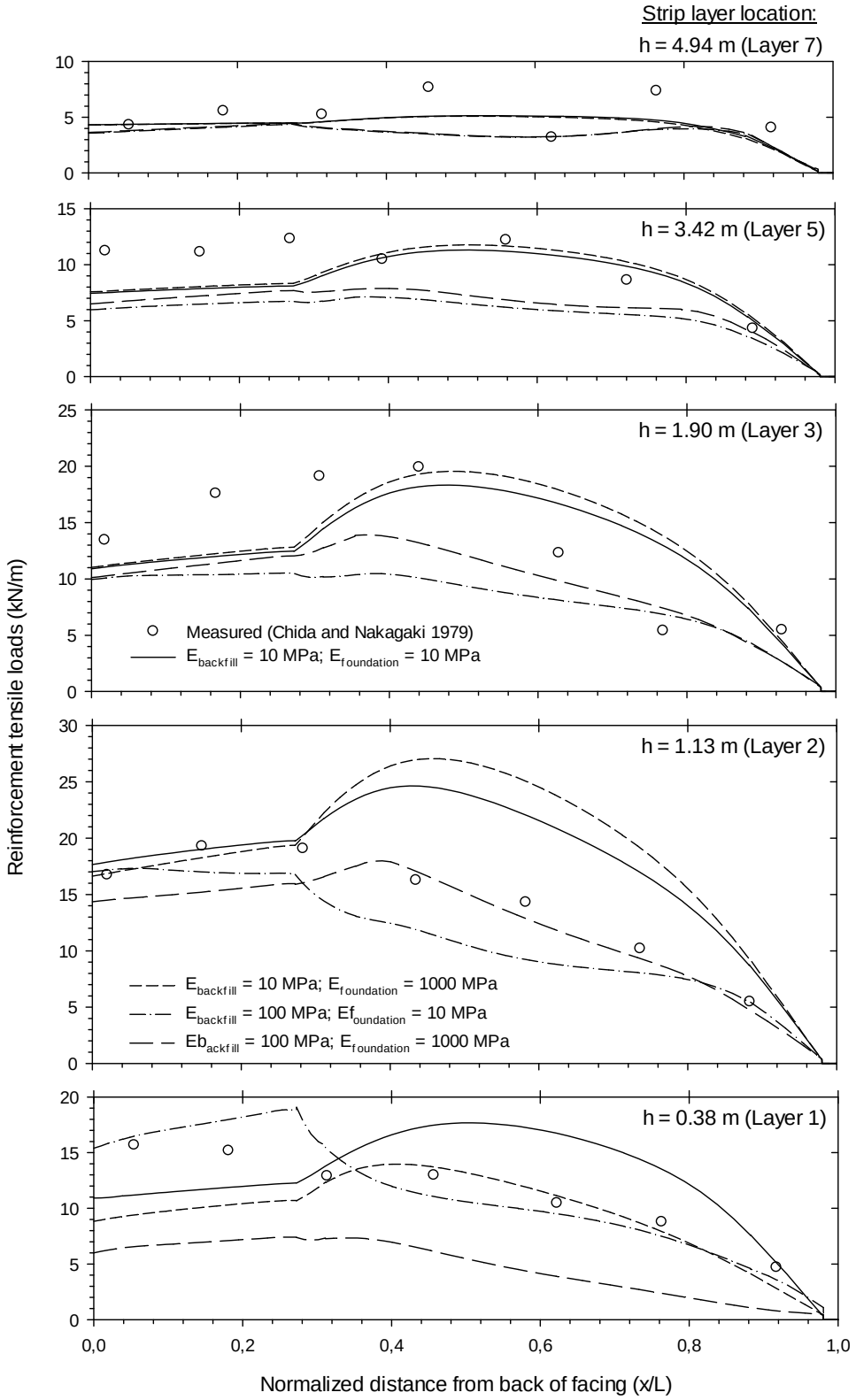

Figure 4.3: Tensile-load distribution of the wall reinforcements at the end of construction. (Normalized distance = distance to the facing of a stress x-point / total length of reinforcement)

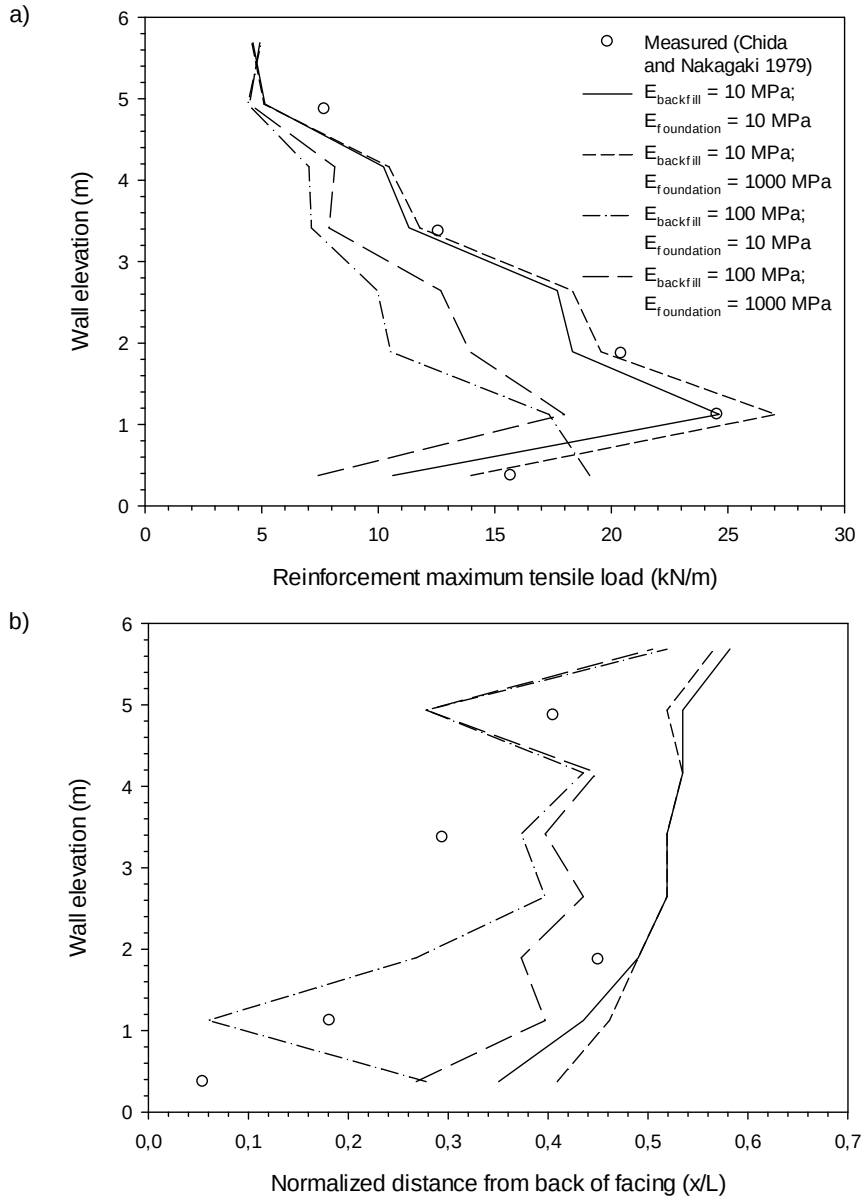

Figure 4.4: Comparison of the maximum reinforcement tensile-loads (a) and their location (b). (Normalized distance = distance to the facing of a stress x-point / total length of reinforcement)

4.1.3.3. Influence of vertical facing stiffness

As noted earlier, the vertical facing stiffness was modified by changing the number of horizontal joints along the facing height of the wall. The reported case (base-case) had three horizontal joins (four panels of 1.5 m-height). Three other cases were considered to investigate the effect of the vertical facing stiffness (see Figure 4.5).

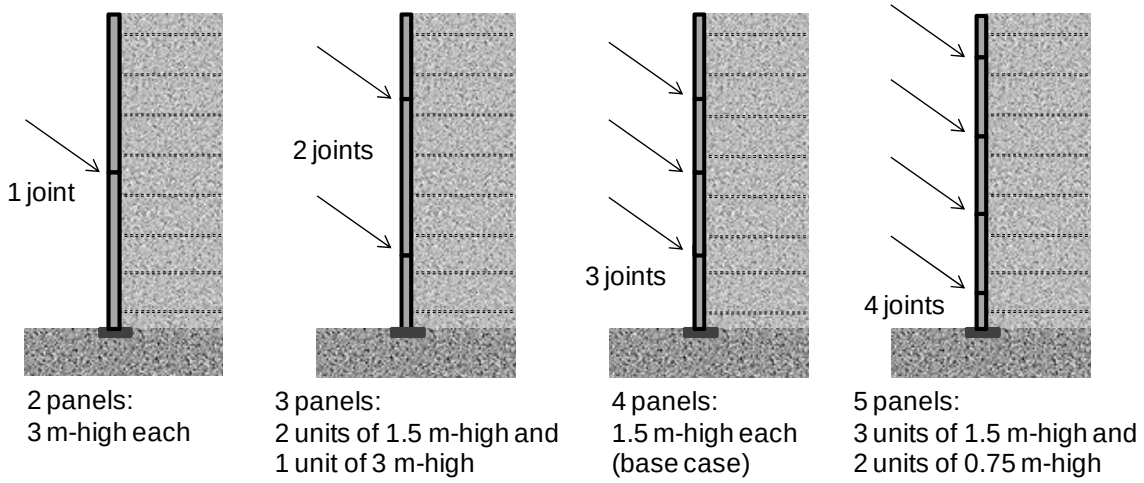

Figure 4.5: Schema about the horizontal joint options considered.

Figure 4.6 shows the numerical model reinforcement tensile-loads with respect to the number of horizontal joints. The values correspond to the maximum load ($T_{maximum}$) of all the reinforcement strips, its related strip, and the normalized distance of T_{max} to the facing in the strip. Reported values obtained from Chida and Nakagaki (1979) are also shown. First, it can be noted that there is little difference in the predicted T_{max} value with respect to the backfill and foundation stiffness combinations (less than 4 kN/m in the case with more divergence, i.e., $E_{backfill}$ = 100 MPa and $E_{foundation}$ = 10 MPa combination). All the T_{max} values (numerical and measured) are located at the bottom zone of the wall (all at the layer located at 1.13 m, except the numerical case with $E_{backfill}$ = 100 MPa and $E_{foundation}$ = 10 MPa). With respect to their location in the reinforcement (normalized distance from the facing), all the T_{max} values are located between 0.3 and 0.5.

Figure 4.7 shows the effect of the foundation stiffness and the vertical facing stiffness on the total vertical loads at base of the facing. Three additional foundation stiffness cases are considered here in order to obtain more data points. It can be observed that higher values of the foundation stiffness (elastic modulus) generate lower values of the total vertical load under the facing. If the total vertical load under the facing with respect to the number horizontal joints is analyzed (Figure 4.6), a significant influence of the vertical facing stiffness on the results can be noted. This influence is less relevant if the lowest modulus of the backfill soil is assumed (i.e., $E_{backfill}$ = 10 MPa, which generates a range of about 3 kN/m between boundary cases). If the backfill soil is assumed with higher stiffness value ($E_{backfill}$ = 100 MPa), the variation of the vertical load is more significant with a range of 15 kN/m for the single joint case, and 20 kN/m for the four joint case.

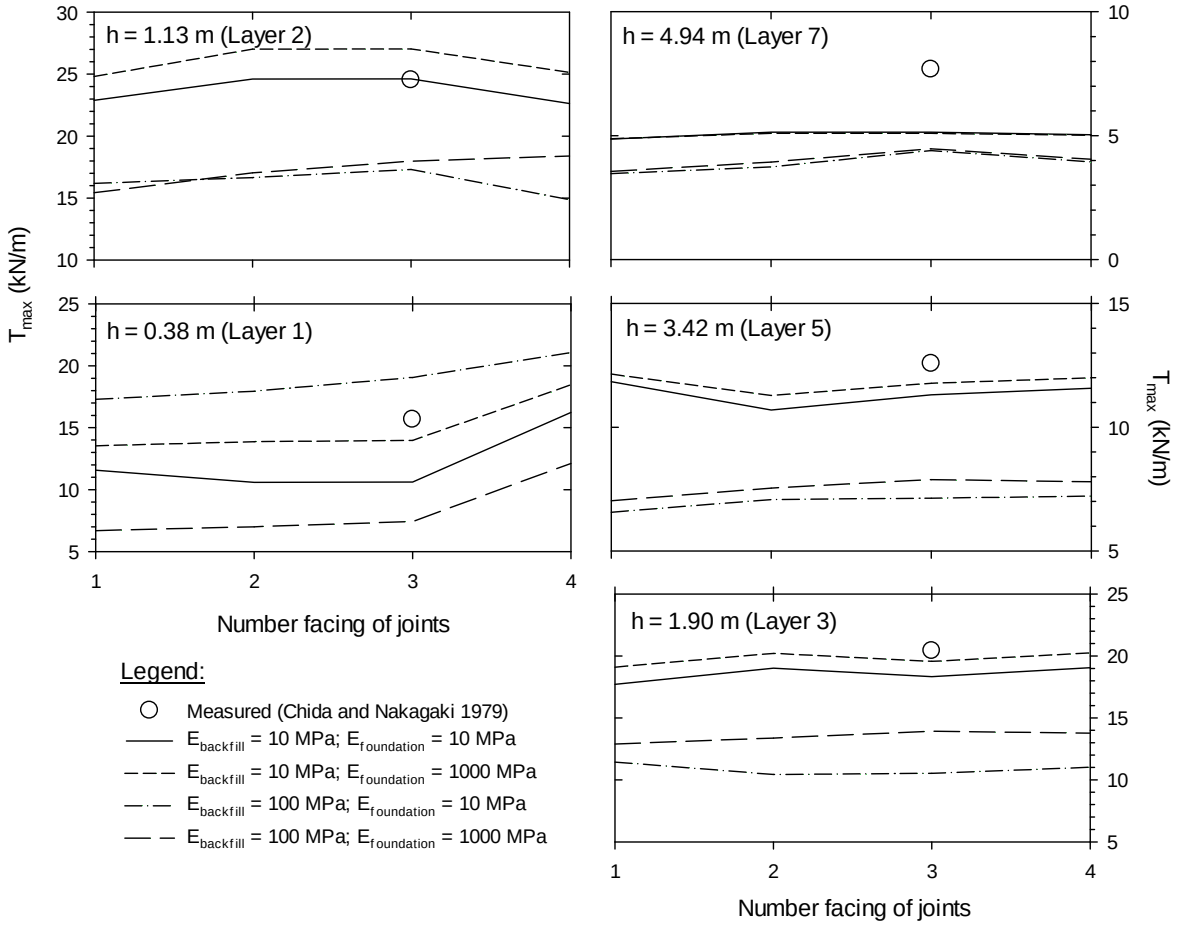

Figure 4.6: Maximum reinforcement loads (T_{max}) with respect to the number of horizontal joints and backfill-foundation stiffness combination.

4.1.4. Conclusions on vertical stiffness results

The mechanical behaviour of reinforced soil walls is complicated due to the mechanical complexity of the component materials, their interactions, wall geometry and soil type/arrangement, in addition to the unquantifiable effects of construction method and quality. Nevertheless, current design methods are typically based on classical notions of soil and reinforcement ultimate strength. Furthermore, internal stability design using conventional analytical solutions assumes that the compressibility of the foundation soil does not influence reinforcement loads.

The numerical simulation results in the current study demonstrate, first, that vertical loads at the base of the facing are affected directly by the backfill and foundation stiffness scenario and the soil-facing interface shear strength; second, there is a significant variation of reinforcement tensile load results depending on the combination of the backfill and foundation stiffness values; and third, the vertical stiffness of the facing (represented by the number of horizontal joints along the facing, that can be also be understood as different

thicknesses of the bearing pad elements) produce significantly different effects on the vertical facing load and the reinforcement tensile loads. These three outcomes cannot be predicted for walls under operational (working stress) conditions using current strength-based design methods for the calculation of reinforcement loads.

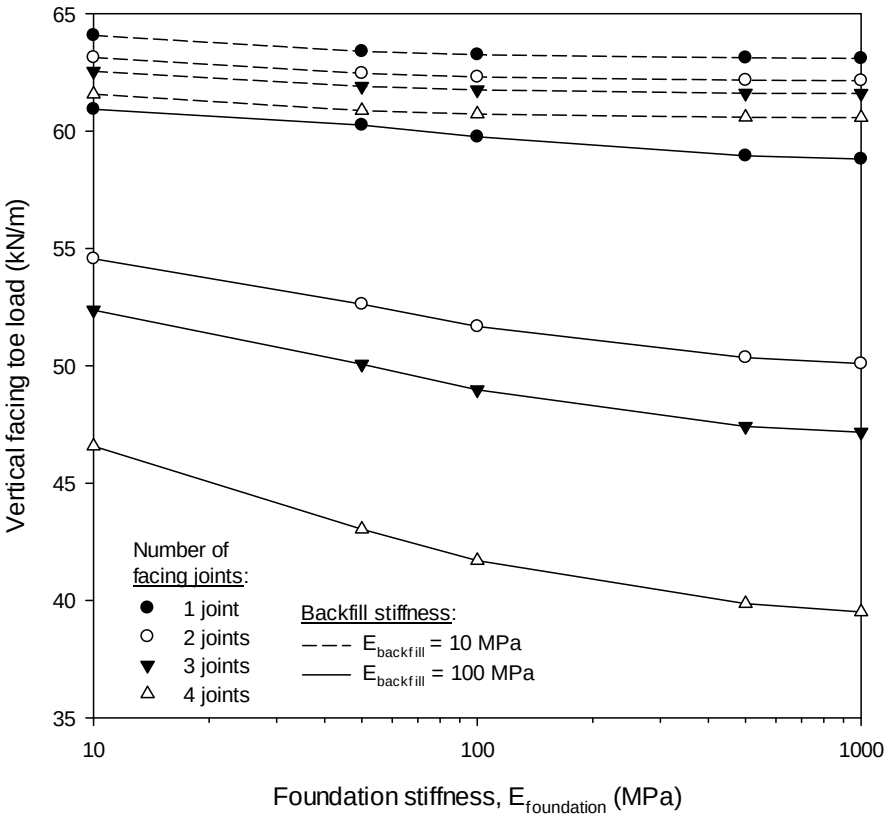

Figure 4.7: Vertical facing toe-load comparison with facing, foundation and backfill stiffness.

4.2. THE USE OF ACTIVELY-TENSIONED POLYMERIC STRIPS

4.2.1. Introduction and Methodology

Mechanically stabilized earth (MSE) walls are used worldwide. However, the mechanical behaviour of these structures is complicated due to the mechanical complexity of the component materials, their interactions, wall geometry, soil type and reinforcement arrangement, in addition to the unquantifiable effects of construction method and quality. Design methodologies for reinforced soil wall systems can be found in national design guidance documents. This section describes the results of a series of numerical simulations that were carried out on an idealized 6 m-high wall using precast concrete panels and backfill soil reinforced with polymeric strips. Current construction practice is to remove any slack in reinforcement materials prior to burial so that reinforcement load capacity is mobilized as soon as possible during construction (Berg et al., 2009). To achieve this condition for polymeric strip reinforced soil wall systems, a pre-tensioning load is applied to the far end of the strips. In this study, four different pre-tensioning loads were considered. The study also considers cases with foundation soils having two very different stiffness values in order to investigate the influence of foundation compressibility on numerical outcomes.

The program PLAXIS (2008) was used to carry out the numerical simulations. This program has been used in related numerical studies of reinforced soil walls by the author (Chapter 1 - Damians et al., 2013a) and has demonstrated good agreement between numerical predictions of reinforcement loads and measured values taken from instrumented structures (Chapter 2 - Damians et al., 2015).

4.2.2. General approach: Polymeric strips and reinforcement installation

Polymeric strips are often used as the reinforcement elements in MSE wall structures. Polymeric strips (Figure 4.8) are made from high-tenacity polyester fibres concentrated in separate parallel bundles (yarns) which provide the axial tensile strength and stiffness. The bundles are coated with a polyethylene sheath to provide protection and interface frictional strength with the surrounding soil. The finished coated strips are manufactured using a die extrusion process. The reinforcement products assumed in this study have four strength capacities (i.e., grades) − 30, 50, 70 and 100 kN based on rapid tensile testing (short-term strength). For design, the long-term strength of the strip is required. The long-term available strength is computed as the short-term strength influenced by a series of material and site-specific strength reduction factors related to potential installation damage, creep and degradation due to potential chemical, biological and ultraviolet attack.

In MSE wall systems, reinforcement elements (polymeric strips in this study) are located within the backfill and transfer the load from the soil material to the strips by frictional interaction. The soil-reinforcement interaction coefficient (C_i) of the strip, which is controlled

by the polyethylene sheath, is normally specified in design codes and confirmed by the strip supplier. Values of $C_i = \tan\delta / \tan\phi$ from 0.7 to 1.5 are typically obtained from pullout tests at different confining pressures (where ϕ is the friction angle of the soil and δ is the soil-reinforcement interface friction angle). In the absence of test data, C_i values of about 0.7–0.8 can be conservatively assumed for polymeric strips (Berg et al., 2009, Lo 1998).

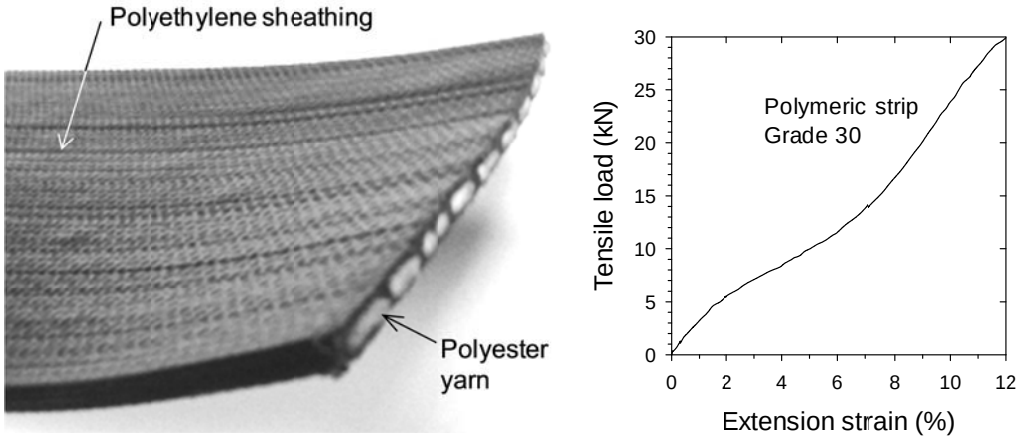

Figure 4.8: Polymeric strip detail (left) and typical load-extension behaviour (right) of Grade 30 strip (Chamberlain & Cooper 2009).

The polymeric strips are placed over compacted backfill soil and pre-tensioned as noted earlier. This is typically achieved by pulling the strips tight from the far end and holding them in this position while they are covered with the next fill layer. The strips may be placed in a continuous wrapped arrangement (loops) (Figure 4.9) or placed as single strip segments (free tail ends). The strip ends are anchored and fixed to the ground using different methods such as rear anchorage bars for the case of continuous strip loops (see Figure 4.9), or pegs drilled or staked through the strips into the backfill (continuous or single strips).

Tensioning of the polymeric strips is then per-formed using different procedures depending on the system (e.g., pulling directly on the rear anchor bar and locking the bar in place with pins, or backfilling over a shallow trench located below the end of the strips and running parallel to the wall face). Regardless of the method, it is a challenge to achieve a uniform pre-tension load in the reinforcement strips between and within each reinforcement layer.

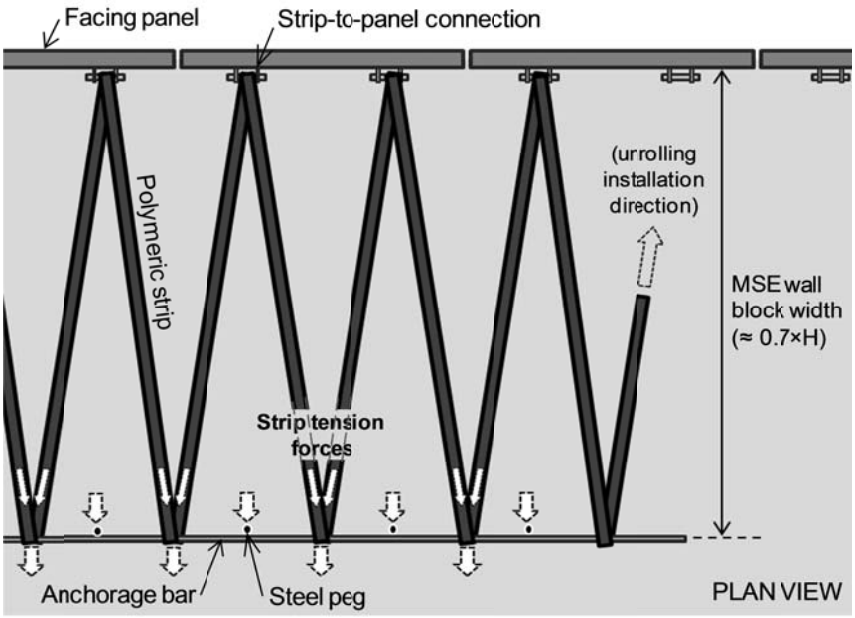

Figure 4.9: Continuous strip installation using an anchorage bar.

4.2.3. Numerical model

4.2.3.1. General features and Material properties

The PLAXIS global geometry, structural components, and the numerical 2D-finite element mesh used to simulate the case study structures are illustrated in Figure 4.10. Eight reinforcement layers were considered within the structural height (i.e., vertical reinforcement spacing of 0.75 m).

The wall facing was modelled as discrete panels of 1.5 m height. The facing was defined by PLAXIS "beam" elements, and was comprised of the panels and elastomeric bearing pads located at the horizontal joints. Material properties for the concrete facing panels and bearing pads are summarized in Table 4.3. Bearing pads are typically used in practice to smoothly distribute vertical loads between the facing panels and to prevent concrete-to-concrete panel contact. The (typical) 20 mm-thick bearing pads are installed in the horizontal joints between adjoining vertical panels. The material type, dimensions and number of bearing pads can vary between projects (Damians et al., 2013a). In the present analyses, two HDPE (high density polyethylene) bearing pads per 1.5 m-wide panel were assumed at each horizontal joint.

Material properties for the three different soil zones (backfill, retained soil and foundation) (Figure 4.10) are summarized in Table 4.4. The first metre of rein-forced soil behind the facing is commonly constructed with less compaction effort and hence was assumed to have one half the stiffness of the compacted soil located further from the facing. Most reinforced soil walls are designed assuming that the wall foundation is rigid and/or does not influence

the magnitude and distribution of reinforcement loads under operational conditions. This assumption may not apply to walls constructed over very compressible foundations. In the current study, two different foundation conditions with respect to compressibility were considered.

Soil materials were modelled as linear elastic perfectly-plastic materials (Mohr-Coulomb failure criterion). Plane-strain boundary conditions were considered for the selection of the internal friction angle of the soils. In program PLAXIS, the soil material properties can be used to define the strength and stiffness of the interfaces between the soil and the structural elements (panels and reinforcement) using a reduction factor (R_i), which is the ratio of interface shear strength to shear strength of the surrounding soil. The values selected in the current study were back-calculated from an instrumented wall (see Chapter 2, as Damians et al., 2015).

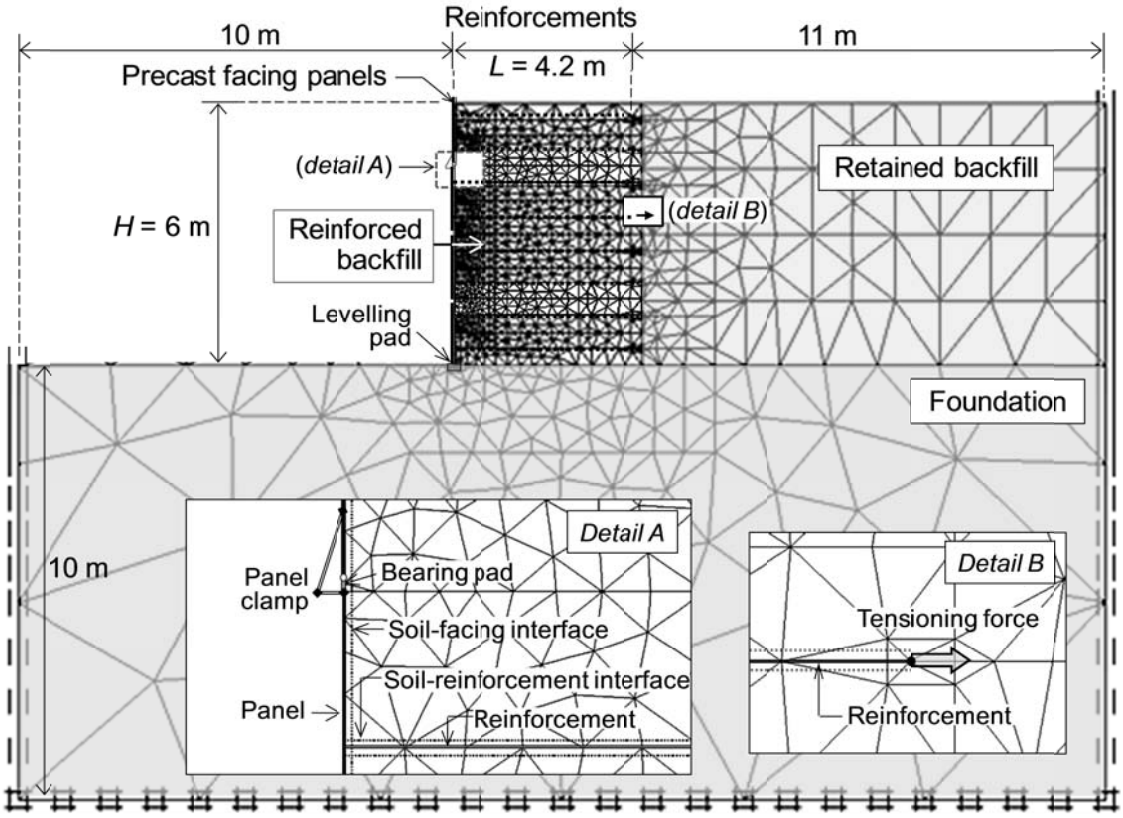

Figure 4.10: PLAXIS numerical model for strip tension analysis.

Reinforcement elements were modelled using "geogrid" PLAXIS elements as continuous sheets that have only axial stiffness and can transmit load to the surrounding soil through interface shear, controlled by the interface reduction factor (i.e., R_i parameter). A soil-reinforcement interaction coefficient $C_{i(strip)}$ = 0.8 was assumed in this study. At each reinforcement-layer elevation there is also a planar area of soil-soil contact only. For this

reason the representative R_i value for each reinforcement layer was computed using Equation 4.2 (which gives the values presented in Table 4.3 − Note (d)).

$$R_i = \frac{1}{A_{\text{layer}}}\left(C_{i\ (\text{soil})} A_{\text{soil/layer}}\right) + \left(C_{i\ (\text{strip})} A_{\text{strips/layer}}\right) \tag{4.2}$$

where: $C_{i(soil)}$ is the soil-soil interaction coefficient ($C_{i(soil)}$ = 1); A_{layer} is the total surface area of each reinforcement layer equal to the panel width (assumed as L_{panel} = 1.5 m) multiplied by the strip length (L_{strip} = 0.7×H = 4.2 m); A_{strip}/layer is the soil-strip contact area equal to the number of strips per layer (n_{strip} = 4 or 6 units matching the number of connections per panel) multiplied by the strip-width (assumed as 85 mm) and by the strip length, and; A_{soil}/layer is the soil-soil contact area per layer (= $A_{layer} - A_{strip}$/layer).

The load/extension test curve presented in Figure 4.8 can be reasonably simplified as a straight line. Thus, the equivalent linear-elastic axial stiffness of the geogrid element for each layer of reinforcement can be computed using Equation 4.3.

$$(EA)_{\text{geogrid}} = \frac{F^*}{\varepsilon}\left(\frac{n_{\text{strips}}}{L_{\text{panel}}}\right) \tag{4.3}$$

where: F^* is the ultimate tensile load of the strip (related to the Grade value) and ε is the actual strain at nominal breaking load F^* ($\varepsilon \approx 0.12$ from Figure 4.8). Table 4.5 presents the resulting axial stiffness of the geogrid elements with regard to the layer height location.

4.2.3.2. Construction sequence modelling: Strip tensioning case studies

The wall construction was modeled in sequential 0.375 m-thick layers. Panel installation was per-formed using stiff beam elements attached to the panels (see Figure 4.10 − Detail A: panel clamp). The beam elements were prevented from rotating to simulate the panel clamp and/or propping devices typically used in practice to temporarily support and align the panel units. No attempt was made to capture compaction effects beyond using different soil elastic modulus values as described earlier. The reinforcement elements were installed in separate construction steps between backfill lifts, together with a pre-tension load applied at the tail-end of all strip layers (see Figure 4.10 − Detail B: tensioning force). Thus, four different strip pre-tension load cases were generated: 0.01 kN/strip (assumed as “no-tension” case), 0.56 kN/strip, 1.13 kN/strip, and 2.25 kN/strip. In addition, after wall construction, a final step with-out a tension load was generated to model a hypothetical sudden loss of tension (e.g., due to corrosion of the steel anchorage device).

Table 4.3. Model properties of facing elements:

Parameters	Panels	Bearing pads (HDPE)
Axial stiffness (MN/m)	6	1.1
Bending stiffness (kNm^2/m)	11	2.1
Weight (kN/m/m)	4.5	0.1
Poisson's ratio	0.15	0.4

Table 4.4. Model properties of backfill and foundation soil materials:

Parameters	Reinforced backfill; distance from face [a]		Foundation	Retained backfill
	> 1.0 m	< 1.0 m		
Unit weight (kN/m^3)	18		20	18
Friction angle [b] (deg)	44		40	30
Dilatancy angle (deg)	14		10	0
Cohesion (kPa)	1		10	5
Elastic modulus (MPa)	50	25	10 & 1000	50
Poisson's ratio	0.3		0.3	0.3
Interface reduction factor, R_i	n/a	0.3 [c] (0.932–0.955) [d]	0.6	1 0

Notes: [a] Backfill properties vary due to lower compaction effort near the facing.

[b] Friction angle assuming plane-strain boundary conditions (i.e., equivalent to about 36º-37º under triaxial conditions).

[c] Soil-facing interface reduction factor (applies to backfill soil < 1.0 m from facing).

[d] Soil-reinforcement interface reduction factor adjusted for number of reinforcement strips per unit panel width.

Table 4.5. Axial stiffness of reinforcement elements: Polymeric strips (Grade 30):

Reinforcement layers	Connections per 1.5 m-width panel	Axial stiffness (kN/m)
8^{th} (top layer)	3	1000
3^{rd} to 7^{th}	2	670
1^{st} (bottom layer) and 2^{nd}	3	1000

4.2.4. Strip tensioning results

The numerical results from the present study correspond to operational (working stress) conditions at the end of construction. However, additional cases were generated assuming a distributed load of 10 kN/m on top of the backfill. These additional sur-charge cases did not generate reinforcement loads or soil shear strains that were practically different from those reported below for non-surcharged cases but did influence vertical facing loads and facing toe

settlements as shown next. A useful performance indicator is the facing load factor (Damians et al., 2013a) defined as the ratio of vertical toe load divided by the self-weight of the wall facing. Load factors are expected to be greater than one due to interface shear mobilized between the back of the facing panels and the backfill, and panel connection down-drag forces. Figure 4.11 shows that the load factor decreases with increasing pre-tension load and foundation stiffness, and increases with surcharge pressure. Negligible toe (leveling pad) settlements were generated for the stiffest foundation soil case. For the relatively soft foundation case, toe settlement increased with surcharging but decreased with increasing pre-tension load.

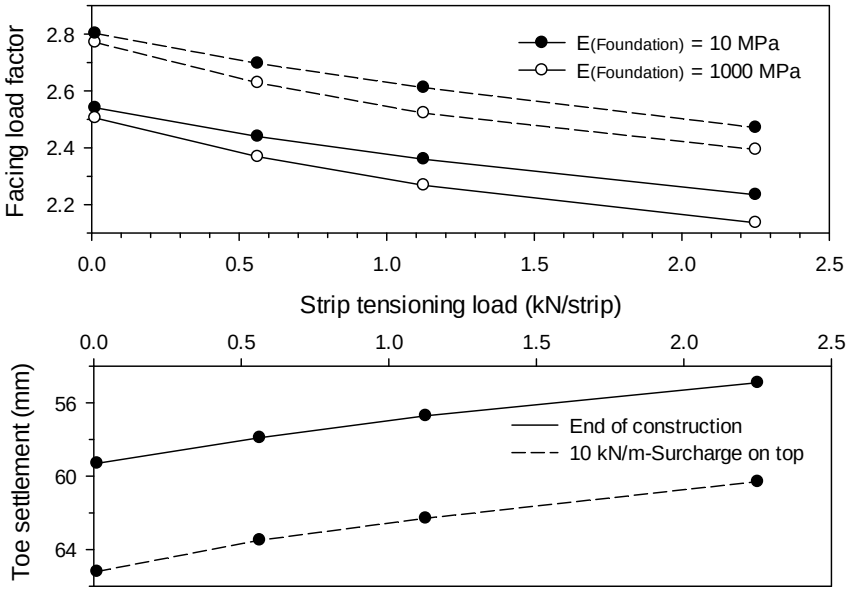

Figure 4.11: Vertical load factor (top) and settlement (bottom) at facing toe.

4.2.4.1. Facing displacements

Figure 4.12 presents computed facing horizontal dis-placements at the end of construction. Increasing the pre-tensioning reduces the outward facing deformations. Tensile loads of 1.13 kN/strip and 0.56 kN/strip resulted in an almost vertical facing alignment for the stiffer and softer foundation cases, respectively. The softer foundation case resulted in 10 mm of horizontal displacement at the wall toe.

4.2.4.2. Reinforcement loads

Computed reinforcement tensile loads for the stiffer foundation (essentially rigid) case at the end of construction are shown in Figure 4.13. The plots show that strip pre-tensioning generates a redistribution of the reinforcement loads that becomes more pronounced with

depth of layer below the wall top. For layers 8 and 6, the maximum pre-tension load of 2.25 kN/strip exceeds the load that is developed for the no-tension case at all locations along the strips. If the tensioning load is lost after construction (e.g., due to corrosion of the anchorage system) the redistribution of load is limited to the vicinity of the strip end where the pre-tensioning load was originally applied. This is because the mobilized interface strip-soil shear strength developed during pre-tensioning and construction remains largely intact.

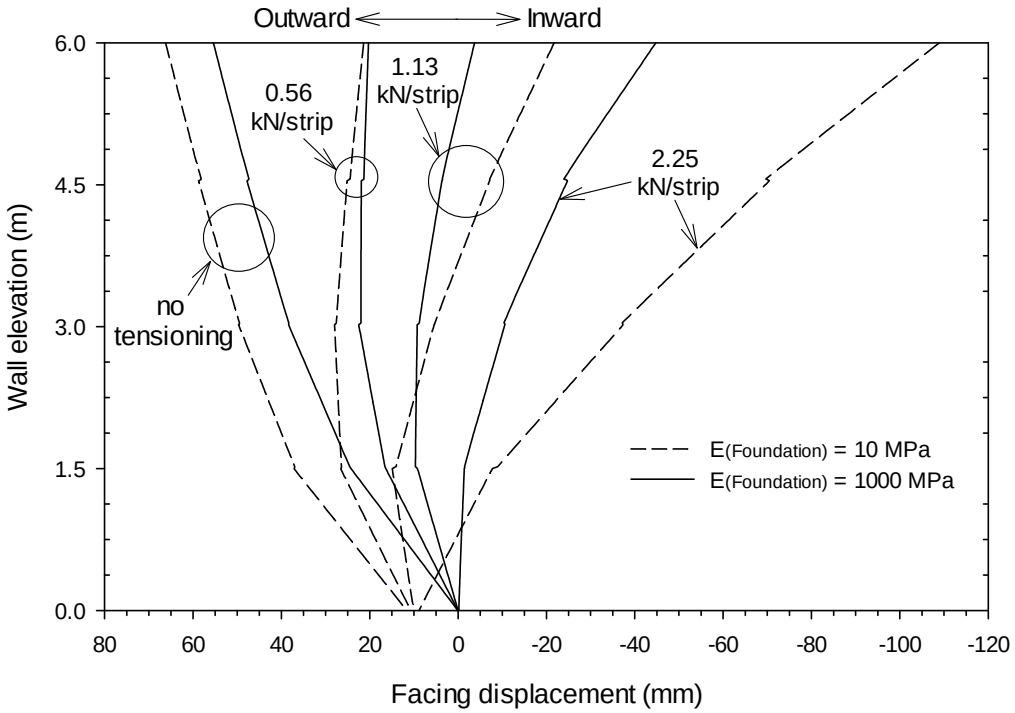

Figure 4.12: Facing displacements at the end of construction.

4.2.4.3. Shear strains and plastic points

Contour plots of shear strains and plastic (failure) points for the stiffer foundation case at the end of construction are presented in Figure 4.14. The internal soil shear zones (0–4% strain range) can be seen to propagate from the heel of the wall but are not fully developed through the height of the reinforced soil zone. This is consistent with the notion of working stress conditions assumed in this study rather than an ultimate internal failure state. Comparison of plots for the cases of pre-tension and no-tension shows a visually apparent reduction in shear strains and plasticity in the reinforced soil zone. This observation is consistent with decreasing wall displacement that results from increasing pre-tension load demonstrated earlier. The shear strain plots show that load transfer between the soil and reinforcement extends to the tail of the reinforcement layers for the pre-tension case which is not the case for the no-tension case.

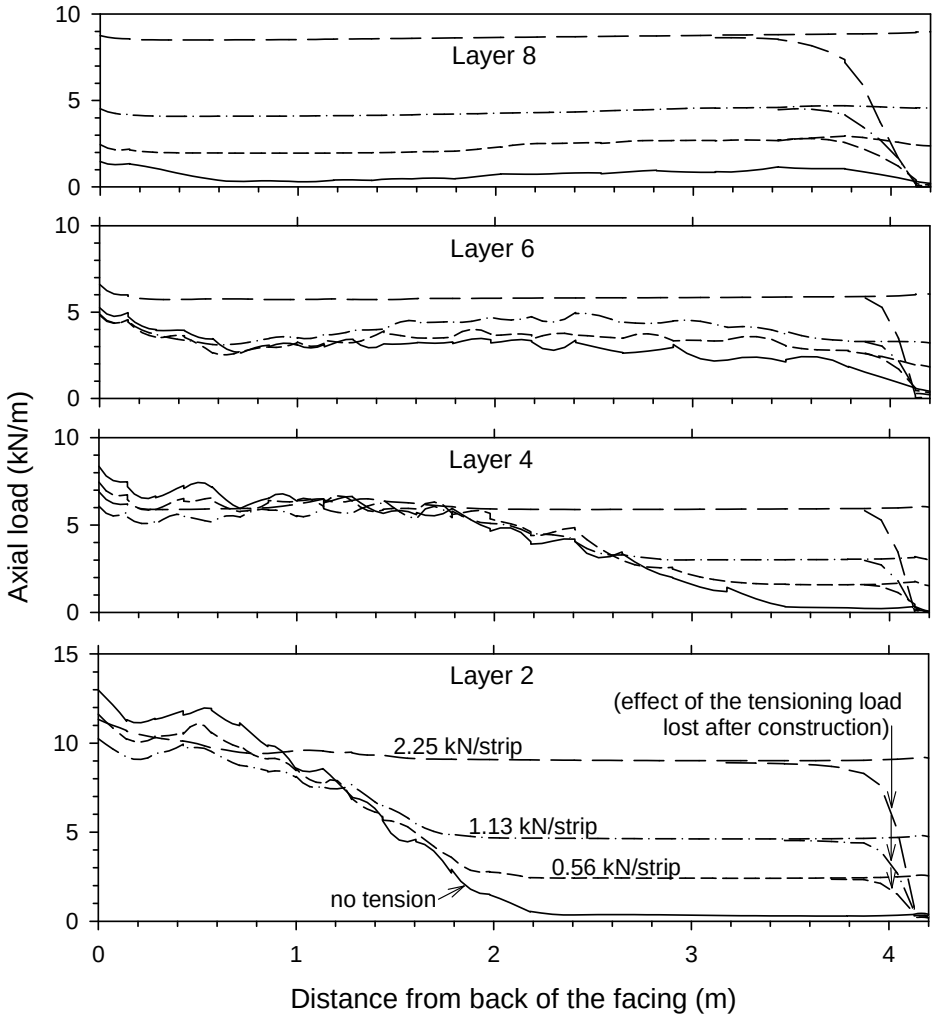

Figure 4.13: Reinforcement loads: Rigid foundation case ($E_{(Foundation)}$ = 1000 MPa) at the end of construction.

4.2.4. Conclusion on strip tensioning results

The numerical simulation results in the current study demonstrate that the polymeric strip installation procedure (i.e., pre-tension or no-tension load applied during construction) has a direct effect on the behaviour of this type of reinforced soil wall. This means that wall performance features at the end of construction can be purposely influenced by using a specified pre-tension load during construction. For example, vertical facing loads, toe settlements and facing displacements can be significantly reduced by applying an appropriate tensioning load at the tail-end of the strip reinforcement layers. In order to achieve this improvement in wall performance it is necessary to use a tensioning device that can measure and control the initial tension load applied to the reinforcement layers at the back anchorage point. The anchorage system must also be designed and installed so that the pre-tension load is maintained during construction. Nevertheless, this may not be a critical long-term

requirement since loss of pre-tension load may be limited to the vicinity of the anchor as demonstrated in this investigation.

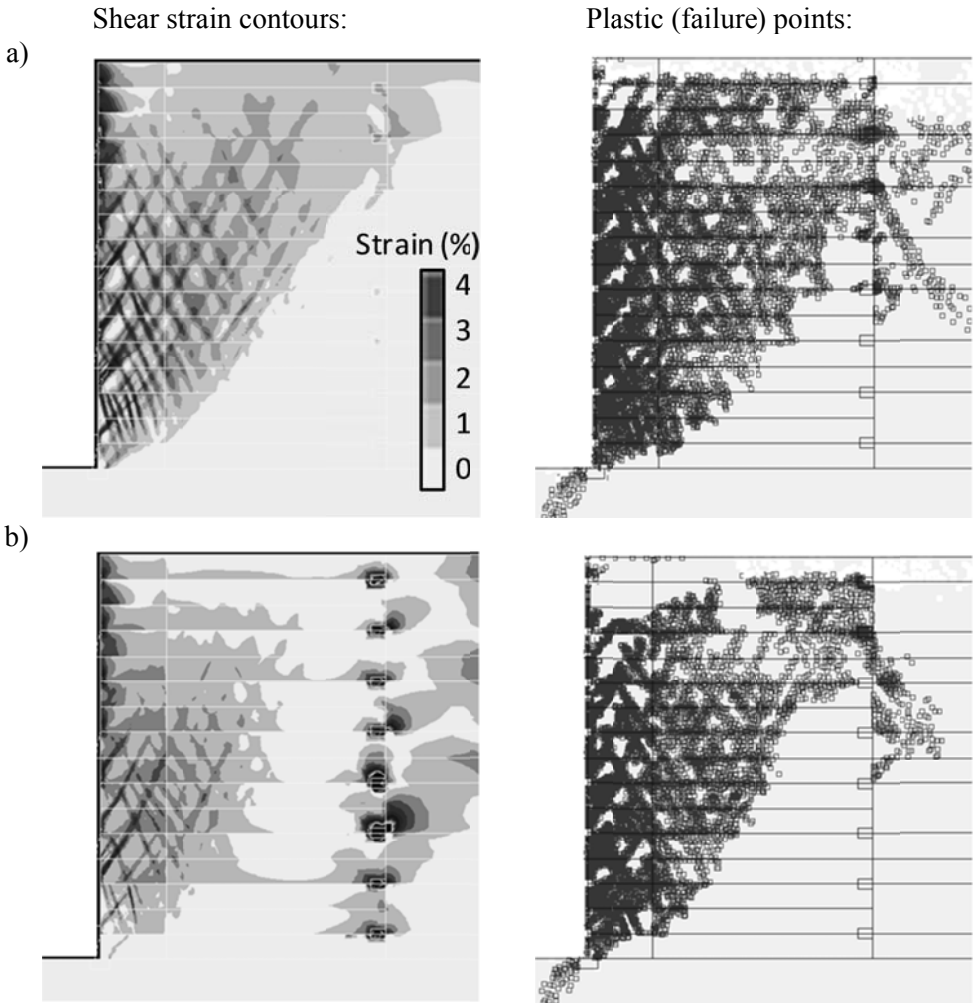

Figure 4.14: Shear strain contours and plastic (failure) points at end of construction for stiff (rigid) foundation case. Strip tensioning cases: no pre-tension (a) and 1.13 kN/strip (b).

CHAPTER 5

COMPARISON OF FINITE ELEMENT AND FINITE DIFFERENCE MODELLING RESULTS WITH MEASURED PERFORMANCE OF A REINFORCED SOIL WALL [1]

5.1. INTRODUCTION

5.1.1. General approach

Mechanically stabilized earth (MSE) walls (reinforced soil walls) are complex mechanical systems. They are comprised of a hard concrete facing in most cases, granular soil backfill and polymeric or steel reinforcement layers. Many walls today are constructed with a dry-stacked modular concrete block facing. Current design methods give recommendations for the internal stability design of these systems so that reinforcement layers do not fail or deform excessively within the soil backfill or at the connections (Berg et al., 2009). These design methods are based on closed-form solutions adapted from conventional earth pressure theory. For geosynthetic (polymeric) reinforced soil walls there is evidence that these design methods are very conservative (Bathurst et al., 2008b). For metallic reinforced soil systems the conservatism is not as great because load equations have been empirically adjusted using measured loads from instrumented walls (Allen et al., 2004). Regardless of the reinforcement type, current design methods are most applicable for walls with simple configurations and competent foundation conditions. For walls falling outside of design guideline envelopes, numerical modelling may be the only alternative for design. However, there are a number of questions that must be addressed when using numerical models for design:

1. Has the numerical model been verified against one or more instrumented structures (Carter et al., 2000)?

[1] Chapter based on Damians, I.P., Bathurst, R.J., Josa, A., and Lloret, A.; 2013. Comparison of finite element and finite difference modelling results with measured performance of a reinforced soil wall. Proceedings of GéoMontréal 2013. 66th Canadian Geotechnical Conference and 11th Joint CGS/IAH-CNC Groundwater Conference. Montréal, Quebec, Canada, 29th September – 3rd October 2013, 7p.

2. Are project-specific material properties available?

3. Will different numerical modelling packages give different design outcomes and, if so, are the differences important?

The current investigation is focused on the last question. Two widely used numerical modelling software packages that use different numerical solution schemes are used to predict performance features of a wire mesh (metallic) reinforced soil wall. One software package is the program FLAC which uses the finite difference method (FDM) solution scheme and the other is the PLAXIS software package that uses the finite element method (FEM). The 2D simulation results are compared to measurements taken from the well-instrumented full-scale experiment noted above and previously reported in the literature.

A very brief description of both software programs follows in the following sections.

5.1.2. Explicit finite difference method: FLAC

FLAC (Fast Lagrangian Analysis of Continua) is a commercial software program developed by ITASCA Consulting Group for engineering mechanics computations. Since 1986 several updated versions have appeared, and the program currently offers a wide range of capabilities to solve complex problems in soil and rock mechanics (Itasca 2005).

FLAC is based on the finite difference method (FDM) to solve partial differential equations. In the FDM the system equations are directly replaced by an algebraic expression at discrete points. The main characteristic of this procedure is that it is able to use an explicit resolution algorithm. Since no global stiffness matrix is formed, large calculations can be made without excessive memory requirement. Due to the explicit solution method, FLAC allows numerical paths to be followed up to plastic collapse. This allows the user to simulate unstable physical processes without numerical divergence issues. The program is well-suited to model large-strain scenarios. For domain discretization, FLAC divides the continua into a finite difference mesh (numerical grid) composed of quadrilateral elements, each of which is internally subdivided into two sets of superimposed constant strain triangles.

Examples of numerical simulation of geosynthetic reinforced soil walls using the program FLAC have been reported by Hatami and Bathurst (2005, 2006) and Huang et al. (2009). Bathurst et al. (2012) used the program FLAC to investigate the influence of foundation compressibility on the behaviour of nominal identical walls constructed with geosynthetic and steel soil reinforcement.

5.1.3. Finite element method: PLAXIS

PLAXIS development began in 1987 at Delft University of Technology with the initial objective to develop a user-friendly finite element code for the analysis of river embankments on soft soils found in Holland. The code has been greatly extended since that time and the PLAXIS software can be used for many geotechnical engineering problems (PLAXIS 2008).

In the finite element method (FEM) the domain is divided into elements. Nodes (where the displacements are calculated) and Gauss points, where loads are calculated, are defined within each element. In PLAXIS 2D, the surfaces and areas are formed by 6-node or 15-node triangles and the element stiffness matrixes are evaluated by 3-point and 12-point Gaussian integrations for 6-node and 15-node triangles, respectively. Due to the general nonlinear relationship between stress increments and strain increments, an approximate formulation of the global stiffness matrix must be formed beforehand, and a global iteration process with a certain tolerance is required to satisfy both the equilibrium condition and constitutive relation under the given boundary and initial conditions.

In previous Chapter 1 (Damians et al., 2013a), Chapter 3 (Damians et al., 2015b), and Chapter 4 (Damians et al., 2013b), PLAXIS was used to investigate the influence of concrete facing unit bearing pad number and compressibility on the behaviour of steel strip reinforced soil walls.

5.1.4. Scope

This Chapter describes the results of a series of numerical simulations with both software programs (FLAC and PLAXIS) that were carried out on a full-scale plane strain 3.6-m high (H) modular block wall constructed with welded wire mesh reinforcement and sand backfill soil.

The accuracy of the FLAC model to predict performance features of the physical wall has been demonstrated in previously published work (Hatami and Bathurst 2005 and 2006, and Huang et al., 2009). In the current study the same verified numerical code is used to model the same wall and to compare predictions with a similar numerical model using the PLAXIS software.

The study presents measured and predicted toe loads, facing displacements, and reinforcement loads at end of construction and during subsequent staged surcharge loading.

A single example of a parametric sensitivity analysis illustrating the influence of friction angle on connection loads is given at the end of the Chapter.

5.2. NUMERICAL MODELS

5.2.1. General

FLAC (version 5.0) and PLAXIS (version 9.2) programs were used to carry out the numerical simulations. As mentioned earlier, the reference case was an instrumented 3.6-m high modular block wall with welded wire mesh reinforcement and sand backfill soil. The physical model was seated on a rigid concrete foundation. The same geometry and boundary conditions were assumed for both numerical models matching the physical experiment (Figure 5.1). The foundation is assumed as rigid, and the toe of the facing was restrained horizontally by a stiff element with an axial spring stiffness of 4 MN/m/m matching the value deduced from measurements at this boundary in the physical test.

The FLAC model domain was discretized using a 50×50 numerical grid (Figure 5.1a). A total of 2009 6-node triangular elements were generated for the PLAXIS model (Figure 5.1b). As noted earlier, PLAXIS allows the use of 15-node elements. However, solving the model constructed with 15-node elements greatly increased computation time with no detectable difference in numerical results.

In order to make fair comparisons between the PLAXIS model and the large strain (Lagrangian) FLAC model, the mesh updating option was selected at each construction step during the PLAXIS simulation.

The same material properties and construction steps matching the physical experiment were used for both models. Construction involved backfilling in 150-mm-thick layers and then applying a transient uniform pressure of 16 kPa to simulate compaction equipment effects. Following construction, a uniform distributed surcharge load (q) was applied in 10 kPa pressure increments up to 80 kPa.

a) FLAC model numerical grid:

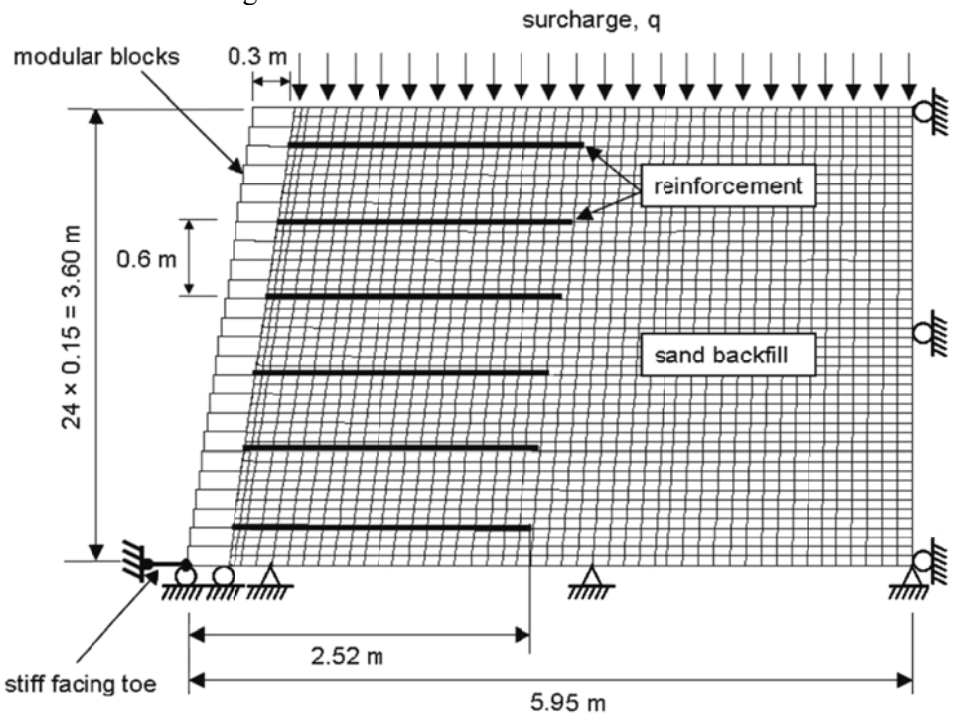

b) PLAXIS model mesh:

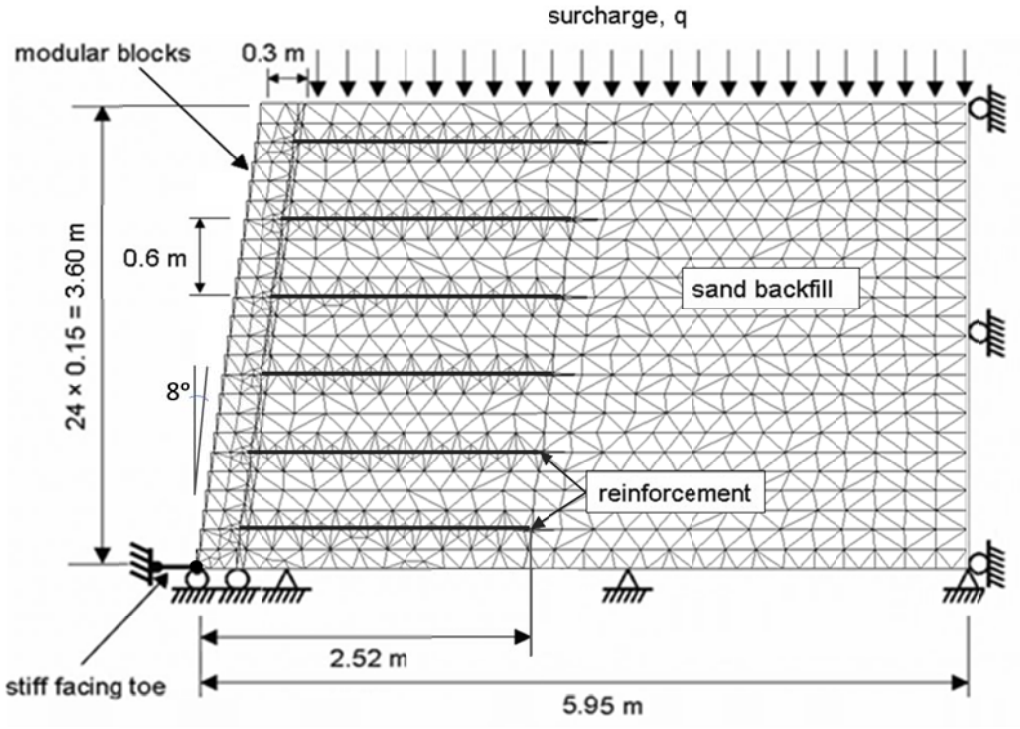

Figure 5.1: Numerical models: FLAC (a) and PLAXIS (b).

5.2.2. Material properties

Reinforcement: The following hyperbolic model proposed by Hatami and Bathurst (2006) was used in the FLAC model:

$$J_t(\varepsilon,t) = \frac{1}{J_0(t)\left(\frac{1}{J_0(t)} + \frac{\eta(t)}{T_f(t)}\varepsilon\right)} \quad (5.1)$$

Where: $J_t(\varepsilon,t)$ is the equivalent tangent stiffness function; $J_0(t)$ is the initial tangent stiffness; $\eta(t)$ is a scaling function; $T_f(t)$ is a stress-rupture function for the reinforcement; ε is strain and t is time (i.e., duration of loading equal to the time to construct the wall).

PLAXIS uses tension elements (called "geogrids") to model soil reinforcement layers. These line elements are assigned an axial stiffness ($J = EA$) and a maximum tension force (N_p). PLAXIS does not provide for user-defined constitutive models for the geogrid elements, so it is was not possible to implement the hyperbolic model described above for the general case of polymeric materials that have stiffness that is strain- and time-dependent.

However, the reinforcement material used in the instrumented wall case was a metallic welded wire mesh (WWM). Therefore the PLAXIS linear-elastic stiffness model was used for this relatively inextensible reinforcement. In the FLAC model, setting $\eta(t) = 0$ in Equation 1 results in the same linear-elastic stiffness for the metallic WWM as in the PLAXIS simulation. Reinforcement model parameters are summarized in Table 5.1.

Table 5.1. Welded wire mesh reinforcement properties:

Model	Parameters	Values
FLAC	$J_0(t)$ (kN/m), $\eta(t)$, $T_f(t)$ (kN/m)	3100, 0, 7
PLAXIS	EA (kN/m), N_p (kN/m)	3100, 7

Backfill soil: Linear elastic model with Mohr-Coulomb failure criterion was used as the constitutive model for the backfill material in both numerical models. This material is high quality medium sand with a narrow size distribution. The model parameters were taken from independent laboratory tests reported by Hatami and Bathurst (2005) and are summarized in Table 5.2. Hatami and Bathurst (2006) and Huang et al. (2009) showed that the linear elastic-plastic model gave sensibly the same results as more complex soil models with hyperbolical stress-strain behaviour at least for working stress conditions.

Interfaces: In the FLAC model case, linear spring-sliders with interface shear strength defined by the Mohr-Coulomb failure criterion were used for the facing-backfill and reinforcement-backfill interfaces (Itasca 2005). In the PLAXIS model, interfaces were modeled with zero-thickness elements (PLAXIS 2008). Typically, PLAXIS interfaces are defined by a reduction factor that is related to the maximum strength of the soil at the interface (i.e., rigidly bonded interface case). This assumption is reasonable for ultimate failure since this interface can be controlled by the friction angle of the soil, but it is only a simplifying assumption for the estimation of the interface stiffness. An alternative strategy is to model the interfaces in PLAXIS by assigning a different constitutive behaviour to interface elements (i.e., different from the surrounding soil).

The results of independent block-block direct shear tests (Hatami and Bathurst 2005) were used to determine the model parameters for block-block interfaces and the same parameters were used in both models (Table 5.3). It should be noted that for the PLAXIS case, the shear modulus value (G) was obtained directly from the interface shear stiffness used in the FLAC model (K_s). This was possible due to the known values of the block-to-block contact geometry and the virtual thickness of the interface FEM model (which depends on the mesh element size and which was 10.5 mm in this case).

Soil-block interface parameter values are summarized in Table 5.3. The FLAC model was simplified by assuming a flat rough facing surface in contact with the backfill (hence, the interface failure criterion is the same as the soil). The interface shear stiffness (K_s) was assumed to be very low. In PLAXIS, the back of the facing column surface was assumed to be stepped as in the physical case. This left a very low density volume of soil below the heel of each block that was assigned very low shear stiffness and no tensile strength. The back vertical sides of the blocks were assumed to have a different reduction factor with respect to the backfill strength (i.e., 1.0, 0.8, 0.6 and 0.4). Nevertheless, no significant variations were detected in numerical results. Hence, a perfectly bonded interface was used in the final simulation runs (reduction factor equal to 1).

The reinforcing materials were assumed to be perfectly bonded to the backfill sand (i.e., rigid interface). This assumption was judged to be reasonable based on the good agreement between numerical predictions that used the same model and measurements of reinforcement loads and strains in two physical tests used to validate the numerical model (Hatami and Bathurst 2006; Huang et al., 2009).

Table 5.2. Sand backfill properties:

Model parameter	Value
γ (unit weight, kN/m^3)	16.8
E (elastic modulus, MPa)	80
ν (Poisson's ratio)	0.3
ϕ (friction angle, degrees)	44
ψ (dilatancy angle, degrees)	11
c (cohesion, kPa)	0.2

Table 5.3. Interface properties:

Parameter	Value:	
	Block-block	Soil-block
FLAC model:		
ϕ (friction angle, degrees)	57	44
ψ (dilation angle, degrees)	0	11
c (cohesion, kPa)	46	0
K_n (normal stiffness, MN/m/m)	1000	100
K_s (shear stiffness, MN/m/m)	40	1
PLAXIS model:		
ϕ (friction angle, degrees)	57	44
ψ (dilation angle, degrees)	0	11
c (cohesion, kPa)	46	0
G (shear modulus, MPa)	1.5[1]	30 and 3[2]

Notes: [1] Equivalent to K_s-value in FLAC model .
[2] Used at the back of the facing blocks and for the horizontal heel of the blocks at the back of the facing column.

5.3. RESULTS

5.3.1. General

The calculations were made using a computer with an 'Intel Core 2 Duo Pa8600' (2.40 GHz) central processor unit. The times to solve the entire problem (i.e., construction and surcharging) were about 20 minutes using FLAC and 30 minutes using PLAXIS. All measured values shown in the figures to follow correspond to the average measured values at each location (no range bars are shown) in order to simplify data presentation.

Figure 5.2a shows the horizontal and vertical components of the total toe load which were generated during construction of the wall. Predicted values for both models are very similar and both sets of predictions are judged to be in good agreement with measured results. Shown in the same plot is the self-weight of the facing column which plots as a straight line. The total predicted and measured vertical loads are greater than the facing column self-weight due to down-drag forces that are generated at the back of the wall facing due to hanging-up of the soil at the connections and interface friction between the concrete facing blocks and the sand backfill. The down-drag loads are generated due to relative vertical movement of the backfill soil during compaction and subsequent outward facing column movement during surcharging.

Figure 5.2b shows the horizontal and vertical toe load components during surcharging. The PLAXIS model can be seen to generally underestimate the measured load values. The FLAC model can be seen to over-estimate measured values at the highest surcharge pressures.

Figures 5.3a and 5.3b show the normalized vertical pressure distribution over the rigid concrete foundation upon which the wall was constructed ($\sigma_v/[\gamma H + q]$) where σ_v is vertical foundation pressure. It can be observed that both models predict similar results. It can be argued that the FLAC prediction for the wall facing contact pressure is more accurate.

Figure 5.4 shows the horizontal displacement profiles of the facing during surcharge loading. The datum is the end of construction. These results show significant and detectable differences between model predictions and measured results. The PLAXIS results consistently underestimate measured displacements. The FLAC results are judged to be accurate at the 20 kPa surcharge level but at higher surcharge levels the FLAC model consistently over-estimated wall displacements. The significant under-prediction using the PLAXIS model occurred even when the mesh updating option was used in PLAXIS.

Figures 5.5a and 5.5b show the connection loads at end of construction and at the end of surcharge loading. Good predictions and similar responses were obtained using both programs at the end of construction, which corresponds to working stress conditions. It appears that the PLAXIS model did better capturing the connection load in the lowermost reinforcement layer. The same is true when the simulations were taken out to a surcharge pressure of 80 kPa. However, at this surcharge pressure level, the FLAC code did better at the top of the wall.

a) During construction:

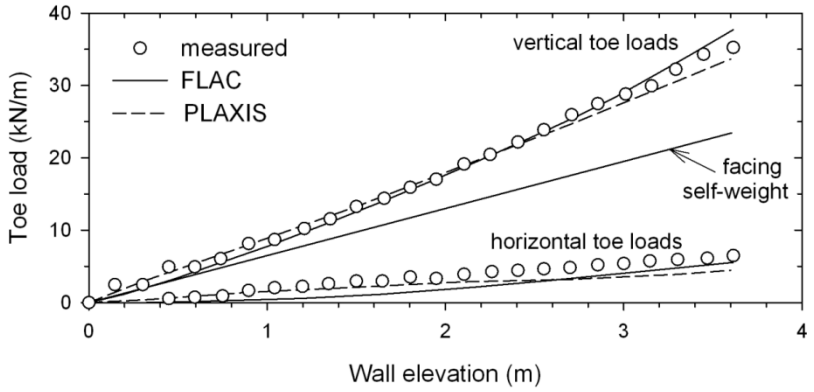

b) During surcharging:

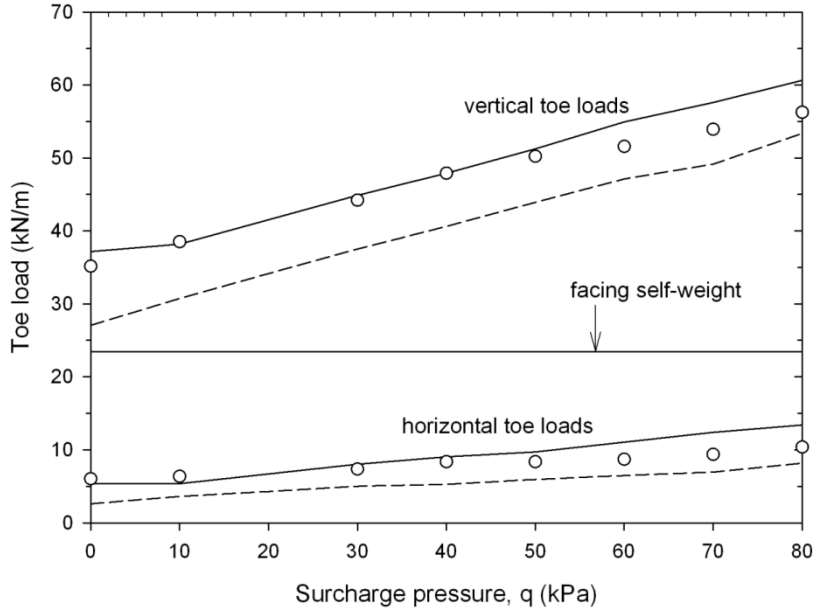

Figure 5.2: Toe loads: during construction (a) and during surcharging (b).

Three of the six reinforcement layers were selected in the current study to compare measured and predicted tensile loads. The measured loads were inferred from strain measurements and the linear stiffness models introduced earlier. Figure 5.6 corresponds to end of construction and Figure 5.7 corresponds to the end of the 80-kPa surcharge load level. Layer 6 is the topmost reinforcement layer. Both computer programs predict loads in the same general range although there are visual differences in the magnitude and distribution of loads between models and between model outcomes and the measured data. The FLAC model gives load distributions that are smoother with the largest loads at the connections. However, it is not possible to conclude that one model is consistently more accurate than the other.

a) During construction:

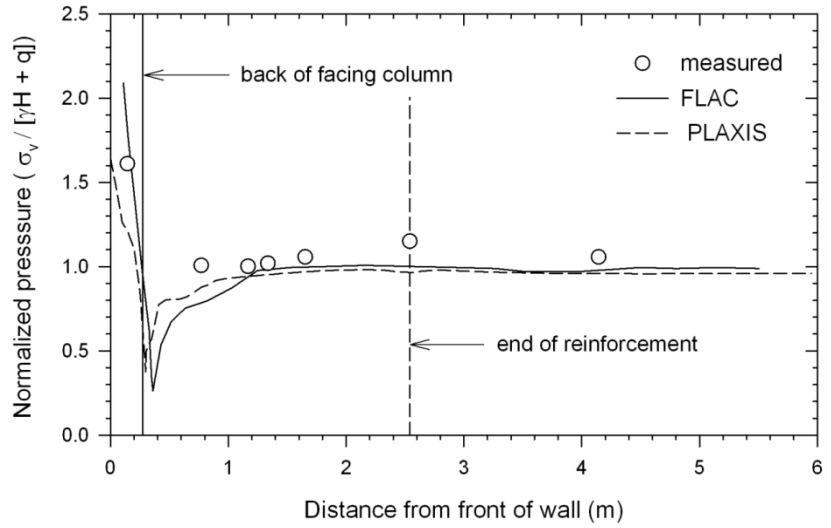

b) Surcharge q = 50 kPa:

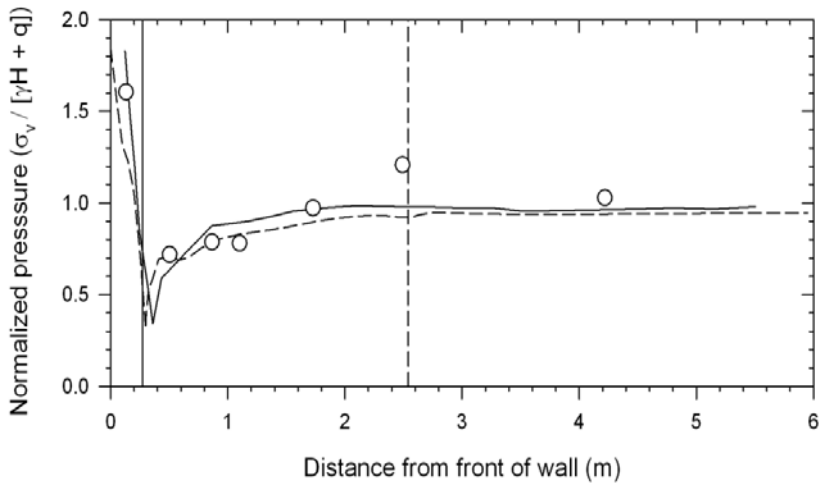

Figure 5.3: Vertical foundation pressure: during construction (a) and under q = 50 kPa-surcharge (b).

5.3.2 Influence of the backfill friction angle

The two numerical modelling approaches described in this study can be used to investigate the sensitivity of wall performance to choice of input parameters. An example follows where the magnitude of the predicted connection load at the second layer of reinforcement during surcharging was investigated using three different backfill friction angles (i.e., 44º (base case), 40º and 36º). All other parameters were kept the same as those reported earlier.

Figure 5.8 shows that both programs gave similar predictions for the same friction angle and that the magnitude of connection load increases with decreasing friction angle of the soil,

which is consistent with expectations based on conventional understanding of earth pressure theory.

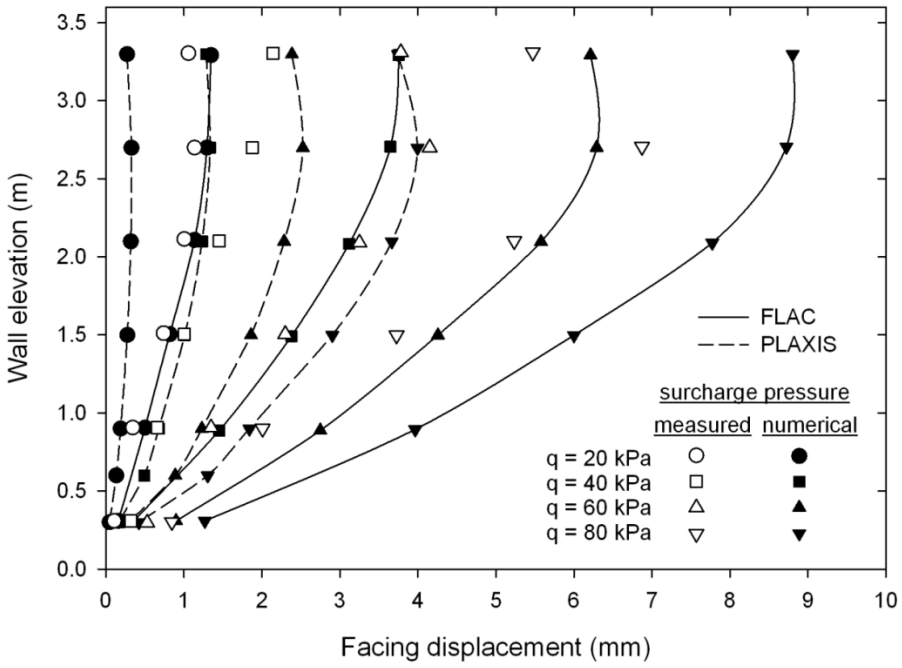

Figure 5.4: Post-construction facing displacements.

a) end of construction: b) surcharge q = 80 kPa:

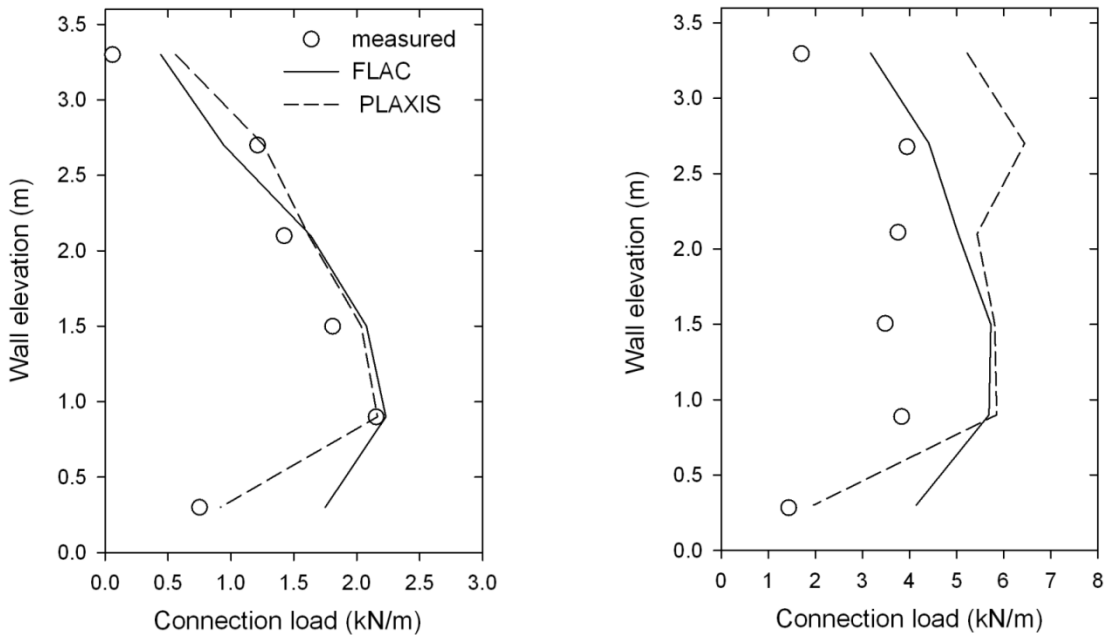

Figure 5.5: Reinforcement loads at the connections: at the end of construction (a) and under q = 80 kPa-surcharge (b).

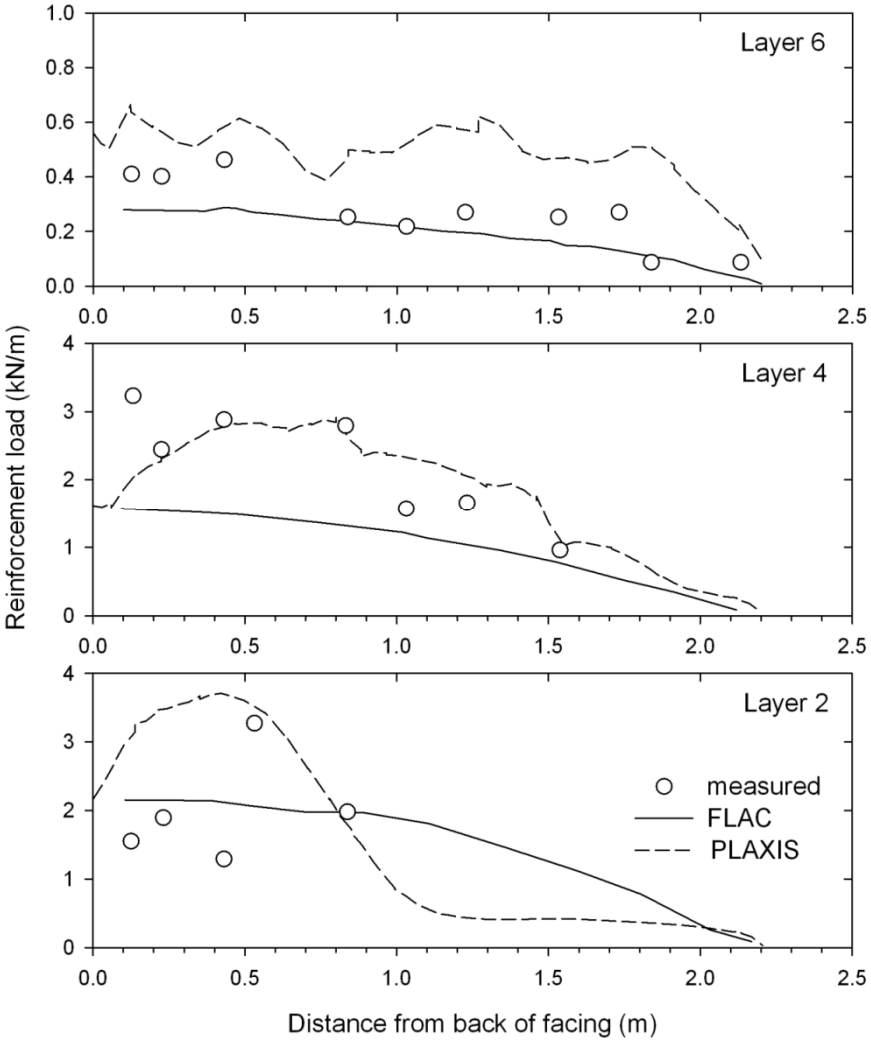

Figure 5.6: Reinforcement load distributions at the end of construction.

5.4. CONCLUSIONS

The mechanical behaviour of reinforced soil walls is mechanically complex because of the different component materials, their interactions, wall geometry, foundation condition and method of construction. An additional complication that was not addressed in this chapter is that there are inevitably unquantifiable effects on wall performance due to construction method and quality. Furthermore, the as-delivered backfill soil materials may satisfy design specifications but may not match the properties of the soil assumed in numerical computations at the design stage. Consequently, regardless of the numerical approach to design a wall, numerical predictions can only be expected to be approximate. With this comment in mind the magnitudes of predicted wall performance features using two different

numerical approaches in this study are judged to have been in satisfactory agreement from a practical point of view even though there were detectable differences in many data plots.

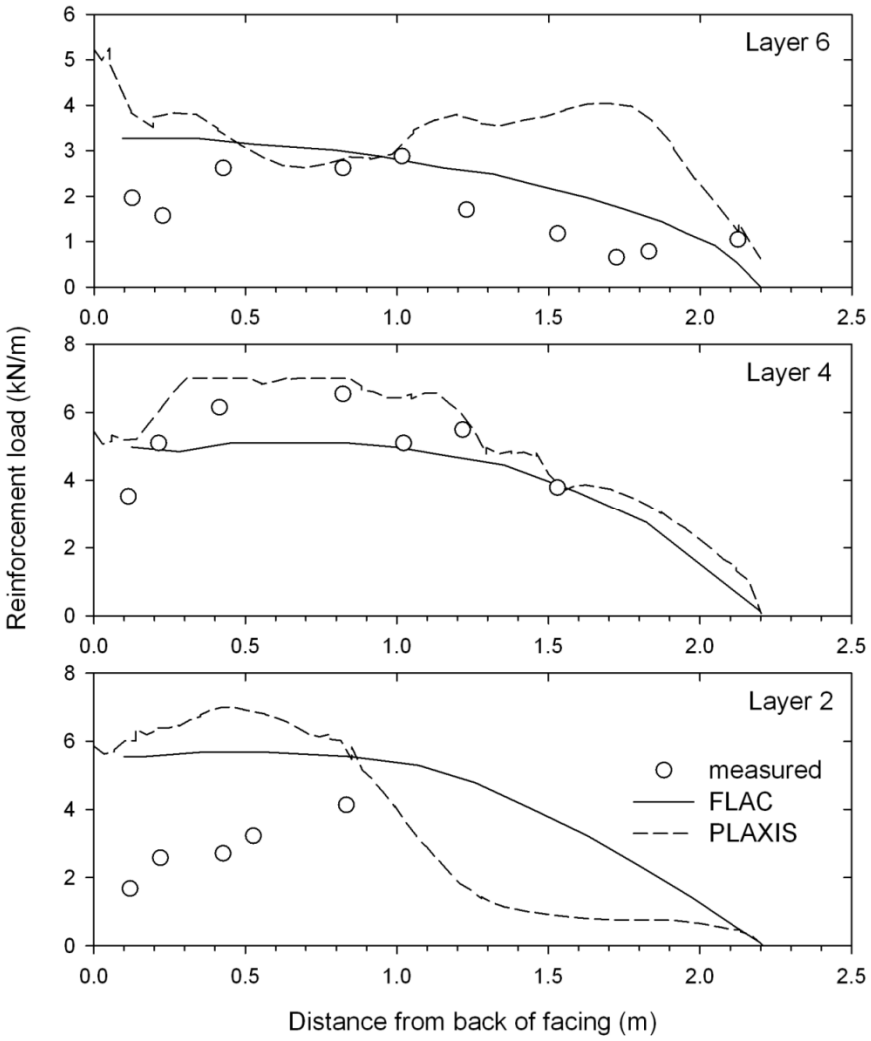

Figure 5.7: Reinforcement load distributions under q = 80 kPa-surcharge.

From the user point of view, the PLAXIS program interface was easier to use and it was easier to make changes to initial and boundary conditions and material properties. FLAC had a longer learning curve. An advantage of the FLAC program is that the software permits user-defined constitutive models to be implemented in the code.

This chapter shows that both these commercial software programs can be used to design complex reinforced soil walls provided that the user has sufficient experience to select appropriate component constitutive model parameters and to correctly judge the reasonableness of all numerical outcomes.

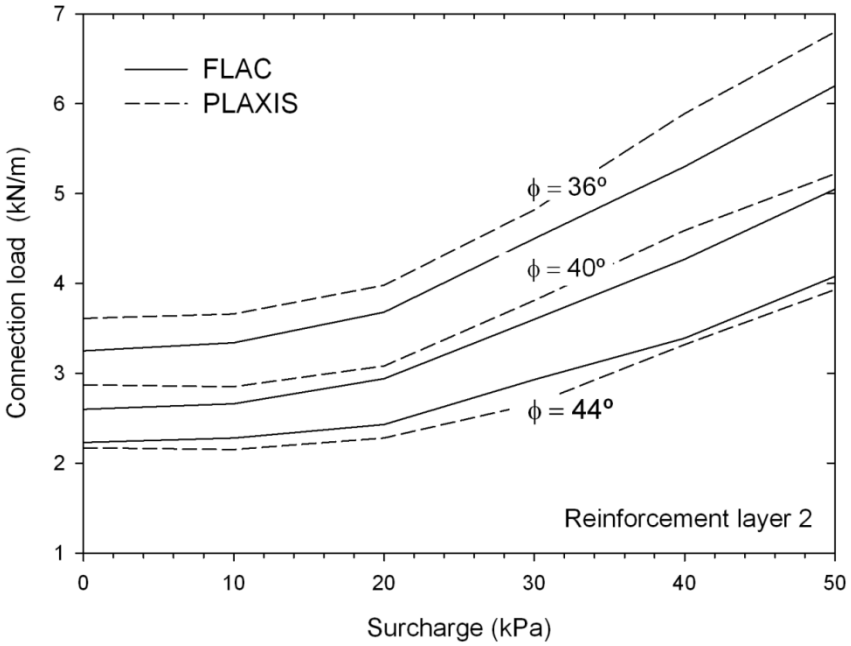

Figure 5.8: Influence of backfill friction angle on connection load in reinforcement layer 2 during surcharging

CHAPTER 6

NUMERICAL STUDY OF THE INFLUENCE OF FOUNDATION COMPRESSIBILITY AND REINFORCEMENT STIFFNESS ON THE BEHAVIOR OF REINFORCED SOIL WALLS [1]

6.1. INTRODUCTION AND GENERAL APROACH

Geosynthetic and metallic reinforced soil walls are constructed with horizontal layers of reinforcement to create a composite gravity mass that acts to resist destabilizing forces generated by the retained soil behind the structure. Internal stability design calculations are carried out to ensure the integrity of the reinforced soil mass. A typical assumption for these calculations is that the wall foundation is rigid and/or does not influence the magnitude and distribution of reinforcement loads under operational conditions. This assumption may not apply to walls constructed over compliant (compressible) foundations. Current study describes the results of a series of numerical simulations that were carried out on idealized 3.6, 6 and 9 m-high modular block walls constructed with two different reinforcement materials and seated on foundations having four different compressibility values. The current study continues an investigation reported by Bathurst et al. (2012). This earlier study was restricted to a single wall height (H = 6 m) and three different foundation conditions. The current study expands this earlier work by investigating a larger number of case studies with three different wall heights and four different foundation compressibility conditions. In addition, the current investigation reports a wider range of response features of the walls than in the earlier study.

The program FLAC (Itasca 2011) was used to carry out the numerical simulations. The initial reference case was based on a pair of instrumented 3.6 m-high modular block walls seated on a rigid foundation and reported by Huang et al. (2009). They used these walls to verify the

[1] Chapter based on Damians, I.P. Bathurst, R.J., Josa, A. and Lloret, A.; 2014. Numerical study of the influence of foundation compressibility and reinforcement stiffness on the behavior of reinforced soil walls. International Journal of Geotechnical Engineering 8(3), 247-259, and also partially based on Bathurst, R.J., Damians, I.P, Josa, A., and Lloret, A.; 2012. Influence of foundation compressibility on reinforcement loads in geosynthetic reinforced soil walls. Proceedings of the 5th European Geosynthetics Congress, Vol.5, pp. 43-47, Valencia, Spain. September 2012.

accuracy of the same FLAC code described in this study by comparing a wide range of measured wall responses to numerically predicted results. In the current study the same verified numerical code is used to model the same wall but with the structure increased to heights of 6 m and 9 m. In all cases, the same sand backfill soil was assumed. The wall facing column and backfill soil were assumed to be seated on a Winkler foundation having three different linear stiffness (compressibility) values and also over a fully-rigid foundation. The Winkler model constrains foundation displacements to the vertical direction. This was undertaken purposely so that the vertical contribution of foundation compressibility to wall reinforcement loads could be isolated. The other variable in this study was the reinforcement type which was assigned two different axial stiffness values.

6.2. NUMERICAL MODEL

6.2.1. General

The FLAC numerical grid is illustrated in Figure 6.1. The facing column is comprised of discrete solid concrete blocks arranged at a facing batter of 8 degrees. The blocks are 0.3 wide from toe to heel and 0.15 m high. The numerical simulation reproduced the sequential bottom-up construction and compaction of the 0.15 m-thick lifts (Huang et al., 2009). No surcharge was applied to the surface of the backfill. The foundation support and rigid horizontal toe support are shown in the figure.

6.2.2. Material properties

The reinforcement materials were assumed as a relatively extensible polypropylene (PP) biaxial geogrid and a relatively inextensible metallic welded wire mesh (WWM). The reinforcement lengths were 70% of the wall height in all cases. The reinforcement vertical spacing was kept constant at S_v = 0.6 m (Figure 6.1) resulting in 6, 10 and 15 layers of reinforcement for wall heights H = 3.6, 6 and 9 m, respectively. The following hyperbolic model was used to describe the load-strain-time behavior of the reinforcement materials under monotonic increasing load (Hatami and Bathurst 2006; Allen and Bathurst 2013a):

$$J_t(\varepsilon,t)=\frac{1}{J_0(t)\left[\frac{1}{J_0(t)}+\chi(t)\varepsilon\right]^2} \tag{6.1}$$

where: $J_t(\varepsilon,t)$ is the equivalent tangent stiffness function; $J_0(t)$ is the initial tangent stiffness; $\chi(t)$ is a scaling function; ε is strain and t is time. The time to construct the 3.6 m-high wall case is assumed as 1000 hours. Longer times would be expected for the higher walls. However, the difference in stiffness values beyond 1000 hours is negligible and a single value for all PP reinforcement cases simplifies the interpretation of simulation results. Setting

$\chi(t)$ = 0 results in a linear-elastic stiffness model that is appropriate for the metallic WWM reinforcement material. Reinforcement model parameters are summarized in Table 6.1.

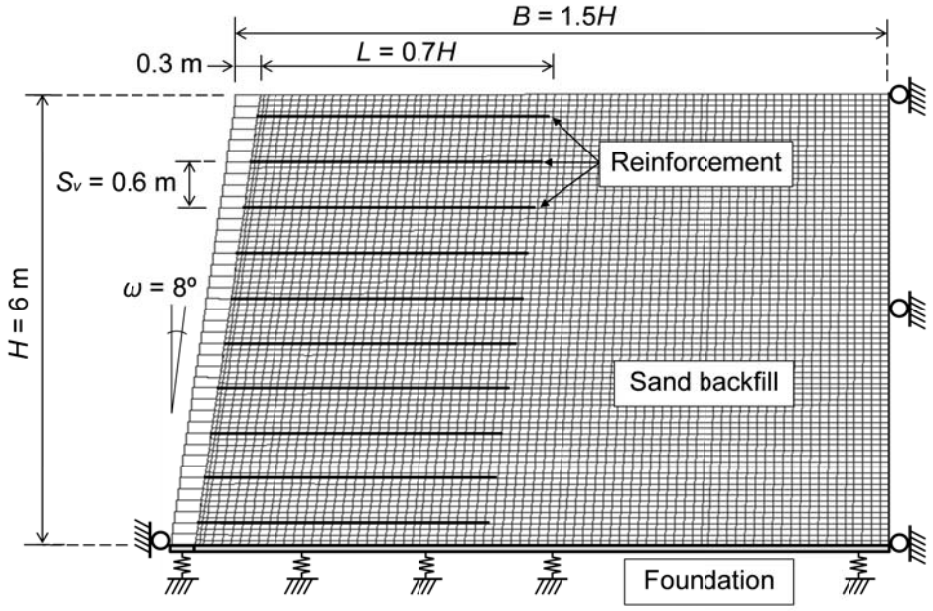

Figure 6.1: Example FLAC numerical model used (H = 6 m case).

Table 6.1. Reinforcement properties at t = 1000 hours:

	Reinforcement type:	
Parameters	PP [(1)]	WWM [(2)]
$J_0(t)$ (kN/m)	115	3100
$\chi(t)$ (m/kN)	0.11	0
T_y (kN/m)	14	14

Notes: [(a)] PP: polypropylene geogrid; [(b)] WWM: welded wire mesh.

The elastic-plastic Mohr-Coulomb (M-C) constitutive model was used for the sand in the numerical model. In the related conference paper the more complicated Lade single-hardening model (Lade 2005) was used. However, Huang et al. (2009) demonstrated that for modular block walls and a rigid foundation, the quantitative model predictions using the simple M-C soil model and the multi-parameter Lade model were similar. Complementary analyses were done comparing both soil models and results are presented in further Section 6.3.3. The advantage of using the simpler model is that numerical simulations can be completed in a shorter time while relative performance outcomes between the various wall cases under operational conditions (i.e., end of construction) are judged to be the same as

those anticipated using the more complicated soil model. The model parameters were taken with some small adjustments from laboratory tests reported by Hatami and Bathurst (2005) and are summarized in Table 6.2. This material is high quality medium sand with a narrow size distribution. The effective stiffness of the backfill sand falls between the two most compressible foundation cases described below.

Linear spring-slider systems with interface shear strength defined by the Mohr-Coulomb failure criterion were used for the facing-backfill (soil-block) and reinforcement-(soil) backfill interfaces (Itasca 2011). The results of independent block-block direct shear tests (Hatami and Bathurst 2005) were used to determine the model parameters summarized in Table 6.3.

The reinforcing materials were assumed to be perfectly bonded to the backfill sand. This assumption was judged to be reasonable based on the good agreement between numerical predictions that used the same model and measurements of reinforcement loads and strains in the two physical tests used to initially validate the numerical model (Huang et al., 2009).

Deformations of the foundation were restricted to the vertical direction. Furthermore, the toe of the wall face was also restrained horizontally. Hence, possible wall deformations due to horizontal sliding at the base of the wall face and/or horizontal deformations in the foundation soil were not considered. This idealized approach was taken in order to isolate the influence of foundation vertical stiffness on reinforced soil wall response as noted earlier.
Extended explanation about the Influence of toe restraint on reinforced soil segmental walls can be found in Huang et al. (2010), and Chen and Bathurst (2013). A 0.25 m-thick foundation soil zone over a fully-rigid lower boundary was actually used in the numerical FLAC grid. By assigning zero Poisson's ratio to this linear elastic zone the deformation response of the foundation is equivalent to a Winkler foundation. The Winkler spring stiffness (subgrade modulus) values are summarized in Table 6.4 together with the matching constrained elastic modulus (E) values assuming a depth of 5 m for the foundation soil or rock over a rigid stratum. The foundation descriptions given in the table are possible matching example types. This compressible zone is defined equally both under backfill and facing. However, complementary analyses considering vertical displacement constrain at facing toe while foundation can settle under backfill was taken into account and results resented in further Section 6.3.4.

Table 6.2. Sand and modular block properties:

Model parameters	Sand backfill	Block
E (Young`s modulus, MPa)	60	23000
v (Poisson`s ratio)	0.3	0.15
ϕ (friction angle, degrees)	44	-
ψ (dilation angle, degrees)	11	-
c (cohesion, kPa)	0.2	-
γ (unit weight, kN/m^3)	16.8	22.0

Table 6.3. Interface properties:

Interface	Values
Block-block	
δ_{bb} (friction angle, degrees)	57
c_{bb} (cohesion, kPa)	46
K_{nbb} (normal stiffness, MN/m/m)	1000
K_{sbb} (shear stiffness, MN/m/m)	40
Soil-block	
δ_{sb} (friction angle, degrees)	44
ψ_{sb} (dilation angle, degrees)	11
c_{bb} (cohesion, kPa)	0
K_{nsb} (normal stiffness, MN/m/m)	100
K_{ssb} (shear stiffness, MN/m/m)	1
Soil-reinforcement	
δ_{sr} (friction angle, degrees)	44[(a)]
s_{sr} (adhesion, kPa)	1000[(a)]
K_{ssr} (shear stiffness, MN/m/m)	1000

Note: [(a)] Fully bonded interface, which is in agreement with numerical simulations using the same materials reported by Huang et al. (2009).

Table 6.4. Foundation cases:

Stiffness (subgrade modulus), k (MPa/m)	E [(a)] (MPa)	Foundation
∞	∞	Rigid
400	~2000	Weathered rock
40	~200	Dense sand with gravel
4	~20	Medium-loose sand

Note: [(a)] Equivalent constrained elastic modulus back-calculated as $E = k \times D$ where D = 5 m depth of foundation and assuming fully-rigid lower boundary.

6.3. RESULTS

6.3.1. General

Displacement vector fields computed for fully-rigid and most compressible foundation cases are plotted in Figure 6.2 (polypropylene geogrid) and Figure 6.3 (welded wire mesh). As expected, the global displacements for the same reinforcement type and wall height are greater for the more compressible foundation condition. However, the displacements are also influenced by the reinforcement stiffness; specifically, for the same foundation condition, the wall deformations are less for the relatively inextensible WWM case than for the more extensible PP geogrid case. An observation that can be made from Figures 6.2 and 6.3 is that the settlements in the vicinity of the wall toe are greater than at locations further into the backfill. This is due to the combined effect of the heavier unit weight of the modular blocks and rotation of the wall face about the horizontally constrained toe.

Figure 6.4 shows contours of soil shear strain for the highest wall in combination with the extensible reinforcement and the two extreme foundation stiffness cases with H = 9 m. For brevity, the soil shear strain plots for the PP reinforcement wall cases with shorter wall heights are not shown. However, as may be expected, the shear strains for these cases were lower and the high shear zones were of shorter length. Similar plots for the WWM reinforcement cases are shown in Figure 6.5, however, the soil shear strains for the much stiffer reinforcement cases were very small (less than 1.5%) even for the soft foundation case (k = 4 MN/m). The plots show that the internal shear zones propagating from the heel of the wall face are not fully-developed from the bottom to the top of the reinforced soil zone. This is consistent with the notion of operational or working stress conditions for the walls in this study. The distinction between working stress conditions and incipient soil failure is important (Allen and Bathurst 2013b). Working stress conditions are a requirement for internal stability design and analysis of walls under operational conditions using empirically calibrated methods such as the K-stiffness Method (Allen et al., 2003, 2004; Bathurst et al., 2005, 2008b). Fully-developed failure mechanisms through the reinforced soil zone mass imply that internal stability design and analysis can be carried out using tie-back wedge methods (or variants) that are based on conventional notions of limit equilibrium. Based on these comments it can be argued that a geogrid reinforcement with greater stiffness would be recommended in practice for the relatively extensible reinforcement wall case and H = 9 m. This stiffer reinforcement would provide a greater margin of safety against a fully-developed internal failure mechanism at end of construction, particularly for the soft foundation case. For walls constructed with relatively inextensible reinforcement materials (e.g., welded wire) the reinforcement will fail before the soil and hence limit-equilibrium based methods of design and analysis are not applicable.

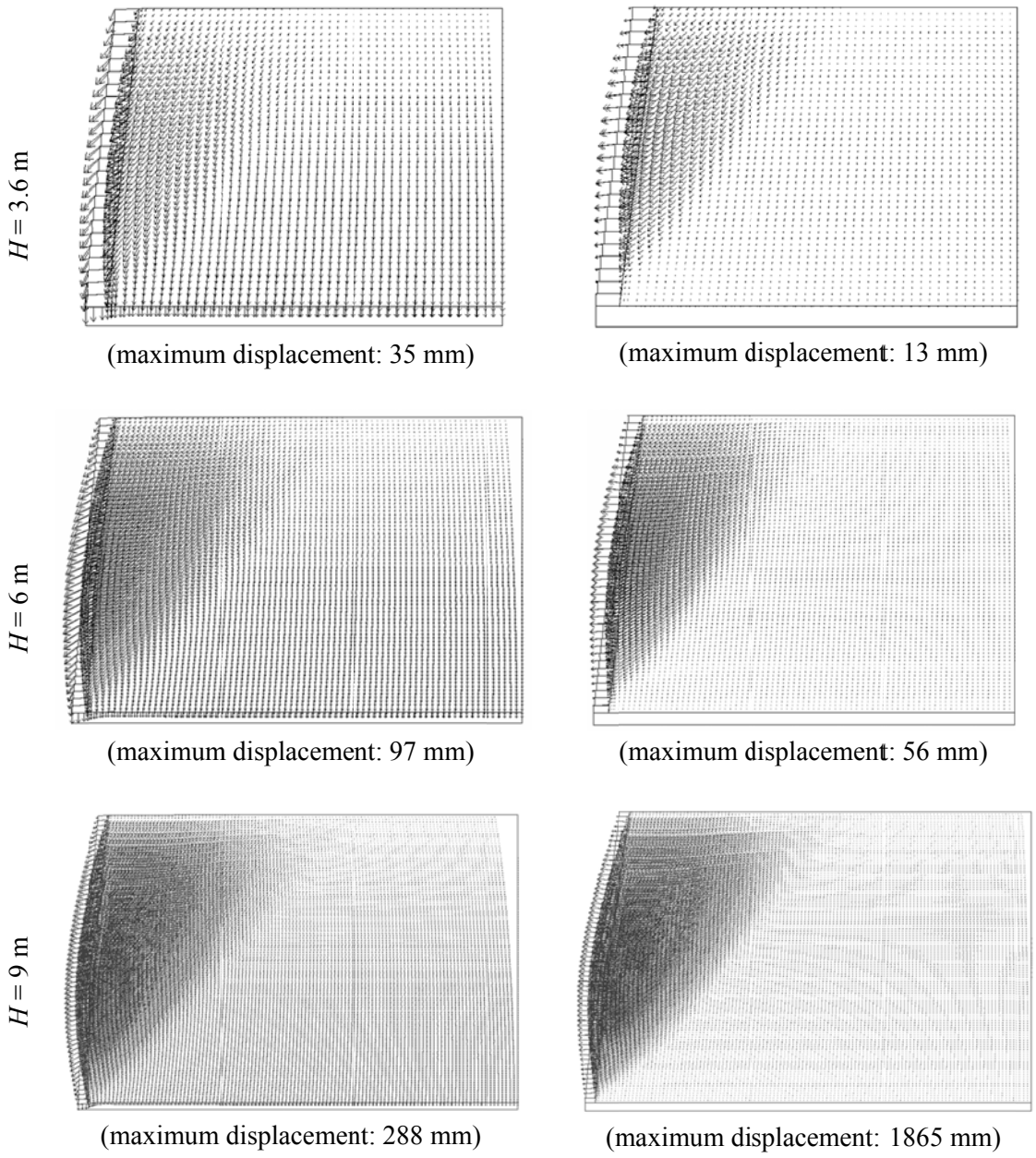

Figure 6.2: Displacement vectors for PP geogrid reinforcement cases: soft foundation (a), and rigid foundation (b).

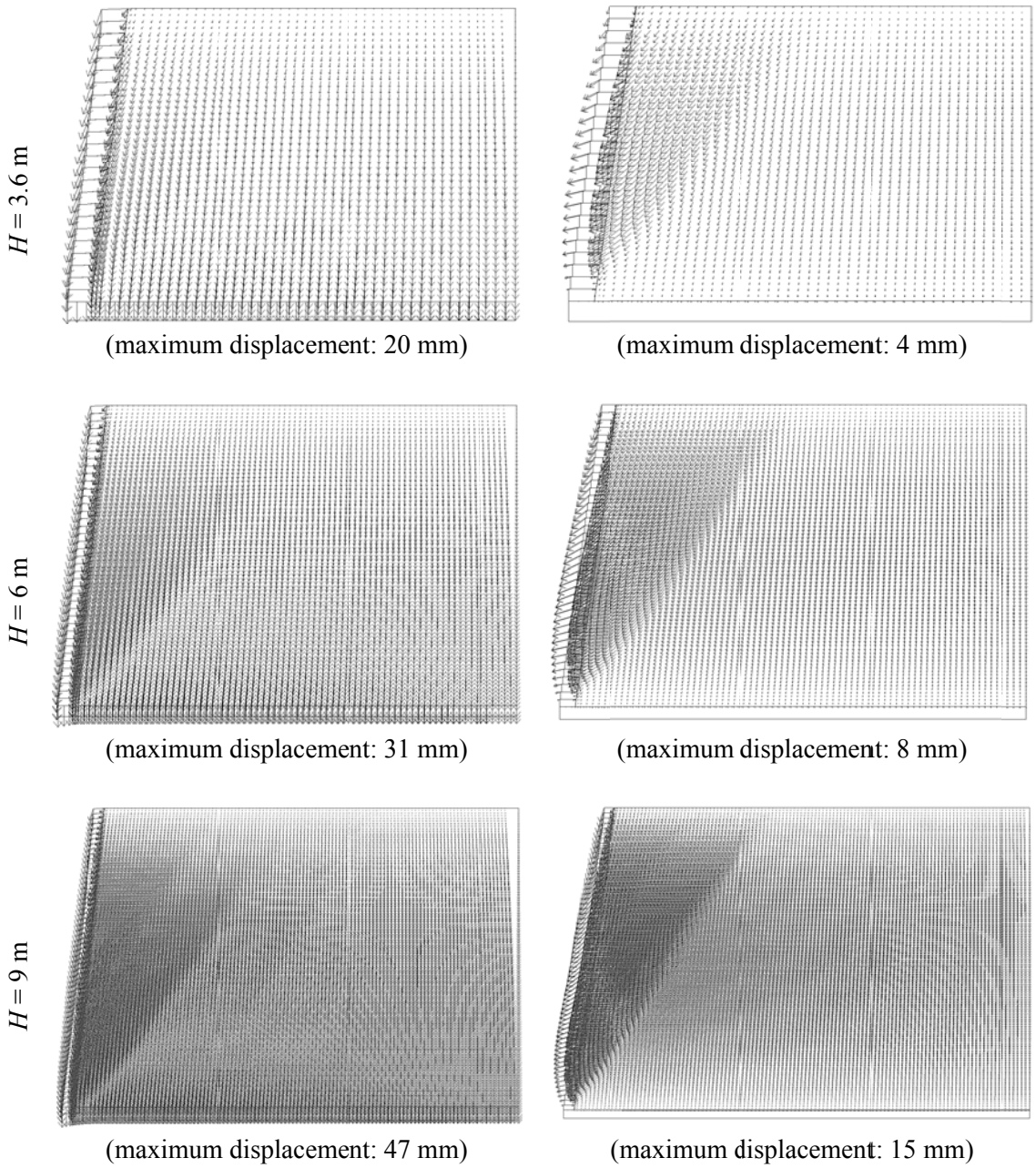

Figure 6.3: Displacement vectors for WWM reinforcement cases: soft foundation (a), and rigid foundation (b).

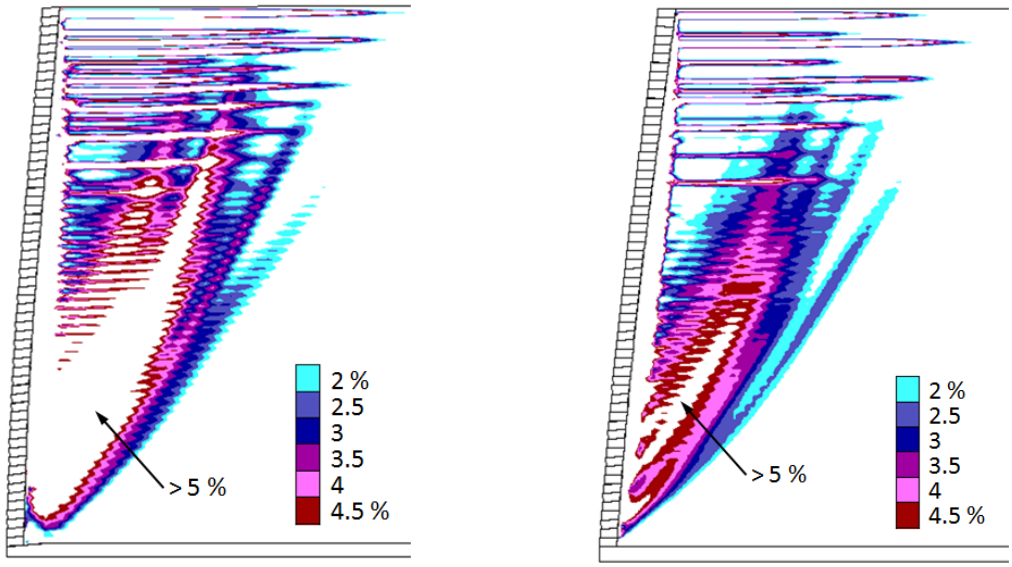

a) soft foundation case (k = 4 MN/m) b) rigid foundation (k = ∞)

Figure 6.4: Soil shear strains for walls with H = 9 m and PP reinforcement: soft foundation (a), and rigid foundation (b).

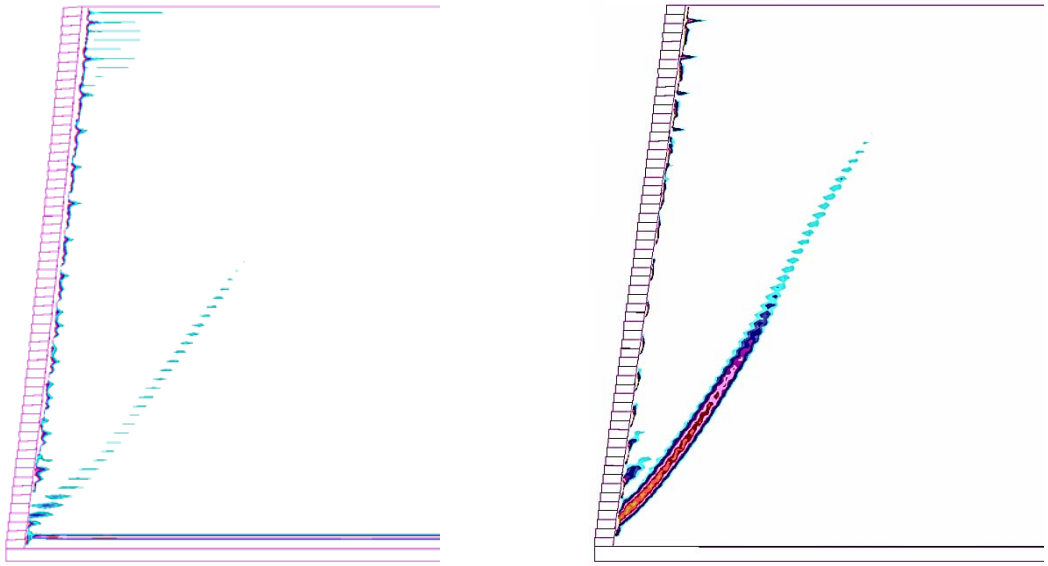

a) soft foundation case (k = 4 MN/m) b) rigid foundation (k = ∞)

Figure 6.5: Soil shear strains for walls with H = 9 m and WWM reinforcement: soft foundation, scaled from 0.9 % (blue) to 1.5% (a), and rigid foundation, scaled from 0.6 % (blue) to 1.5% (b).

Horizontal facing displacements (Δx) are normalized with wall height (H) and plotted in Figure 6.6. It should be noted that the displacements at each elevation are taken with respect to the time the block-soil layer was placed. Hence, these displacements are with respect to a moving datum and should not be confused with the actual wall profile at the end of construction. The plots show that facing displacements are larger for the more extensible reinforcement when all other conditions are the same. For both relatively extensible and inextensible reinforcement cases the facing displacements increase with increasing foundation compressibility.

The influence of reinforcement stiffness and wall height on horizontal wall displacements (moving datum) can be appreciated from the plots in Figure 6.7. The magnitudes of horizontal displacement are low enough for the cases with WWM reinforcement that the influence of wall height and magnitude of foundation compressibility is not of practical concern. However, for the more extensible reinforcement condition, both wall height and foundation stiffness have a large influence on wall displacements.

Tensile reinforcement loads in selected layers are summarized in Figure 6.8 and Figure 6.9 for PP geogrid and WWM cases, respectively. Figure 6.8 shows that the maximum reinforcement loads occur at the connections with the wall face irrespective of foundation condition. The loads at the connections and at all other locations along the length of the reinforcement layers generally increase with increasing foundation compliance. There are detectable greater reinforcement loads for the case with k = 400 MN/m compared to the rigid foundation condition. The reinforcement loads for the same wall height (H = 6 m) but with the relatively inextensible WWM reinforcement (Figure 6.9) are much greater. Similar to the PP reinforcement cases, the maximum tensile loads (typically) occur at the connections. However, unlike the matching PP geogrid reinforcement cases, the differences in tensile loads for the rigid and k = 400 MN/m foundation conditions are negligible. The high connection loads also persist deeper into the reinforced soil zone particularly for the top three layers compared to the same three layers in the matching PP reinforced soil wall case. Although comparable plots for the other walls in this study are not presented here, the same observations noted above for both sets of walls (PP and WWM) also apply to walls with H = 3.6 m and 9 m.

Figures 6.10 and 6.11 show axial loads in reinforcement layers at the same depth below the top of the wall (2.7 m) and layers closest to the wall mid-height for all simulation cases in the current study. The data in Figure 6.10a show that for walls with H = 6 and 9 m, the reinforcement loads are comparable at normalized distances in the range of 0.1 to 0.2 from the back of the wall. The plots in Figure 6.10b show that the influence of foundation compressibility is more pronounced for the low height WWM reinforced wall (H = 3.6 m) than for the higher walls. This is attributed to the greater influence of proximity to the rigid horizontal toe boundary condition for the low-height wall with very stiff reinforcement. Figures 6.11a and 6.11b show that when load distributions are plotted for reinforcement

layers located in the vicinity of the mid-height of the walls, the load curves appear to cluster together according to wall height.

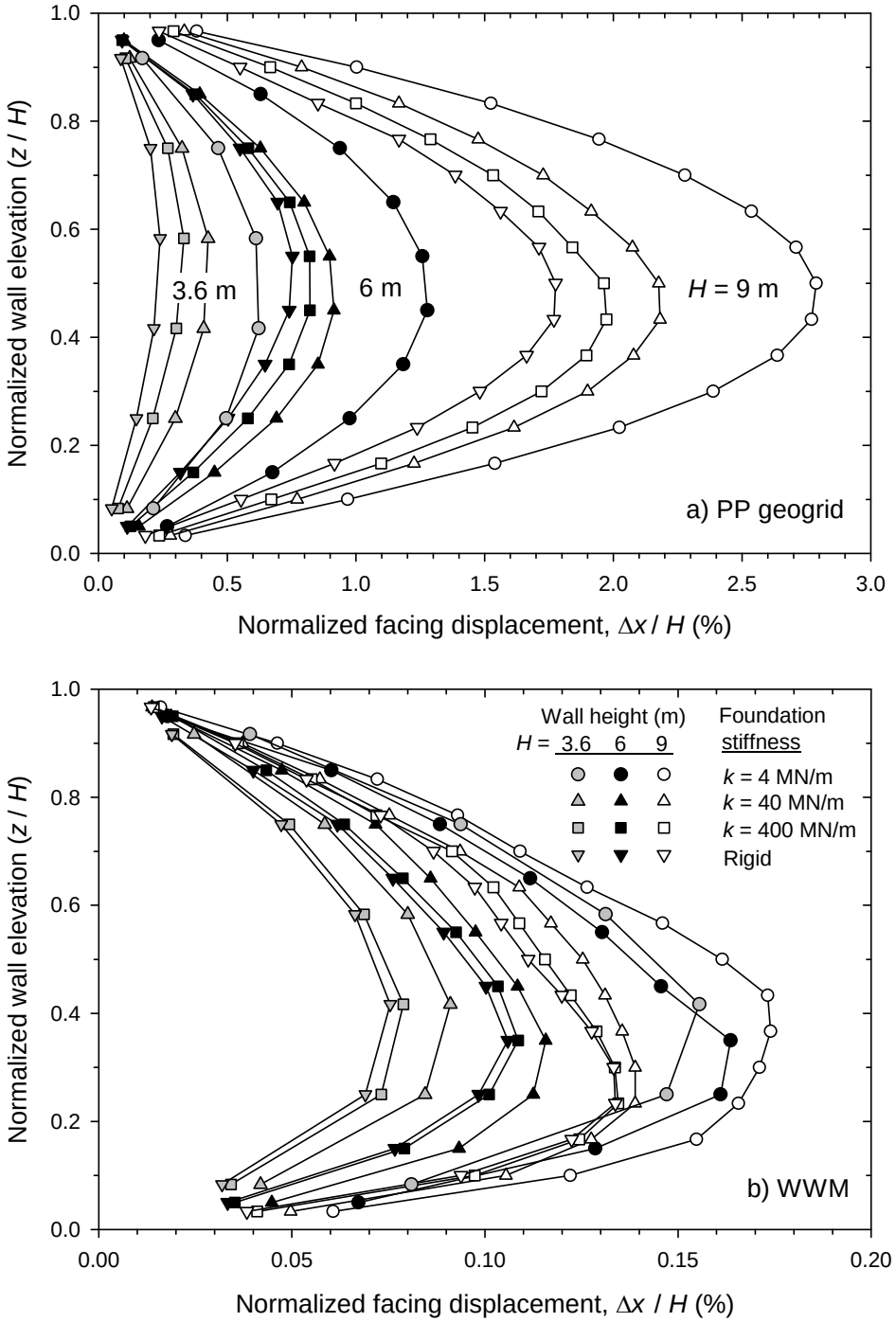

Figure 6.6: Normalized-relative horizontal facing displacements: PP reinforcement (a), and WWM reinforcement (b). Note: *z* is elevation above the base of the wall.

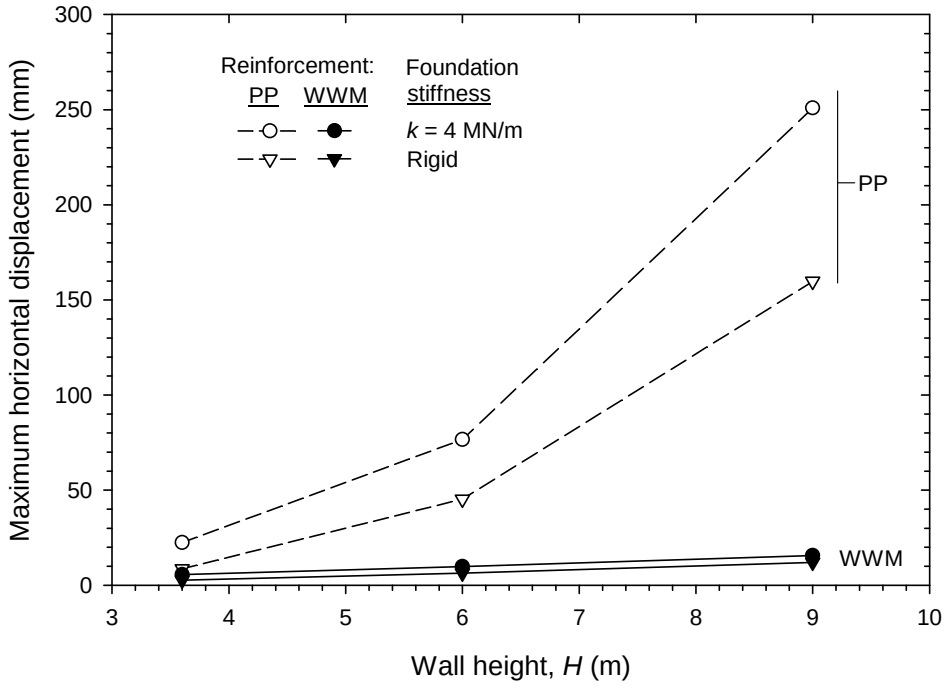

Figure 6.7: Maximum horizontal displacements with respect to reinforcement type and wall height.

The influence of foundation compressibility on reinforcement connection loads for WWM and PP geogrid materials for all wall cases is presented in Figure 6.12. The connection loads increase with foundation compressibility. However, for the same foundation case, the loads in the reinforcement layers are greater for the stiffer material. This outcome demonstrates that rupture (or yield) strength of a reinforcement material is not a reliable indicator of load in reinforced soil walls under operational conditions. Recall that both materials were assigned the same strengths but very different stiffness values. Regardless of the reinforcement type and foundation condition, the connection loads are not uniform through the height of the walls.

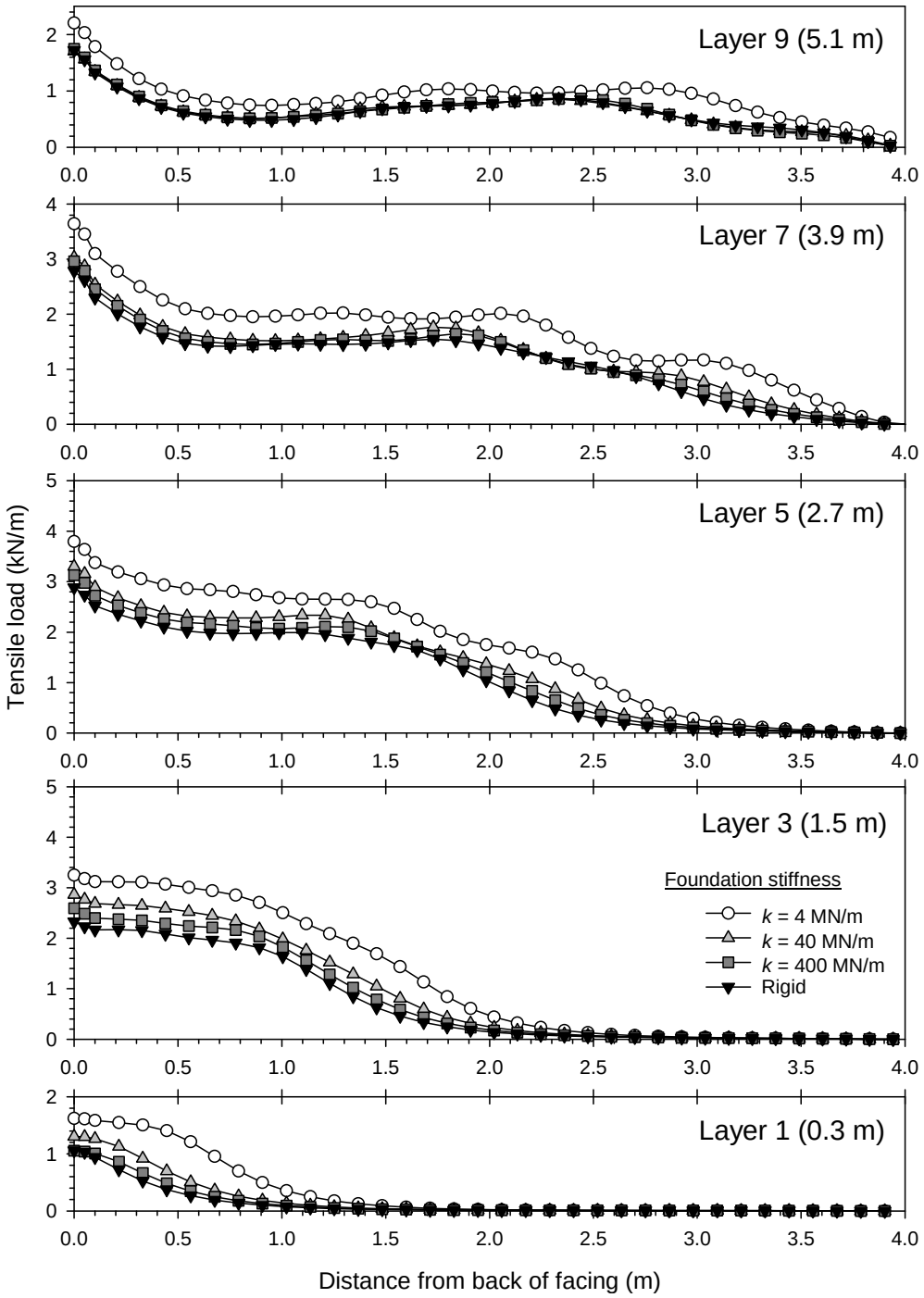

Figure 6.8: Reinforcement tensile loads at end of construction for cases with H = 6 m, PP geogrid reinforcement and four different foundation stiffness cases.

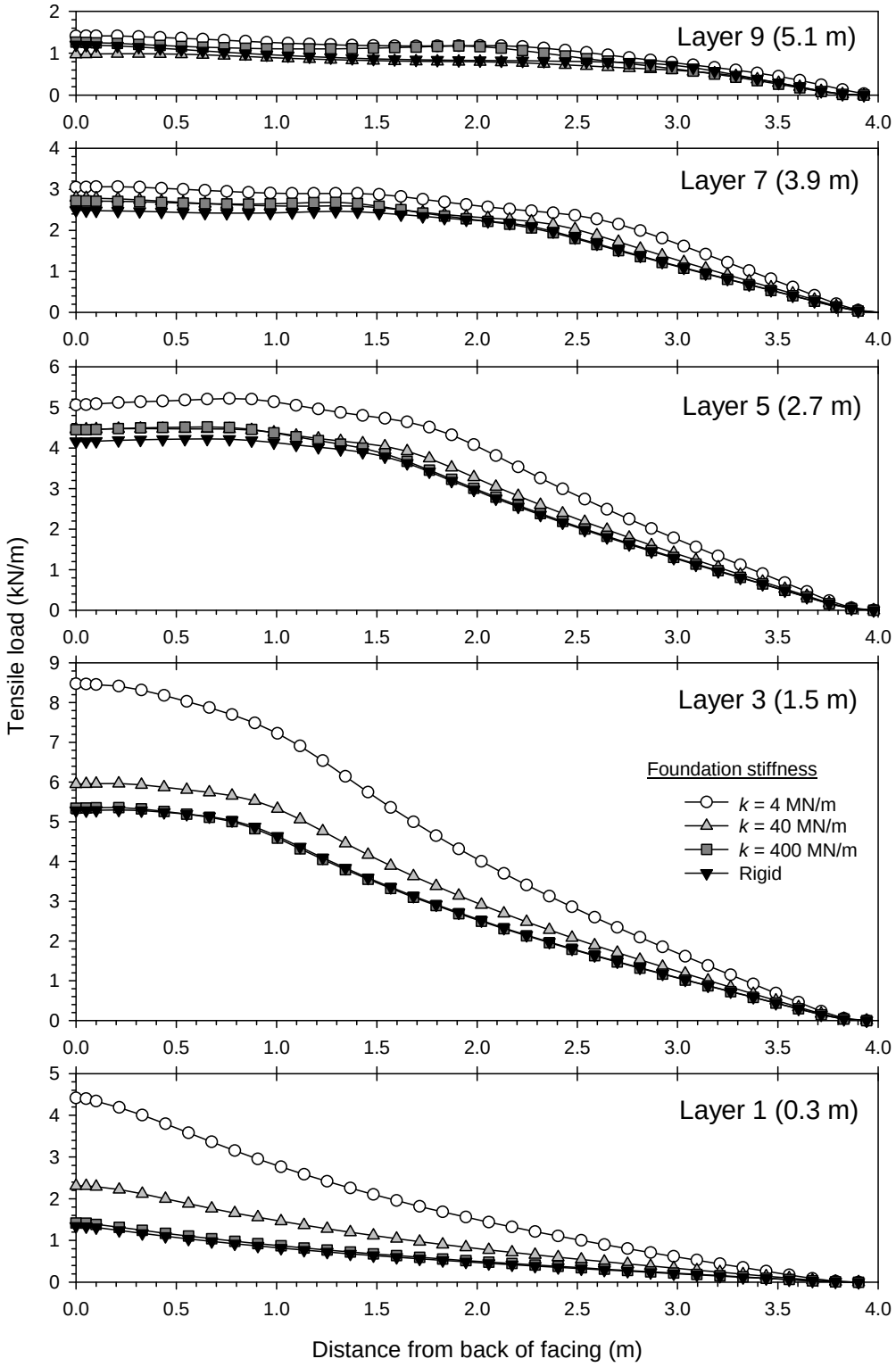

Figure 6.9: Reinforcement tensile loads at end of construction for cases with H = 6 m, WWM reinforcement and four different foundation stiffness cases.

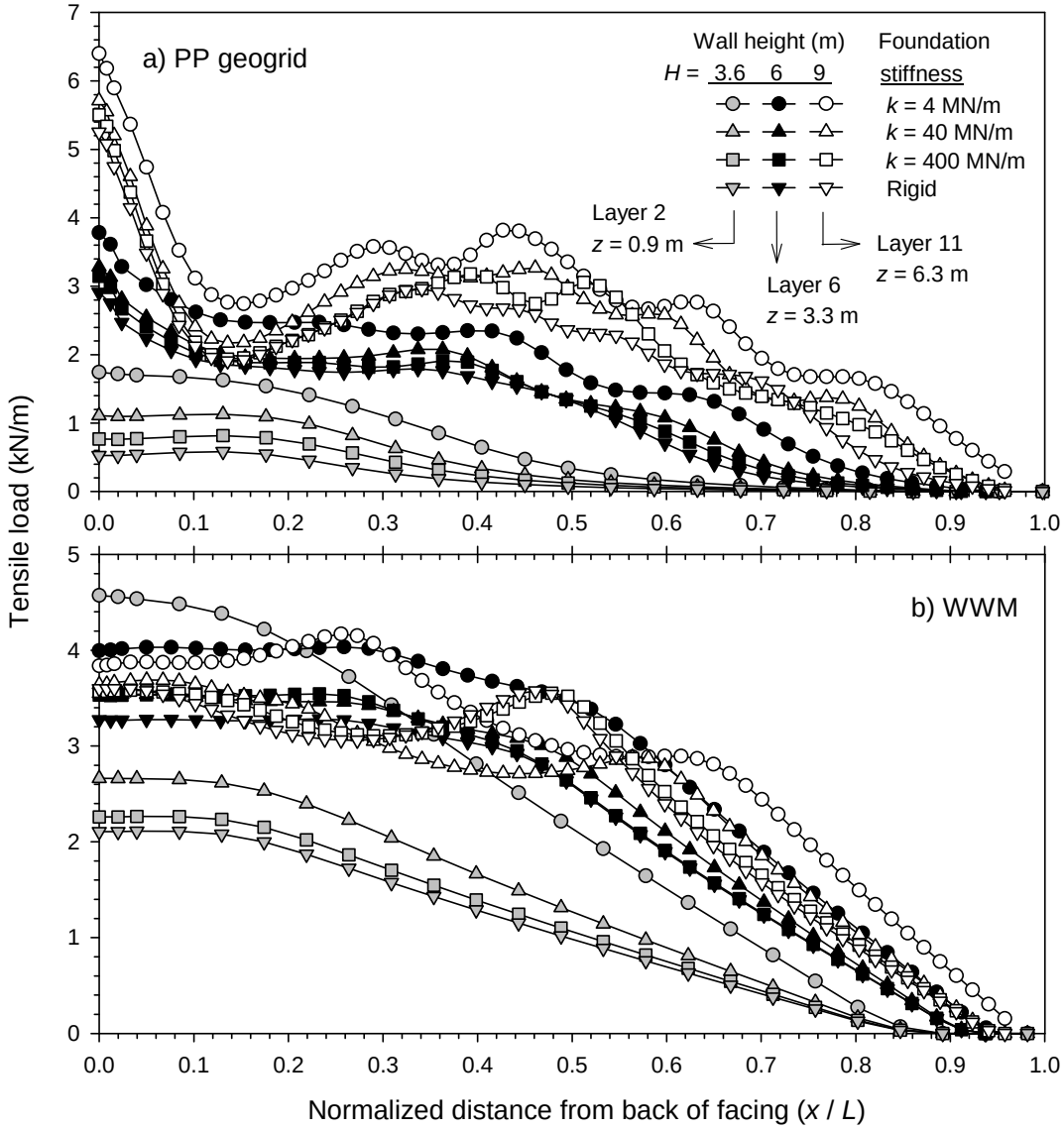

Figure 6.9: Comparison of axial loads in reinforcement layer 2 at 2.7 m below top of wall for walls with H = 3.6, 6 and 9 m: PP geogrid (a), and WWM reinforcement (b). Note: x is the distance from the back of the wall facing and L is the reinforcement length.

The connection loads are attenuated at the base of the wall due to proximity to the horizontally constrained toe boundary. The shapes of the connection load profile with depth are similar for each reinforcement type. However, there is a detectable trend towards a linear increase in load with depth over the top two thirds of the wall for the stiffer WWM reinforcement cases than for the more extensible polymeric reinforcement cases. The non-linear connection load profiles are qualitatively similar to peak axial load profiles deduced from measurements of steel reinforced soil walls (Allen et al., 2004) and reinforced soil walls constructed with more extensible polymeric reinforcement (Bathurst et al., 2008b). An important practical implication of the trends in the load distributions in Figure 6.12a is that

the shape of the load distribution profiles is better captured by a trapezoidal shape (which has also been observed in instrumented field walls) compared to a linear increasing (triangular) shape as assumed in current limit equilibrium-based design methods.

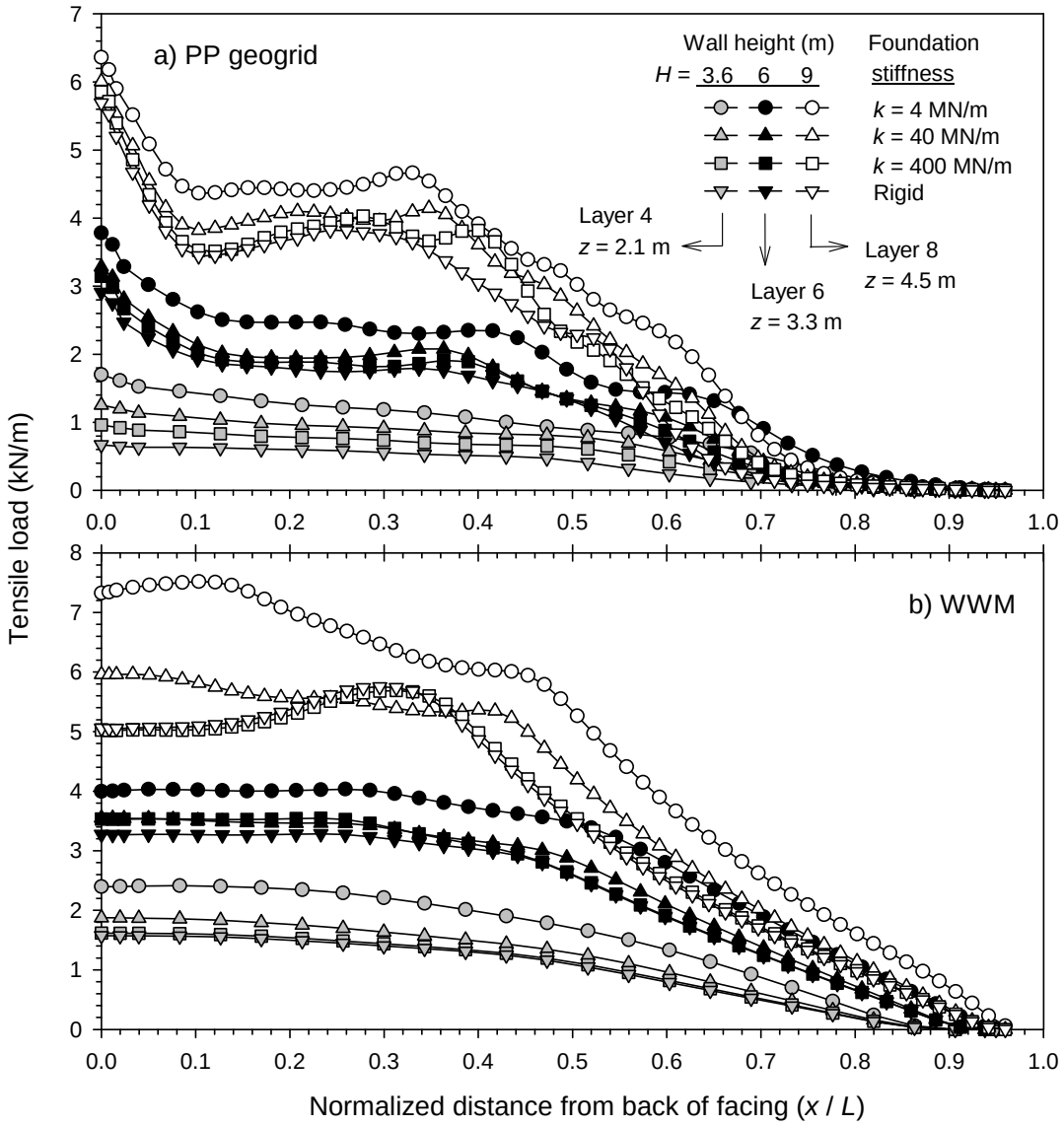

Figure 6.10: Comparison of axial loads in reinforcement layer closest to mid-height of wall for walls with H = 3.6, 6 and 9 m: PP geogrid (a), and WWM reinforcement (b). Note: x is the distance from the back of the wall facing and L is the reinforcement length.

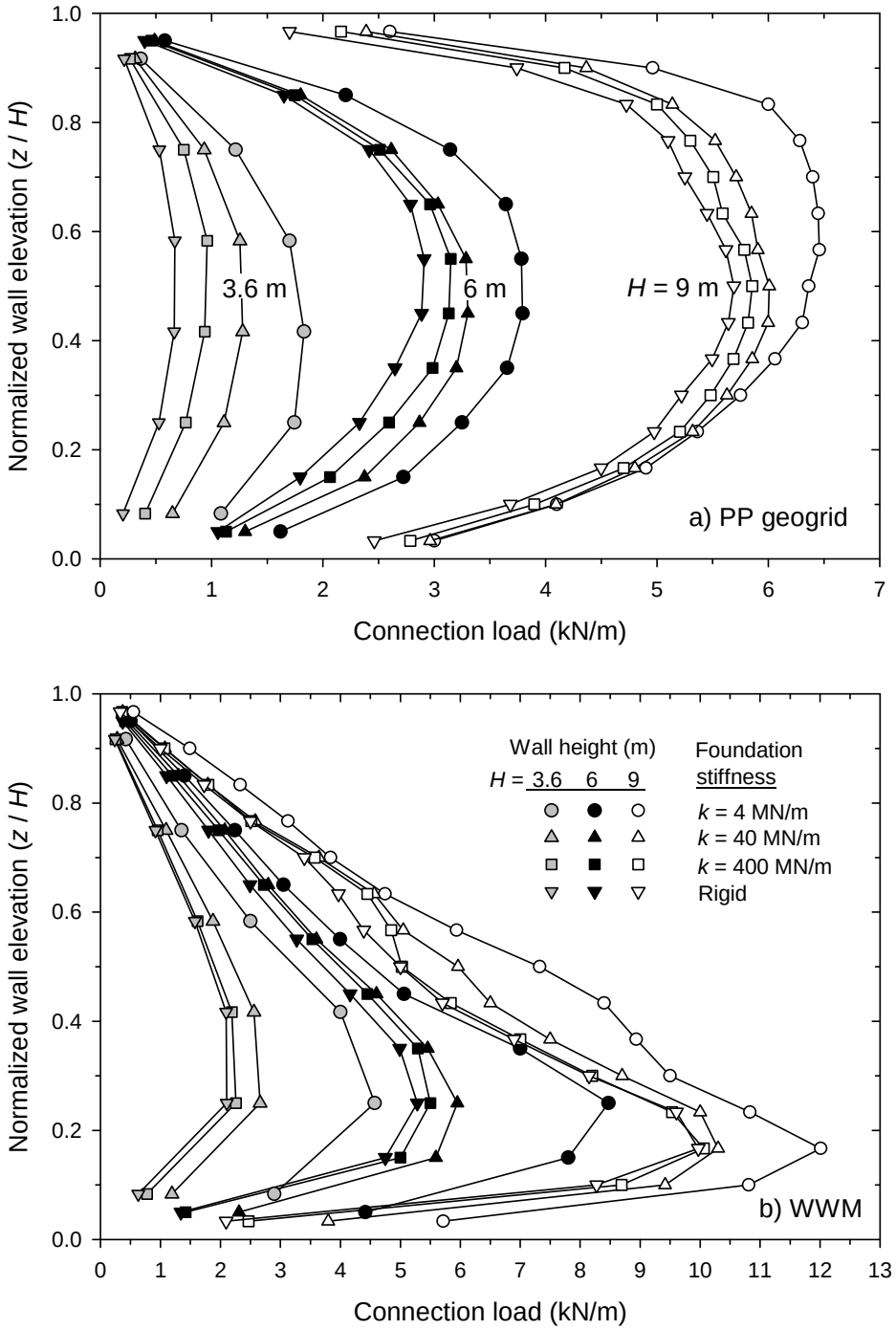

Figure 6.12: Connection loads: PP geogrid (a), and WWM reinforcement (b). Note: z is elevation above the base of the wall.

Figure 6.13 plots the normalized vertical load acting directly below the base of the wall facing at the end of construction for all cases analyzed. The base foundation pressures (σ_v) were normalized by dividing the computed values by the product of the unit weight of the

blocks and the wall height (H). In general, the toe load increases with increasing foundation stiffness when all other conditions are the same. With the exception of the WWM reinforced soil walls with the most compressible foundation (k = 4 MN/m; E = 20 MPa), the toe loads are greater than the self-weight of the facing column. The data curves for the WWM wall cases that cross below the facing self-weight reference line correspond to foundation compressibility which is less than the equivalent stiffness of the backfill soil (E = 60 MPa; see Table 6.2). The result is greater vertical settlement of the foundation behind the facing column than directly below the facing toe. This unusual condition leads to connection up-drag loads on the connections. The influence of the relative stiffness of the backfill soil and the foundation soil is not examined in the current study but confirms the observation made in Chapter 1 (Damians et al., 2013a) that the relative stiffness of the backfill soil and foundation soil can have an important quantitative influence on the magnitude of reinforcement loads at the connections.

Toe loads in excess of column facing self-weight have been recorded for instrumented geogrid and metallic reinforced soil walls in the field and in the laboratory (Damians et al., 2013a; Huang et al., 2009) when these walls have been constructed on competent foundations. The additional load has been attributed to shear and down-drag forces generated at the wall facing-backfill interface and at the facing-reinforcement connections. For the same wall height, the toe load is greater for the more extensible PP geogrid reinforcement case than for the matching WWM case. This is attributed to the greater outward displacement of the wall facing for each PP reinforcement case which leads to greater down-drag loads compared to the matching WWM case.

Figure 6.14 shows the distribution of foundation pressures below and behind the facing column for all analysis cases. The foundation pressures (σ_v) have been normalized by dividing the computed values by the product of the unit weight of the soil (γ) above the foundation and the wall height (H). At the location of the wall facing base, the unit weight of the modular blocks is used in this calculation. The data plots show that influence of wall height on the distribution of normalized foundation pressures behind the wall facing is negligible for both soft and rigid foundation cases. However, the distance over which foundation pressures are attenuated behind the wall face is greater for the rigid foundation cases than for the soft foundation cases (compare left-hand side figures to right-hand side figures).

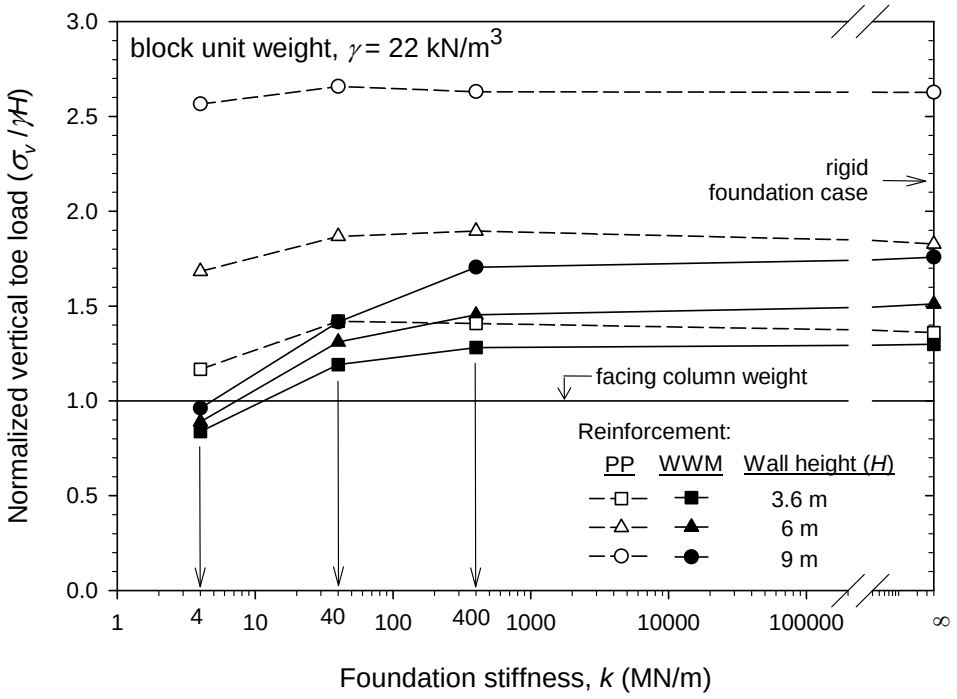

Figure 6.13: Normalized vertical toe load at facing.

6.3.2. Influence of toe fixity (rigid foundation under facing)

Previous cases assumed equal foundation compressible behaviour under the facing and under the backfill. However, this should not the representative in particular real cases as if specific foundation is emplaced just under the facing. To perform this differential settlement effect between the facing and the backfill, additional constrain in vertical displacements was considered in previous foundation compressibility cases with H = 6 m (logically, with the exception of the rigid foundation case). Figure 6.15 presents the FLAC numerical model with detail in the prescribed fixity assumed at foundation facing toe.

Figure 6.16 presents the normalized-relative horizontal facing displacements for soft foundation under backfill and facing, and soft foundation only under backfill (i.e., toe fixed) model cases. Contrary to previous cases, the restrain in vertical displacement at facing toe generates inverse response from foundation compressibility degrees for both PP and WWM reinforcement cases: the greater compressibility under backfill (i.e., the greater differential settlement), the less facing displacement. As expected, the higher foundation stiffness the more similar responses between both toe fixity conditions analyzed.

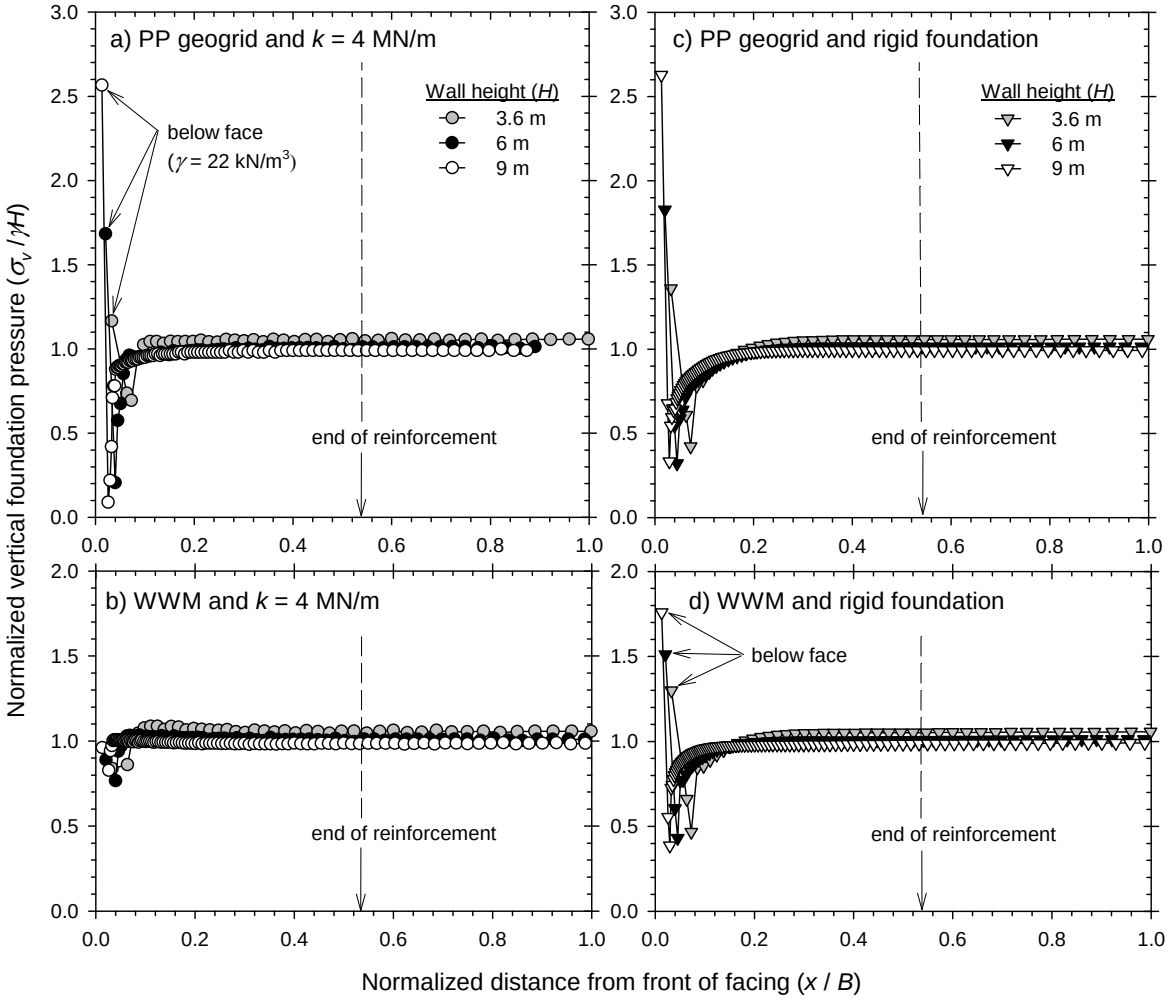

Figure 6.14: Normalized vertical foundation pressures: PP reinforcement and soft foundation (a), WWM reinforcement and soft foundation (b), PP reinforcement and rigid foundation (c), and WWM reinforcement and rigid foundation (d). Note: x is the distance from the front (toe) of the wall and B is the width of the numerical model.

Figure 6.17 and 6.18 show the tensile reinforcement loads in selected layers for PP geogrid and WWM cases, respectively, with H = 6 m. Both foundation compressibility under backfill and facing, and under backfill only (i.e., toe fixed) cases were analyzed, for two different foundation stiffness cases. As detected, not much variations of tensile load distribution was obtained in case of stiffer foundation despite the facing toe fixity condition (i.e., k = 400 MN/m). However, significant reduction of tensile loads were obtained in softer foundation (k = 4 MN/m) and facing toe fixity case, with a reached trend similar to stiffer foundation case (except for bottom reinforcement layers).

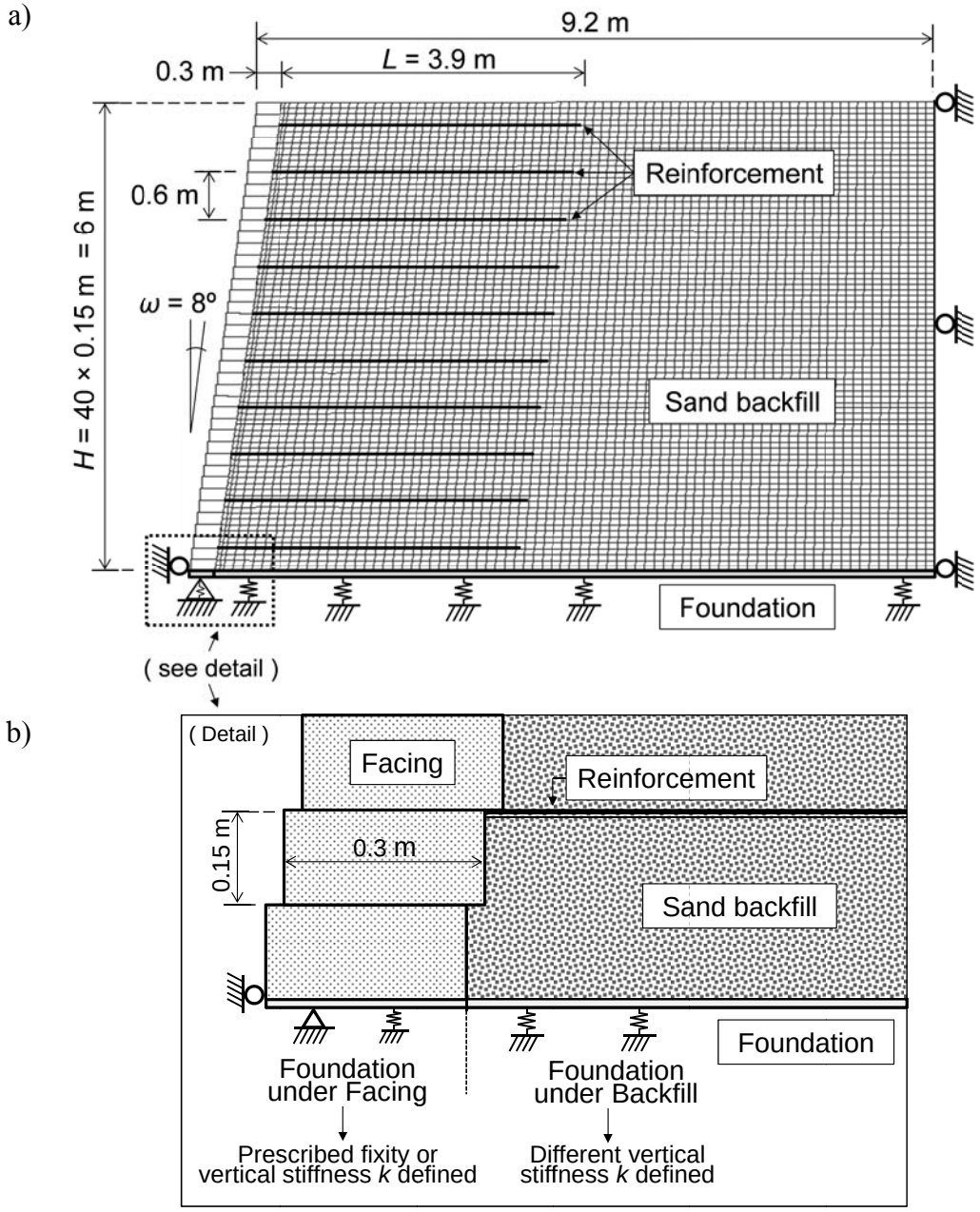

Figure 6.15: FLAC numerical model with H = 6 m: global view (a) and foundation detailed schema (b).

Connection loads for foundation compressibility under backfill and facing case, and just under backfill case (i.e., toe fixed) are presented in Figure 6.19 (H = 6 m). Similar responses were obtained despite the different foundation compressibility toe conditions. However, somewhat lower resulting values were reached in all foundation compressibility scenarios for toe fixity condition. Different from facing displacement results, same sequential resulting order was obtained between foundation compressibility under backfill and facing case, and foundation compressibility just under backfill (i.e., toe fixed) case.

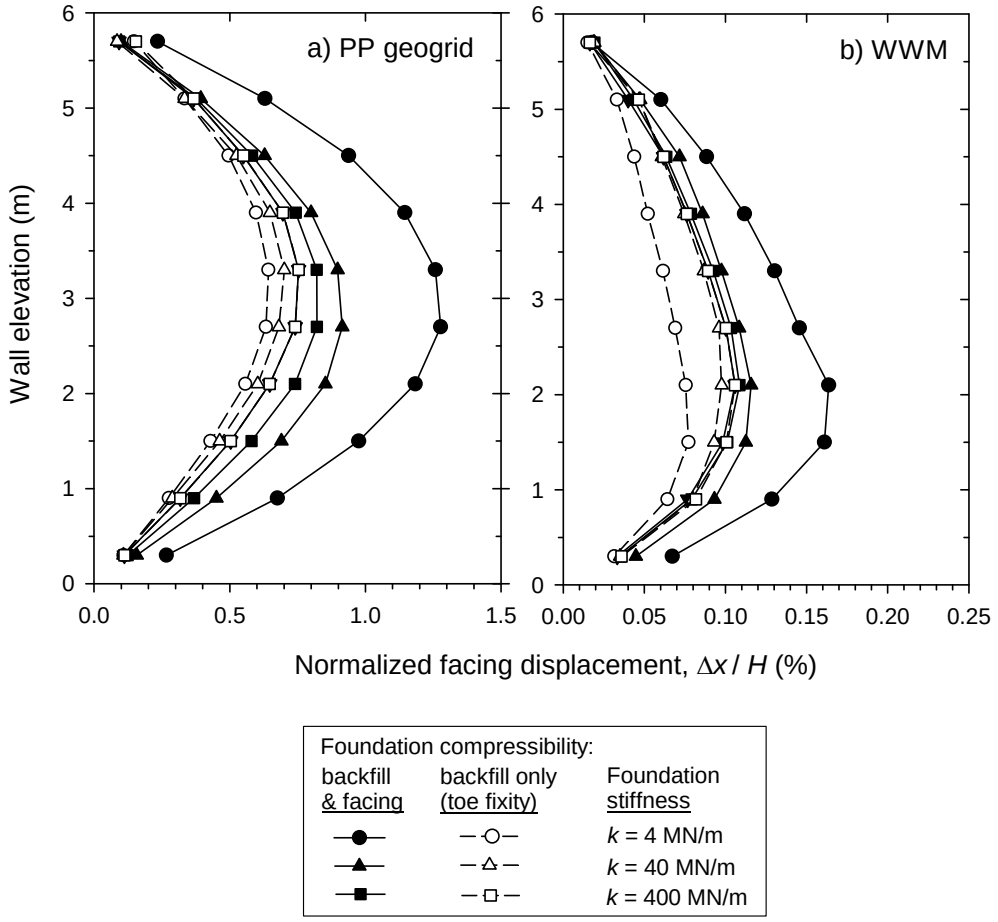

Figure 6.16: Normalized-relative horizontal facing displacements for foundation compressibility under backfill and facing case, and under backfill (i.e., toe fixed) case, with H = 6 m: PP geogrid (a), and WWM reinforcement (b).

Vertical load under the facing models with H = 6 m assuming facing toe foundation fixity case is shown in Figure 6.20. As commented, for softer foundation, larger vertical load is generated under the facing. But if the foundation has the same stiffness compressibility under the facing that under the backfill, the vertical load is significantly lower than the case of toe fixity. This is because the facing, that is much weighty than the soil, generates larger settlements than the backfill. In this scenario, the reinforcement seems to pull the facing up, reducing the vertical load. If foundation under facing is stiffer than under backfill (case example assuming particular foundation under facing, higher vertical facing toe loads are reached due to the down-drag loads at reinforcement-to-facing connections. This increases of vertical facing load due to the toe fixity was determined to be about 1.9 times the case of equal foundation under facing and backfill in WWM, and about 1.2 times in PP geogrid.

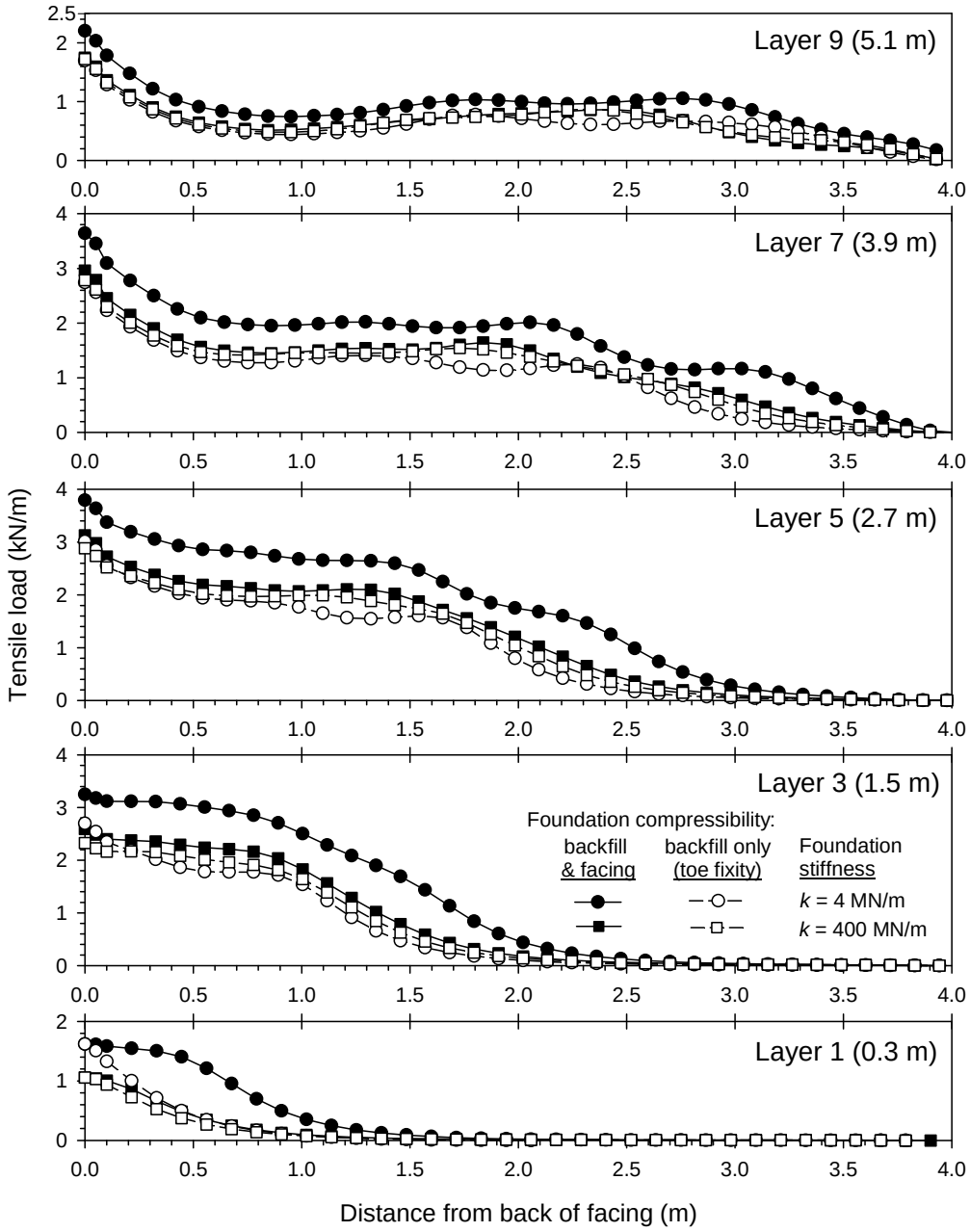

Figure 6.17: Reinforcement tensile for foundation compressibility under backfill and facing case, and under backfill (i.e., toe fixed) case, with H = 6 m: PP geogrid reinforcement and two different foundation stiffness cases.

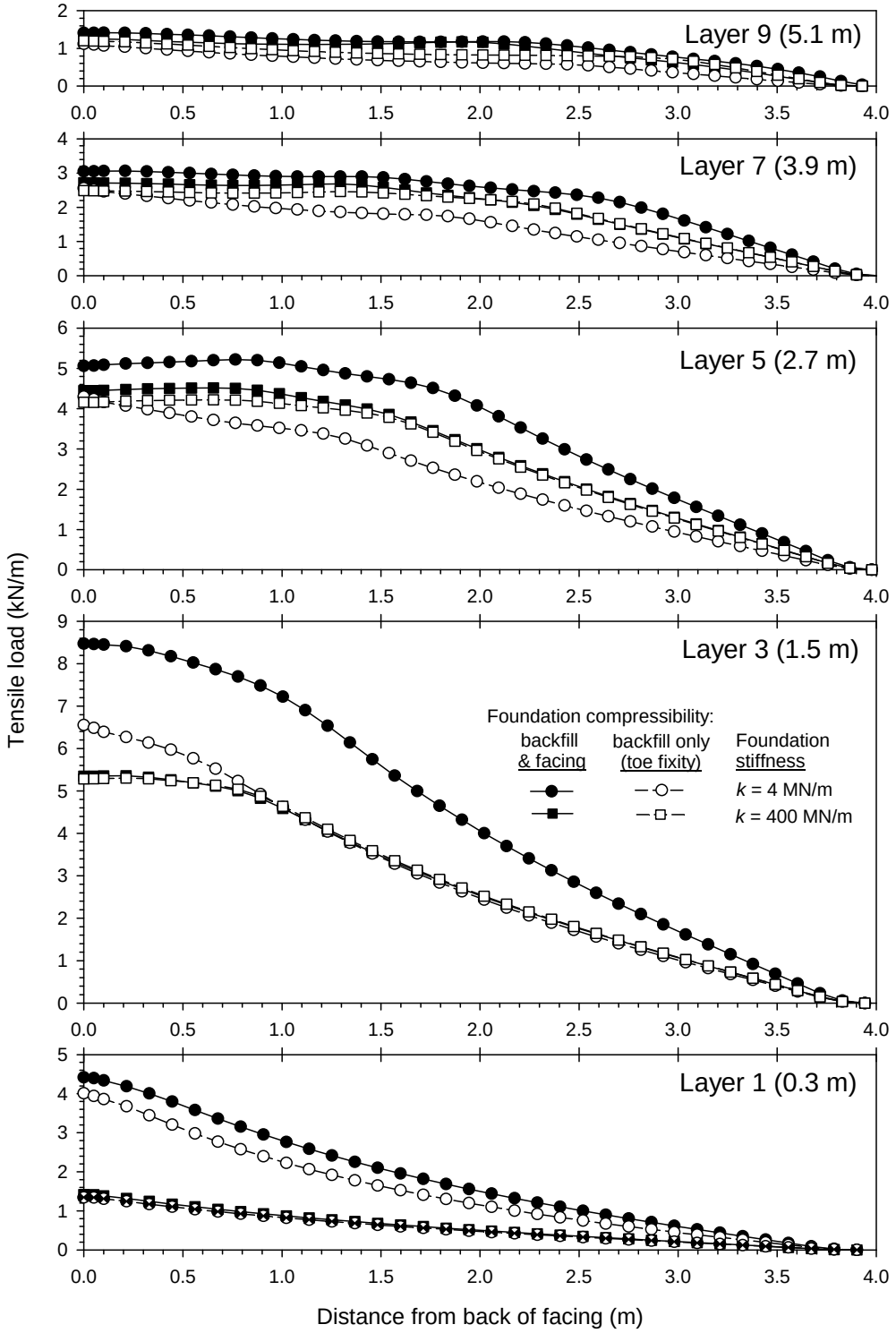

Figure 6.18: Reinforcement tensile for foundation compressibility under backfill and facing case, and under backfill (i.e., toe fixed) case, with H = 6 m: WWM reinforcement and two different foundation stiffness cases.

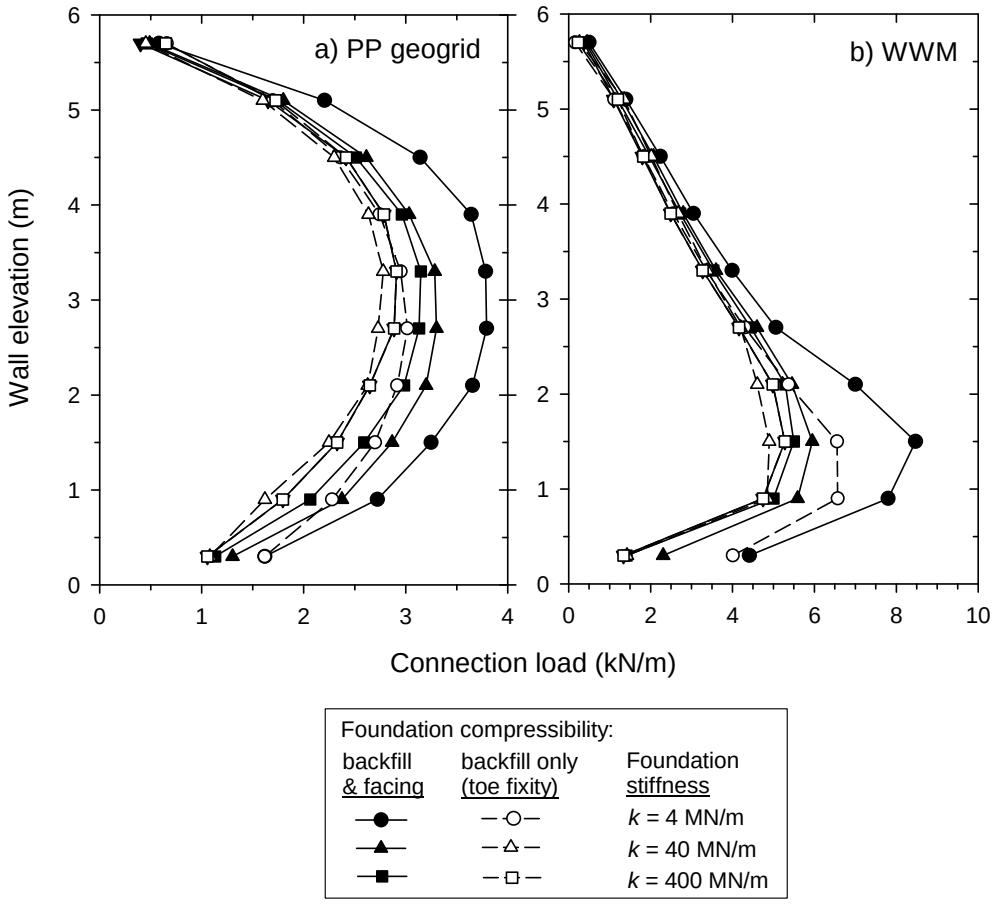

Figure 6.19: Connection loads for foundation compressibility under backfill and facing case, and under backfill (i.e., toe fixed) case, with H = 6 m: PP geogrid (a), and WWM reinforcement (b).

6.3.3. Influence of the soil model selection (M-C and Lade)

Additionally to the elastic-plastic Mohr-Coulomb failure criteria, the Lade single-hardening (Lade 2005) constitutive model for sand was also used in the numerical model. The model parameters were taken from laboratory tests reported by Hatami and Bathurst (2005) and are summarized in Table 6.5. The proposed parameters for Lade model are in agreement and proper correspondence the toe ones assumed in previous results and presented in Table 6.2 for elastic-plastic model and Mohr-Coulomb (M-C) failure criterion.

Normalized-relative horizontal facing displacements for Mohr-Coulomb and Lade models with H = 6 m are shown in Figure 6.21 for WWM and PP geogrid reinforcement scenarios. Despite similar tendencies were obtained in both reinforcement cases, Mohr-Coulomb resulted with higher response values in PP geogrid cases, and lower in WWM cases.

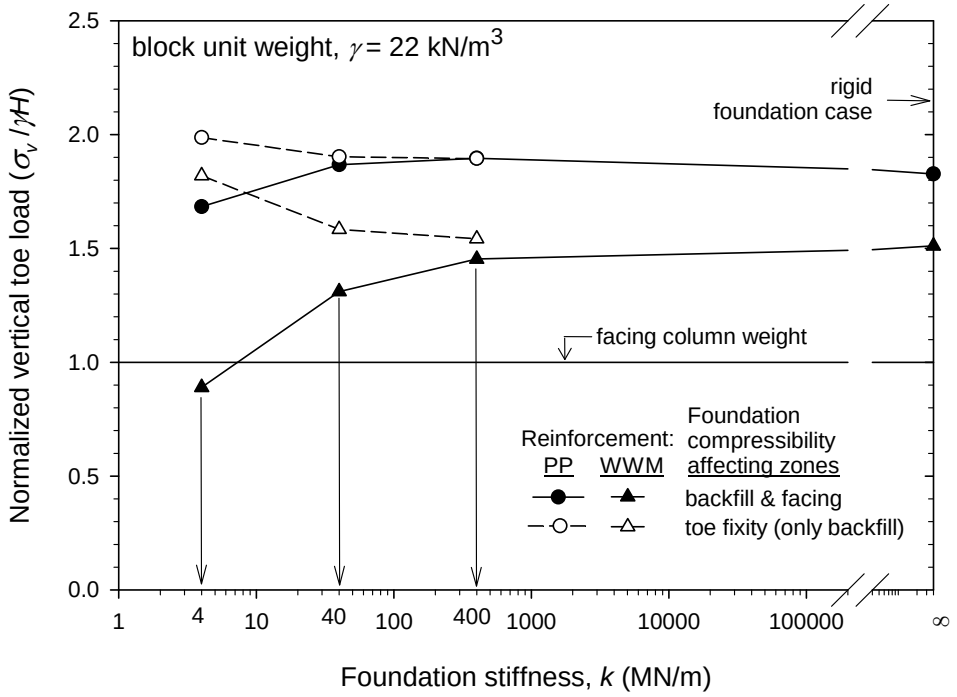

Figure 6.20: Vertical load under the facing models with H = 6 m: facing toe foundation fixity case included.

Table 6.5. Sand backfill properties with Lade model (equivalent to Table 6.2):

Model parameters	Values
M, λ, v (elastic properties)	955, 0.25, 0.3
m, η_1, a (failure criterion)	0.107, 36, 1.97×10^{-3}
Ψ_2, μ (plastic potential)	-3.65, 2.425
h, α (yield criterion)	0.432, 0.34
C, p (hardening/softening law)	0.11×10^{-3}, 1.22
γ (unit weight, kN/m^3)	16.8

Figures 6.22 and 6.23 show the reinforcement tensile loads at end of construction Mohr-Coulomb and Lade models with H = 6 m for PP geogrid and WWM reinforcement cases, respectively, and two different foundation stiffness cases. Consequent to previous results, lower tensile loads were obtained in PP geogrid cases if Lade model is assumed, for both stiff and soft foundation cases analyzed. In WWM reinforcement case, higher tensile loads were obtained in case of soft foundation in all reinforcement layers with the exception of the first-bottom one. However, lower tensile loads were obtained in the first half of wall height in Lade model for rigid foundation case.

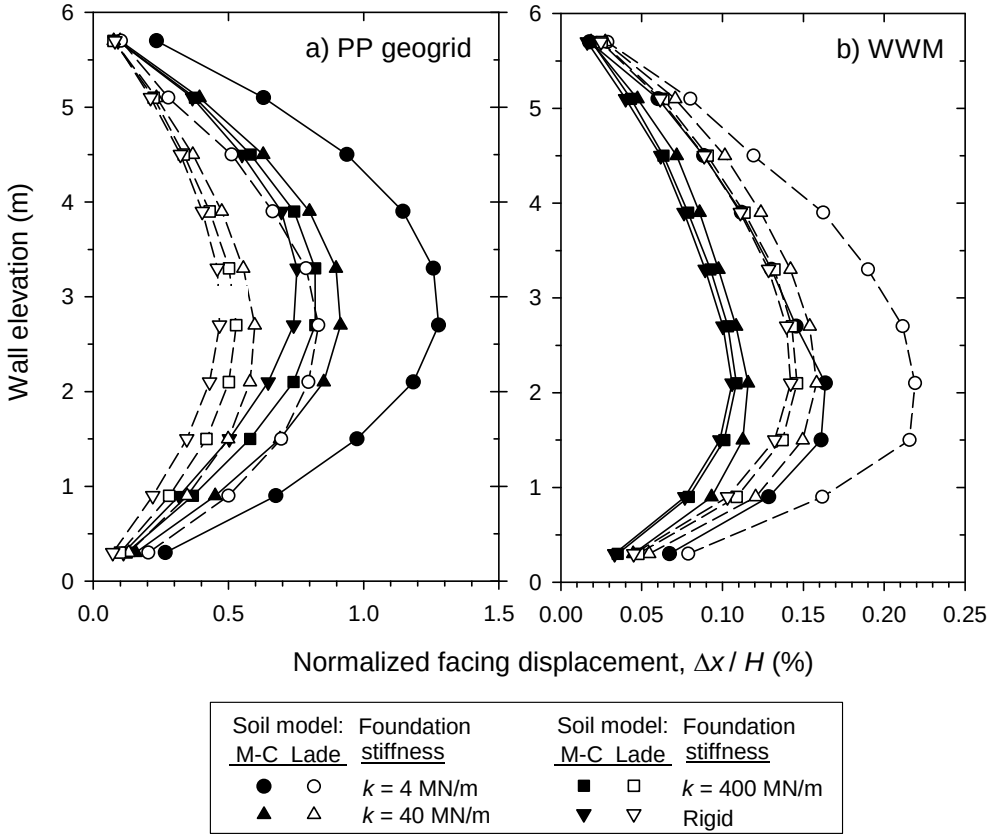

Figure 6.21: Normalized-relative horizontal facing displacements for Mohr-Coulomb and Lade models with H = 6 m: PP geogrid (a), and WWM reinforcement (b).

Connection loads in WWM and PP geogrid reinforcement cases for Mohr-Coulomb and Lade models with H = 6 m are shown in Figure 6.24. As observed, similar to the facing displacement results, lower results were generally obtained if Lade model is considered, than in Mohr-Coulomb. In case of WWM reinforcement, very similar response was obtained between both models. A general comparison between the soil-models considered over the reinforcement strains is done in this section (Lade versus Mohr-Coulomb response). This comparison has been made defining a strain ratio equal to the strain results at 0.2 m back to the facing obtained with the Mohr-Coulomb criterion (previous section results) over the ones obtained for Lade model, i.e., $\varepsilon_{(Mohr\text{-}Coulomb;\ at\ 0.2\ m)} / \varepsilon_{(Lade;\ at\ 0.2\ m)}$. The reinforcement location of this strain ratio is at 0.2 m back to the facing, which is the zone between the facing and the 1st half meter of the reinforcement length where in all cases shown before (Figures 6.8 and 6.9) has been localized the maximum stress-strain response. Figure 6.25 exposes this reinforcement strain comparison with regards to the strain ratio mentioned. The comparison between strains reached in Lade and Mohr-Coulomb shows that both models have similar response for WWM reinforcement cases (Figure 6.25b), with slightly tendency of higher results under Lade soil model for reinforcement layers located at higher wall heights: from

about $\varepsilon_{(Mohr\text{-}Coulomb;\ at\ 0.2\ m)} / \varepsilon_{(Lade;\ at\ 0.2\ m)} = 1.0$ (average) at bottom reinforcement layer, up to $\varepsilon_{(Mohr\text{-}Coulomb;\ at\ 0.2\ m)} / \varepsilon_{(Lade;\ at\ 0.2\ m)} = 0.65$ (average) at top layer.

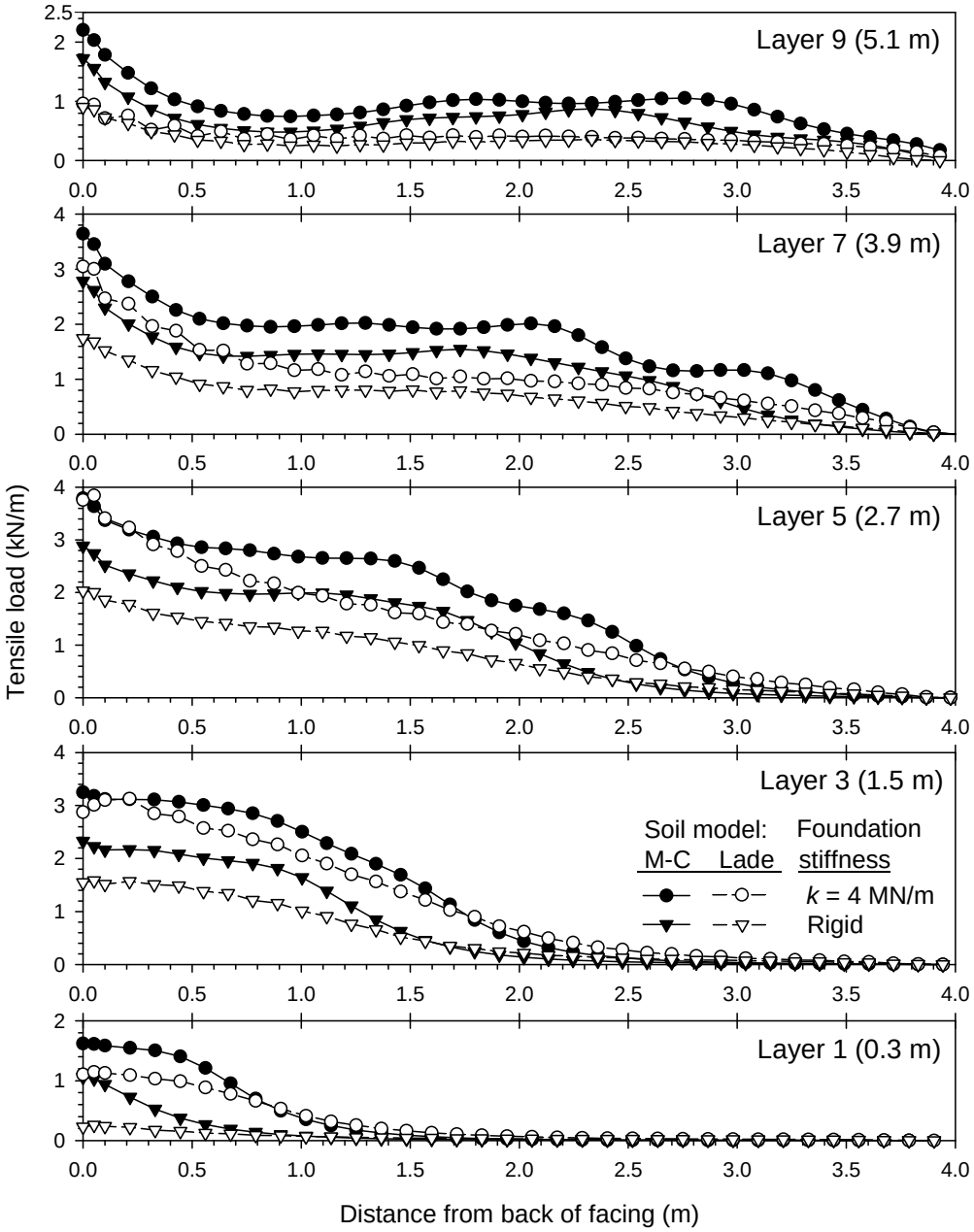

Figure 6.22: Reinforcement tensile loads at end of construction Mohr-Coulomb and Lade models with H = 6 m, PP geogrid reinforcement and two different foundation stiffness cases.

On the other hand, significant variations were obtained for PP geogrid reinforcement cases, with higher Mohr-Coulomb strain results in all foundation compressibility scenarios and at all the reinforcements layers: $\varepsilon_{(Mohr\text{-}Coulomb;\ at\ 0.2\ m)} / \varepsilon_{(Lade;\ at\ 0.2\ m)} = 1.8$ (average), with a tendency of lowest results under Lade soil model for reinforcement layers located at higher wall

heights (inverse to the previous WWM case). The greater difference was obtained at bottom reinforcement layer under rigid foundation, were Mohr-Coulomb strain results reached more than 3 times the strains obtained under Lade model.

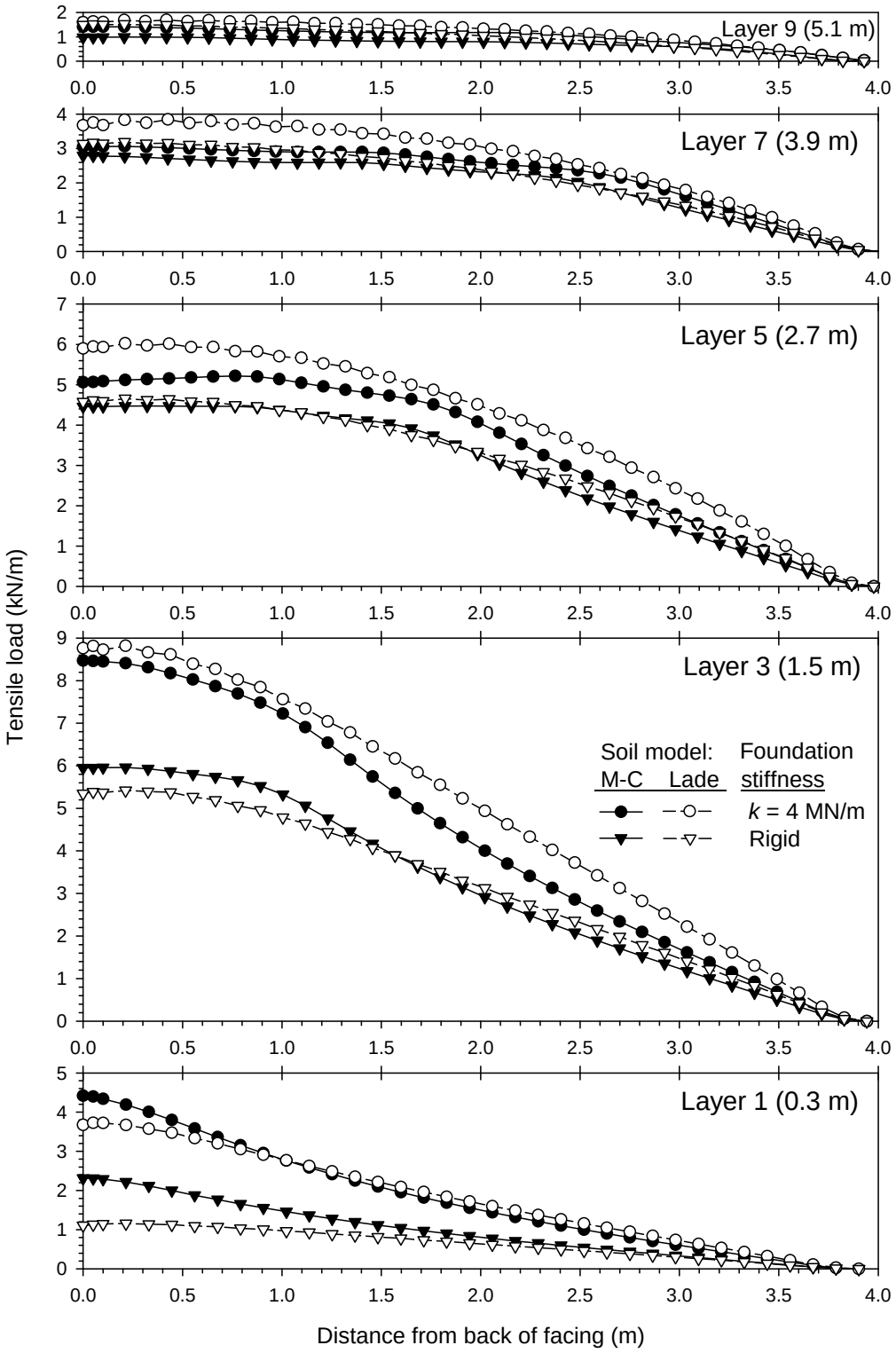

Figure 6.23: Reinforcement tensile loads at end of construction Mohr-Coulomb and Lade models with H = 6 m, WWM reinforcement and two different foundation stiffness cases.

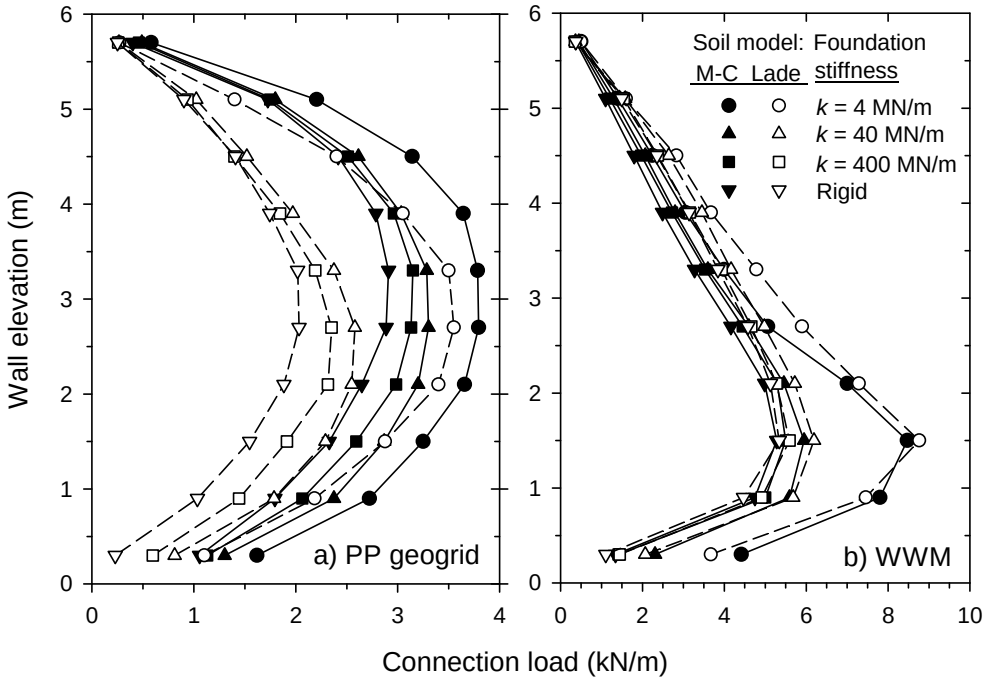

Figure 6.24: Connection loads for Mohr-Coulomb and Lade models with H = 6 m: PP geogrid (a), and WWM reinforcement (b).

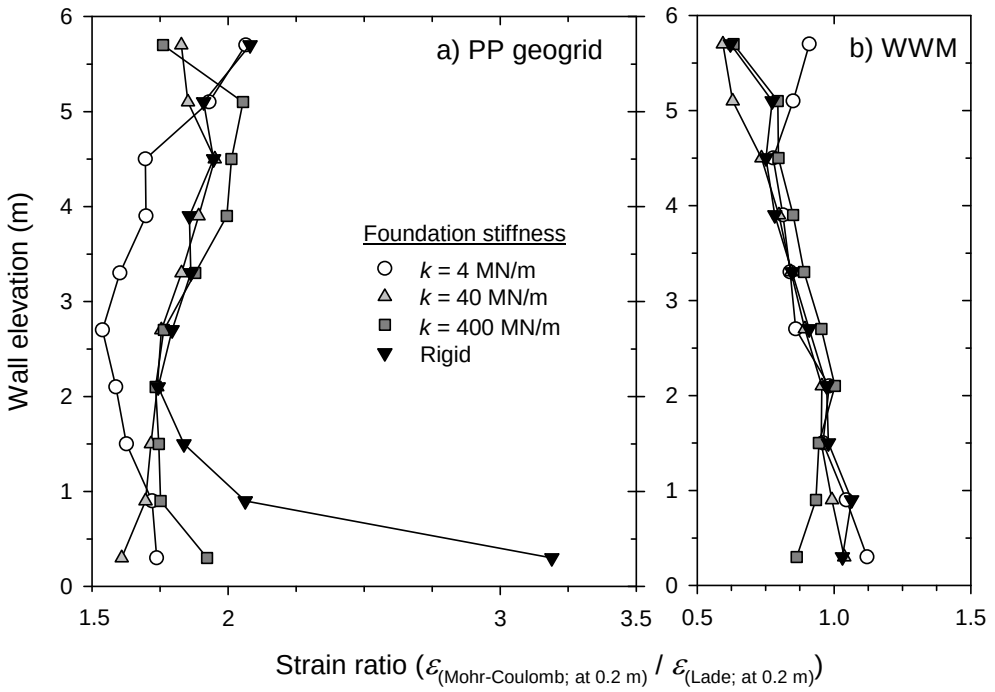

Figure 6.25: Reinforcement strain ratio between Lade and Mohr-Coulomb model results with H= 6 m at 0.2 m back to the facing: PP geogrid (a), and WWM reinforcement (b).

6.4. CONCLUSIONS

The physical behavior of reinforced soil walls is complicated due to the mechanical complexity of the component materials, their interactions, wall geometry and soil stratigraphy/arrangement, in addition to the unquantifiable effects of construction method and quality. Nevertheless, current design methods are typically based on classical notions of soil and reinforcement ultimate strength. Furthermore, internal stability design using conventional analytical solutions assumes that the compressibility of the foundation soil does not influence reinforcement loads.

This current investigation is a modest attempt to isolate the contribution of foundation vertical stiffness on reinforced soil wall behaviour. The modeling is admittedly simple because it considers the foundation support as deformable only in the vertical direction. In field structures, additional horizontal deformations may occur in the foundation soils. However, predicting this performance is complicated by the choice of constitutive model assigned to the foundation soil and the choice of magnitude of input parameter values. The simplest approach to isolate the effect of the foundation on the performance of a wall is to treat the structure support as a Winkler foundation with linear spring stiffness.

The numerical simulation results in the current study demonstrate that wall facing deformations, connection loads and axial strains in the reinforcement layers all increase with decreasing foundation stiffness. However, the magnitude of wall displacements, maximum reinforcement loads (or strains) and vertical toe loads for the two different reinforcement materials considered, is influenced more by the relative stiffness of the two reinforcement materials than by the compressibility of the foundation when all other conditions are the same. This outcome cannot be predicted for walls under operational (working stress) conditions using current limit equilibrium (strength-based) design methods for the calculation of reinforcement loads.

The relative displacement between the facing and the backfill is influenced by the relative compressibility of the backfill soil and the foundation soil, and reinforcement stiffness. The numerical results in this study have shown that as foundation stiffness decreases to very low values, the reinforcement connection loads can actually decrease which may be judged to be counter intuitive. However, as reinforcement stiffness decreases and all other factors remain unchanged the wall facing displacements will increase and wall connection loads will increase due to larger down-drag loads.

CHAPTER 7

EQUIVALENT INTERFACE PROPERTIES TO MODEL SOIL-FACING INTERACTIONS WITH ZERO-THICKNESS AND CONTINUUME ELEMENT METHODOLOGIES [1]

7.1. INTRODUCTION AND GENERAL APPROACH

Soil-facing mechanical interactions play an important role in the behavior of earth retaining walls. Generally, numerical analysis of earth retaining structures requires the use of interface elements between dissimilar component materials to model soil-structure interactions and to capture the transfer of normal and shear stresses through these discontinuities. In finite element method software programs, soil-structure interactions can be modelled using special interface tools as "zero-thickness" interface elements between the soil and structural components. These elements use a strength/stiffness reduction factor that is applied to the soil adjacent to the interface. In this study, because the software program used (CODE_BRIGHT; Olivella et al., 1996) has no specific tool to model interfaces, continuum elements has been used to model soil-structure and soil-reinforcement interactions. The continuum element approach could allow to a more control of the interface features (i.e., material strength and stiffness properties) as well as the element sizes and shapes at the interfaces. A methodology and proposed parameter values for continuum elements are presented in next sections, with providing the same numerical outcomes as those using zero-thickness elements in already calibrated 2D models.

Soil-facing interaction may not require 3D modelling, as 2D modelling (plain strain) has been demonstrated to reach good performance. However, in some cases, the use of continuum elements will derive on non-expected results when using elastic-plastic soil models, as fluctuations on stresses once soil plastic flow occurred. Furthermore, because soil-facing

[1] Chapter partially based on Damians, I.P., Yu, Y., Lloret, A., Bathurst, R.J., and Josa, A.; 2015. Equivalent interface properties to model soil-facing interactions with zero-thickness and continuum element methodologies. Proceedings of the XV Pan-American Conference on Soil Mechanics and Geotechnical Engineering (XV PCSMGE): From Fundamentals to Applications in Geotechnics. Buenos Aires, Argentina, 15th – 18th November 2015, pp.1065-1072.

interaction is required in 3D to be included in the entire reinforced soil wall modelling, 3D soil-facing interface shall be generated and properly calibrated.

Thus, the main objectives of this chapter are, first, to examine the load transfer between the soil and the facing component within a small concrete earth retaining wall segment using both zero-thickness (PLAXIS) and spring elements (FLAC), with additionally also continuum elements at the interfaces in finite element and finite difference programs. Secondly, to present numerical model details for equivalent interface property values using the default different interface modelling methods available or the proposed methodology with continuum elements. The chapter shows that the different interface modelling approaches can give very similar results using equivalent interface property values, and demonstrates the influence of choice of numerical mesh size on the numerical outcomes when continuum elements are used at the interfaces.

7.2. GENERAL PROBLEM DEFINITION

A small concrete earth retaining structure segment was considered to examine the load transfer from the backfill soil to the adjacent facing structure using both zero-thickness elements and continuum elements with the same interface property values (Figure 7.1). The concrete facing was 0.5 m thick and 1.5 m high. The retained backfill soil was 2.5 m long and 1.5 m high. Both the soil and concrete facing were discretized using 15-node elements. The left side of the concrete facing and the right side of the backfill soil were fixed in x-direction and free in y-direction. The bottom of both the concrete facing and backfill soil was fixed in y-direction only. A uniformly distributed surcharge load was applied to the top surface of the backfill soil at three different magnitudes (q = 10, 50 and 100 kPa).

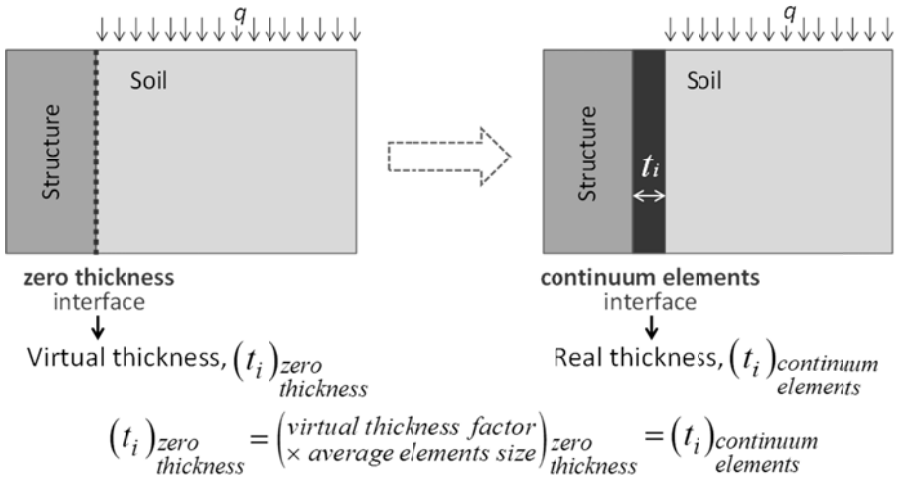

Figure 7.1: Interface modelling approaches with zero-thickness elements and continuum elements.

The soil was modelled as linear elastic with Mohr-Coulomb failure criterion. The parameter values for the backfill soil are shown in Table 7.1. The concrete facing was modelled as linear elastic with elastic modulus of 32 GPa, Poisson's ratio of 0.15 and a unit weight of 25 kN/m^3. The interface strength and stiffness can be very different depending on the interacting materials (Potyondy, 1961). Thus, five different strength/stiffness reduction factors (R_i = 0.3, 0.45, 0.6, 0.8 and 1.0) were considered; the corresponding interface property values are shown in Table 7.2.

As an elastic-plastic model with the Mohr-Coulomb failure criterion, the proposed continuum element interfaces have strength properties of friction angle (ϕ_i), cohesion (c_i), and dilatancy angle (assumed with a fixed value of ψ_i = 0º). The stiffness of the interface is controlled by the Young's modulus (E_i) and the Poisson's ratio (assumed with a fixed value of ν_i = 0.45).

Table 7.1. Soil properties:

Soil parameters	Value	Units
Unit weight, γ_{soil}	18.0	kN/m^3
Cohesion, c_{soil}	1.0	kPa
Friction angle, ϕ_{soil}	44.0	degrees
Dilatancy angle, ψ_{soil}	14.0	degrees
Elastic modulus, E_{soil}	5.0 and 50.0	MPa
Poisson's ratio, ν_{soil}	0.3	-
Strength/stiffness reduction factor, R_i	0.3, 0.45, 0.6, 0.8 and 1.0	-

Table 7.2. Interface properties (related to E_{soil} = 5 MPa):

Parameters	Strength/stiffness reduction factor, R_i					Units
	0.3	0.45	0.6	0.8	1.0	
Cohesion, c_i	0.3	0.45	0.6	0.8	1.0	kPa
Friction angle, ϕ_i	16.2	23.5	30.1	37.7	44.0	degrees
Shear modulus, G_i	0.17	0.39	0.69	1.23	1.92	MPa
Elastic modulus, E_i	0.50	1.13	2.01	3.57	5.00	MPa

The parameter relations between the soil and the interface material can be understood as a strength/stiffness reduction factor ($R_i \leq 1.0$) directly applied to the properties of the adjacent soil. Thus, to set the interface material properties the following parameter relations are considered:

$$c_i = R_i c_{soil} \tag{7.1}$$

$$\phi_i = \tan^{-1}(R_i \tan \phi_{soil}) \tag{7.2}$$

$$G_i = R_i^2 G_{soil} = R_i^2 \left(\frac{E_{soil}}{2(1+\nu_{soil})} \right) \tag{7.4}$$

$$E_{\text{oed,i}} = 2G_{\text{i}} \frac{1-\nu_{\text{i}}}{1-2\nu_{\text{i}}} \tag{7.5}$$

Where: c_{soil} is the soil cohesion; ϕ_{soil} is the soil friction angle; E_{soil} is the Young's modulus of the soil; G_{soil} and G_i are the shear modulus of the soil and the interface, respectively, and $E_{oed,i}$ corresponds to the oedometer modulus of the interface material (because, as mentioned, ν_i = 0.45).

From Eq.7.4, Young's modulus of the interface can be consequently deduced as follows:

$$E_i = 2G_i\left(1+\nu_i\right) = R_i^2\left(\frac{E_{soil}}{(1+\nu_{soil})}\right)\left(1+\nu_i\right) = 1.45R_i^2\left(\frac{E_{soil}}{(1+\nu_{soil})}\right) \tag{7.6}$$

First approach in 2D will provide better understanding about the mesh size to analyze soil-facing interaction.

7.3. 2D MODELLING

7.3.1. Interface 2D model and properties with PLAXIS

To model an interface with continuum elements, a real interface zone between the dissimilar materials with the thickness equal to the virtual thickness from the zero-thickness elements is generated (Figure 7.1). The material properties of this zone are also taken to be the same as those from the zero-thickness elements (Figure 7.1). For cases where different finite element meshes (with different average element sizes) are considered, the virtual thickness factor can be slightly adjusted to keep the same interface virtual thickness. Otherwise specified, the actual thickness value considered was 18 mm, corresponding to the exact value used during calculation. This value can be found in the Output program (a post-processor in PLAXIS).

7.3.1.1. Effect of the mesh size and elements type

Figure 7.2 shows three different finite element meshes (i.e., coarse, fine and optimized) that were generated to examine the effect of element size at the interface zone on the load transfer between the soil and facing structure. Among these three meshes, the coarse mesh (Figure 7.2a) had the highest element aspect ratio within the real interface zone, the optimized mesh (Figure 7.2c) had the lowest element aspect ratio in the region where the analysis is focused (and fewer total number of elements), and the element aspect ratio of the fine mesh (Figure 7.2b) was between that if the coarse and optimized meshes. When zero-thickness elements were used at the interface between the soil and facing, the interface virtual thickness was, as commented, 18 mm. When using continuum elements to simulate the soil-facing interaction the same 18 mm-value of real zone thickness was modelled (see Figure 7.2 – Details).

a) Coarse mesh:

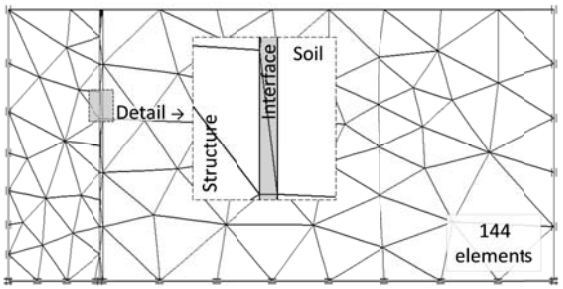

b) Fine mesh:

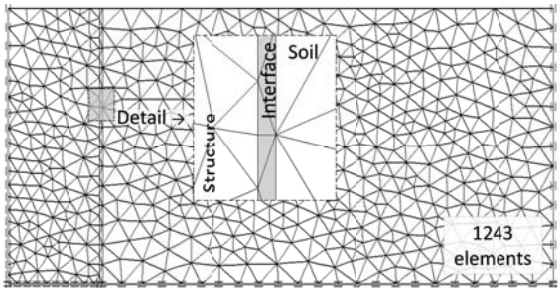

c) Optimized mesh:

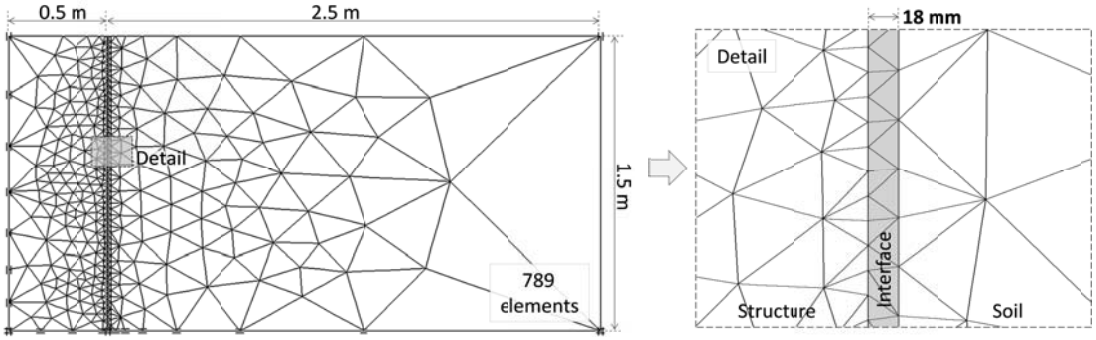

Figure 7.2: Three different finite element meshes for the same soil-structure interaction example in PLAXIS: coarse mesh (a), fine mesh (b), and optimized mesh (c) with the same interface thickness of t_i = 0.018 m.

Figure 7.3 shows the normal and shear stresses acting at the interface between the facing and backfill soil with the three different meshes and using the strength/stiffness reduction factor of R_i = 0.8 where both zero-thickness elements and continuum elements are considered. The use of R_i = 0.8 results in an interface friction angle of about 38º, which is similar to the measured friction angle between smooth-concrete and sand (Potyondy, 1961; Samtani and Nowatzki, 2006). The numerical modelling showed that for the cases examined with zero-thickness elements, the finite element mesh had a minor effect on the normal and shear stresses at the interface between the soil and facing. However, when using continuum elements both interface normal and shear stresses fluctuated once soil plastic flow occurred for all three meshes. The results also showed that the optimized mesh with the lowest interface continuum element aspect ratio experienced the smallest stress fluctuation amplitudes.

The total horizontal and vertical forces acting at the interface are shown in Tables 7.3 and 7.4, respectively. Both total horizontal and vertical forces using zero-thickness elements are in good agreement with results using continuum elements and the finite element mesh had a minor effect on the total horizontal and vertical forces for both zero-thickness elements and continuum elements.

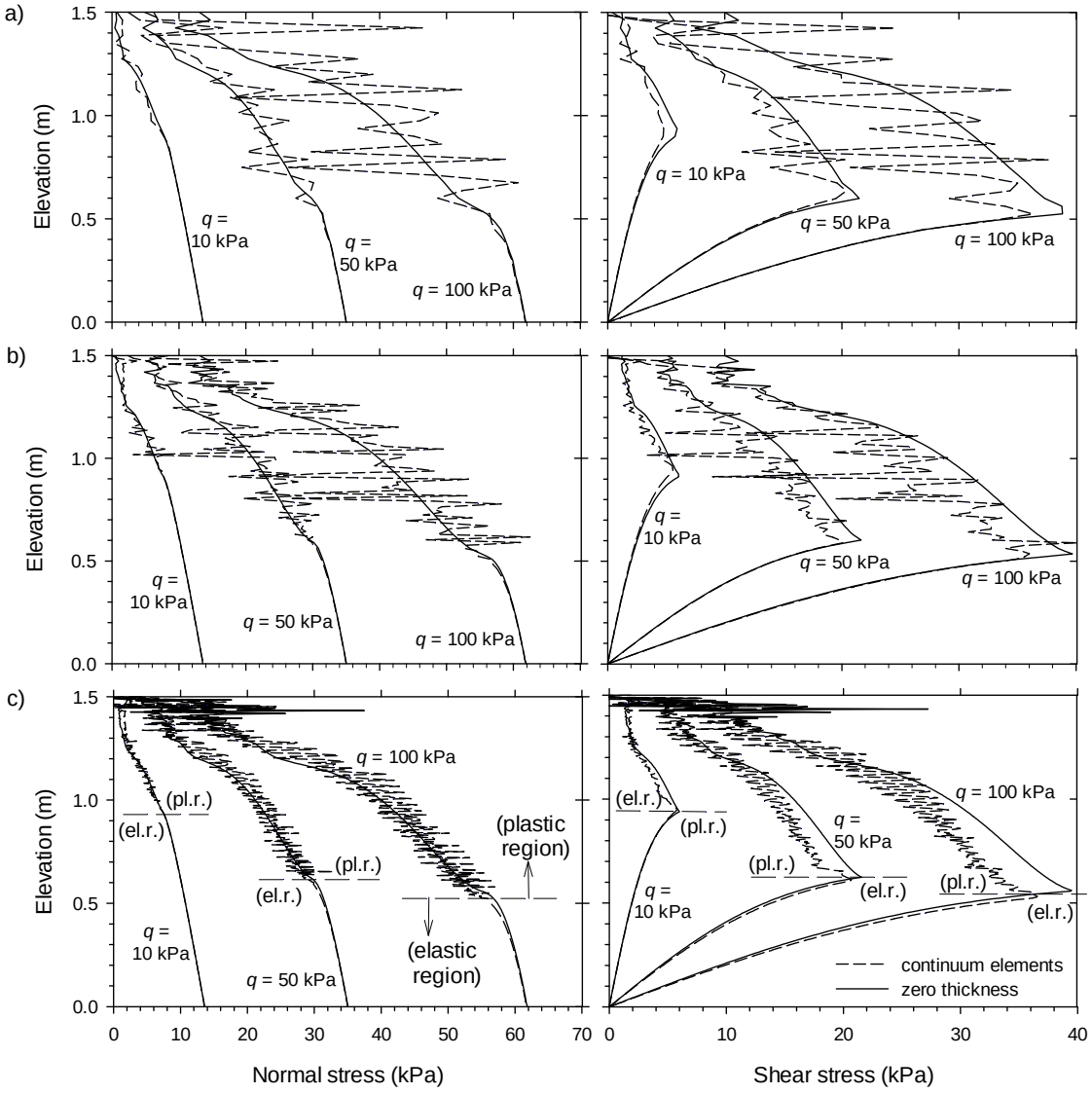

Figure 7.3: PLAXIS load transfer from backfill soil to facing panel: Effect of the finite element mesh on the normal and shear stresses at the interface between the facing structure and backfill soil: coarse mesh (a), fine mesh (b), and optimized mesh (c). Cases with $R_i = 0.8$.

7.3.1.2. Effect of the strength/stiffness reduction factor

Figure 7.4 shows the normal and shear stresses at the interface between the facing structure and backfill soil for the three different strength/stiffness reduction factors investigated. The modelling results showed that for the continuum elements, increasing the strength/stiffness reduction factor (i.e., increasing the interface stiffness) resulted in greater amplitude of both normal and shear stress fluctuations in the plastic region when other conditions were equal. However, as shown in Figure 7.5a, the total vertical loads (i.e., equivalent force from shear stresses) at the interface between the facing and backfill soil from the continuum elements are in good agreement with those from simulations with zero-thickness elements.

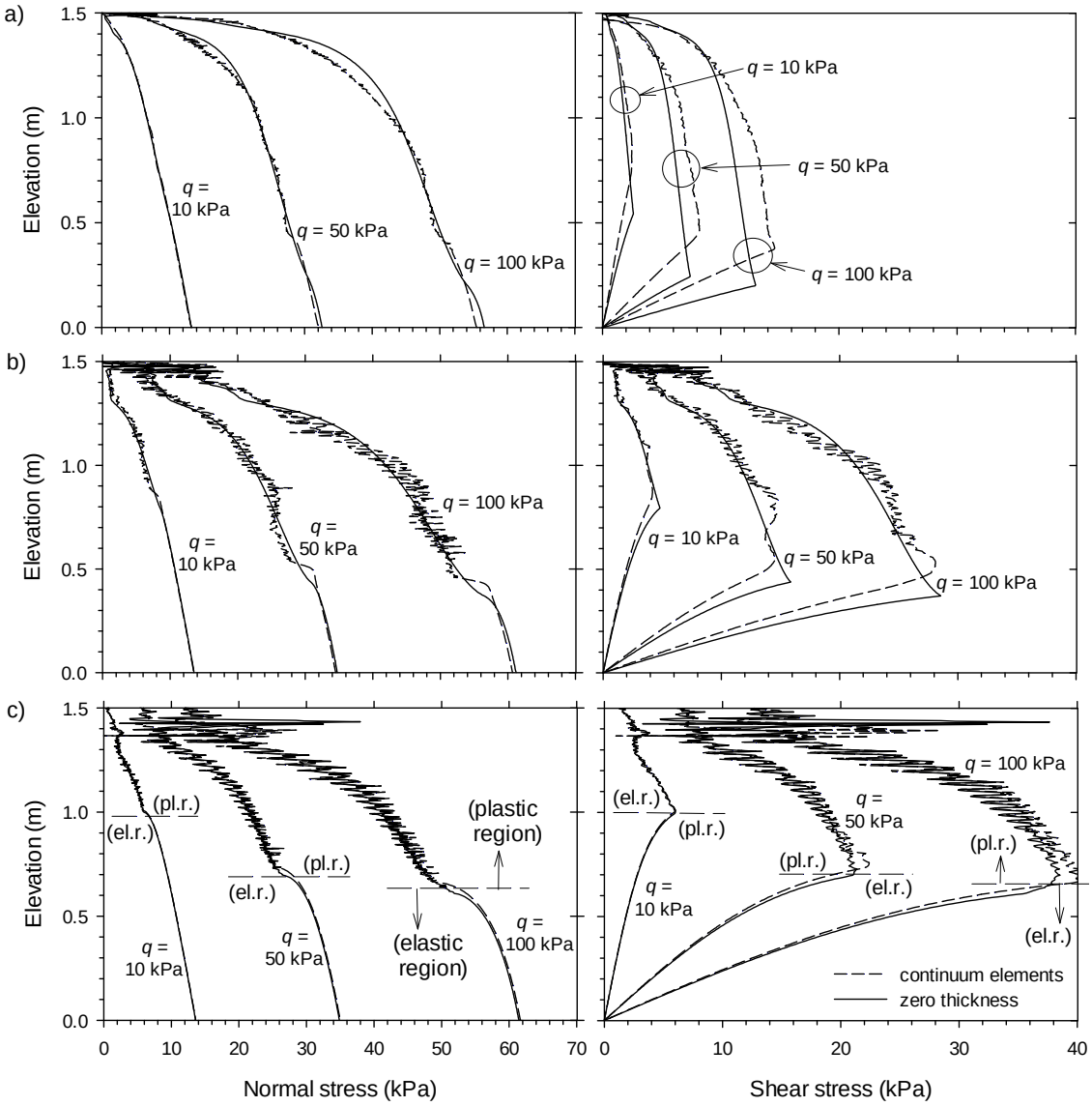

Figure 7.**4**: PLAXIS load transfer from backfill soil to facing panel: Normal and shear stresses at the interface between facing structure and backfill soil with optimized mesh for three different strength/stiffness reduction factors: $R_i = 0.3$ (a), $R_i = 0.6$ (b), and $R_i = 1.0$ (c).

Table 7.3. Total horizontal force (kN/m) from normal stresses at the interface for coarse, fine and optimized meshes with zero-thickness elements and continuum elements for modelling the interface (R_i = 0.8):

Surcharge,	Zero-thickness elements			Continuum elements		
q (kPa)	Coarse	Fine	Optimized	Coarse	Fine	Optimized
10	12.06	12.06	12.08	12.29	12.22	12.11
50	36.11	36.15	35.95	36.31	36.71	36.12
100	66.25	66.19	65.93	67.33	67.20	66.62

Table 7.4. Total vertical force (kN/m) from shear stresses at the interface for coarse, fine and optimized meshes with zero-thickness elements and continuum elements at the interface (R_i=0.8):

Surcharge,	Zero-thickness elements			Continuum elements		
q (kPa)	Coarse	Fine	Optimized	Coarse	Fine	Optimized
10	3.75	3.76	3.74	3.67	3.78	3.69
50	16.66	16.60	16.72	16.25	16.42	15.91
100	32.25	32.15	32.57	31.68	31.65	31.79

7.3.2. Equivalent interface properties between FLAC and PLAXIS

The interface friction angle, cohesion, dilatancy angle, and tensile strength in FLAC are the same as those in PLAXIS and the same parameter values can be set directly in both programs. If the normal stiffness (k_n) and shear stiffness (k_s) from FLAC are known, the equivalent interface properties in PLAXIS can be found using the following equations (Yu et al., 2014 and 2015b):

$$E_{\mathrm{i}} = \frac{\left(3k_{\mathrm{n}} - 4k_{\mathrm{s}}\right)k_{\mathrm{s}}t_{\mathrm{i}}}{k_{\mathrm{n}} - k_{\mathrm{s}}} \tag{7.7}$$

$$v_{\mathrm{i}} = \frac{k_{\mathrm{n}} - 2k_{\mathrm{s}}}{2\left(k_{\mathrm{n}} - k_{\mathrm{s}}\right)} \tag{7.8}$$

$$E_{\mathrm{oed,i}} = k_{\mathrm{n}}t_{\mathrm{i}} \tag{7.9}$$

$$G_{\mathrm{i}} = k_{\mathrm{s}}t_{\mathrm{i}} \tag{7.10}$$

where t_{i} is the virtual thickness of the interface which is related to average element size in PLAXIS (the exact value used during calculation can be found in the Output post-processor program in PLAXIS).

If Young's modulus and Poisson's ratio (or compression modulus and shear modulus) are available from PLAXIS, the following equations can be used to compute the equivalent interface properties in FLAC as:

$$k_{\mathrm{n}} = \frac{E_{\mathrm{i}}\left(1-v_{\mathrm{i}}\right)}{\left(1+v_{\mathrm{i}}\right)\left(1-2v_{\mathrm{i}}\right)t_{\mathrm{i}}} = \frac{E_{\mathrm{oed,i}}}{t_{\mathrm{i}}} \tag{7.11}$$

$$k_{\mathrm{s}} = \frac{E_{\mathrm{i}}}{2\left(1+v_{\mathrm{i}}\right)t_{\mathrm{i}}} = \frac{G_{\mathrm{i}}}{t_{\mathrm{i}}} \tag{7.12}$$

7.3.3. Interface 2D model and properties with FLAC

The interfaces in FLAC can be defined as glued, unglued, or bonded interfaces depending on the application. For the later purpose of comparison with PLAXIS, unglued interfaces (where the slip or/and opening of interfaces is allowed and the plastic shear displacement occurs after the shear stress exceeds a maximum shear strength controlled by the Coulomb shear-strength criterion) are used in this section (Yu et al., 2014 and 2015b). The interface properties are friction angle (φ_i), cohesion (c_i), dilation angle (ψ_i), tensile strength ($\sigma_{t,i}$), normal stiffness (k_n), and shear stiffness (k_s) (Itasca 2011). The interface shear strength is governed by the Coulomb failure criterion. Both soil and interface material properties are in agreement as the ones presented in Tables 7.1 and 7.2. The normal stress and shear stress (τ_s) are calculated based on the interface normal displacement (u_n) and shear displacement (u_s) using the following equations:

$$\sigma_{\mathrm{n}} = k_{\mathrm{n}} u_{\mathrm{n}} \tag{7.13}$$

$$\tau_{\mathrm{s}} = \begin{cases} k_{\mathrm{s}} u_{\mathrm{s}} & k_{\mathrm{s}} u_{\mathrm{s}} \le \tau_{\mathrm{s,max}} \\ \tau_{\mathrm{s,max}} & k_{\mathrm{s}} u_{\mathrm{s}} > \tau_{\mathrm{s,max}} \end{cases} \tag{7.14}$$

Figure 7.5 presents FLAC finite difference meshes considerer: coarse mesh, otherwise, fine mesh, with the same interface thickness of t_i = 0.018 m (same as in previous PLACIS model case also). These two cases were modelled assuming both default interface elements (named springs) or with considering an actual material with t_i = 0.018 m-thickness. The same methodology as explained before was taken into account to transform from non-thickness (spring) interface to 0.018 m-thick continuum interface material.

Results comparing both interface methodology are presented in Figure 7.6, for a strength/stiffness reduction factor R_i = 0.8. Comparison of normal and shear stresses transfer from backfill soil to facing panel at the interface between the facing structure and backfill soil resulted in a small differences between default and reference elements (spring) and continuum material interface trick. Maybe larger differences were obtained with regards to the ones shown in PLAXIS program (Figures 7.3 and 7.4), however, non-fluctuation effect was obtained in FLAC models.

a) Coarse mesh: b) Fine mesh:

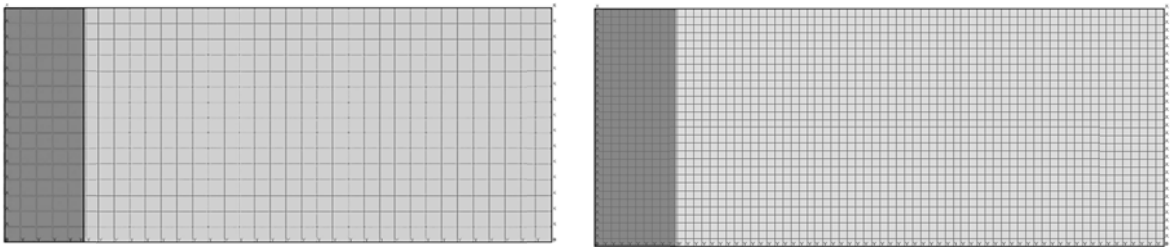

Figure 7.5: FLAC finite difference meshes for the same soil-structure interaction example: coarse mesh (a), and fine mesh (b), with the same interface thickness of $t_i = 0.018$ m.

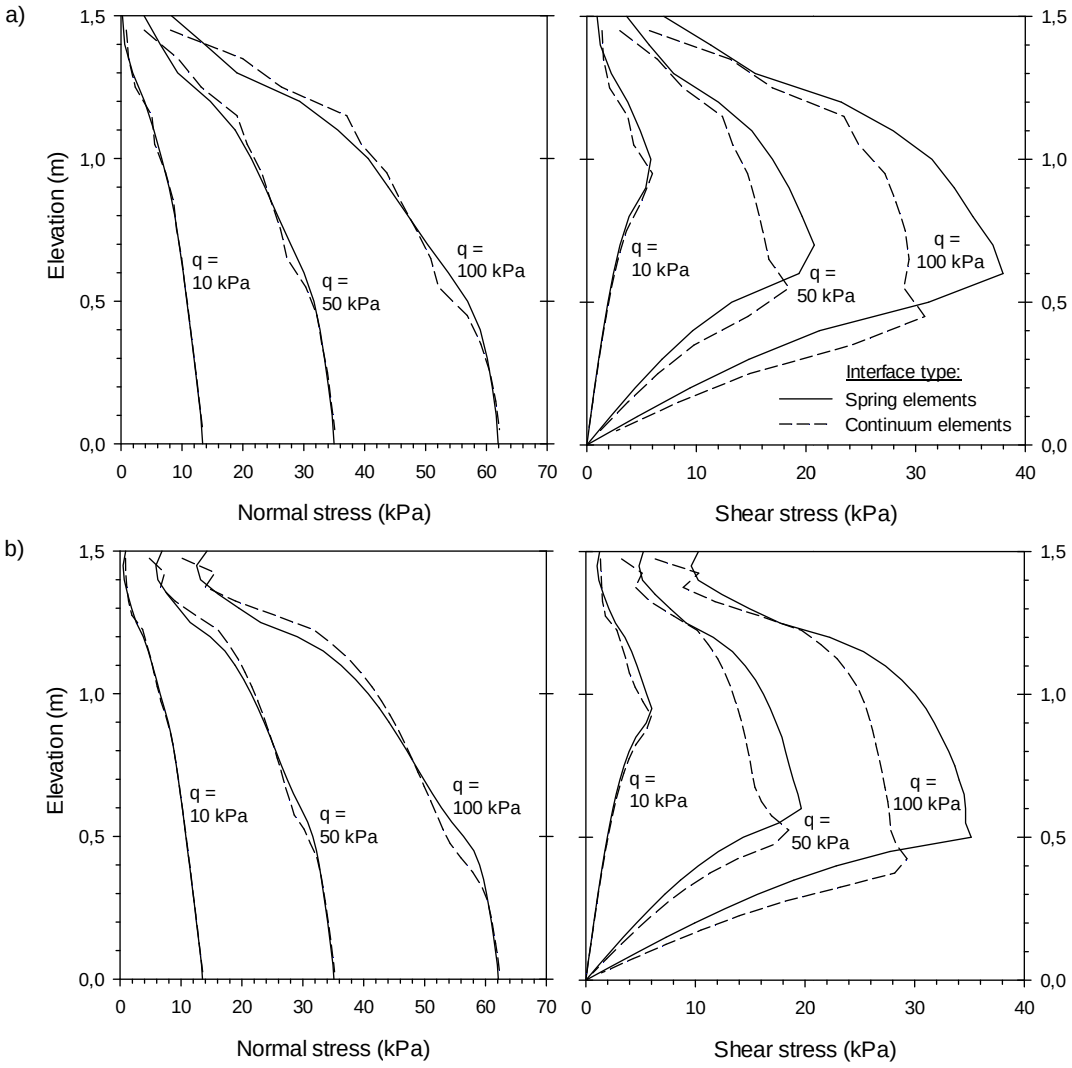

Figure 7.6: FLAC coarse mesh (a) and fine mesh (b) comparison to load transfer from backfill soil to facing panel: Normal and shear stresses at the interface between the facing structure and backfill soil for a strength/stiffness reduction factor $R_i = 0.8$.

Figure 7.7 presents the same previous results but grouping by interface element type, so comparison between the meshing size can be directly deduced. As it can be observed, not much differences were obtained between coarse and fine mesh cases.

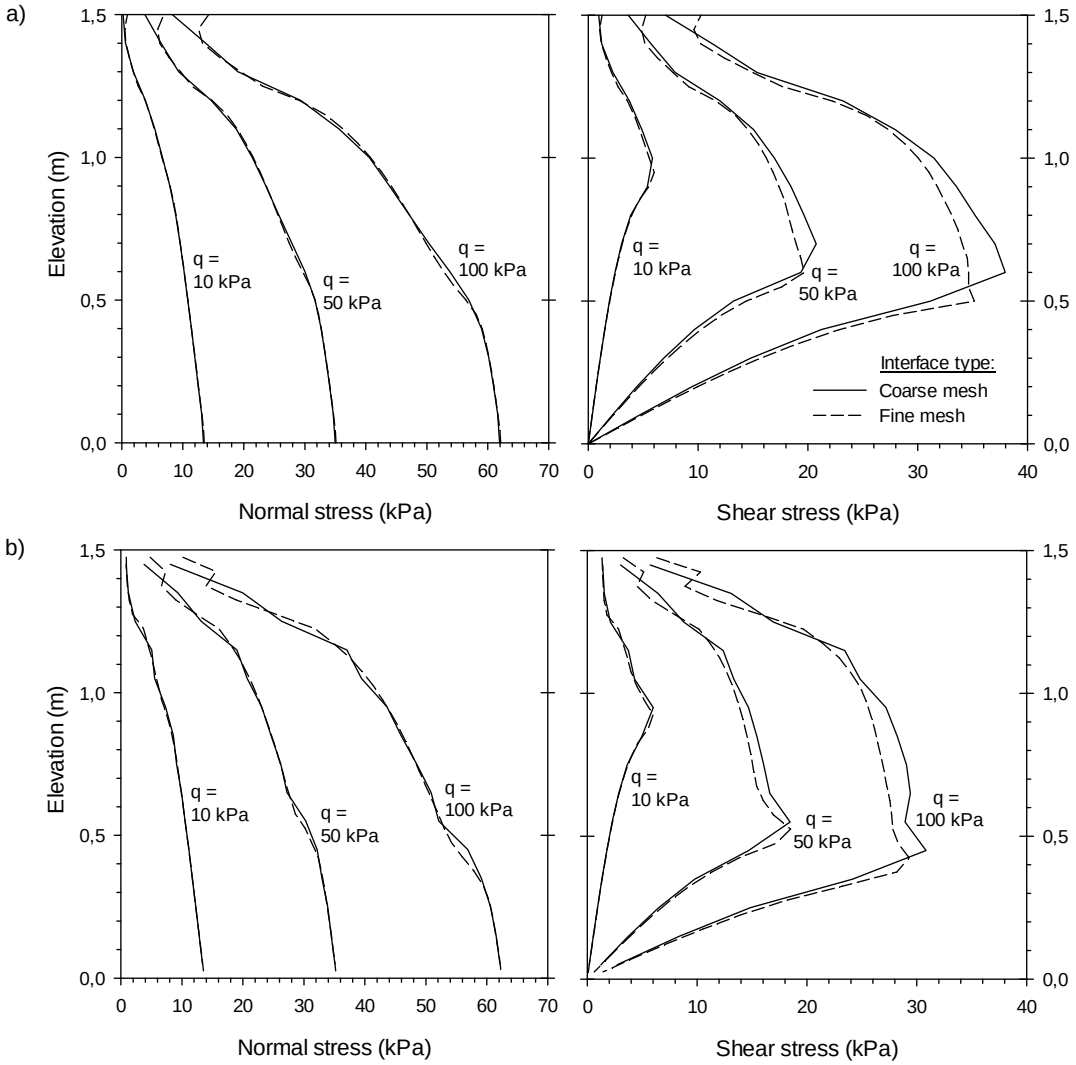

Figure 7.7: FLAC spring (a) and continuum (b) interface elements with coarse mesh and fine mesh comparison to load transfer from backfill soil to facing panel: Normal and shear stresses at the interface between the facing structure and backfill soil for a strength/stiffness reduction factor $R_i = 0.8$.

Figure 7.8 presents FLAC spring and continuum elements interface comparison to load transfer from backfill soil to facing panel for two different strength/stiffness reduction factors: $R_i = 0.3$ (a), and $R_i = 1.0$ (b). As it can be observed, non-fluctuation was obtained even for rigid interface case (worst fluctuation case in PLAXIS comparison).

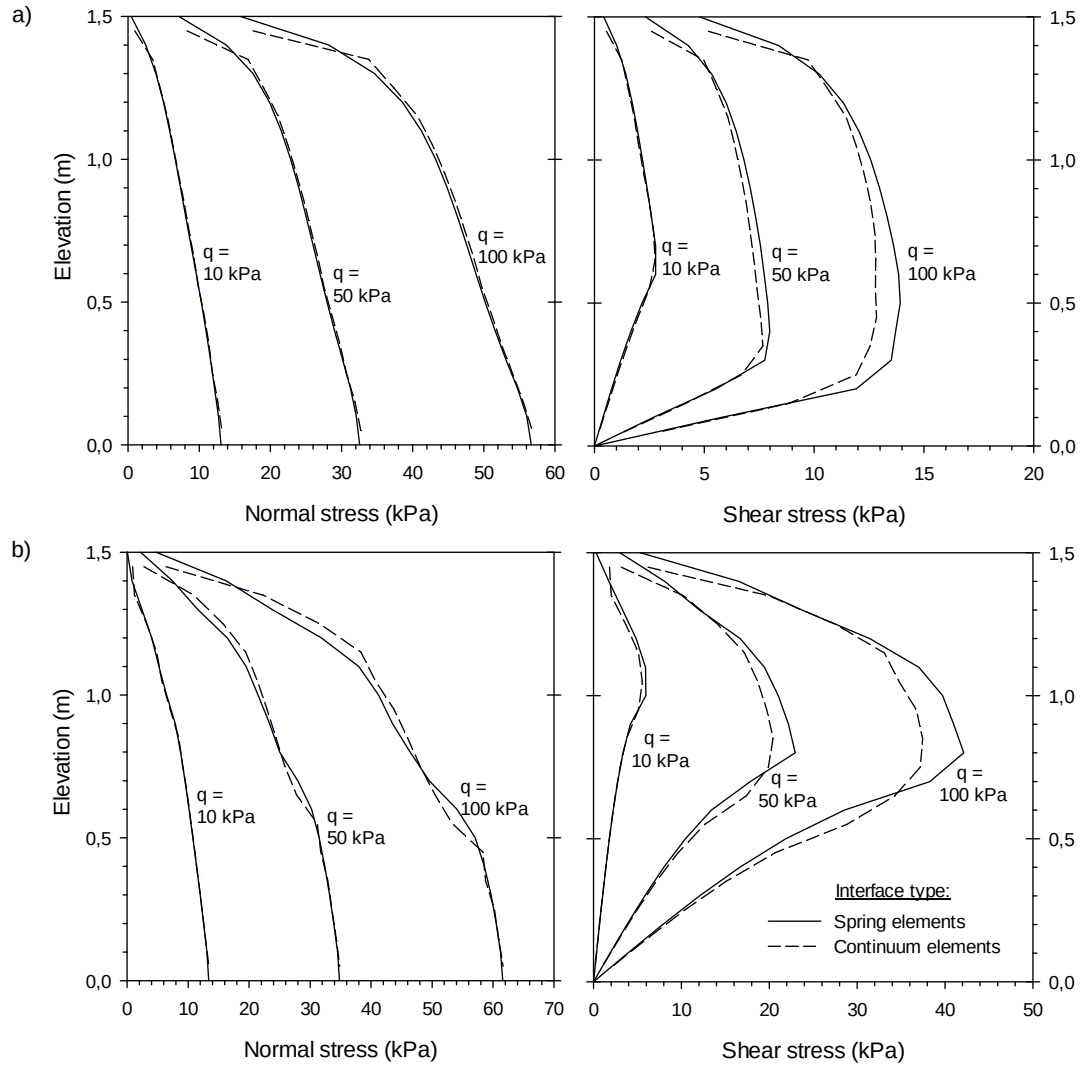

Figure 7.8: FLAC spring and continuum elements interface comparison to load transfer from backfill soil to facing panel: Normal and shear stresses at the interface between facing structure and backfill soil with fine mesh for two different strength/stiffness reduction factors: R_i = 0.3 (a), and R_i = 1.0 (b).

As commented, to next FLAC-PLAXIS comparison purposes, unglued interfaces were assumed, where the slip or/and opening behaviour of interfaces is allowed and the plastic shear displacement occurs after the shear stress exceeds a maximum shear strength controlled by the Coulomb shear-strength criterion. This is also compatible with the further continuum material interface modelling using CODE_BRIGHT FEM program (both 2D and 3D interface modelling).

7.3.4. Interface 2D model and properties with CODE_BRIGHT

7.3.4.1. Problem definition: Soil material modelling features

Continuum elements interface were considered in CODE_BRIGHT to simulate the soil-facing interaction with 18 mm-thick real zone was modelled. As in previous cases, the structure (facing concrete panel) was modelled as linear elastic with elastic modulus of 32 GPa, Poisson's ratio of 0.15 and a unit weight of 25 kN/m^3. Soil material was modelled with Drucker-Prager failure criterion (i.e., circular cone in the principal stress space). In the program, the soil friction angle (ϕ) is defined with the critical state slope M-line in order to obtain correct shear strength. In case of assuming the Mohr-Coulomb failure criteria circumscribing the Drucker-Prager failure criteria (see Figure 7.9), strength is then defined as:

$$M = \frac{6\sin\phi}{3-\sin\phi} \quad \text{(triaxial compression state)} \tag{7.15}$$

which relates to triaxial compression behaviour of material, $M_{compression}$, i.e., $\sigma_1 > \sigma_2 = \sigma_3$, where σ_1, σ_2, and σ_3 are the main stress states: σ_1 (major stress) $\geq \sigma_2 \geq \sigma_3$ (minor stress)). In the other hand, in case of assuming Drucker-Prager circle failure criteria to be inscribed within the Mohr-Coulomb failure criteria (see Figure 7.9), the strength is defined as:

$$M = \frac{6\sin\phi}{3+\sin\phi} \quad \text{(triaxial extension state)} \tag{7.16}$$

which relates to triaxial extension behaviour of material, $M_{extension}$, i.e., $\sigma_1 = \sigma_2 > \sigma_3$. Thus, the stress states with regards to Mohr-Coulomb failure criteria can be defined as with the M-parameter assuming a proper compression otherwise extension state.

As noticed, proper material constitutive modelling assuming M-values requires to previously determine the material state in terms of intermedia main stress scenario (i.e., $\sigma_2 = \sigma_3$ in compression, otherwise extension if $\sigma_2 = \sigma_1$). In common scenarios and in the ones assumed in current study, compression state corresponds to the better suitability case. Thus, soil model properties are the ones as already presented in Table 7.1, with proper fixing the $M_{compression}$ parameter value: $M_{compression} = 1.808$.

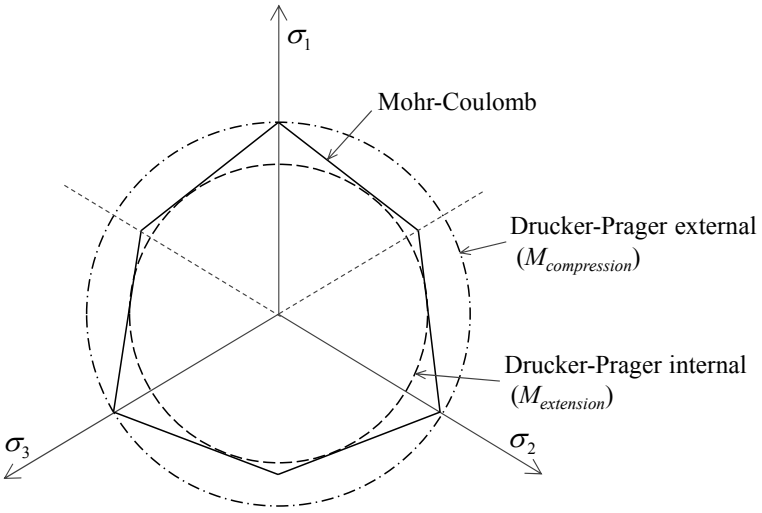

Figure 7.9: Mohr-Coulomb and Drucker-Prager yielding criteria surfaces.

Interface material demonstrated to be best fitted within compression and extension states. Table 7.5 show same parameters as in previous Table 7.2 but including *M*-values for compression, extension, and intermedia ($M_{average}$) case states. Despite results demonstrated interface material *M*-value to be actually within compression and extension values, default $M_{compression}$ values were assumed to develop soil-facing interaction in this chapter.

Table 7.5. Interface properties (related to E_{soil} = 5 MPa):

Parameters	Strength/stiffness reduction factor, R_i					Units
	0.3	0.45	0.6	0.8	1.0	
Cohesion, c_i	0.3	0.45	0.6	0.8	1.0	kPa
Friction angle, ϕ_i	16.2	23.5	30.1	37.7	44.0	degrees
$M_{compression}$	0.613	0.919	1.204	1.536	1.808	-
$M_{extension}$	0.509	0.704	0.859	1.016	1.128	-
$M_{average}$	0.561	0.811	1.031	1.276	1.468	-
Shear modulus, G_i	0.17	0.39	0.69	1.23	1.92	MPa
Elastic modulus, E_i	0.50	1.13	2.01	3.57	5.00	MPa

7.3.4.2. Effect of the mesh size and elements type

Four different finite element 2D meshes were generated in CODE_BRIGHT: unstructured or irregular (but optimized) mesh with linear-triangular elements (Figure 7.10a), linear-triangular structured-mesh (Figure 7.10b), bilinear-quadrilateral structured-fine-mesh (Figure 7.10c), and bilinear-quadrilateral structured-coarse-mesh (Figure 7.10d). With these elements it was possible to examine the effect of element size at the interface zone on the load transfer between the soil and facing structure.

Among these three meshes, the irregular mesh presented in Figure 7.10a had the highest element aspect ratio far from the analyzed soil-structure zone, but the optimized shape becomes to a finer aspect ratio in interface zone. Structured fine mesh presented in Figure 7.10b has fine definition in all regions. However, triangular linear elements with analytical integration may not be the best ones because the simple linear interpolation definition of this element type. This type of elements could not work very well when shear strains occur with limitations on volumetric strains development. As noticed, Figure 7.10b and 710c have same number of nodes even triangular has double number of elements. However, both Figures 7.10c and 710d are quadrilateral structured elements, which imply bilinear interpolation and numerical integration with quadrature of 4 Gauss points and are probably better to perform soil-structure interactions for regular shear strains scenarios (despite the larger computational efforts required).

a) 583 triangular elements (320 nodes):

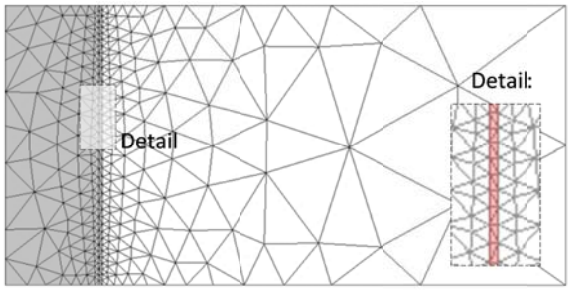

b) 9150 triangular elements (4712 nodes):

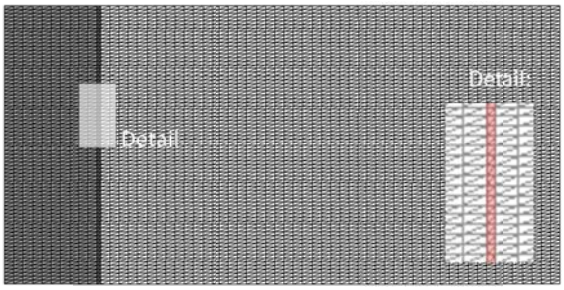

c) 4575 quadrilateral elem. (4712 nodes):

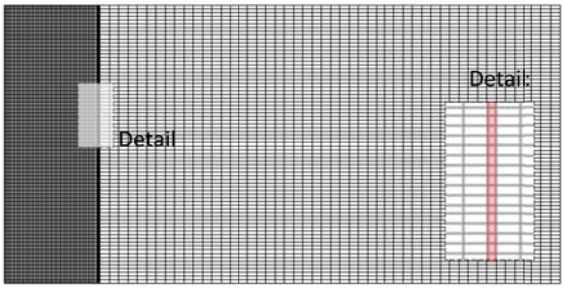

d) 390 quadrilateral elements (432 nodes):

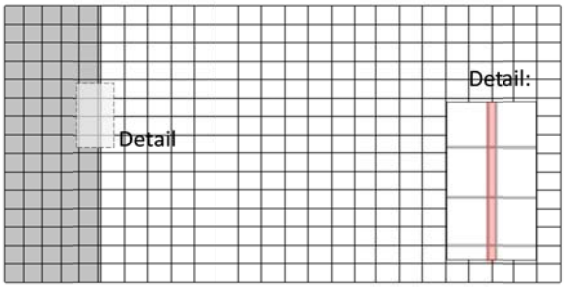

Figure 7.10: Three different finite element meshes for the same soil-structure interaction example in CODE_BRIGHT, with the same interface virtual thickness of t_i = 18 mm: unstructured mesh with linear-triangular elements (a), linear-triangular structured-mesh (b), bilinear-quadrilateral structured-fine-mesh (c), and bilinear-quadrilateral structured-coarse-mesh (d).

Settlement resulting under q = 100 kPa-surcharge for the different meshes previously presented are shown in Figure 7.11 (R_i = 0.8). As observed, despite the different meshing element types, well agreement was obtained between four alternatives and all of them, with a maximum settlement value of 2.33 cm in triangular linear elements (both optimized and fine mesh cases), and 2.32 cm in quadrilateral bilinear elements.

Figure 7.12 presents the total shear strains evolution under q = 50 kPa and 100 kPa surcharges (R_i = 0.8). Because results are scaled from 100 kPa surcharge in each meshing case, similar colour distribution is obtained between meshing type with the exception of the quadrilateral coarse mesh (greater zone affected due to elements size). However, despite the similar responses in soil settlement regarding the different mesh types used (Figure 7.11), a strains difference from about 13% in structured triangle mesh up to 19% in structured quadrilateral fine mesh were obtained.

Results about load transfer from backfill soil to facing panel are plotted in Figure 7.13 for two cases of interface strength/stiffness reduction factors (R_i = 0.8 and R_i = 0.3). Despite variations noticed in previous results, triangular structured mesh improves results with avoiding the fluctuation trends obtained in both normal and shear stress results when unstructured (but optimized) mesh are considered. In quadrilateral elements case, small differences were obtained between meshing size. As observed, these differences were even smaller when softer (and weaker) interface reduction factor was considered.

a) 583 triangular elements (320 nodes):

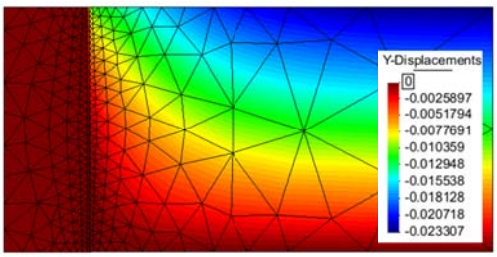

b) 9150 triangular elements (4712 nodes):

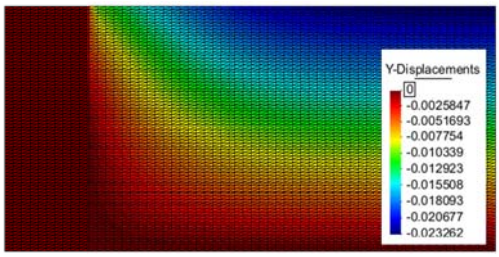

c) 4575 quadrilateral elem. (4712 nodes):

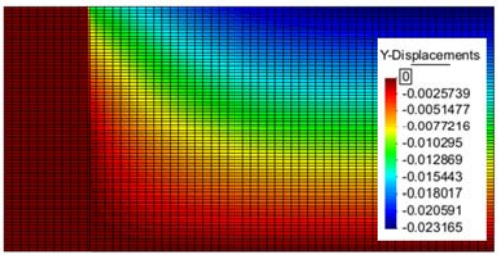

d) 390 quadrilateral elements (432 nodes):

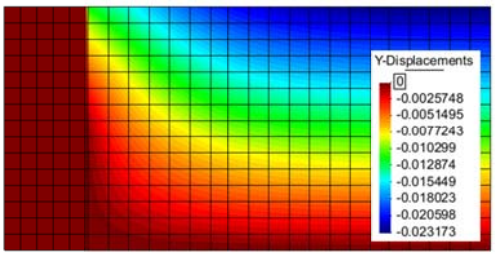

Figure 7.11: CODE_BRIGHT settlements (m) under q = 100 kPa-surcharge for the different meshes assumed: unstructured mesh with triangular elements (a), triangular structured-mesh (b), quadrilateral structured-fine-mesh (c), and quadrilateral structured-coarse-mesh (d). Cases with t_i = 0.018m and R_i = 0.8.

a) Unstructured-Triangle/irregular mesh:

q = 50 kPa *q* = 100 kPa

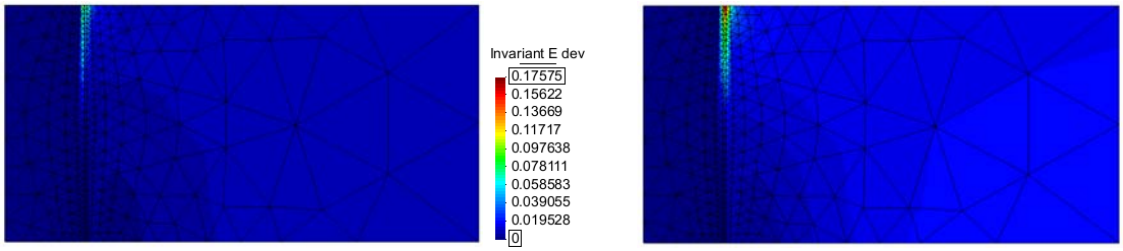

b) Structured-Triangle/fine mesh:

q = 50 kPa *q* = 100 kPa

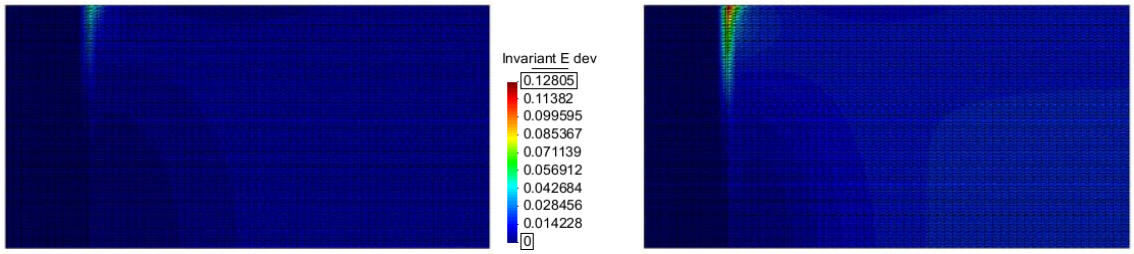

c) Structured-Quadrilateral/fine mesh:

q = 50 kPa *q* = 100 kPa

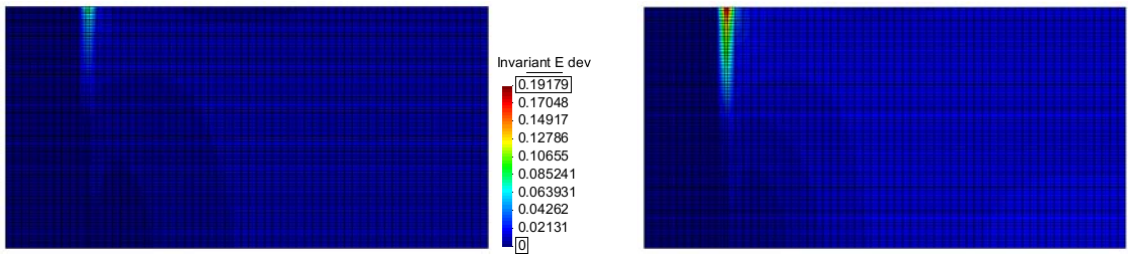

d) Structured-Quadrilateral/coarse mesh:

q = 50 kPa *q* = 100 kPa

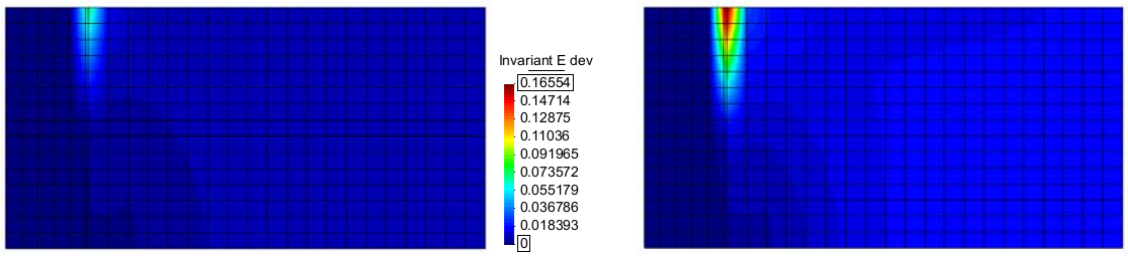

Figure 7.12: CODE_BRIGHT total shear strains evolution (q =50 kPa and 100 kPa) results for the different meshes assumed: unstructured mesh with triangles (a), triangular structured-mesh (b), quadrilateral structured-fine-mesh (c), and quadrilateral structured-coarse-mesh (d). Cases with t_i = 0.018m and R_i = 0.8.

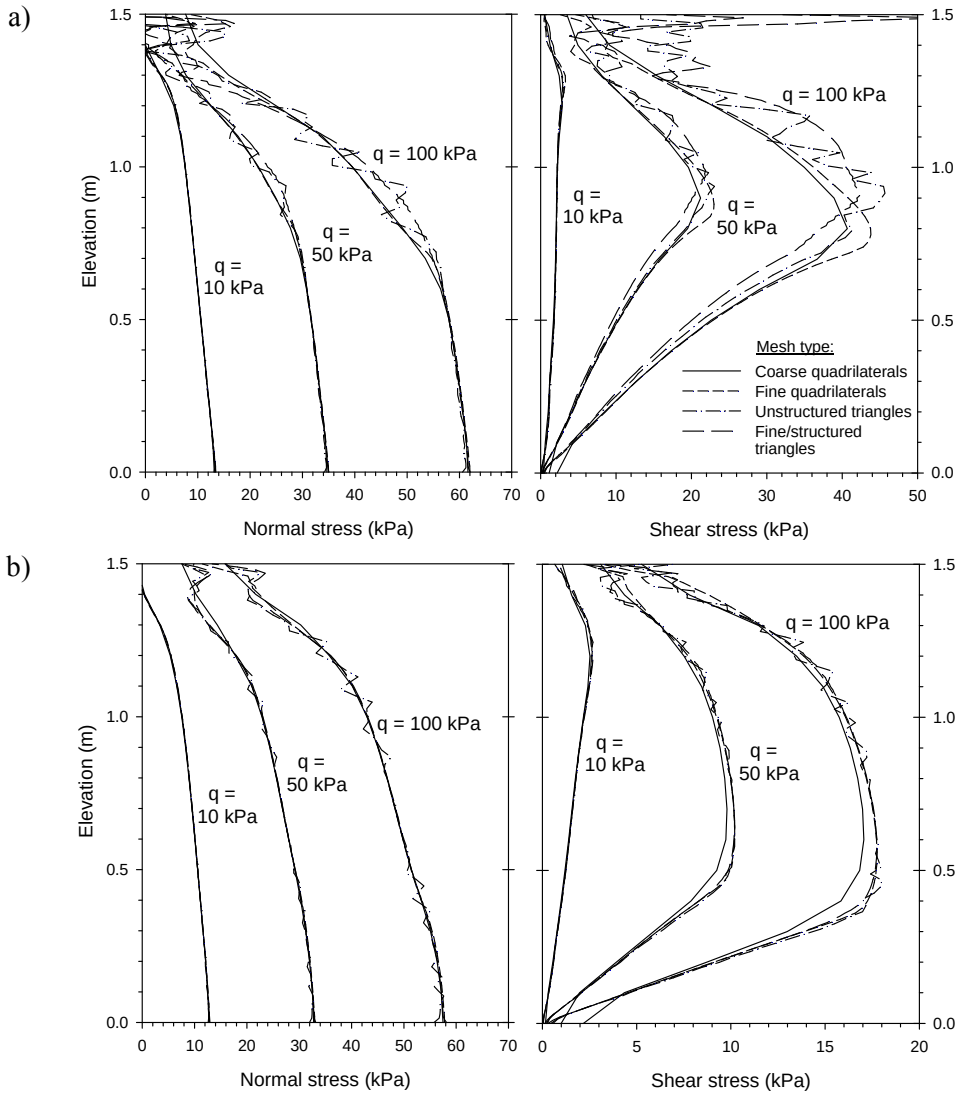

Figure 7.13: CODE_BRIGHT load transfer from backfill soil to facing panel: Normal and shear stresses at x = 0.509 m cross-section (i.e., at middle of the interface media; t_i = 0.018 m) with regards to the mesh type (unstructured or structured triangular, otherwise coarse or fine quadrilateral). Cases with: R_i = 0.8 (a), and R_i = 0.3 (b).

Figure 7.14 presents the normal and shear load transfer from backfill soil to facing panel with regards to the critical state slope M-parameter defining interface strength (see explanation in Section 7.3.2.1). Different results were obtained due to the M-value selected, regarding to the related triaxial state. As observed, triaxial compression and extension state trends (i.e., $M_{compression}$ and $M_{extension}$) generate a region of possible results. Differences between both compression and extension states are, however, not dramatic (e.g., similar differences were obtained in FLAC results with regards to interface definition by springs or continuum material; see Figure 7.6). Results from an average value of M are also plotted ($M_{average}$) falling between both boundary triaxial states. The comparison results obtained between both

compression and extension triaxial states for the CODE_BRIGHT continuum interface modelling, and the continuum interface modelling by PLAXIS and FLAC is presented in Figure 7.15 (R_i = 0.8 and R_i = 0.3 cases). Despite the fluctuations from PLAXIS model response, quite well approach was obtained between FLAC and PLAXIS modelling (Yu et al., 2014 and 2015b). With regards to CODE_BRIGHT comparison response, as shown, PLAXIS and FLAC results were approximately well defined within the region ranged by compression and extension triaxial *M*-values response. As commented, even maybe a proper interface is fitted by the average *M*-value, the $M_{compresion}$ was assumed to be the default value for the remaining interface behavior response analyses in this current Chapter.

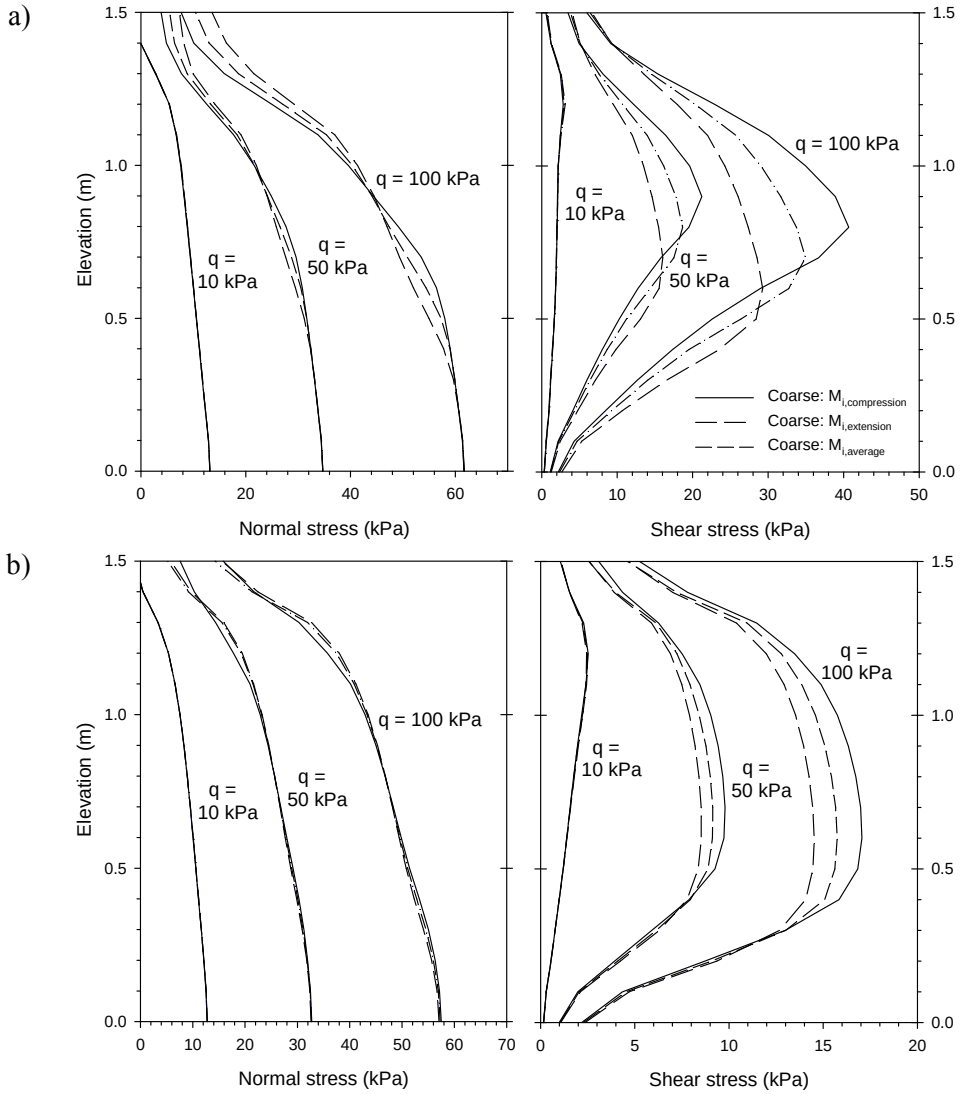

Figure 7.14: CODE_BRIGHT load transfer from backfill soil to facing panel: Normal and shear stresses with regards to the M_i-parameter ($M_{compression}$ –default assumed case– compared to $M_{extension}$ and $M_{average}$). Cases with: R_i = 0.8 (a), and R_i = 0.3 (b).

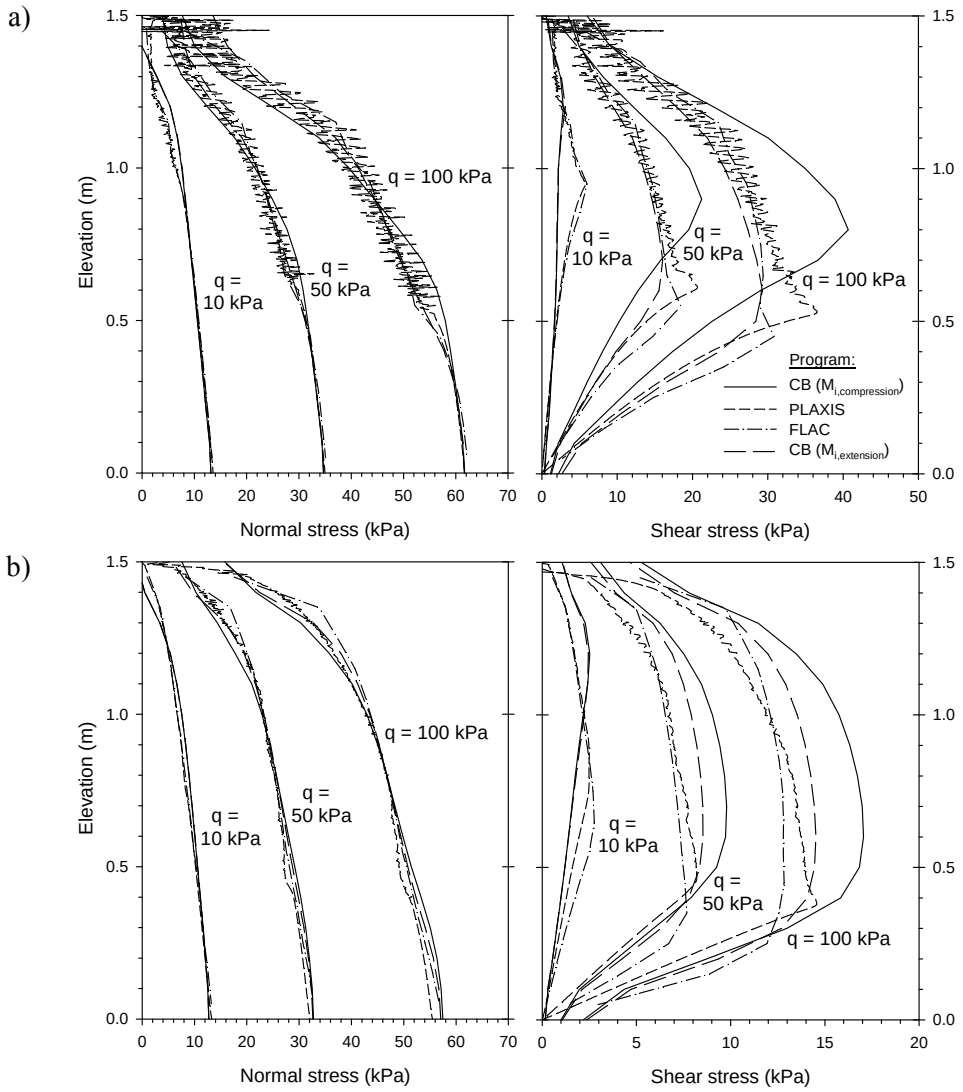

Figure 7.15: Load transfer from backfill soil to facing panel: Normal and shear stresses comparison with regards to PLAXIS (continuum elements interface; optimized mesh), FLAC (continuum elements interface; coarse mesh), and CODE_BRIGHT (both M_i-compression and M_i-extension scenarios performed). Cases with $R_i = 0.8$ (a), and $R_i = 0.3$ (b).

7.3.4.3. Effect of the strength/stiffness reduction factor

Complementary to Figure 7.12, Figure 7.16 shows the normal and shear stresses at the interface between the facing structure and backfill soil for other three different strength/stiffness reduction factors investigated in CODE_BRIGHT modelling with using quadrilateral coarse mesh elements (mesh case shown in Figure 7.10d). As previously deduced, the modelling results showed that the increasing of the strength/stiffness reduction factor R_i (i.e., increasing the interface stiffness) resulted in a consequent smaller shear strains and relative displacements affected region: from about 13% in rigid interface to 22% in R_i =

0.3 case. Note that, despite the maximum displacement reached is obviously similar in right boundary contour (free displacement condition), the displacement distribution significantly change though the soil-panel interaction between the three strength/stiffness interaction factors analyzed.

Results about the normal and shear stresses transfer from backfill soil to facing panel due the interface strength/stiffness reduction factor under 100 kPa and 50 kPa-surcharge loading are analyzed in Figure 7.17. As observed, despite the stress magnitude was logically different between *q*-loading cases analyzed, very similar trending shapes were obtained. Significant variations were obtained with regards to the R_i-values considered, with a consequent variation of the affected plastic zone (i.e., peak shear stress value location).

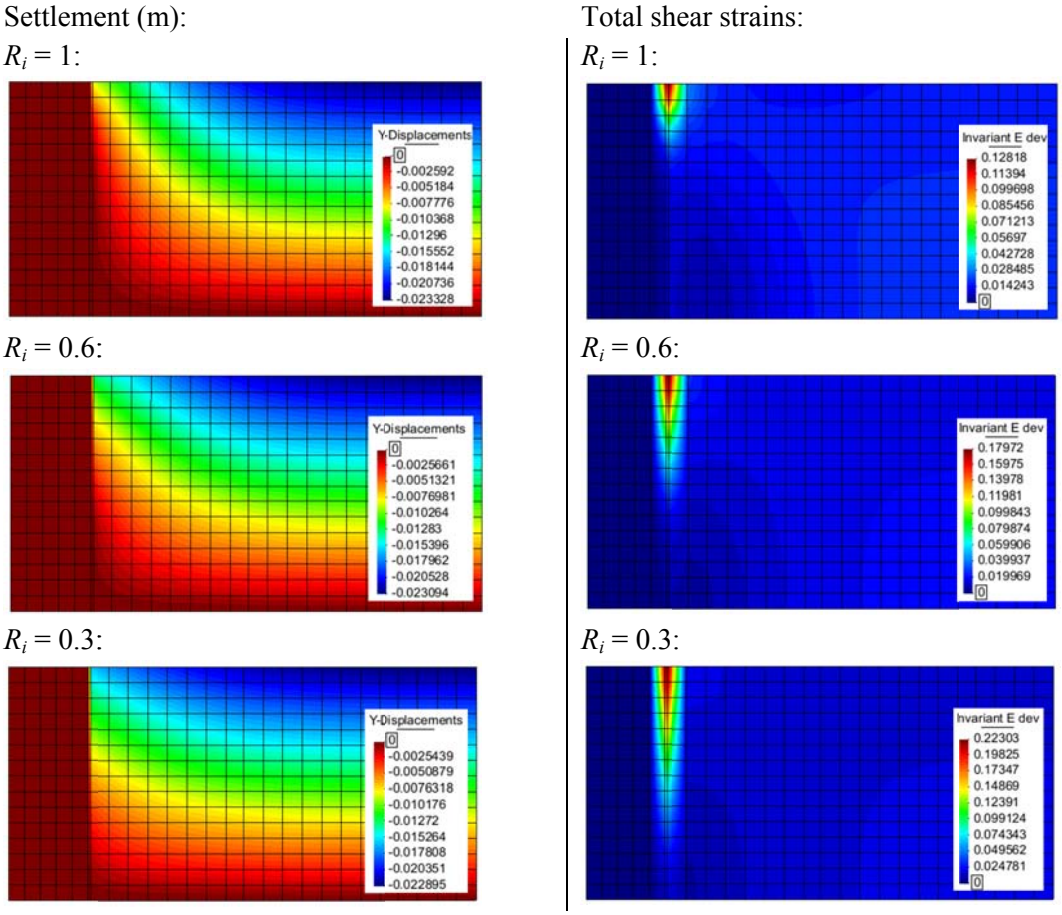

Figure 7.16: CODE_BRIGHT settlement and total shear strains evolution obtained at q = 100 kPa-surcharge for different strength/stiffness interaction factors.

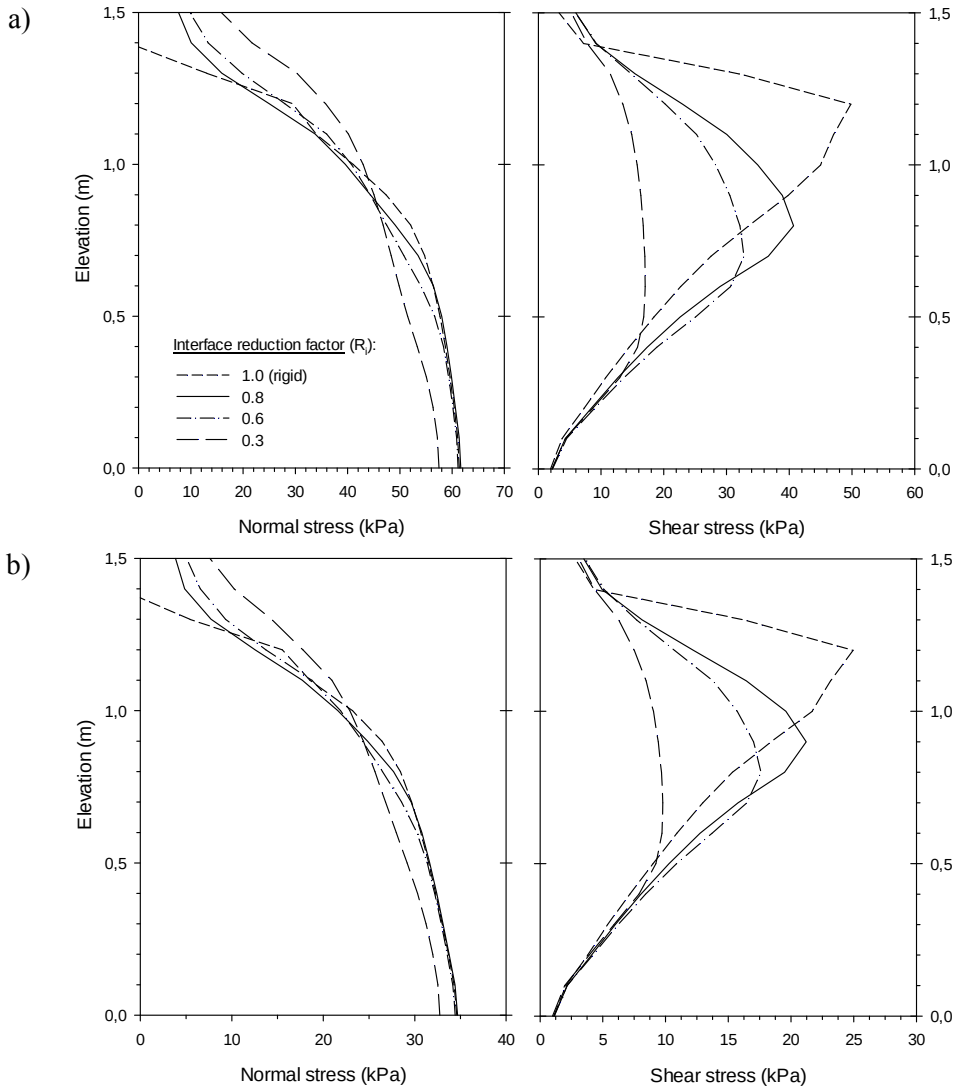

Figure 7.17: CODE_BRIGHT load transfer from backfill soil to facing panel: Normal and shear stresses comparison with regards to interface strength/stiffness reduction factor (R_i-values). Cases with q = 100 kPa (a), and 50 kPa (b).

7.3.4.4. Effect of the interface thickness

Modelling of an 18 mm-thick (t_i) interface zone between dissimilar materials in full-height earth retaining walls using continuum elements can be problematic due to the large difference in shape and size geometry between the different components within the retaining wall. Thus, it should be desirable to increase the interface thickness while keeping the same normal and shear stresses transferred between the soil and structures.

In this section two complementary interface thicknesses of t_i^* = 50 and 100 mm were examined using quadrilateral structured-coarse mesh case (Figure 7.18, which correspond to

complementary cases from Figure 7.10b – t_i = 18 mm-thick case). To keep the same interface stiffness, the new shear modulus (G_i^*) of the interface was calculated as:

$$G_i^* = \left(G_i / t_i\right) t_i^* \tag{7.17}$$

where: the Poisson's ratio results equal between both interface thickness cases (i.e., $v_i^* = v_i$ = 0.45), and the new oedometer modulus ($E_{oed,i}^*$) and elastic modulus (E_i^*) can be calculated from already explained Equations 7.5 and 7.6, respectively, with the new shear modulus (G_i^*) and Poisson's ratio (v_i^* = 0.45). Table 7.6 presents the equivalent interface properties for the case studies assumed with regards to the additional interface thickness cases examined (as commented, t_i^* = 50 and 100 mm).

a) t_i = 0.05 m: b) t_i = 0.10 m:

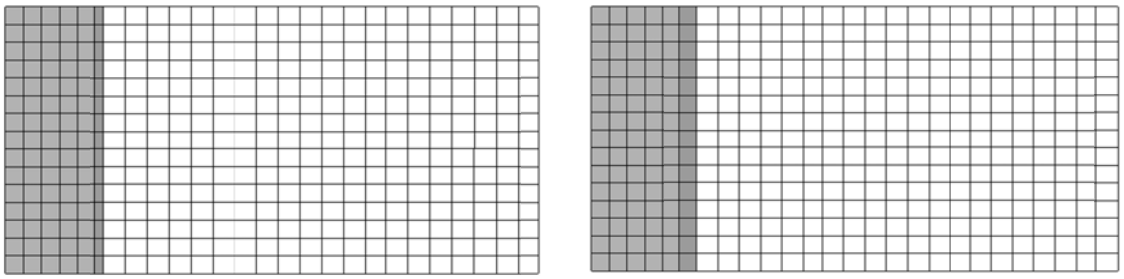

Figure 7.18: Two different interface thicknesses in quadrilateral structured-coarse mesh case: t_i = 0.05 m (a), and t_i = 0.10 m (b).

Table 7.6. Stiffness interface properties for t_i = 0.018 m (previous analyzed cases), t_i = 0.05 m and t_i = 0.10 m, related to E_{soil} = 5 MPa:

Parameters		t_i = 0.018 m		t_i = 0.05 m		t_i = 0.10 m		Units
	(R_i):	0.3	0.8	0.3	0.8	0.3	0.8	
Shear modulus, G_i^*		0.17	1.23	0.48	3.42	0.96	6.84	MPa
Elastic modulus, E_i^*		0.50	3.57	1.39	9.92	2.79	19.83	MPa

The obtained settlements and shear strains (deviatoric invariant) evolution results for both interface thicknesses assumed (t_i = 0.05 m and t_i = 0.10 m) are presented in Figure 7.19 (case with R_i = 0.8) and Figure 7.20 (R_i = 0.3). As shown, very similar response was obtained between the three interface thickness cases (ti = 18 mm case results already presented in previous Figures 7.11d, 7.12d for R_i = 0.8, and Figure 7.16 for R_i = 0.3) under q = 50 kPa and 100 kPa-surcharge scenarios. As shown in previous cases, the reduction of the interface strength/stiffness interaction factor implies an increase of the affected shear strains localization zone.

a) t_i = 0.05 m:
Settlement (m)

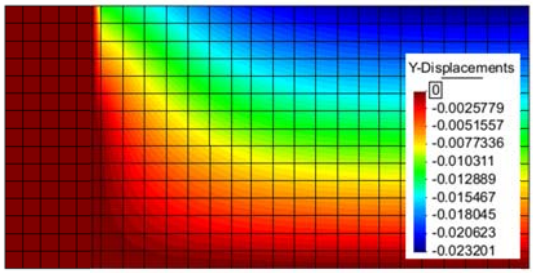

b) t_i = 0.10 m:
Settlement (m)

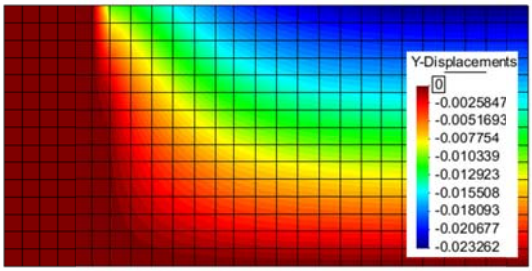

Deviatoric invariant (-):
q = 50 kPa

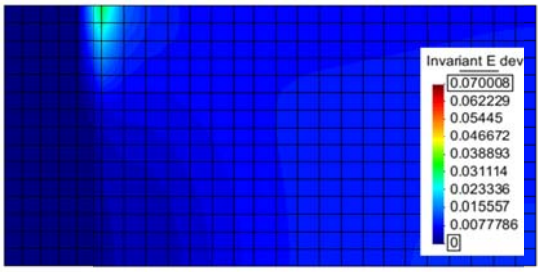

Deviatoric invariant (-):
q = 50 kPa

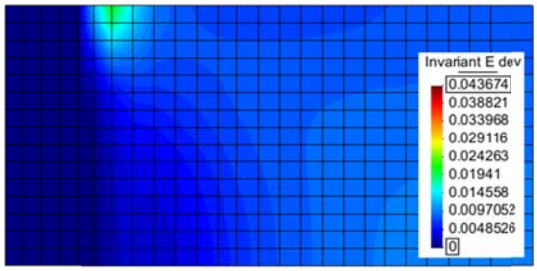

q = 100 kPa

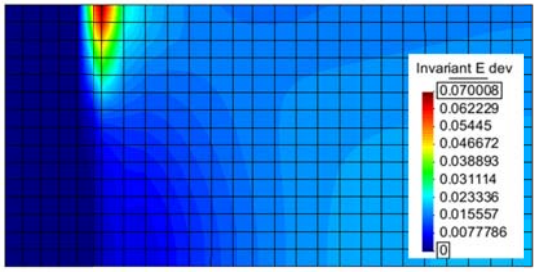

q = 100 kPa

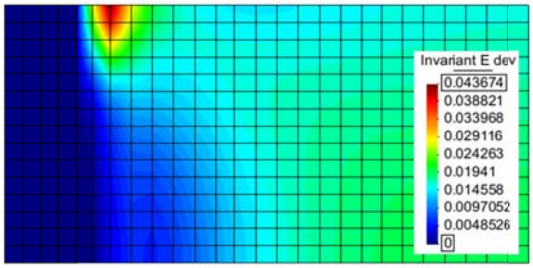

Figure 7.19: Settlement (q = 100 kPa-surcharge) and total shear strains evolution results for interface thickness t_i = 0.05 m (a) and t_i = 0.10 m (b) continuum element interface thicknesses. R_i = 0.8.

Normal and shear stresses transfer from backfill soil to facing panel results are presented in Figure 7.21, comparing the three interface thickness cases under q = 10 kPa, 50 kPa and 100 kPa-surcharge cases, and R_i = 0.8 and R_i = 0.3 interface strength/stiffness interaction cases. Results were obtained from a cross section location at 9 mm-distance from facing panel (i.e., at x = 0.509 m-distance from left boundary), which corresponds to line located within the t_i = 18 mm interface thickness case. As shown, very similar response was obtained between the three interface thickness cases.

a) t_i = 0.05 m:
Settlement (m)

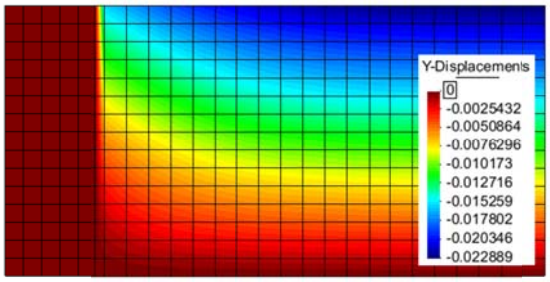

b) t_i = 0.10 m:
Settlement (m)

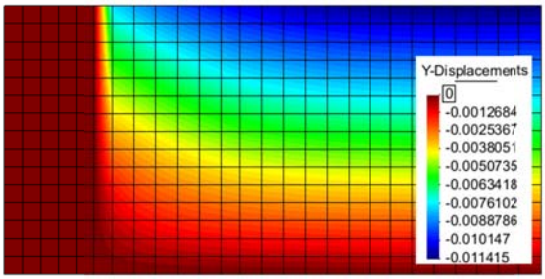

Deviatoric invariant (-):
q = 50 kPa

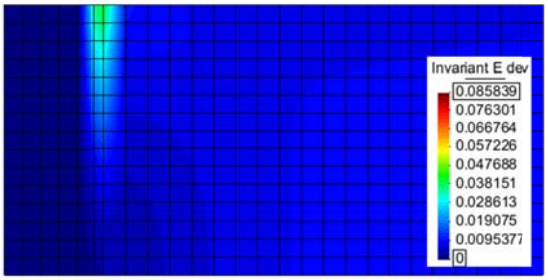

Deviatoric invariant (-):
q = 50 kPa

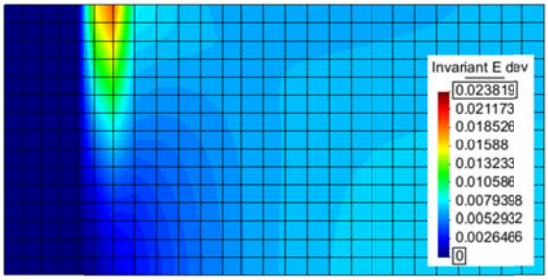

q = 100 kPa

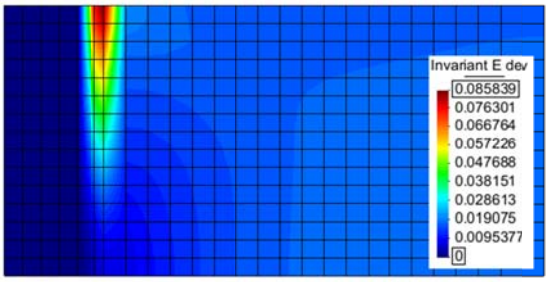

q = 100 kPa

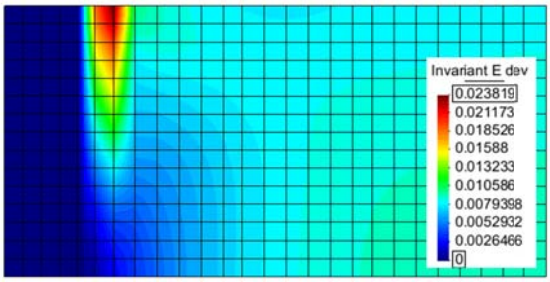

Figure 7.20: Settlement (q = 100 kPa-surcharge) and total shear strains evolution results for interface thickness t_i = 0.05 m (a) and t_i = 0.10 m (b). R_i = 0.3.

Additionally to Figure 7.21 results, Figure 7.22 presents the same results but with locating the cross-section in the middle of each interface thickness: at 9 mm-distance in t_i = 18 mm-thick case, at 25 mm-distance in t_i = 50 mm-thick case, and at 50 mm-distance in t_i = 100 mm-thick case. As shown, practically no differences were obtained in comparison to the previous fixed cross-section location.

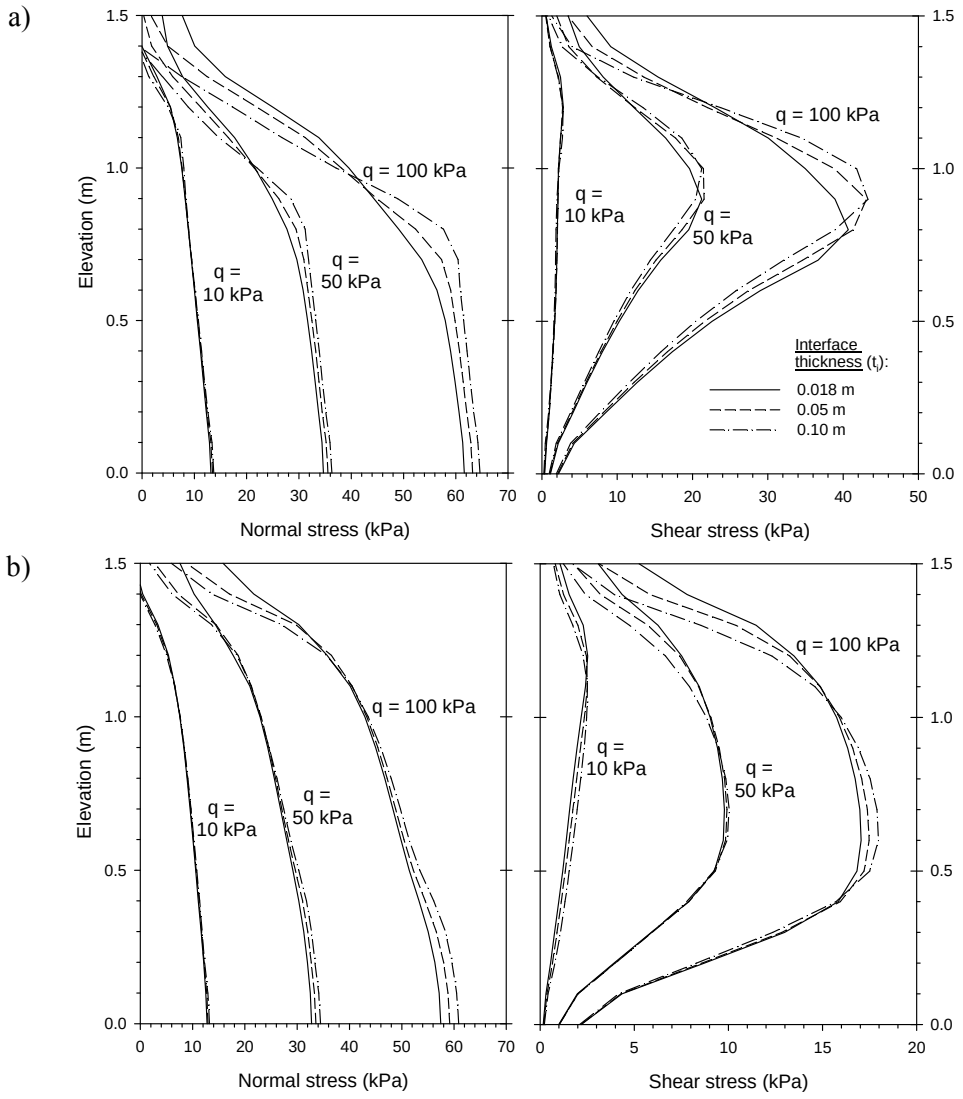

Figure 7.21: CODE_BRIGHT load transfer from backfill soil to facing panel: Normal and shear stresses comparison with regards to interface thickness (t_i = 0.018 m, 0.05 m, and 0.10 m). Cross-section at x = 0.509 m. Cases with R_i = 0.8 (a), and R_i = 0.3 (b).

The numerical results demonstrated that the increased interface thickness cases had a minor effect on the total vertical load at the interface between the facing and backfill soil if the equivalent interface stiffness was kept the same. Thus, a real interface zone between the dissimilar materials using continuum elements with a thickness greater than the virtual interface thickness using zero-thickness elements can be generated to model the soil-structure interactions and give similar numerical outcomes if the soil property values within the real interface zone are properly calculated based on the same interface stiffness.

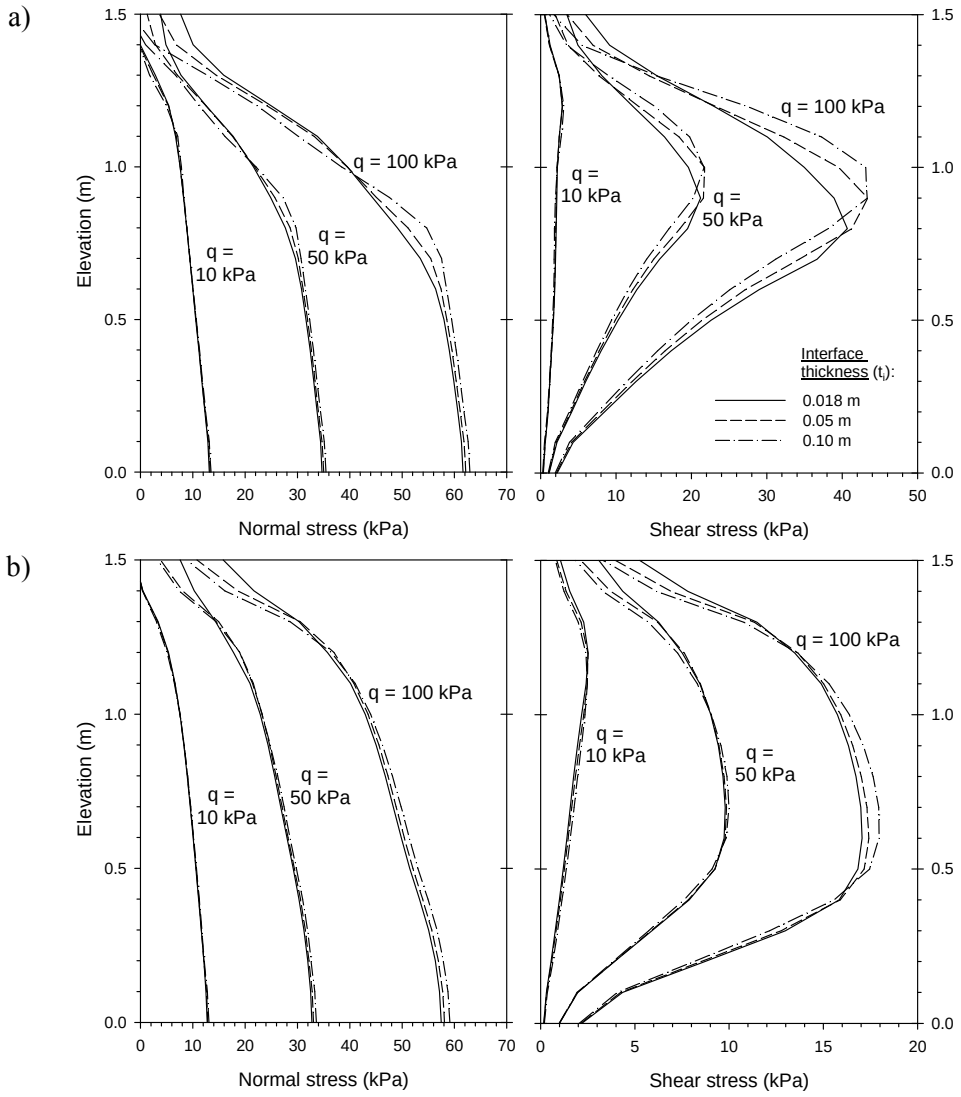

Figure 7.22: Load transfer from backfill soil to facing panel: CODE_BRIGHT normal and shear stresses comparison with regards to interface thickness (t_i = 0.018 m, 0.05 m, and 0.10 m): Cross-section at the middle of the interface thickness (i.e., x = 0.509 for t_i = 0.018 m; x = 0.525 for t_i = 0.05 m; and x = 0.55 for t_i = 0.1 m). Cases with R_i = 0.8 (a), and R_i = 0.3 (b).

7.4. CODE_BRIGHT 3D MODELLING

Four different 3D models were generated to perform the soil-facing interactions using continuum elements to fit the previous 2D results (Section 7.3.4). As in previous cases, different numerical meshes were assumed to detect any possible differences. Figure 7.23 presents the different meshes considered, from hexahedron coarse mesh case (related to previous structured quadrilateral 2D coarse mesh default case; see Figure 7.10b), up to three different tetrahedron quality meshes.

a) Hexahedron with coarse and structured (3D) mesh

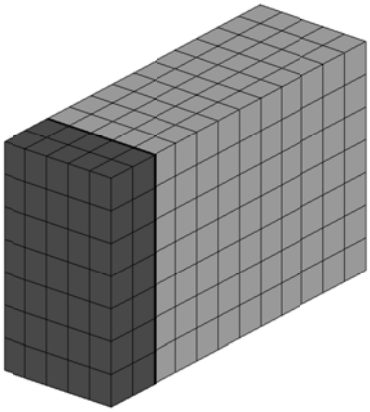

b) Tetrahedron with coarse and structured (3D) mesh

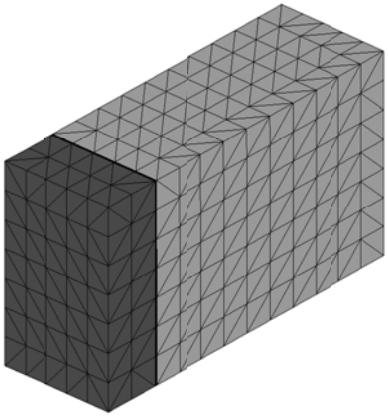

a) Tetrahedron with medium and structured (3D) mesh

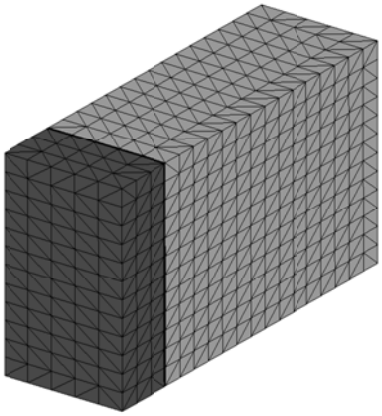

b) Tetrahedron with irregular unstructured (3D) mesh

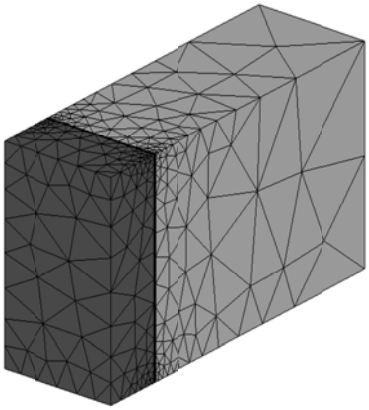

Figure 7.23: Two different finite element meshes for the same soil-structure interaction 3D example in CODE_BRIGHT: coarse structured (trilinear hexahedron elements) mesh (a), and optimized unstructured (linear tetrahedron elements) mesh (b), with the same interface virtual thickness t_i = 0.018 m.

7.4.1. Effect of the mesh size, elements type, and interface reduction factor

Figure 7.24 presents the resulting settlements under 100 kPa top surface surcharge scenario. As shown, very similar with practically no different settlement response were obtained between the four 3D modelling cases.

The total shear strains generation is presented in Figure 7.25. The higher strains value was similar between the four mesh cases analyzed (from about 16% to 18%). As it can be observed, the cutting plane direction which divides one hexahedron into two tetrahedron eases the shear strain to be developed up to somehow undesired direction (compare Figures 7.25a and 7.25b and see top-left elements, and then also in Figure 7.25c). Despite this effect,

only unstructured meshing case (Figure 7.25d) was judged to generate major differential response.

a) Hexahedron coarse mesh:

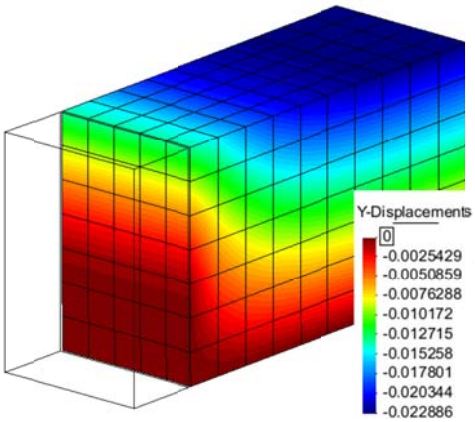

b) Tetrahedron structured-coarse mesh:

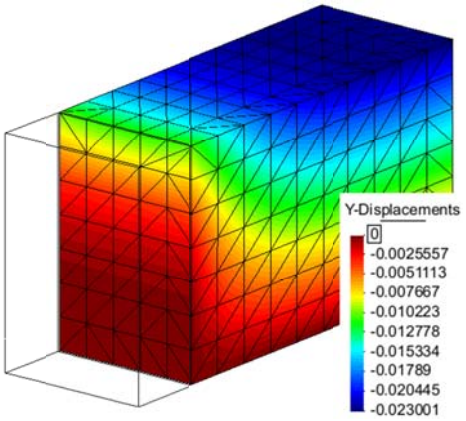

c) Tetrahedron structured-medium mesh:

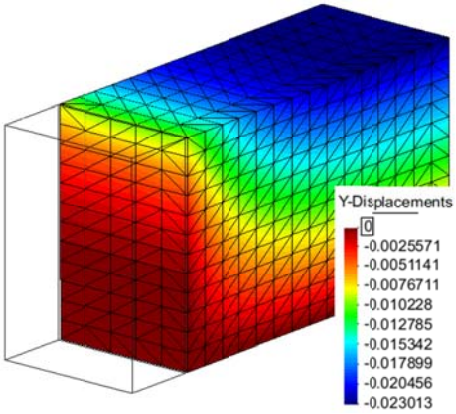

d) Tetrahedron unstructured mesh:

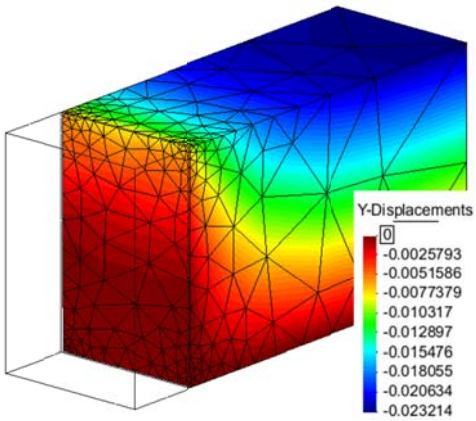

Figure 7.24: Settlement results (m) under q = 100 kPa-surcharge on top: hexahedron structured-coarse mesh (a), tetrahedron structured-coarse mesh (b), tetrahedron structured-medium mesh (c), and tetrahedron unstructured irregular-mesh (d). Cases with t_i = 0.018 m and R_i = 0.8.

Figure 7.26 presents the normal and shear stresses transfer from backfill soil to facing panel through in a cross-section located at 9 mm-distance from facing (i.e., in the middle of the interface media; t_i = 0.018 m) with regards to previous 3D mesh types considered and quadrilateral structured 2D coarse meshing model case (cases with R_i = 0.8 and R_i = 0.3). As shown, even not equal, reasonable similar responses were obtained between 2D and equivalent 3D hexahedron structured coarse cases. Tetrahedron elements returned more differences with regards to hexahedron case, with maybe more differential evidence in unstructured mesh case (as in previous 2D modelling cases).

a) Hexahedron coarse mesh:

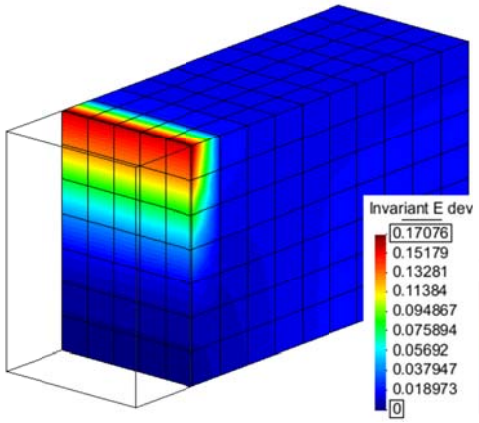

b) Tetrahedron structured-coarse mesh:

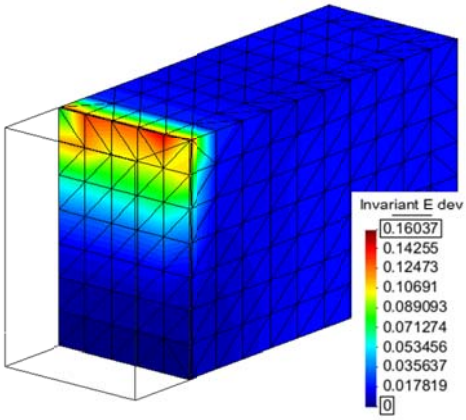

c) Tetrahedron structured-medium mesh:

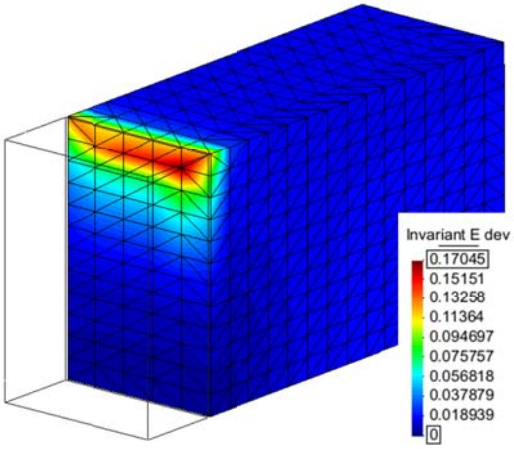

d) Tetrahedron unstructured mesh:

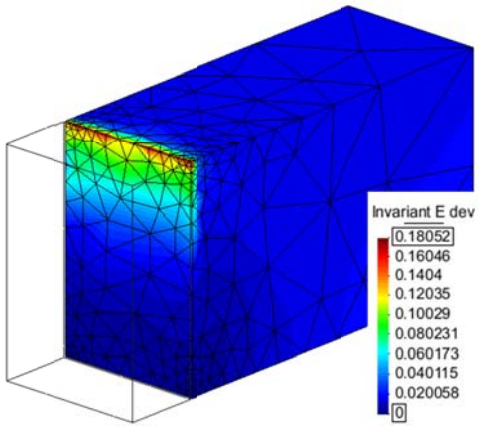

Figure 7.25: Total shear strains (-) results under q = 100 kPa-surcharge on top: hexahedron structured-coarse mesh (a), tetrahedron structured-coarse mesh (b), tetrahedron structured-medium mesh (c), and tetrahedron unstructured irregular-mesh (d). Cases with t_i = 0.018 m and R_i = 0.8.

Figure 7.27 presents the resulting settlements under q = 100 kPa-surcharge scenario for hexahedron elements structured coarse mesh comparing R_i = 0.8 and R_i = 0.3 strength/stiffness interaction factor cases. As expected and shown in previous 2D cases (e.g., Figure 7.16), different affectation area was generated consequent to the interface strength/stiffness. The shear strains (deviatoric invariant) evolution results are shown in Figure 7.28 (also R_i = 0.8 and R_i = 0.3 cases, under 50 kPa and 100 kPa-surcharge on top scenarios; results ranged from q = 100 kPa cases). As expected, logically higher strains were generated under the higher surcharge loading, and also due to the lowest interface strength/stiffness interaction factor.

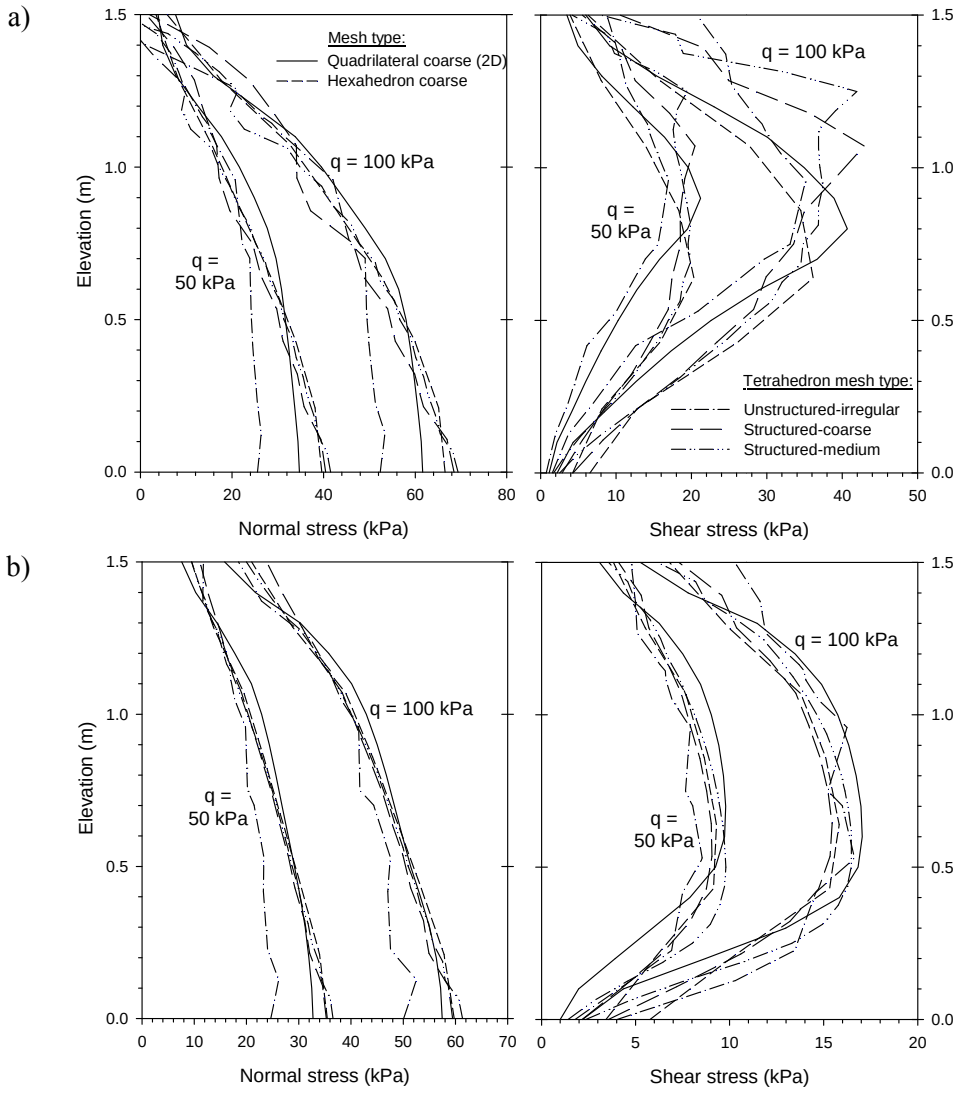

Figure 7.26: Load transfer from backfill soil to facing panel: Normal and shear stresses at x = 0.509 m cross-section with regards to the 3D mesh type (coarse and optimized). Cases with R_i = 0.8 (a), and R_i = 0.3 (b).

a) R_i = 0.8 b) R_i = 0.3

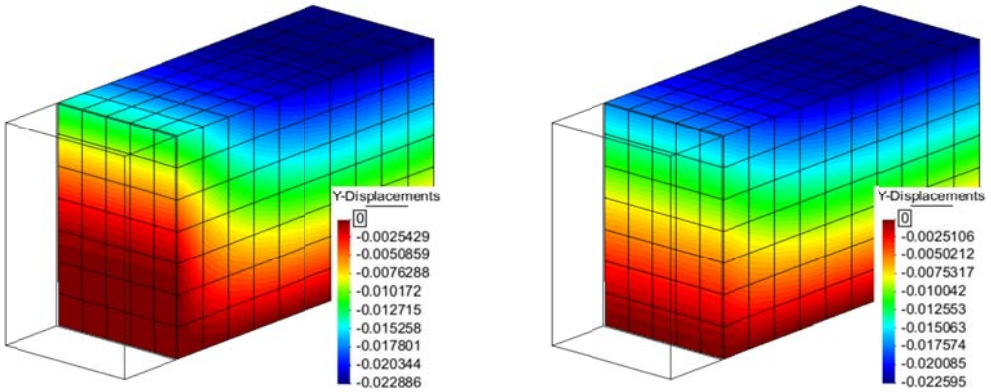

Figure 7.27: Settlement results (m) under q = 100 kPa-surcharge on top for hexahedron elements structured coarse mesh: R_i = 0.8 (a) and R_i = 0.3 (b). Cases with t_i = 0.018 m.

a) R_i = 0.8
q = 50 kPa

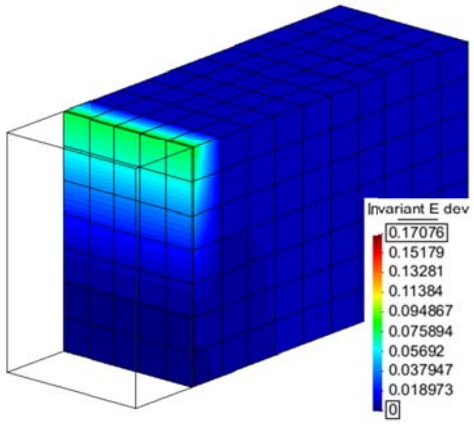

b) R_i = 0.3
q = 50 kPa

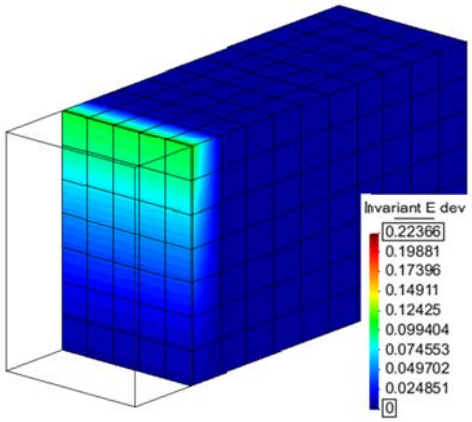

q = 100 kPa

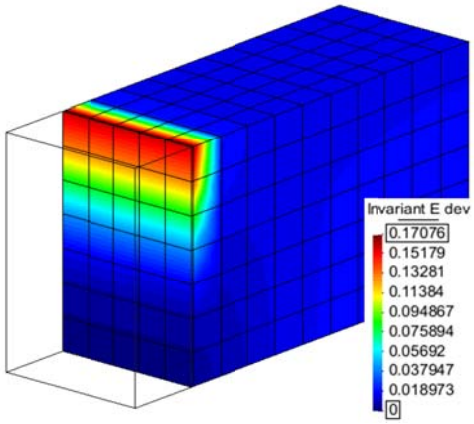

q = 100 kPa

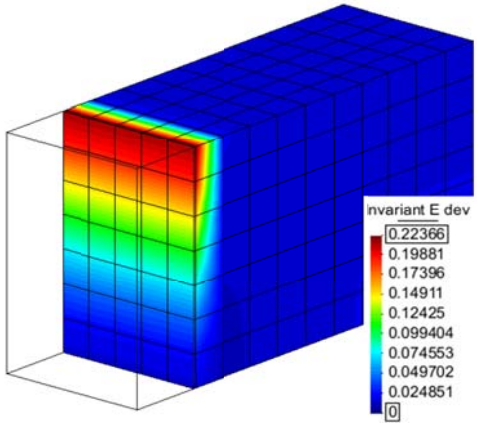

Figure 7.28: Total shear strains (-) evolution results for hexahedron elements with structured coarse mesh: R_i = 0.8 (a) and R_i = 0.3 (b). Cases with t_i = 0.018 m.

7.4.2. Effect of the interface thickness

From structured coarse mesh with hexahedron elements, two other complementary different thicknesses of the soil-facing interface were considered: t_i = 0.05 m and t_i = 0.10 m, as in previous 2D cases, with the same material properties (Table 7.6).

Figure 7.29 presents both mesh cases, generated based on previous the hexahedron structured coarse mesh type and methodology explained in Section 7.3.2.4.

a) t_i = 0.05 m: b) t_i = 0.10 m:

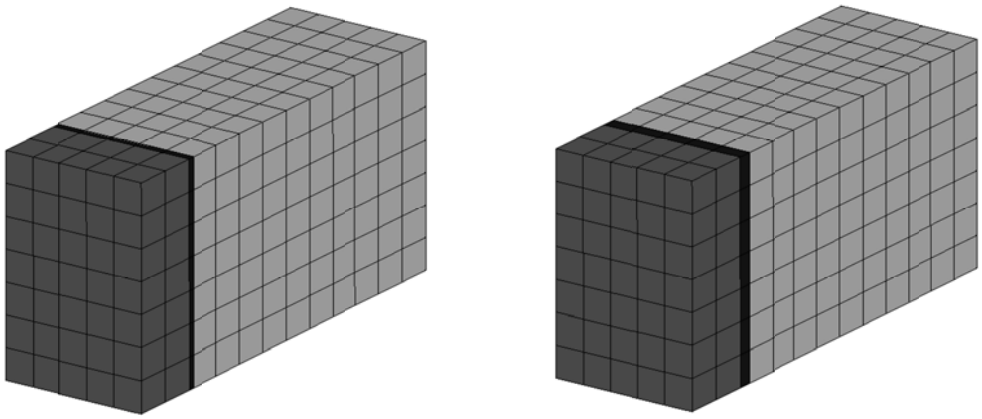

Figure 7.29: Two different interface thicknesses: t_i = 0.05 m (a), and t_i = 0.10 m (b). hexahedron structured-coarse (3D) mesh case.

Figure 7.30 presents the resulting settlement under 100 kPa-surcharge scenario for both interface thicknesses (i.e., t_i = 0.05 m and t_i = 0.10 m). As in previous 2D model cases analyzed, negligible differences were obtained with interface thickness increasing (very similar settlement distribution between both alternatives in each particular R_i-case).

The shear strains obtained under 50 kPa and 100 kPa-surcharge are presented in Figure 7.31 (R_i = 0.8) and Figure 7.32 (R_i = 0.3). Again, practically no differences were obtained between both interface thickness equivalent cases.

Finally, Figure 7.33 presents the normal and shear stresses transfer from backfill soil to facing panel with R_i = 0.8 and R_i = 0.3 between the three interface thicknesses analyzed (i.e., t_i = 0.018 m, 0.05 m, and 0.10 m) at a cross-section plane located at 9 mm-distance from facing panel (i.e., in the middle of t_i = 0.018 m-thick case). Also the previous 2D model case was included (previous Figure 7.10d-case). As shown, reasonably well agreement was obtained between all cases. However, the most different trends were obtained between 2D and 3D model cases, with variations more or less within the same order of magnitude as in the element type comparison results (see Figure 7.26 – elastic regime)..

a) t_i = 0.05 m:
R_i = 0.3

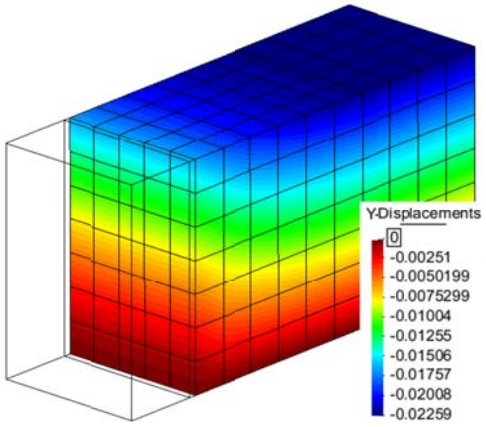

b) t_i = 0.10 m:
R_i = 0.3

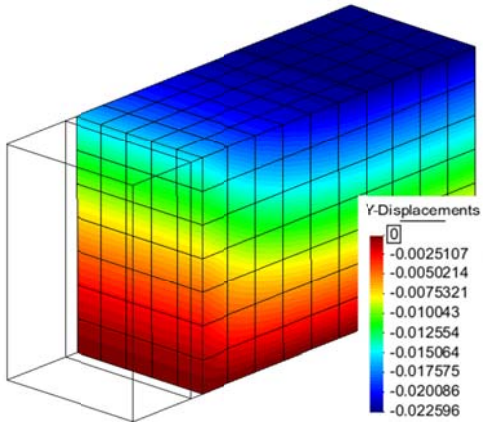

R_i = 0.8

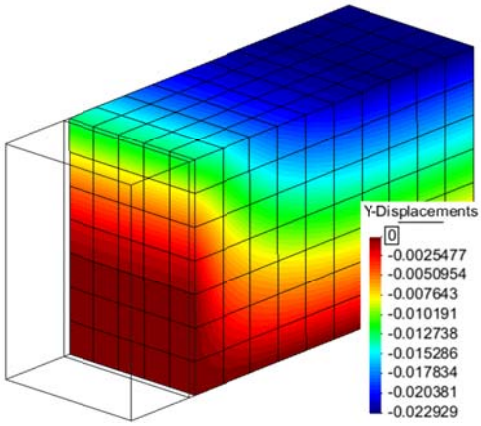

R_i = 0.8

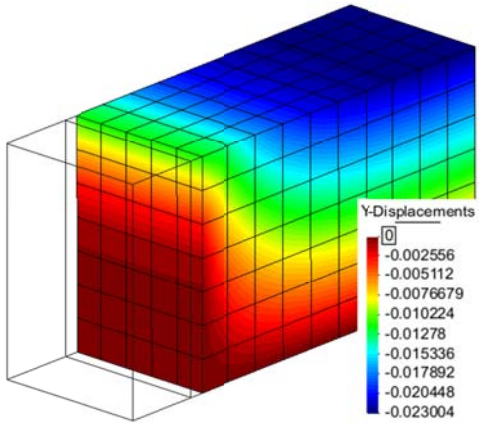

Figure 7.30: Settlement results (m) under q = 100 kPa-surcharge on top for interface thickness t_i = 0.05 m (a) and t_i = 0.10 m (b).

7.5. CONCLUSIONS

This chapter presents numerical predictions of normal and shear stresses at the interface between soil and a concrete facing using two interface modelling approaches (i.e., zero-thickness elements and continuum elements) with equivalent interface properties based on the Mohr-Coulomb failure criterion. A small earth retaining wall segment was used to demonstrate how the interfaces between the dissimilar materials can be modelled using both zero-thickness elements and continuum elements to capture soil-structure interactions. Based on the cases and conditions examined, the following conclusions are made:

The finite element mesh had a minor influence on the predicted normal and shear stresses at the interface between the facing panel and backfill soil when using zero-thickness elements. Fluctuations of normal and shear stresses for the interface with continuum elements were

observed once the soil within the interface zone reached plasticity (failed). However, the total vertical and horizontal loads at the interface from continuum elements generally agreed with those from zero-thickness or spring elements in both PLAXIS and FLAC models.

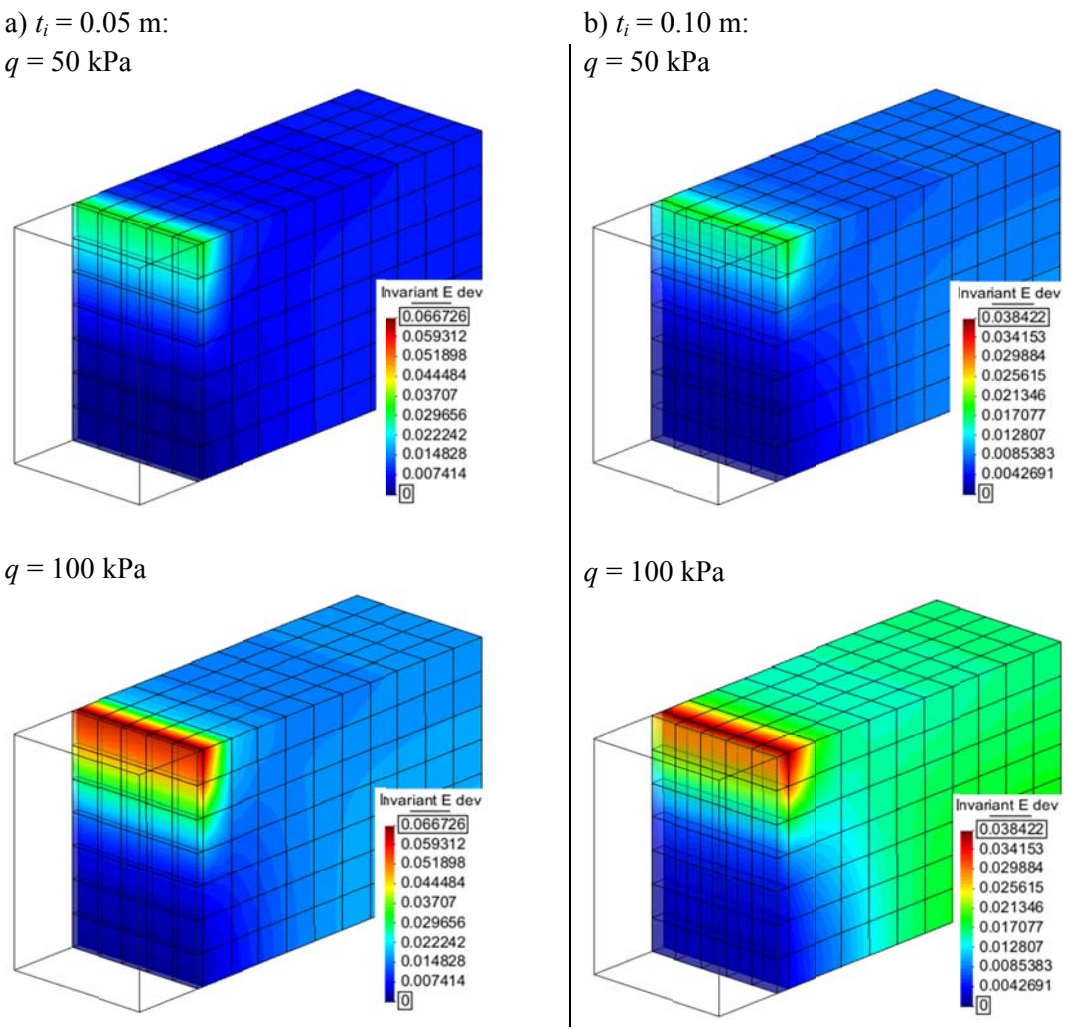

Figure 7.31: Total shear strains (-) evolution results: t_i = 0.05 m (a) and t_i = 0.10 m (b) continuum element interface thicknesses. Cases with R_i = 0.8.

For the interface with continuum elements, the finite element mesh with the lowest element aspect ratio (e.g., optimized mesh among the three meshes examined in this chapter) had the smallest normal and shear stress fluctuation amplitudes. Increasing the strength/stiffness reduction factor (i.e., increasing the interface stiffness) resulted in larger fluctuation amplitudes of normal and shear stresses when other conditions were the same.

a) t_i = 0.05 m:
q = 50 kPa

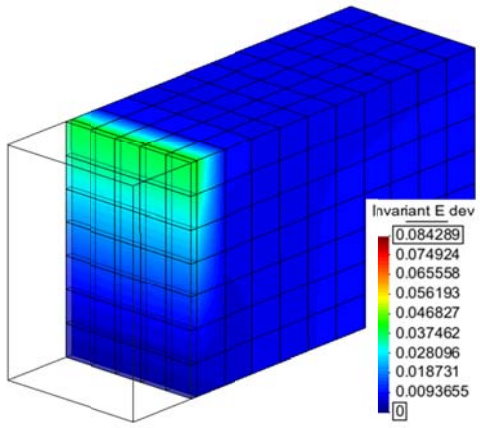

b) t_i = 0.10 m:
q = 50 kPa

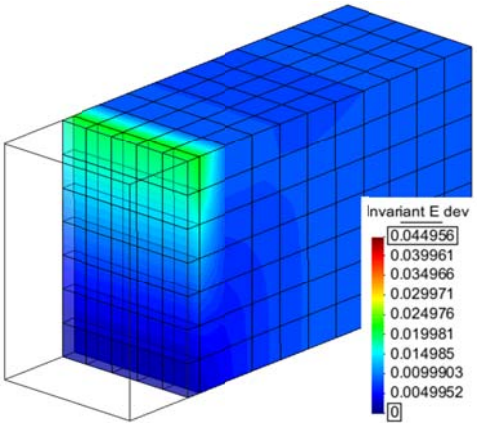

q = 100 kPa

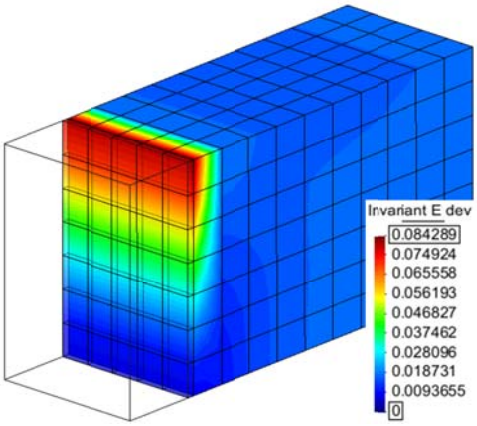

q = 100 kPa

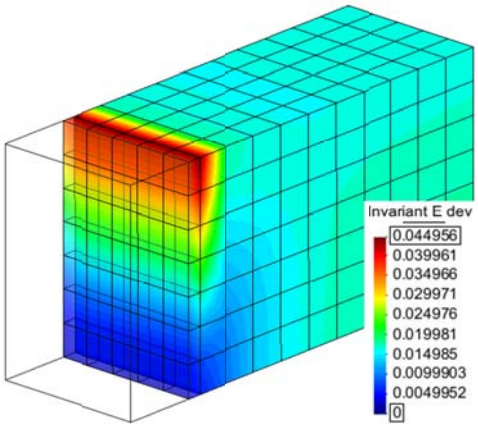

Figure 7.32: Total shear strains (-) evolution results: t_i = 0.05 m (a) and t_i = 0.10 m (b) continuum element interface thicknesses. Cases with R_i = 0.3.

The real interface zone using continuum elements with a thickness greater than the interface virtual thickness from zero-thickness or spring elements can be used to generate similar numerical outcomes for finite element models with continuum elements and zero-thickness elements, if the equivalent interface stiffness is kept the same for both methods.

The 3D modelling generated by CODE_BRIGHT and assuming the interface defined by continuum elements demonstrated a good agreement with the 2D models and other interface methodologies from PLAXIS and FLAC.

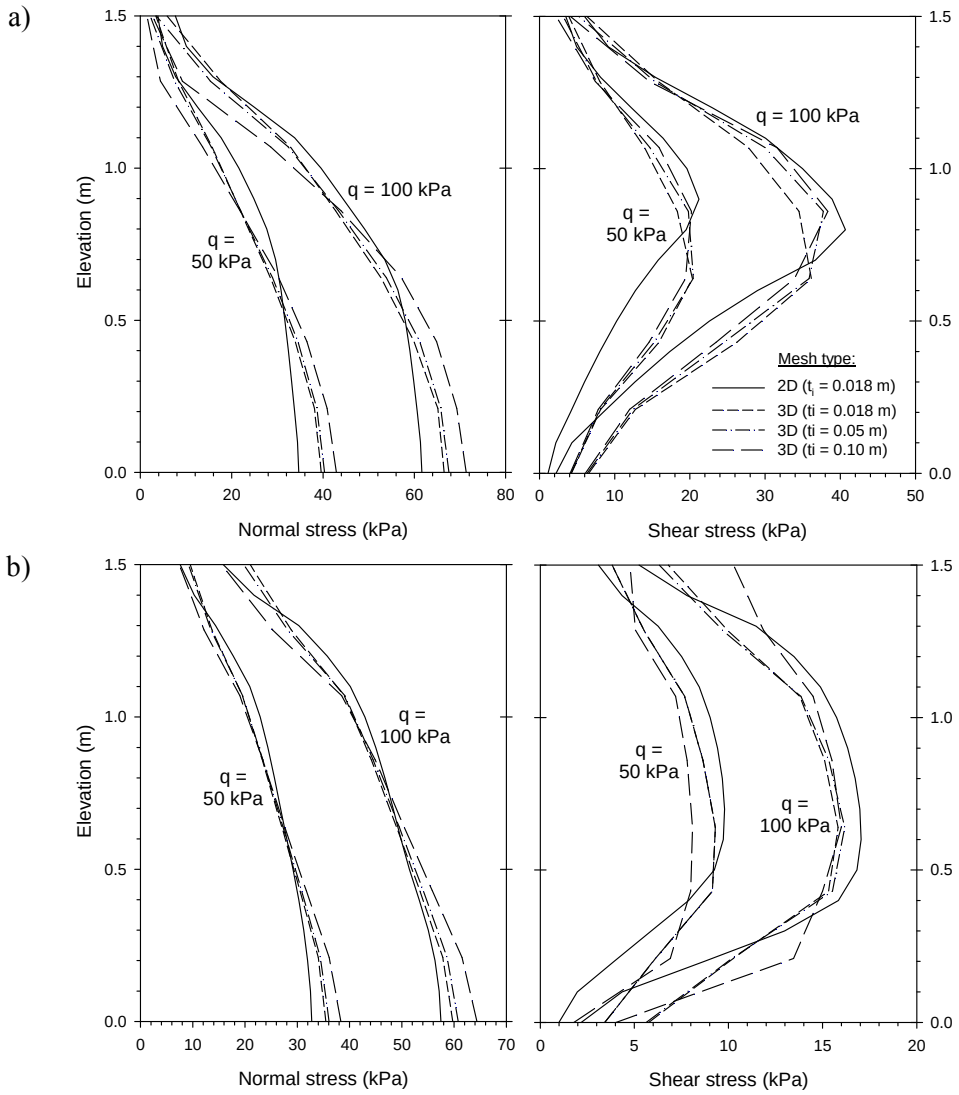

Figure 7.33: Load transfer from backfill soil to facing panel: Normal and shear stresses comparison with regards to interface thickness (t_i = 0.018 m, 0.05 m, and 0.10 m): Cross-section at x = 0.509 m. Cases with R_i = 0.8 (a), and R_i = 0.3 (b).

CHAPTER 8

SOIL-REINFORCEMENT INTERACTION: 3D MODELLING OF REINFORCEMENT PULLOUT TESTS

8.1. INTRODUCTION

Accurate design of reinforced soil-retaining walls requires knowledge of the actual interface shear behaviour of the reinforcement elements. Typically, these types of structure operate under working stress conditions (i.e., far away from failure), so they do not generate enough strain to fully develop soil-reinforcement interface strength. Nevertheless, interfaces must have adequate stiffness and shear strength. Therefore, pullout tests are particularly useful to examine interface behaviour and to quantify interface stiffness and strength. These parameters allow reinforcement design optimization to be carried out and/or to determine an adequate number of reinforcement elements to ensure safety.

Pullout tests are used to determine the soil-reinforcement interaction under different confinement conditions. Basically, reinforcement samples (e.g., steel ladders, polymeric strips, etc.) are placed inside the pullout box with compacted and vertically loaded filling material to perform real conditions (i.e., real reinforcement layer depth location). This test deals with the pulling out (extraction) of polymeric strip soil-reinforcement from the soil environment (filled material). The axial tensile load and reinforcement displacements developed and obtained from pullout testing are used in order to determine the behaviour and resistance of the strips under this particular mechanism.

An implementation methodology of steel ladder and polymeric strips pullout testing is described in this section, with generating enough normalized information about the in-lab pullout testing procedures. The designed pullout box allows the right development of pullout tests, as required, to determine and fix the fundamental parameters implied in the soil-reinforcement interaction when pullout mechanism occurs. Due to the optimized geometry of the pullout box and the common components required (typically used for many tasks in a mechanical workshop space or lab), the pullout testing can be easily performed in-lab, but also in-situ with carrying the equipment to the construction area. Explanations and features presented through in this described methodology are in agreement with ASTM D6706-01 (2013) and EN 13738 (2004) guidelines, and learnings from many reported cases in the

literature (e.g., Palmeira 2009, among others). A list of the required devices and tools to the performance of pullout tests is provided. Explanation of preliminary works necessary and the checklist of operational sequence for a successful test performance are also included in this Chapter. This described methodology was followed to carry on then a series of pullout tests both to steel ladders and polymeric strips samples. A summary of these results is presented to compare the measured data with theoretical/calculated data from international codes. Particular cases of steel ladder and polymeric strip pullout tests are also tested and analyzed.

A 3D model was then generated to analyze pullout tests. A base case is defined (with regular properties regarding to typical soil used in MSE wall structures) and parametrical sensitivity analysis performed from this base case. Finally, a calibration was done with regards to the previous steel ladder and polymeric strip cases presented, with a proper definition of soil, reinforcement, and interface materials.

8.2. PRINCIPLE AND SCOPE OF THE PULLOUT TESTS

The aim of the pullout tests is to determine the real pullout friction factor at different soil depths by evaluating the maximum pullout strength of particular reinforcement and particular soil types. This test deals with the pulling out (extraction) of reinforcement samples from the soil environment (filled material) applying an incrementally horizontal pulling force to the polymeric strips embedded between two layers of soil in the test box, for a specific vertical pressure applied on the top layer of fill soil. The test is finished when the reinforcement sample fails, pullout occurs, or a predetermined reinforcement displacement is reached.

The mechanical interfaces problem (i.e., soil-structure interaction) is a typical issue in geotechnical engineering, and soil-reinforcement interaction is not an exception. In this case, the load-displacement development of the system during this interaction could be not easy to predict (pullout or direct shear interaction). The strength and stiffness of this interaction (which can be understood as an anchorage of the reinforcement in the soil) have the direct influence of the soil material type (soil properties), type of reinforcement (geometrical properties, but also its axial stiffness), and boundary conditions (confinement pressure, moisture conditions, etc.). Because that, it is important to develop analytical reliable tools to evaluate these interactions, according to specific reinforcement, soil type and normal pressure conditions.

Current international Codes provide theoretical expressions to obtain pullout strength for particular cases, with assuming a certain values previously unknown. These values are typically in agreement for most common cases due to the empirical approaches with regards to historical report updates. When new materials appear in the market (as the high-grade polymeric strips are), some of the proposed expressions to determine parameters could not be representative, so new tests should be performed to determine the real strength of the interface and to deduce most representative interaction parameters.

The different depth locations of the strips in real scenarios are represented by applying consequent vertical pressures over the strip sample. During the test, the pullout force is continually determined and the strip sample displacements are measured, at least, at two points of the reinforcement (head and rear tail locations). The sample displacements are measured simultaneously by transducer gauges with regards to the applied pulling force. The correlation between displacements and applied load (i.e., pullout strength) depends on the reinforcement type (i.e., steel ladder dimensions, polymeric strip grade, etc.), the features of the soil placed in the box (which includes stiffness and strength properties, but also compaction level), the confining pressure conditions, and also, in particular cases, the rate of pullout displacement (pore pressure effects in case of an eventual undrained soil with fines and water content, and higher saturation degree).

8.3. PULLOUT TESTS IN BOX

8.3.1. Test components and testing materials

8.3.1.1. Test components

The **pullout box** is a rigid box made of steel open at its top. ASTM D6706-1 (2013) recommendations were followed for the dimensions of the box used. The plan dimensions are 1250 mm-length, 500 mm-width, and 550-750 mm-high (see Figure 8.1). These sizes are consequent with restrictions over the minimum embedment length of the strip specimen, the minimum depth of the soil in the box above or below the specimen (about 6 times the D_{85} or 3 times the maximum particle size), and the lateral boundaries to ensure minimum effect of the sidewalls boundaries over the sample tested. At its front side has an opening through which strip passed to connect to pulling mechanism and front clamps. At the rear side there are two openings that strips pass through. Openings are located at the same horizontal height level, at the middle of the box height assuming the same deep of soil bellow and above the strip. The box has two out-front arms where pulling jack sits and acts as a reaction to the jack to generate the extraction strip force. In order to avoid the influence of boundary conditions, a load transfer metal sleeve where the strip is passed through has to be fitted at the front side opening. The sleeve shall consist of two thin plates and properly fixed to the front side of the box. The sleeve plates must have a minimum length of 15 cm into the pullout box, but is recommended that this value is the same as the total soil depth above the strip (i.e., above or below the opening level).

The **pullout force device** (i.e., jack pump with calibration certificate; see Figure 8.2a) must be able to ensure the strip sample extraction out from the box at each confining pressure scenario required (i.e., vertical stress level condition), and must have the capability to apply the pullout force at a constant rate of displacement typically of 1 mm/min (with 10 % of tolerance deviation). This rate displacement can be significantly lower (about 0.05 mm/m) in case of pore pressure development anticipation. The pullout force must be applied at the same horizontal level than the strip (i.e., front opening level).

Figure 8.1: Pullout box samples.

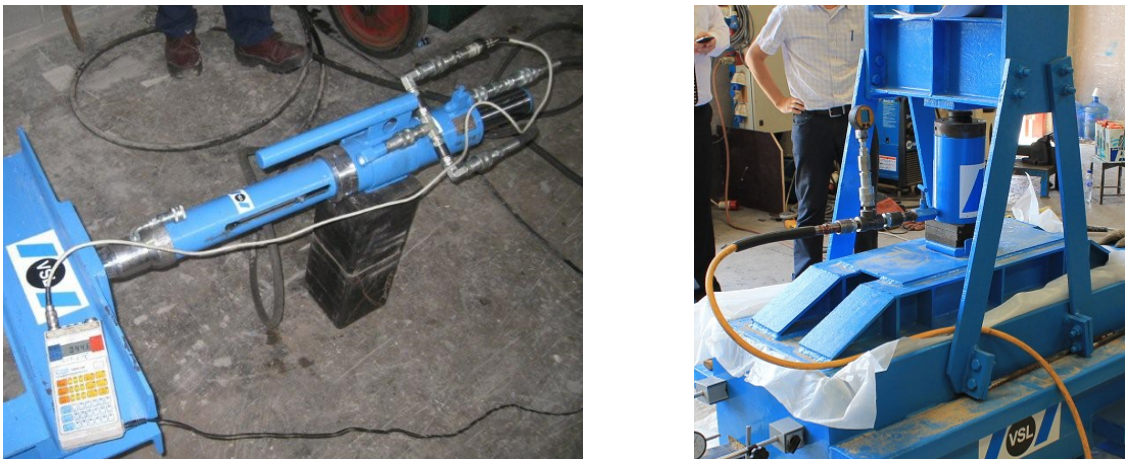

Figure 8.2: Pulling jack (a), and vertically pushing jack (b).

The **vertical loading device** (Figure 8.2b) has to be capable to anticipate stresses up to 300 kPa and should maintain the applied normal stress within ±2 % of the required one. The vertical stress applied to the upper layer of soil must remain constant and uniform during the test. To this purpose, a flexible pneumatic or hydraulic bag or diaphragm is required, which must be continuous (one rectangular bag piece) and must cover the entire upper fill-soil area above the specimen length. A reaction plate placed must be placed over the flexible loading bag, properly connected and fixed to the box, ensuring no openings where the flexible bag can be extruded through when loading. In case of cohesionless and stiffer granular soil, another optional however less accurate way to apply vertical loading is installing a loading plate over the top of the soil and apply the normal stress with a pushing jack device. In this case, the loading plate must be flat and rigid enough, and a reaction beam must be installed and right fixed to the pullout box, with appropriate rigid beam-legs connected with strength bolts, to sit the pushing jack stand between them. The soil must be isolated to the loading

plate with a plastic sheet and over covered of fine sand (about 20 mm-thick) to generate a better stress distribution. Is necessary to mention that this vertical loading solution is significantly less accurate due to the non-uniform distribution of the normal stress over the soil (under rigid loading conditions, the soil reaction generates stress accumulations at the edges and a consequent stress reduction under the central zone). Because that, the pushing jack over the loading plate device is only recommended for low confining pressure scenarios, where less divergences between the stresses at the edges and the central zone are expected. It is recommended to include several load cells over the upper layer of filled material (bellow the fine sand layer) to determine the true vertical pressure transmitted from the loading plate and to check its distribution and verify uniformity along the pullout box plan area. These load cells must be installed at representative locations (i.e., corners, side box edges, middle-central, and at half location from the central and the edges). Additionally, load cells may be installed within the fill and at the layer where the sample is placed (beside the strip specimen at a minimum 100 mm-distance), to determine the normal load transmitted to the strip specimen.

The reinforcement pullout **clamping device** is located at the front side (Figures 8.4a, 8.4c, and 8.4e) and must connect the strip or the ladder to the pullout force system without slipping and providing uniform load transmission to the sample without implying any damage. In case of V-shape of the polymeric strip specimens, the pullout clamp must ensure the no development of relative displacements after the rolling up of the strip around the circular pullout beam.

The horizontal **displacements control system** of the reinforcement consists of a comparator/transducer device with 0.01 mm-accuracy. In case of steel ladder pullout tests in where no inextensible behaviour is expected single device is required (Figure 8.4a), however, both front and rear measurements are recommended. In case of polymeric strip pullout tests, at least two movement comparators are required (front and rear clamps; Figure 8.4c and 8.4d), otherwise three movement comparator devices in case of V-shape strip, one positioned at the front clamp and the two others at the rear clamps of the strip's end tails (Figure 8.4e and 8.4f). These rear clamps required to measure the tail ends of the strip must assure free displacement with no generating additional strength to the pullout resistance (affecting as an apparent cohesion). Typically, dial gauges, electronic displacement transducers or spring-loaded deflection gauge with calibration certificate are used.

When clearly extensible strip reinforcements have to be tested or extensible behaviour is expected to be performed due to particular conditions of the test (i.e., low strip grade and/or very high confining pressures), in-soil displacement devices should be also required, and thus included, to measure internal displacements and to determine the location of the relative displacements generation along the specimen due to the pullout. These measurements can be very relevant to detect the extensible behaviour of low grade strips under higher confining pressure conditions. At least two additional measurements have to be obtained along each strip inside the box (at proportional space between them, including the pullout head and both tails measurements). These measurements can be done with attaching wire gauges

(inextensible thin steel cables) over the strips with pinning one end of the wire to the specimen and installing displacement transducers (four units) at the other wires ends, of the box to the rear. To reduce friction between wires and the surrounding soil, the cables can be covered with enough lubricant, or installed inside a thin rubber tube filled with oil or grease. Special attention must be taken to install the wires assuring that any slack is eliminated (Berg et al., 2009).

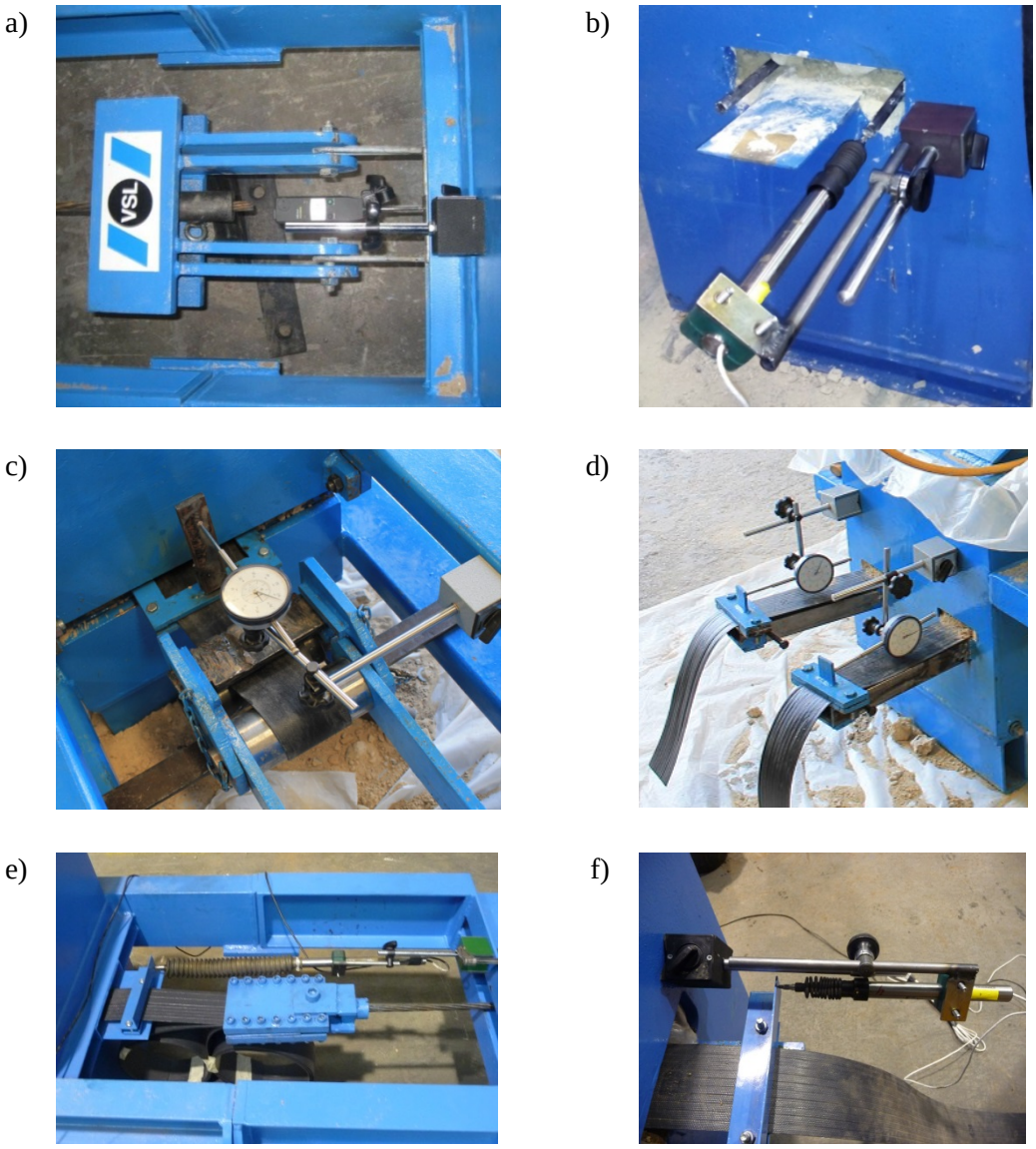

Figure 8.4: Reinforcement clamp devices and displacement transducers examples: steel ladder at front (a) and rear (b); V-shape polymeric strip at front (c) and rear tail end (d); and single polymeric strip front clamp (e) and rear tail end (f).

Several **compaction tools** can be used to compact the soil, as light compaction devices (e.g., portable vibratory plate compactor; (see Figure 8.5a), and/or hand compactors to be used

alternatively or to the edges and corner areas (see Figure 8.5b). The fill soil material must reach representative and uniform density to perform real conditions at the whole filled area. A **densitometer apparatus** may be necessary to easy determine the reached unit weight of the fill soil at each layer compaction step in the pullout box (see Figure 8.5b).

a) b) c)

Figure 8.5: Compactor equipment: plate compactor (a), hand compactor (b), and soil nuclear densitometer (c) to measure/verify the soil unit weight during compaction.

To reduce the side wall friction and fill adhesion, a lubricant (oil or grease) should be spread on the sidewalls of the box and a plastic sheet or silk fabric can be installed inside the surface of the pullout box. In case of no shear friction guarantee at the lateral box boundaries, it could be important to include vertical pressure cells to determine the true distribution of vertical stress from the loading plate to the soil, and the actual vertical pressure arriving to the reinforcement level layer.

8.3.1.2. Testing materials

Pullout tests are used to analyze the soil-reinforcement interaction, so the testing materials are the reinforcement elements (steel ladders and polymeric strips in the current study; see Figure 8.5) and the fill-soil material.

Steel ladders reinforcement system are typically manufactured from cold-drawn steel wire comprising longitudinal and transverse wires that are fusion-welded at the intersections to form long and narrow mesh elements (see Figure 8.6). Different connection systems can be performed in steel loop reinforcements. The longitudinal wires consist of smooth bars with diameter ranging from typically 8 mm to 12 mm. They provide the required tensile resistance for the reinforcement system. As mentioned above, the reinforcement-soil interaction is provided mainly by the transverse wires of the ladder (passive resistance). The transverse bars have similar diameters than longitudinal ones. In the steel ladder specimens to be tested, the distance between the longitudinal bars was about 160-170 mm (ladder's width), and the transversal bars spacing was 150 mm otherwise 300 mm. The spacing between transversal

bars usually depends on the required pullout resistance. Ladders located at top of wall require higher pullout strength and hence can have a smaller transverse wire spacing while those located at the bottom of wall require less pullout friction and hence have larger transverse wire spacing. A minimum of 50% of the longitudinal bars tensile strength must be capable of being transferred by the weld between the longitudinal and transversal bars. Galvanization of the steel ladder is conducted to protect it against corrosion and hence to ensure the durability of the reinforcing system for a specified design life of the structure. Usually, the ladders are hot-dip galvanized to a certain thickness, which depends on code and project specifications (e.g., minimum thicknesses of 70 µm according to EN 14475 (2011) and 85 µm according to AASHTO 2014). However, a certain sacrificial thickness of the black steel itself is considered in sizing the required reinforcement during design.

a) b)

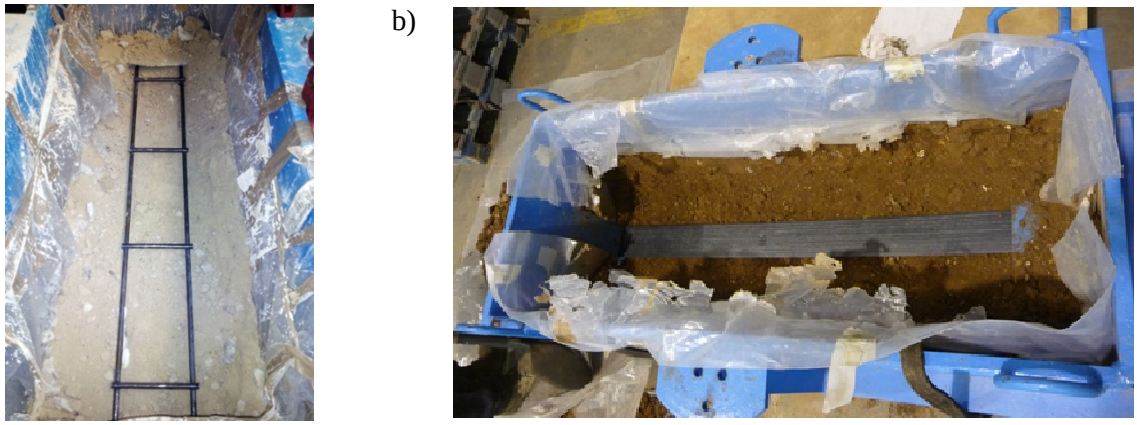

Figure 8.5: Reinforcement samples: steel ladder (a) and polymeric strip (b). Pictures taken after pullout tests performances.

Polymeric strips are often used as the reinforcement elements in MSE wall structures. Polymeric strips (Figure 8.7) are made from high-tenacity polyester fibers concentrated in separate parallel bundles (yarns) which provide the axial tensile strength and stiffness. The bundles are coated with a polyethylene sheath to provide protection and interface frictional strength with the surrounding soil. The finished coated strips are manufactured using a die extrusion process. The reinforcement products assumed in this study have four strength capacities (i.e., Grades) − 30, 50, 70 and 100 kN based on rapid tensile testing (short-term strength). For design, the long-term strength of the strip is required. The long-term available strength is computed as the short-term strength influenced by a series of material and site-specific strength reduction factors related to potential installation damage, creep and degradation due to potential chemical, biological and ultraviolet attack. In MSE wall systems, reinforcement elements (polymeric strips in this study) are located within the backfill and transfer the load from the soil material to the strips by frictional interaction.

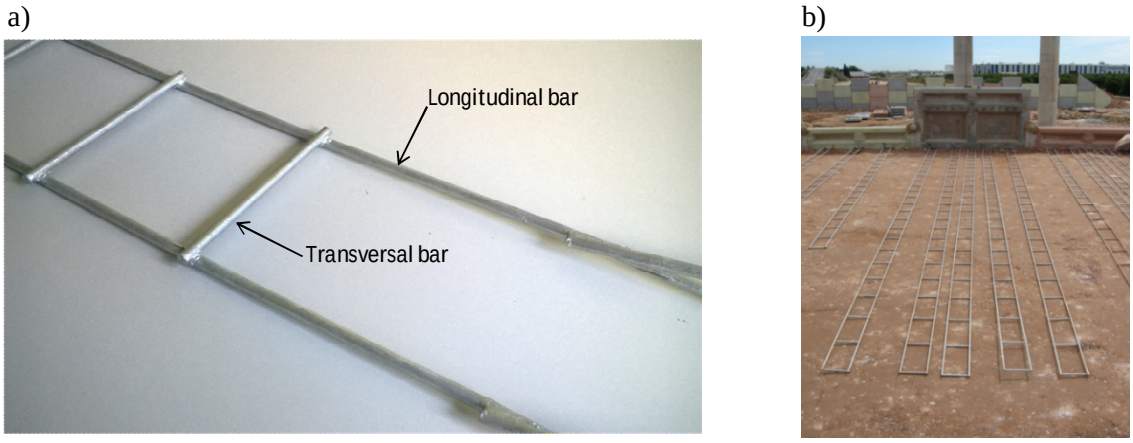

Figure 8.6. Steel ladder specimen detail (a) and on-site installation example (b).

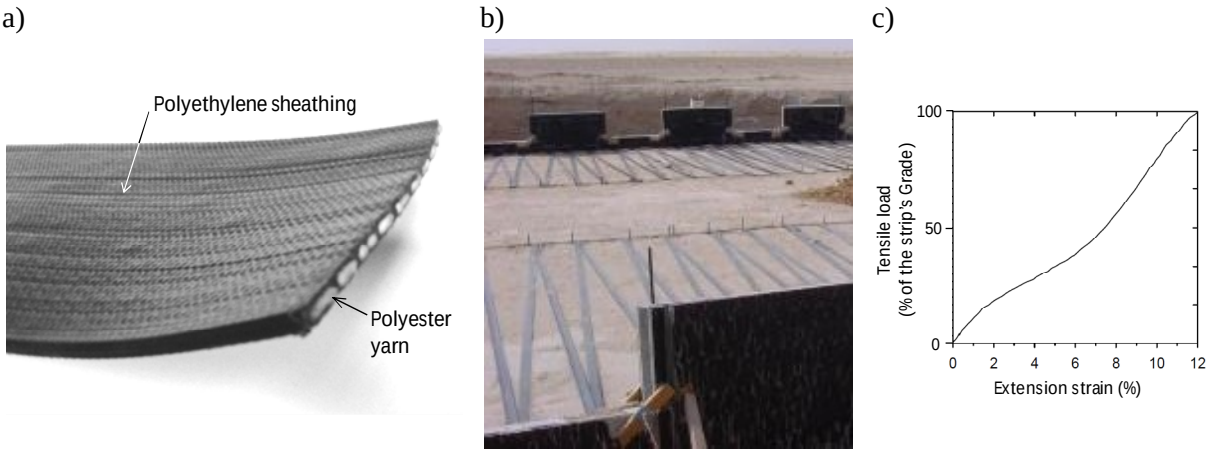

Figure 8.7. Polymeric strip detail (a), on-site installation example (b), and typical load-extension behaviour (c) of polymeric strips (Chamberlain & Cooper 2009).

The **fill-soil** to be used for the test shall be the same soil used for the project site. It is necessary to have the following soil parameters to correlate the pullout resistance with the type of soil used:

- gradation curve to determine D_{10}, D_{30}, D_{60}
- plasticity index
- maximum density and optimum moisture content (at 95% Modified Proctor test)
- angle of internal friction
- cohesion (if any)

Gradation code criteria examples are presented in Table 8.1 (American AASHTO 2014), Table 8.2 (European EN 14475 2011), and Table 8.3 (Australian RTA QA-R57 2005). A

summary of the requirements specified in Codes about the gradation of the backfill material to be used in MSE wall systems is presented in Figure 8.8 (shadowed area for soil types 1 and 2 according to Table 8.3; i.e., excluding soil Type 3-Intermediate). The criteria specified in RTA QA-R57 (2005) have been also added in order to full-fit the gradation area. As it can be observed, different maximum soil particle sizes are required with regards to the reinforcement type. Also, as specified in AASHTO (2014), soil gradation shall not be gap-graded and must satisfy well-graded classification (in accordance with the Unified Soil Classification System in the American Society for Testing Materials - ASTM D2487 2011), which implies, for a sand soil (SW), required Coefficient of Uniformity ($C_u = D_{60}/D_{10}$) greater than 6 ($C_u > 6$), and a Coefficient of curvature (curve-shape parameter, defined by $C_c = (D_{30})^2/(D_{60} \times D_{10})$) from 1 to 3 ($1 < C_c < 3$). For a gravel to be classified as well-graded (GW) the following criteria must be met: $C_u > 4$, and $1 < C_c < 3$. Thus, not all gradation curves within the shadowed area in Figure 8.8 necessarily satisfy soil gradation requirements and proper well-gradation is required according to AASHTO. In case of RTA QA-R57 (2005), $C_u \geq 5$ must be satisfied. With regards to the soil plasticity (plasticity index PI, related to fine soil particles portion) different limitations are specified. Tables 8.1, 8.2, and 8.3 summarize gradation and plasticity requirements according to the mentioned Codes. Table 8.2 shows the features about the soil classification types mentioned in Figure 8.8 (i.e., Type 1, Type 2, and Type 3 according to draining, granular, and intermediate, respectively).

About soil density and strength criteria, as specified in AASHTO, the fill material to be used in the reinforced backfill structures must comply with the project requirements for electro-chemical properties (later explained in more details) as well as all mechanical grading requirements, density (unit weight of about 18 – 20 kN/m^3 for dry scenarios and 20 – 22 kN/m^3 when saturated) and strength (a minimum measured effective friction angle of 34º). Moisture content and backfill density must be carefully controlled during construction (compaction works) in order to obtain strength and interaction values. Complementary electrochemical requirements shall be satisfied by a soil to allow its usage as reinforced backfill material in a MSE wall system, but only mechanical properties are analyzed in this study.

Table 8.1. Geomechanical properties for reinforced backfill applications according to AASHTO (2014):

	U.S. sieve size	Percentage passing (%)
Gradation	102 mm for steel reinforcement 19 mm for polymeric reinforcements [(a)]	100
	No. 40 (0.425 mm)	0 - 60
	No. 200 (0.075 mm)	0 - 15
Plasticity Index, P*I*	PI ≤ 6	

Note: [(a)] Unless full scale installation damage tests are conducted.

Table 8.2. Geomechanical properties for reinforced backfill, adapted from EN 14475 (2011):

		Fill type:			
		Type 1 (draining)	Type 2 (granular)		Type 3 (intermediate)
Geomechanical properties	% in weight smaller than 80 micron	< 5 %	< 12 %	12 to 35 %	12 to 35 %
	% in weight smaller than 20 micron	n.a.	n.a.	< 10 %	> 10 %
	Plasticity Index, PI	n.a.	n.a.	n.a.	< 25
Application	Parts of structure exposed to flooding and / or rapid water draw-down	often used	sometimes used	sometimes used	not recommended
	Structure supporting bridge abutments, railways, buildings		often used		subject to specific study [(a)]
	High reinforced backfill walls				sometimes used
Reinforcement type	Smooth strips or rods (metallic or polymeric)	often used	often used		subject to specific study [(b)]
	Ribbed strips or rods, ladders, bar mats, meshes, grids, sheets (metallic or polymeric)				sometimes used
Facing type	Rigid	often used	often used		not recommended [(a)]
	Semi flexible				subject to specific study [(c)]
	Flexible				often used

Notes: [(a)] If adequate compaction is not achieved then differential settlements between facing and reinforcement may occur which may overload the connection.
[(b)] The fill-reinforcement interaction should be assessed for long term and during construction conditions.
[(c)] Special attention should be paid to the control of the alignment of the facing units during construction.

Table 8.3. Geomechanical properties for reinf. backfill applications, modified and according to RTA QA (R57):

	Sieve size [(a)]	Percentage passing (%)
Gradation	% Passing 9.5 mm	25 - 100
	% Passing 2.36 mm	15 - 100
	% Passing 600 micron	10 - 100
	% Passing 75 micron	0 - 15
Coefficient of Uniformity, C_u	$\geqq 5$	
Liquid Limit, *LL*	$\leqq 30$	
Plasticity Index, *PI*	$\leqq 12$	

Note: [(a)] Maximum size (mm) prior to placement and compaction must be 150 mm for steel and 75 mm for polymeric reinforcements. For all soil reinforcements, maximum size of granular material must not be greater than one third of layer thickness.

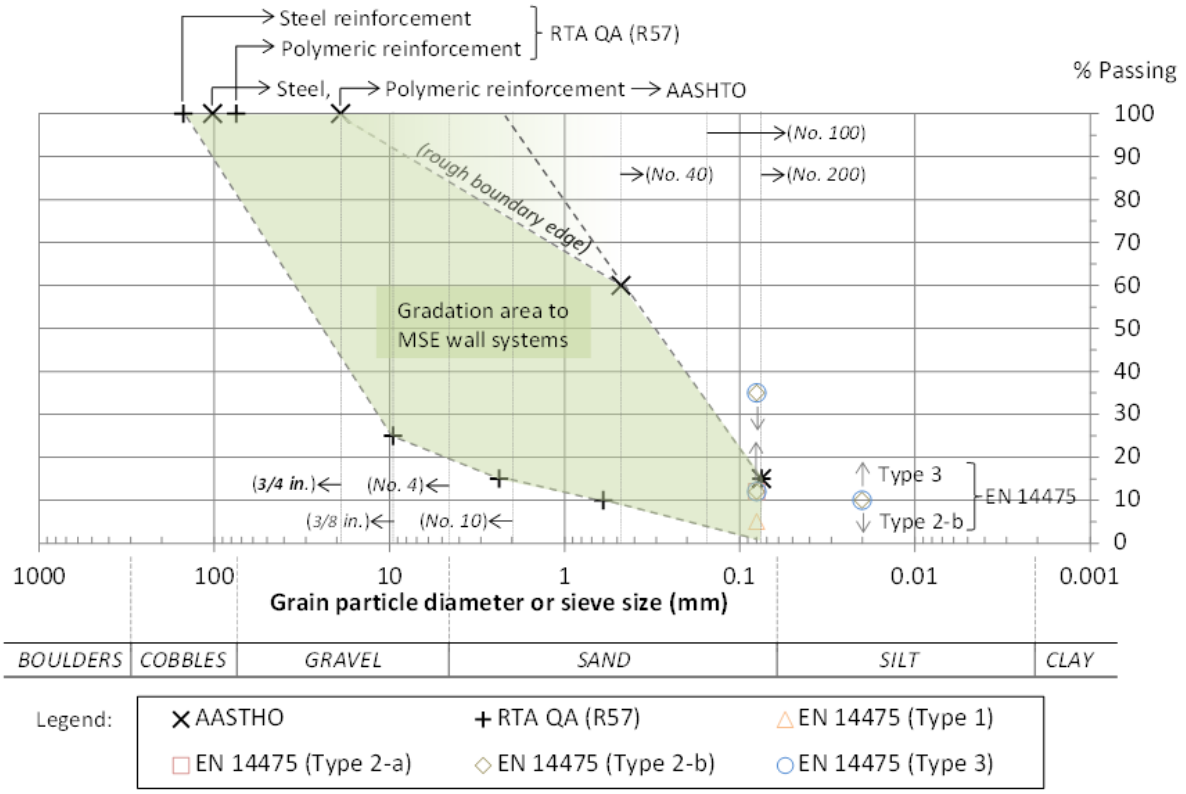

Figure 8.8: Summary of gradation criteria for selected reinforced-backfill according to AASHTO (1014), EN 14475 (2011), and RTA QA-R57 (2005), standards.

8.3.2. Test preparation and procedure

Select the steel or strips grade that will be used in the tests and cut the selected strips to be 4 meters in length (which is enough for box dimension and loop/clamping devices). The amount of soil should be in agreement with respect to the box geometry dimensions, the soil type and the moisture content (i.e., the required dry unit weight of the soil). About 0.35-0.50 m^3 of soil material are necessary to fully fill the box, achieve the desired/required dry unit weight, and perform a single pullout test. The specified fill-soil amount is based on one single pullout test (i.e., pullout test box volume). Typically not the entire fill-soil volume is required to perform subsequent tests, but at least half-height of the box shall be replaced by new soil to further test, corresponding to the soil placed above the reinforcement specimen, plus bout 5-10 cm thick of soil below the reinforcement specimen layer. Additional amount of soil material is also required for laboratory testing to determine soil parameters (about 50 dm^3 of additional material). According to the desired dry unit weight and the compaction effort to use, the number (or thickness) of soil lifts is selected. It is important to select the equivalent soil depths to then calculate corresponding vertical pressure that will be applied to the soil

fill, and to evaluate the theoretical pullout resistance of the strips for each scenario to be performed.

8.3.2.1. Test preparation

Prior to the soil filling, the four side wall surfaces of the pullout box must be clean to reduce the shear load transfer along these interfaces. As mentioned, it is recommended to spread lubricant with plastic films or silk fabric cover installation on the sidewalls of the pullout box can be necessary to reduce lateral friction effects and to eliminate fill adhesion, which, if no enough box dimensions is assured (or at least no enough spacing between reinforcement and side boundaries of the box), it can affect to testing results by reducing the effect of the vertical pressure and/or reorganization of the main stresses direction in fill soil.

Sequentially, place, spread, compact and level the soil layers into the box with appropriate thickness (about 150 mm-thick). The soil placement procedure should allow for a uniform soil dry unit weight along the pullout box. Is recommended to test the unit weight of each compacted layer to compare it with the maximum one obtained from Modified Proctor test (≥95 %). When the fill layer reaches the box openings level at the half height of the box, the sleeve plates must be installed at the front face-side opening. The fill must be leveled about 10 mm over the box openings to avoid dragging forces of the strips, so a portion of soil must be removed at the front face of the wall where the sleeve plates have to be installed.

After the sleeve-plates installation, the reinforcement specimen must be placed over the fill soil, passed through the front opening within the sleeve box entrance, right looped at the tensioning device anchorage, and both end tails passed through the rear openings (see Figure 8.9a). The strips shall be in the middle of sleeve plates and shall not be overlapped once they are out of the sleeve inside the box. At the rear zone the strips shall not be in contact with the sidewalls assuring a minimum of 100 mm-separation.

Prepare the pulling mechanism, jacks, pumps, and prepare the necessary connections with displacement transducer gauges. In case of polymeric strips, it is important to take into account that the strips must be properly aligned and any slack of the strip shall be avoided (hold tight the specimen by pulling from the back side openings). Ensure center point of shaft is aligned to middle of test box. The front clamp must be then installed, but without tighten the bolts already. The rear clamps to install displacement transducers must be temporarily tightened and the clamps with pins properly held, and a slight initial pulling force must be applied to perform the initial brief strained of the specimen without slacks. The front clamp should be then properly installed by fixing the bolts.

If required, install the in-soil displacement devices, properly connected to the displacement transducer devices at the rear of the box. As mentioned, any slack of the inextensible cables must be eliminated prior to spreading of the next fill soil layer. Then, the sequence of placing, spreading, compacting and leveling the fill soil must be repeated until reaching the indicated level on the side walls of the box.

After the required fill soil level is reached in the pullout box the vertical loading device must be installed. As previously mentioned, there are two available options: the main one (and thus, preferred one) is vertical load transfer by a diaphragm and a pneumatic or hydraulic pump device, which shall be properly placed over the top fill soil layer (Figure 8.9b). The top plate must be then installed and right fixed to the pullout box keeping the diaphragm inside. If none diaphragm neither pneumatic/hydraulic bag is selected to apply the normal stress over the fill soil, a plastic sheet and 5-10 mm-thick of fine sand must be spread over the plastic sheet at the top of the box. Then, the loading plate and the pushing jack must be installed, and the necessary connections with gages and pump for jacking must be prepared.

a) b)

Figure 8.9: Inside pullout box view with V-shape polymeric strip specimen placement above half-height of the box filled and compacted (a) and reaction beam placement over the pneumatic bag (b).

The vertical loading device must be properly calibrated and any change pressure during the test should be noted. The normal stress can be then applied to the specified vertical loading to the pullout test. As mentioned, it is important to determine that the stress will remain constant during testing. The rear clamps must be then released and pins removed, the location of the dial gauges adjusted and their bolts slightly tighten by hand to the fixed support. The pullout initial load must be reduced to 0. Figure 8.10a presents a frontal view with all this components at this stage of preparation (V-shape strip case).

After the desired normal pressure is reached, the gauge readings can be seated to zero and proceed to the pullout test execution. As mentioned, if the displacement transducers are not electronic, two cameras can be used to simultaneously record the gauge readings. If fill soil consolidation is required (so excess soil pore pressure can be eliminated) and to perform particular field conditions, enough time interval between the vertical load application and the pullout force loading must be considered. Figure 8.10b presents a rear view with all components at this stage of preparation (single strip case).

a)

b)

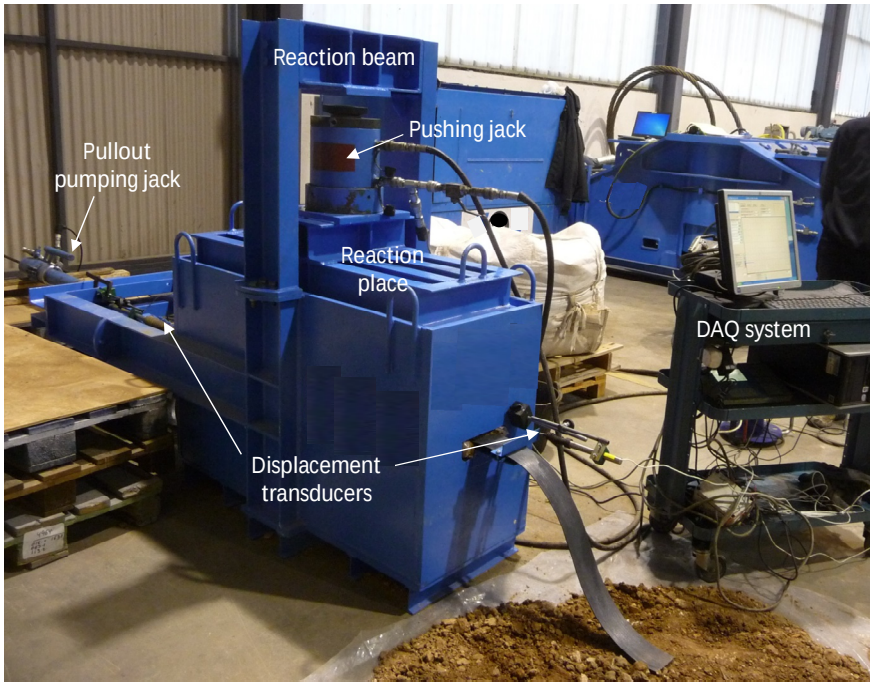

Figure 8.10: Testing polymeric strip pullout components set-up: front view of the pullout box with some components already installed (a), and rear view with monitoring control station-data acquisition system (b).

8.3.2.1. Test procedure

The complete connection of the pullout system should be ensured by applying a slight load with the pullout force jack and then take initial gauge readings. To apply a controlled pulling load so that the movement of the front clamp will be a constant rate displacement of 1 mm/min (±10 %). In case of expected soil pore pressures (soils with fine content really close to a full saturation degree) development during the test (e.g., significant fine-graded soil particles presence and moisture content), the rate displacement must be reduced slow enough to dissipate them. For regular rate displacement applied (i.e., 1 mm/min), the pullout pressure and reinforcement specimen displacement measurements shall be taken continuously or at intervals which correspond to a displacement of 0.2 mm or 6 second intervals of time. Pullout test shall proceed until the specimen fails, pullout failure occurs (i.e., pullout load becoming stable or a maximum is reached with respect to the strip displacement). In case of steel ladders (inextensible reinforcement), if no peak load is reached pullout load may continue increasing up to 20 mm-displacement at the front clamp. In case of polymeric strip, pullout loading shall continue increasing up to 15 mm-displacement is obtained at the back end of the specimen. After the pullout is reached (or pullout agreement decision), the pullout/pushing loading jacks and the top reaction plate must be released. The upper layers of soil must be removed with special attention to not modify/damage the reinforcement sample to allow its proper inspection. The test must be repeated for all vertical pressures and strip's grade required.

8.3.3. Theoretical calculations

The stress transfer mechanism through soil-reinforcement pullout interaction depends on reinforcement type. Figure 8.11 and Figure 8.12 present a schematic sectioned view for a general case of the pullout test in polymeric strip and steel ladder cases, respectively. Whereas in strips and sheets reinforcement type the pullout resistance (P_r) must be equal just to the frictional shear stresses (τ developed at the whole contact area between the strip reinforcement and the fill soil), complementary passive strength or bearing resistance (σ_b) is also developed in the bar-mat, ladder, grid, or even ribbed strip reinforcement types due to the transversal bar member surfaces.

According to this, in polymeric strips case (Figure 8.11) the pullout resistance (P_r, in total force units) can be understood theoretically as:

$$P_r = 2\int_{x=0}^{x=L_e'} T\,dx = 2w\int_{x=0}^{x=L_e'} \tau\,dx = 2wL_e'(a+\sigma_n^T f') = 2wL_e'(a+\sigma_n^T \tan\delta) \quad (8.1)$$

Where each parameter corresponds to:

T: is the transferred stress through the soil-reinforcement pullout interaction, corresponding to the frictional shear stresses (τ) in strips reinforcement case;

$L_e^{'}$: is the strip length to test (i.e., net sample length) projected to the orthogonal, which can refer directly to the strip length (L_e) for straight elements with no slanted installation (as steel ladders of single polymeric strip sample;

w: is the width of the strip, so ($2wL_e^{'}$) refers to the whole strip area in contact with the soil (number 2 due to both sides of the strip);

σ_n^{Total}: corresponds to the total vertical (normal) pressure developed at the reinforcement level (see later explanation);

a: is the soil-strip adherence (related to "soil cohesion" when soil-soil interaction);

f': is the friction interaction factor between the soil and the reinforcement, where, in case of strips is related to the tan(δ);

δ: is the friction angle of the soil-reinforcement interaction.

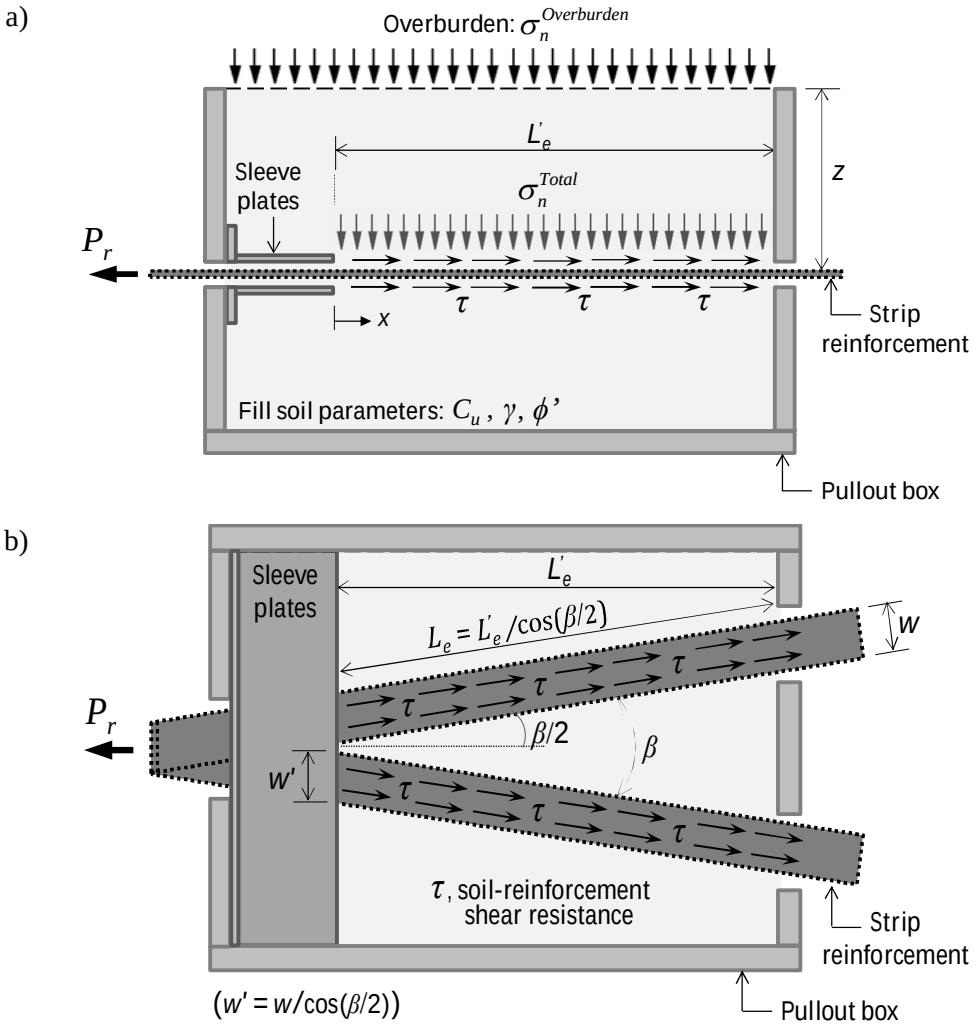

Figure 8.11: Polymeric strip pullout test: lateral-vertical section view of a general case (a) and plan section view adapted to V-shape strip case (b).

Assuming no adherence (i.e., no cohesion presence in the soil) and the particular scenario of V-shape geometrical disposition of the strip sample into the pullout box (see Figure 8.11b) the pullout resistance results, consequently, as follows:

$$P_r = 2\left(2(wL_e)\sigma_n^T \tan\delta\right)\cos\left(\beta/2\right) = 4wL_e^{'}\sigma_n^T \tan\delta \tag{8.2}$$

Where the added (×2) corresponds to the number of strip tails and β is the angle between strip tails in the pullout box (due to the V-shape). Must be noted that orthogonal projection of the strip area returns no modification ($L_e w = L_e^{'} w^{'}$).

In steel ladders case (Figure 8.12), as commented, the transferred stresses through the soil-reinforcement pullout interaction are a combination of frictional (τ developed through the longitudinal bars) and passive resistance (σ_b developed on the transversal bars) components. Thus, the friction interaction factor between the soil and the reinforcement (*f'*) is a combination between them (frictional + passive). It is not easy to properly define *f'*, however, the different available Codes (see next section) propose different semi-empirical definitions according to the reinforcement geometry (transversal bars thickness and separation) and soil gradation. The friction interaction factor could be defined as follows (Berg et al., 2009):

$$f' = F_q \alpha_\beta + \tan\delta \tag{8.3}$$

Where:

- F_q: is the embedment or confining bearing capacity factor, defined as the bearing resistance developed on transversal bars (i.e., $F_q = \sigma_b / \sigma_n^T$);
- α_β: is a bearing factor for passive resistance which is based on thickness per unit width of the bearing member;
- δ: is the friction angle of the soil-reinforcement interaction.

In steel ladder or bar-mat cases the frictional contribution through the longitudinal bars can be neglected, and thus, assume the pullout capacity to be because of bearing resistance only. However, on the other hand, the thickness of the transversal members is usually small compared to the depth, thus, the *f'* value probably takes more relevance due to the soil dilatancy, general reinforcement roughness, and initial soil stress states (Jewell et al., 1984) instead of purely passive of punching resistance. Both frictional and passive approaches results in a bearing capacity factor consistently increasing with friction angle. However, reported studies (as in Palmeira and Milligan 1989 and Matsui et al., 1996) have shown that neither shear failure nor punching on transversal members provide good predictions of pullout capacity of grids when compared with measured values from laboratory pullout tests. The reported study done by Yu and Bathurst (2015) demonstrated good accuracy of results with using empirical-based expressions of more fine definition of the bearing capacity factor. In this study, the pullout resistance or capacity is defined as:

$$P_r = n_b t w N_q \tag{8.4}$$

Where:

n_b: is the number of transversal bar (i.e., equal to ratio between the reinforcement length and the transversal bars separation, $n_b = (L_e / S_t)+1$;

t : is the thickness of the transversal bars;

N_b: is an empirically-based dimensionless bearing capacity factor. Assuming the best fit values as proposed by Yu and Bathurst (2015), $N_q = 43/\sqrt{(n_b \sigma_n^{Total} / p_a)}$ is deduced, where p_a corresponds to the atmospheric pressure: p_a = 101 kPa.

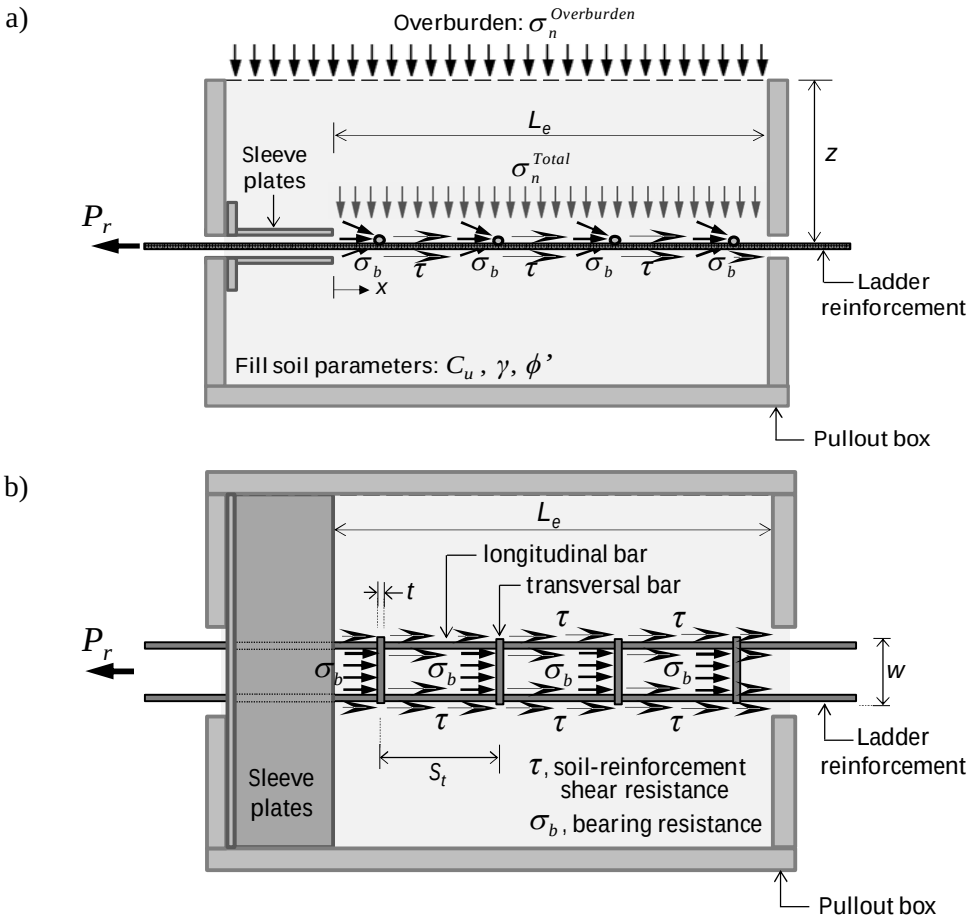

Figure 8.12: Steel ladder pullout test: lateral-vertical section (a) and plan section (b) views.

The normal stress σ_n^{Total} applied to the strip should consider the overburden pressure and the self-weight of the fill soil material. If no friction along the boundaries of the pullout box is guaranteed (front, back, and sidewalls), the total vertical stress can be defined as follows:

$$\sigma_n^{Total} = \sigma_v^{Total} = \sigma_v^{Overburden} + (\gamma z) \quad (8.5)$$

If uniform vertical stress is not reached and/or arching effects are expected to be developed in the pullout box (due to lateral boundaries soil-box friction with consequent reduction of the vertical stress developed in depth), Equation 8.4 could not be satisfied with resulting vertical stresses significantly lower than the expected one. Thus, other expressions must be used, as the following one:

$$\sigma_v^{Total} = \frac{B\left(\gamma - 2c/B\right)}{2K_a \tan\phi'}\left(1 - e^{-2K_a \tan\phi\left(\frac{z}{B}\right)}\right) + \left(\sigma_v^{Overburden} e^{-2K_a \tan\phi\left(\frac{z}{B}\right)}\right) \quad (8.6)$$

Where:

- B: width of the yielding soil-reinforcement (equal to the width of the pullout box as first approximation);
- K: earth pressure coefficient, typically assumed as active (K_a), so defined as $K_a = \tan^2\left(45 - (\phi/2)\right)$ for vertical boundaries and horizontal top surface,
- γ: unit weight of the fill soil;
- ϕ': effective friction angle of the fill soil.

As commented, to avoid any unknown about the vertical pressure to consider in calculations, and to definitively fix the vertical pressure developed over the strip sample, it could be interesting to install load cells during pullout tests at the strip level.

8.3.4. Pullout equations and variables to consider according to international Codes

Several international codes provide expressions and charts to determine the theoretical pullout force when pullout tests data is not available and there is no option to perform this type of testing. These provided default data can be used for different reinforcements and soil types to deduce the pullout strength in design analysis. It is clear that this default data could be not much accurate or extremely conservative, and the option to perform pullout test for the conditions required is always preferable to then fix more accurate design parameters. The development of several pullout tests performed under the same boundary conditions generated enough data to obtain a patron of steel ladders and polymeric strips pullout behaviour and the consequent accuracy when fixing pullout equations (i.e., fixing the most representative soil-reinforcement interaction parameter values) in design performance.

This section has the purpose to expose the theoretical expressions proposed in AASHTO (2014, and related Berg et al., 2009) and French standard (NF P 94-270, 2009) to determine ultimate pullout resistance when polymeric strips are used as reinforcement in mechanically stabilized earth retained walls. A summarized explanation of the pullout resistance presented by these Codes is presented. It is necessary to mention that the theoretical developments from

these codes are tried to be uniformed with exposing each pullout expression in terms of pullout resistance per strip unit (P_r), but with the original nomenclature for the other equation terms, and obtaining final easier equations to compare.

8.3.4.1. AASHTO LRFD

In American Association of State Highway and Transportation Officials, Load Resistance Factor Design: Bridge Design Specifications (AASHTO 2014) the pullout resistance is given as:

$$P_r = CwL_e\sigma_v(F^*\alpha) \tag{8.7}$$

Where:

- w: is the reinforcement width in case of polymeric strip, or the transversal bar width (distance between outside longitudinal bars; which can be different from longitudinal bars width) in steel ladder case;
- L_e: is the length of the reinforcement in the resisting zone; assuming orthogonal disposition with respect to the facing, results: $L_e = L_e^{'}$;
- C: is the overall reinforcement surface area geometry factor based on gross perimeter of the reinforcement (equal to 2 for strips and ladders, i.e., two sides);
- σ_v: is the vertical stress at the reinforcement level in the resistance zone;
- α: is a scale effect correction factor, which is assumed to be 1 for inextensible reinforcements (steel ladders), and less than 1 for extensible reinforcements (see explanation below);
- F^*: refers to the pullout friction factor, corresponding to the soil-reinforcement transferred strength relation. As explained below, in case of smooth strips, this factor, which is mainly controlled by friction shear stresses development, can be understood as $F^* = \tan\delta = C_i \tan\phi$ (where ϕ is the friction angle of the soil, δ is the soil-reinforcement interaction friction angle, and C_i corresponds to the interaction coefficient, i.e., $C_i = \tan\delta/\tan\phi$). In case of steel ladders, friction and passive resistance is occurring, and F^* default values related to transversal bars thickness and separation are recommended.

AASHTO specifies that α and F^* are parameters which "shall be determined from product-specific pullout tests in the project backfill material or equivalent soil, or they can be estimated empirically/theoretically". AASHTO proposes values of α which cannot be applied for polymeric strips (α = 0.6 for geotextiles and α = 0.8 for geogrid reinforcements) as this reinforcements type are not clearly extensible reinforcement if the extensible/inextensible behaviour is understood with regards to the soil deformation relation. Polymeric strips have been instrumented in-site conditions, demonstrating somehow inextensible behaviour results (Luo et al., 2015), and thus, α = 1 could be assumed. The proper scale effect correction factor value, α cannot be determined from shear direct test and must be analytically derived. As

mentioned, α is assumed to be 1 for inextensible reinforcements, and less than 1 for extensible reinforcements. The Federal Highway Administration guidelines (Berg et al., 2009 - Appendix B) proposes a procedure from particular instrumentation to obtain α-values. The most important to analyze the scale effect is to increase the instrumentation capacity when pullout arises with measuring displacements in several point along the strip sample. Briefly explained, after obtaining the step-by-step displacements along the mobilized length of the reinforcements (named L_p, which in extensible reinforcements varies according to the pullout load), the pullout resistance with respect to the parameter $\sigma_v \times L_p$ can be obtained, i.e., different slopes (F^*-values) of the P_r with respect to (σ_v L_p) are obtained. Thus, the scale effect correction factor value (α) that must be used for design corresponds to the asymptotic approach of the residual over peak values of F^* (i.e., $\alpha = F^*_{residual} / F^*_{peak}$) which corresponds to the lower bound).

Similar problem happens when F^* is wanted to be deduced. In case of polymeric strips, again, no specification for polymeric strip reinforcements is presented. To propose a default value of $F^* = 0.67\tan\phi$ (i.e., $C_i = 0.67$) as a lower bound value to geotextiles and geogrid reinforcements for all wall elevation locations could derive into a not representative or excessively conservative value. Shear direct test (ASTM D5321 2008) can be useful to obtain F^* when strip reinforcement type, and it would be equal to the peak resistance developed (i.e., $F^* = \tan\delta_{peak}$). The probably main objection of this F^*-value obtained from regular direct shear tests is the soil material limitations of this essay, with the possibility of generating non-representative results in case of particular material types (i.e., coarse gravel with uniform gradation) due to the direct shear testing box dimension and the reinforcement fill material requirements imposed by the national codes (particular analysis and decision on obtaining F^*-values must be done in this case). Polymeric strips manufacturers use to provide their own default C_i values (typically less conservative than Code values).

No explicit mention about bar-mats neither steel ladders F^*-values are provided in AASHTO, However, F^* can be understood as a relation between steel grid openings geometry and a bearing capacity factor (n_q), as follows:

$$F^* = n_q(t / S_t) \tag{8.8}$$

Where:

t: is the thickness of the transversal bar members;

S_t: is the separation between transversal bar members (see Figure 8.12);

The AASHTO-default values for the pullout friction factor of steel grid reinforcements are given, as a function of the reinforcement layer depth location (z), and summarized in Figure 8.13.

Equaling pullout resistance capacity P_r from previous Equations 8.8 (including Equation 8.8 definition) and 8.4 (i.e., $P_r = CwL_e\sigma_v(F^*\alpha) = 2wL_e\sigma_v n_q(t/S_t) = n_b tw\sigma_v N_q$, with assuming

inextensible reinforcement (i.e., $\alpha = 1$), a relation between bearing capacity factors relation is obtained as $2n_q = N_q$. From Figure 8.13, $n_q = 20$ is given at $z = 0$ level, and $n_q = 10$ for $z \geq 6$ m layer locations. These values are more or less in agreement with N_q values proposed by Mitchell and Villet (1987) (from Bloomfield 1984 data), where $N_q = 40$ at $z = 0$ level, and $N_q = 15$ for $z \geq 6$ m layer locations.

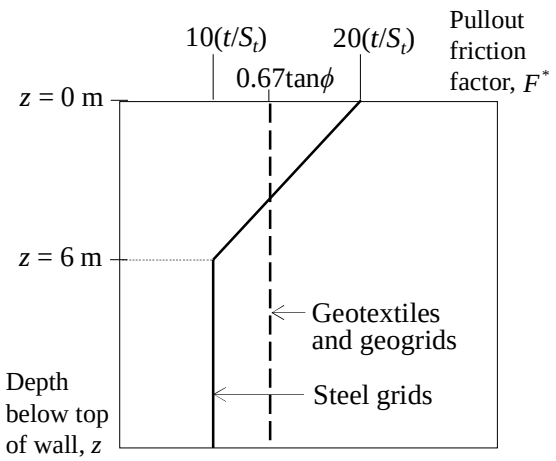

- No explicit mention to steel ladder reinforcement type is provided and values given to steel grid reinforcement type are considered;
- t is the thickness of the transversal bar members, and S_t is the separation between transversal bar members;
- no explicit mention to polymeric strips is provided and values given to geotextiles and geogrids are considered.

Figure 8.13: Summary of the default pullout friction factor F^* in more agreement to be applied in steel ladder and polymeric strip reinforcement types (according to AASHTO 2014).

8.3.4.2. NF P 94-270

French standard (NF P 94-270, 2009) defines the pullout strength as:

$$P_r = P_s L_s \tau_{max} \tag{8.9}$$

Where:

τ_{max}: is the apparent mobilized shear strength at a certain reinforcement depth, defined as: $\tau_{max} = \sigma_v \mu^*_{(z)}$, where σ_v is the vertical stress and $\mu^*_{(z)}$ is the apparent coefficient of interaction (lately extended explanation);

P_s: is the cross-section reinforcement perimeter, defined as defined as: $P_s = 2w$, where w is reinforcement width, equal to the total steel ladder width, without taking into account larger protrude than $s_y/3$ (in case) where s_y corresponds to the spacing between longitudinal bars;

L_s: is the effective reinforcement length. In case of steel ladders the pullout effective reinforcement length is defined as: $L_s = (n_s - 1)s_x$, where n_x is the number of transversal bars and s_x is the spacing between transversal bars.

Thus, $P_s L_s$ corresponds to the reinforcement surface contact where the friction interaction is mobilized. Previous Equation 8.9 can be then derived into the following one:

$$P_r = (2w)(n_b - 1)s_x(\sigma_v \mu^*_{(z)}) \quad (8.10)$$

The apparent soil-reinforcement interaction coefficient ($\mu^*_{(z)}$) must be obtained from pullout tests, preferable in-situ as recommended into NF (real in-situ tests, this is, pullout execution during wall construction and at different depths. The execution and interpretation of the pullout tests must be done according to NF P 94-222 (1995) for inextensible reinforcements, and NF P 94-232-1 (2001) for extensible reinforcements.

Similar to the AASHTO case, the $\mu^*_{(z)}$ -value must be distinguished along the depth location (h_a) of the reinforcement layer to analyze:

$$\begin{cases} \mu^*_{(z)} = \mu^*_0 \dfrac{h_0 - h_a}{h_0} + \mu^*_1 \dfrac{h_a}{h_0} & \text{for } h_a \le h_0 \text{ (with } h_0 = 6 \text{ m)} \quad (8.11) \\ \mu^*_{(z)} = \mu^*_1 & \text{for } h_a > h_0 \text{ (with } h_0 = 6 \text{ m)} \quad (8.12) \end{cases}$$

To evaluate Equations 8.12 and 8.13, in case of geosynthetic strips, the values of μ^*_0 and μ^*_1 as a function of the soil type presented in Table 8.4 are recommended:

Table 8.4. Apparent coefficient of soil- reinforcement interaction μ^*_{0-1} (NF P 94-270):

		Steel ladders:			Polymeric strips:			
Backfill type [a]:		1 and 2			1	2		3
Gradation [b]:	C_u	$D_{50} \le d_x$ [c]	$D_{50} > d_x$ [c]	C_u	-	D_{70} > 2 mm	D_{70} < 2 mm	-
μ^*_0	>2	$35(d_x / 2s_x)$	$70(d_x / 2s_x)$	≤ 2	1.1		1.0	$\dfrac{\tan\phi}{\tan 36}$
				>2	1.3		1.1	$1.1\left(\dfrac{\tan\phi}{\tan 36}\right)$
μ^*_1		$15(d_x / 2s_x)$	$30(d_x / 2s_x)$	-	$0.9(\tan\phi)$		$0.8(\tan\phi)$	

Notes: [a] Backfill types division according to EN 14475: Type 1: Draining material; Type 2: Granular material; Type 3: Intermediate material.

[b] C_u corresponds to the coefficient of uniformity: $C_u = (D_{60} / D_{10})$.

[c] d_x is the diameter of the transversal bars.

As it can be observed from previous values of μ^*_0 and μ^*_1 (Table 8.4) and Equations 8.11 and 8.12, the resulting values of the apparent soil-reinforcement interaction coefficient ($\mu^*_{(z)}$) returns a bilinear path development as a function of the depth below the top of the wall (i.e., normal stress applied to the reinforcement layer), with an inflexion point at 6 m-depth.

8.3.4.3. Summary between the theoretical development and Codes

After having seen AASHTO (and related Berg et al., 2009) and NF codes with respect to the pullout resistance and its intrinsic parameters, a summary is presented in this section. As it has been observed, the main equation concept development is the same in the codes, with only variations in the parameter's nomenclature and the way of understand the reinforcement-soil interaction. To uniform all expressions, a friction-interaction factor (*f'*) can be defined and a general equation referred to single strip or ladder is obtained:

$$P_r = f'\left(2wL_e'\sigma_v\right) \tag{8.14}$$

Linking *f'* to the analyzed Code's expressions with regards to the parameters used to represent soil-reinforcement interactions, the relations presented in Table 8.5 are obtained.

Figure 8.14 shows the comparison between AASHTO and NF codes with regards to the soil-reinforcement friction-interaction factor to consider in design. To do the comparison, a base case with transversal bars diameter of t(AASHTO) = d_x(NF) = 10 mm and transversal bars separation S_t(AASHTO) = s_x(NF) = 300 mm has been assumed for steel ladders cases; and soil friction angle about 36º with $C_u > 2$ for polymeric strips comparison case.

Table 8.5. Friction-interaction factor (*f'*) definition according to AASHTO and NF:

Code:	friction-interaction factor, *f'*	Comments:
AASHTO	$f' = F^*\alpha$	- Non specified values for polymeric strips, and recommendation on performing specific tests (i.e., Pullout and Direct Shear tests). Approaches can be deduced, with: $0.6 \leq \alpha \leq 1$, and $F^* = 0.67\tan\phi$. - Non specified values for steel ladder neither bar-mat reinforcement types (steel grid bilinear default values to be considered?)
NF	$f' = \mu^*_{(z)}$	- Bilinear performance as per Equations 8.11 and 8.12, and Table 8.4. - NF recommends perform Pullout tests to obtain representative and proper $\mu^*_{(z)}$ values under particular soil conditions and reinforcement system.

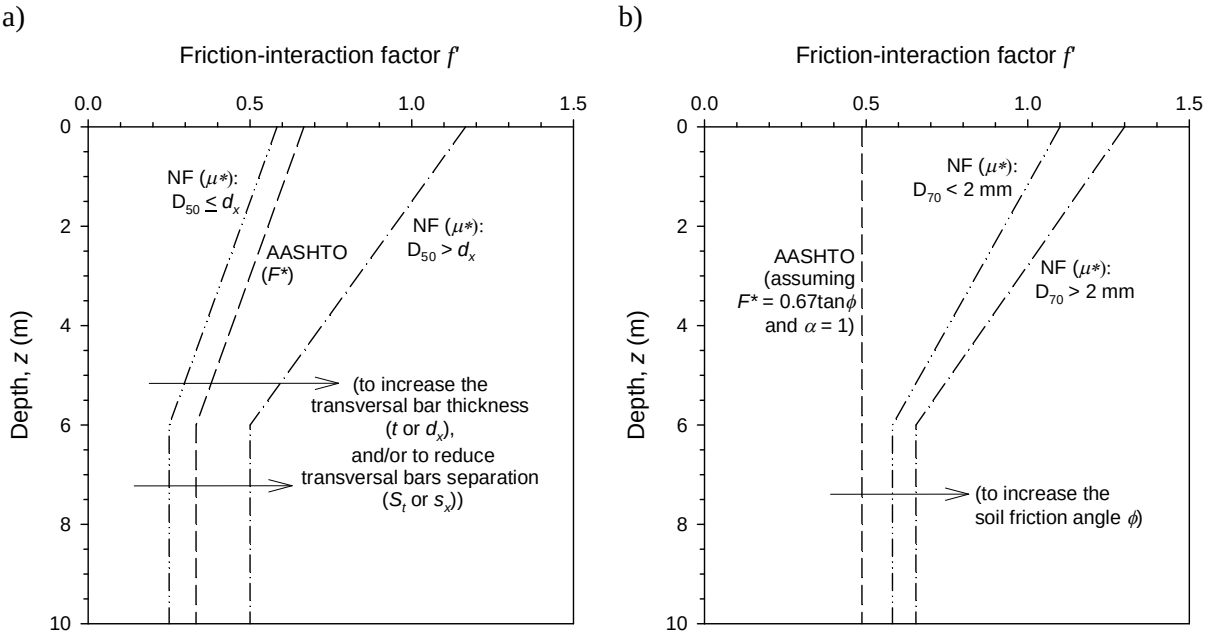

Figure 8.14: Friction-interaction factor (*f'*) according to AASHTO and NF codes adapted to steel strips (a) and polymeric ladders (b) under backfill soil types 1 (draining) and 2 (granular). Notes: in steel ladder case transversal bar thickness and separation assumed to be 10 and 300 mm, respectively; backfill friction angle assumed to be to 36º with soil $C_u > 2$ for polymeric strip case.

As commented, no explicit values of polymeric strips interaction are provided in AASHTO. C_i = (2/3) has been assumed due to AASHTO, however, the soil-reinforcement interaction coefficient (C_i) of the strip, which is controlled by the polyethylene sheath, is normally specified in design codes and confirmed by the strip supplier. Values of $C_i = \tan\delta / \tan\phi$ from 0.7 to 1.5 are typically obtained from pullout tests at different confining pressures. In the absence of test data, C_i values of about 0.7 – 0.8 can be conservatively assumed for polymeric strips (Berg et al., 2009, Lo 1998).

As concluding explanations, it seems clear that, to carry out several pullout testing to reinforcements of a particular system (steel ladders and polymeric strips in this case) under different confining pressures (i.e., performing different depth reinforcement layer locations) and under the same methodology (to uniform the practical stepping procedures and theoretical analyses) is strongly required. After enough tests developed, the obtained data will helps to refine the particular system design with the more accurate fixity of the currently uncertain-default parameter values referred to the soil-reinforcement interaction.

8.3.5. Particular test features and results

8.3.5.1. Steel ladder pullout tests

Series of steel ladder pullout test were performed according to test execution as explained in previous sections. A summary of the obtained results from 36 tests is presented in this section. 12 different soils were considered (i.e., 12 series of tests with different confinement pressures), however, all presented data was obtained from granular fills with friction angles from 31º up to 40º, unit weights from 18.8 up to 22.5 kN/m^3, and $C_u > 2$ in all soils. With regards to the reinforcement elements (i.e., steel ladders), different transversal bar thickness (8 and 12 mm-thick), and transversal bars separation (8 and 150 and 300 mm-thick) were considered, and results are classified accordingly. The obtained data is classified under AASHTO and NF codes, to detect variations with regards to the default code parametrization and actual measured values.

Figures 8.15 and 8.16 presents the measured (from tests) times the calculated (using AASHTO and NF default values, with no inclusion of material resistance nor load factors) friction interaction factors (*f'*; see Table 8.5) under different confinement pressures (i.e., normal stress applied to the testes specimen, or equivalent soil depth *z* from top surface in case of a real MSE wall). This measured/calculated ratio allows to detect agreement between the considered codes and the actual steel ladder pullout behaviour: if this measured/calculated ratio is equal to 1, perfect correspondence is reached; if the ratio is greater than 1 means conservative code values, otherwise tending to lack of safety for ratio lower than 1. Whereas in Figure 8.15 the data is classified with regards to the transversal bar thickness (t or d_x parameters according to AASHTO and NF nomenclature, respectively), in Figure 8.16 the classification is with regards to the transversal bars spacing (S_t or s_x parameters according to AASHTO and NF nomenclature, respectively). As it can be observed, similar trends were obtained, with huge over conservative code design values at low confinement pressures in both transversal bar thickness and separation classification and in both codes. At high confinement the measured/calculated ratio is tending to 1 in all cases, with almost non-values below. However, pullout interaction is not mush relevant at high confinement pressures (e.g., *z*-equivalent greater than 10), as the MSE wall internal design verifications are controlled by the ultimate tensile reinforcement strength at those locations (where the reinforcement resistance zone is already enough for shear strength). As per results obtained from NF comparison, data from soil gradation where the sieve size passing the 50% of soil mass (D_{50}) is lower than the transversal bar thickness (i.e., $D_{50} \leq d_x$) results with a bit greater measured/calculated ratio (i.e., even more conservative) in almost all cases under the same (similar) confinement pressure scenario.

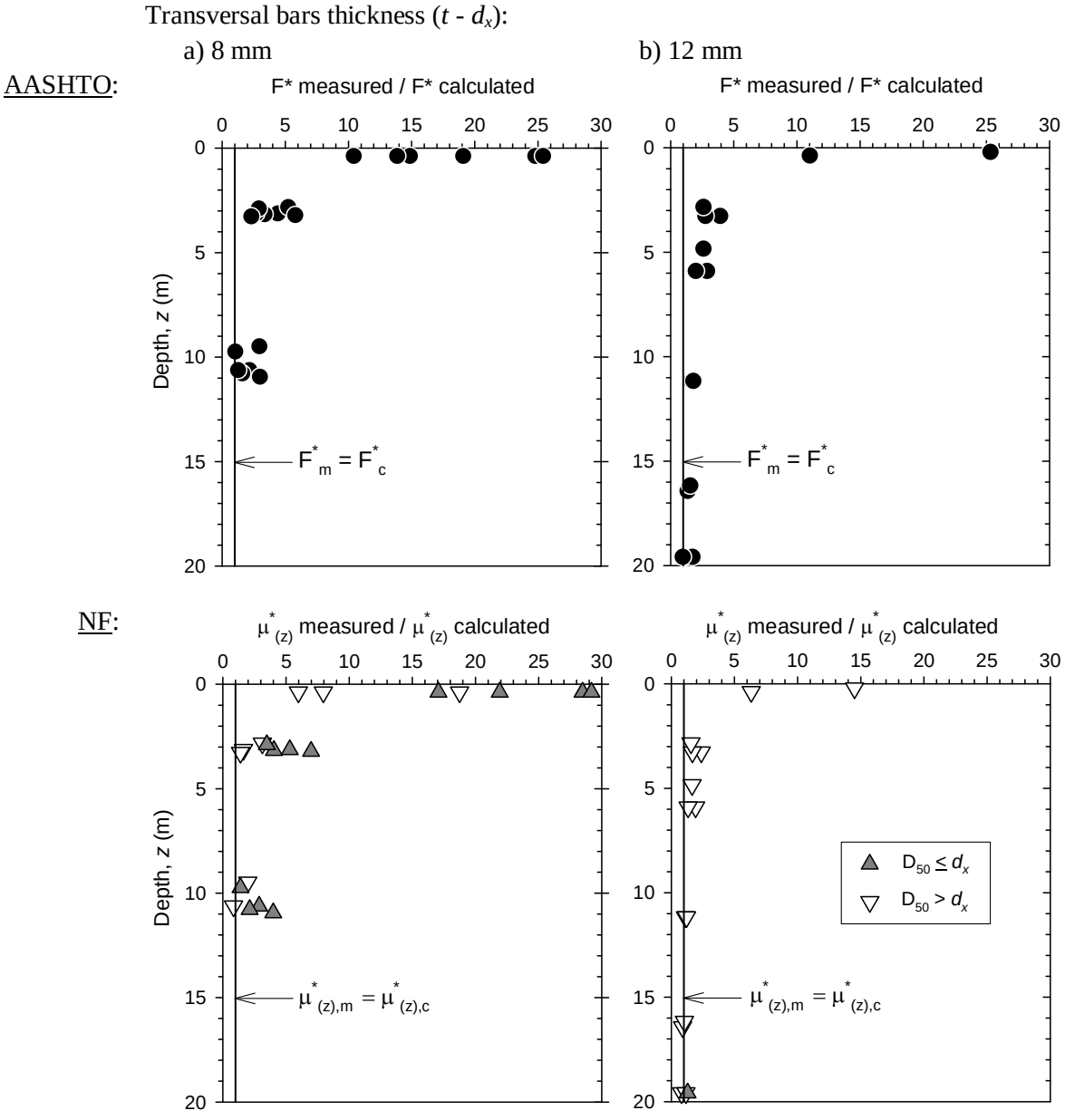

Figure 8.15: Measured/calculated friction-interaction factor (*f*') ratio for pullout steel ladder reinforcement according to AASHTO ($f' = F^*$) and NF ($f' = \mu^*_{(z)}$): transversal bars diameter (t or d_x) equal to 8 mm (a) and 12 mm (b) cases.

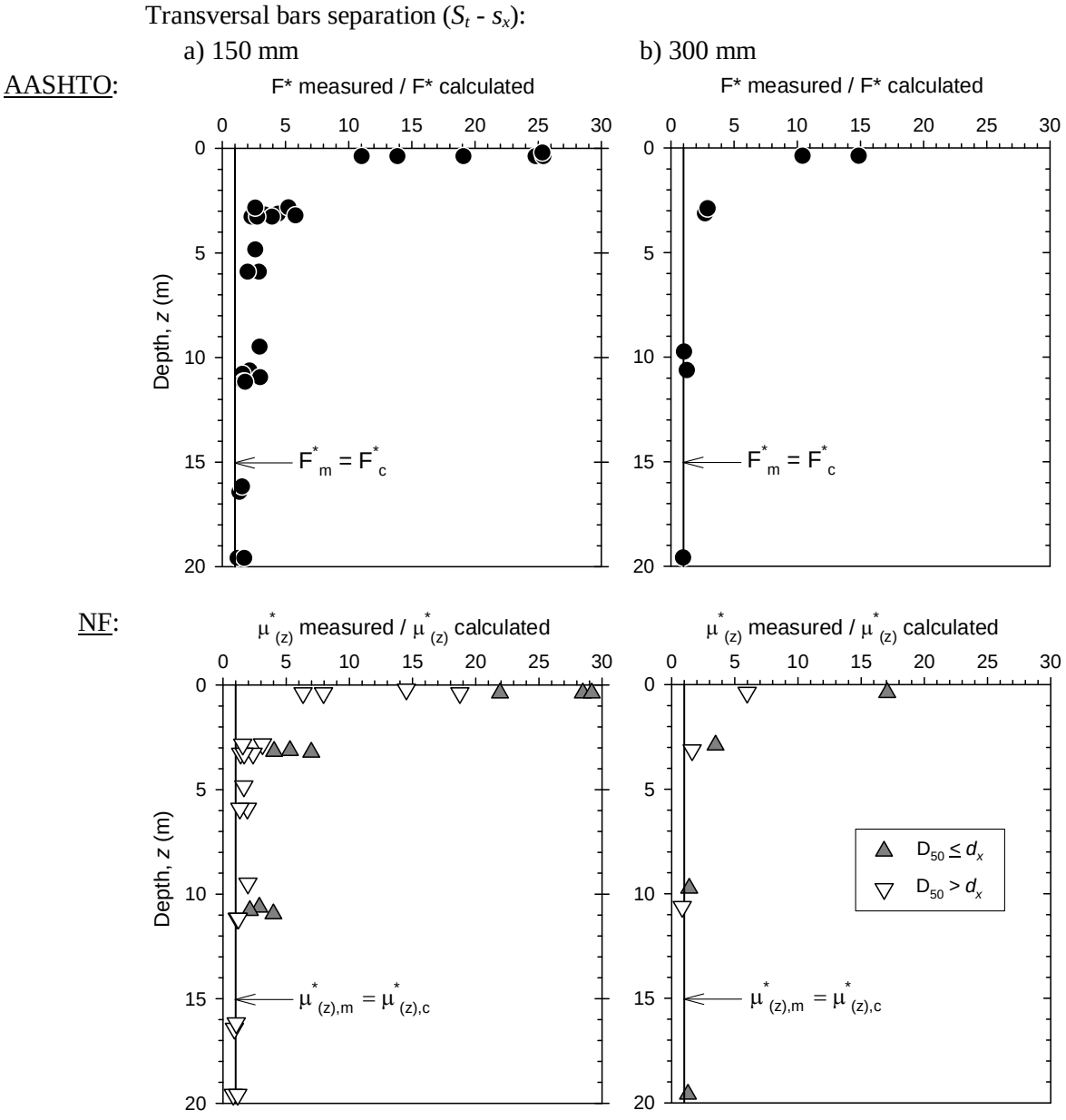

Figure 8.16: Measured/calculated friction-interaction factor (*f*') ratio for pullout steel ladder reinforcement according to AASHTO ($f' = F^*$) and NF ($f' = \mu^*_{(z)}$): transversal bars separation (t or d_x) equal to 150 mm (a) and 300 mm (b) cases.

Calculated against measured pullout friction interaction factor data under logarithmic representation is presented in Figure 8.17. As it can be observed, again, almost all data obtained is above default design codes parametrization (i.e., above the 1:1 line), which derives into conservative default values, more conservative as confining pressure decreases (right-up direction in plots).

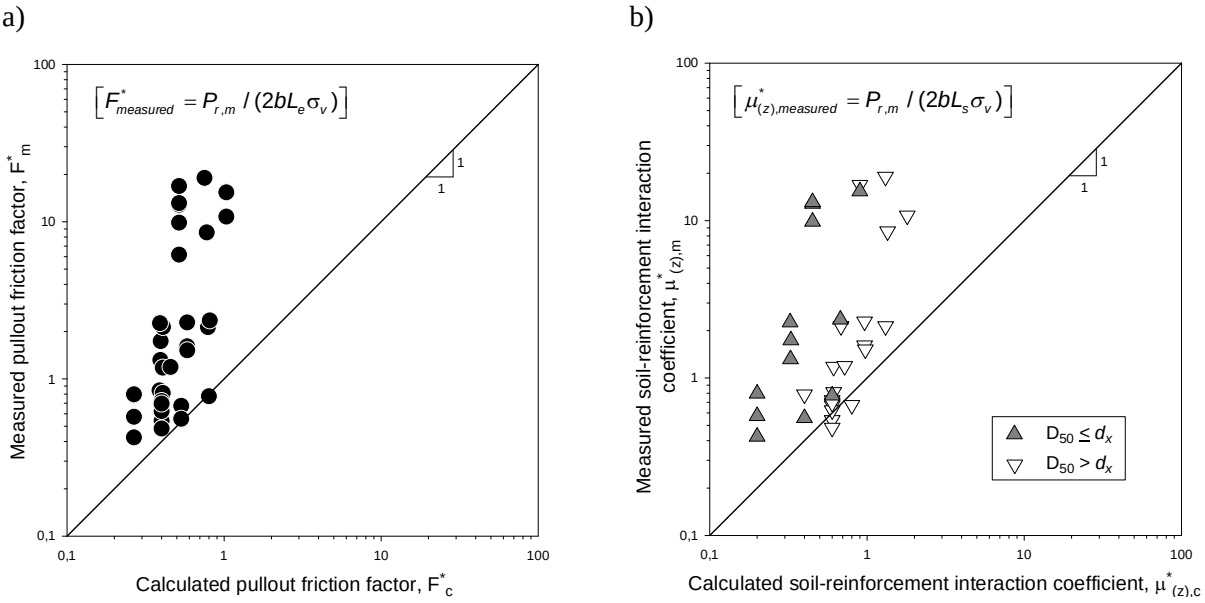

Figure 8.17: Measured/calculated friction-interaction factor (*f'*) ratio for pullout steel ladder reinforcement according to AASHTO (a) and NF (b).

Figure 8.18 presents the ratio between the apparent soil-reinforcement interaction friction angle (δ value, deduced from tests and defined here as $\delta = \tan^{-1}(f')$) and the actual soil friction angle. As it can be observed (Figure 8.18), quite high values of the apparent interaction friction angles were obtained at low confining pressures (even reaching $\delta > 80^o$). This is in agreement with reported values from Ingold (1983), where different steel ladders were tested in $\phi = 35^o$ sandy soil and considerably larger values than ϕ were calculated for the angles of bond stress. This increase of the friction at low normal stresses can be understood as derived from the effects of soil dilation (maybe even because of it only). It can be observed also how the obtained ratio-values trend is decreasing with increasing the normal stress or soil confinement (i.e., equivalent depth). This δ values decreasing effect reaches even lower values of soil friction angle at equivalent locations where *z* is deeper than 10 m. The fact that the rated angles become less than 1 (i.e., $\delta < \phi$) could derive into the understanding of that not only bearing strength capacity is developed in steel ladders-soil interaction (as this should be representative in case of all data with $\delta \geq \phi$), but also frictional (where typically $\delta < \phi$ values are reached, being the soil friction angle the higher boundary of δ values).

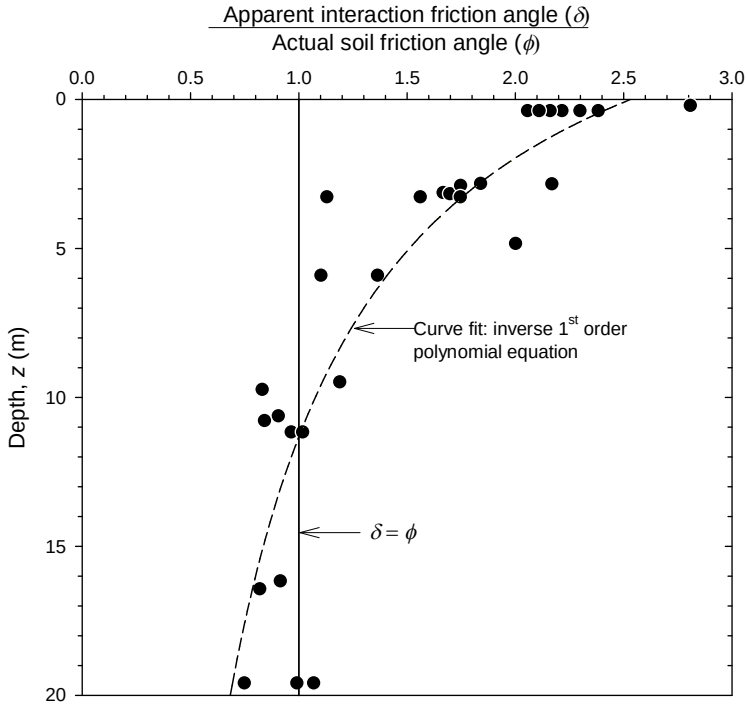

Figure 8.18: Ratio between the obtained apparent pullout interaction friction angle (δ) and the actual soil friction angle (ϕ) of the pullout test soil-fills.

Similarly to Figure 8.17, Figure 8.19 presents the measured against AASHTO-calculated pullout capacity (P_r) under logarithmic representation of all the tested data (36 points). As it can be clearly observed, again, at low confinement pressures the overestimation is significantly increasing. The same data can be plotted within all steel-bar-mat pullout tests data obtained from bibliography (data collected by Yu and Bathurst 2015, with a total of 356 pullout tests; see Figure 8.19a). Apart from the different confinement, no much distinction is obtained between the current data presented and the data obtained by Jayawickrama et al., (2013) (grey points).

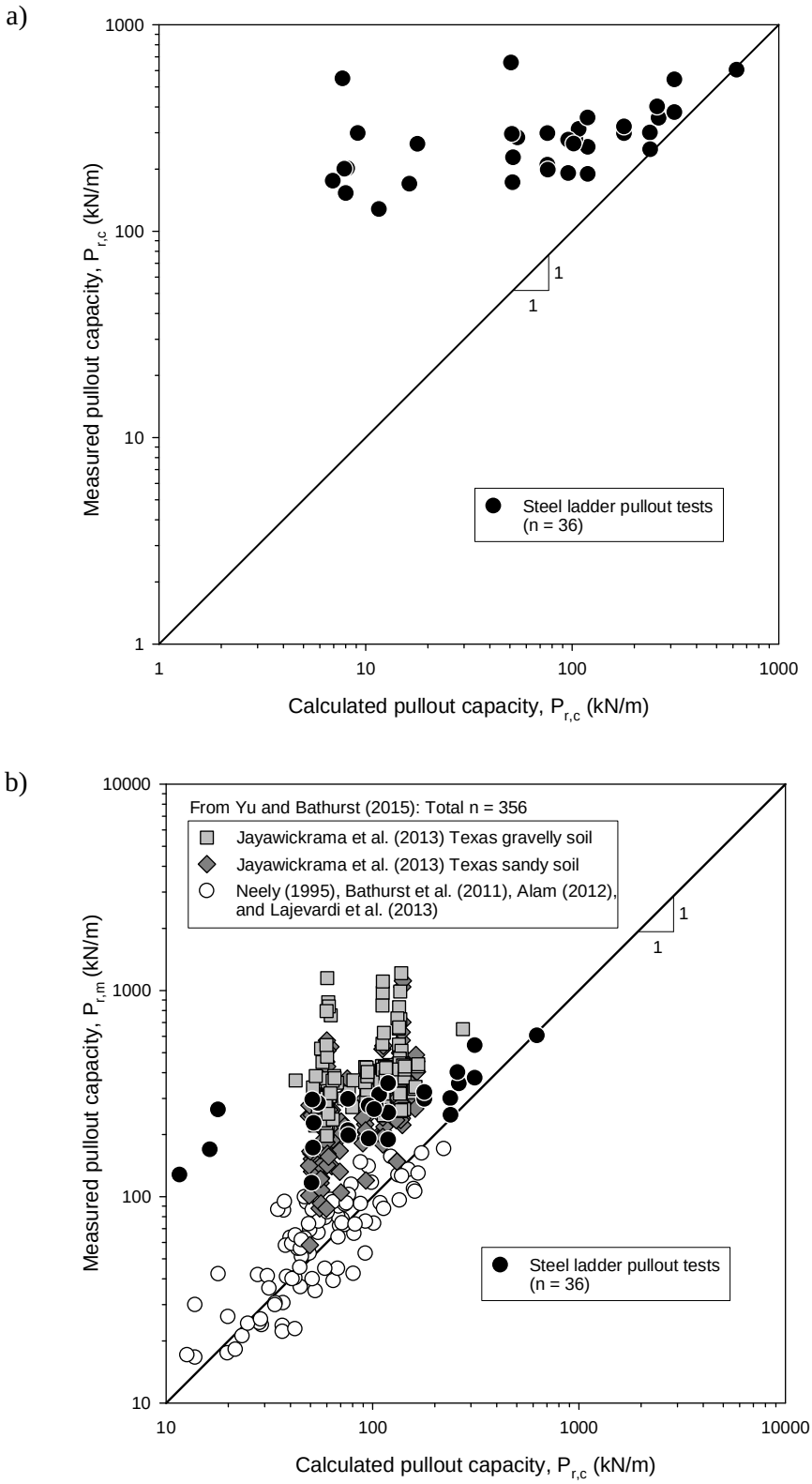

Figure 8.19: Measured/calculated pullout strength capacity (P_r) according to AASHTO: summary of steel ladder reinforcement tests (a) and comparison with other bar-mat reported cases (b; adapted from Yu and Bathurst 2015).

A particular steel ladder pullout test case is presented as example. The material parameters are summarized in Table 8.6. Fill soil material corresponds to a well-graded gravely sand, and resulting gradation curve is as in Figure 8.20.

Table 8.6. Steel ladder pullout test parameters:

Materials:	Parameters (and units)	Values:
Fill soil: Gravely sand (GW)	Unit density, γ (kN/m^3)	19.7
	Friction angle, ϕ (degrees) [(a)]	41
	Cohesion, c (kPa) [(a)]	0.5
	Sieve size passing 50% of soil, D_{50} (mm)	5 - 6
	Coefficient of uniformity, C_u (-)	40
	Coefficient of curvature, C_c (-)	1.81
	Plasticity index, PI (-)	0
Steel ladder	Transversal bar diameters (mm)	8
	Transversal bars separation (mm)	300
	Length, L_e (mm)	1.05
	Width, w (mm)	168

Note: [(a)] From direct shear tests

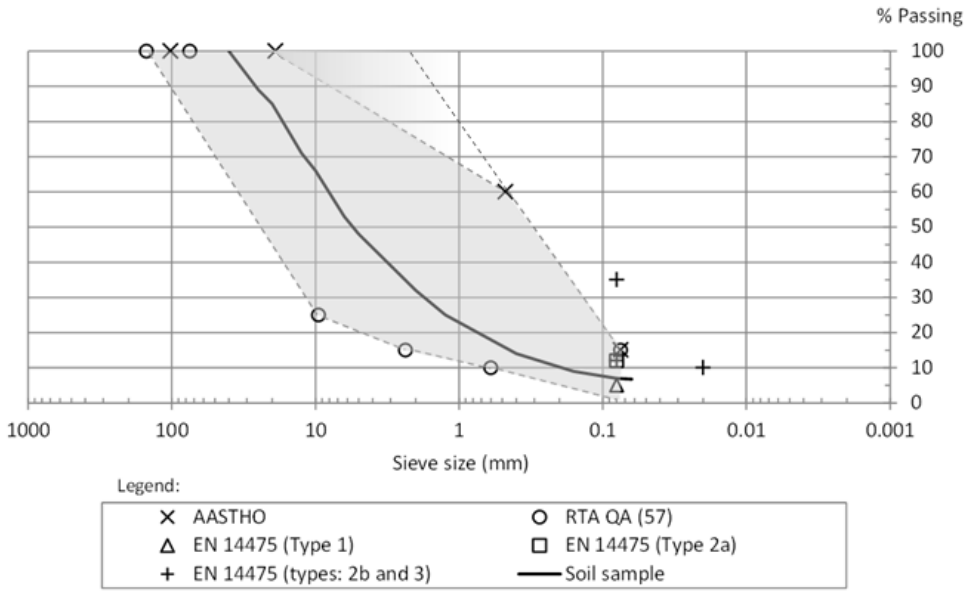

Figure 8.20: Fill soil gradation used for steel ladder pullout tests.

Results from pullout tests (i.e., measured pullout capacity against reinforcement displacement monitored at the front clamp) are presented in Figure 8.21. Three different normal stresses

were considered, performing different theoretical reinforcement depth locations: *z*-equivalent = 0.375 m, 3.10 m, and 10.625 m-depth. Data is presented up to peak pullout test was reached, with no clear peak obtained (i.e., no sudden loss of strength capacity after peak, so horizontal fluent failure after the maximum pullout value in 0.375 and 10.625 m-depth cases). With fixing pullout as the strength capacity obtained at 15 mm-displacement, values of 34.0 kN, 38.3 kN, and 43.0 kN were reached for 0.375 m, 3.10 m, and 10.625 m of equivalent depth scenarios, respectively.

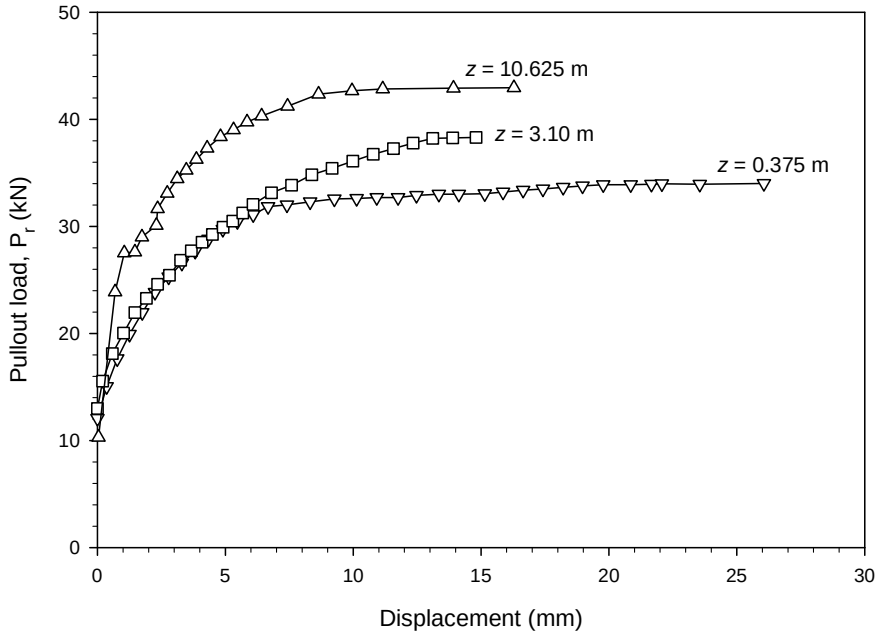

Figure 8.21: Steel ladders pullout test results: pullout load vs displacement.

From the obtained data, friction interaction factor (*f*`) can be measured at the three different confining pressures. Figure 8.22 presents both measured and AASHTO-calculated factors. As observed, quite greater values were obtained at low confining pressures, demonstrating over conservative default values assuming AASHTO steel grid classification (as no particular mention to steel ladder is given in AASHTO). Values of $f' = 0.57$, $f' = 1.7$, and $f' = 12.5$ were reached for $z_{eq.} = 0.375$ m, $z_{eq.} = 3.10$ m, and $z_{eq.} = 10.625$ m-depth scenarios, respectively. In case of friction interaction factor relation to the fill-soil friction (i.e., as $f' = \tan\delta = C_i \tan\phi_{soil}$), the apparent soil-reinforcement interaction friction angles obtained are $\delta = 29.7^o$ ($C_i = 0.66$) for $z_{eq.} = 10.625$ m, $\delta = 59.5^o$ ($C_i = 1.96$) for $z_{eq.} = 3.10$ m, and $\delta = 85.4^o$ ($C_i = 14.38$) for $z_{eq.} = 0.375$ m.

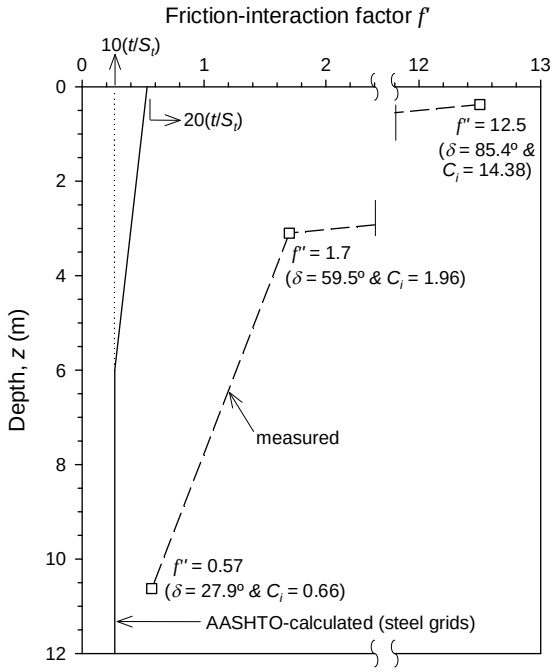

Figure 8.22: Friction interaction factor (*f'*) for steel ladders pullout tests: AASHTO default values (steel grids actually) and measured from performed tests. (Note: $f' = F^*\alpha = F^*$, as $\alpha = 1$ in inextensible reinforcement types).

8.3.5.2. Polymeric strip pullout test

Polymeric strip pullout tests were carried out at three different normal stresses and results presented in this section. The material parameters are summarized in Table 8.7. Fill soil material corresponds to a low plasticity silty sand, and resulting gradation curve is as in Figure 8.23. As it can be noticed, soil does not properly satisfy the parametrization required as presented in previous Tables 8.1 and 8.2, neither soil gradation is fitted within the gradation area (draining and granular fill types). However, the fill soil fails into Type 3 – intermediate fill as per EN 14475 (2011) fine soil gradation and *PI* features so it could be suitable if pullout tests results in a good soil-reinforcement interaction performance (see Table 8.2 – Note [(b)]). It should be also noticed also that some value of cohesion was obtained in direct shear tests.

Table 8.7. Polymeric strip pullout test parameters:

Materials:	Parameters (and units)	Values:
Fill soil: Low plasticity silty sand (SM(L))	Unit density, γ (kN/m^3)	21
	Friction angle, ϕ (degrees) [(a)]	31.4
	Cohesion, c (kPa) [(a)]	14
	Sieve size passing 50% of soil, D_{50} (mm)	3 - 4
	Coefficient of uniformity, C_u (-)	~700
	Coefficient of curvature, C_c (-)	0.275
	Plasticity index, PI (-)	6.6
Polymeric strip	Grade (short-term strength: kN)	70
	Width, w (mm)	90

Note: [(a)] From direct shear tests

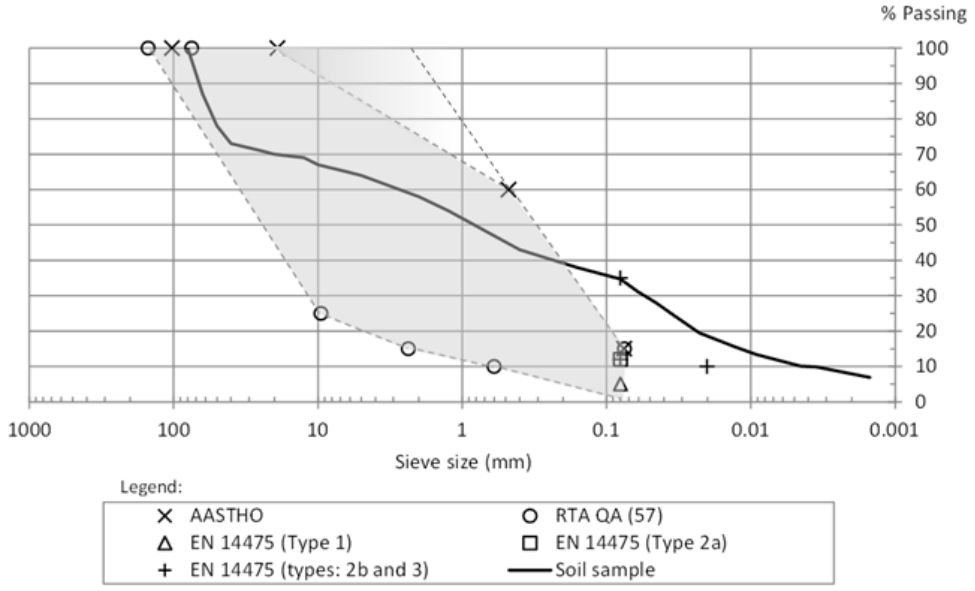

Figure 8.23: Fill soil gradation used for polymeric strip pullout tests. (Note: fine particles gradation obtained by sedimentation (Casagrande densimeter method)).

Figures 8.24 and 8.25 present the results from polymeric strip pullout tests. Measured pullout capacity against reinforcement displacement monitored at both front and real clamps are presented in Figure 8.24, while displacements evolution in both clamps are presented in Figure 8.25 to identify extensibility behaviour of the strips. As in previous case, three different normal stresses were considered, performing different theoretical reinforcement depth locations: *z*-equivalent = 1 m, 3.6 m and 7.0 m-depth. Data is presented up to peak pullout test was reached, obtaining pullout strength values of 2.57 kN, 6.09 kN, and 9.46 kN for 1.0 m, 3.5 m, and 7.0 m of equivalent depth scenarios, respectively.

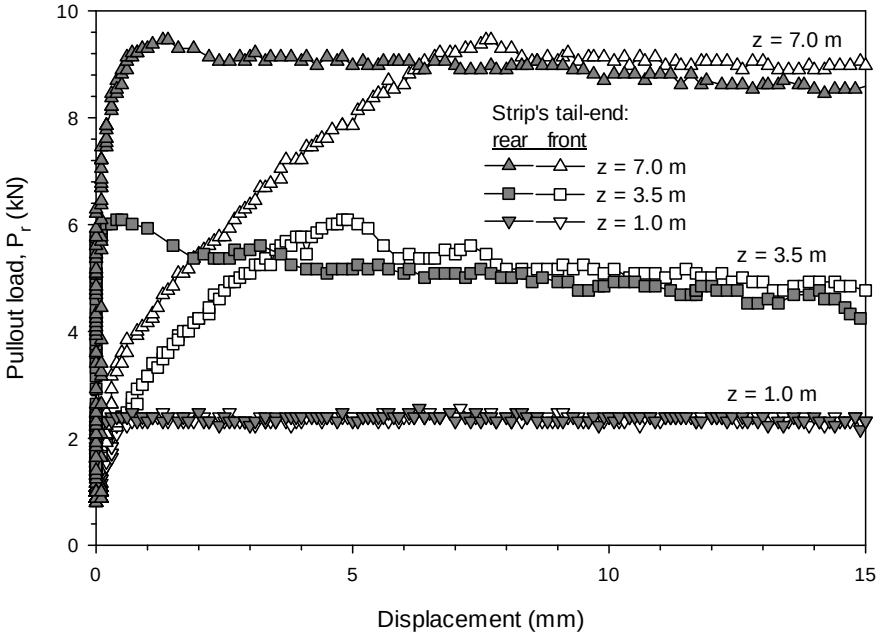

Figure 8.24: Polymeric strips pullout test results: pullout load vs displacement.

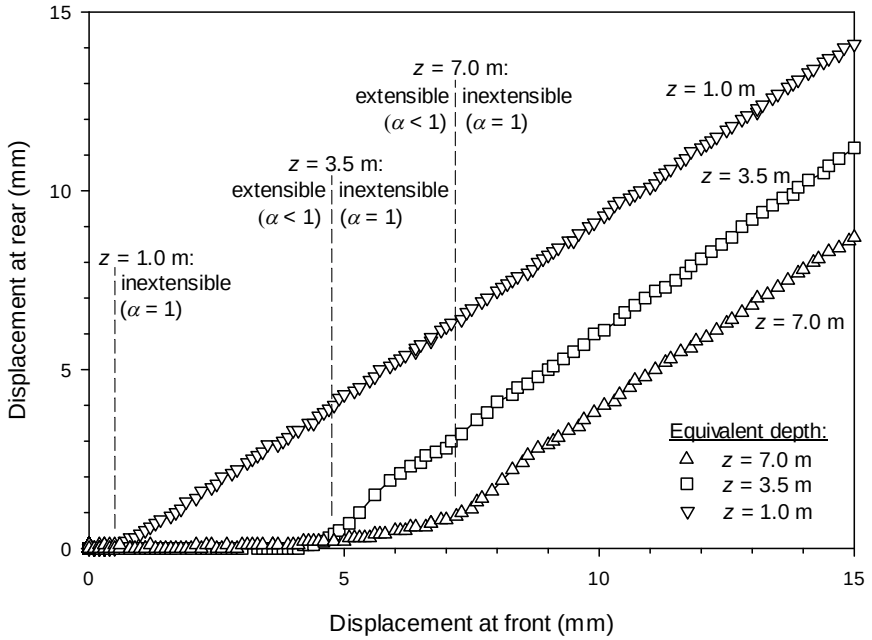

Figure 8.25: Polymeric strips pullout test results: front-rear displacements comparison.

From the obtained data, friction interaction factor (*f*`) can be measured at the three different confining pressures (see Figure 8.26a). The scale effect correction factor α, which relates to the reinforcement extensibility, must be assumed. As it can be observed, α values of about 0.8

to 1 can be assumed for polymeric strips reinforcement, regarding soil confining scenarios. Alternatively, Figure 8.26b presents both measured and AASHTO-calculated factors. As observed, first, not straight linear values were obtained, and second, clearly greater values at low confining pressures were reached, demonstrating over conservative default values assuming AASHTO with $F^* = 0.4$ at these locations (corresponding to geotextile and geogrid reinforcement types; see Figure 8.13). It must be remained that non explicit F^* values are given in AASHTO for polymeric strip reinforcements. However, $F^* = 0.4$ value appeared to be in agreement under at confining scenarios with equivalent depth greater than 5 m (i.e., $z_{eq.}$>5 m).

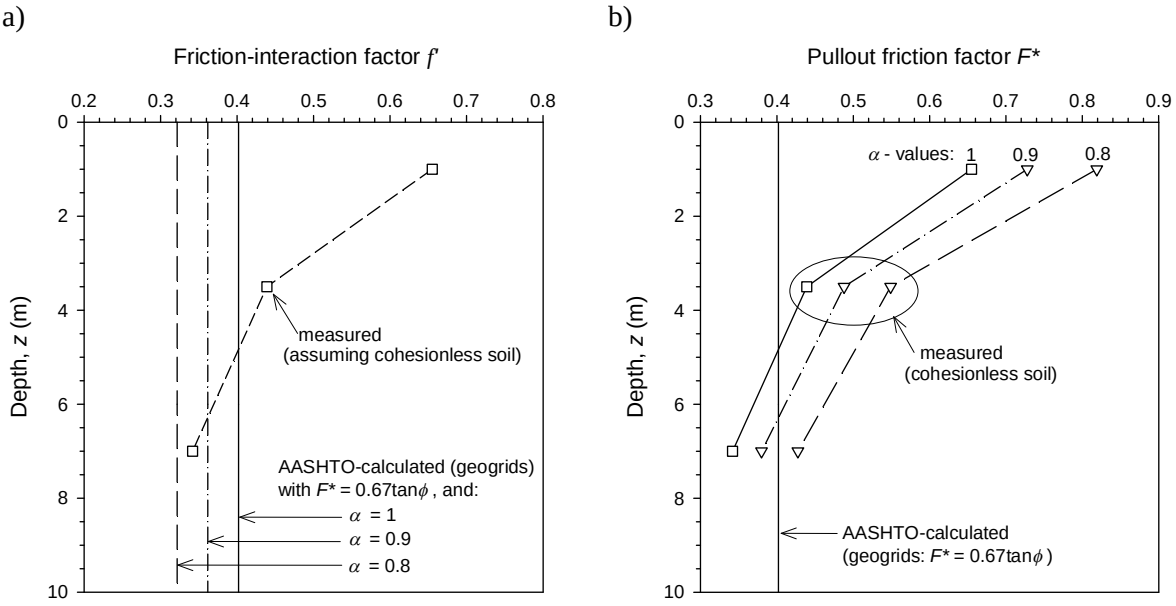

Figure 8.26: Calculated and measured comparison of friction interaction factor ($f' = \alpha F^*$) (a) and AASHTO pullout friction factor (F^*) (b) for polymeric strips pullout tests.

8.4. NUMERICAL 3D MODEL

A 3D model with CODE_BRIGHT program (Olivella et al., 1996) was generated to analyze pullout tests. As in previous Chapter methodology, soil-reinforcement interaction was modelled with assuming a certain thickness of material from continuum media. A base case is first defined, which considers common strength-stiffness features for a regular soil to be used in MSE wall structures. Results from several parametrical sensitivity analysis with regards to base case are then presented. Finally, a calibration was done with regards to two real monitored pullout tests, one with steel ladder and other with polymeric strip.

8.4.1. Model features

8.4.1.1. General

Figure 8.27 shows the finite element 3D model pullout box geometry developed. As detailed, box has 0.75 m-high, 0.50 m-width, and 1.25 m-length. 200 mm-length of rigid sleeves were generated at the frontal box opening (see Figure 8.27e), with proper displacement fixities (as detailed below). The reinforcement had, in all cases of analysis, strip's dimension with 50 mm-width, 5 mm-thick, and 1050 mm-length of analysis (i.e., L_e from previous Equations development). As in previous Chapter 7 (soil-facing interaction performance), also here the reinforcement-backfill interface was modeled by a certain thickness of continuum elements surrounding the reinforcement strip with 50 mm-thick on both lateral and vertical sides (global cross-section dimensions of 105 mm-high × 150 mm-width; see Figure 8.27f).

The finite element 3D model structured-mesh considered for the analyses had a total of 3276 nodes corresponding to 2838 (tri)linear hexahedron -or brick- elements with selective integration, disposed as:

- Backfill: (6×4)(above and below) × (4×5)(laterals) × 11(length)
- Interface: (6×7)(above and below) × (7×5)(laterals) × 10(length)
- Reinforcement: 5(high) × 6(width) × 11(length)

These number-of-element dimensions correspond to an optimal performance dimensions after several tests carried out to obtain an asymptotic pullout results from coarse mesh (exploitation: premature convergence) to very fine mesh (exploration: higher computational cost). Some example results from this calibration analysis with regards to meshing size are presented later (see Section 8.4.2.1, within base case first results).

The full pullout calculation process generated takes three stages or intervals:

- 1st interval: the first one corresponds to an initial equilibrium state (calculation time steps from 0 to 10).

- 2nd interval: the second one corresponds to the confining pressure scenario with a vertical surcharge application at top of the box (ramp loading; steps from 0 to 11).
- 3rd interval: the third one is the application of the pullout load (steps from 11 to 12).

The pullout was performed by prescribing a constant velocity-displacement of 2×10^{-6} m/s at the front of the reinforcement strip at the beginning of the third stage (i.e., step 11), which generates 17.28 cm of pullout displacement at the end of the stage (i.e., at the end of the step 12). A 52.5 kPa-surcharge loading ($\Delta\sigma_v$) were assumed at the top boundary, performing an equivalent reinforcement depth location of z = 3 m. Thus, theoretical total vertical surcharge of $\sigma_{v(total)}$ = 60 kPa acting at the reinforcement sample, as reinforcement is placed at the middle height of the box (i.e., at 0.375 depth from top boundary) and soil fill unit weight was assumed to be 20 kN/m^3 (see next section 8.4.1.2 and Table 8.8).

With regards to the remaining boundary conditions (i.e., box sides), displacements in the orthogonal directions are not allowed, with the exception of the top-horizontal surface (to apply vertical surcharge). The interface areas at front and back surfaces have also prescribed displacement at the orthogonal directions at the first and second intervals (i.e., steps from 0 to 11), but non-prescribed displacement conditions when pullout (third interval). As mentioned, the reinforcement has the prescribed pullout displacement at the front, but free-end displacement at the back.

8.4.1.2. Materials: Base case parameters

The reinforcement material was modeled as a linear elastic material, which is a good assumption for steel reinforcements (e.g., steel strips or ladders) and probably also for actual polymeric strips. Soil materials (i.e., the fill soil and the soil-reinforcement interface materials) were modeled by a linear elastic stiffness (Young's modulus and Poisson's ratio parameters) with elastic-plastic law at strength-failure (controlled by the cohesion, friction angle, and dilatancy angle). As mentioned in previous Chapter, soil-reinforcement interface material was modelled with assuming an average value of M in both soil-facing and soil-structure interface definition (see Section 7.3.4.1).

Table 8.8 presents the constitutive model material parameters assumed for the Base case. The parameter's values correspond to a steel strip pullout performed in a regular granular fill soil material, with strength/stiffness values in agreement with the reinforced backfill material reported in Runser (1999) already performed numerically in Chapters 2 and 4. Obtained results from the triaxial tests modelled are presented in Figure 8.28. As can be observed, quite good agreement was obtained between the numerically calculated and measured stress-strain performance at different confining pressures.

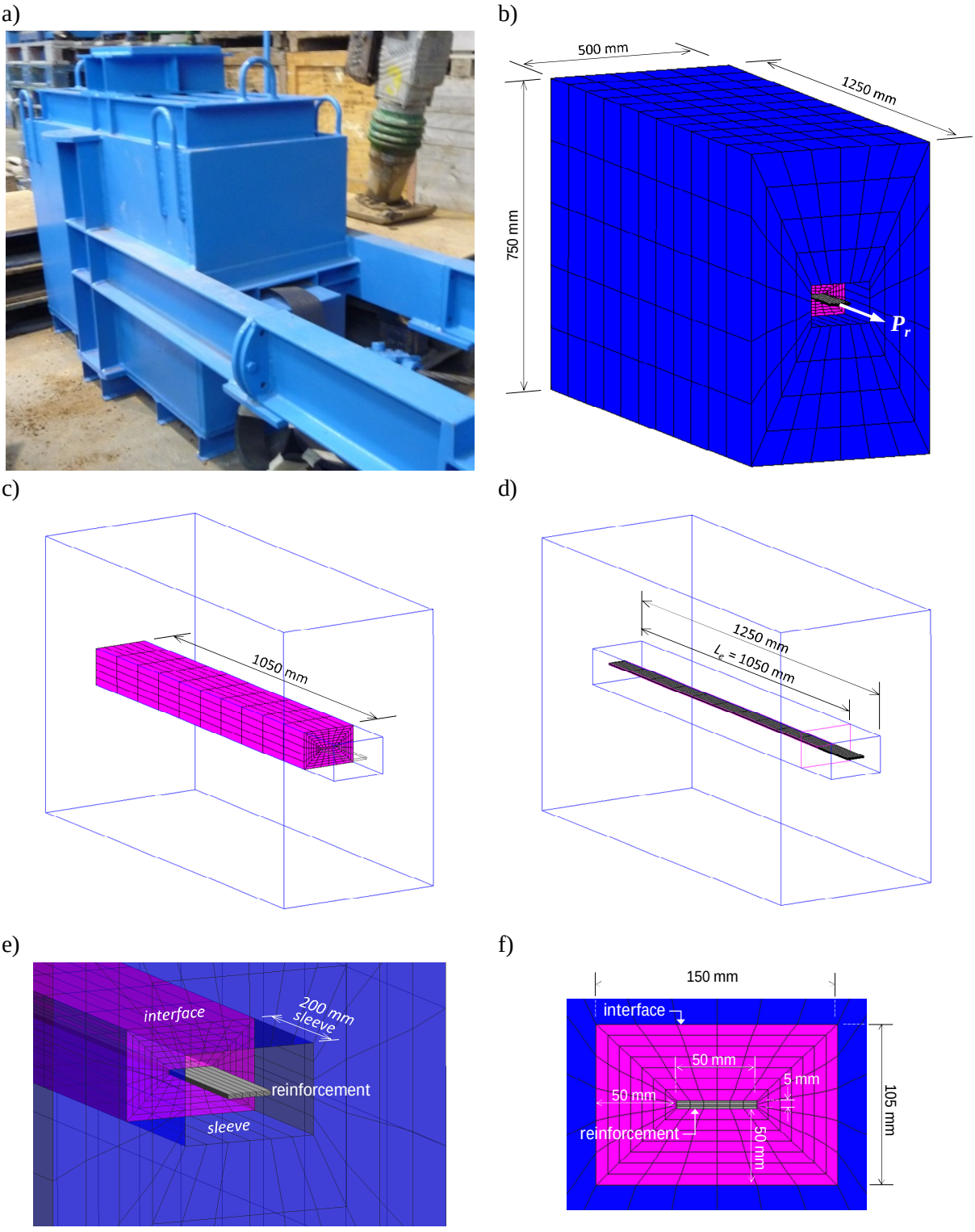

Figure 8.27: Pullout box: real pullout box (a) and 3D model mesh and geometry dimensions (b); interface material (c) and reinforcement (d); front box opening detail (e) and interface frontal view (f).

Table 8.8. Material parameters for Pullout Base case:

Parameters:	Materials:		
	Reinforcement	Fill soil	Interface
Unit weight, γ_n (kN/m^3)	75	20	
Elastic stiffness modulus, E (MPa)	210 000	20	
Poisson's ratio, v (-)	0.3	0.3	0.45 [(a)]
Cohesion, c (kPa)	-	1	1
Friction angle, ϕ and δ (deg.)	-	ϕ_s = 38	δ = 28.7 [(b)]
Dilatancy angle, ψ (deg.)	-	8 [(c)]	8 [(d)]

Notes: [(a)] Despite Poisson's ratio demonstrated to have no much significant effect on pullout capacity, higher v-value (i.e., v_i = 0.45) was considered to best fit pullout capacity under high vertical pressure cases to mobilize confinement (i.e., to increase mean stress p-invariant) and reduce unrealistic volumetric interface plasticization.

[(b)] δ = 28.8º ($=\phi_i$) is equivalent to an interface reduction factor of R_i = tanδ/tanϕ = 0.7, which corresponds to an AASHTO pullout friction factor (F^*) equal to tanδ = tan(28.7º) = 0.55 (i.e., F^* = tanδ = $R_i$tanϕ = 0.7tan38º = 0.55).

[(c)] Dilatancy angle assumed as $\psi = \phi_s - 30$º.

[(d)] Interface dilatancy angle assumed as equal to fill-soil dilatancy angle.

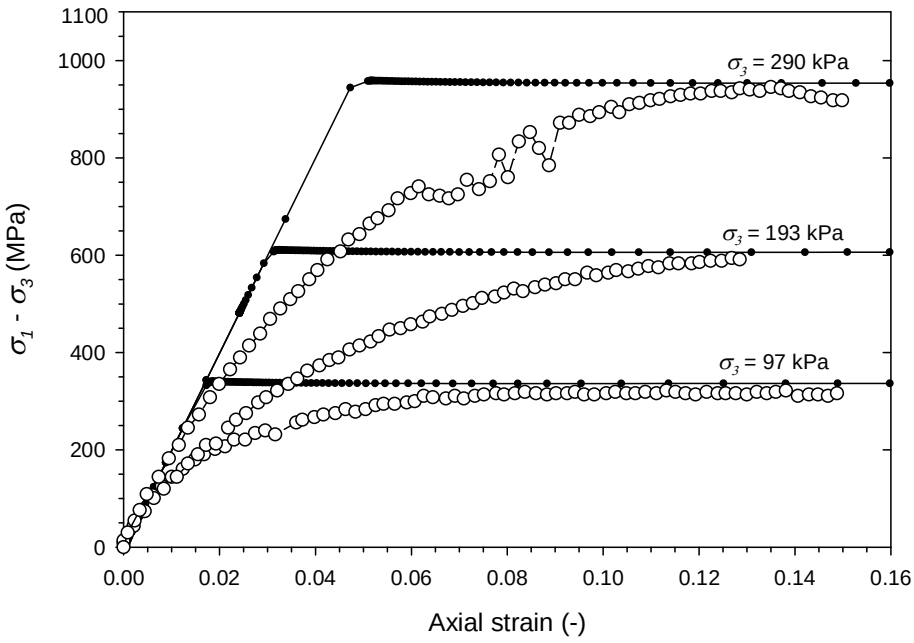

Figure 8.28: Real and Base case model soil triaxial tests behaviour at different confining pressures. (Note: real triaxial soil data as in Chapter 3, adapted from Runser 1999).

8.4.2. First results

8.4.2.1. Base case

Results of the Base case (E_r = 210 GPa, $E_s = E_i$ = 20 MPa, ϕ_s = 38º, δ = 29º (=ϕ_i); see Table 8.8) are presented in this section. Figure 8.29 presents the results of the global geometry deformation at the end of pullout performance ($\Delta d_{Pullout}$ = 173 mm-displacement reached). Different pictures are plotted with-without considering meshing detail and materials transparency. Reinforcement became extruded from interface material, and, as it can be observed, pullout displacements generate significant upwards vertical displacements due to soil-dilatancy effects. This effect becomes more significant at head-frontal edge of the reinforcement due to the boundary conditions of prescribed displacements, but it is not caused by the axial strains of the reinforcement (which can be assumed as inextensible).

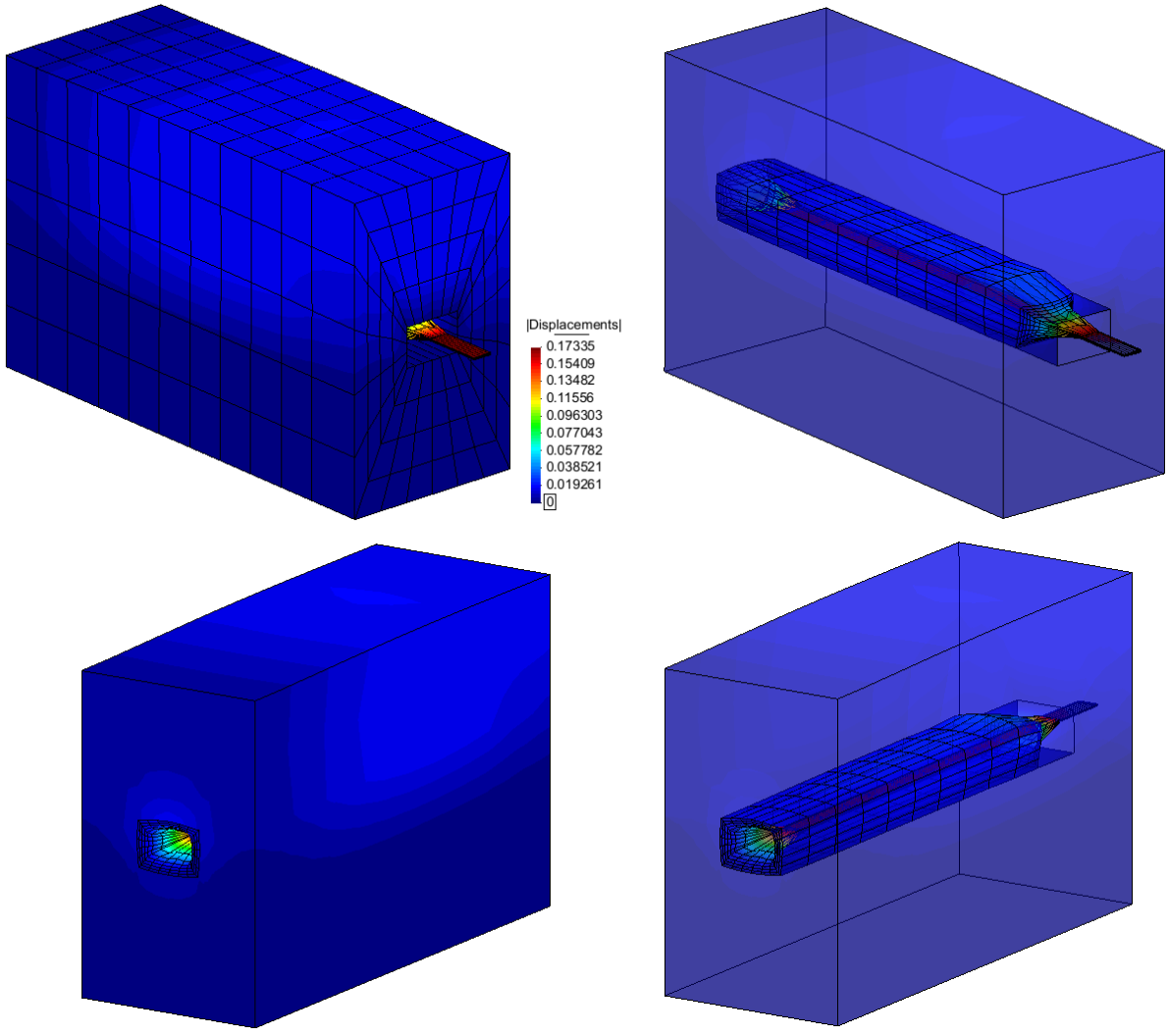

Figure 8.29: Base case total displacements and global model deformation (real scale).

The pullout load evolution with regards to the head horizontal displacement results is presented in Figure 9.30. As expected and observed from real tests, load strength is increasing up to a certain level of axial displacements, in where soil-reinforcement reaches failure (at about $\Delta d_{Pullout}$ = 3 mm-displacement), and then, reinforcement pullout displacement progresses with almost no changes of strength (plastic regime). Indeed, there is strength increasing due to dilatancy, as has been considered with a fixed-perpetual value in the model. A positive dilatancy angle implies that in drained conditions the soil will continue to dilate as long as shear deformation happens. This is not much realistic as typically soils reach a critical dilatant state at some point and further shear deformation will occur without volume changes. However, dilatancy has a main influence in actual soil-reinforcement interaction under shear loading and, even without having the soil model a critical state cap for dilatant conditions, realistic effects were expected for the displacement range assumed.

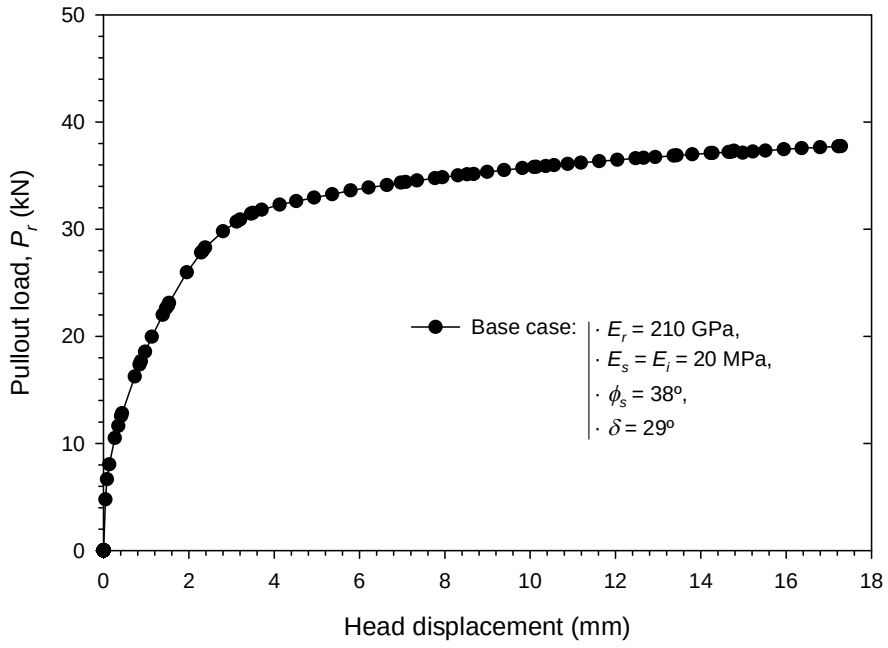

Figure 8.30: Base case reinforcement pullout load – axial displacement response.

Example pullout trends from sensitivity of the finite element meshing analysis are presented in Figures 8.31 and 8.32. Different finite element meshing refinement criteria were considered at interface material definition (with assuming the same structured and hexahedron element features), which corresponds to the number of elements within the interface thickness (i.e., number of elements between the reinforcement and the backfill). Also different cases with different number of elements at the whole 3D model were considered (i.e., soil thickness above/below and lateral sides of the reinforcement, and also

the number of elements defining the reinforcement length), which is related to a certain meshing proportion with regards to the interface meshing refinement processes previously stated. As example, an additional case with linear tetrahedron structured mesh is plotted, generated with an interface composed by 3-6 elements (depending of the crossing line location). Linear tetrahedron elements may not be as accurate as the trilinear hexahedra ones if large shear strains are performed. However, the obtained results with structured mesh demonstrate fairly good agreement between element type alternatives at initial stages of stress-strain (in the example trend plotted: pullout stiffness at head displacements less than 3 mm). These elements may be required for complex geometries under particular conditions (i.e., low shear strains development) with feasible and confidence results. As it will be explained in next Chapter, this elements type were required to reach numerical convergence in case of entire reinforced soil wall finite element 3D models performance (as the trilinear hexahedra became complicated and somehow inconvenient to work on in cases where elastic-plastic soil models and staged construction were required).

As it can be observed in Figure 8.31, in case of pullout-displacement test evolution, clear trending improvement can be reached with meshing refinement from a single interface element case up to 10 interface elements case, with reducing the pullout strength capacity asymptotically. About 35% load reduction was obtained from the worst case (1 element: $P_r \approx$ 54 kN) up to the best and asymptotic case (10 elements: $P_r \approx 37$ kN)). However, as expected, different computation times were required (from about 1 hour in the fastest case, up to 37 hours in the slowest case), logically inversely proportional to the results improvement or interface meshing refinement. Figure 8.32a presents the computational time results (CPU time) of the different meshing refinement sensitivity cases analyzed (Note that the refinement meshing criteria specified in the figure is referred to the whole model meshing apart from the interface material 1-10 elements definition). As it can be observed, different times are obtained, significantly increasing with mesh refinement and becoming somehow unworkable (unacceptable waiting times). Alternatively, Figure 8.32b presents the comparison between both mesh refinement cases. Similar trends are obtained between both cases, but significant less accuracy in coarse mesh cases (i.e., greater pullout strength values). As mentioned above, this “coarse” status is referring to the meshing refinement at backfill and reinforcement materials in vertical and both horizontal directions, which derives into a more proportional mesh as the interface thickness is defined with more elements.

Finally, as commented in Section 8.4.1.1, the 7 interface thickness elements case was the reference and Base case selected to the further tests in this Chapter (hexahedron elements - structured mesh). This case was considered to be the best performance case, optimizing the computer time (CPU time) and with good agreement in terms of the asymptotic pullout value case (most refined mesh case, with higher CPU time).

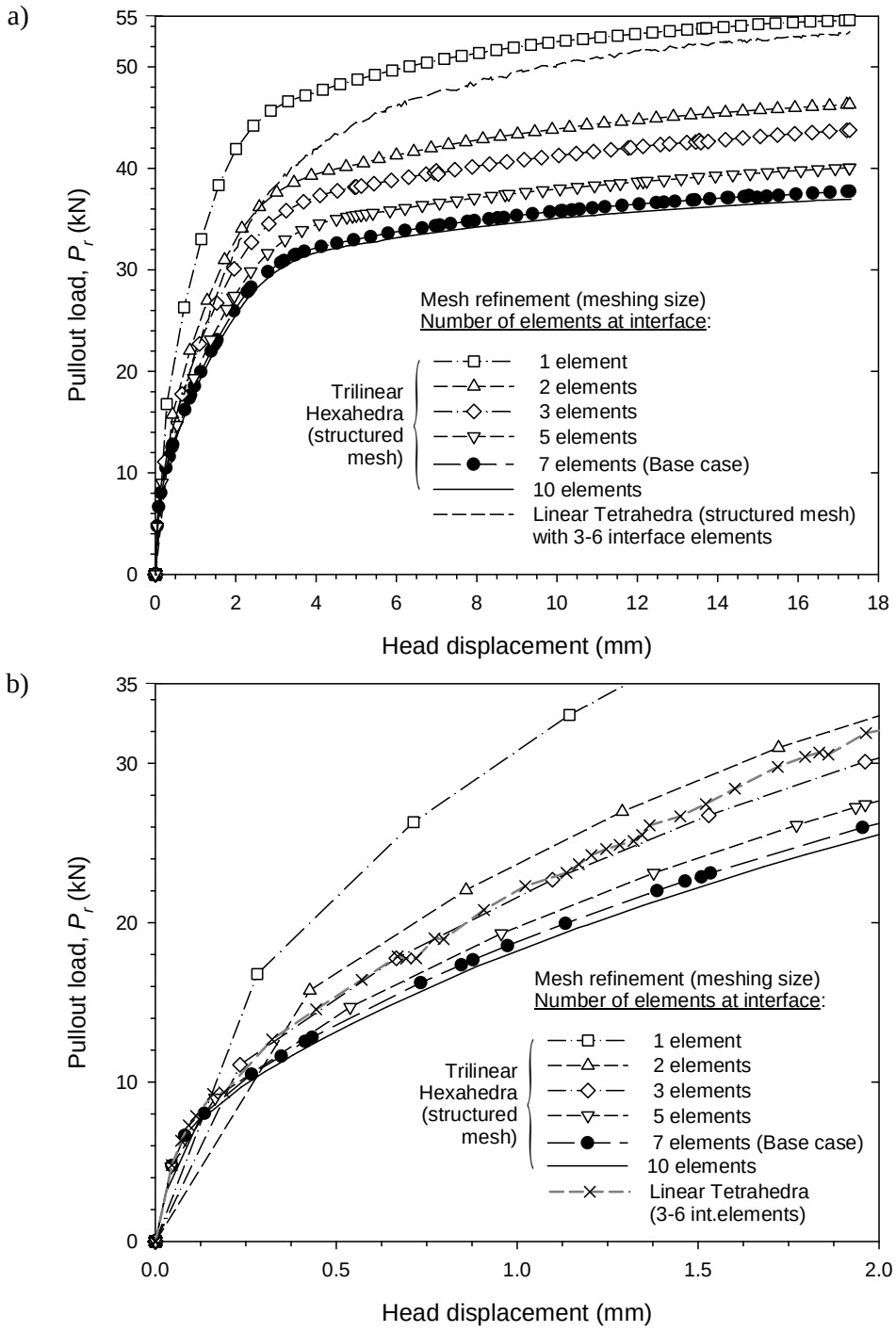

Figure 8.31: Reinforcement pullout load – axial displacement response with regards to the interface material finite element mesh refinement.

Again with the optimized mesh base case (number of elements as listed in Section 8.4.1.1; which are the meshing features followed for all the cases in following analysis), results of the vertical displacements of backfill and interface materials at different time-steps can be observed in Figures 8.33. As it can be observed and already commented, positive-upward displacements are generated during pullout. These displacements (positive → upwards,

negative → downwards) are more relevant within the interface due to the greater shear strains in soil-reinforcement interaction, and near the prescribed boundary conditions assumed on frontal opening sleeves. The displacements within the soil decreases with soil height as the due to the surcharge loading considered at the top boundary.

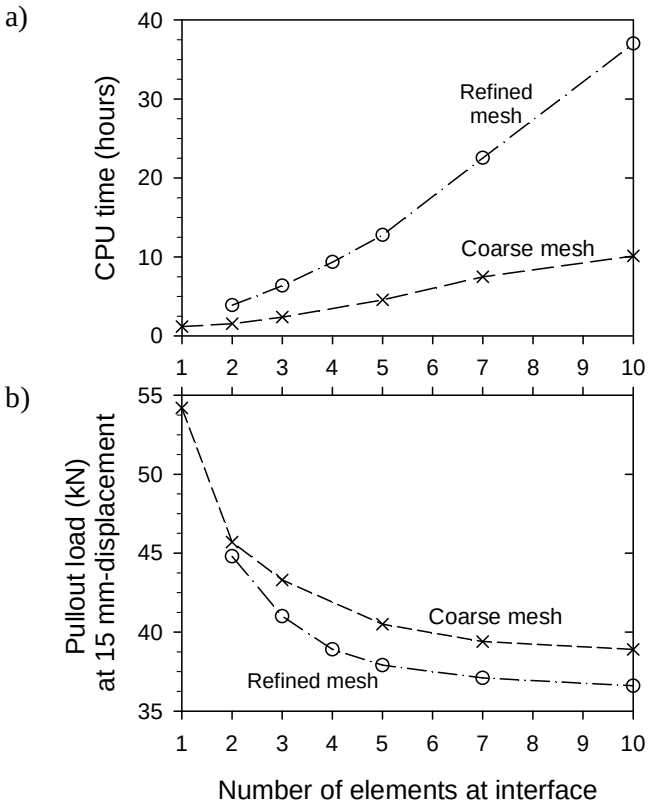

Figure 8.32: Computational time (a) and pullout strength (b) comparison with regards to the finite element mesh refinement.

Similarly to previous results, the vertical stress results evolution during pullout performance are presented in Figure 8.34. Significant increasing of vertical stress is generated during pullout. As observed, the maximums are localized at the central zone of the reinforcement, with reaching values of about 10 times the vertical stress assumed just for soil self-weight (plus surcharge loading, i.e., soil self-weight assuming the *z*-equivalent of 3 m-depth). Very minor positive values of vertical stresses (i.e., tensile stress) are generated at the lateral-side corner-boundaries, which can be assumed as nonexistent, as they are appearing due to numerical equilibrium with the prescribed conditions at boundary planes (prescribed normal displacements).

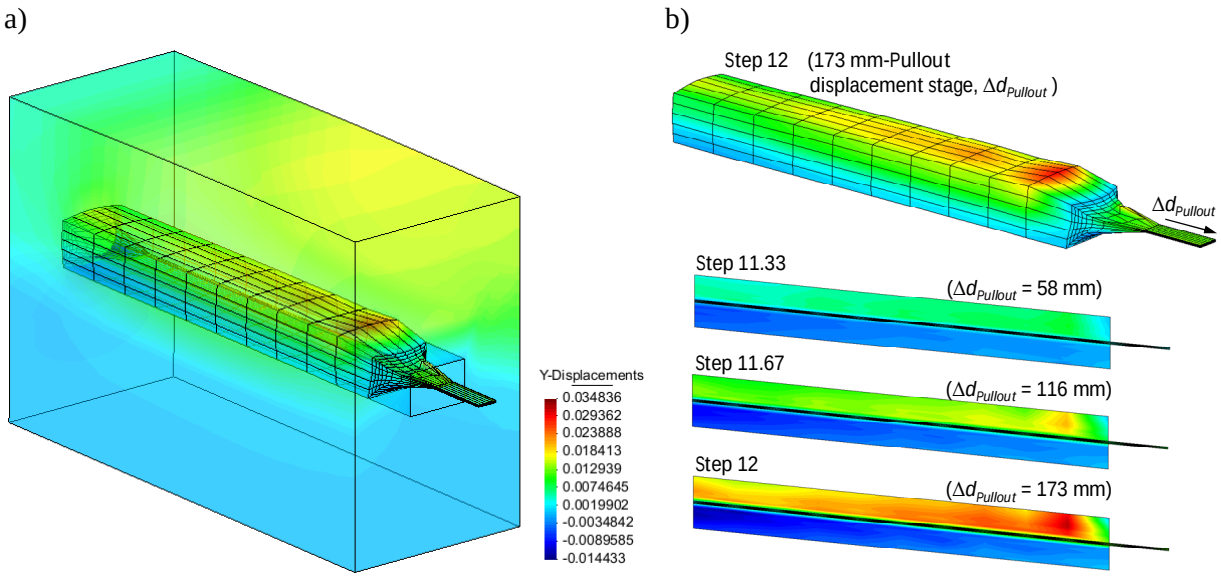

Figure 8.33: Base case vertical displacements (m) development: entire model (a) and at interface with their evolution in time (i.e., steps) on interface vertical cross-length-section (b).

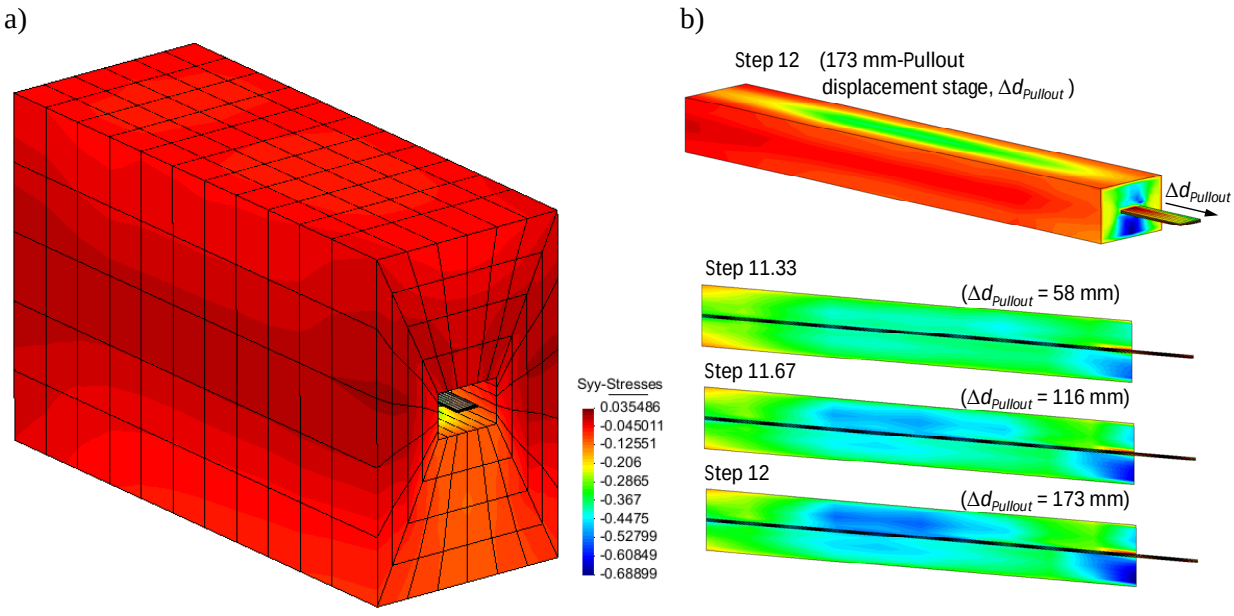

Figure 8.34: Base case vertical stress (MPa) development: entire model (a) and at interface with their evolution in time (i.e., steps) on interface vertical cross-length-section (b).

Vertical displacement and stress generated in Step 12 ($\Delta d_{Pullout}$ = 173 mm) at different reinforcement length locations can be observed in Figures 8.35a and 8.35b, respectively, with results representation at several cross-section planes. The vertical cross sections considered are located at 0.41 m, 0.725 m, and 1.04 m vertical cross-transversal-sections from head of

reinforcement (i.e., at 0.21 m, 0.525 m, and 0.84 m within reinforcement sample, as per 0.2 m-sleeve at front box opening; see Figure 8.27e).

a) Vertical displacements:

b) Vertical stresses:

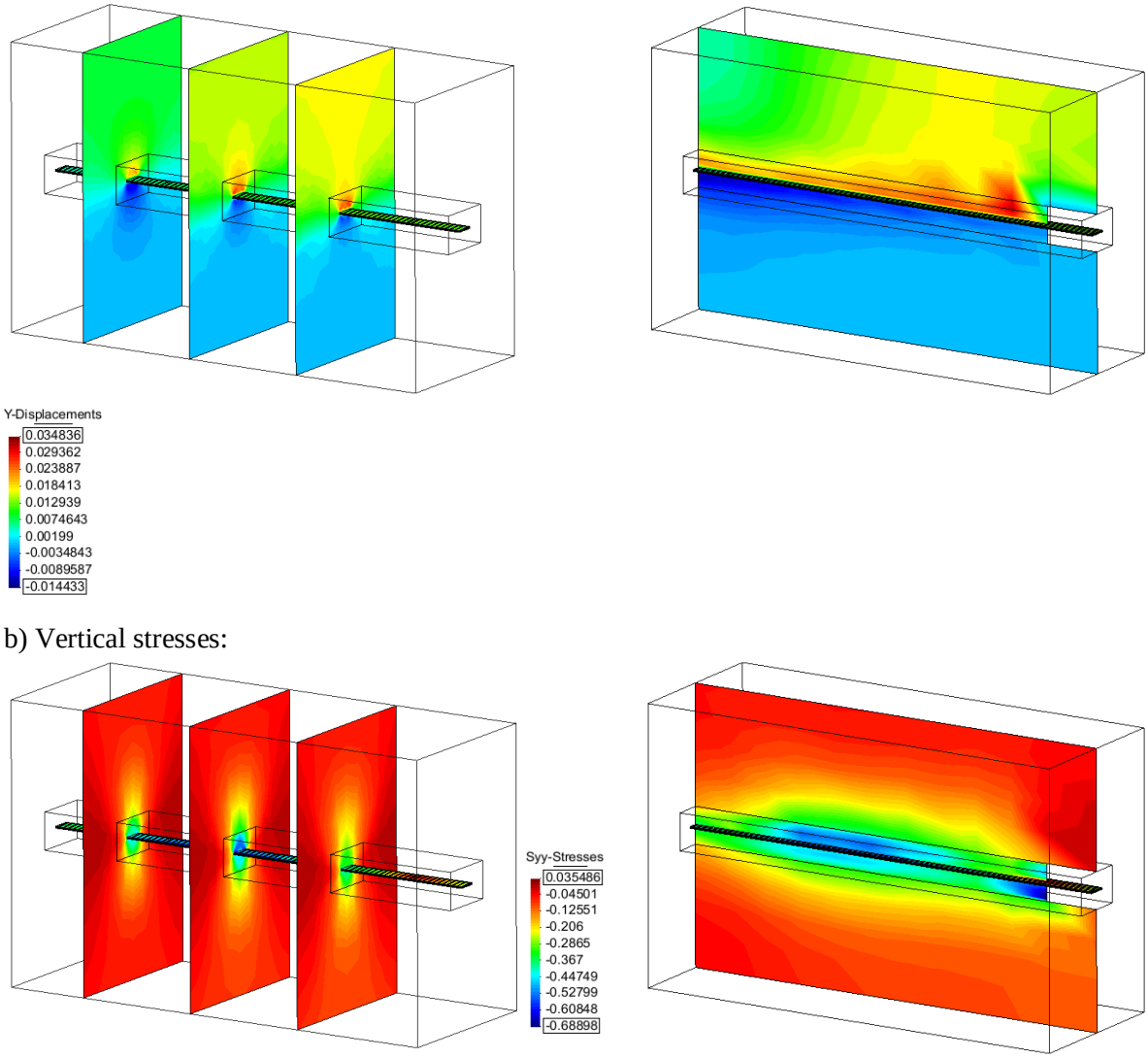

Figure 8.35. Base case vertical displacements (a) and stresses (b) at several vertical cross-sections. Results at Step 12 ($\Delta d_{Pullout}$ = 173 mm).

Plots of the shear and vertical stresses time evolution along the soil-reinforcement interaction are presented in Figures 8.36a and 8.36b. Shear stresses are presented as they occur in both upper and bottom sides of the reinforcement though it longitudinal direction, with almost symmetric trends. As expected, both stresses increase with time (i.e., increase with pullout displacement) in almost all reinforcement length. Initial stress values (i.e., 0 mm-displacement at Step 11) are presented. At this Step (11), non-shear stresses were obtained

and about 60 kPa were achieved, which corresponds to the self-weight of the soil at the equivalent depth (i.e., $\sigma_v = \gamma_n \times z_{eq.}$). Divergences from this reference value was obtained near the head frontal box opening were the sleeve was modeled (tending to $\sigma_v = 0$ at the contact with the sleeve).

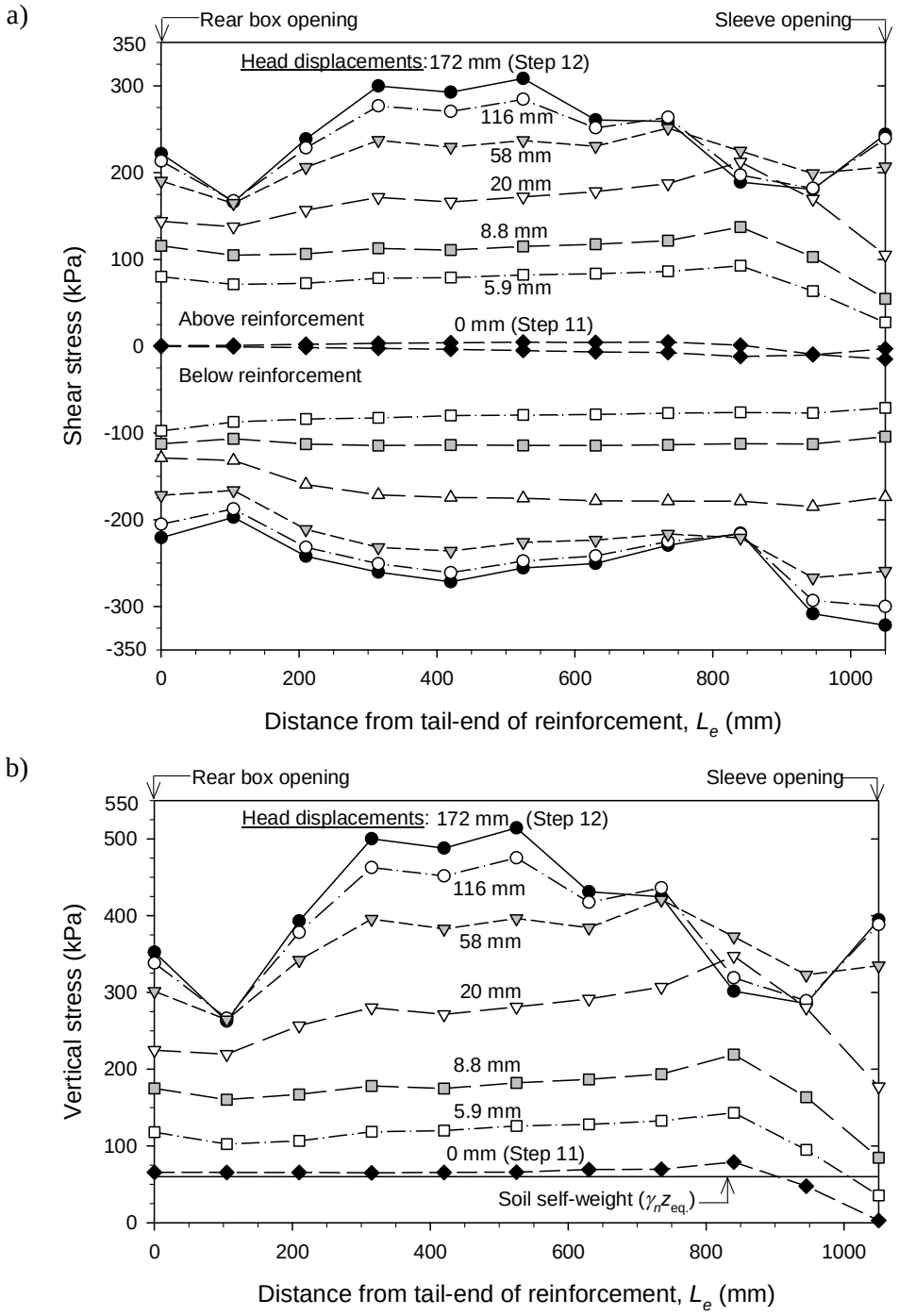

Figure 8.36: Shear (a) and vertical stresses (b) due to reinforcement head displacement evolution (i.e., pullout time step) in Base case (E_r = 210 GPa, $E_s = E_i$ = 20 MPa, ϕ_s = 38º, δ = 28.7º (R_i = 0.7)).

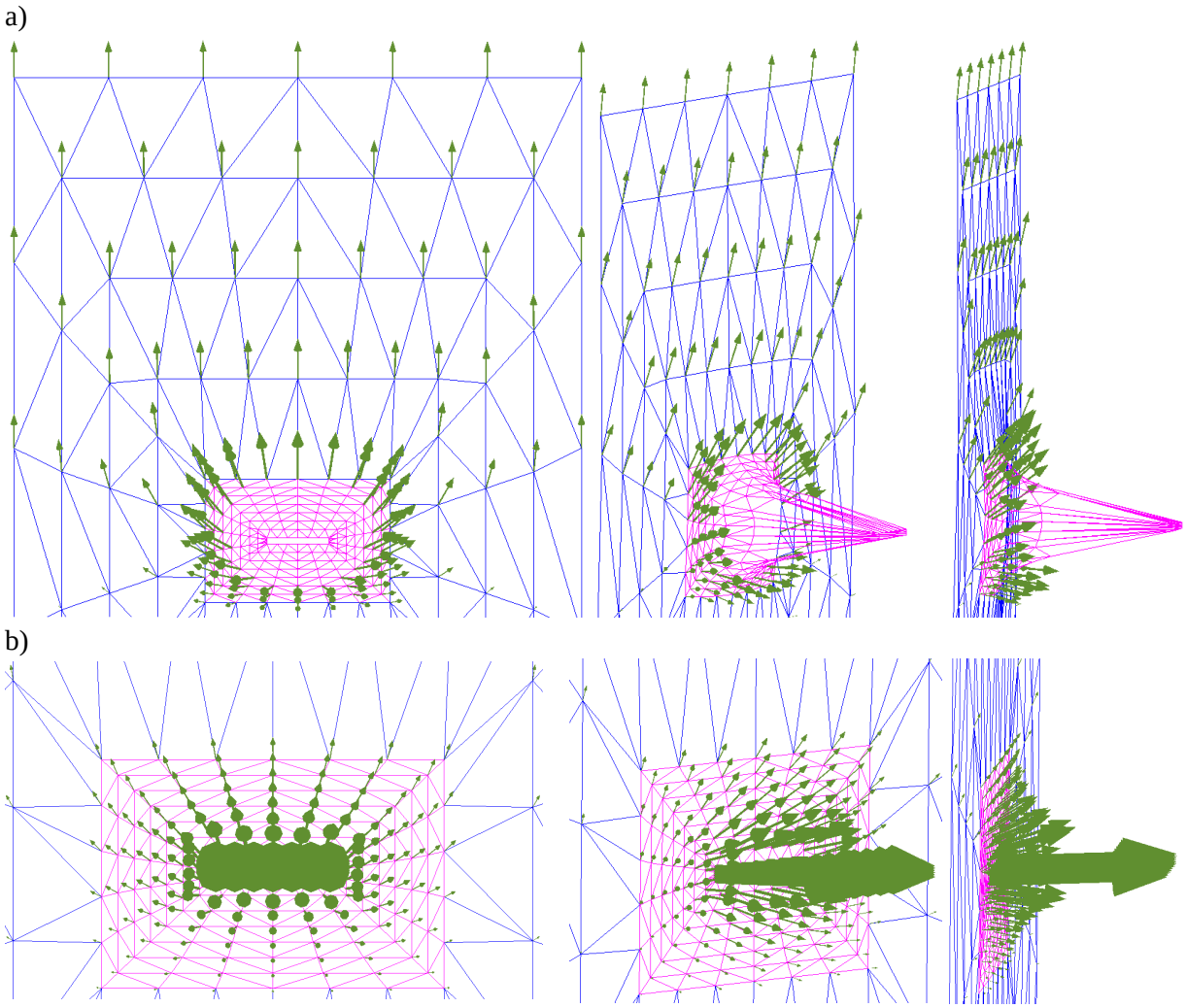

Figure 8.35: Total displacement vectors of fill-soil (a) and interface (b) at Step 12 in a vertical cross section in the middle of the reinforcement (at 0.525 m from tail-end of reinforcement).

As observed in plot from Figure 8.36b, about 10 times the self-weight of fill-soil assuming the equivalent depth of 3 m was reached in the middle of the reinforcement: about 525 kPa at Step 12 and 60 kPa at Step 11. This vertical stress increasing is due to soil dilatancy during pullout displacement (were high shear strains were generated), and arching effect within the soil.

Displacement at Step 12 at a central vertical cross-section (i.e., located at 0.725 m from head of reinforcement) are represented in Figure 8.37 (analysis within the soil and detailed within the interface). From rotary vector displacement plots it can be observed that not only upward displacements were generated but also forward displacements (i.e., as pullout direction).

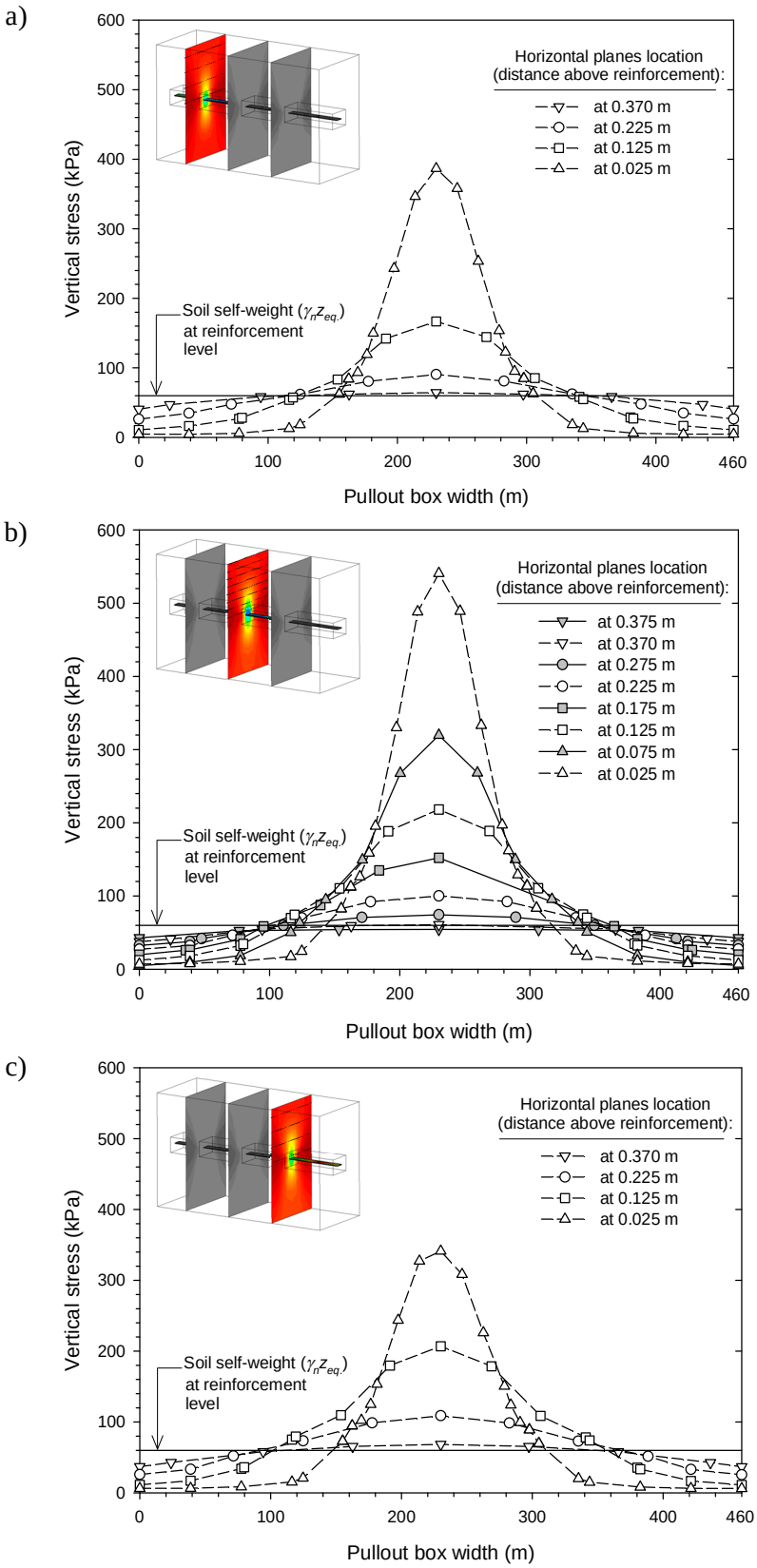

Figure 8.38: Vertical stress development (b) of interface in different horizontal planes from reinforcement layer at Step 12, within several vertical cross section planes: at 0.210 m (a), 0.525 m (b), and 0.840 m (c) from tail-end of reinforcement.

Figure 8.38 presents vertical stress-values at Step 12 (reinforcement pullout already performed) in several horizontal planes located above reinforcements, within three different vertical planes crossing reinforcement (see Figure 8.35b-left). As observed previously when vertical stresses were analyzed just above the reinforcement (Figure 8.36), the presented results demonstrates a huge variation between vertical pressure development at locations above the reinforcement and locations away the reinforcement at the lateral sides.

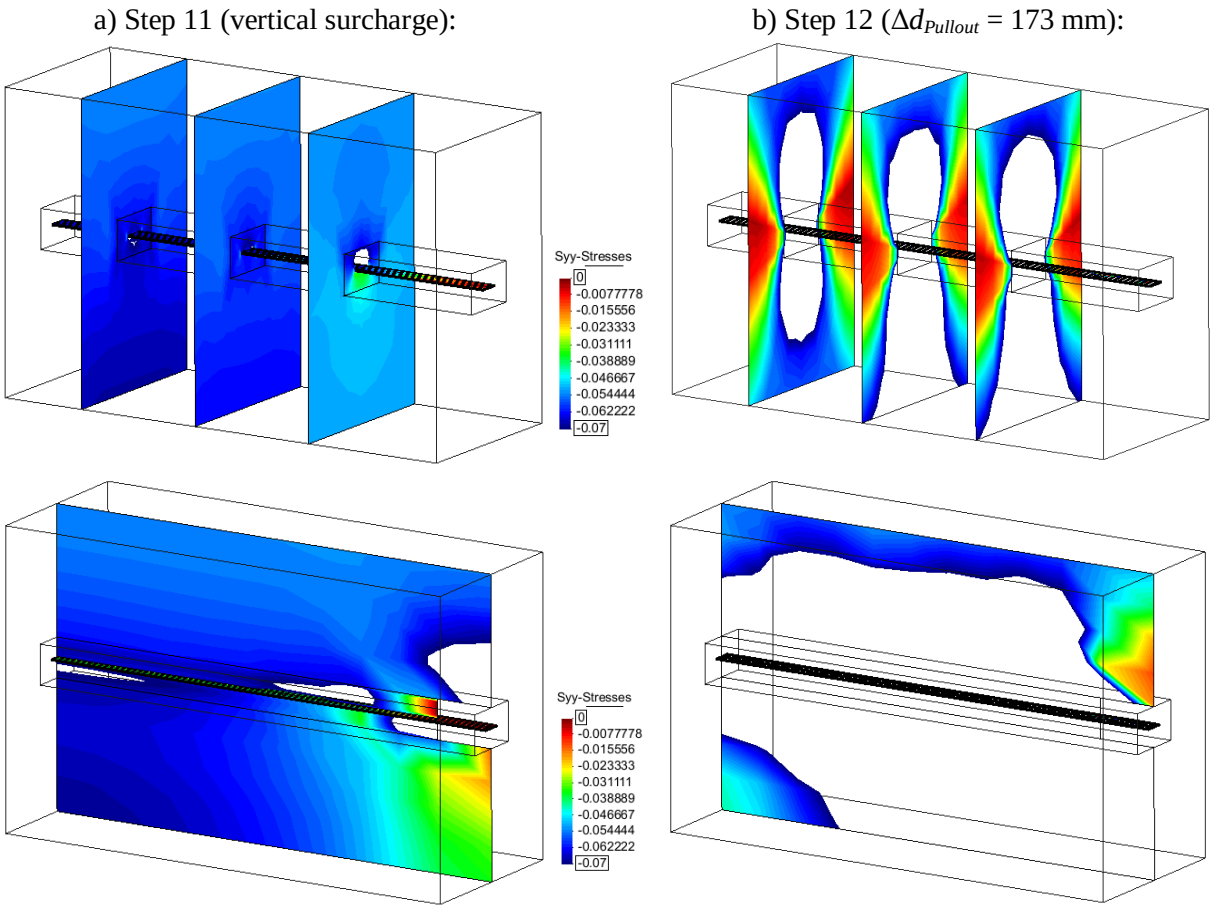

Figure 8.37: Base case vertical stresses at step 11 (a) and step 12 (b) at several vertical cross-sections with regards to vertical stresses ranging from 0 to 70 kPa.

This vertical pressure increment (Figure 8.38) with regards to the vertical pressure assuming the equivalent depth ($z_{eq.}$, i.e., fill-soil depth within the box at this horizontal plane + surcharge loading applied on top surface) is generated due to the shear strains by the reinforcement pullout performance and due to the fill-soil dilatancy effect (increasing of volume due to shear, with upward displacements generation). Even these differences on vertical pressure distribution (for example, with reaching values of about 10 times the self-

weight of fill-soil assuming the equivalent depth of 3 m) the mean stress in horizontal planes is maintained as per the equivalent fill-soil depth pressure at any plane location due to soil arching-effect. This distribution is several times higher than the pressure due to the self-weight of fill-soil above the reinforcement, and times lower at the lateral sides. The equivalent resultant load at any horizontal plane is maintained and equal to the equivalent soil self-weight at the horizontal plane of analysis. As expected and presented in Figure 8.38, the vertical pressure distribution curvature shape (or magnitude of the vertical pressure at the central zone with regards to the vertical pressure distribution at the lateral sides) is related to horizontal plane location (i.e., vertical distance above the reinforcement element), with a reduction of the vertical stress as the horizontal plane of analysis moves away from reinforcement, up to a vertical pressure almost equal to the surcharge loading at top surface boundary.

Alternatively to previous results, Figure 8.39 presents vertical stresses comparison between steps 11 and 12 with ranged results from 0 to 70 kPa at several cross-section planes representation (i.e., from no vertical pressure up to about 3 m-depth fill-soil pressure). The interest of this representation is to identify the 70 kPa non-colored edge region at the end of pullout, which represents the regular vertical stress generated just after vertical surcharge load (i.e., about the vertical stress due to the equivalent depth loads only). As it can be observed, the soil dilatancy affects a significant region of the soil area.

Figures 8.40 and 8.41 present deviatoric and volumetric total strains, respectively, at different cross-section planes with regards to time evolution. Both strains increase with pullout displacement, derived from shear strains and dilatancy effect. As observed, not only vertical strains are obtained (i.e., above and below reinforcement sides) and also shear/volumetric strains are obtained at both lateral sides of the reinforcement, even with the small thickness assumed (5 mm-thick).

a) Step 11:

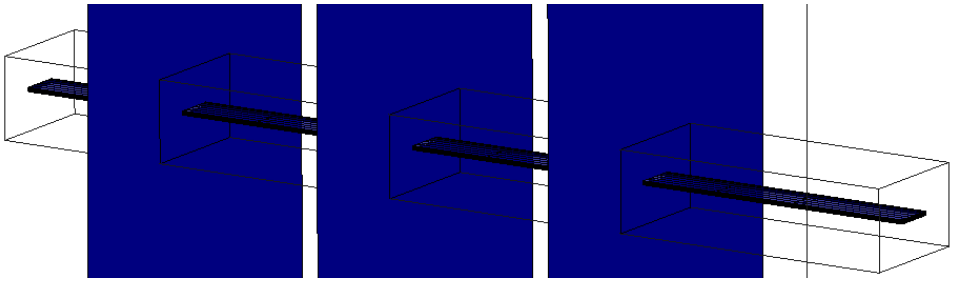

b) Step 11.33 ($\Delta d_{Pullout}$ = 58 mm):

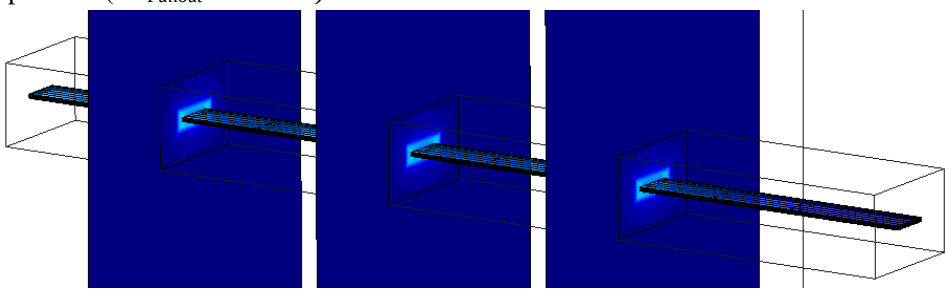

c) Step 11.67 ($\Delta d_{Pullout}$ = 116 mm):

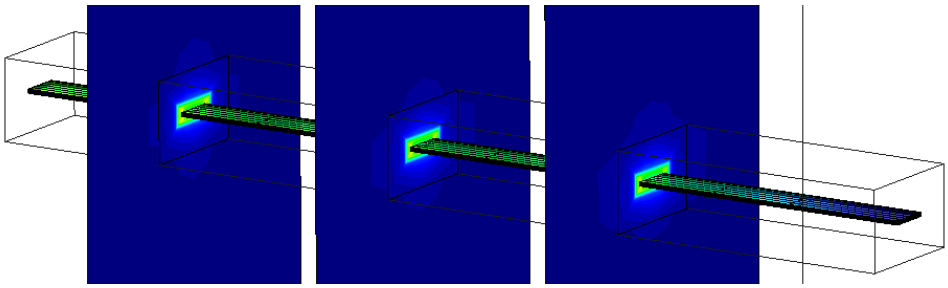

d) Step 12 ($\Delta d_{Pullout}$ = 173 mm):

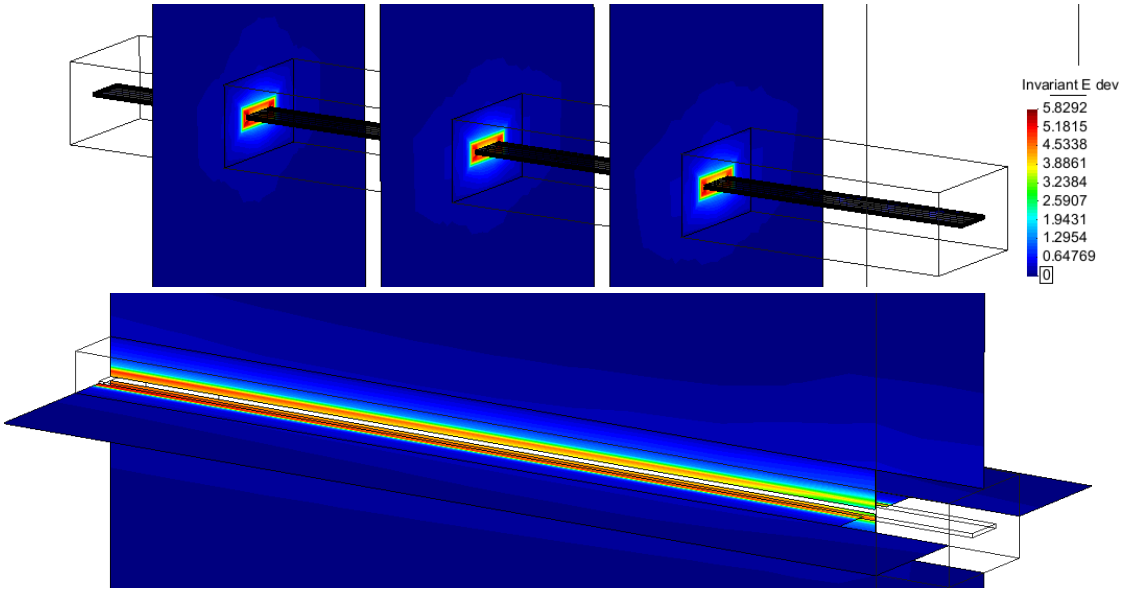

Figure 8.40: Base case deviatoric strains evolution.

a) Step 11:

b) Step 11.33 ($\Delta d_{Pullout}$ = 58 mm):

c) Step 11.67 ($\Delta d_{Pullout}$ = 116 mm):

d) Step 12 ($\Delta d_{Pullout}$ = 173 mm):

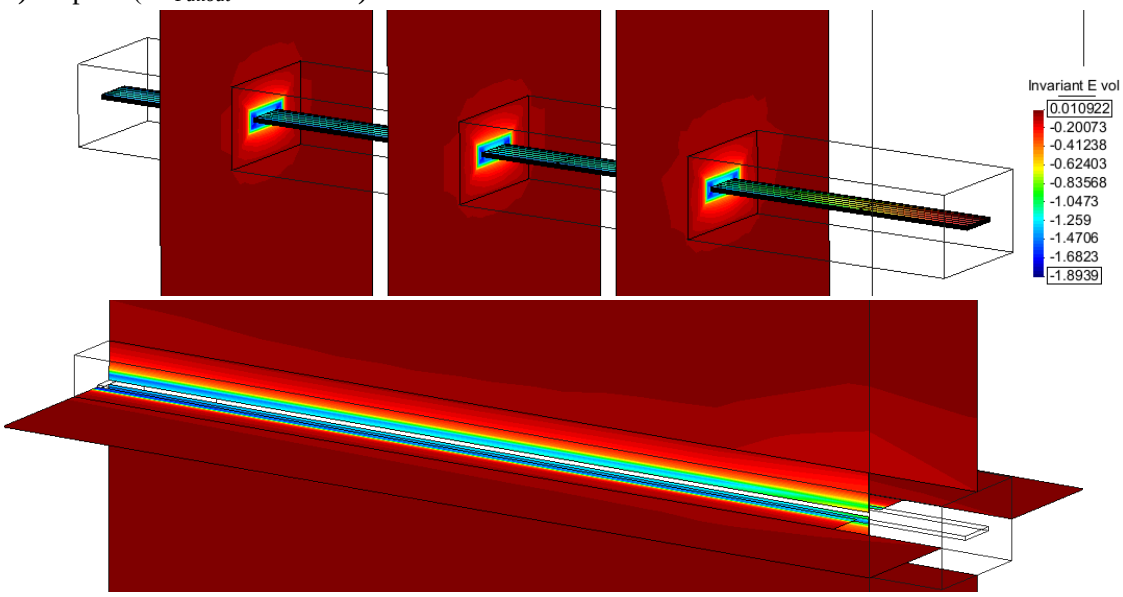

Figure 8.41: Base case volumetric strains evolution.

8.4.2.2. Sensitivity analysis

In this section, parametric changes from Base case are assumed to perform sensitivity analysis and to detect trending variations with these changes. Table 8.9 presents the parameter variations to perform the sensitivity analysis. Basically, the idea was to detect trends due to soil and interface strength and stiffness. The confinement pressure variations effect is analyzed in further Section 8.4.3 (calibration of real pullout tests).

Table 8.9. Sensitivity variations from Base case:

Sensitivity on [(a)]:	Base case value:	Variation cases:	Case number:
• Soil friction angle, ϕ_s	$\phi_s = 38^o$ ($R_i = 0.7$; $\delta = 28.7^o$)	Maintaining R_i: $\phi_s = 32^o$ ($R_i = 0.7$; $\delta = 23.6^o$)	1
		$\phi_s = 44^o$ ($R_i = 0.7$; $\delta = 34.1^o$)	2
		Maintaining δ: $\phi_s = 32^o$ ($R_i = 0.88$; $\delta = 28.7^o$)	3
		$\phi_s = 44^o$ ($R_i = 0.57$; $\delta = 28.7^o$)	4
• Soil and interface dilatancy [(b)], ψ_s and ψ_i	$\psi_s = \psi_i = 8^o$	$\psi_s = \psi_i = 3^o$	5
		$\psi_s = \psi_i = 13^o$	6
• Soil-reinforcement friction interaction factor, f' (and interface friction angle, δ)	$f' = 0.55$ ($R_i = 0.7$; $\delta = 28.7^o$)	$f' = 0.66$ ($R_i = 0.85$; $\delta = 33.6^o$)	7
		$f' = 0.78$ ($R_i = 1$; $\delta = 38^o$)	8
• Soil (and interface) stiffness, E_s and E_i	$E_s = E_i = 20$ MPa	$E_s = 50$ MPa and $E_i = 20$ MPa	9
		$E_s = E_i = 50$ MPa	10
		$E_s = 20$ MPa and $E_i = 50$ MPa	11
• Reinforcement stiffness, E_r	$E_r = 210000$ MPa	$E_r = 500$ MPa	12

Note: [(a)] Non-mentioned parameters remain the same as in Base case.

[(b)] Despite the dilatancy definition (already stated in Table 8.8 - Note [(c)]; $\psi = \phi_s - 30^o$), the interface material dilatancy angle was assumed as equal to fill-soil dilatancy angle in Base case, and with the same value (i.e., $\psi = 8^o$) for the complementary cases.

Figures from 8.42 to 8.45 present the results of the pullout axial load at head of reinforcement with respect to axial head-displacement, for the different sensitivity cases. Sensitivity on fill-soil friction angle is presented in Figure 8.42. As it can be observed, as the strength and stiffness increase, higher values of pullout load are reached. With maintaining the interface friction angle (i.e., cases 3 and 4 with δ = 28.7º) the obtained trending deviation from Base case is lesser than in case of maintaining the interface strength reduction factor (i.e., cases 1 and 2 with R_i = 0.7), as the interface friction angle became much different. Interface friction angle (δ) seems to generate equal increasing pullout load slope under the same soil friction angle scenario.

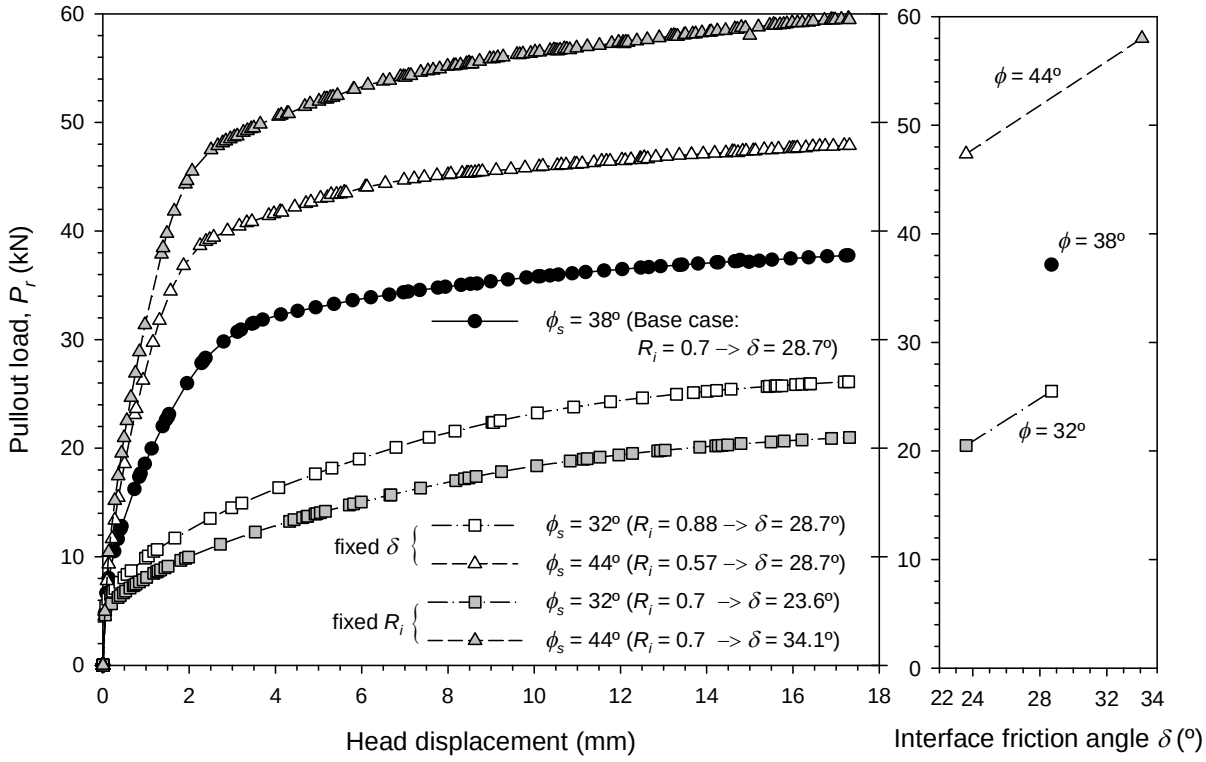

Figure 8.42: Axial reinforcement pullout load – axial displacement responses with regards to variations on interface friction angle (cases 1, 2, 3, and 4).

Figure 8.43 presents the results of the interface and soil dilatancy angle variations from Base case with ψ = 8º. Also related with to fill-soil strength variation, as the dilatancy angle increases the higher values also of pullout load are reached with also different sloping trends. Not shown in this figure, the higher stiffness of soil mixed with higher values of dilatancy perform higher strength, as the dilatancy generates positive volumetric strains and vertical pressure increasing (as already explained in Figures 8.37, 8.38 and 8.41) and soil stiffness appears as a disability to move. Figure 8.44 presents the results of the interface strength

variations up to rigid interface case (case 8 with R_i = 1). As in previous cases, as the interface strength increases the higher values also of pullout load are reached.

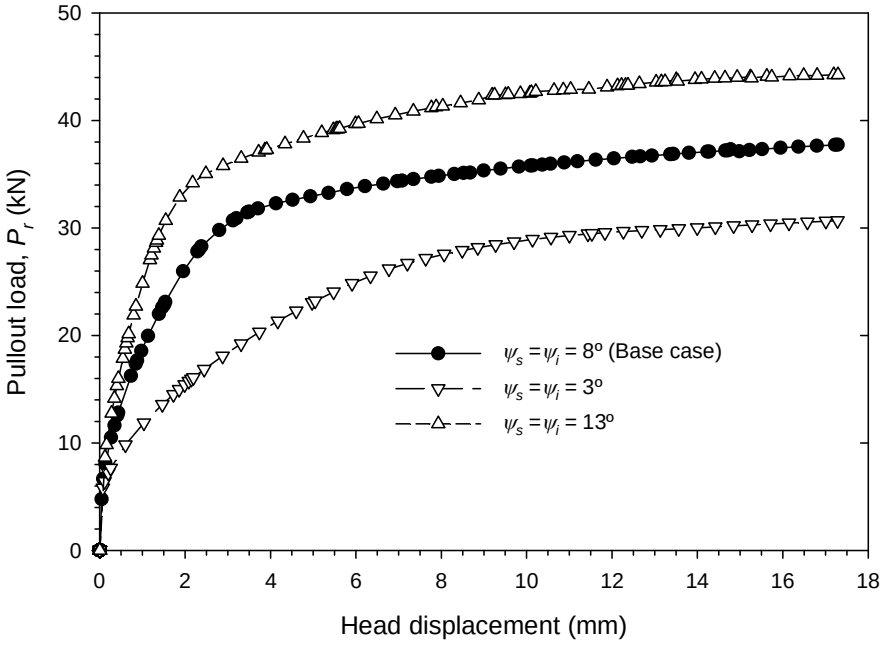

Figure 8.43: Axial reinforcement pullout load – axial displacement responses with regards to variations on soil and interface dilatancy angle variations (cases 5 and 6).

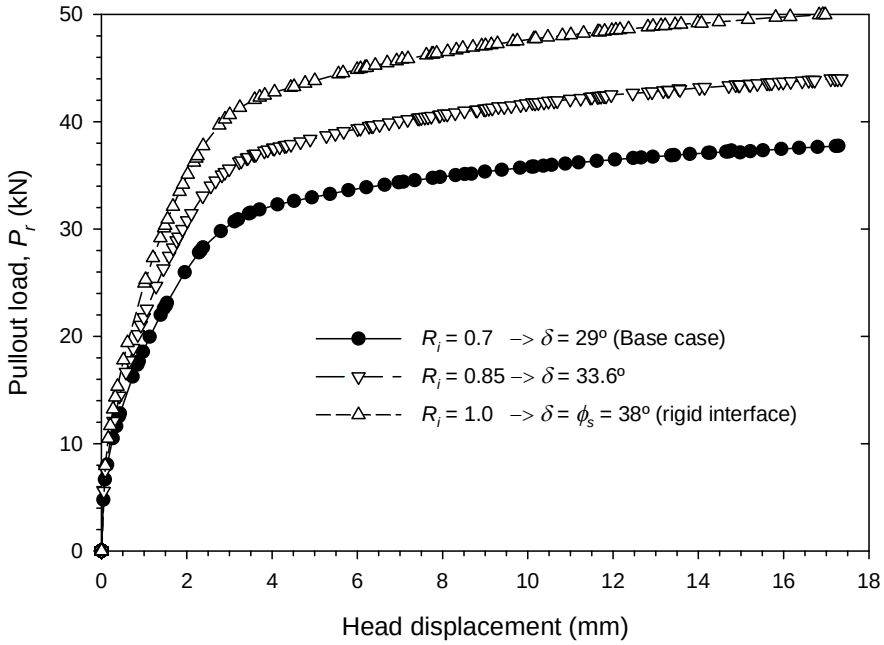

Figure 8.44: Axial reinforcement pullout load – axial displacement responses with regards to variations on interface strength/stiffness reduction factor (cases 7 and 8).

Figure 8.45 presents the resulting fill-soil and interface stiffness variation. As it can be deduced, soil/interface stiffness had a significant influence at the elastic regime of the pullout phenomena, but the pullout load (i.e., within plastic regime: load from where the increase of displacement generates not much changes in strength) remain likely the same. The small variation of the pullout load from soil/interface increased stiffness cases is, again, due to dilatancy: stiffer soil material generates more restriction of vertical displacement due to dilatant effect, and thus, a bit higher pullout load is required. As it can be observed, not much pullout changes were obtained with maintaining the interface material stiffness equal to the Base case, which means that, under the considered conditions, soil stiffness (and not interface stiffness) has the major influence on pullout strength. As commented in Table 8.8 – Note [(a)],

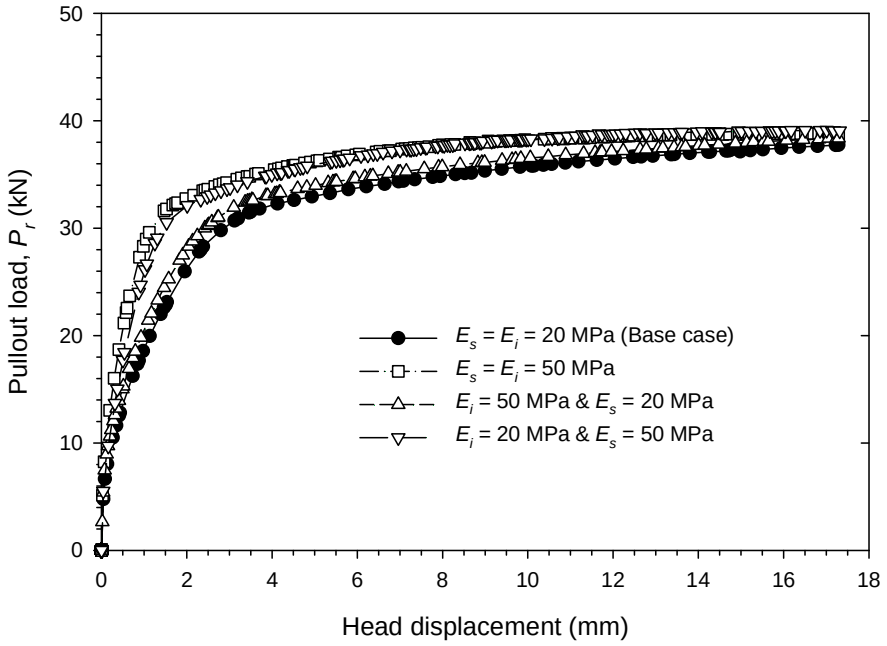

Figure 8.45: Axial reinforcement pullout load – axial displacement responses with regards to variations on soil/interface stiffness (cases 9, 10, and 11).

Reinforcement stiffness influence is presented in Figure 8.46. Reinforcement stiffness is related to reinforcement extensibility. Reinforcement stiffness of the Base case (E_r = 210 GPa) can be perfectly assumed as inextensible (steel). As it is observed, pullout stiffness decreases with decreasing reinforcement stiffness, but, as in previous soil-stiffness case, pullout load (i.e., critical load in where there is the elastic-plastic stress-regime change) remain likely the same. Both rear and frontal reinforcement displacements are plotted for E_r = 500 MPa extensible reinforcement case. As expected, different final pullout displacement were reached due to tensile dilation of reinforcement element.

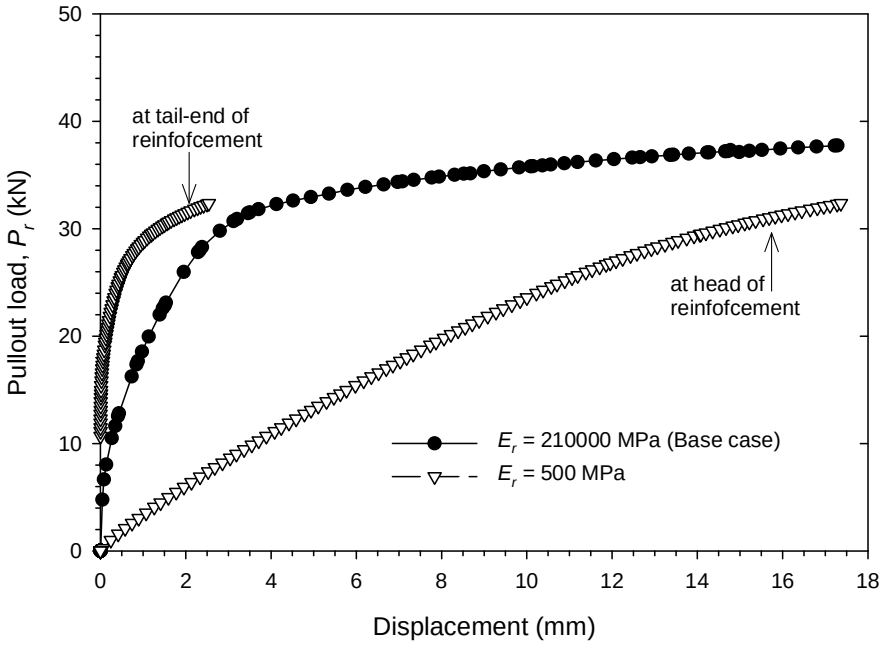

Figure 8.46: Axial reinforcement pullout load – axial displacement responses with regards to variations on reinforcement stiffness (case 12).

Results from shear and vertical stresses generation along the reinforcement at Step 12 ($\Delta d_{Pullout}$ = 173 mm) are presented in Figures from 8.47 to 8.51, with regards to material parametric change. Figure 8.47 presents the comparison results obtained from soil friction angle changes (i.e., soil strength). As expected, higher stresses are obtained with increasing the soil friction angle. Figure 8.48 presents the comparison results obtained from soil and interface dilatancy angle changes. As in previous cases, higher stresses are obtained with increasing the soil dilatancy. Figure 8.49 presents the comparison results obtained from interface strength (interface friction angle from 28.7º (Base case; R_i = 0.7) to 31º (rigid interface). As in previous case, higher shear stresses are obtained with increasing the interface strength; however, no much significant variations were obtained in vertical stresses (with the exception of the near opening-sleeve location). Soil/stiffness variations with regards to shear and vertical stresses are plotted in Figure 8.50. As it can be observed, no much stress variations are obtained due to stiffness changes. Figure 8.51 presents shear and vertical stress results with regards to reinforcement stiffness variation. Whereas shear stresses remain roughly constant along the reinforcement, soft reinforcement (i.e., extensible reinforcement) generated an increase of shear stresses, with higher values at the front. This appears to be logical as per the shear strains magnitudes, which resulted greater near the frontal opening sleeve due to the reinforcement extensibility. Consequent to the shear stresses (and shear strains), vertical stresses also increased with the reinforcement proximity to the head opening due to the related soil and interface material dilatancy.

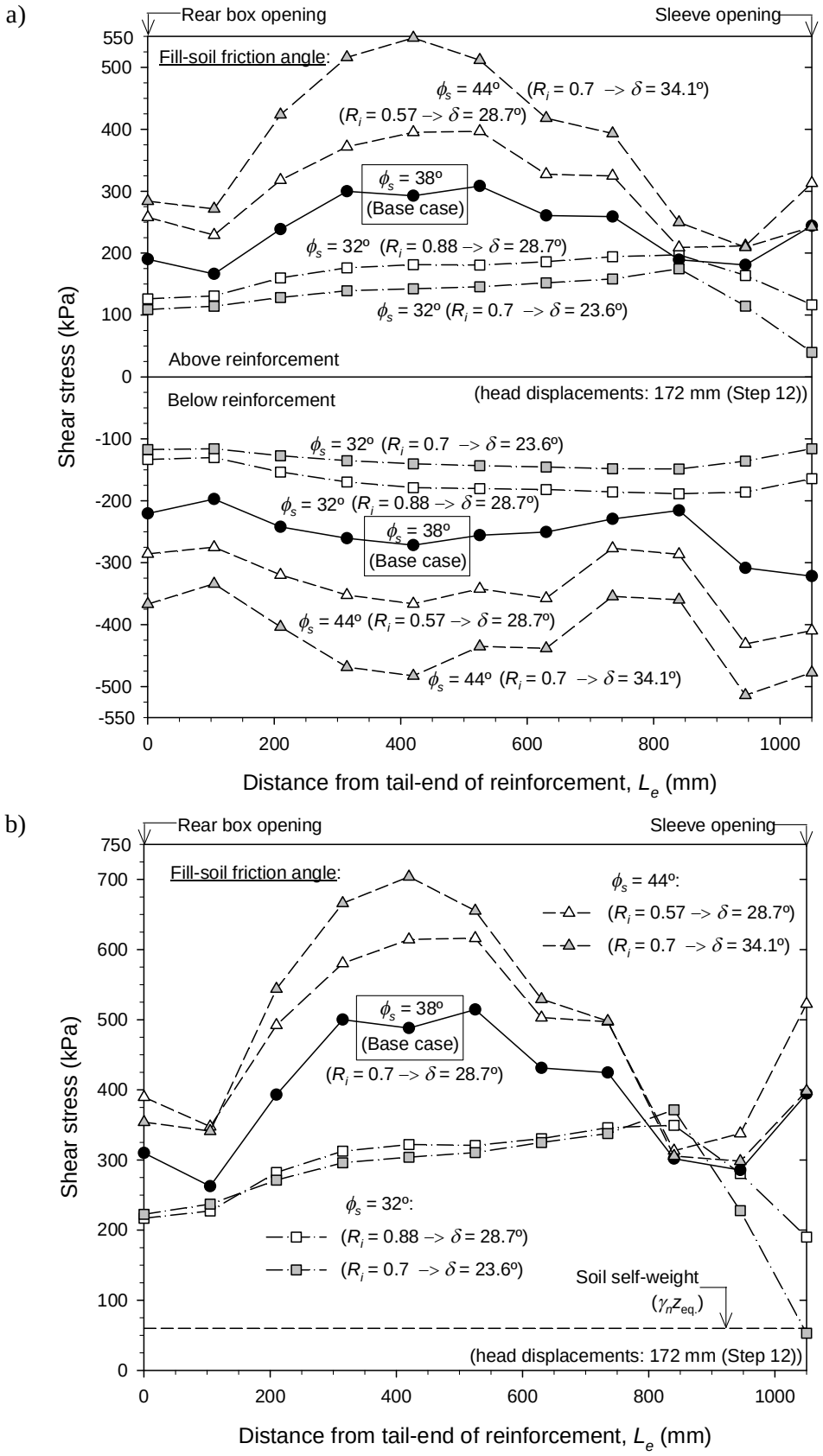

Figure 8.47: Shear (a) and vertical (b) stresses sensitivity with regards to soil friction angle ϕ variation. Cases 1, 2, 3, and 4.

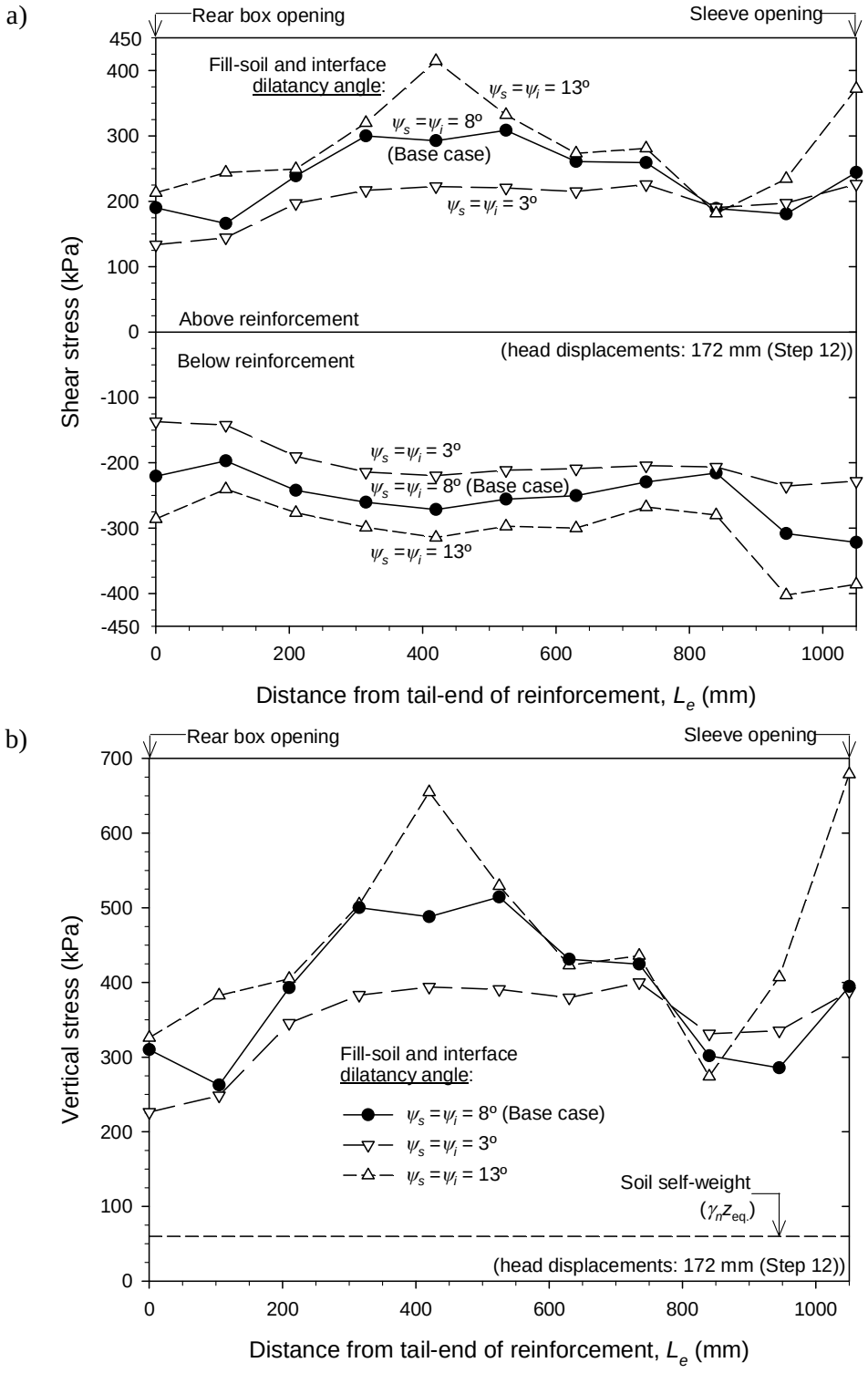

Figure 8.48: Shear (a) and vertical (b) stresses sensitivity with regards to soil and interface dilatancy angle ψ_s & ψ_i variations. Cases 5 and 6.

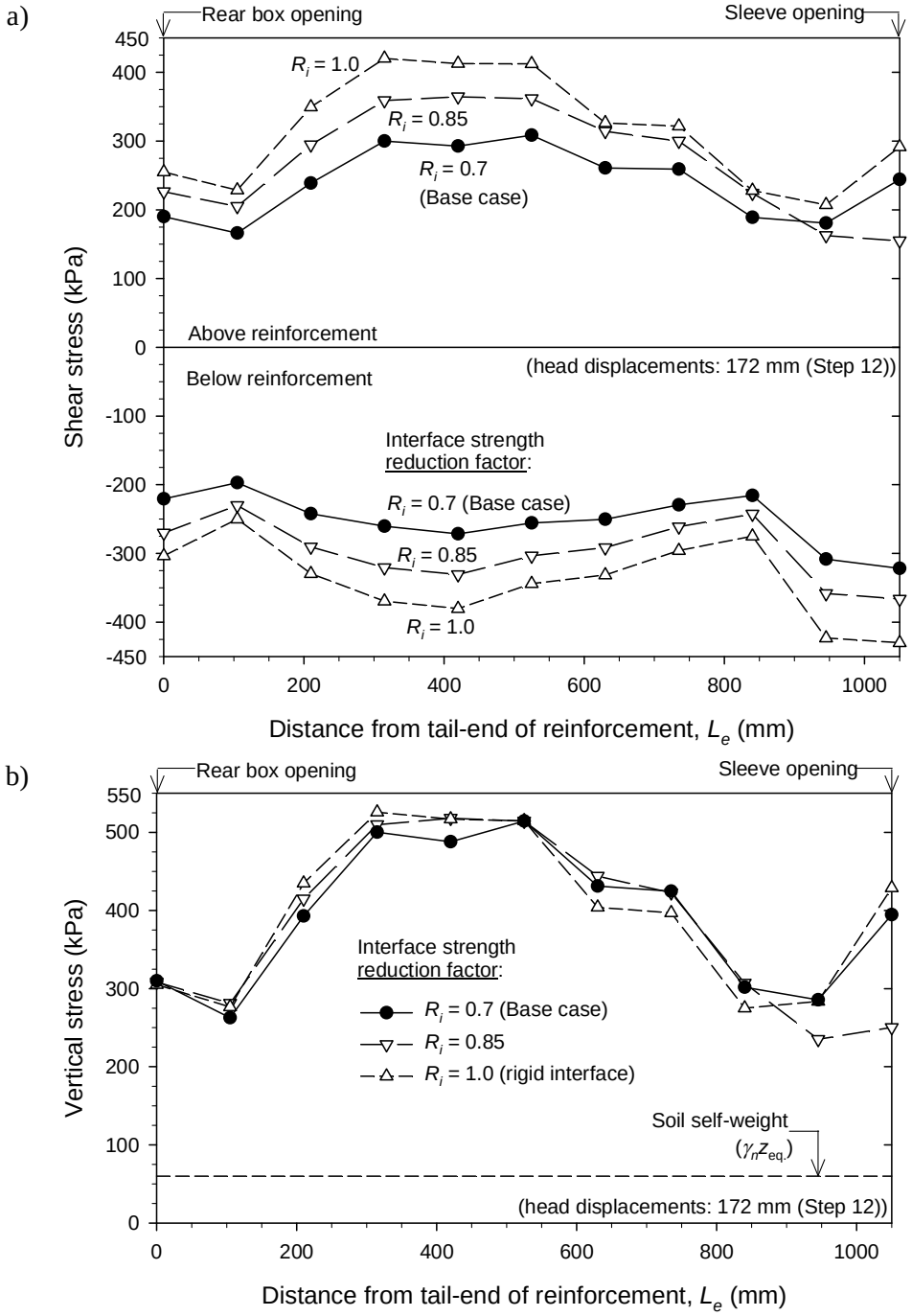

Figure 8.49: Shear (a) and vertical (b) stresses sensitivity with regards to interface strength/stiffness reduction factor R_i variation. Cases 7 and 8.

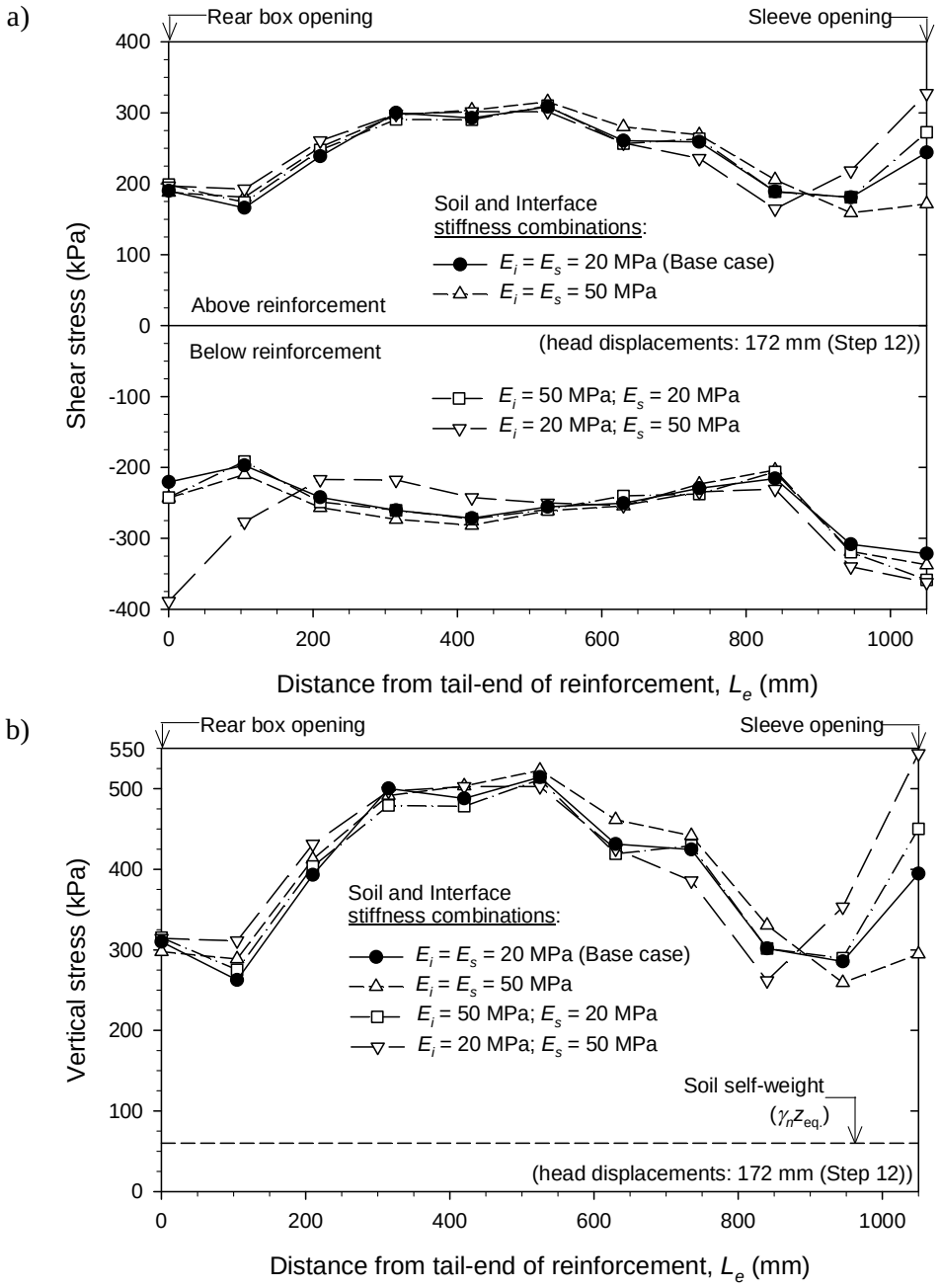

Figure 8.50: Shear (a) and vertical (b) stresses sensitivity with regards to soil/interface stiffness E_i variation. Cases 9, 10, and 11.

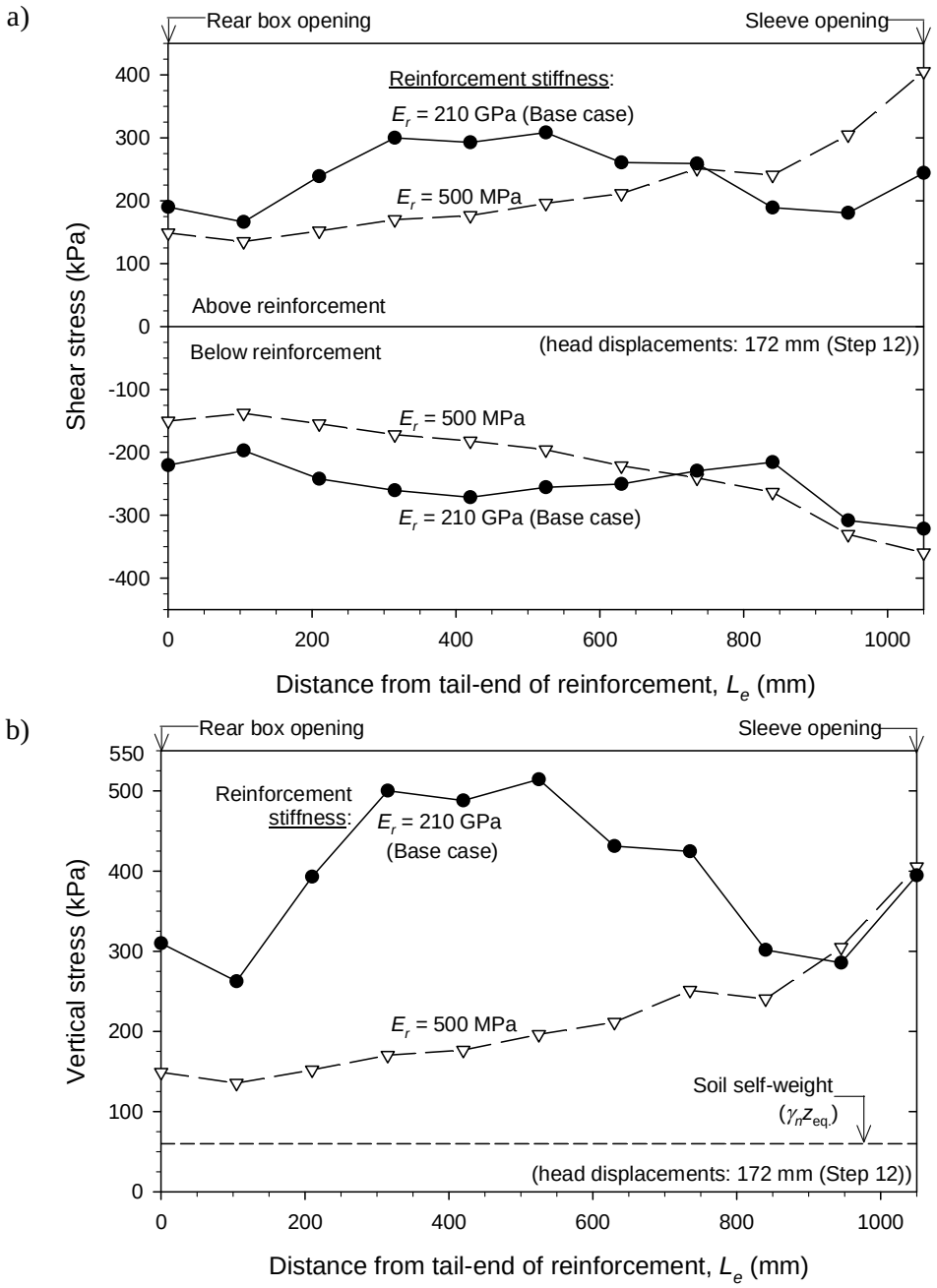

Figure 8.51: Shear (a) and vertical (b) stresses sensitivity with regards to reinforcement stiffness E_r variation. Case 12.

8.4.3. Calibration results from actual Pullout tests

The previous model is here adapted to perform and to suit the pullout behaviour of the particular testing cases presented in sections 8.3.5.1 (steel ladder case, see Figure 8.21) and 8.3.5.2 (polymeric strip case, see Figures 8.24 and 8.25).

8.4.3.1. Steel ladders

Table 8.10 presents de model parameters considered to steel ladders particular case, with parametric values suitable to the actual ones shown in Table 8.6. Both results from instrumented tests (dotted/scatted trends) and 3D model (trending lines) are presented in Figure 8.52 for AASHTO default and calibrated *F**-value cases.

Table 8.10. Model material properties for steel ladder pullout case:

Parameters	Materials: Steel ladder	Fill soil	Interface			
Unit weight (kN/m^3)	75	20	20			
Elastic modulus, E (MPa)	84446 [(a)]	30 [(b)]	30			
Poisson's ratio, ν (-)	0.3	0.3	0.45 [(c)]			
				Equivalent depths [(d)]: z = 0.4 m	z = 3 m	z = 10.5 m
Cohesion, c (kPa) [(e)]	-	1		1	1	1
Friction angle, ϕ-soil and δ-interface (deg.)	-	40	· default [(e)]: (F^* value=)	28 (0.52)	22 (0.4)	15 (0.27)
			· calibrated: (F^* value=)	89 (~60)	27 (0.5)	13 (0.23)
Dilatancy angle, ψ (deg.) [(g)]	-	10		10	10	10

Notes: [(a)] Equivalent stiffness from steel modulus (210 GPa) and actual steel ladder geometry (8 mm-diameter two longitudinal bars), converted to 50 mm-width × 5 mm-thick reinforcement 3D-model geometry.

[(b)] Value approximated from final in-fill settlement reached after tests, which is in agreement with soil material type (gravely sand) and performed compaction; as explained in previous sensitivity analysis (and demonstrated below for this current case) fill soil and interface stiffness variations implies different pullout-displacement trend, which can be properly refined to improve real pullout-displacement trend.

[(c)] Despite Poisson's ratio demonstrated to have no significant effect on pullout capacity, higher ν-value (i.e., ν = 0.45) was considered to best fit pullout capacity under high vertical pressure cases to mobilize confinement (i.e., to increase p-stress invariant) and reduce unrealistic volumetric interface plasticization.

[(d)] Equivalent depths from actual fill-soil layer height above the reinforcement and surcharge loading applied on top of pullout box.

[(e)] Even being a cohesionless soil, non-zero cohesion value has been assumed for the numerical model to ensure numerical stability at very low confining pressure.

[(f)] Default values from AASHTO pullout friction factor F^* for steel grid reinforcement (bilinear value; see Figure 8.13), i.e., from $F^* = 10(t/S_t) = 10 \times (8\text{ mm} / 300\text{ mm}) = 0.27$ (at depths $z \geq 6$ m) linearly increasing up to $F^* = 20(t/S_t) = 20 \times (8\text{ mm} / 300\text{ mm}) = 0.53$ (at $z = 0$).

[(g)] Assumed as $\psi = \phi - 30^o$.

a) AASHTO default F^*-values: from F^*= 0.27 (at $z \geq 6$ m) to 0.53 (at z = 0):

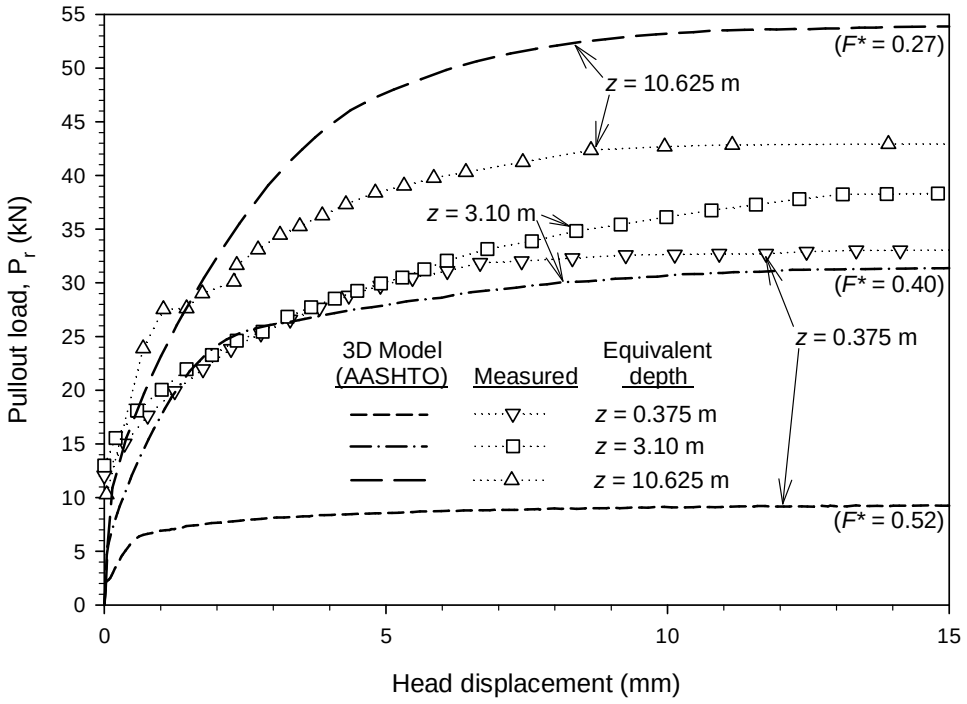

b) Calibrated/best fit F^*-values:

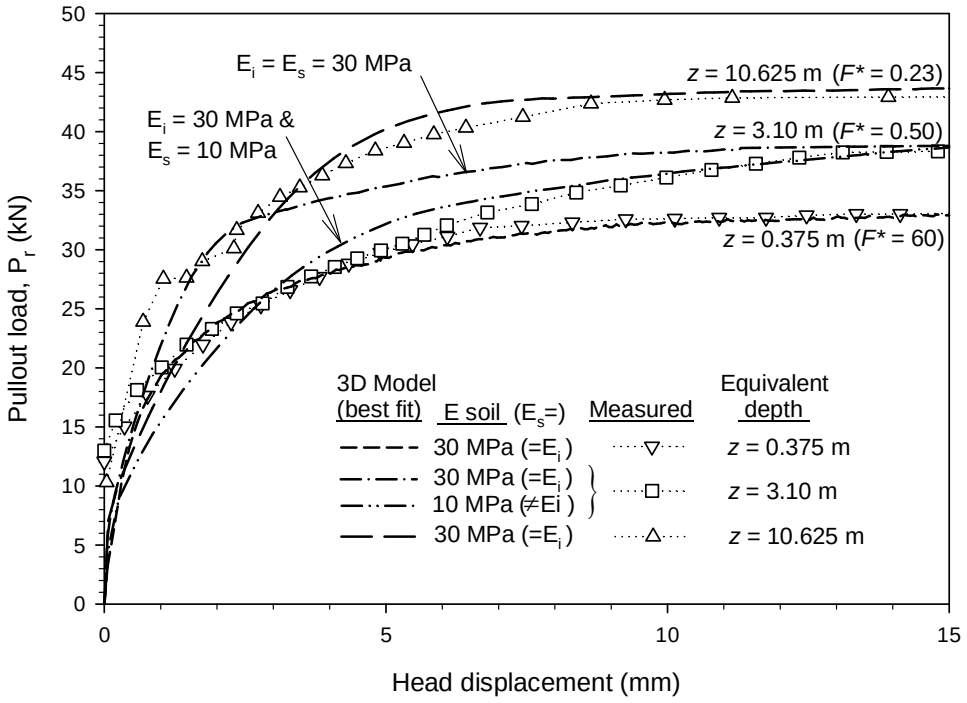

Figure 8.52: Comparison between real and 3D model steel ladder pullout tests results: AASHTO default (a) and calibrated (b) F^*-values.

As it can be observed in Figure 8.52a, if AASHTO-calculated friction factor default values (F^*) are assumed not much agreement was reached between real and numerical results. Whereas too low pullout load was obtained at low confining pressure ($z_{eq.}$ = 0.375 m-depth) too high pullout load was reached at high confining pressure ($z_{eq.}$ = 10.3625 m-depth). Despite lower numerical result was also obtained at the intermedia confining scenario ($z_{eq.}$ = 3.10 m-depth), this was the best matched case.

Results with modifications on F^*-values are presented in Figure 8.52b, while other parameters remain the same as in previous case. As it can be noticed, clear improved trends (in terms of modeled-measured results agreement) were obtained. As noticed in measured data for $z_{eq.}$ = 3.10 m-depth case, initial stiffness was not much well fitted neither expected between the data obtained at higher and lower confining cases. After the learnings from previous section 8.4.2.2 (pullout sensitivity analysis), just with changing the fill-soil stiffness modulus from E_s = 30 MPa to E_s = 10 MPa clear better agreement was reached.

Figure 8.53 presents the comparison between the AASHTO-calculated, measured (as already presented in Figure 8.22), and calibrated friction-interaction factors from the different confining pressure cases analyzed. As it can be observed, reasonable agreement was obtained between the 3D model parameters and the AASHTO default ones, despite in low confining case, where a much greater value of *f'* was required (even greater than the one calculated from measurements).

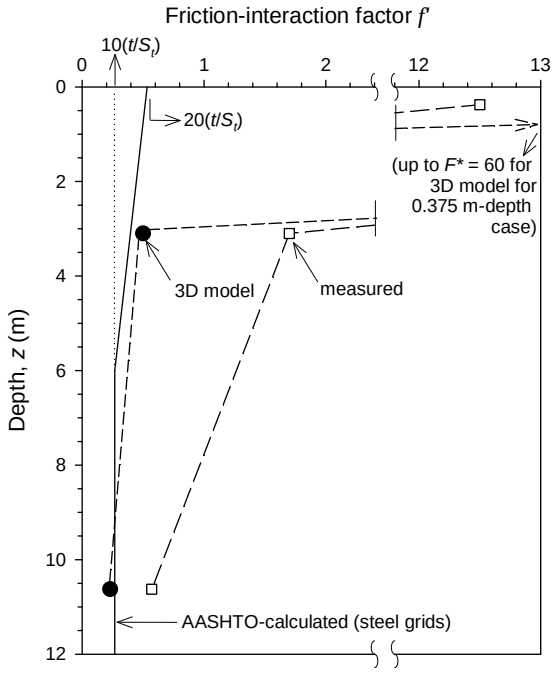

Figure 8.52: Comparison of AASHTO-calculated (steel grids), measured and 3D model-calibrated friction interaction factor (*f'*) for steel ladder pullout performed tests. (Note: $f' = F^*\alpha = F^*$, as α = 1 in inextensible reinforcement types).

8.4.3.2. Polymeric strips

Table 8.11 presents de model parameters considered to polymeric strips particular case, with parametric values suitable to the actual ones shown in Table 8.7. Both results from instrumented tests (dotted/scatted trends) and 3D model (trending lines) are presented in Figure 8.54 and 8.55 for AASHTO default (geogrids) and calibrated F^*-value cases.

As it can be observed in Figure 8.54a, if AASHTO-calculated friction factor "default" values (F^*) are assumed (not explicit F^*-values are proposed for polymeric strips, but geogrid/geotextile reinforcement values are considered) quite fine agreement was reached between real and numerical results with the exception of low confining pressure case ($z_{eq.}$ = 1.0 m-depth). As identified during model results development, cohesion had a huge effect in results. As specified in Table 8.11 - Note [(e)], first approach of interface cohesion value was considered with the same reduction as in frictional strength (i.e., $c_{interface} = R_i \times c_{soil} = (\tan\delta / \tan\phi_s)\, c_{soil} = (\tan(22^o) / \tan(31^o))\, c_{soil} = 0.67 c_{soil}$. Thus, a fixed $c_{interface}$ value equal to 0.67×14 kPa = 9.4 kPa was assumed at this stage in every confining pressure scenario (i.e., in all $z_{eq.}$ case).

With just refining of the pullout-friction factor (F^*) and interface cohesion values (c_i), clear improved trends were obtained in terms of measured and 3D model results comparison (see Figure 8.54b). In these cases, instead of constant F^* value in depth, about linear increasing values with reducing equivalent depth was considered (see later Figure 8.56), so F^* = 0.4 at $z_{eq.}$= 7.0 m-depth, F^* = 0.5 at $z_{eq.}$= 3.5 m-depth, and F^* = 0.56 at $z_{eq.}$= 1.0 m-depth. A minor cohesion value (c_i = 1 kPa) was considered at low confining pressure scenario, and increasing with depth up to soil cohesion value (i.e., $c_i = c_{soil}$ = 14 kPa) at higher conifing scenario case ($z_{eq.}$ = 7.0 m-depth). As shown in Figure 8.55, good agreement was reached between the measured and 3D model predictions on reinforcement head and reinforcement tail-end displacements comparison.

Figure 8.56 presents the comparison between the AASHTO-calculated, measured (as already presented in Figure 8.26), and calibrated friction-interaction factors from the different confining pressure cases analyzed. As demonstrated, not constant F^* value is required to improve the pullout performance in polymeric strip reinforcement. As it can be observed, reasonable agreement was obtained between the 3D model parameters and measured ones assuming cohesionless soil. The scale effect correction factor (α value) appeared to be in good agreement as α = 0.9 for the confining pressure scenarios with $z_{eq.}$> 3.5 m-depth. Figure 8.57 presents the same results as in Figure 8.52, but with including the effect of cohesion within the calculated and measured pullout friction factor (see Equations 8.14 and 8.15).

Table 8.11. Model material properties for polymeric strip pullout cases:

Parameters	Materials: Polymeric strip	Fill soil	Interface		
Unit weight (kN/m^3)	75	21	21		
Elastic modulus, E (MPa)	500 [(a)]	10 [(b)]	10 [(b)]		
Poisson's ratio, v (-)	0.3	0.3	0.45 [(c)]		
			Equivalent depths [(d)]:		
			z = 1.0 m	z = 3.5 m	z = 7.0 m
Cohesion, c (kPa)	-	14	· default [(e)]:	9.4	9.4
			· calibrated [(f)]:	1	14
Friction angle, ϕ-soil and δ-interface (deg.)	-	31	· default [(g)]: (F^* value=)	22 (0.4)	22 (0.4)
			· calibrated: (F^* value=)	29 (0.56)	26.5 (0.5)
Dilatancy angle, ψ (deg.) [(h)]	-	1		0	0

Notes: [(a)] Despite not much coincident with the reported stiffness for polymeric strips Grade 70 kN (about 2500 MPa, as may be deduced from Lawson 1991, and explicitly stated in Abdelouhab et al., 2011), after fixing other unknowns (as soil stiffness, see below), values of E_{strip} from 500 to 700 MPa demonstrated to give the best agreement with the measured pullout performance (see Figure 8.54).

[(b)] Value approximated from fill-soil settlement after applying vertical surchage, which is in agreement with soil material type (silty sand) and performed compaction.

[(c)] Despite Poisson's ratio demonstrated to have no much significant effect on pullout capacity, higher v_i-value (i.e., v_i = 0.45) was considered to best fit pullout capacity under high vertical pressure cases, to mobilize confinement (i.e., to increase mean stress p-invariant) and reduce unrealistic volumetric interface plasticization.

[(d)] Equivalent depths from actual fill-soil layer height above the reinforcement and surcharge loading applied on top of pullout box.

[(e)] Default interface cohesion value obtained from interface strength reduction (i.e., $c_{interface} = R_i \times c_{soil} = (\tan\delta / \tan\phi_s)\, c_{soil}$. $= (\tan(22^o) / \tan(31^o))\, c_{soil} = 0.67 c_{soil}$. Thus, default $c_{interface}$ value equal to 0.67×14 kPa = 9.4 kPa.

[(f)] Calibrated or best fit cohesion values as obtained from direct shear point-by-point data (i.e., less cohesion at low confining pressure, but also greater friction angle at that location).

[(g)] Default values from AASHTO pullout friction factor F^* for geotextile and geogrid reinforcement type (single linear value; see Figure 8.13) which corresponds to $\delta = \tan^{-1}(F^*) = \tan^{-1}(C_i \times \tan\phi) = \tan^{-1}(0.67\tan(31^o)) = \tan^{-1}(0.4) = 21.9^o$.

[(h)] $\psi = \phi_s - 30^o = 1$; however, interface material assumed as non-dilatant (i.e., $\psi = 0$).

a) AASHTO default F^*-value: $F^* = 0.4$:

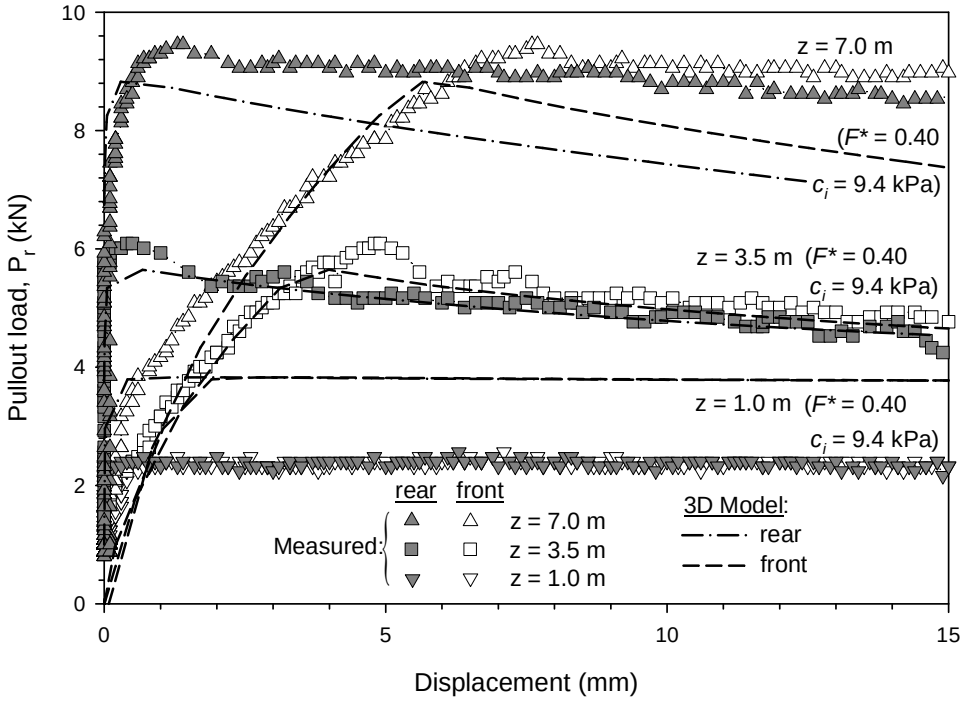

b) Calibrated/best fit F^* and interface cohesion (c_i) values:

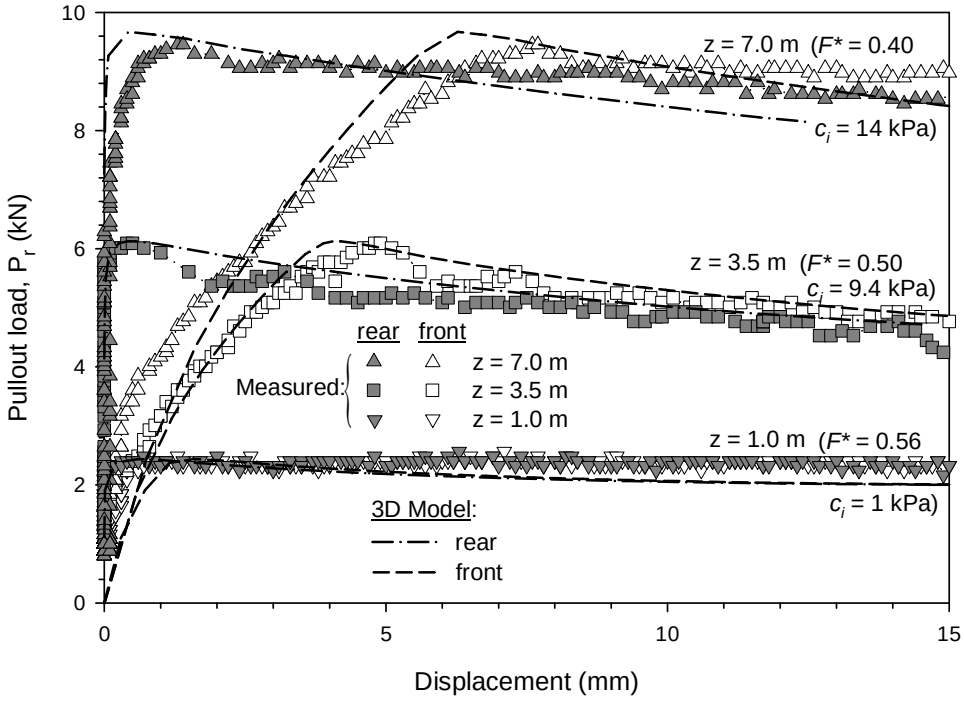

Figure 8.54: Comparison between real and 3D model polymeric strip pullout tests results: AASHTO default (a) and calibrated (b) F^*-values.

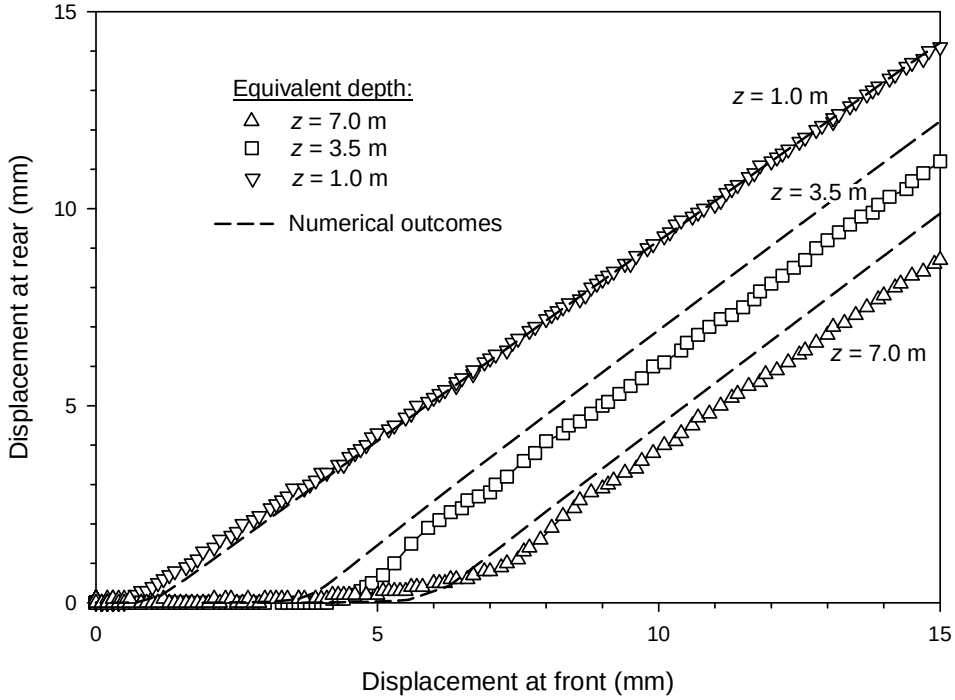

Figure 8.55: Comparison between real and 3D model polymeric strip pullout tests results: head and tail-end reinforcement displacements comparison.

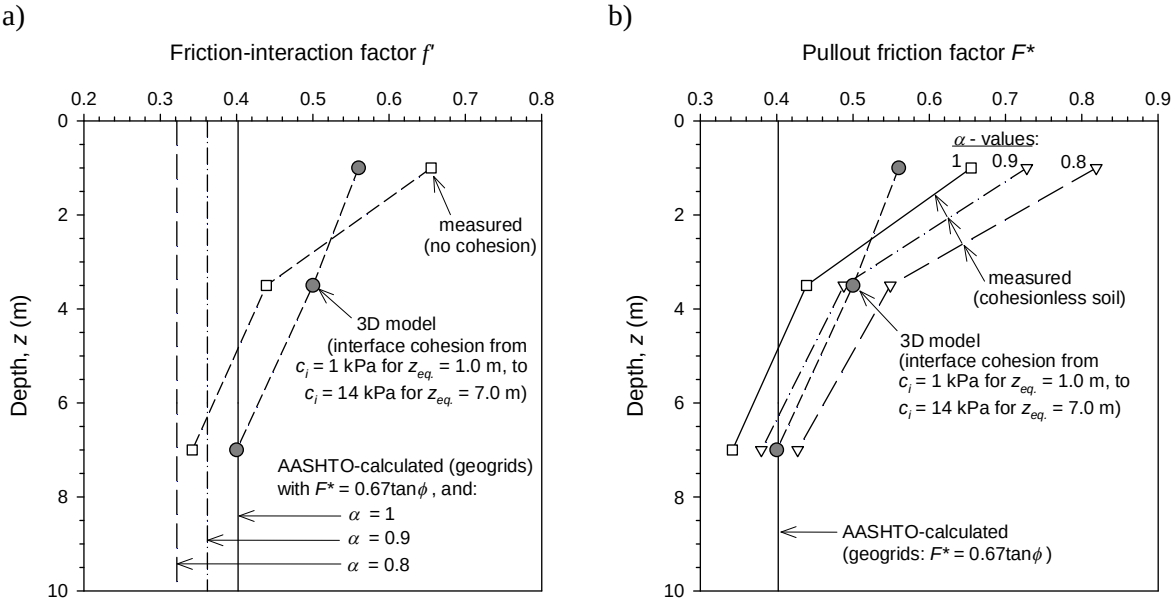

Figure 8.56: Comparison of calculated, measured and 3D model-calibrated friction interaction factor ($f' = \alpha F^*$) (a) and AASHTO-calculated (geogrids) pullout friction factor (F^*) (b) for polymeric strips pullout performed tests.

As presented in Tables 8.7 and 8.11, actual soil responded with some cohesion at direct shear tests (c_{soil} = 14 kPa). Despite non-cohesion soil materials are considered in AASHTO developments (see previous Equation 8.7), easy equation modifications can be performed to include cohesion. A comparison was performed and new friction-interaction factor deduced with including cohesion component within Equation 8.7.

$$P_r = CwL_e\sigma_v(F^*\alpha) + CwL_e(c_i\alpha) \quad (8.14)$$

Where, as in previous Equation 8.8:

$\left[CwL_e\sigma_v(F^*\alpha)\right]$ is the frictional strength component, as in Equation 8.8;

$\left[CwL_e(c_i\alpha)\right]$ is the component from cohesion strength;

P_r: Pullout strength.

w: is the reinforcement width in case of polymeric strip: w = 90 mm (Table 8.7).

L_e: is the length of the reinforcement sample: L_e = 1.05 m.

C: is the overall reinforcement surface area geometry factor based on gross perimeter of the reinforcement (equal to 2 for strips, i.e., two sides).

σ_v: is the vertical stress at the reinforcement level: $\sigma_v = \gamma_n \times z_{eq.}$

α: is a scale effect correction factor, which is assumed to be 1 for inextensible reinforcements (steel ladders), and less than 1 for extensible reinforcements. As commented, AASHTO proposes values of α which cannot be applied for polymeric strips (α = 0.6 for geotextiles and α = 0.8 for geogrid reinforcements) as this reinforcements type are not clearly extensible reinforcement if the extensible/inextensible behaviour is understood with regards to the soil deformation relation. Note that this factor has been assumed to be applied both in frictional and cohesional components of the equation.

F^*: is the pullout friction factor, corresponding to the soil-reinforcement transferred strength relation. As explained below it can be defined as $F^* = \tan\delta = C_i \times \tan\phi$ (where ϕ is the friction angle of the soil, δ is the soil-reinforcement interaction friction angle, and C_i corresponds to the interaction coefficient: $C_i = \tan\delta / \tan\phi$, assuming a default value of C_i = 0.67 for geogrids and geotextiles in AASHTO.

c_i: is the cohesion as soil-reinforcement interaction (i.e., interface), understood as soil-reinforcement adherence, with assuming a reduction of the shear strength derived from cohesion value (for example, with the same as in soil-strip reinforcement interaction frictional component, i.e., $c_{interface} = C_i \times c_{soil}$).

Thus, from previous Equation 8.14, the friction-interaction factor ($f' = F^*\alpha$) results as follows:

$$F^*\alpha = f' = \frac{P_r}{CwL_e\sigma_v} - \frac{\alpha c_i}{\sigma_v} \tag{8.15}$$

a) including cohesive soil assumption with interface adherence equal to $c_i = 0.67c_{soil}$:

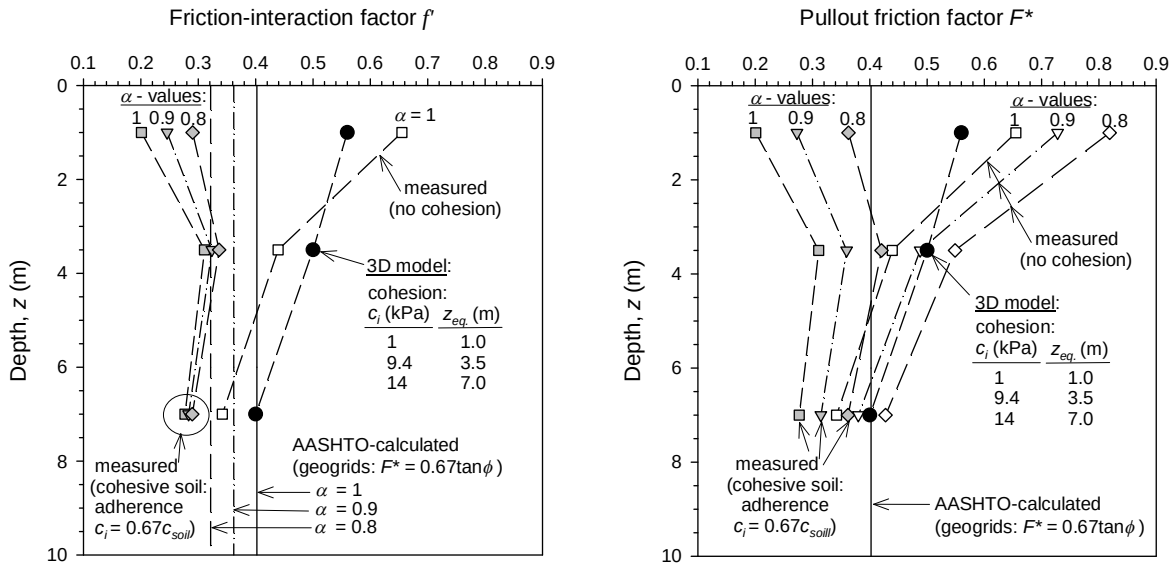

b) including cohesive soil assumption with interface adherence equal to: c_i = 1 kPa at $z_{eq.}$=1m, c_i = $0.67c_s$ = 9.4 kPa at $z_{eq.}$= 3.5 m, and $c_i = c_s$ = 14 kPa at $z_{eq.}$= 7.0 m, corresponding to 3D model best fit pullout performance:

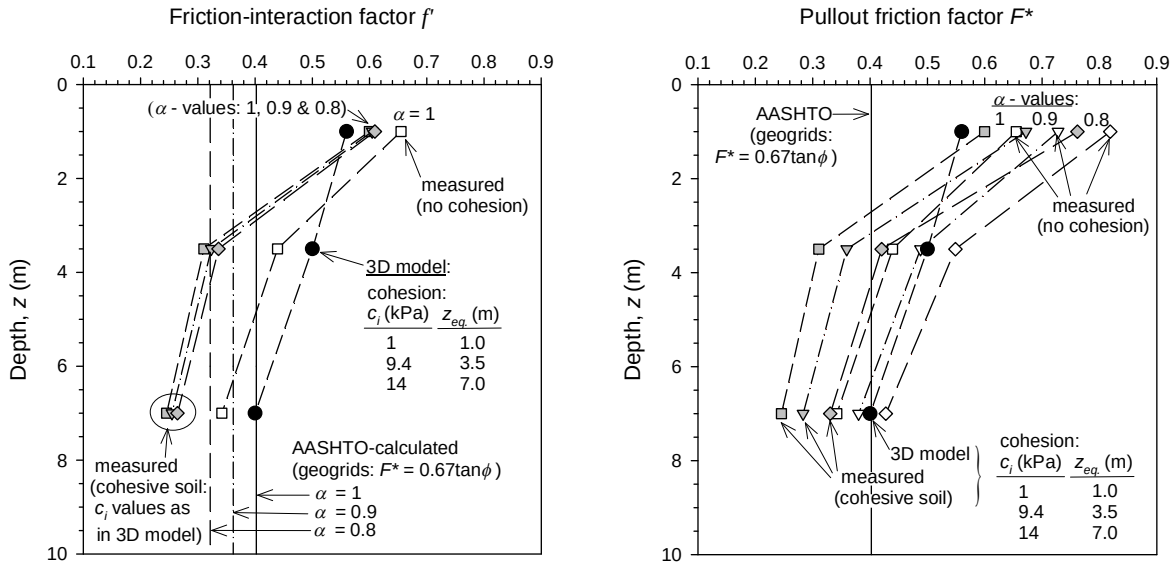

Figure 8.57: Comparison of calculated, measured and 3D model-calibrated friction interaction factor ($f' = \alpha F^*$) and AASHTO-calculated (geogrids) pullout friction factor (F^*) for polymeric strips pullout performed tests with and without cohesion values: a fixed interface adherence equal to $c_i = 0.67c_s$ (a), and variable interface adherence as obtained in best fit results from 3D model (b).

8.5. CONCLUSIONS

This chapter has described the details of proper in-lab pullout testing requirements, standard procedures, and proper execution of these tests. Results of several pullout testing series performed particularly in both steel ladders and polymeric strips reinforcement types have been presented. 3D numerical finite element modelling has been generated, presented, and explained, intended to analyze this kind of tests and with special focusing results variation due to sensitivity on typical parameter changes (basically the strength and stiffness of different component materials). As in previous Chapter 7, the same methodology about the interface definition with using continuum material elements has been presented also here for the soil-reinforcement interaction. Finally, after a reasonable estimation of fill-soil and interface material properties, a comparison with two measured pullout test cases has made, using a CODE_BRIGHT numerical code, with a proposed model calibration for this kind of tests, reinforcement types, and fill-soil scenarios given.

Advanced numerical 3D modelling for steel and polymeric reinforcement pullout tests using the finite element commercial software package CODE_BRIGHT have been developed and analyzed in this chapter. The resulting approaches and presented methodology may of interest for designers when soil-reinforcement pullout interaction is intended to be analyzed, complementary to the strategy of laboratory pullout testing series. Before design engineers can develop confidence in the accuracy of the numerical predictions of reinforcement pullout performance using commercial programs, program predictions must be tested against measurements recorded for instrumented pullout cases following proper testing procedures and accurate testing execution. Then, from a properly calibrated numerical model, easy parametric analysis can be done, providing information about non-tested complementary scenarios.

The chapter demonstrates a good agreement between the measured performance values from in-lab pullout tests and the numerical approach using an interface material as soil-reinforcement interaction. The presented results from pullout test led to better estimate the soil-reinforcement pullout interaction factors proposed by the codes when steel ladders and polymeric strip reinforcements are considered. The numerical approaches allow the prediction in case of parametric value changes from a properly defined base case.

CHAPTER 9

3D MODEL OF REINFORCED SOIL WALLS

9.1. INTRODUCTION

Numerical 2D models to perform mechanically stabilized earth (MSE) retaining wall full-height structures have been extendedly used and presented in previous Chapters 1 - 6. As demonstrated, proper calibration has been possible even for non-planar reinforcement cases (i.e., strips or bars; see Chapters 2 and 4). The simplification from real 3D to 2D plane strain has been possible by the transformation of the structural components width dimensions and the actual amount per width of any discrete component (basically, bearing pads and linear reinforcements, if required) to equivalent 1 m-width components (which becomes to an equivalent sheet in case of reinforcements). As the main (or weak) stress-strain directions of these kind of structures is quite well localized due to the slice symmetry assumed along the running direction of the wall, the transformation to a plane-strain continuum-slice is assumed to be, in general, faithfully representative.

However, in cases where linear reinforcement (i.e., strips, bars, ladders, etc.) are used, it could be interesting to have a more complete understanding of the system behaviour. Under this scenario, it may be necessary to identify divergences on results which can appear between locations through the less representative plane space direction (i.e., running wall direction). These variations have been already identified in previous Chapter 8 in the context of the Pullout tests performance. In those cases, relevant variability was obtained on vertical pressures through the width direction of the pullout box (i.e., on the horizontal and opposite to the reinforcement displacement direction) due to the real soil-soil vertical transfer of the shear stresses (see Figure 8.38).

A simplified 3D finite element model with CODE_BRIGHT software program (Olivella et al., 1996) has been developed to analyze a 6 m-high mechanically stabilized earth strip-reinforcement retaining wall structure. The purpose of this model is to be capable to achieve more accurate and faithfully behaviour results beyond the scope of the two-dimensional models. As known, the most relevant behaviour contribution of this type of structures is the soil-structure interfaces definition. After the followed methodology, results achieved, and

learnings obtained from previous Chapters 7 and 8, proper interface features have been implemented in this full-scale 3D model.

Despite some other models can be found in the literature about geotechnical engineering field, three-dimensional numerical models and methodology is still having young and limited knowledge scope. The main reasons of this are due to the multiple numerical troubles that appear working with these models, and probably also due to the complexity of the computer programs available for generate, solve, and working with 3D modelling. About reinforced soil or even soil nailing topic, not many references can be found. Anyhow, most of them are assuming planar reinforcement (Bergado and Teerawattanasuk 2008, Yoo and Kim 2008, Skejic and Balic 2015) so the 3D model may lose its intrinsic capabilities and resolution potential.

9.2. MODEL FEATURES

9.2.1. Model geometry, numerical mesh, and material components definition

Figure 9.1 presents the 3D finite element model mesh generated including main dimensions and related material components to perform reinforced soil earth retaining structures. Reinforced backfill, retained fill, and foundation were the soil materials defined. Concrete facing panels, soil reinforcement strip elements, and bearing pads were also modelled as structural material components of the system. Soil-Facing and soil-reinforcement were also defined as interface materials with continuum element methodology (as in previous Chapters 7 and 8).

The numerical model generated was shaped by a structured (and somehow coarse) mesh comprising 38430 linear tetrahedron elements which generates 7288 nodes. Despite this type of elements may not be the best one (trilinear hexahedron may would be preferable), concerns about numerical convergence and excessive calculation timing in initial models led to the decision to select tetrahedrons. As the model was intended to perform working stress conditions scenarios (which means far away from failure and less strains development) and after the comparison results reached within previous Chapters 7 and 8 interface models, the decision about the use of tetrahedron instead of hexahedron was expected to not generate results falling much away between both element types and making tetrahedron equally representative. Several solved cases confirmed this, with assuming the same coarse mesh size. Finest mesh also generated convergence problems and excessive computational times in some particular material properties cases. The final mesh was capable to solve all projected sensitivity case, with calculation times comprised between an hour (faster case) and a 4 days (slower cases).

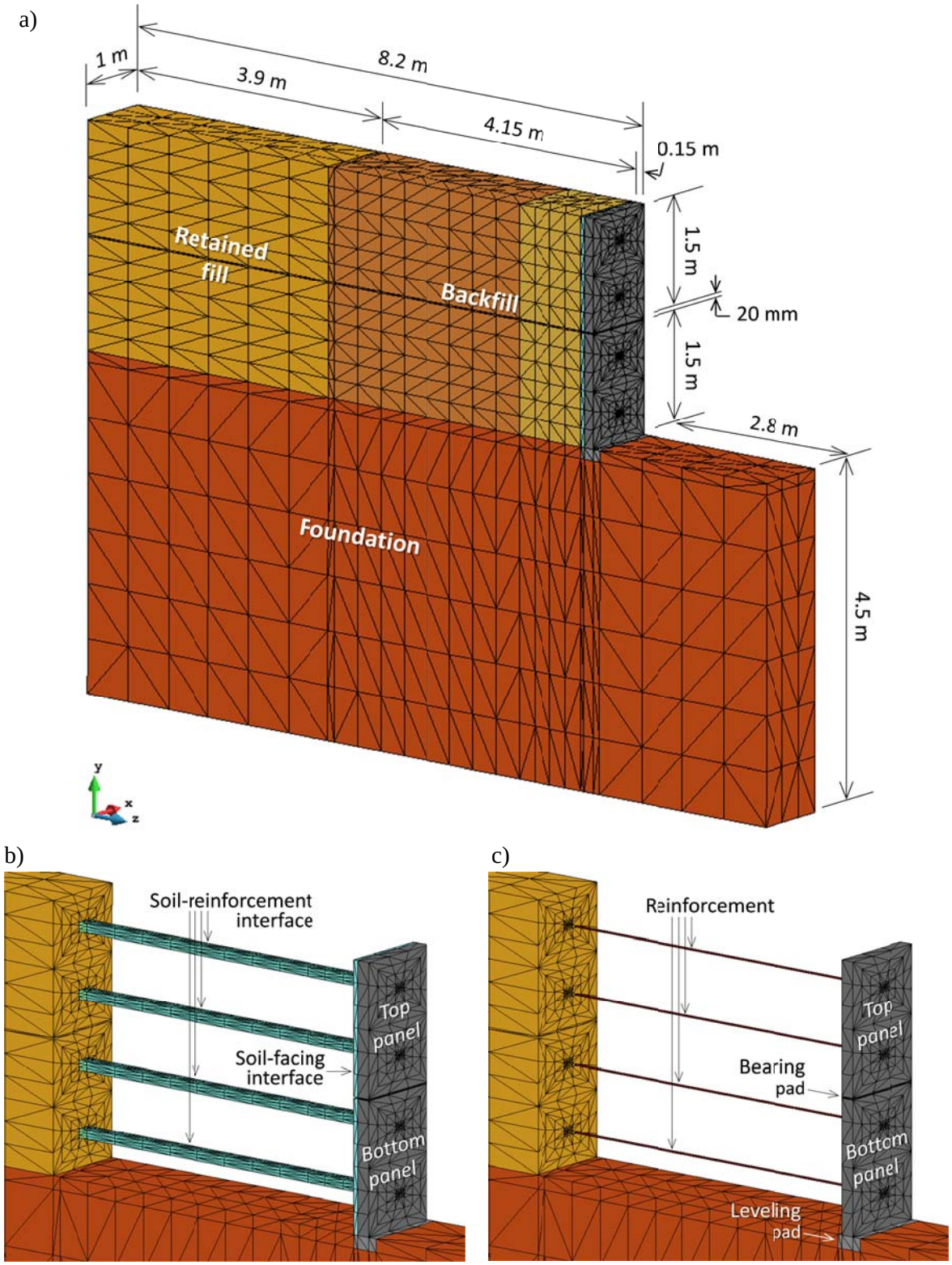

Figure 9.1: 3D model mesh, geometry, components and main dimensions: whole geometry (a), interfaces (b), and structural components detail (c).

The model has 3 m-high dimension and has all components to generate the least common denominator of a full-height MSE wall scenario. As the calculation for 3D numerical modelling derive into somehow tedious work (in terms of computational time required in addition to other complementary issues related to numerical convergence due to solver strategies), a simplified 3 m-high model was considered to model 6 m-high equivalent wall cases with applying a certain surcharge degree on top surface above the 3 m-high model case. Extended explanation about this is done in next section.

As it can be observed in Figures 9.1b and 9.2 (gray-blue lines and region), the same continuum elements interface methodology was considered to perform soil-facing and soil-reinforcement interactions as in previous Chapters 7 and 8, respectively. As it can be noticed, in soil-reinforcement interaction case (Figure 9.2b) the definition of the interface is coarser (i.e., less thick elements) than the assumed in Pullout test models. However, as mentioned before, the aim of the model was to perform working stress conditions, which relates to low shear-strains development in soil-reinforcement interactions and allows the use of coarse meshing zones with still maintaining an expected good response. The variations from assuming different elements amount of interface thickness, directly related to the computational time required so reach solution was also analyzed in Chapter 8 (see Figure 8.32).

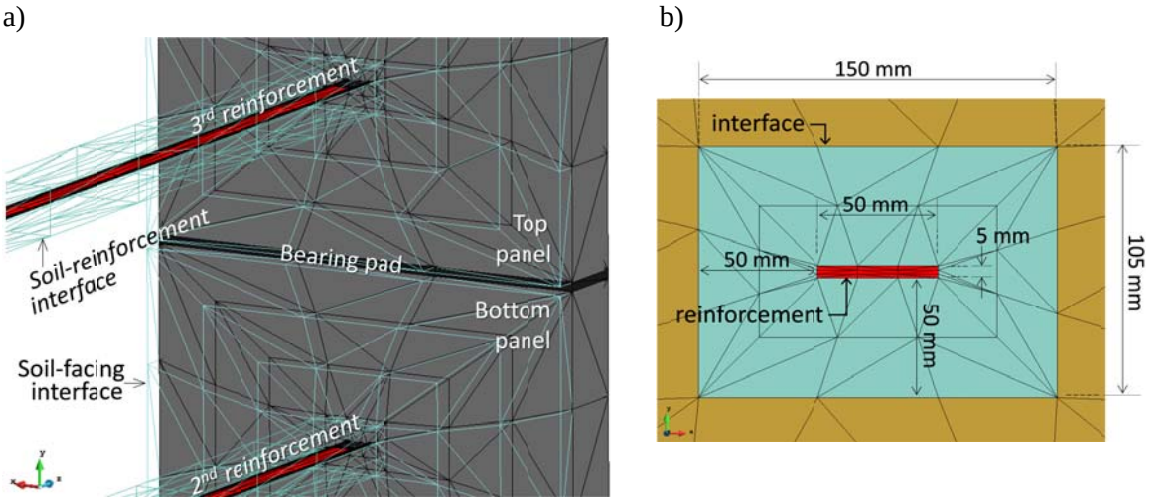

Figure 9.2: 3D model mesh: facing panel joint and reinforcement connection detail (a) and soil-reinforcement interface measurements definition (b).

Bearing pads are modelled as entire bearing piece dimension between panels (See Figure 9.2a). Proper transformation was made in order to represent the particular amount of pieces per joint, pads geometry and stiffness. Reinforcement elements were modeled as strip with 50 mm-wide × 5 mm-thick dimension (see Figure 9.2b). This dimension generates slightly larger

cross-section area than other steel strip dimensions reported (e.g., 50 mm-wide × 4 mm-thick as reported in Abdelouhab et al. (2011), or 100 mm-wide × 2.3 mm-thick as reported in Chida and Nakagaki (1979), among others). However, not only the stiffness per area is important but also the reinforcement elements perimeter due to the shear strength development. As explained in next section, proper equivalences can be done consequent to the stiffness (steel or polymeric) and the real cross-section area of the actual linear reinforcement strip (even ladder and bar cases) with regards to the modelled strip geometry.

9.2.2. Interval data (staged construction) and boundary conditions

Figure 9.3 shows the stepped construction modeling process, with backfill + reinforcement layer thickness of 0.75 m at each step after initial equilibrium and panels emplacement.

As commented, a simplified 3 m-high model was considered to model 6 m-equivalent wall height construction. This was achieved with applying a certain surcharge degree and distribution on top surface above the 3 m-high model case (see Figure 9.3h). This surcharge application was performed as follows: after the step-by-step calculation up to the 3 m-high, the stress state at the base-line (i.e., both vertical (σ_v) and shear (τ) stresses below the reinforced soil mass) was obtained. These vertical pressure and shear stress distribution (i.e., σ_v,τ stresses state below the retained fill should not be equal to that below reinforced backfill materials nor under facing panels) are then applied at the top of the 3 m-high model surface to generate an equivalent 6 m-high wall scenario. With fixing this stress state (σ_v,τ) at the top plane of the 3 m-high structure the model was then calculated up to the consequent final 6 m-equivalent wall height construction case. In other words, the foundation vertical and shear stress values obtained at 3 m-high structure were the ones assumed to be applied as ramp-loading above the structure with a simplified distribution to perform 6 m-high wall construction times.

This methodology allows to project and approximate loads generation of models with higher heights in case of rectangular reinforced block shape $H \times L$ at the lowest part of the structure (of course, with proper dimensions of the reinforced block length and adjustment of the appropriate least common denominator component measurements and properties).

Displacements in the orthogonal directions of the edge planes are not allowed, with the exception of the top-horizontal surface (where to apply the vertical surcharge). Both vertical and horizontal displacements were not allowed at the bottom foundation plane (full fixity condition). Actually this is not strictly a fully realistic boundary condition, but after some starting trial calculations was considered to fit better response than free horizontal displacement allowance. To take into account the propping panels effect of actual construction procedure, facing panels were assumed to be horizontally fixed (not vertically) up to the 7^{th} step.

a) Step 1: initial stresses (foundation)

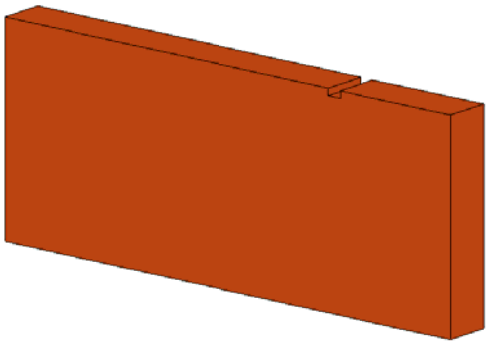

b) Step 2: leveling pad and 1st panel

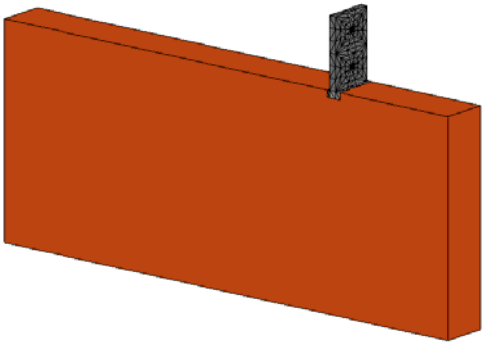

c) Step 3: 0.75 m soil layer

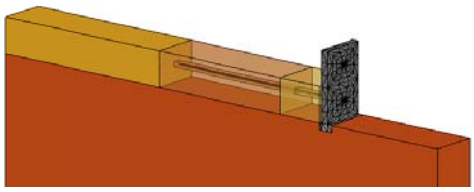

d) Step 4: bearing pad & 2nd panel

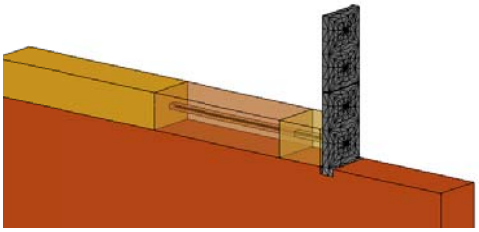

e) Step 5: 1.5 m soil layer

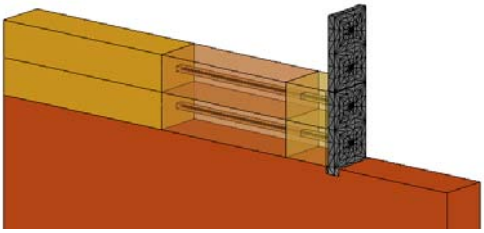

f) Step 6: 2.25 m soil layer

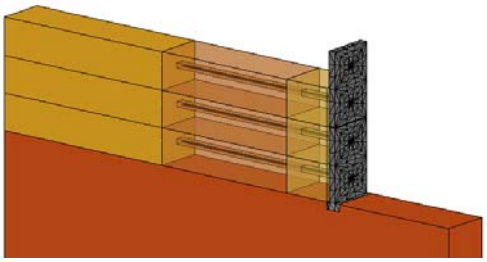

g) Step 7: 3.0 m soil layer

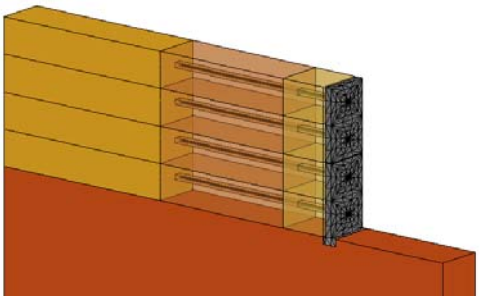

h) Step 8: vertical pressures on top (6.0 m soil layer – equivalent)

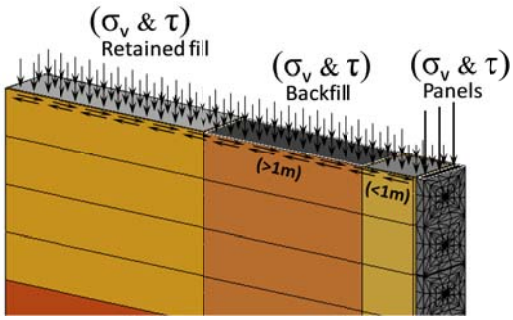

Figure 9.3: Stepped construction modeling process: from initial equilibrium at Step 1 (a) to 3 m soil pressure distribution on top of the 3 m model construction to generate 6 m-equivalent wall height construction at Step 8 (h).

9.2.3. Material properties and case studies:

All material properties assumed for the Base case are shown in Tables 9.1, 9.2 and 9.3. Table 9.2 presents the Base case soil materials (backfill, retained fill, and foundation) constitutive model parameters assumed as linear elastic-plastic. The parameter values assumed are in line with previous 2D numerical analysis (see Chapters 1-4), representing a suitable granular material to be installed as reinforced backfill. The good response under triaxial conditions was already demonstrated in previous Chapter 8 (see Figure 8.28). Both reinforced backfill and retained fill were assumed to have same strength-stiffness properties. A 50% reduction on stiffness was assumed within the first meter near the facing to take into account the typical reduction compaction efforts which occurs during construction. This reduction stiffness praxis was already done in previous 2D numerical analysis. Stiffness variability is also analyzed for both backfill and foundation materials and presented later.

Table 9.1. Soil materials parameters for 3D MSE wall model - Base case:

Parameters:	Soil materials:		
	Backfill [(a)]:		Foundation
	(> 1.0 m from face) [(b)]	(< 1.0 m from face)	
Unit weight, γ_n (kN/m^3)	18		20
Elastic stiffness modulus, E (MPa)	20	10	45 [(c)]
Poisson's ratio, ν (-)	0.3		0.3
Cohesion, c (kPa)	1		5
Friction angle, ϕ (deg.)	44		36
Dilatancy angle, ψ (deg.)	14		6

Notes: [(a)] Assumed to include both reinforced and retained backfill materials.
[(b)] Retained fill assumed to have the same strength-stiffness soil properties as Backfill zone far away than 1.0 m from facing.
[(c)] Equivalent to E_f = 100 MPa in case of foundation layer with 10 m-depth:
$E_{f\,(4.5\text{ m-depth})}$ = 4.5 m × ($E_{f\,(10\text{ m-depth})}$ / 10 m) = 4.5 m (100 MPa / 10 m) = 45 MPa.

Table 9.2 presents the Base case properties of the non-soil material components, as reinforcements, panels and bearing pads. These were modelled to be linear-elastic. As explained in Table 9.1 – Note [(a)], proper equivalences can be done consequent to the steel stiffness and any real cross-section area of a particular linear reinforcement strip with regards to the modelled strip geometry. In the assumed case, the strips modelled are equivalent to a 50 mm-width × 5 mm-thick strip emplaced in a two horizontal connections 1.35 m-width panel. Similar procedure was done for the High Density Polyethylene (HDPE) bearing pads

(assuming two pads installed in 1.35 m-width horizontal panel joints). In this case, also reduced (almost zero) Poisson's ratio was considered to take into account the real non-massive and ribbed shape of the pads, that allow most of the compression deformation with negligible lateral expansion. This was found to have a direct effect as per the front face boundary condition imposed at facing panels (i.e., propping) and to better perform pads compression during construction. Reinforcement and bearing pads stiffness variability is also analyzed for both materials and presented later.

Table 9.2. Non-soil material parameters for 3D MSE wall model - Base case:

Parameters:	Materials:		
	Reinforcements (steel) [(a)]	Panels	Bearing pads (HDPE) [(b)]
Unit weight, γ_n (kN/m^3)	75	24	10
Elastic stiffness modulus, E (MPa)	130000	32000	3.3
Poisson's ratio, v (-)	0.3	0.2	0.1 [(c)]

Notes: [(a)] Equivalent stiffness from steel stiffness modulus (210 GPa) and 2 steel strips amount disposed in 1.35 m panel-width with 50 mm-width x 3 mm-thick cross-section geometry. Note that the proper elastic stiffness value to be incorporated into the model has to be converted to 50 mm-width × 5 mm-thick reinforcement 3D-model geometry.

[(b)] Equivalent stiffness from 2 HDPE pads installed in 1.35 m panel-width × 0.14 m panel-thick joint adapted to 1 HDPE in 1 m-width × 0.15 m-thick panel measurements in 3D model.

[(c)] Reduced Poisson's ratio value to take into account the real ribbed geometry of the bearing pads (i.e., non-massive) and boundary conditions between panels, which use to allow compression with negligible lateral expansion.

Table 9.3 presents both soil-facing and soil-reinforcement interface material properties for the Base case. The learnings achieved in previous Chapters 7 and 8 were considered to the 3D full-height wall model. A strength-stiffness reduction factor of $R_{i\ (facing)} = 0.6$ was considered in soil-facing interaction (with assuming non-dilatancy effect), and about $R_{i\ (reinforcement)} = 0.52$ (equivalent to $F^* = 0.5$; see Chapter 8) to the soil-reinforcement interaction (maintaining both backfill stiffness and backfill dilatancy value, which demonstrate good agreement in previous Chapter 8). Despite this value is known to not be constant in depth at low confining pressure states, as the model is performing wall depths from $z = 3$ m to $z = 6$ m, it is assumed to generate enough confining pressure to allow the use of a constant value. This assumption is in agreement with instrumented data reported by Chida and Nakagaki (1979) for an equivalent wall height ($H = 6$ m) and steel strip reinforcement. Variability on reduction factors for both soil-facing and soil-reinforcement interfaces is also analyzed and presented later.

Table 9.3. Interface materials parameters for 3D MSE wall model - Base case:

Parameters:	Interface materials:	
	Soil-facing [(a)]	Soil-reinforcement [(b)]
Unit weight, γ_n (kN/m^3)	19	19
Elastic stiffness modulus, E (MPa)	4.02	20
Poisson's ratio, ν (-)	0.45	0.45
Cohesion, c (kPa)	0.6	1
Friction angle, δ (deg.)	30.1	26.6
Dilatancy angle, ψ (deg.)	0	14 [(c)]

Notes: [(a)] Soil-facing interface strength-stiffness reduction factor assumed equal to R_i = 0.6, which affects both stiffness and strength (see Equations 7.1 to 7.6 in previous Chapter 7).

[(b)] Soil-reinforcement steel strip interaction assuming δ = 26.6º (= ϕ_i) is equivalent to an interface reduction factor of R_i=tanδ/tanϕ = 0.52, which corresponds to a pullout friction factor (F^*) equal to tanδ = tan(26.6º) = 0.50 (i.e., F^* = tanδ = $R_i$tanϕ = 0.52tan44º = 0.50), fairly well fitting AASHTO requirements (F^* = 0.4 for smooth steel strips). This value is assumed to remain constant at reinforcement locations deeper than 3 m from top of wall (i.e., all reinforcement layers modeled), which is in good agreement with Chida and Nakagaki (1979) as performed by Yu et al. (2015a).

[(c)] Interface dilatancy angle assumed as equal to fill-soil dilatancy angle in soil-reinforcement interaction.

Table 9.4 presents and define the complementary 10 cases generates to perform sensitivity analysis from Base case. All these cases can be divided in two groups. First group of sensitivity cases are arranged by cases 1, 2, 3 and 4, in where just different backfill and foundation stiffness combinations were generated to perform different stress-strain opposite scenarios. Second group is composed by the rest of cases (cases from 5 to 8) where particular variations were generated in a single parameter in each grouping case (cases 5 and 5b to bearing pad stiffness variation, cases 6a and 6b to reinforcement stiffness, case 7 to soil-facing interaction factor variation, and, finally, case 8 to soil-reinforcement interaction variation). Any non-mentioned parameter in each sensitivity case remains constant and equal to the Base case.

Table 9.4. Sensitivity variations from Base case:

Sensitivity on [a]:	Base case values (case number 0):	Variation cases:	Case number:
• Backfill stiffness, E_b	E_b = 20 MPa ($E_{b(1st\text{-}m)}$ = 10 MPa)	E_b = 10 MPa ($E_{b(1st\text{-}m)}$ = 5 MPa) [b]	1 & 2
		E_b = 100 MPa ($E_{b(1st\text{-}m)}$ = 50 MPa) [c]	3 & 4
• Foundation stiffness, E_f	E_f = 13.5 MPa	E_f = 4.5 MPa [d]	1 & 3
		E_f = 45 MPa [d]	2
		E_f = 450 MPa [d]	4
• Bearing pads stiffness, E_p	HDPE: E_p = 3.3 MPa	EPDM: E_p = 0.4 MPa	5 & 5b [e]
• Reinforcement stiffness, E_r	Steel: E_r = 130000 MPa	Polymeric [f]: E_r = 5000 MPa & E_r = 500 MPa	6a 6b
• Soil-facing interface strength-stiffness reduction factor, R_i	R_i = 0.6 (E_i = 4.02 MPa)	R_i = 0.3 (E_i = 1.0 MPa)	7
• Soil-reinforcement pullout friction factor, F^*	F^* = 0.50	F^*- variable [g, h]: from F^* = 0.28 at bottom layer, to F^* = 0.38 at top layer	8

Note: [a] Non-mentioned parameters remain the same as in Base case.

[b] Soil-facing interface stiffness ($E_{i(\text{soil-facing})}$) equal to 2.01 MPa as per R_i = 0.6 reduction stiffness relation ($E_{i\,(\text{soil-reinforcement})} = E_{backfill}$).

[c] $E_{i(\text{s-f})}$ = 20.1 MPa as per R_i = 0.6 value (and $E_{i(\text{s-r})} = E_b$).

[d] $E_{f\,(4.5\text{ m-depth})} = 4.5\text{ m} \times (E_{f\,(10\text{ m-depth})} / 10\text{ m})$, so for E_f = 4.5, 45, and 450 MPa correspond to an equivalent $E_{f\,(10\text{ m-depth})}$ = 10, 100, and 1000 MPa, respectively.

[e] Additional 5b-case with foundation stiffness E_f = 13.5 MPa was considered in order to represent the best fit FLAC 2D model case from Yu et al. (2015a) with regards to Chida and Nakagaki (1979) steel strip reinforced and instrumented wall case. Also E_r = 270 MPa, which corresponds to the equivalent stiffness from steel stiffness modulus (200 GPa) and 2 steel strips amount disposed in 1.35 m panel-width with 100 mm-width x 2.3 mm-thick cross-section geometry (as in Chida and Nakagaki 1979).

[f] Assumed soil-reinforcement interaction factor R_i = 0.67 in case of polymeric reinforcement interaction (as per AASHTO 2014) so a pullout friction factor $F^* = \tan\delta = R_i\tan\phi = 0.67\tan 44^o = 0.65$, which returns an interaction friction angle equal to $\delta = 32.9^o$.

[g] Assuming steel ladder reinforcement (8 mm bars diameter) and the related bilinear soil-reinforcement strength interaction, the following four values were considered: F^* = 0.38 at z_i = 3.375 m, F^* = 0.35 at z_i = 4.125 m, F^* = 0.32 at z_i = 4.877 m, F^* = 0.28 at z_i = 5.627 m (which are related with the AASHTO definition: $F^* = 20t/S_t$ at z = 0 m up to $F^* = 10\ t/S_t$ at $z \geq 6$ m).

[h] Reinforcement stiffness consequently changed to E_r = 113000 MPa, equivalent to 2 units steel ladder units with 8 mm longitudinal bars diameter (two longitudinal bars per ladder).

As commented in previous section (see explanation on Figure 9.3h), the foundation vertical and shear stress values obtained at 3 m-high structure were the ones assumed to be applied above the structure with a simplified distribution to perform 6 m-high wall construction times. Both shear and vertical stresses obtained after 3 m-high construction (7^{th} step) are summarized and grouped in four different application top surface zones, representing the actual non-uniform vertical pressure distribution obtained. Table 9.5 presents these foundation stress states (σ_v,τ) applied as ramp-loading surcharge at top surface in last calculation step.

Table 9.5. Foundation stress state (σ_v,τ) reached at H = 3 m to perform H = 6 m-equivalent wall height construction cases (i.e., stresses applied at top surface in 8^{th} step):

Sensitivity cases:	Top stresses (kPa)	Zone (see Figure 9.3h):			
		Facing panels	Reinforced backfill:		Retained fill
			(<1 m from facing)	(>1 m from facing)	
Case 0 (Base case)	σ_v	216.88	29.29	51.72	53.67
	τ	61.03	5.48	1.80	-0.12
Case 1	σ_v	256.10	31.82	49.04	53.40
	τ	68.0	6.12	2.05	-0.11
Case 2	σ_v	193.67	30.15	52.80	53.64
	τ	46.1	1.90	1.33	0.05
Case 3	σ_v	277.09	44.32	45.68	51.07
	τ	94.2	10.62	1.64	0.41
Case 4	σ_v	183.59	32.80	52.65	53.60
	τ	48.69	4.18	1.55	-0.05
Case 5	σ_v	204.44	29.80	52.34	53.67
	τ	62.2	6.47	1.51	-0.18
Case 5b	σ_v	232.25	31.40	50.38	53.56
	τ	68.0	8.29	1.91	-0.21
Case 6a	σ_v	209.63	30.26	51.90	53.67
	τ	62.38	6.54	1.93	-0.12
Case 6b	σ_v	207.81	30.52	51.93	53.67
	τ	62.77	6.77	1.93	-0.13
Case 7	σ_v	207.21	30.00	52.07	53.67
	τ	63.18	6.27	1.66	-0.15
Case 8	σ_v	216.21	29.36	51.71	53.68
	τ	61.20	5.53	1.80	-0.13

9.3. BASE CASE RESULTS

9.3.1. Global displacements

Figures 9.4a-c show the vertical displacements obtained at different construction steps (1.5 m, 3 m, and 6 m-equivalent). As it can be seen, the maximum displacements location is consequent to the construction step stage, appearing at a certain depth below the surface. Figure 9.4d shows the horizontal displacements obtained at 6 m-equivalent wall height construction. Maximum outward displacement was obtained in a bulb-shape between both panels region.

a) H = 1.5 m

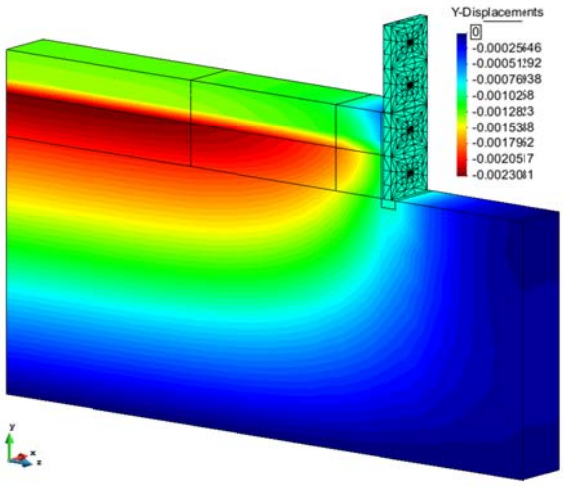

b) H = 3 m

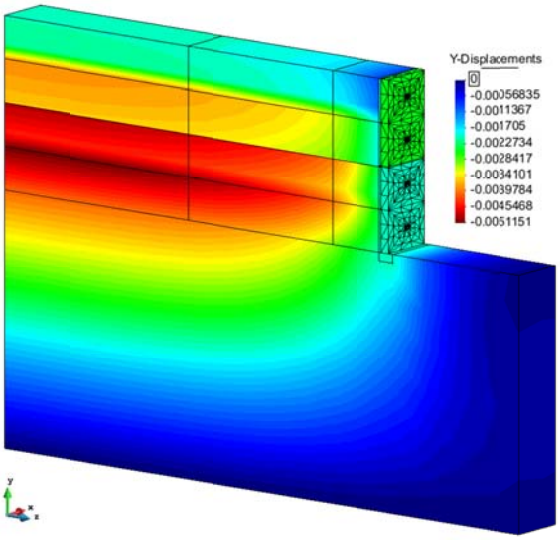

c) H = 6 m-equivalent

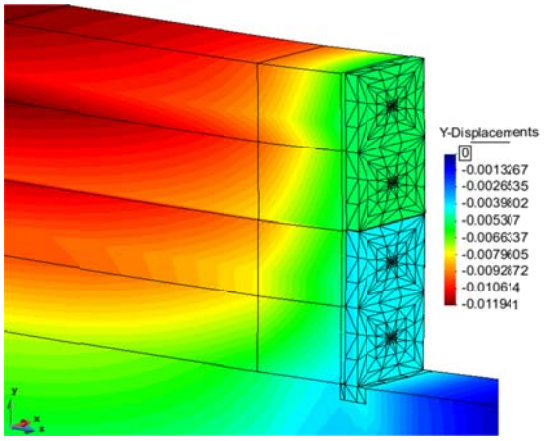

d) H = 6 m-equivalent

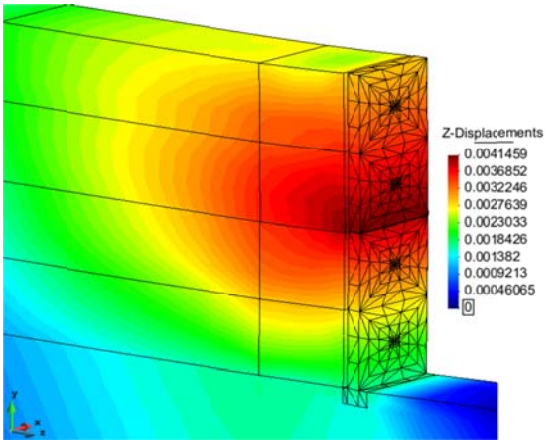

Figure 9.4: Vertical displacements at different construction steps: 1.5 m (a), 3 m (b), and 6 m-equivalent wall height construction. Horizontal displacements at 6 m-equivalent wall height construction (d). (Base case).

Figure 9.5 presents the lateral displacements plotted at several vertical sections after 6 m-high wall construction. The magnitude of the displacements resulted in a reduction of magnitude as far as the section is displacements magnitude is away from facing. As observed, the vertical boundary (and related displacement conditions) behind the structure seems to slightly affect results in the section located at 6 m-distance from facing. However, this was not expecting to influence main results of the structure (i.e., locations closer to the facing, reinforced soil and reinforcement elements).

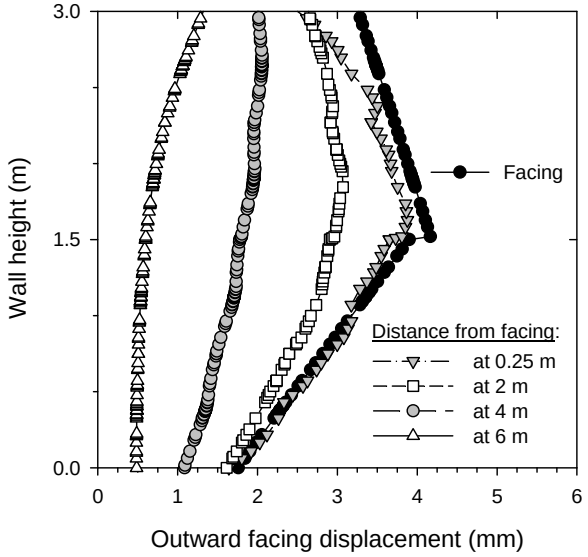

Figure 9.5: Lateral displacement at several vertical sections after 6 m-high wall construction. (Base case).

A rear view detailing the back of panels and reinforcement vertical displacement (without showing backfill material) is presented in Figure 9.6. Displacements were ranged to be similar to the maximum ones obtained in the whole model analysis with all materials selected at 6 m-equivalent wall height construction (Figure 9.4c). In these figures, deformed mesh was amplified 20 times in each construction step. As observed, very similar to the soil settlement also the reinforcement reached a certain degree of deformation during construction after loading (e.g., about 1 cm at 6 m-equivalent construction stage).

More detained results settlement plots are presented in Figure 9.7. As shown Figure 9.7a, soil settlement at 3rd reinforcement layer level (sections at 0.25 m and 0.125 m-distance from lateral boundary) resulted very similar than 3rd reinforcement vertical displacement and deformed shape (section at 0.5 m-distance from lateral boundary). The maximum settlement values reached were about 10 mm whereas top panel settled about 5 mm. Comparison between settlements obtained in all reinforcement layers at 3 m and 6 m-equivalent wall height construction times are plotted in Figure 9.7b. As expected, different response was

obtained at 3 m and 6 m-equivalent wall height construction. Larger settlements were obtained at 3rd and 4th reinforcement at 6 m-equivalent height whereas the smallest settlement was, as expected, at bottom reinforcement layer under the same step surcharge. The order from largest to smallest settlement is opposite in 3 m wall height construction (7th step).

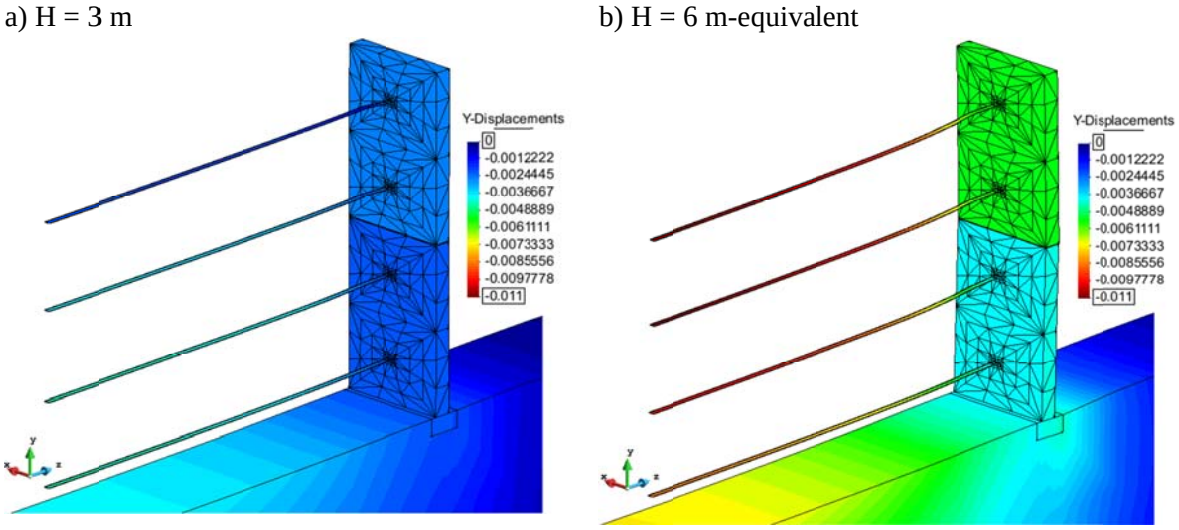

Figure 9.6: Vertical displacements detailed at soil-facing interface rear view: 3 m (a), and 6 m-equivalent (b) wall height construction. Displacements ranging 0 – 11 mm and deformed mesh amplified 20 times. (Base case).

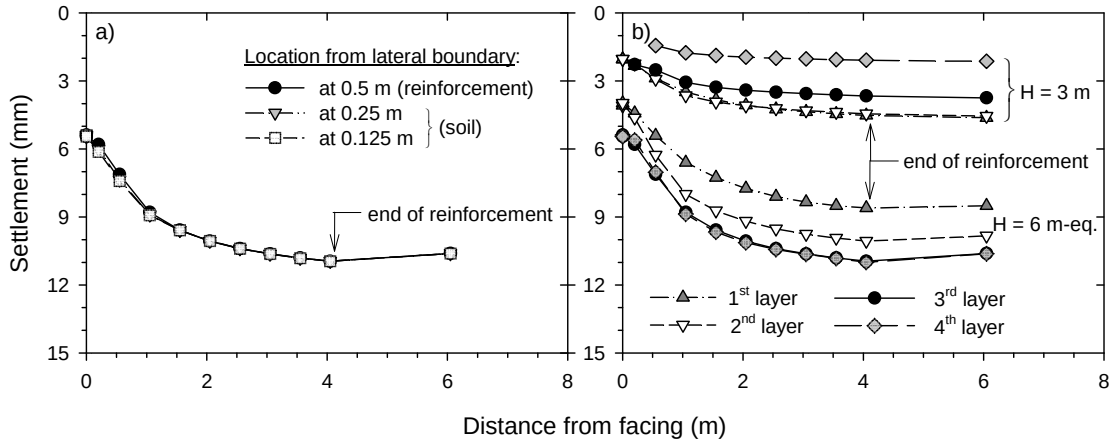

Figure 9.7: Settlement at reinforcement layers: comparison with regards to lateral boundary distance location at 3rd reinforcement layer level (a), and comparison between reinforcement layers at different construction stages (b). (Base case).

Figure 9.8 shows the vertical displacements occurring within soil-facing zone through two different cross-sections at different distances from lateral boundary. To a better isolation of desired results the magnitude of the vertical displacements was selected to be ranging from 3 to 6 mm. Was possible to identify the effect of the existing reinforcement within the soil at 0.5 m-distance section (Figure 9.8a) with regards to the soil-soil interaction (section at 0.25 m-distance; Figure 9.8b). As shown, just slightly divergences can be detected between both results, with numerical highlighted zones near the connections above the reinforcements.

a) b)

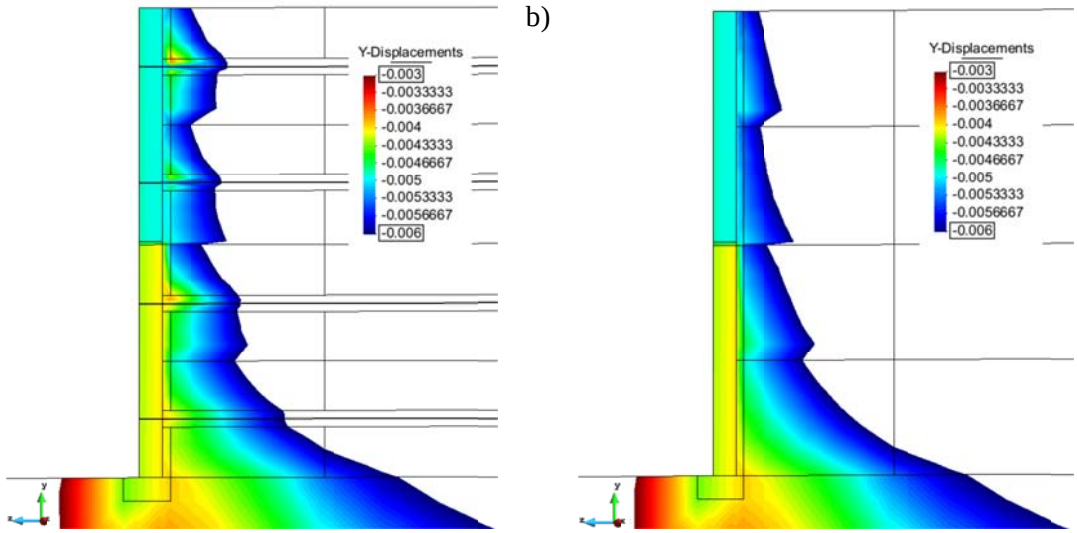

Figure 9.8: Settlements within soil-facing zone at a cross-section at 0.5 m from lateral boundary (a) and at 0.25 m from lateral boundary (b). Note: settlements ranging from 3 to 6 mm. (Base case).

Additionally to Figures 9.7a and 9.8, Figure 9.9 presents the vertical displacements obtained at each reinforcement horizontal plane layer at the end of construction (H = 6 m-eq.). As observed in the detailed views presented in Figures 9.9b to 9.9e (with specific restriction of ranging results), non-uniform vertical displacements were obtained around the reinforcement-to-facing connections (slightly lesser reinforcement connection displacement than soil settlement).

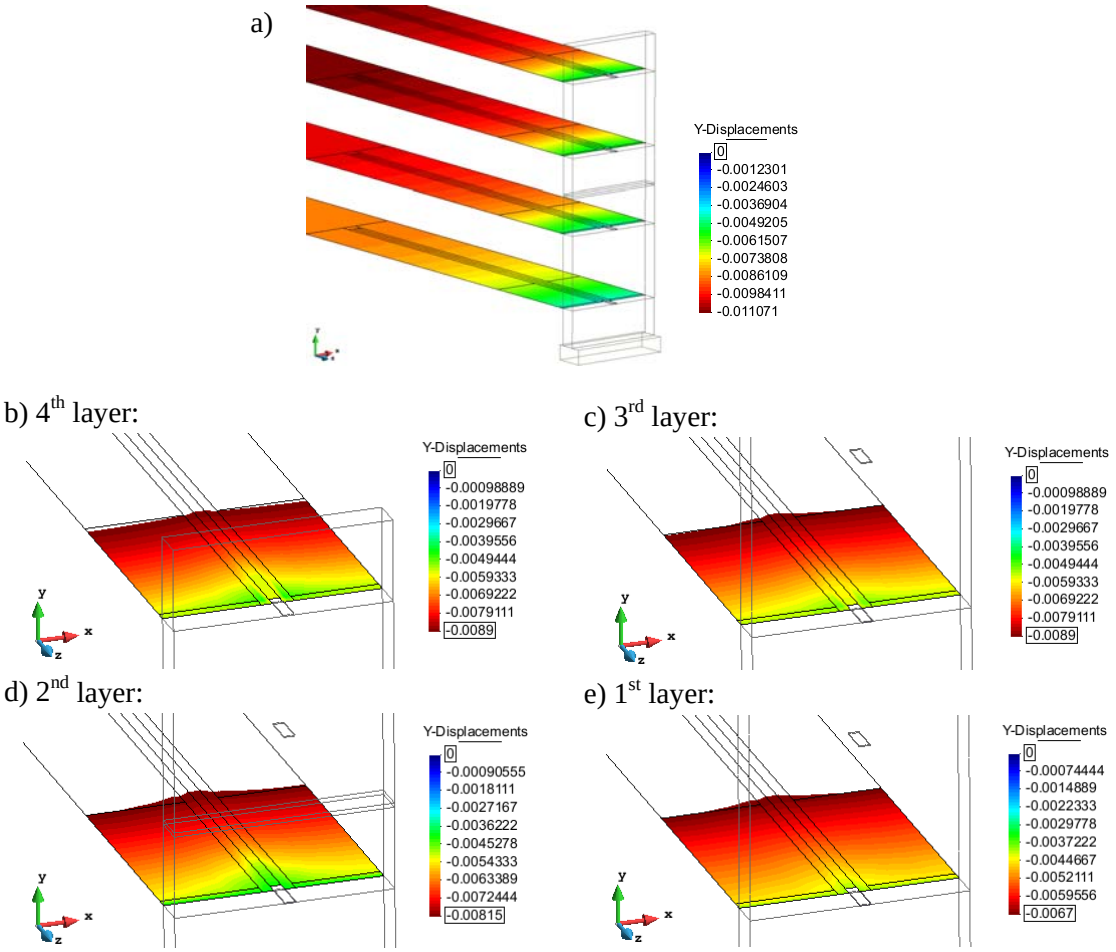

Figure 9.9: Vertical displacements obtained at reinforcement layers horizontal planes.

9.3.2. Stress-strain response

Figure 9.10 shows the vertical soil stresses distribution at 3 m and 6 m-equivalent wall height construction steps. Note that only soil stresses wanted to be analyzed in this figures, thus, consequent ranging of values were selected to discriminate greater stress results appearing in structural components or interfaces (in contact of structural components, which can develop stress due to the shared node between and smooth contour results plotting condition). Greater vertical pressures and are logically obtained in 6 m-equivalent wall step (about 175 kPa the maximum) than in 3 m-high (about 140 kPa), with a clear reduction of vertical stresses at the low compacted soil zone near the facing in both construction steps.

As mentioned, the vertical boundary plane behind the structure looks to slightly affect results in that particular surrounding area. An example can be found in vertical stress results with the non-uniform color development detected in that contour at top zone (Figure 9.10b, top-background retained fill corners). This is translated to a non-fully developed initial stresses. However, as mentioned, this was not expecting to influence main results of the structure.

a) H = 3 m b) H = 6 m-equivalent

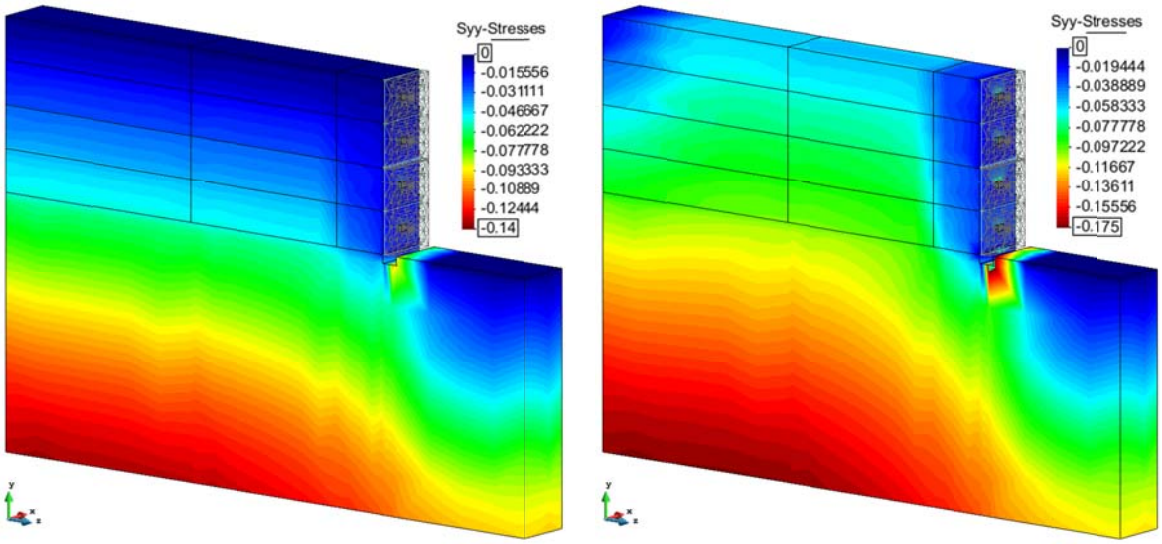

Figure 9.10: Vertical soil stresses at 3 m (a) and 6 m-equivalent (b) wall height construction times. (Base case).

Figure 9.11 presents the vertical foundation pressure distribution developed under the backfill. As it can be observed, non-uniform vertical foundation pressure distribution was obtained in both construction stages. Whereas far from facing vertical pressure achieves the self-weight of the soil above (in 6 m-equivalent case was not fully reached, but close enough), vertical pressure is dramatically reduced close to the facing, and then increases under the facing (i.e., vertical facing toe load) up to values much higher than the self-weight of panels (i.e., vertical facing load factor: $(\sigma_v / (H\gamma_{panels})) > 1$). Similar foundation pressure trends have been already obtained in Chapters 2, 5, and 6, and already reported by Damians et al., 2014 and 2015a, and Huang et al., 2009.

As explained in Section 9.2.2, the vertical pressure values obtained at 3 m-high structure were the ones assumed to be applied above the structure with a simplified distribution to perform 6 m-high wall construction times (an as mentioned, with including also the shear stresses developed).

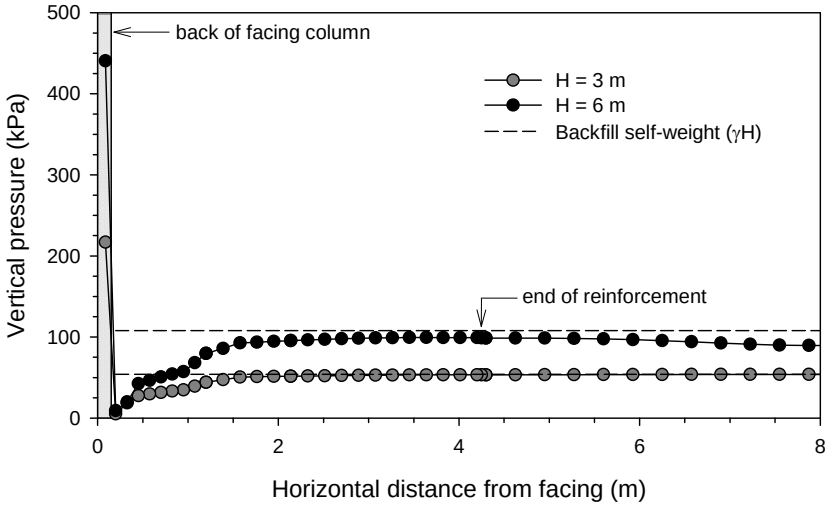

Figure 9.11: Vertical foundation pressure at 3 and 6 m-equivalent wall height construction times. (Base case).

As demonstrated in previous Chapter 8, the presence of linear reinforcements buried into the soil generates loads transferred from soil to reinforcement by shear (or, in case of transversal elements or ribbed reinforcements, also by bearing). In case of granular soil materials (as the assumed backfill material, featuring commonly granular draining material as per design code requirements), soil dilatancy effects are generate at low confining states due to the soil-reinforcement interaction. In case of relative soil-reinforcement displacement is developed, this dilatant property results into a positive volumetric strains around the reinforcement (i.e., upper vertical displacement above reinforcement) and a consequent increasing of vertical pressure values.

Figure 9.12 shows the Base case vertical pressures development obtained at several vertical cross-section planes within the backfill. As it can be detected, non-uniformed vertical pressure distribution is obtained. Figures 9.12 c and 9.12d shows the results plotted with iso-stress lines. This latest format results makes easy the detection of vertical stress discontinuities.

a) H = 3 m b) H = 6 m-equivalent

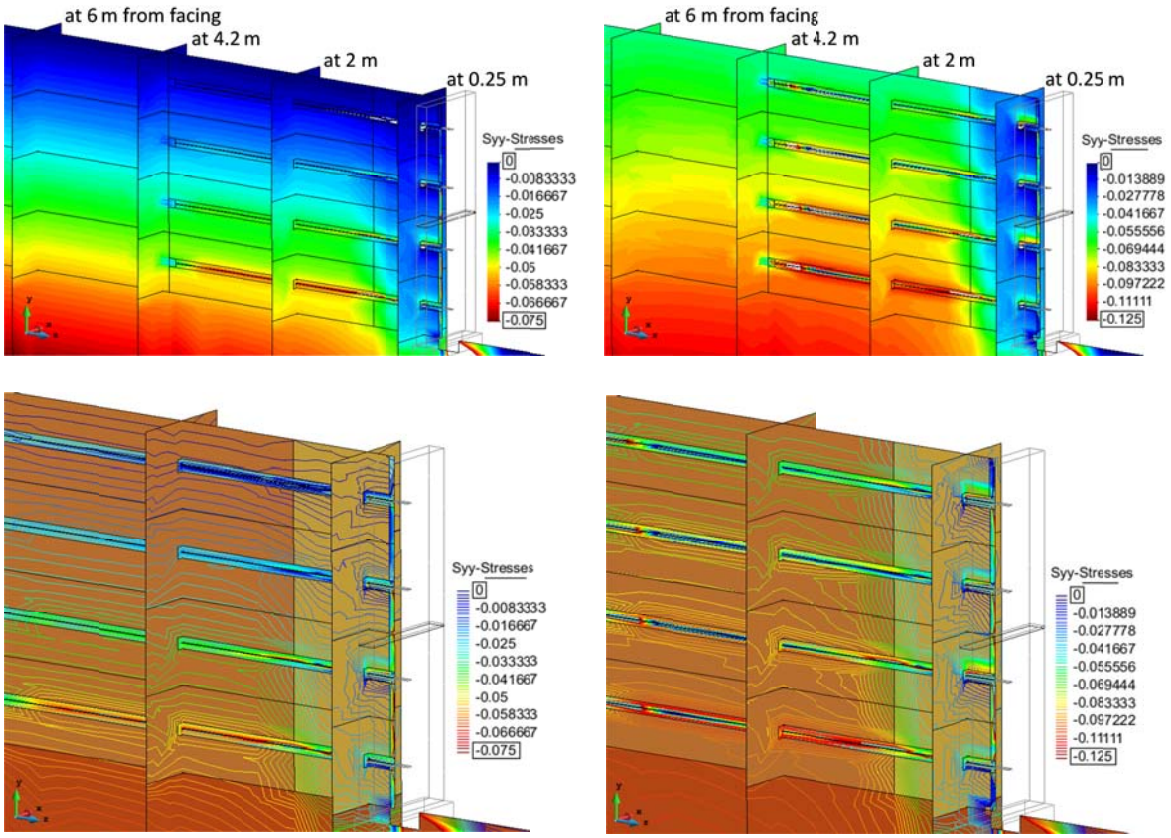

Figure 9.12: Vertical pressure obtained at several vertical cross-section planes after 3 m (a) and 6 m-equivalent (b) wall height construction times. Contour iso-stress lines also attached to a better distinction of results. (Base case).

Figures 9.13 and 9.14 present the vertical pressure horizontally developed in reinforcement layers at 0.25 m and 2.0 m distances from facing, respectively (Base case). As results are plotted with regards to horizontal distance (i.e., pressure development with regards to distance from lateral boundary), this allows to determine three-dimensional effects of the model (further than two-dimensional simplification restrictions). As shown, greater divergence of results was obtained at 0.25 m from facing location, where greater relative soil-reinforcement displacements were achieved with consequent soil dilatancy development only above the reinforcement. This dilatant behaviour (positive volumetric strains) affects both above and below reinforcement strip locations at 2.0 m from facing, and affects in a major manner near reinforcement (i.e., higher vertical stress values at 0.25 cm than 10 cm distance from reinforcement). At 2.0 m from facing (Figure 9.14) the difference between vertical pressure results at reinforcement location (0.5 m from lateral boundary) and at lateral boundary achieved factors from 1.25 to 1.4 (i.e., times greater in the middle of the graph and below the reinforcements). These factors increased up to 2.25 and 5.6 at 0.25 m from facing (Figure 9.13) above reinforcements. As already shown in Figure 9.11, at 0.25 m from facing results (corresponding to the low compacted backfill zone), vertical pressure is much lower than the backfill self-weight.

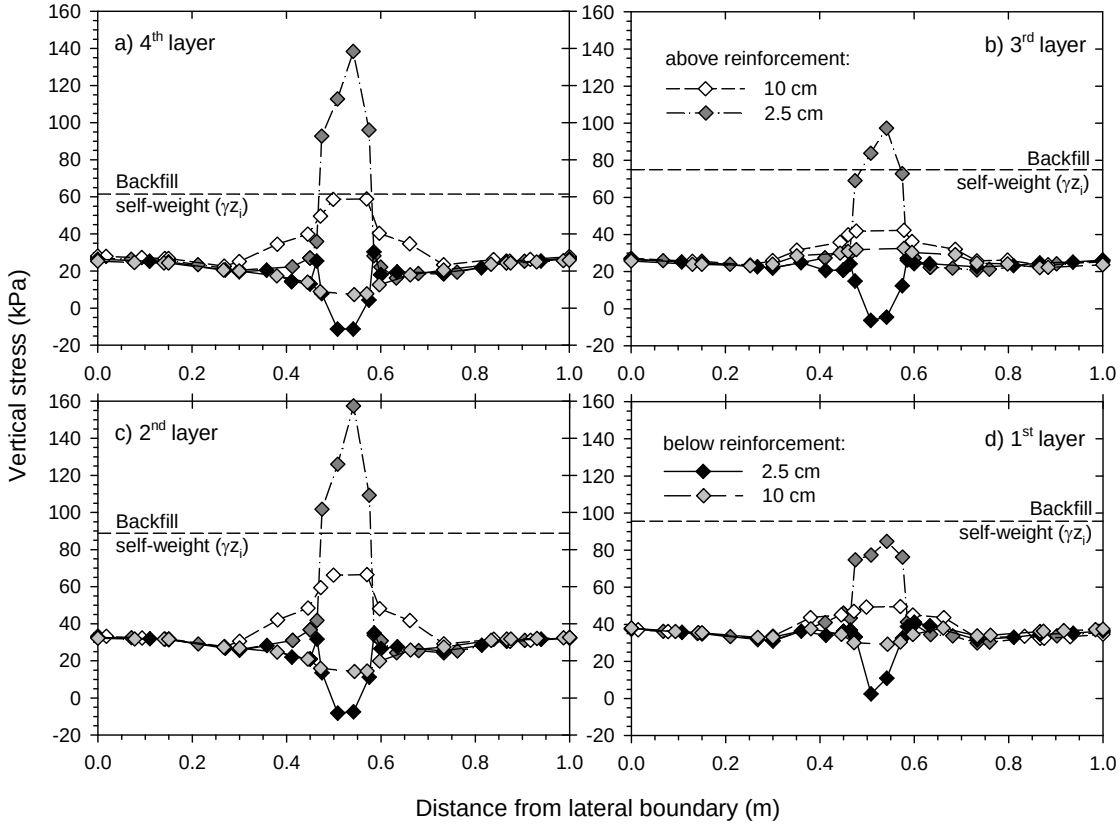

Figure 9.13: Vertical pressure at reinforcement layers location at 0.25 m from facing.

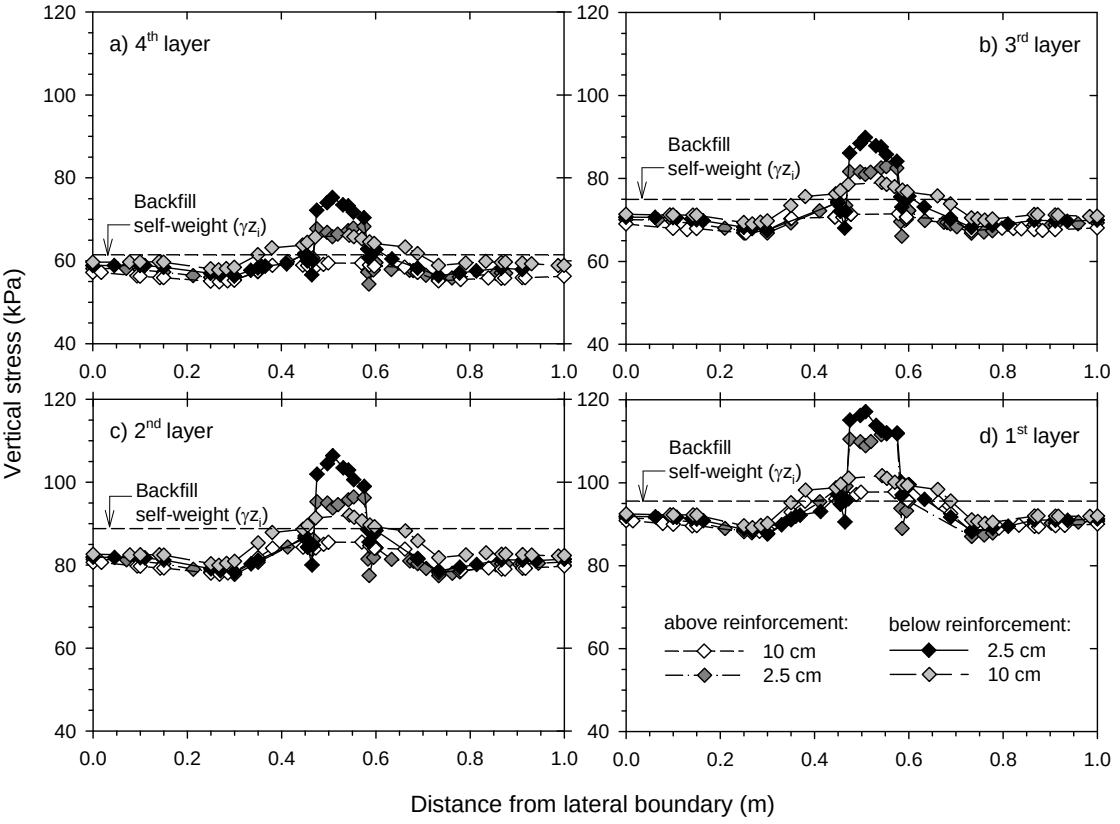

Figure 9.14: Vertical pressure at reinforcement layers location at 2.0 m from facing.

Figure 9.15 presents the same horizontal plane vertical pressure development as in previous results but at location away from reinforcements (just after reinforcement tail-end in Figure 9.15a and 2 meters after the reinforcement tail-end in Figure 9.15b. Whereas the vertical pressure distribution generated localized reduction just after reinforcements (probably due reinforcement displacement and consequent relaxation of stresses), stresses remain almost constant at 6.0 m from facing (about 2 m after the tail-end of reinforcements).

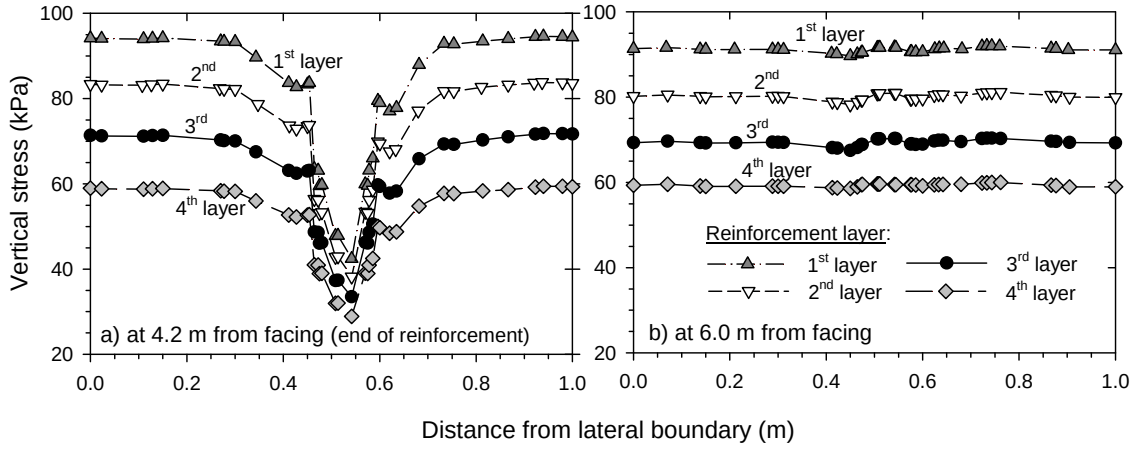

Figure 9.15: Vertical pressure at reinforcement layers location at 4.2 m (a) and 6.0 m (b) from facing. (Base case).

Both volumetric and shear (or deviatoric) plastic strains developed at 6 m-equivalent wall height construction stage are presented Figure 9.16. Results obtained from structural components (i.e., facing panels and reinforcements) are not shown within the ranging results, but indeed yes the soil-structure interface components (i.e., soil-facing and soil-reinforcement interfaces). Consequent to the previous results, Figures 9.16b and 9.16d show how plastic volumetric strains are developed around reinforcements due to soil dilatancy effects. These results are in agreement with previous Figure 9.13 results.

9.3.3. Lateral earth pressure

The horizontal earth pressure generated at Base case 6 m-equivalent wall height construction stage at different distance planes from facing are presented in Figure 9.17. To determine three-dimensional effects of the model and verify 2D reduction suitability, results obtained in different cross-section distance from lateral boundary are analyzed to detect any discrepancy between results at reinforcement section (0.5 m horizontal distance from boundary) and soil-soil sections (0.25 and 0.125 m horizontal distance from boundary). As observed, results obtained away from reinforcements are almost the same with no distinction with regards to lateral boundary distance. However, results obtained within the reinforced backfill region

actually present major differences as far as the results are obtained at reinforcement locations (third column of results) or at soil-soil locations (first and second column). This is not possible to detect in a two dimensional model simplification.

Results are plotted in comparison with the theoretical ones from lateral earth pressure coefficient of the reinforced backfill (i.e., $\sigma_h = \sigma_v K_r$) which is commonly defined proportionally to the active earth pressure (K_r/K_a). As shown, despite the distance from boundary, factors within K_r/K_a = 1.25 to 2.0 are required to best fit lateral earth pressure trends within reinforced zone, closer to active state near the facing. Within the foundation, lateral earth pressure results in trends well ranged between active (top of foundation) and at-rest (bottom of foundation) earth pressure states.

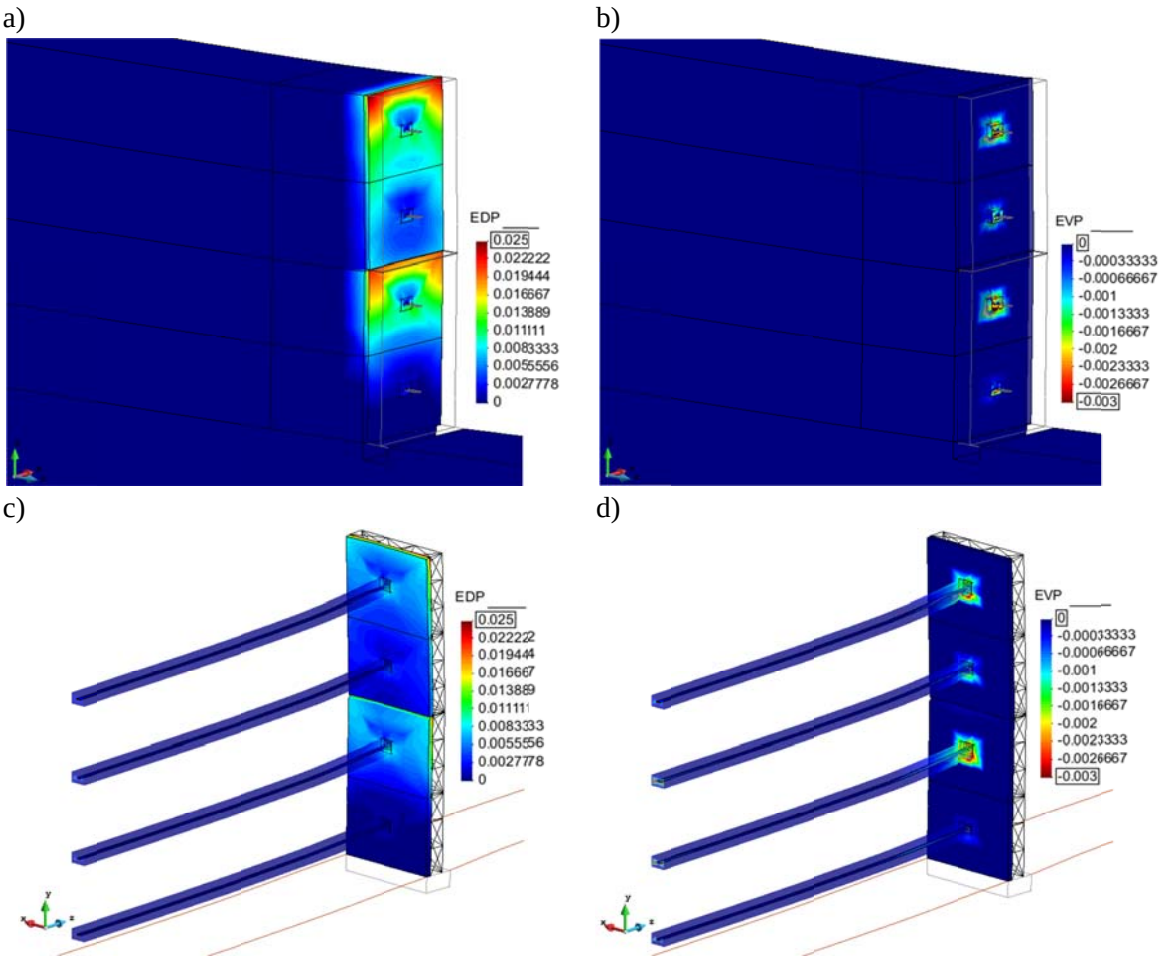

Figure 9.16: Plastic strains at 6 m-equivalent wall height construction: shear (a and c; up to 2.5%) and volumetric (b and d; up to 0.3%). Transparent soil-reinforcement and soil-facing interface rear view (c and d). (Base case)

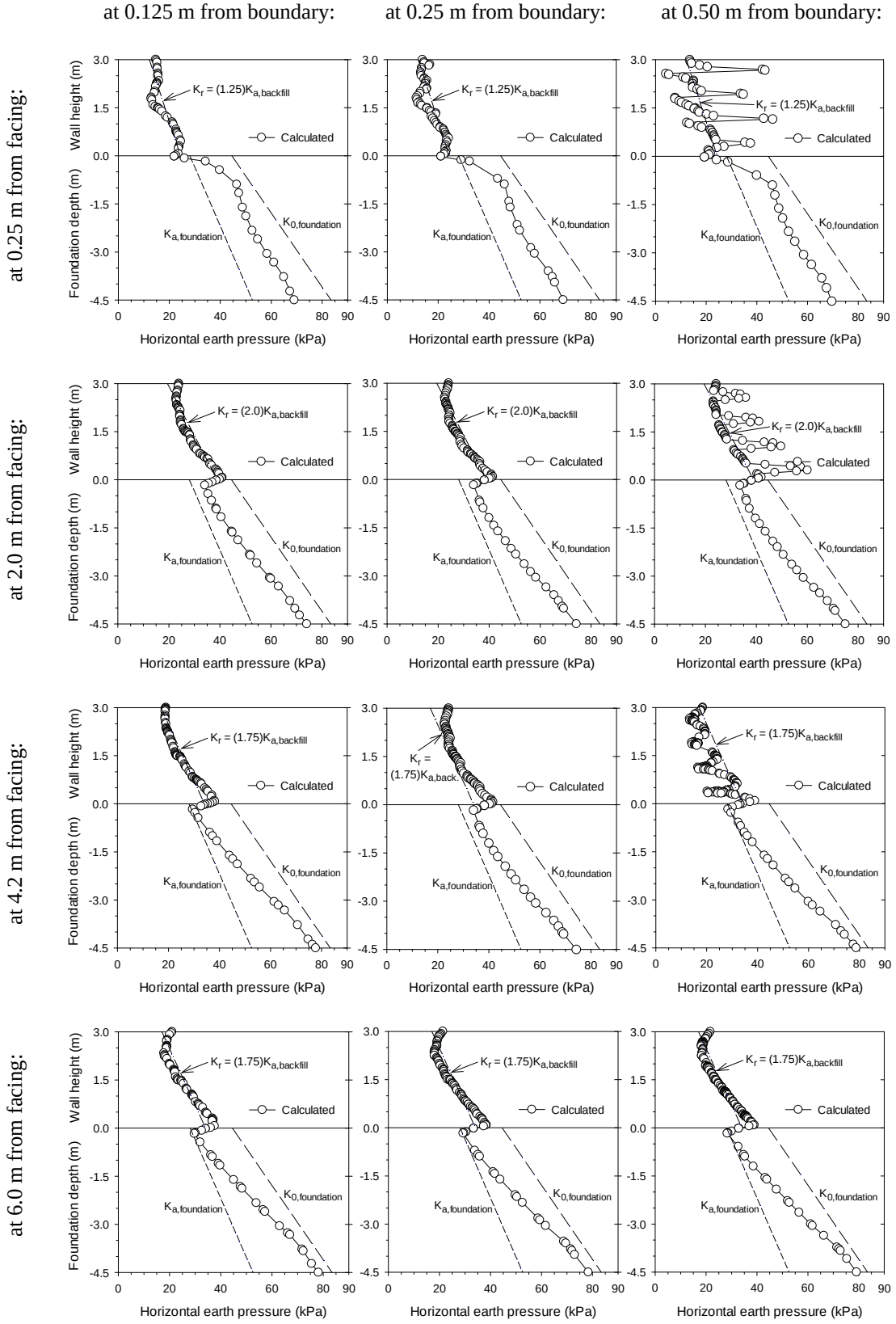

Figure 9.17: Horizontal earth pressure at different distances from facing. (Base case).

9.3.4. Reinforcement loads

Figure 9.18 shows the resulting tensile reinforcement loads predicted in Base case. Despite the differences from models and previous scenarios assumed, results are within same ranging results as the ones obtained in Chapters 4 and 6 for steel reinforced 6 m-high wall cases. Better comparison between real data (from Chida and Nakagaki 1979 reported case) and best fitting 3D model is provided in next section once sensitivity analyses are developed and results from Case 5b presented (see Table 9.4).

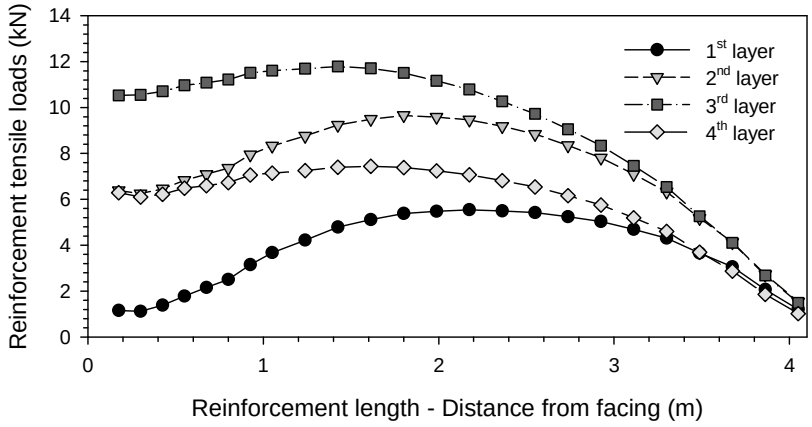

Figure 9.18: Tensile reinforcement loads predicted in Base case (case 0).

9.4. SENSITIVITY ANALYSIS

This section presents the results obtained from the different sensitivity cases proposed in Table 9.4. As commented, all cases modify just a single parameter value to perform another feasible case scenario. From trending results variability it was possible to identify which parameters and magnitude of these parameters play a main role in terms of parametrical sensitivity in MSE walls.

9.4.1. Vertical facing toe load

Figure 9.19 presents the variability of the vertical facing toe load factor 3D model results obtained from backfill and foundation stiffness combination cases (cases from 1 to 4; see Table 9.4) at H = 6 m-equivalent wall height construction stage. Additionally, results obtained from 2D PLAXIS model assuming the same scenarios and material component features are also presented. Two different PLAXIS models were generated modeling facing panels as beam or plate structural elements (line elements defined by flexural and axial stiffness) otherwise assuming a defined continuum material area with elastic concrete

properties (as in 3D model presented methodology; see Table 9.2) (see Chapters from 1 to 4 to notice particular and extended details of the 2D PLAXIS model featured by beam elements). Both material and beam elements were generated to model the same facing components properties (concrete and bearing pad). However, different performance was obtained probably due to geometrical discrepancies between both facing model cases (e.g., hinges at beam-to-beam connections with related ease rotation at toe, among others). Despite the differences between both modeled facing elements, results are within the same magnitude and sensitivity variation tendencies (i.e., similar shaped region of results due to soil material stiffness combinations), also obtained in the 3D modeling cases.

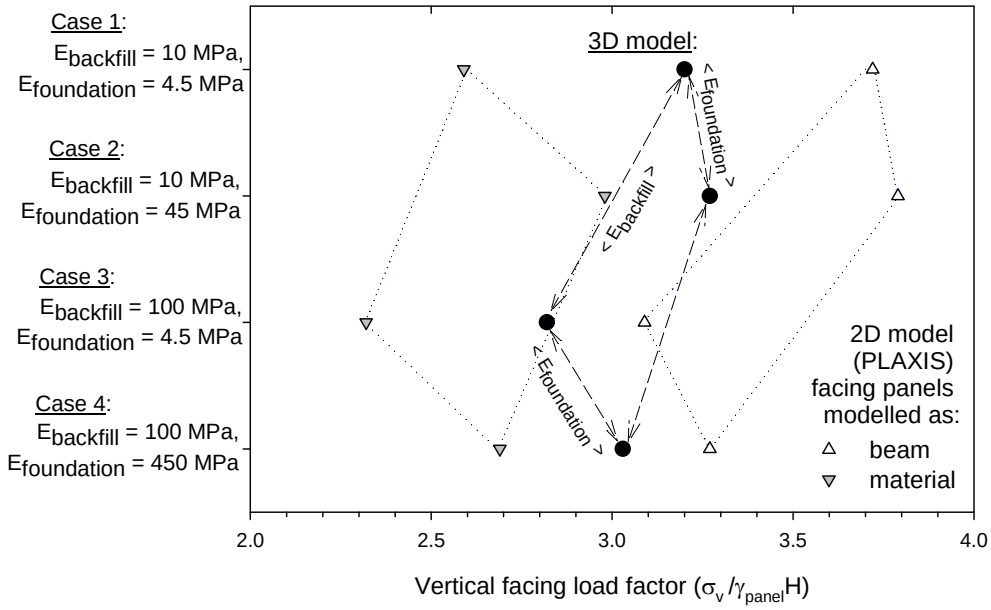

Figure 9.19: Vertical facing load factor comparison with regards to backfill/foundation stiffness combination cases (i.e., cases 1, 2, 3, and 4).

Figure 9.20 presents the vertical facing toe load comparison between the other sensitivity cases. The bearing pad lowest stiffness scenarios (cases 5 and 5b) were the ones where less vertical facing toe load was obtained. Reported Chida and Nakagaki (1979) data was plotted to compare with the best fitted values (case 5b) and quite good agreement was obtained. Reduction of reinforcement stiffness cases 6a and 6b also presented a reduced value of vertical facing load with regards to the steel reinforcement case (Base case). Similarly, the reduction of the soil-facing interface strength-stiffness factor (case 7) and soil-reinforcement pullout friction interface factor generate less vertical facing toe loads than Base case.

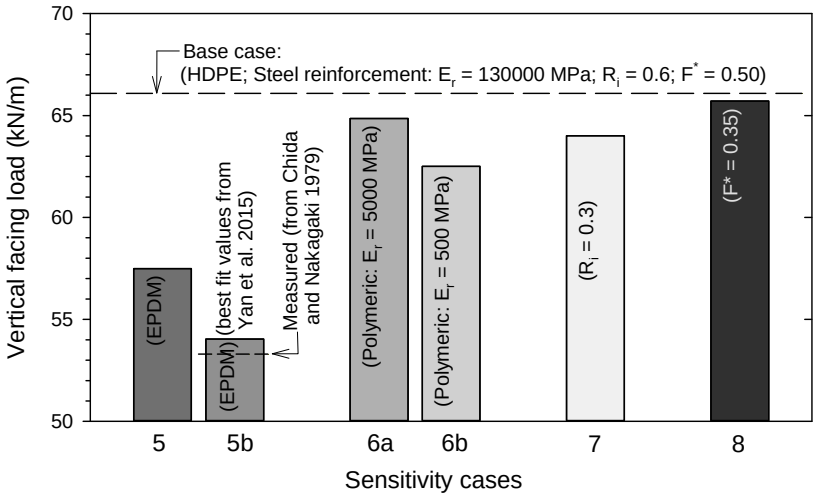

Figure 9.20: Vertical facing toe load comparison cases.

9.4.2. Facing movement

9.4.2.1. Vertical panel joint-gap

Results from horizontal panel joint gap compression obtained at H = 6 m-equivalent wall height construction stage are presented in Figure 9.21. As observed, incremental gap-aperture tendency was reached through case 1, 2, 3, and 4 sequence scenarios (see Figure 9.21a), reaching values from 18 mm in softer backfill and foundation scenario (Case 1) to less than a millimeter compression in stiffer backfill and almost rigid foundation scenario (Case 4).

Base case achieved about 6.5% compression at H = 6 m-equivalent wall height construction stage (i.e., about 18.7 mm-gap). Comparison with regards to other sensitivity cases (see Figure 9.21b) show how the bearing pad stiffness, as assumed, directly affected the gap-closure at the end of construction (the lesser EPDM stiffness the higher compression, up to 24% and 28% compression in cases 5 and 5b, respectively). The other sensitivity cases did not show much variations from Base case result. Unexpected practically not different response was obtained in soil-facing interface strength-stiffness reduction factor R_i = 0.3 (Case 7) although indeed a significant variation was obtained in previous vertical facing toe load results (Figure 9.20).

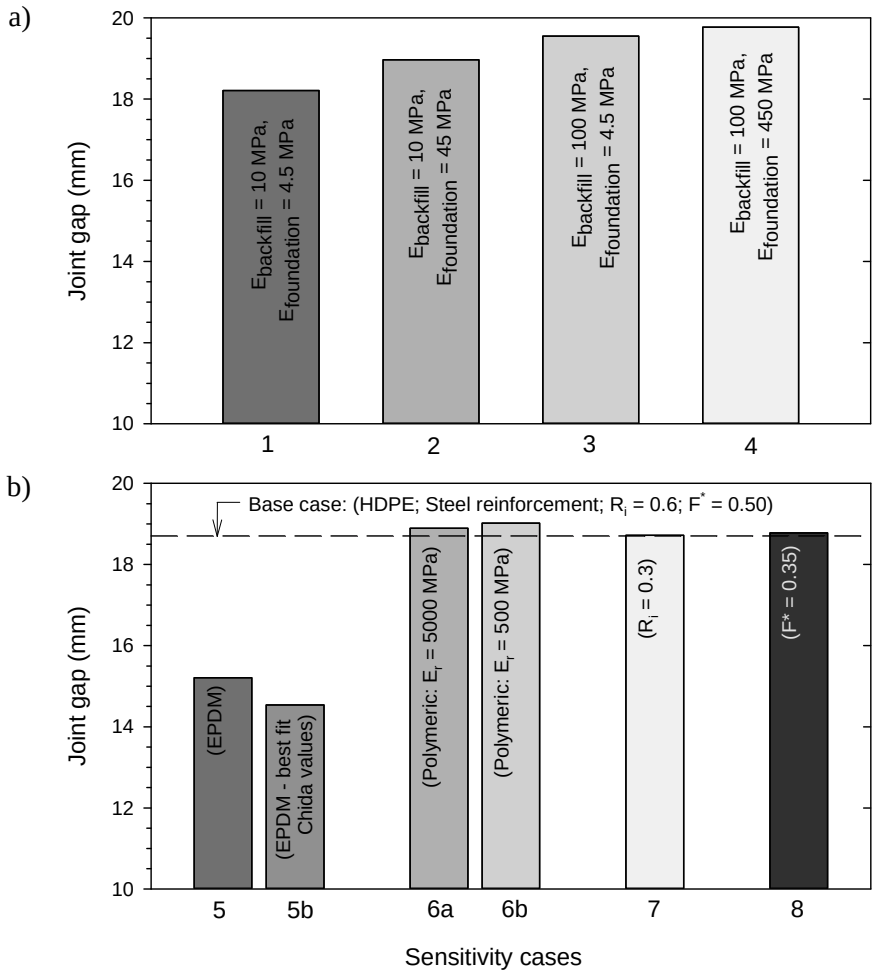

Figure 9.21: Panel joint gap comparison cases: backfill-foundation stiffness cases 1, 2, 3 and 4 (a), and other sensitivity cases 0, 5, 6, 7, and 8 (b).

9.4.2.2. Lateral displacement and differential settlement

Figure 9.22 shows the obtained lateral facing displacement comparison with regards to backfill / foundation stiffness combination cases (i.e., cases 1, 2, 3, and 4). As expected, the softer backfill / foundation scenario (Case 1) generated the higher outward facing displacements. In the other hand, the also softer foundation scenario but with stiffer backfill (Case 3) generated inward facing displacements at facing height above 2.5 m.

Results from the complementary sensitivity cases are presented in Figure 9.23. As noticed, so assume softer EPDM bearing pad generated greater outward displacement above panel joint locations. Also the reduction of reinforcement stiffness cases generate also greater outward facing panel displacements, as expected due to the more evident extensibility behaviour which relates to the reinforcement stiffness loss. Cases 7 and 8 did not present much variability in terms of facing lateral displacement.

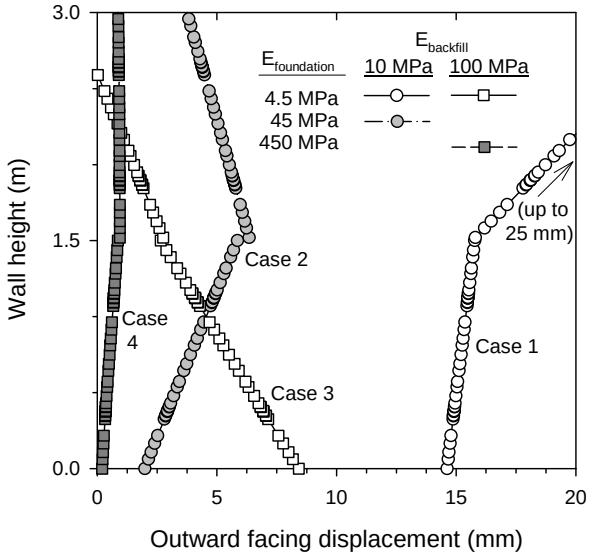

Figure 9.22: Lateral facing displacement comparison with regards to backfill / foundation stiffness combination cases (i.e., cases 1, 2, 3, and 4).

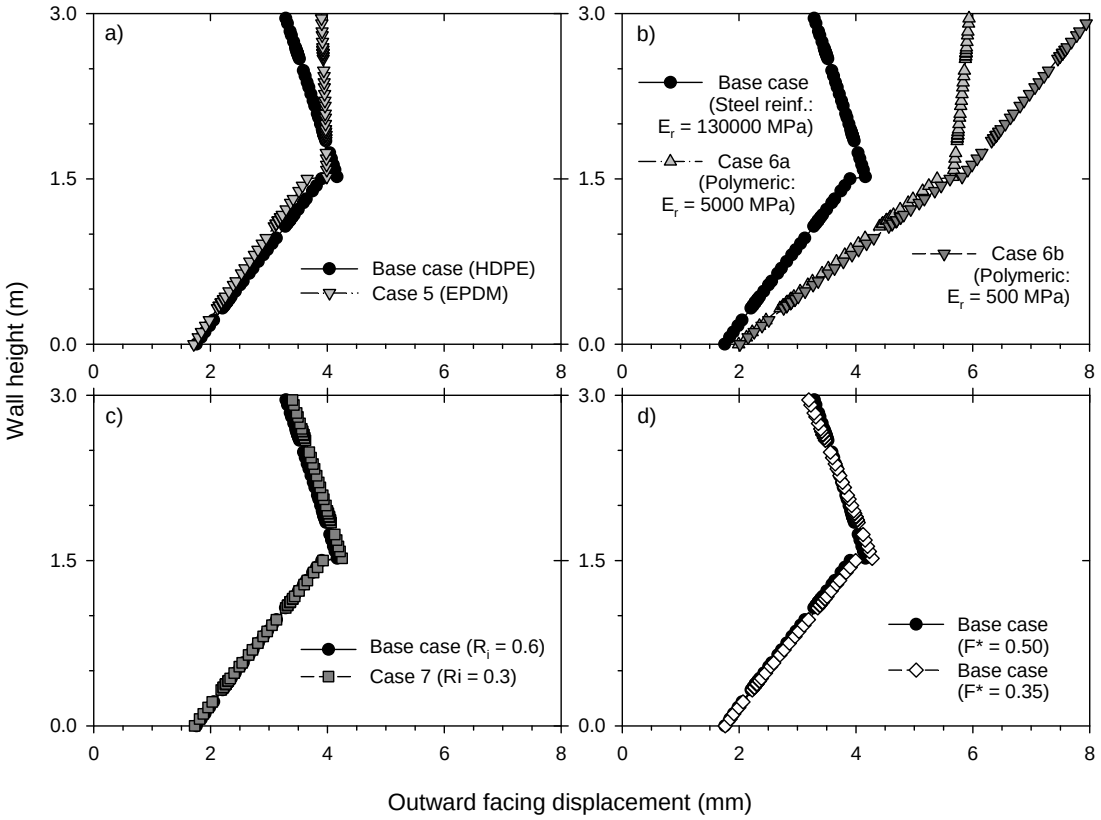

Figure 9.23: Lateral facing displacement comparison cases: Bearing pad stiffness (a), reinforcement stiffness (b), soil-facing interaction (c) and soil-reinforcement interaction factors (d).

9.4.3. Soil/reinforcement settlement

The settlement at 3rd reinforcement layer location comparison cases are presented in Figure 9.24. Similar responses were obtained in all cases (just bit differences in cases 7 and 8 as per Figures 9.24c and 9.24d, respectively). However, variations due to gap closure in EPDM Case 5 were obtained (i.e., 2nd panel settlement with the consequent reinforcement-to-panel connection displacement). In cases 6a and 6b there were no variation between them, however, the much different reinforcement stiffness variations with regards to the steel cases generated a different settlement trend with a more dropping shape near the facing (see Figure 9.24b).

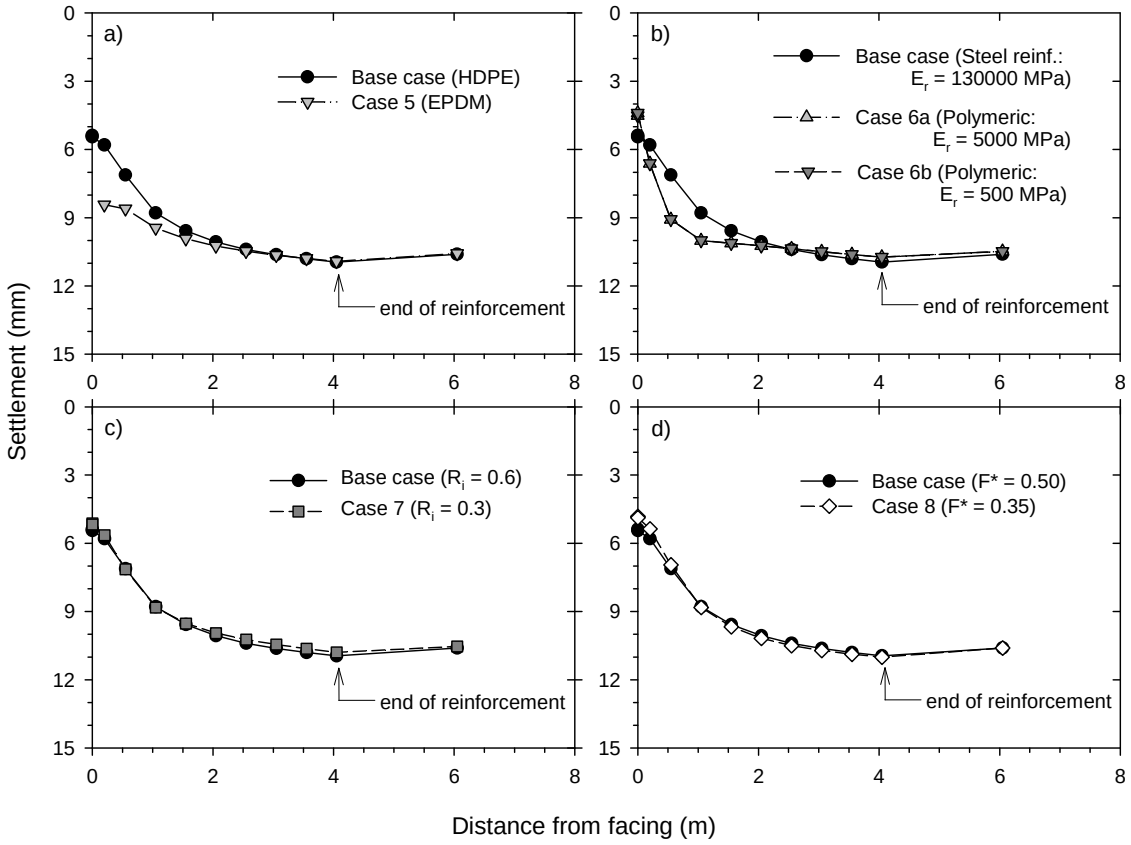

Figure 9.24: Settlement at 3rd reinforcement location comparison cases: Bearing pad stiffness (a), reinforcement stiffness (b), soil-facing interaction (c) and soil-reinforcement interaction factors (d).

9.4.4. Reinforcement loads

Figure 9.25 presents the tensile loads predicted at 3rd reinforcement layer with regards to backfill/foundation stiffness combination cases (i.e., cases 1, 2, 3, and 4). As noticed, the higher tensile loads were obtained in Case 1 scenario (softer backfill and foundation materials). The more variations in tensile reinforcement load distribution were caused in

softer backfill cases 1 and 2 despite in case of stiffer backfill the variations are practically negligible.

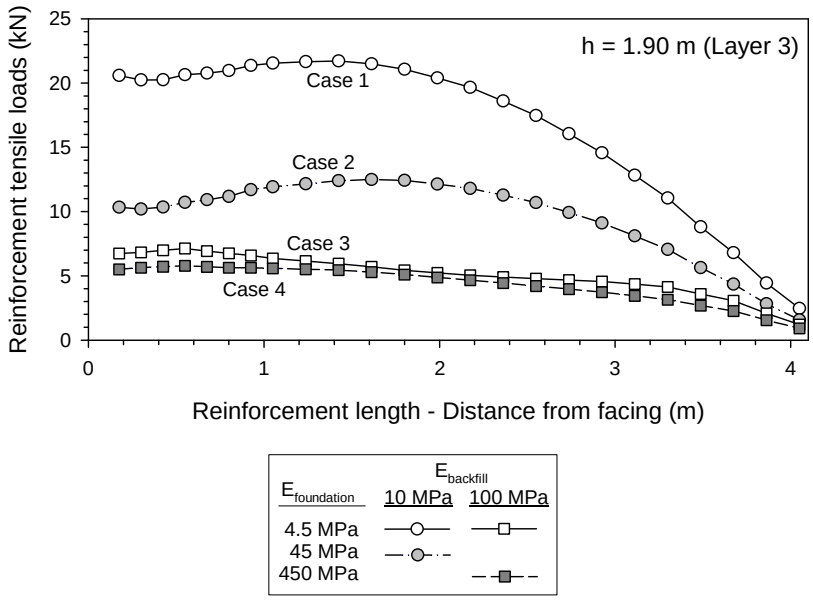

Figure 9.25: Tensile loads predicted at 3rd reinforcement layer with regards to backfill/foundation stiffness combination cases (i.e., cases 1, 2, 3, and 4).

Figure 9.26 presents results from best fit parameter values to perform Chida and Nakagaki (1979) reported 6 m-high wall case. Measured and predicted tensile loads at 3rd reinforcement layer are presented. Both PLAXIS and FLAC 2D numerical model results were also included. PLAXIS facing panels modeling (beam otherwise continuum material panel) did not result in significant changes, and thus, only beam results are plotted. FLAC model results correspond to the best fit values from Yu et al. (2015a). Despite the results obtained are not fully coincident, practically quite fine agreement was reached between three model cases (3D model CODE_BRIGHT model closer close to FLAC 2D model than PLAXIS 2D model), and fitting quite well the reported tensile loads by Chida and Nakagakiy (1979) 6 m-high steel strip reinforced soil wall instrumentation.

The 3rd reinforcement layer tensile loads were also used to perform the sensitivity analyses between Base case and the other cases. Figure 9.27 presents results with regards to bearing pad stiffness variation. As shown, practically not differences were obtained between HDPE and EPDM bearing pad stiffness.

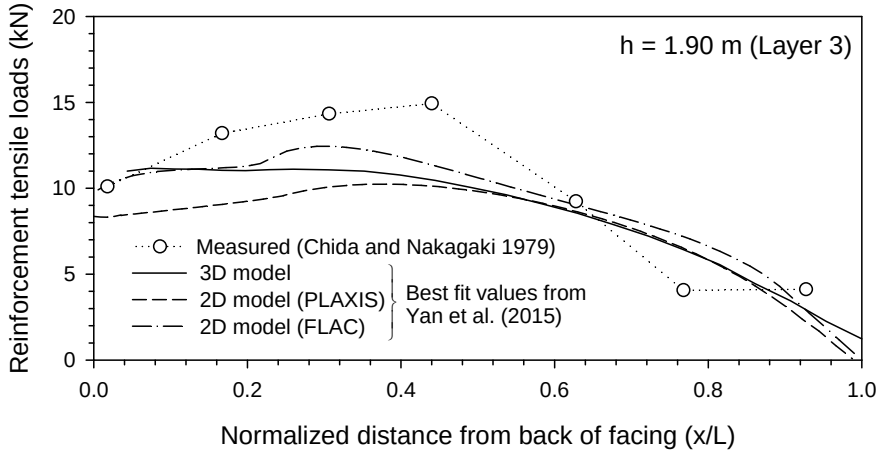

Figure 9.26: Measured and predicted tensile loads at 3rd reinforcement layer: Model with assuming best fit values from Yu et al. (2015a).

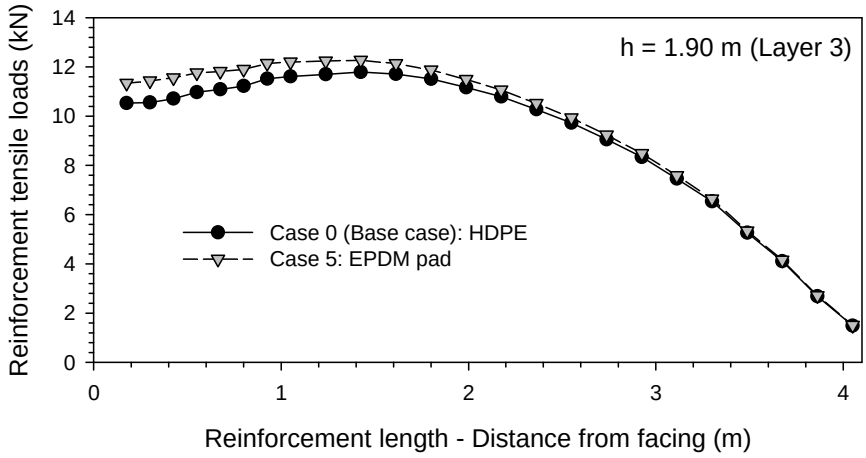

Figure 9.27: Tensile loads predicted at 3rd reinforcement layer with regards to bearing pad stiffness variation: case 0 (Base case) with HPDE, and case 5 with EPDM.

The effect of the reinforcement stiffness reduction cases 6a and 6b is shown in Figure 9.28. As observed and expected, the lesser stiffness the lesser also tensile loads developed. This is in agreement with results presented in Chapter 6 for welded wire mesh reinforcement and polypropylene reinforcement comparison cases.

Figure 9.29 presents comparison of the 3rd reinforcement layer tensile load results with regards to soil-facing interface strength-stiffness reduction factor variation. As observed and as in bearing pad stiffness comparison case, not relevant differences were obtained between the Base case (with R_i = 0.6) and Case 7 (with R_i = 0.3).

The effect of the soil-reinforcement pullout friction factor variation is presented in Figure 9.30. As observed, Base case (with a constant value F^* = 0.5 in all reinforcement layers) developed higher tensile loads developed than Case 8, where lower not constant in depth pullout factor F^* was assumed (equal to F^* = 0.35 in 3rd reinforcement layer; see Table 9.4 – Note [g]).

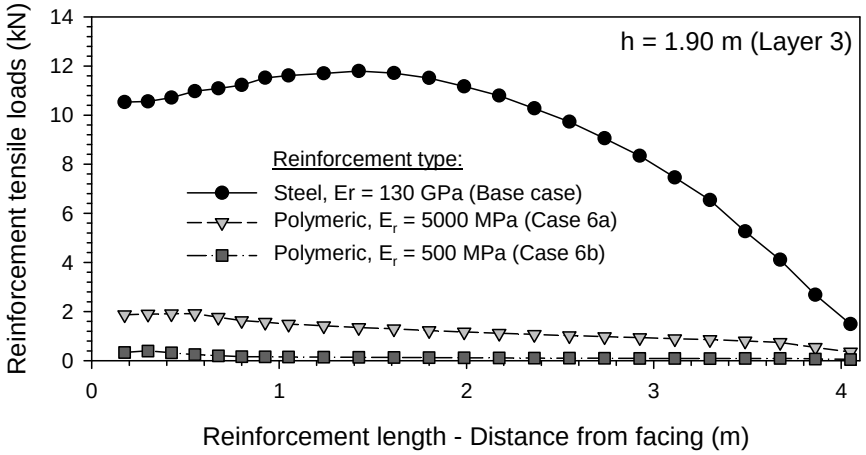

Figure 9.30: Tensile loads predicted at 3rd reinforcement layer with regards to reinforcement stiffness: Base case (steel) and cases 6a-b (polymeric).

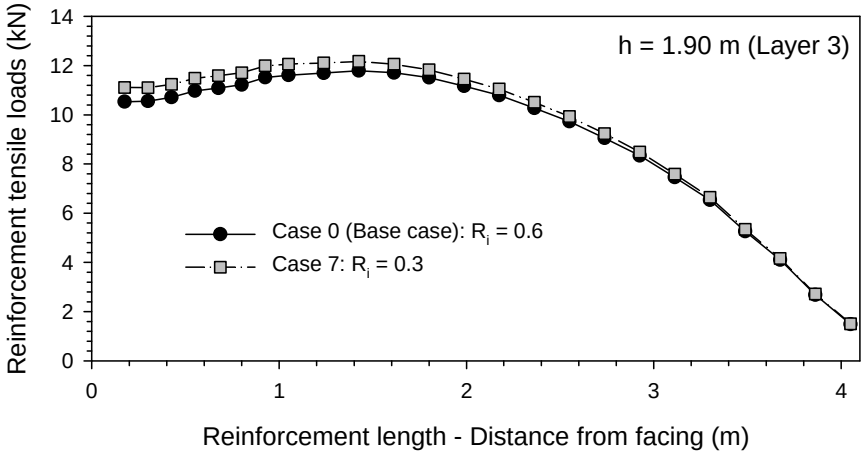

Figure 9.29: Tensile loads predicted at 3rd reinforcement layer with regards to soil-facing interface strength-stiffness reduction factor variation: case 0 (Base case) with R_i = 0.6, and case 7 with R_i = 0.3.

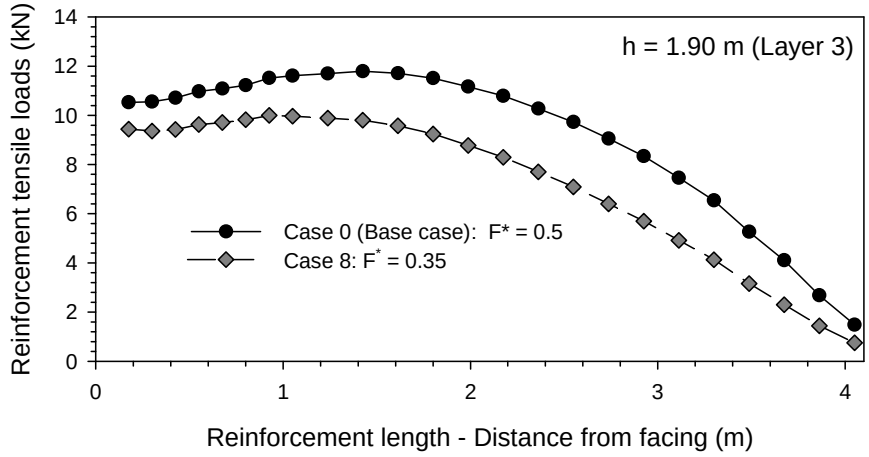

Figure 9.30: Tensile loads predicted at 3rd reinforcement layer with regards to soil-reinforcement pullout friction factor variation: case 0 (Base case) with F^* = 0.5 (constant in all reinforcement layers), and case 8 with F^* = 0.35 (corresponding to this 3rd reinforcement layer; see Table 9.4 – Note (g)).

9.5. CONCLUSIONS

The stress-strain behaviour of reinforced soil walls is complicated due to the mechanical complexity of the component materials and their interactions. In this current investigation, a 3D numerical finite element modelling was generated to analyze a 6 m-high mechanically stabilized earth reinforced soil wall structure. The same continuum elements interface methodology as in previous chapters (7 and 8) was considered in this current study to perform soil-facing and soil-reinforcement interactions.

In this investigation, a simple equivalent 3 m-high model was implemented to perform 6 m-high structure. The purpose of this model was to be capable to achieve more accurate and faithfully behaviour results beyond the scope of the two-dimensional models. The results obtained demonstrated that there is an actual 3D-effect in this kind of structures, not possible to be detected with 2D models analysis. Despite in many cases these 3D effects may not be such relevant to justify the use of these complex models (in addition to the related computational issues), the current study showed that this effects could be detected, if required, in particular cases of interest.

The numerical simulation results presented demonstrate satisfactory agreement with reported data from a similar instrumented real wall. The methodology presented looks promising to achieve further results to other geometries, structural material data, and even under different boundary conditions.

CHAPTER 10

ENVIRONMENTAL ASSESSMENT OF EARTH RETAINING WALL STRUCTURES [1]

10.1. INTRODUCTION

10.1.1. General approach

The benefits of performing environmental impact assessments of proposed civil engineering works, which include earth retaining wall (ERW) structures, are now generally accepted and a life cycle assessment (LCA) framework for these assessments is now in place (ISO 14040:2006). Currently, there are many different ERW systems available on the market, but they can all be broadly classified into gravity, cantilever and mechanically stabilized earth (MSE) categories. On a project-specific basis the final solution must be designed to be constructible, satisfy minimum performance and safety criteria while at the same time optimizing material quantities to minimize costs. A number of studies have demonstrated the economic benefits of MSE walls constructed with geosynthetic (polymeric) materials compared to conventional concrete wall solutions (e.g., Christopher, 2014; Khan and Sikder, 2004; Koerner et al., 1998; Koerner and Koerner, 2011). However, the final choice of solution seldom includes optimization of resource consumption to reduce potential environmental impacts. This can most often be ascribed to lack of awareness and/or political will. However, there is also the challenge of selecting a methodology that provides a common framework that designers can use to compare relative impacts of different ERW solutions, finding and familiarization with toolkits used to implement the methodology (i.e., software), selecting which environmental impacts to use in analyses and then choosing which database(s) to find these inputs (Rebitzer et al., 2004; Pennington et al., 2004).

[1] Chapter based on Damians, I.P., Bathurst, R.J., Adroguer E., Josa, A., and Lloret, A.; 2016. Environmental assessment of earth retaining wall structures. ICE Environmental Geotechnics. 10.1680/jenge.15.00040.

This study is focused on a methodology to assess the environmental impacts of ERWs using examples of the wall types identified earlier. The details of the approach are in general conformity with recommendations found in ISO 14044:2006. The example structures fall within gravity, cantilever and MSE wall classifications and all are constructed with a hard (concrete) facing. These structures were selected to capture a wide range of earth retaining wall solutions that are currently available to design engineers. One set of MSE walls was designed using galvanized steel soil reinforcement and the other set using polymeric reinforcement. The walls were first designed to have typical geometries, satisfy minimum margins of safety against instability based on current practice, and to minimize material quantities. Two life cycle assessment (LCA) methods were used to compute different environmental impacts of each wall type constructed to heights of 3, 5, 10 and 15 m. Each LCA analysis was carried out using an environmental inventory of the materials, materials transportation and construction activities for each wall together with an available database of environmental impact indicators.

10.1.2. Background

10.1.2.1. Assessment of environmental impacts using life cycle assessment (LCA)

Environmental impacts can be defined as the set of possible effects and consequences on the environment from a modification of the natural land as a result of human works or any other activities (Rebitzer et al., 2004). Any structure and construction material implies the consumption of resources and emission of substances into the natural environment, generating a series of environmental impacts that should be identified and minimized. A methodology that can be used to address environmental impacts is the life cycle assessment (LCA) approach, which is used to estimate the environmental impacts resulting from the life-cycle stages of a product or service, i.e., from raw material extraction to site delivery (cradle-to-gate) or to end-of-life (cradle-to-grave) (ISO 14044:2006). Some applications of LCA are for product development and improvement, strategic planning, public policy making and marketing (ISO 14040:2006). Recently the European Committee for Standardisation (CEN) introduced a protocol for identifying “cradle-to-gate” LCA of construction products (EN 15804:2012). An example of environmental impacts from cradle-to-gate of two different polymeric (geogrid) products (one square-metre basis) is provided by Frischknecht et al. (2014).

Environmental impacts are one factor in project/structure sustainability assessment which has emerged as a key concept in all engineering fields. The other factors are social, functional and economic. Overviews of current approaches to sustainability assessment in civil and geotechnical engineering appear in papers by MacAskill and Guthrie (2013) and Basu et al. (2014). A complete sustainability assessment of ERWs is not addressed in the current study.

10.1.2.2. Previous related work

There are many examples in the literature on the ecological impacts of using different materials in civil engineering works (e.g., Kreijger, 1987; Hammond and Jones, 2008). Inui et al. (2011) carried out a study of four pile wall solutions using energy consumption, CO_2 and four other gas emissions as metrics to quantify environmental impacts using alternative solutions. Jones (1996, 2002) gives examples of both the economic advantages of MSE walls over conventional concrete structures as well as the benefits of the former in terms of reduced energy and water consumption, dust emissions and SO_2 emissions, among a number of environmental impact indicators. The WRAP (2010) study includes examples of sustainability analyses for different wall options based on cost of materials and transportation, and embodied CO_2 as the environmental impact indicator. Heerten (2012) studied the benefits of geosynthetics in two geotechnical applications including a MSE and conventional wall solution based on cumulative energy demand (CED) and CO_2 emissions. Rafalko et al. (2010) and Stucki et al. (2011) carried out similar LCAs on MSE and conventional concrete walls using the same environmental impact indicators. Fraser et al. (2012) and Wallbaum et al. (2014) examined a wider range of environmental impacts for a single MSE wall solution and a competing conventional concrete wall option. In all these wall case studies, the geosynthetics solutions were shown to be a better option than conventional concrete walls based on environmental impacts.

Previous work on LCAs applied to ERWs has focused on environmental impacts during manufacture of the component materials used in a particular wall type and transportation of materials. These studies have provided insight on environmental impacts of ERW structures but have been limited to a single structure of each wall type (e.g., one set of dimensions) and most often did not consider the influence of different construction procedures (e.g. soil type, placement and compaction). The current study extends previous related work by considering a wider range of ERW types and dimensions, different construction procedures, quality of backfill together with a wide range of environmental impact categories.

10.2. CASE STUDIES AND METHODOLOGY

10.2.1. Earth retaining wall cases and functional unit

Figure 10.1 shows the three types of wall considered in this investigation. As noted earlier, MSE wall analyses considered both steel soil reinforcement and polymeric reinforcement cases. The dimensions of the walls were first optimized by carrying out conventional stability analyses to satisfy recommendations found in AASHTO (2014) and ACI (2002). The backfill and foundation soil material properties used in these calculations are shown in Table 10.1. The GEO5 geotechnical software suite (Fine, 2010) was used to carry out external stability calculations. The internal steel reinforcement arrangement for the cantilever walls was carried out using program CYPECAD (CYPE 2014). Wall dimensions and soil reinforcement

arrangement are summarized in Table 10.2. Analyses were carried out on a one-metre running length of wall face basis. This one-metre slice also serves as the functional unit defined in LCA terminology as the reference unit for inputs and outputs that enable alternative strategies to be compared and analysed with respect to environmental impacts due to consumption of materials, construction activities, transportation and the like (ISO 14044:2006). The case study geometries assumed a level ground surface in front of the wall and a horizontal backfill slope. The functional unit in this study does not consider materials or activities below the maximum depth of the base of each structure (including below the wall footing for MSE wall cases). The water table is assumed to be at a depth below the foundation surface where it cannot influence analysis and design outcomes. Environmental impacts due to site preparation and final grading are expected to be similar regardless of wall type and are not considered in this study. The design life of the structures was taken as 100 years.

In order to simplify comparisons of environmental impacts between different MSE solutions the same reinforcement-to-facing galvanized steel connection system was assumed for both steel and polymeric reinforced soil walls. Regardless, the choice of connection system was judged to have negligible influence when compared to other wall components which have much larger mass contributions. The same backfill soil material was assumed for the conventional wall structures and for the retained soil zone in the MSE wall cases. In practice, the choice of material in the reinforced soil zone for MSE walls (i.e., polymeric or galvanized steel soil reinforcement) may differ based on reinforcement-related durability requirements (e.g., Tanyu et al., 2008; AASHTO 2014). The steel reinforced concrete facing panels used for the MSE walls were the same geometry in both cases. However, the amount of rebar and number of connections per panel did increase with height. The gravity wall structures were assumed to be constructed without internal structural steel. Any small amount of steel reinforcement used close to the surface of these structures was neglected. To simplify the cantilever wall case geometry, the base slab was not extended to form a T-shape wall and counterfort elements were also not used. This arrangement did result in some additional flexural steel rebar at the stem-base connection compared to the T-section alternative.

Figure 10.2 shows main material mass quantities (concrete, steel and backfill) corresponding to the structures with optimized dimensions for each wall height using conventional design practice. As expected, gravity wall solutions require the most concrete for walls of equal height followed by cantilever walls. Cantilever wall solutions require the most steel (i.e., rebar). The concrete consumption for MSE walls is relatively small and limited to the facing panels. Since the panel units have the same dimensions for all MSE wall examples, concrete consumption increases linearly with height. The MSE walls with steel reinforcement require more steel than for the matching polymeric soil reinforcement solutions because this material is used in the concrete panels and to manufacture the steel soil reinforcement. The consumption of soil is largest for the MSE walls since backfill soil is used for both the reinforced soil zone and the wedge of retained soil immediately behind the reinforced soil zone.

a) Gravity:

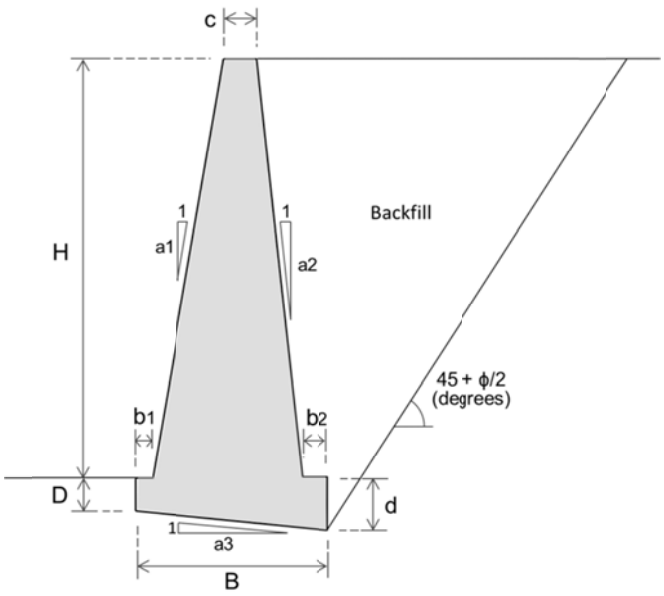

b) Cantilever:

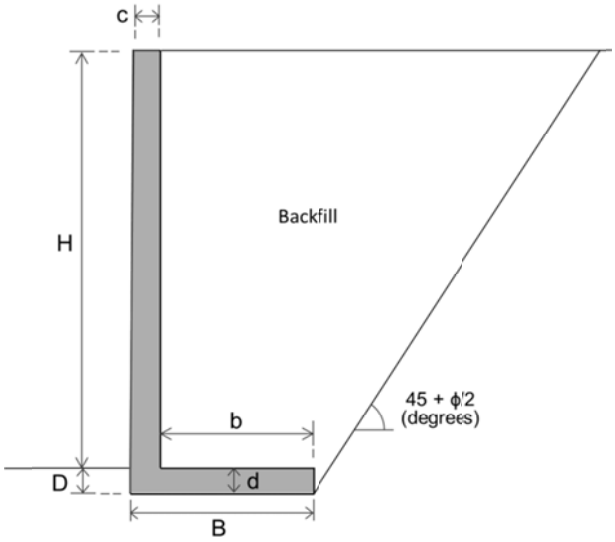

c) MSE wall:

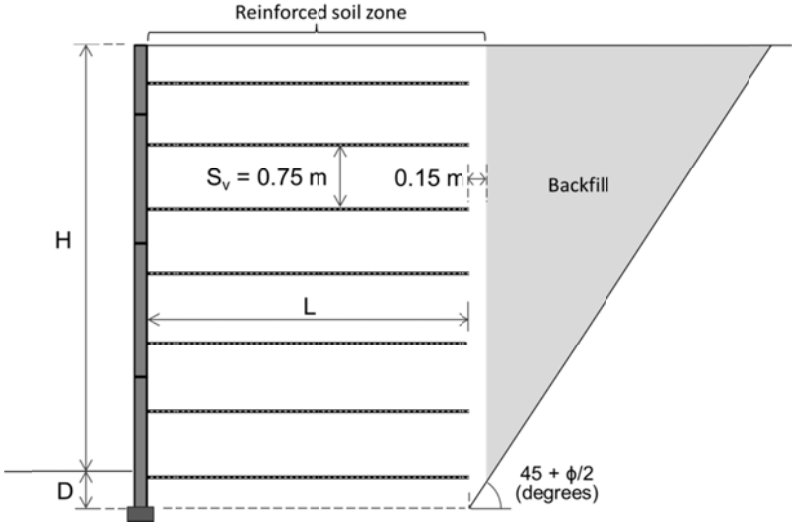

Figure 10.1: Geometry and parameter definitions: gravity (a), cantilever (b), and MSE walls (c).

Table 10.1. Backfill and foundation soil material properties:

Parameter	Backfill	Foundation
Unit weight (kN/m^3)	20	20
Friction angle (degrees)	30 (Gravity and cantilever) 34 (MSE wall cases)	30
Cohesion (kPa)	0	0
Soil/structure interface friction angle (degrees)	24	27

Table 10.2. Wall dimensions and soil reinforcement arrangement:

Wall type	Parameter or number [a]		Wall height [b] (H)			
			3 m	5 m	10 m	15 m
Gravity	D	m	0.25	0.40	0.90	1.20
	B	m	1.33	2.31	4.69	6.97
	c	m	0.30	0.40	0.80	1.20
	b_1	m	0.10	0.20	0.45	0.60
	b_2	m	0.15	0.30	0.65	1.00
	d	m	0.38	0.63	1.37	1.90
	a_1	m	6.00	6.00	6.00	6.00
	a_2	m	10.70	8.60	8.90	9.00
	a_3	m	10.00	10.00	10.00	10.00
Cantilever	D (= d)	m	0.25	0.40	1.00	1.70
	B	m	1.30	2.20	4.60	7.40
	c	m	0.25	0.25	0.40	0.80
	b	m	1.05	1.90	3.70	6.00
MSE [c]	D	m	0.40	0.60	1.25	1.50
	L (= 0.7×(H+D))	m	2.40	3.90	7.90	11.60
	Number of reinforcement layers		5	8	15	22

Notes: [a] see Figure 10.1.

[b] H = wall height over above the ground surface at front of wall (Figure 10.1).

[c] facing panel height assumed as 1.5 m. Vertical reinforcement spacing S_v = 0.75 m (Figure 10.1c) and is the same for steel and polymeric reinforcement cases.

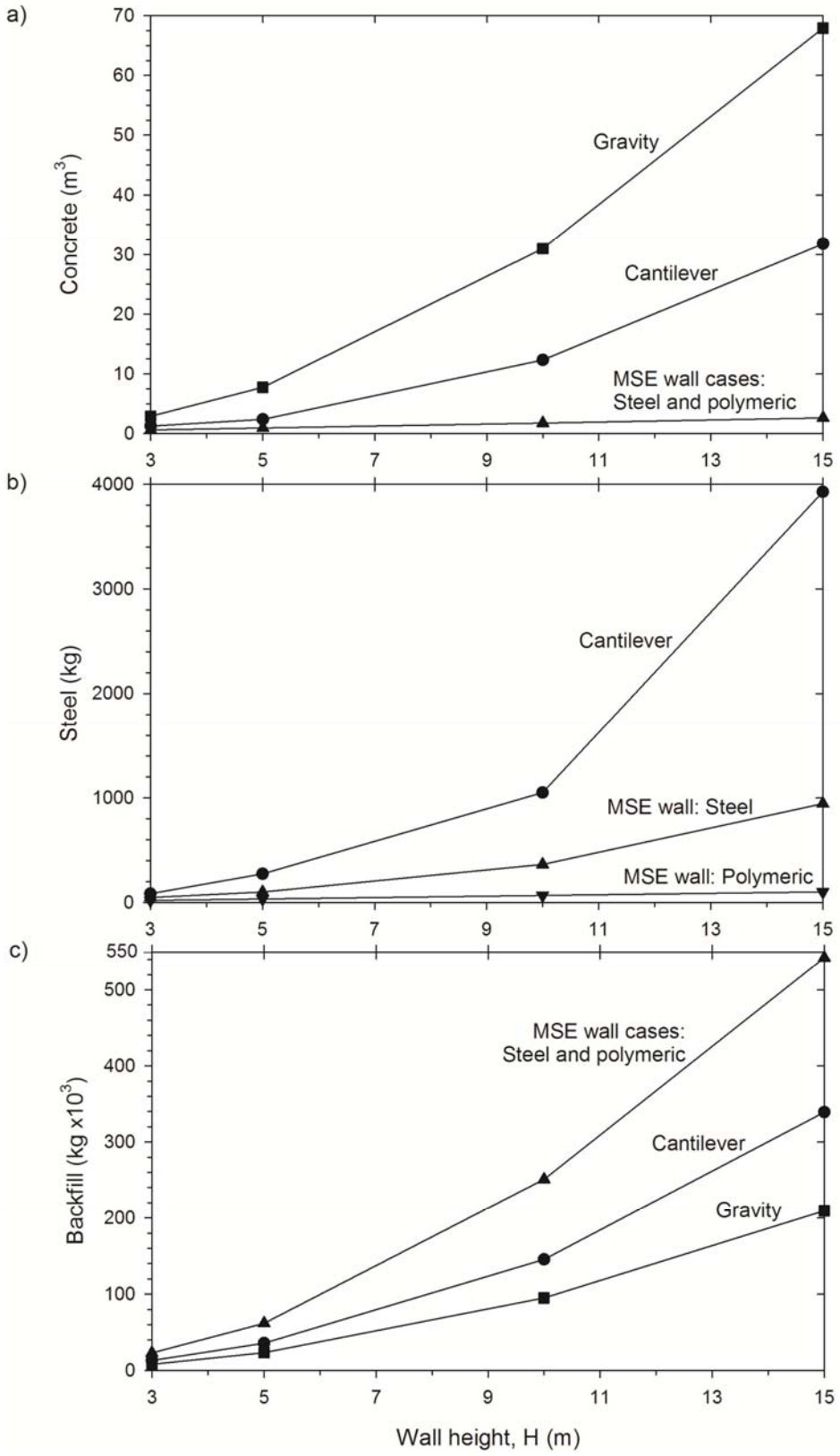

Figure 10.2. Main material quantities required for each wall type based on a one-metre running length of wall (functional unit): (a) concrete, (b) steel and (c) backfill.

10.2.2. Environmental assessment methodology

10.2.2.1. System boundary and environmental inventory database

In civil engineering applications, the life-cycle stages can be defined from "cradle-to-grave" (i.e., raw materials extraction from natural environment to final disposal and any recycling options at the end-of-life phase) with intermediate stages corresponding to materials processing to produce the required components, materials/components transportation, installation works, maintenance works during service life and final demolition. This concept is illustrated in Figure 10.3. The components in this figure define the system boundary for a full LCA (ISO 14040:2006; ISO 14044:2006) in this study. In fact, a preliminary sensitivity analysis showed that maintenance (service life) could be excluded from analyses. Similarly, post-construction consumptions of electricity and diesel were found to have negligible environmental impacts (i.e., < 0.5% of environmental indicator values selected in this study) and so were ignored. To simplify the analyses, the environmental impacts of demolition were also ignored. Hence, the life cycle system boundaries in this study are best described as "cradle-to-operational" corresponding to end-of-construction time frames.

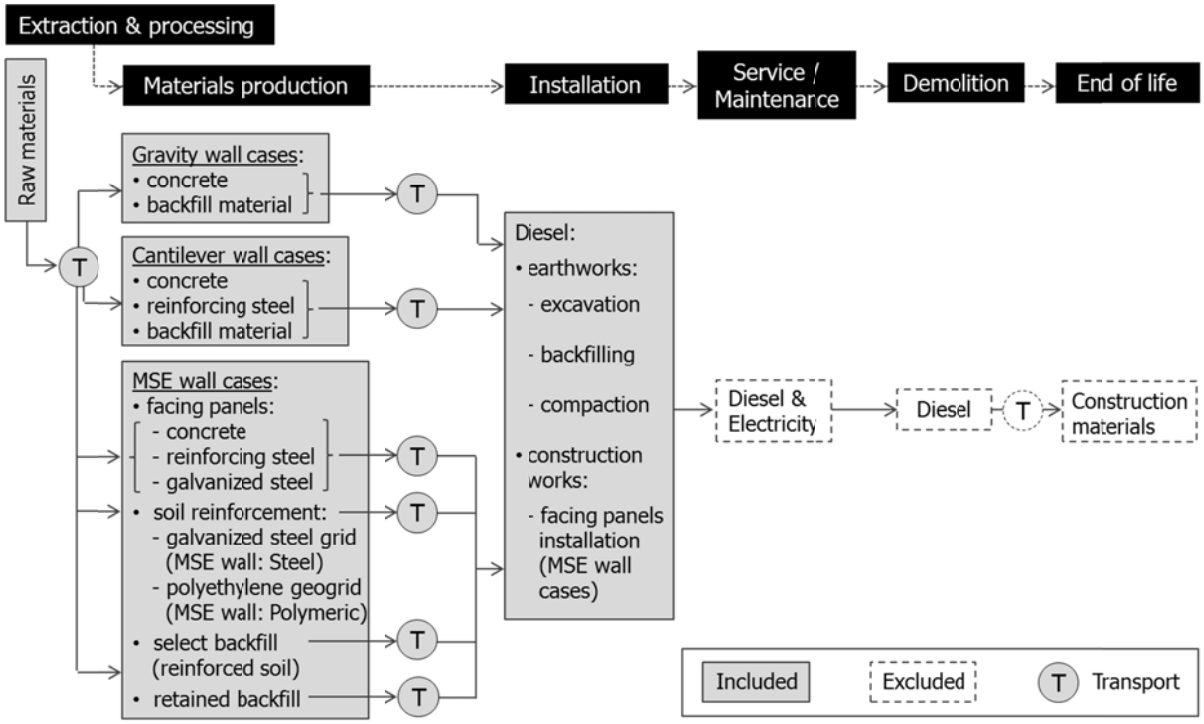

Figure 10.3: Flow chart showing the components of cradle-to-grave system for the wall types in this study.

Table 10.3 presents the environmental inventory of materials and construction-related activities in the current study. It should be noted that environmental impacts due to electricity consumption for extraction and manufacturing processes vary from country to country and from region to region (e.g., different emissions are generated from nuclear, hydro and coal power plants). In the analyses to follow, "global values" from the Ecoinvent v3.1 (Ecoinvent Centre, 2014) database (described later) were used for the environmental inventory.

Imported backfill soils were assumed for the gravity and cantilever wall cases and for the retained soil portion of the MSE walls. In practice the quality of the backfill may be expected to be greater in the order of gravity/cantilever, MSE (polymeric reinforcement) and MSE wall (steel reinforcement) based on typical specifications related to durability issues for steel and polymeric soil reinforcement categories in MSE walls as noted earlier. To simplify calculations, these distinctions were not considered directly based on source of material in this study. However, the higher quality backfill typically required for MSE structures was reflected by environmental impacts associated with a greater haul distance between off-site source and construction site (10 km) as noted at the bottom of Table 10.3. It is possible on a project-specific basis that local soil could be available, in which case the transportation-related environmental costs noted above would disappear.

The placement and compaction of soil material can be expected to vary for different wall types. The soil for the gravity and cantilever walls and the retained soil for the MSE wall cases were assumed to be compacted in 0.3 m-thick lifts. The reinforced zone soils were assumed to be compacted in 0.15 m-lifts and to extend 0.15 m beyond the free end of the reinforcement layers (Figure 10.1c).

On-site concrete formwork and facing alignment tools for the MSE wall facing panels were not included in analyses since they were assumed to be reusable. A transportation distance of 10 km was assumed for concrete mix trucks in diesel consumption calculations. Lorry transportation distance for steel and precast concrete panels was assumed as 100 km. Diesel consumption was also considered during panel facing installation based on an average installation time of 0.04 h/m^2 per facing. This includes lifting the panels from the lorry to the ground, and on-site transportation and panel placement by a skid-steer loader.

10.2.2.2. Environmental impact calculation and LCA tools

There are some differences in the details of LCA models to quantify environmental impacts (Rebitzer et al., 2004). However, most identify midpoint indicators (such as any quantification of intermediate effects or impact categories representing pollutants) and endpoint indicators (which are based on damage models) (Bare et al., 2000). The ReCiPe method (Goedkoop et al., 2008) was selected in this investigation to compute both midpoint and endpoint indicators identified in Figure 10.4 (described in more detail below). The method is included in the SimaPro 8.0.2 software (PRé Consultants B.V., 2010) that was used to carry out all LCA calculations in this study.

Table 10.3. Environmental inventory of materials, construction activities and transportation on per metre length of wall basis (functional unit):

Case	Category	Related items and components	Units	Wall height (*H*)			
				3 m	5 m	10 m	15 m
Gravity	Structural materials	Concrete	m^3	2.5	6.7	27.3	60.1
	Soil materials	Retained backfill[(a)]	tonnes	8.1	23.3	95.1	209
	Earthworks	Excavation	m^3	0.6	1.2	5.3	10.8
		Backfilling and compaction	h ($\times 10^{-3}$)	0.5	1. 5	5.9	13.3
	Transportation	Concrete	km	10	10	10	10
Cantilever	Structural materials	Concrete	m^3	1.1	2.3	11.1	29.1
		Reinforcing steel (rebar)	tonnes	0.08	0.27	1.04	3.93
	Soil materials	Retained backfill[(a)]	tonnes	13.2	35.9	139	339
	Earthworks	Excavation	m^3	0.3	0.9	4.6	12.6
		Backfilling and compaction	h ($\times 10^{-3}$)	1.0	2.8	11.0	25.8
	Transportation	Concrete and steel	km	10	10	10	10
MSE wall: Steel and Polymeric	Structural materials	Precast panels [(b)]	m^2	3.4	5.6	11.1	16.6
		Concrete (levelling pad)	m^3	0.05	0.05	0.05	0.05
		Soil reinforcement:					
		- Galvanized steel grid	kg	25	54	296	844
		- Polymeric grid [(c)]	kg	4	10	66	187
	Soil materials	Reinforced and retained backfill [(a)]	tonnes	23.0	61.8	250	542
	Installation	Panels installation	h	0.1	0.2	0.4	0.6
	Earthworks	Excavation	m^3	1.8	3.9	7.0	12.5
		Backfilling and compaction	h ($\times 10^{-3}$)	3.5	9.2	33.1	72.0
	Transportation	Panels and reinforcement	km	100	100	100	100
		Select backfill		10	10	10	10

Notes: [(a)] backfill soils are assumed to be processed at source (e.g., screened and washed).

[(b)] facing precast panels include: concrete (m^3), reinforcing steel (kg) and galvanized steel for the connections (kg).

[(c)] high-density polyethylene (HDPE) geogrid materials were used in calculations. The average strength and hence mass of these materials increased with depth below the wall crest to satisfy reinforcement load demand computed during design.

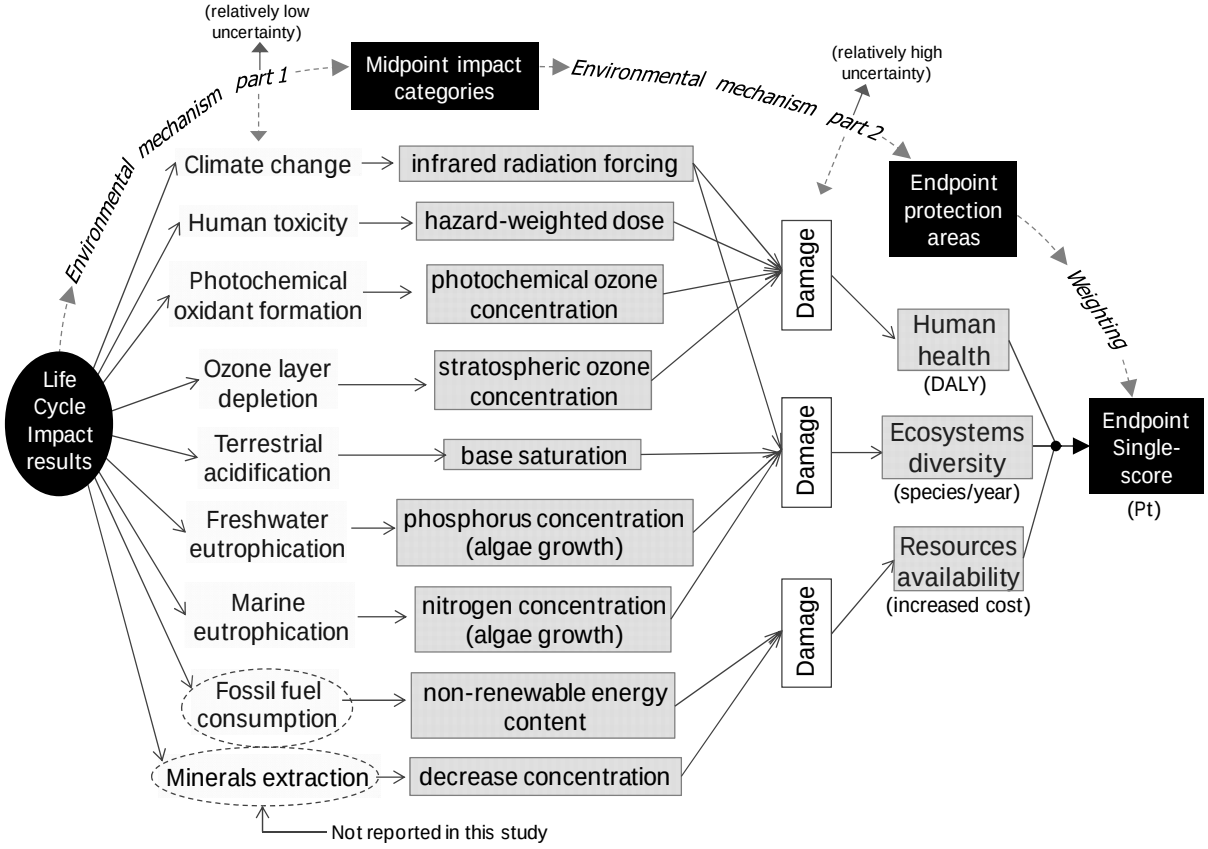

Figure 10.4: Relationship between the life cycle impacts, midpoint indicators and endpoint indicators in the ReCiPe method (modified from Goedkoop et al., 2008).

The "hierarchist" theory option was selected in the ReCiPe method. This option assumes a 100 year-time frame and reflects the most common policy principles to take into account other subjectivities when conversion steps are generated from the raw pollutant materials – life cycle impacts– to midpoint impact categories, and from the latter to final endpoint indicators. Both midpoint and endpoint level indicators have advantages and disadvantages. Midpoints provide more certainty in the results while endpoints are more useful for decision making since they are expressed as a single numerical score (Bare et al., 2000). The Ecoinvent v3.1 database (Ecoinvent Centre, 2014) that is included in the SimaPro software was used to select environmental impact indicator (input) values resulting from material and energy consumption. Global values were used to ensure fair comparisons between wall types. These input values are based on a mix of values taken from around the world as the name implies.

It should be noted that there are other databases available in the literature with other values for environmental impact indicators for the same materials and for different regions. Raja et al. (2015) give one relevant example to the current study when they point out that embodied carbon values (in kg CO_2e/kg of plastic) vary based on plastic (polymer) type, stage of

manufacture, geosynthetic product type and between databases (e.g., between ICE database (Hammond and Jones, 2011) and Ecoinvent v2.2 databases compared in their study). Differences in embodied carbon values for HDPE taken from the Ecoinvent v3.1 database and the ICE database are 1.91 kg CO_2e/kg and 1.93 kg CO_2e/kg, respectively. The differences are negligible and hence the choice of database for this material is not a concern. The quantitative influence of other input values found in other databases on midpoint impact outcomes was not investigated in the current study.

There are a total of 18 environmental midpoint impact categories that are simultaneously evaluated in the ReCiPe method at midpoint level (Goedkoop et al., 2008). Figure 10.4 presents the relationship between the life cycle impacts, midpoint indicators and endpoint indicators for nine categories. Some appear in the studies cited earlier (Stucki et al., 2011; Fraser et al., 2012; Heerten, 2012). The seven environmental midpoint impact categories and units that are reported in the current study are listed below:

- **Climate change**: global warming potential (GWP); kg CO_2 to air-equivalent ("equivalent" corresponds to the effect of a kilogramme of greenhouse gas relative to that of a kilogramme CO_2 to air).
- **Human toxicity**: human toxicity potential (HTP); kg of 1.4 dichlorobenzene (14DCB) to urban air-equivalent.
- **Photochemical oxidant formation**: photochemical oxidant formation potential (POFP); kg of non-methane volatile organic carbon compound (NMVOC) to air-equivalent.
- **Ozone depletion**: ozone depletion potential (ODP); kg of chlorofluorocarbon (CFC-11) to air-equivalent.
- **Terrestrial acidification**: terrestrial acidification potential (TAP); kg SO_2 to air-equivalent.
- **Freshwater eutrophication**: freshwater eutrophication potential (FEP); kg P to freshwater-equivalent.
- **Marine eutrophication**: marine eutrophication potential (MEP); kg N to freshwater-equivalent.

These categories were judged to be of most interest for the class of structures in the current LCA study at global, regional and local scales.

There is scientific agreement on the environmental impacts from LCA to different endpoint damage categories. The ReCiPe method converts and aggregates midpoint impact categories into the following protection areas with respect to related damage (Figure 10.4):

- **Human health**: disability-adjusted loss of life years (DALY); years.
- **Ecosystem diversity**: loss of species during a year; species/year.
- **Resources availability**: increased cost; dollars.

These damage categories can then be weighted based on socio-political preferences, perceived uncertainty in the calculations for any categories and the like, to compute a single final dimensionless endpoint score for LCA. The higher the LCA value the greater the negative environmental impact and the less desirable the case study option. As noted earlier, this score can then be used for decision making between design options.

Another widely used environmental impact indicator is based on the cumulative energy demand (CED) model (Frischknecht et al., 2007). This is the model for the second LCA mentioned in the introduction. This model (also available in the SimaPro software) is used to evaluate energy consumption over the life-cycle of a good or service.

10.3. ENVIRONMENTAL ASSESSMENT RESULTS

10.3.1. Global warming potential (GWP) and cumulative energy demand (CED)

The most familiar quantities for environmental impact evaluations are mass CO_2 equivalent, used as an indicator of global warming potential (GWP), and cumulative energy demand (CED) measured in joules. These results are presented in Figure 10.5 as a function of wall height and type. These values are taken from the first LCA using the ReCiPe method for mass CO_2 equivalent and the second LCA using the CED method. These are total values computed for “cradle-to-operational” timeframes corresponding to the end of construction for each wall case.

As expected, CO_2 equivalent and CED can be seen to increase with wall height for each wall type. The relative order of decreasing total amounts for gravity, cantilever, MSE wall (steel reinforcement) and MSE wall (polymeric reinforcement) is preserved at each wall height for CO_2 equivalent emissions (Figure 10.5a). The same is true for CED in Figure 10.5b with the exception of the 15 m-high gravity and cantilever wall cases. This is due to increasing CED impact of steel rebar content in the cantilever wall from 10 to 15 m height compared to the concrete gravity wall structure constructed without rebar. The larger contribution of the backfill soil to CO_2 equivalent emissions and CED in both plots for the MSE wall options compared to matching gravity and cantilever wall cases is due to the larger volumes of soil used in these structures. In all cases the sum of the contributions of concrete and steel components are the largest contributors to total CO_2 equivalent emissions and CED with the possible exception of the MSE wall case with height of 15 m and polymeric reinforcement. For this case, the contribution of concrete and steel is about the same as that for the soil. Both plots show that the contribution to total CO_2 equivalent emissions and CED of construction activities and materials transportation to site are very small compared to the contribution due to the production of the materials alone.

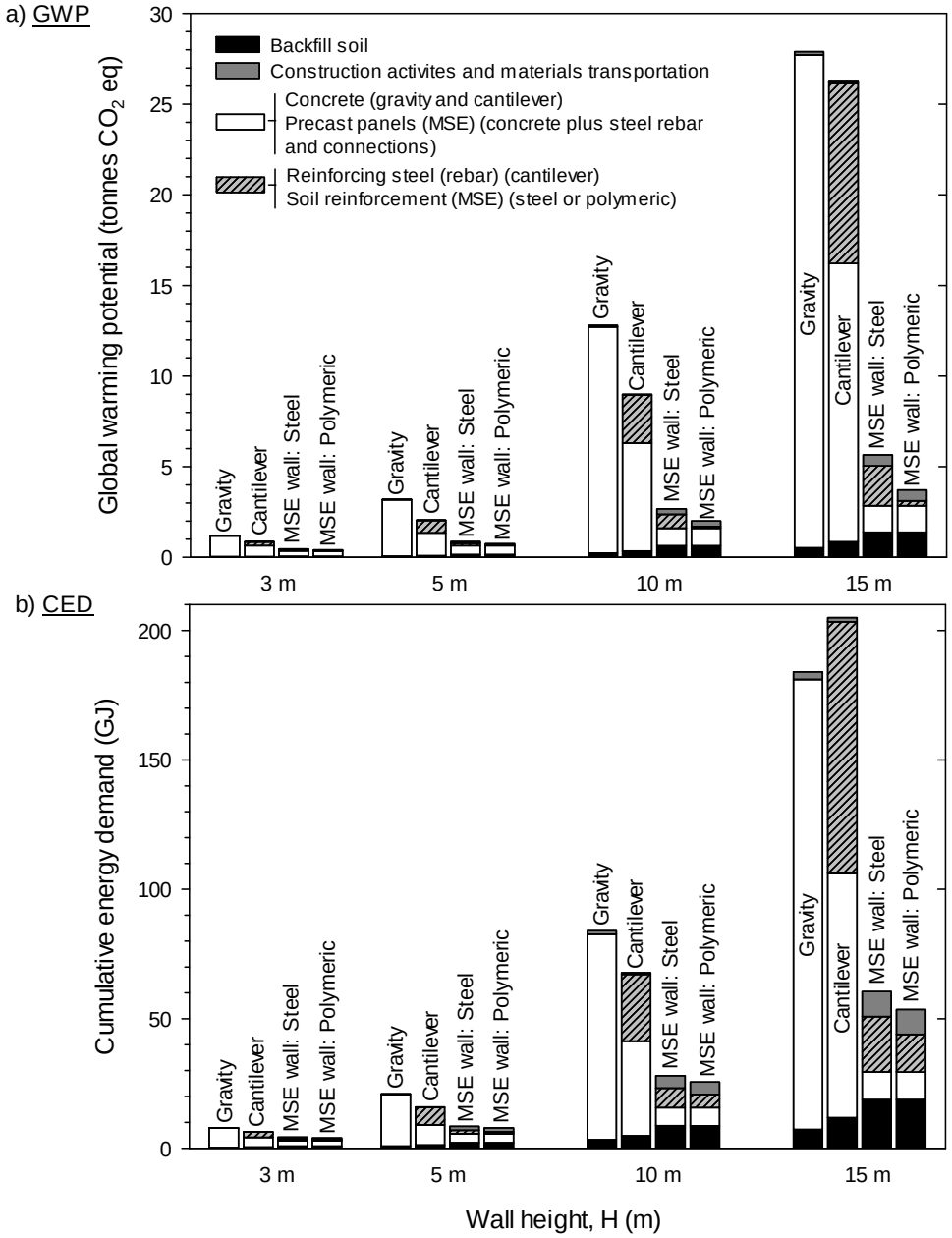

Figure 10.5: Total (a) global warming potential (GWP), and (b) cumulative energy demand (CED) for earth retaining wall alternatives with respect to wall height, material categories, materials transportation and construction activities. Note: Based on a one-metre running length of wall (functional unit).

Table 10.4 shows comparisons of CO_2 equivalent values and energy consumption using the LCA method and the Ecoinvent database in the current study, with data reported in earlier related studies. The data from these earlier studies is judged to be in reasonable agreement despite differences in details of LCA methods employed, differences in polymeric

reinforcement products and suppliers, and different environmental impact indicator databases.

Table 10.4. Comparison of results with data reported by Stucki et al. (2011), Rafalko et al. (2010), and Heerten (2012):

Source	*H* (m)	Climate change (kg CO_2 eq.)		Energy consumption (GJ)	
		Gravity	MSE [(b)]	Gravity	MSE [(b)]
Stucki et al. (2011)	3.0	1300	230	13	3.1
current study		1200	410	7.9	3.9
Rafalko et al. (2010) [(a)]	4.6	3200[(c)]	850	17[(c)]	7.7
current study	5.0	3200	880/750 [(d)]	21	8.5/7.8 [(d)]
Heerten (2012) [(a)]	5.5	3600	670	30	9

Notes: [(a)] Reported results converted to 1 m-width wall to match functional unit in current study and results reported by Stucki et al. (2011).

[(b)] Polymeric soil reinforcement used in studies by Heerten (2012) and Stucki et al. (2011).

[(c)] Concrete and soil materials only.

[(d)] Both steel and polymeric (steel/polymeric) reinforcement types are included.

Figure 10.6 presents the relative contributions to global warming potential and cumulative energy demand for the material components, construction activities and materials transportation of MSE wall alternatives. For example, for the case of a MSE wall with steel soil reinforcement and a height of 15 m (Figure 6a), the backfill soil, construction and materials transportation, and structural components contribute 24%, 11% and 65%, respectively, to GWP. The 65% contribution of the structural components can be attributed to the precast concrete panels (26%) and the steel soil reinforcement (39%). The four plots show that the relative impact of construction activities and materials transportation is smallest (10% to 20%) and sensibly constant across all wall heights. In all cases the two environmental indicators (GWP and CED) decrease with wall height at a decreasing rate for structural components, and increase with wall height at a decreasing rate for the backfill soil component. These trends are most pronounced for the MSE wall cases with polymeric soil reinforcement (Figure 10.6c).

10.3.2. Midpoint results

The CO_2 equivalent values presented in the previous section are a midpoint indicator. Figure 10.7 shows the values of the six other midpoint indicators selected for LCA in the current study plotted against wall height for the four ERW types. As expected, all indicators increase

with wall height. The large increase in rate with height for the conventional gravity wall solutions reflects the larger and non-linear increase in concrete required to construct these structures to greater height (see Figure 10.2a). The same trend for the cantilever wall cases is due to the non-linear increase in steel rebar needed to construct the cantilever walls to greater height (see Figure 10.2b). Increases in environmental indicators are less for MSE wall options and the increases in potential impacts with height of wall are generally more linear.

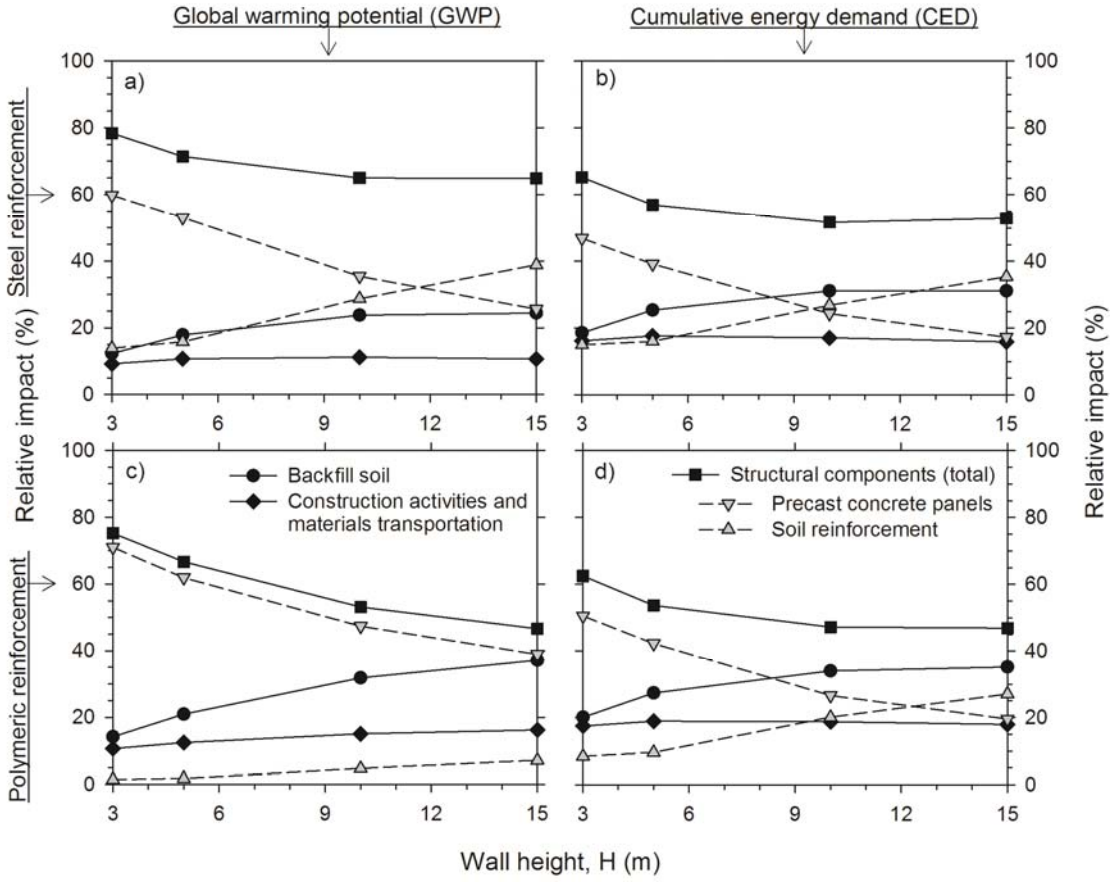

Figure 10.6: Global warming potential (GWP) (a-c) and cumulative energy demand (CED) (b-d) results for MSE wall alternatives based on wall height soil, structural materials, construction activities and materials transportation, and soil reinforcement type: (a-b) steel, and (c-d) polymeric. Note: Based on a one-metre running length of wall (functional unit).

10.3.3. Relative midpoint indicator impacts, global warming potential (GWP) and CED

Figure 10.8 shows the relative impacts for the eight categories in the current study. The gravity walls solutions have the highest impact for six out of eight categories for walls from H = 3 to 10 m. At H = 15 m, the cantilever walls have the largest impact in five of eight categories. In every category and at every height the steel and polymeric MSE wall cases give

lower relative impact values. These values range from a maximum of about 50% at H = 3 m to 30% or less for H = 15 m. Between the steel and polymeric solutions, the environmental impact potentials of MSE polymeric wall cases are always less, but often only by a small amount.

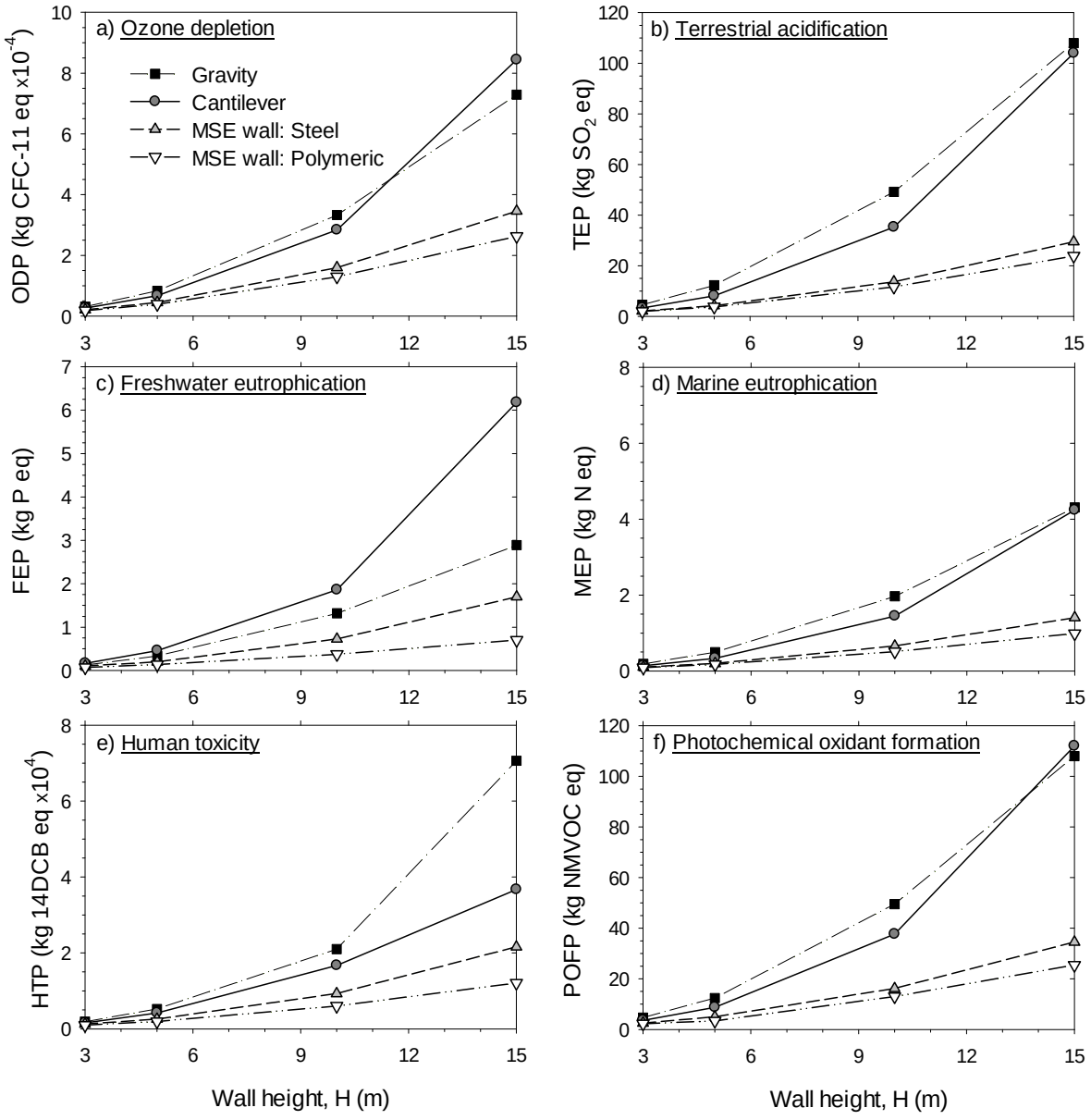

Figure 10.7: Total midpoint environmental indicator impact values versus wall height for each ERW type. Note: Based on a one-metre running length of wall (functional unit).

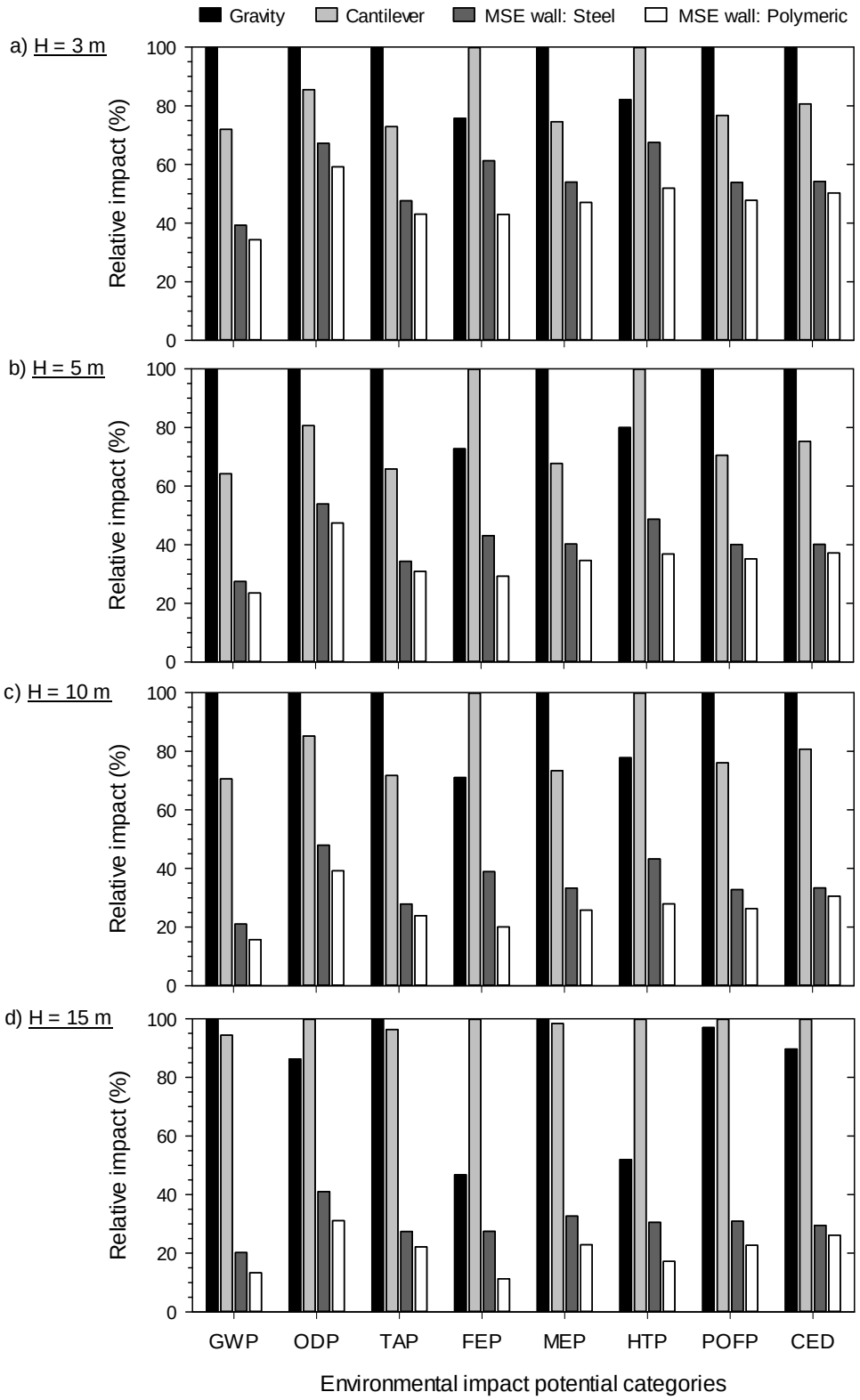

Figure 10.8: Relative environmental impact indicators for different wall solutions constructed to height of (a) 3 m, (b) 5 m, (c) 10 m, and (d) 15 m. Notes: Relative impact is with respect to worst case in each potential impact category. Based on a one-metre running length of wall (functional unit).

10.3.4. Endpoint results

As mentioned earlier, endpoint indicators are based on damage models, which can be used for decision making in categories of potential damage to human health (understood as disability-adjusted loss of life years), ecosystem diversity (related to loss of species during a year) and natural resources availability (related to increased cost). These damage categories were computed individually and then aggregated to give final (unweighted) endpoint single numerical scores for all wall cases (Figure 10.4).

Figure 10.9 presents the endpoint results as relative damage assessments for the four wall cases and wall height scenarios taken with respect to the worst case in each data group. The gravity wall alternative returned greater damage to human health and ecosystems indicators at 3, 5 and 10 m wall heights. The damage to natural resources was greatest in all cases for the cantilever wall option. Significantly better performance was obtained for the MSE wall alternatives, ranging from a maximum relative value of 65% (steel MSE wall case and H = 3 m in natural resources category) to 15% (polymeric MSE wall case and H = 15 m in human health category).

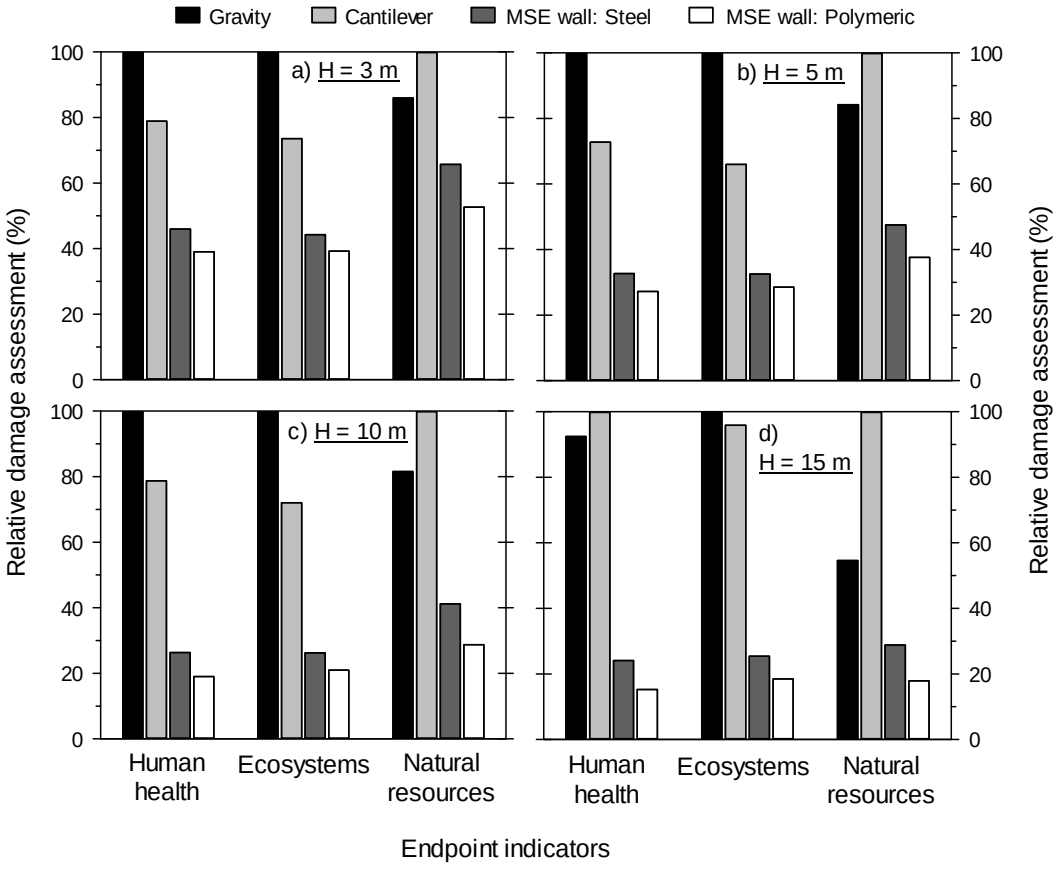

Figure 10.9: Endpoint indicator scores presented as relative damage values for all wall types and wall heights. Note: Based on a one-metre running length of wall (functional unit).

Figure 10.10 presents the final endpoint single scores for the four wall options and wall height scenarios. In each endpoint category there are similar trends to those described in Figure 10.9. It can be seen that there is an order of magnitude difference between contributing and total endpoint scores at H = 3 m and 1 m. The large spreads in contributory and total endpoint numerical scores across all analysis cases in this study demonstrate that the methodology allows differences in damage potential to be easily identified. The endpoint scores decrease in the order of gravity, cantilever, MSE walls with steel reinforcement and MSE walls with polymeric reinforcement, with the exception of the H = 15 m cases where the gravity and cantilever outcomes are reversed. Human health damage accounts for largest impact component and contributes 40% to 50% of the total scores in each wall category regardless of wall type. Figure 10.10 shows that endpoint scores are very sensitive to wall height. To explore this effect further the contributing endpoint data have been replotted in Figure 10.11 as a function of wall height. Not unexpected, there is a nonlinear increase in damage endpoint scores with wall height. The nonlinear trend is most obvious for the cantilever wall cases at H= 10 m (Figure 10.11b). This is attributed to the marked increase in steel rebar at this height which has been noted earlier in reference to Figure 10.2b.

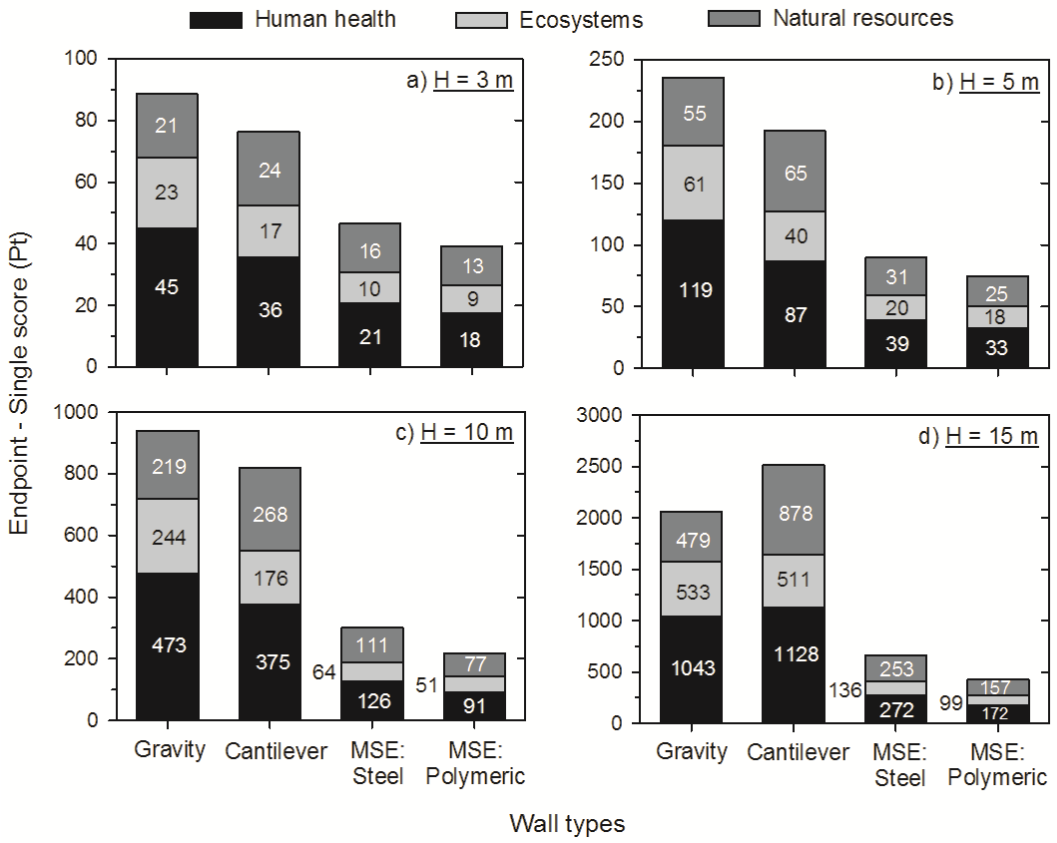

Figure 10.10: Endpoint single score results and endpoint indicator contributions for all wall types and wall heights. Note change of scale with wall height. Based on a one-metre running length of wall (functional unit).

10.4. DISCUSSION AND CONCLUSIONS

Sustainability assessment is emerging as a desirable design component of structures in civil engineering works. A key part of any sustainability assessment is a life cycle assessment (LCA) which is used to quantify the environmental impacts of candidate design solutions.

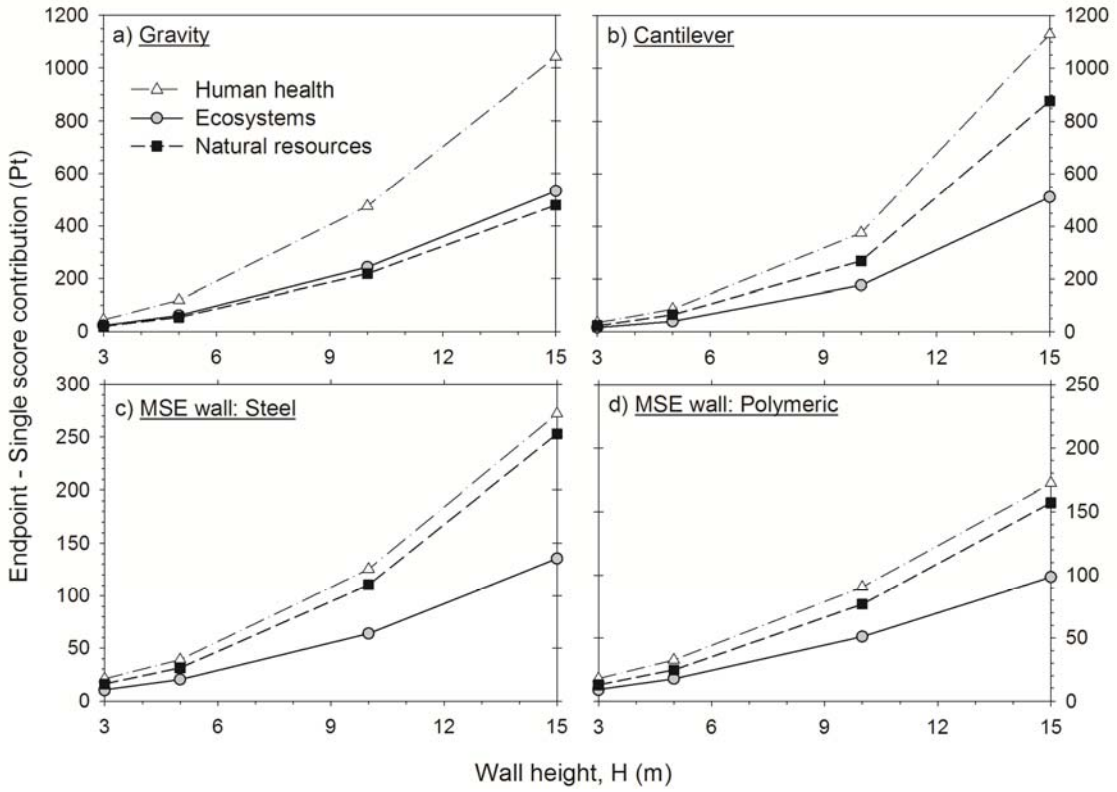

Figure 10.11: Contributions to endpoint single score results plotted against wall height for each wall type. Note: Based on a one-metre running length of wall (functional unit).

This study identifies and explains the principal parts and stages in a LCA and how they apply to the example of environmental impact assessment of typical earth retaining wall solutions. Analyses were carried out for four earth retaining wall options that perform the same function over cradle-to-operational time frames (i.e., up to end of construction). The walls were conventional gravity and cantilever types, and MSE walls constructed with steel and polymeric soil reinforcement options. The analyses included walls constructed to four different heights. The major conclusions from this study are:

1. For each wall height, MSE wall solutions resulted in lower environmental impacts than gravity and cantilever wall solutions as measured by global warming potential,

cumulative energy demand, six major midpoint environmental indicator categories, three endpoint damage categories and in terms of overall endpoint scores.

2. The quantitative environmental benefits of MSE walls in all categories over conventional wall options were seen to increase markedly with increasing wall height.

3. The reason for the better environmental performance of the MSE solutions compared to the gravity wall options was the use of soil backfill as the principle structural component rather than concrete. The better environmental impact performance of the MSE solutions compared to the cantilever wall solutions was again the use of soil as the major structural component, but also because less steel was required.

4. The general approach showed that differences in environmental impacts between MSE walls constructed with steel and polymeric soil reinforcement were detectable in favour of the MSE polymeric options. However, the differences were small enough not to be of practical significance when compared to conventional solutions.

The LCA methodology adopted in the current study was able to quantitatively distinguish between the component environmental impacts of different wall solutions and thus provide a practical numerical score-based tool for designers to choose between candidate solutions. Simplifying assumptions were used in the problem definition for all the wall types in this study but variations in such details will not change the conclusion that MSE walls are a better environmental solution compared to conventional treatments. The methodology described here can be used to explore strategies to further reduce environmental impacts of all earth retaining wall types. For example, the use of recycled construction and demolition waste could be used as the backfill soil for conventional wall types and for the retained and reinforced soil zones in polymeric MSE wall structures (Santos et al., 2012, 2013; Vieira and Pereira, 2015).

In practice, the final choice between the earth retaining wall solutions in this study for a given height must also be based on cost as well as societal and functional factors which are part of a larger sustainability assessment. The LCA described in this Chapte has been included as the environmental impact component in a sustainability study. Results and methodology of a full sustainability evaluation are presented in next Chapter 11.

CHAPTER 11

SUSTAINABILITY ASSESSMENT OF EARTH RETAINING WALL STRUCTURES [1]

11.1. INTRODUCTION

11.1.1. General

Historically, final solutions for civil engineering projects have been optimized based on minimum costs and maximum functionality while satisfying acceptable margins of safety. Examples of civil engineering works are buildings, pavements, bridges, foundations, and earth retaining walls to name only a few. Furthermore, sustainability criteria as an integral part of civil engineering design decision making are becoming more common (e.g., Aguado et al., 2012; MacAskill and Guthrie 2013) including geotechnical engineering projects (Holt et al., 2010; Basu et al., 2014). Sustainability and sustainable development includes the capacity to carry out an activity (such as manufacturing or constructing a product or structure) with minimal or no impact (EN 15804 2012; Josa and Alavedra 2006; Brundtland et el., 1987). However, more broadly defined, sustainability is related to satisfying three sets of requirements (pillars) based on environmental, economic and societal/functional criteria (CEN/TC350 2012; ISO 14040 2006). Sustainability objectives can vary between project types and within different categories due to differences in costs of materials, construction and maintenance, environmental and societal impacts, etc. Sustainable design involves finding a satisfactory balance between these competing objectives (Basu and Puppala 2015; Josa and Alavedra 2006; Josa et al., 2008). A key feature of sustainable design is a structure or project lifetime "cradle-to-grave" perspective, although "cradle-to-operation" or "cradle-to-gate" are also common (ISO 14040 2006; ISO 14044 2006).

[1] Chapter based on Damians, I.P., Bathurst, R.J., Adroguer E., Josa, A., and Lloret, A.; 2016. Sustainability assessment of earth retaining wall structures. ICE Environmental Geotechnics. (in-press)

Earth retaining walls (ERWs) are ubiquitous on the civil engineering landscape. Many different types of wall solutions are available to designers with advantages and disadvantages depending on the application (Jones 2002). Design methodologies for these structures are well established and proven. ERWs can be broadly classified into conventional (cantilever and gravity) and mechanically stabilized earth (MSE) categories (e.g., Figure 11.1). While walls of different types can be designed to perform the same function, MSE structures constructed to the same height as cantilever walls have been shown to be less expensive (Berg et al., 2009; Tanyu et al., 2008; Khan and Sikder 2004; Jones 1996, 2002; Koerner and Soong 2001).

Jones (1996) reported the results of an "ecology audit" on an example 6 m-high reinforced concrete cantilever wall and a steel MSE wall of the same height. Based on eight different indictors he concluded that the MSE wall was much more efficient. Lee and Basu (2015) demonstrated a sustainability study of a pair of steel and polymeric geogrid reinforced MSE walls of the same height using a sustainability assessment framework comprising of the three pillars introduced earlier but with some simplifications. Their study also showed that the MSE wall structure was the most sustainable option but cautioned that relative outcomes are sensitive to choice and weighting of indicator criteria.

In previous Chapter 10 the environmental impacts associated with the different wall types shown in Figure 10.1 (i.e., gravity, cantilever and MSE structures; constructed to different heights) were examined using a life cycle analysis (LCA) approach. This previous study demonstrated that the environmental impacts (defined by midpoint and endpoint indicators) most often decreased in the order of gravity, cantilever, steel MSE and polymeric MSE wall types.

The current Chapter extends the earlier study from previous Chapter 10 (reported also in by Damians et al., 2016) by reporting the results of sustainability analyses for the same suite of earth retaining walls (i.e., gravity, cantilever, steel and geogrid MSE structures) constructed to heights of 3, 5, 10 and 15 m. The environmental impacts from the LCA analyses performed previously by the author are used for the environmental pillar identified above as one of the three components of a proper sustainability assessment.

11.1.2. Sustainability assessment principles

A sustainability assessment model based on value theory and multi-attribute assumptions was used in the current investigation and implemented using the Value Integrated Model for Sustainable Evaluations (MIVES) methodology/software tool (Josa et al., 2008). The program can be used for quantitative sustainability assessment of any defined functional unit for which input and outputs can be related for each requirement level (pillar) using multi-criteria analyses. As an example, the functional unit in the current study is a one-metre slice in the running length direction of each earth retaining wall structure option. The sustainability

assessment methodology and outcomes using the MIVES approach can be understood by referring to the flow chart in Figure 11.2. Sustainability requirements refer to environmental, economic and societal/functional pillars. Each of these categories is defined by one or more criteria with three or more quantifiable indicators. Each multi-criteria analysis ends with a single numerical score (V_{final}) suitable for objective decision making between candidate project alternatives.

An important feature of the MIVES assessment model used in the current study is that the different wall options are not evaluated in isolation and then the best option selected from a comparison of final scores. Rather, the strength of each option is influenced by the strength of the competing options at each stage of the calculations in Figure 11.1 for the three categories identified above.

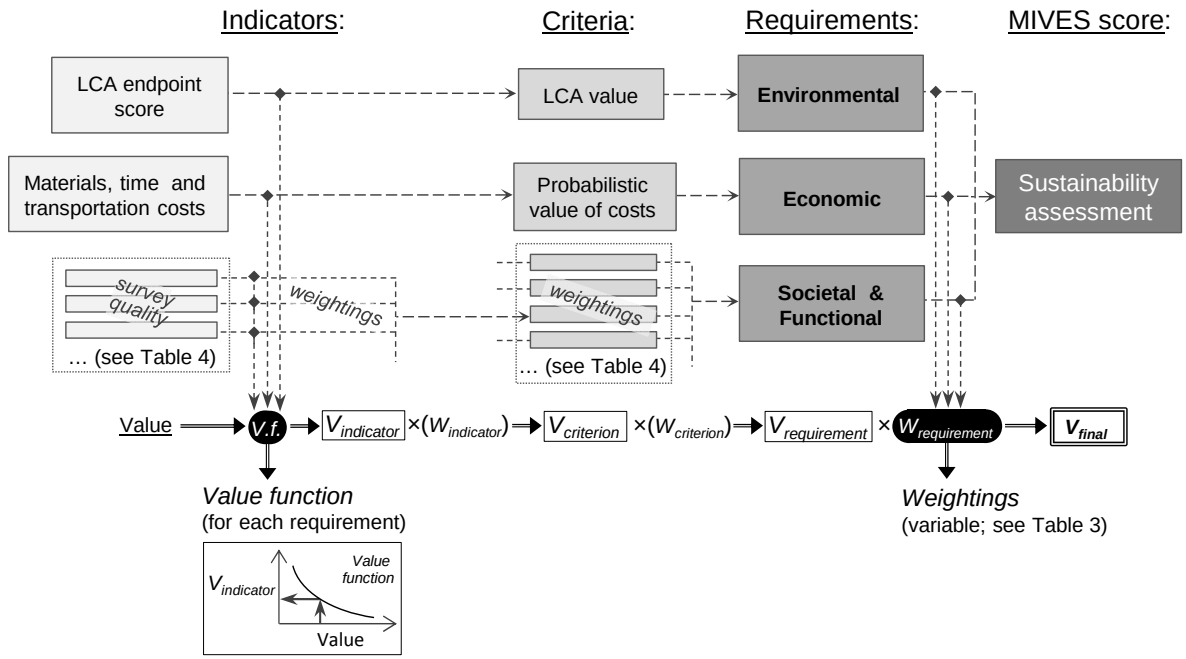

Figure 11.1: Sustainability assessment flow chart.

Additional details for each pillar in the sustainability assessment methodology are described in next:

The **environmental pillar** is focused on environmental impacts and is most often carried out using a life cycle assessment (LCA) approach (e.g., Chapter 10 - Damians et al., 2016). An LCA should ideally consider all possible environmental impacts of any construction process and materials used in the project works (ISO 14044 2006). Midpoint (*Mp*) indicators (e.g., tonnes of equivalent carbon dioxide (CO_2eq) are used to identify intermediate effects of pollutants, and damage models are used to compute endpoint (*Ep*) indicators which are combined to give a final effects LCA endpoint score. Quantification of environmental impacts is well established in the scientific literature and databases are available. Damage

categories can be weighted based on socio-political preferences, and uncertainty in calculations when computing the final (dimensionless) endpoint score for project alternatives in LCA. This score can then be used for decision making based on environmental impacts alone (Bare et al., 2000).

The **economic pillar** focuses on project costs. These costs accrue from manufacture and transportation of construction materials, anticipated material losses, on-site fabrication of structure components including labour, and the like. For "cradle-to-grave" sustainability assessment these costs include operation and maintenance of the structure/project and final dismantling and disposal of materials.

The **societal/functional pillar** captures requirements related to such issues as aesthetics, safety, ease of design and constructability, amongst many other considerations. These issues vary with regard to subjective importance and assessment. A practical strategy to quantify these issues is to develop a survey tool that can be filled out by stakeholders and professionals in the same knowledge field. The results can be weighted using analytic hierarchy process (AHP) techniques (Saaty 2008). An example survey for the wall case study alternatives in the current investigation is described later.

11.2. EARTH RETAINING WALL SUSTAINABLE ASSESSMENT CASE STUDY

In previous Chapter 10, Figure 10.1 shows the three types of wall considered in this investigation. The MSE wall analyses considered both steel and polymeric (geogrid) soil reinforcement cases. The dimensions of the walls were first optimized by carrying out conventional stability analyses to satisfy recommendations found in AASHTO (2014) and ACI (2002). Wall dimensions and soil reinforcement arrangement are summarized in Table 11.1. Analyses were carried out on a one-metre running length of wall face basis. This one-metre slice, also serves as the functional unit defined in LCA terminology as the reference unit for inputs and outputs that enable alternative strategies to be compared and analysed with respect to environmental impacts (ISO 14044 2006). Wall geometry, ground conditions and material mechanical properties used in stability analyses to select optimal structure dimensions can be found in previous Chapter 10 and for brevity are not repeated here.

Table 11.2 summarises the inventory of materials and actions related to each case study analysis for which environmental impacts can be assigned. Included in this table are additional amounts of materials and other project inputs that are required to make up for losses in these items. For example, the nominal amount of concrete estimated during the design of a gravity structure is increased by 5% to 12% to make up for expected losses. In a project-specific sustainability assessment, the amount of loss for each entry will be influenced in most cases by the height of the structure. To simplify analyses, no variances in unit excavation volumes were considered in the current study. However, in a project-specific sustainability study this variance from a nominal estimate is likely available. Table 11.2 also

includes variations from unit costs for inventory items that are used later in the economic pillar calculations.

As in previous Chapter 10, the case study timeframe was taken as cradle-to-operational (i.e., to end of construction) and the design life of the structures was taken as 100 years. The same time frame (system boundary) and design life are used for all three pillars in this Chapter. The design life is a required input to the sustainability study costing component of any earth retaining wall structure even if the system boundary is cradle-to-operation. For example, issues related to durability and/or creep of the soil reinforcing elements in an MSE wall and connections must be considered at the time of structure design.

11.3. SUSTAINABLE ASSESSMENYT COMPUTATIONAL DETAILS FOR WALL CASE STUDIES

11.3.1. General

The process of assigning values and weighting to each indicator–criteria–requirement level to arrive at a final MIVES score (V_{final}) is shown in the flow chart in Figure 11.1. The values (*Value*) for LCA endpoints, midpoints and societal/functional scores are relative dimensionless numbers while the values for the economic pillar are in cost units (e.g., euros-€). A value function for each requirement level (pillar) is used to convert each original indicator value to a dimensionless indicator value ($V_{indicator}$) between 0 and 1. Value functions can have different forms (i.e., linear, concave, convex, sigmoidal; see Alarcon et al., 2011). Example value functions and their meaning are presented later.

The next step is to compute the criterion value for each indicator level ($V_{criterion}$) using Equation 11.1:

$$V_{criterion} = \sum_{i=1}^{n} V_{indicator} \times W_{indicator} \tag{11.1}$$

Each of these values is multiplied by a weighting factor ($W_{indicator}$) at the indicator level. As an example, rather than using endpoint scores in the LCA, different weights could be assigned to the CO_2eq and cumulative energy demands (CED) outputs reported in previous Chapter 10 (Damians et al., 2016) and the sum of the resulting weighted scores used for $V_{indicator}$ for the environmental requirement level. In the current study the endpoint scores based on the LCA reported by the author in the previous Chapter are used and hence the weighting factor is 1.0. Similarly, a single cost indicator with a corresponding weighting factor of 1.0 is used for the economic pillar in this study, but different weightings could be assigned to different cost components. As an example the cost of items consumed early in a project may be more certain than the costs for materials procured later in the project. In the current study, multiple indicators (n = 17) are used in the societal and functional requirement

level with different weighting factors applied to each indicator based on the results of a survey simulation.

Table 11.2. Materials, time and transportation inventory including additional amounts for losses and variation in nominal unit costs:

Cases	Category	Related items and components	Units	Wall height (H) (nominal values)				Additional % amount to account for losses		Variation on nominal unit costs	
				3 m	5 m	10 m	15 m	min.	max.	min.	max.
Gravity	Structural materials	Concrete	m^3	2.5	6.7	27.3	60.1	5%	12%	-10%	15%
	Soil materials	Retained backfill	tonnes	8.1	23.3	95.1	209	5%	12%	-10%	15%
	Earthworks	Excavation	m^3	0.6	1.2	5.3	10.8	0%	0%	-10%	15%
		Backfilling and compaction time	h ($\times 10^{-3}$)	0.5	1.5	5.9	13.3	5%	12%	-10%	15%
	Transportation	Concrete	km	10	10	10	10	5%	12%	-10%	15%
Cantilever	Structural materials	Concrete	m^3	1.1	2.3	11.1	29.1	5%	12%	-10%	15%
		Reinforcing steel (rebar)	tonnes	0.08	0.27	1.04	3.93	5%	12%	-10%	15%
	Soil materials	Retained backfill	tonnes	13.2	35.9	139	339	5%	12%	-10%	15%
	Earthworks	Excavation	m^3	0.3	0.9	4.6	12.6	0%	0%	-10%	15%
		Backfilling and compaction time	h ($\times 10^{-3}$)	1.0	2.8	11.0	25.8	5%	12%	-10%	15%
	Transportation	Concrete and steel	km	10	10	10	10	5%	12%	-10%	15%
MSE walls: Steel and Polymeric	Structural materials	Precast panels [(a)]	m^2	3.4	5.6	11.1	16.6	3%	7%	-10%	20%
		Concrete (levelling pad)	m^3	0.05	0.05	0.05	0.05	5%	12%	-10%	15%
		Soil reinforcement: Steel grid	kg	25	54	296	844	5%	12%	-10%	15%
		Soil reinforcement: Polymeric geogrid [(b)]	kg	4	10	66	187	3%	7%	-10%	20%
	Soil materials	Reinforced and retained backfill	tonnes	23.0	61.8	251	542	5%	12%	-10%	15%
	Installation	Panel installation time	h	0.1	0.2	0.4	0.6	3%	7%	-10%	20%
	Earthworks	Excavation	m^3	1.8	3.9	7.0	12.5	0%	0%	-10%	15%
		Backfilling and compaction time	h ($\times 10^{-3}$)	3.5	9.2	33.1	72.0	5%	12%	-10%	15%
	Transportation	Panels and reinforcement	km	100	100	100	100	3%	7%	-10%	20%
		Select backfill	km	10	10	10	10	5%	12%	-30%	40%

Notes: [(a)] facing precast panels include: concrete (m^3), reinforcing steel (kg) and galvanized steel for the connections (kg).

[(b)] high-density polyethylene (HDPE) geogrid materials were used in calculations. The average strength and hence mass of these materials increased with wall height to satisfy reinforcement load demand computed during design.

The next step is to sum the product of each criterion value and matching weighting factor ($W_{criterion}$) to arrive at a single score for each requirement level, hence:

$$V_{requirement} = \sum_{j=1}^{m} V_{criterion} \times W_{criterion} \quad (11.2)$$

In the example sustainability assessment of the earth retaining walls in this Chapter, only one criterion was considered at environmental and economic levels and hence these weighting factors are again 1.0. However, a total of m = 5 criteria are identified in the societal and functional requirement category. An advantage of the MIVES software is that indicator values ($V_{indicator}$) and criterion values ($V_{criterion}$) can be evaluated deterministically or probabilistically.

Final weighting values ($W_{requirement}$) are applied to the scores for each requirement level ($V_{requirement}$) to arrive at the final MIVES score (i.e., V_{final}) for the problem case being assessed (e.g., each wall option in this study). Example sets of requirement-level weighting factors are presented in Table 11.3. The example values reflect possible preferences of different stakeholders with respect to the subjective importance of each assessment pillar in arriving at a final MIVES score for each project alternative (e.g., wall solution option). However, these values are used to demonstrate the methodology and are not meant to be a general guide.

Table 11.3. Example requirement weighting scenarios:

Stakeholder group/ pillar weighting scenario	Weightings for requirement levels (pillars) ($W_{requirement}$) (see Figure 10.2)		
	Environmental	Economic	Societal and functional
A (reference case)	1/3	1/3	1/3
B	**2/3**	1/6	1/6
C	1/6	**2/3**	1/6
D	1/6	1/6	**2/3**

11.3.2. Environmental pillar

SimaPro software (Pré Consultants B.V. 2010) was used to compute the single endpoint LCA value for the environmental requirement (pillar). Included in the SimaPro software is the Ecoinvent v3.1 database (Ecoinvent 2014) and ReCiPe (Goedkoop 2008; ReCiPe 2014) method, among others. Details of the general approach and its implementation using the same walls in the current study can be found in previous Chapter 10 (as in Damians et al., 2016).

The higher the LCA value the greater the negative environmental impact and hence the less desirable the case study option from an environmental impact perspective.

A value function having an exponential decay formulation (Alarcon et al., 2011) was used in Equation 11.1 and is plotted in Figure 11.2a. This function is the default "concave" function in the MIVES software toolkit. High LCA endpoint values in Figure 11.2a translate to low value function multipliers. The non-linear function favours environmentally friendly solutions and discriminates against relatively poor solutions. In the current Chapter the author imposed two additional constraints on value function outcomes. Endpoint values that were twice the average value of all four solution alternatives for a given wall height were assigned a score of zero and endpoint values with a score less than 50% of the average of all solutions were assigned a value of 1.0. This strategy was used to ensure that obvious low environmental impact cases were assigned a maximum value and solutions with very high environmental impact with respect to the other solutions were not rewarded with a non-zero value. A total of four cases in the current study were assigned a value of 1.0 and two were assigned a value of zero using these rules. As noted earlier, both indicator- and criterion-level weighting factors were assigned a value of 1.0 in the current study.

11.3.3. Economic pillar

An inventory of project consumables is required as the starting point for economic level calculations in the flow chart of Figure 11.1. Table 11.2 summarises the materials, time and transportation items for walls in the current study. For each category item and wall height option, the cost of that item can be computed knowing the unit cost. In order to carry out these calculations, unit costs were taken from a construction materials database used in Barcelona (ITeC 2014). Nevertheless, the relative outcomes from the economic level component of the sustainability assessment in the current study are judged by the author not to be prejudiced by the use of this database.

Because material losses and costs have uncertainty, (Table 11.2), a probabilistic approach was used to estimate the economic level $V_{indicator}$ value for each wall option. First, the minimum possible total cost of each wall solution was computed using the sum of nominal item amounts plus minimum additional item amounts times the associated minimum costs (i.e., nominal cost adjusted by negative unit cost variance shown in Table 11.2). Hence, this calculation considers minimum loss amounts and minimum unit costs. The maximum possible total cost of each wall solution was computed as the sum of nominal item amounts plus corresponding maximum additional item amounts times the associated maximum costs (i.e., nominal cost adjusted by positive unit cost variance shown in Table 11.2). Hence, this calculation assumes maximum loss amounts and maximum unit costs. Wall solution costs were assumed to be randomly distributed between these values according to a triangular probability density function. The mode value for the triangular distribution for each wall solution was taken as the sum of nominal item amounts plus average of each additional item amount multiplied by the matching nominal item cost. The triangular cost frequency

distributions for the 16 wall option-height cases in the current study are plotted in Figure 11.3. The choice of a triangular frequency distribution is common practice when available data is limited. In this particular application, knowledge is limited to a typical (most frequent) cost (i.e., mode), and best estimates of the minimum and maximum range of cost for a single wall type of particular height. In sustainability assessment studies with more cost data, other frequency distributions could be used.

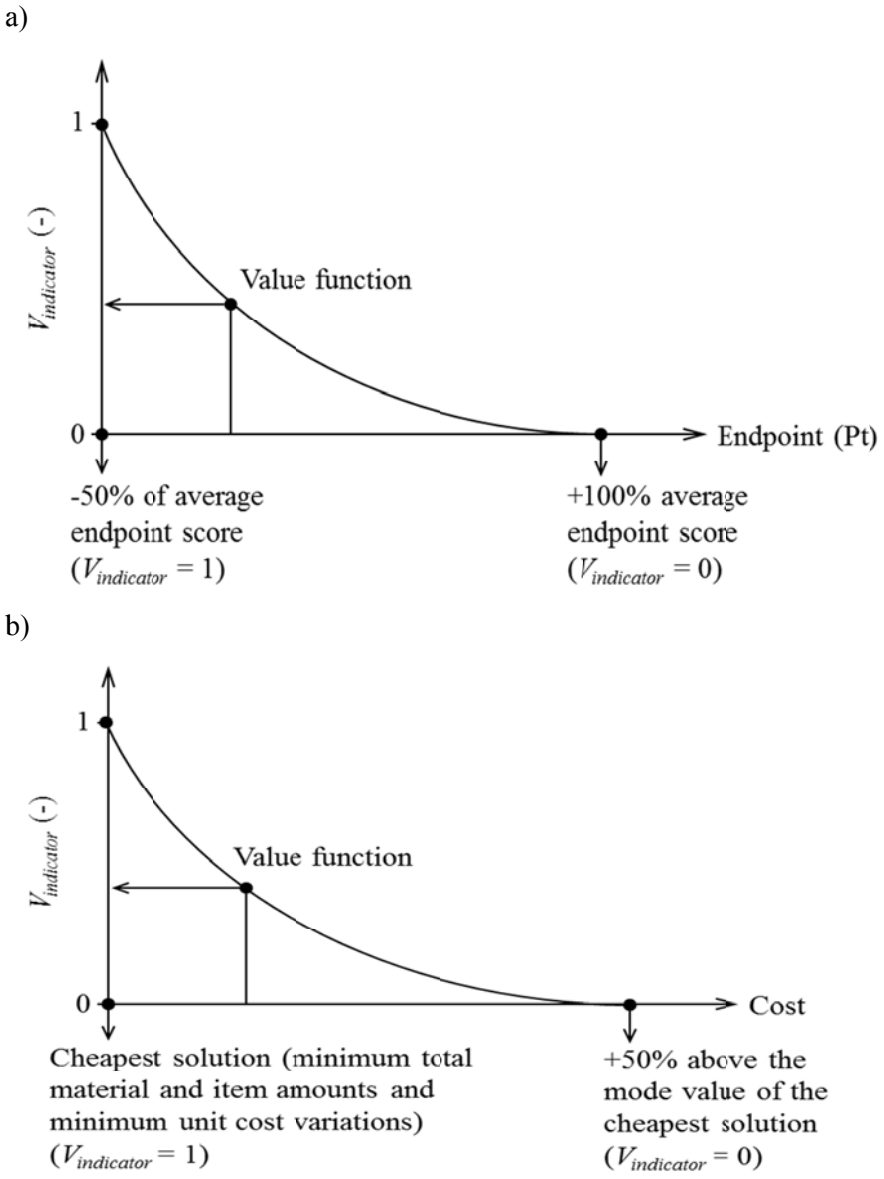

Figure 11.2: Value function concepts and limits for environmental (a) and economic (b) level analyses.

Superimposed on the figures are the average cost of steel and geosynthetic reinforced MSE walls in the USA reported by Koerner et al. (1998) adjusted for year and currency. Only those

cases where cost values fall within the cost range of each plot are shown. The USA study was restricted to state-funded wall projects. The walls ranged from 3 m to 11.5 m in height and included conventional gravity structures. The relative order of costs based on wall type is the same in the current study and in the USA data. It is interesting to observe that the USA data for polymeric MSE walls fall within the cost range for similar structures assumed in the current investigation. However, with the exception of the steel MSE wall in Figure 11.3c the average costs reported in the USA study were greater than the maximum value of the cost axis in these plots for steel MSE walls and gravity walls. This may be expected since unit costs can vary widely between countries and regions; the same is true for structures that are built for public and private sectors.

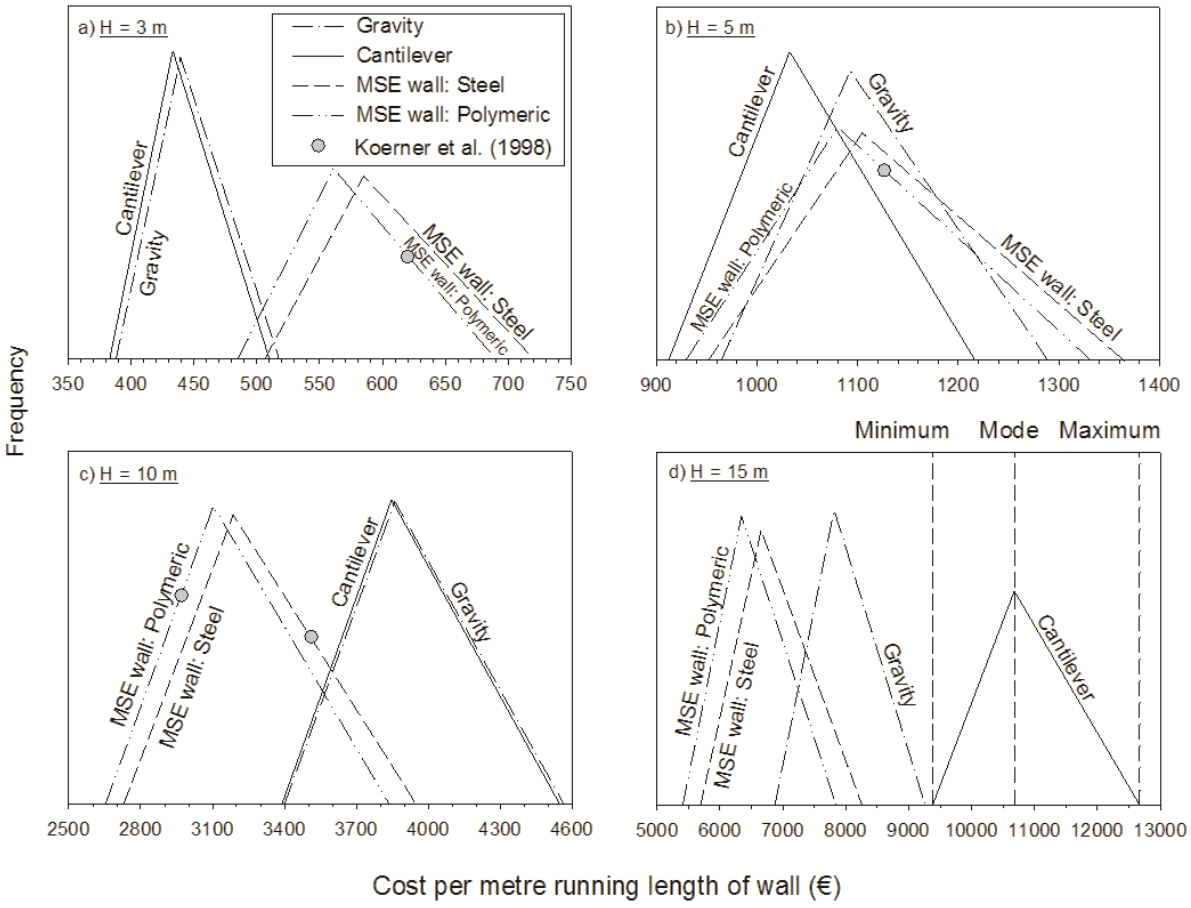

Figure 11.3: Triangular cost frequency distributions for wall options and different wall heights.

The triangular frequency distribution function for each wall solution was used to generate random cost values for the wall solution using Monte Carlo simulation. Each random cost variable was converted to an indicator value using the economic requirement value function (transformation). The result is an array of random $V_{indicator}$ values between 1 and 0. The mode

value of this array of random values was taken as $V_{indicator}$ for the economic level in the sustainability assessment flow chart in Figure 11.1.

A similar type of value function as that used in the environmental level analyses was used for the economic value function and for the same reasons (Figure 11.2b) (i.e., reward low cost solutions and discourage high cost solutions). A value of 1.0 was assigned to the minimum possible cost of all solution options. Maximum cost outcomes that were more than 50% of the mode value of the cheapest solution were assigned a value of zero. Since criteria and requirement weighting factors were taken as 1.0 in this study, then $V_{final} = V_{requirement} = V_{indicator}$.

11.3.4. Societal and functional pillar

A collection of indicator items is required as a first step in carrying out the societal and functional pillar portion of any sustainability assessment study. These data can be acquired from the results of a focused survey designed around the type of project solutions under investigation and taken by project stakeholders and knowledge professionals in the subject area. An example survey for the wall sustainability assessment in the current study is described in this section. The calculation of $V_{requirement}$ for the societal and function level follows the flow path shown in Figure 11.1. The value function that appears in this string of calculations was linear with a score of 1 transformed to 0 and a score of 5 transformed to 1. Weighting values for indicator and criteria items were deduced from survey results described next.

For the purposes of this study, indicator descriptions were first compiled from 200 undergraduate and 50 graduate students enrolled in geotechnical engineering design classes following discussions with the instructors (AJ, AL and IPD) regarding their opinion of primary concerns for the four wall alternatives in this study. The descriptors were then refined based on the experience of two of IPD and RJB with actual retaining wall projects. The indicator descriptions were assigned by numbers and grouped into the five criteria categories shown on the survey form that appears in Table 11.4. The integer scoring system from 1 to 5 assigns higher numbers to better MIVES outcomes for each indicator. The survey form also includes a subjective weighting to be assigned to the relative importance of each of the five criteria categories identified on the form. This survey form was filled out by the students in the classes noted above and also by 10 experienced earth retaining wall designers. The actual scores that appear in the survey form of Table 11.4 are those of a respondent in the latter group. The final scores were aggregated and weighted as discussed later in the Chapter.

The scores in the completed survey form are presented for demonstration purposes only. The contents of survey forms of this type are hugely subjective and outcomes are significantly influenced by the number and experience of the respondent sample. Nevertheless, the final weighted scores were judged by the author to be reasonable and to not unfairly prejudice final MIVES scores for each of the four wall options in each height category.

Table 11.4. Societal and functional criteria and indicators and example survey form:

		$W_{criterion}$ (see Eq. 11.2)			$W_{indicator}$ (see Eq. 11.1)	$V_{indicator}$ (see Eq. 11.1)			
						Scores (1= worst to 5 = best) [(a)]			
						Wall type			
Criteria	Criterion number, m = 5	Criteria weightings assigned by respondent (%)	Indicator number, n = 17	Indicator description	Indicator weightings assigned by respondent (%)	Gravity	Cantilever	MSE Steel	MSE Polymeric
Marketing considerations	1	25	1	Acceptance of wall type	25	4	5	3	2
			2	Labour requirements (less is better)	15	5	4	3	3
			3	Research and development that was required for the wall type category (more R&D for the technology will result in higher)	10	1	1	4	5
			4	Use of local materials and technology (more is better)	25	5	5	2	3
			5	Specialist/trained workers provided by wall system supplier (more is better)	15	1	1	4	3
			6	Land use (less is better)	10	4	4	3	3
Design & construction methodology	2	25	7	Ease of design	20	5	3	3	2
			8	Safety during construction	25	3	3	3	3
			9	Ease of construction	30	2	2	4	5
			10	Duration of construction	25	2	2	3	4
Aesthetics	3	15	11	Aesthetics	100	2	3	4	4
Reliability	4	20	12	Ease of repair (higher score means easier to repair)	25	2	2	3	3
			13	Ease of routine maintenance (higher score means easier to maintain)	25	5	5	3	3
			14	Expectation of satisfactory performance	25	5	4	3	3
			15	Consequences of poor performance requiring repair (low consequence is better)	25	2	2	3	3
Resilience	5	15	16	Flexibility to increase or decrease height during construction	50	2	1	2	2
			17	Susceptibility to changing site conditions from design (e.g., water)	50	2	2	3	4

Note: [(a)] There are no constraints on wall type scores as long as scores are integer values and fall within 1 and 5.

11.4. EARTH RETAINING WALL SUSTAINABLE ASSESSMENT RESULTS

11.4.1. Environmental pillar results

One advantage of the ReCiPe method and Ecoinvent database that are included in the SimaPro software, is that midpoint and endpoint environmental impacts can be computed for different categories. Examples are given in the companion LCA of the same walls in this study by Damians et al. (2016). Two additional examples are shown in Figure 11.4 for midpoint values associated with global warming potential and energy demand. The plots show that in each environmental impact (midpoint) category the conventional wall solutions (gravity and cantilever) are more damaging than MSE wall solutions. All indicators increase non-linearly with increasing wall height. There is a marked increase in CO_2eq and cumulative energy demand for the cantilever wall option which is attributed to the large increase in steel reinforcement required to provide flexural strength at the stem-base connection (Damians et al., 2016). The reason for the better environmental performance of the MSE solutions compared to the gravity wall options was the use of soil backfill as the major structural component rather than concrete. The reduced environmental impact of the MSE solutions compared to the cantilever wall solutions was the use of soil as the major structural component and less steel.

Endpoint damage can be aggregated into a single score based on expected impacts to human health, ecosystems, and natural resources. Figure 11.5 presents the final endpoint single scores (*Ep*-score) computed for the four wall types and wall height scenarios investigated. The relative contributions of each impact category are also shown. As expected the endpoint scores for each wall type increase with wall height. For each wall height, the endpoint scores decrease in the order of gravity, cantilever, MSE walls with steel reinforcement and MSE walls with polymeric reinforcement, with the exception of the H = 15 m cases where the gravity and cantilever outcomes are reversed. Human health damage accounts for the single largest impact component and contributes 40% to 51% of the total scores in each wall category regardless of wall type. Additional discussion of the LCA results in the current study can be found in previous Chapter 10.

Each endpoint score (*Ep*) is then transformed to a $V_{requirement}$ value using a value function as described earlier and illustrated in Figure 11.2a. The results of these calculations are summarized in Figure 11.6. Based on environmental impact alone, the MSE wall options are superior to the conventional wall options. Among the two best options, the polymeric MSE wall option is better than the steel MSE wall option at lower wall heights.

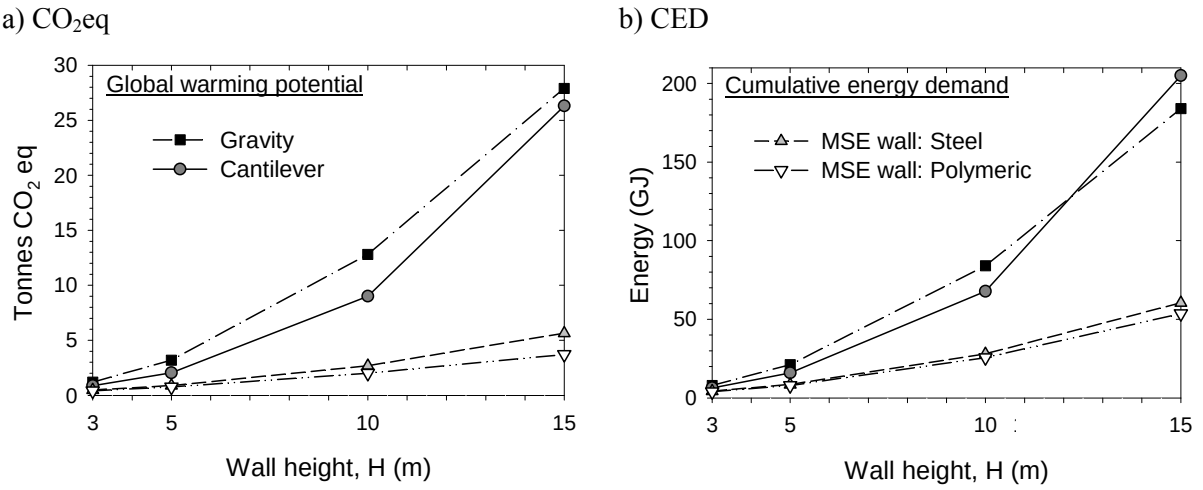

Figure 11.4: Environmental midpoint indicator results for wall options with different heights: (a) global warming potential in tonnes CO_2eq, and (b) cumulative energy demand (CED) in gigajoules (GJ).

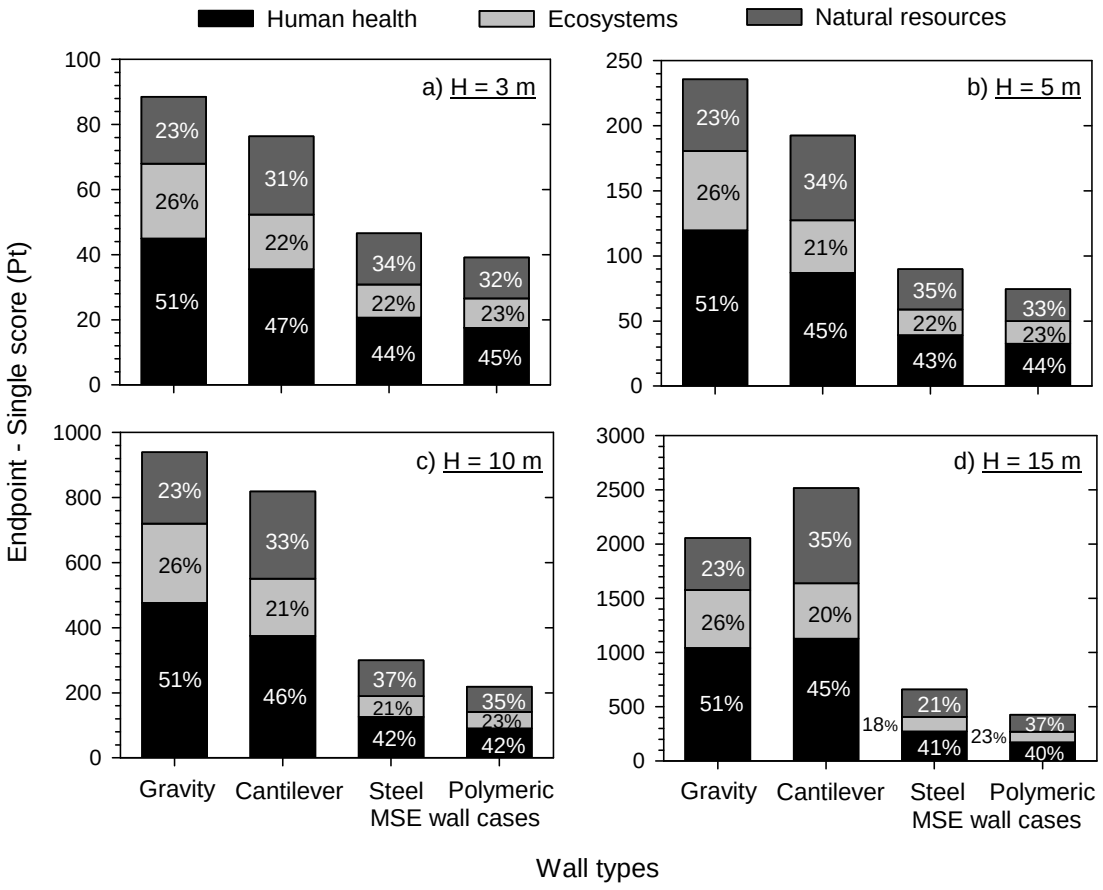

Figure 11.5: Endpoint single score results and relative endpoint indicator contributions for all wall types and wall heights. Note change of scale with wall height (after Damians et al., 2016).

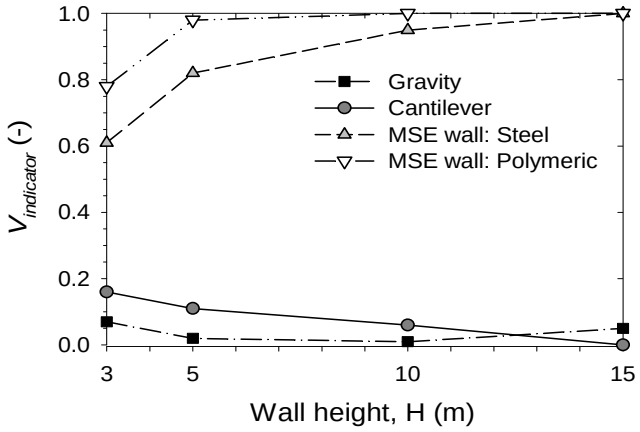

Figure 11.6: Environmental indicator values at requirement level for the four wall options constructed to different heights.

11.4.2. Economic pillar results

The ITeC-BEDEC (ITeC 2014) wall-construction cost inventory database was used in this investigation. Unit costs for some specialized items not found in this reference were generated separately based on the experience of the author with the local (Spanish) market. In addition, the inventory database includes the cost of typical transportation and installation in addition to manufacturing costs. These costs were adjusted by assuming that the facing panels and select backfill were transported 100 km and 10 km, respectively. Again, these haulage distances were judged to better reflect typical local project conditions. Materials, time and transportation inventory items are shown in Table 11.2. The meaning of the material loss and nominal cost variances has been explained earlier in the Chapter.

Figure 11.7 summarizes the total cost of each alternative solution as a function of wall height. The rate of increase in wall costs with height is most pronounced for the cantilever wall option. For walls with height of 5 m there is little economic advantage of one type of wall over another. The two MSE wall solutions are the cheapest at greater height with a small but detectable lower cost for the polymeric MSE wall solution compared to the steel MSE wall option. At a height of 15 m, the gravity and cantilever wall options are approximately 20% and 70% more expensive, respectively, than the MSE wall alternatives. The qualitative trends of increasing cost with increasing wall height has also been noted in the study by Koerner et al. (1998) based on a survey of different wall types constructed for the public sector. Data from their study are superimposed on Figure 11.7. Interestingly there is reasonable agreement between their study and the costs computed in this study for MSE walls up to (say) 12 m where comparable data are available. However, this may be fortuitous because the walls were constructed in different countries at different times and costs were compiled differently in the current study and in the Koerner et al. (2008) study.

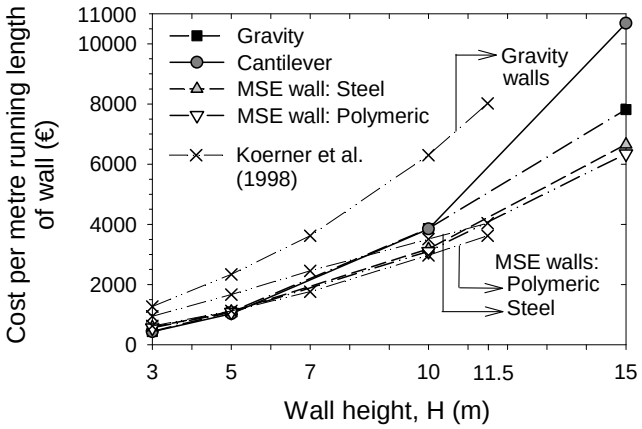

Figure 11.7: Total cost of each wall option using the mode cost for the corresponding triangular frequency distribution for wall costs.

Differences in costs of the different wall types of similar 3 m and 5 m height in the current study are easier to detect in Figure 11.8. It can be seen that for short walls of 3 m height, the MSE walls are about 30% more expensive than gravity and cantilever wall options. At a height of 5 m, the four wall options have similar total cost. At greater height, the MSE walls are consistently cheaper which agrees with comments made earlier regarding Figure 11.7. Additional cost component data can be extracted from the economic portion of the sustainability component using the ITeC-BEDEC (ITeC 2014) wall-construction cost inventory database. Figure 11.8 shows a breakout of the wall costs based on 1) labour, 2) construction equipment, 3) materials, and 4) transportation. These types of breakout are common for cost estimating. The plots do show that conventional gravity and cantilever wall options are more labour intensive than the two MSE wall options. On the other hand, transportation costs are higher for the MSE walls, at least in this study. For walls of 10 m and 15 m height in this study the largest cost component is due to materials for all types. Figure 11.9 shows a breakout of the relative material component costs for the wall options in the current study. The general trends of decreasing relative cost of the panels and relative increasing costs of the steel reinforcement and backfill soil with increasing height of the steel MSE walls cases are consistent with trends reported by Jones (1996).

Figure 11.10 presents computed economic level indicator scores based on the value function shown in Figure 11.2b and the costs of all solutions in the same height category. Some points in Figure 11.10 are zero or close to zero because the much higher relative cost of that solution removed it from consideration based on economics alone (e.g., MSE walls with H = 3 m and conventional walls with H = 15 m). Clearly the magnitude of indicator scores ($V_{indicator}$) will be influenced by the value function selected and the criterion adopted to assign zero for solutions with costs greater than the mode cost. As more cost data becomes available for competing wall types of similar height, then criteria to select both the maximum and minimum cost limits for the value function in the economic pillar analyses can be improved.

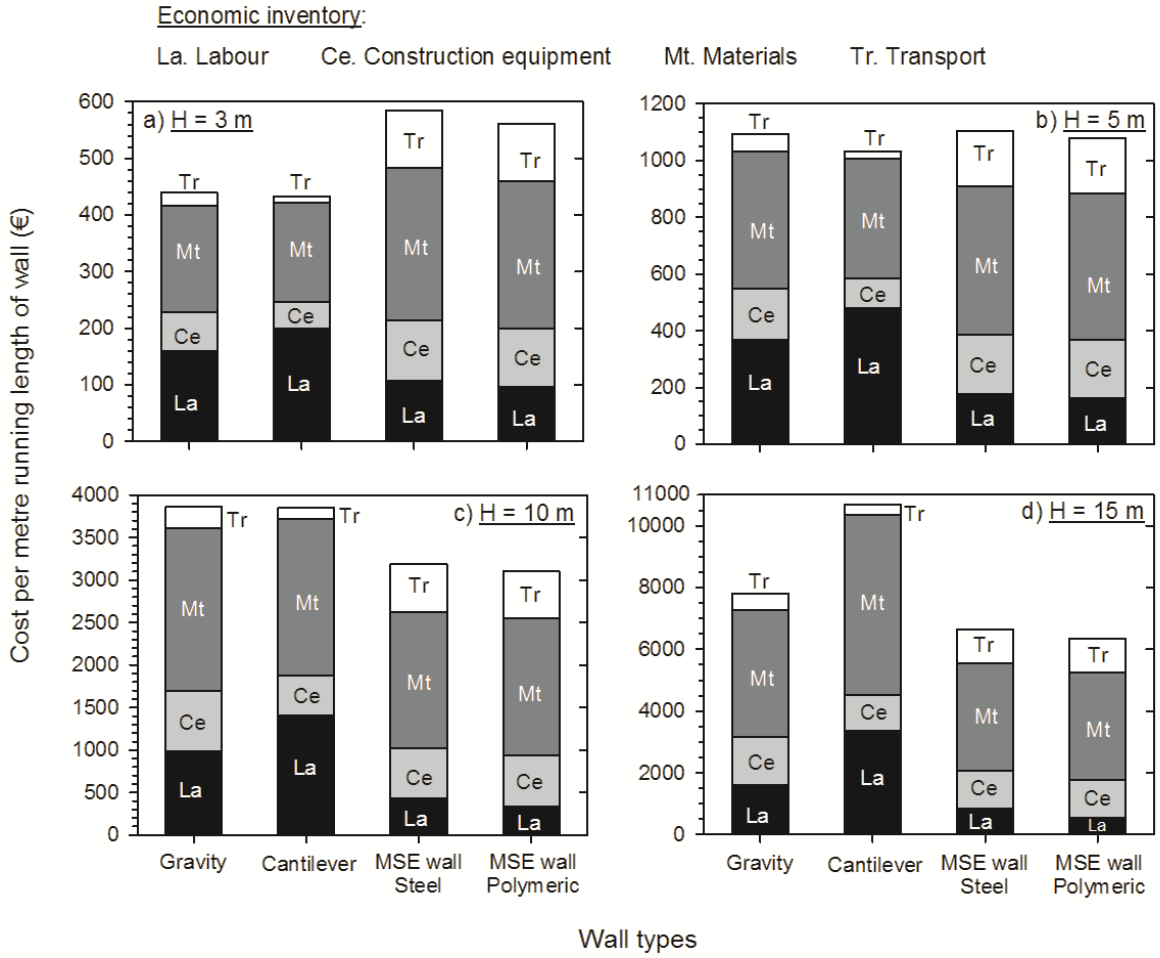

Figure 11.8: Economic inventory for different wall options and different wall heights using mode prices.

11.4.3. Societal and functional pillar results

Table 11.4 was discussed earlier and shows the results of the survey by one example respondent. From each survey form a value of $V_{requirement}$ was computed using Equation 11.1 and then Equation 11.2 for each wall type. The percentage values shown in the table were converted to decimal values in these computations. The average of the scores for each of the three survey populations was computed and then a final $V_{requirement}$ score assigned to each wall type by weighting the score for each group according to 20% for undergraduate students, 30% for graduate students, and 50% for the knowledge professionals. The final computed $V_{requirement}$ values were 0.53 (gravity), 0.54 (cantilever), 0.57 (MSE steel) and 0.58 (MSE polymeric). The numerical values can be seen to be greater (better) in the order listed here with the polymeric MSE wall option ranked best. However, the difference in numerical values is not large. This is interpreted to mean that for the population of respondents that were sampled the overall preference of one wall type over another was not significant. However, scoring outcomes in the societal and functional category can be expected to be

influenced by the design of the sample form and the weighting assigned to each item in the form and the final sample group weightings assigned by the author. As one example, the survey form did not identify wall height as an indicator item in this pillar category. In some jurisdictions in North America there are restrictions on the height of some types of MSE walls constructed with modular block facings.

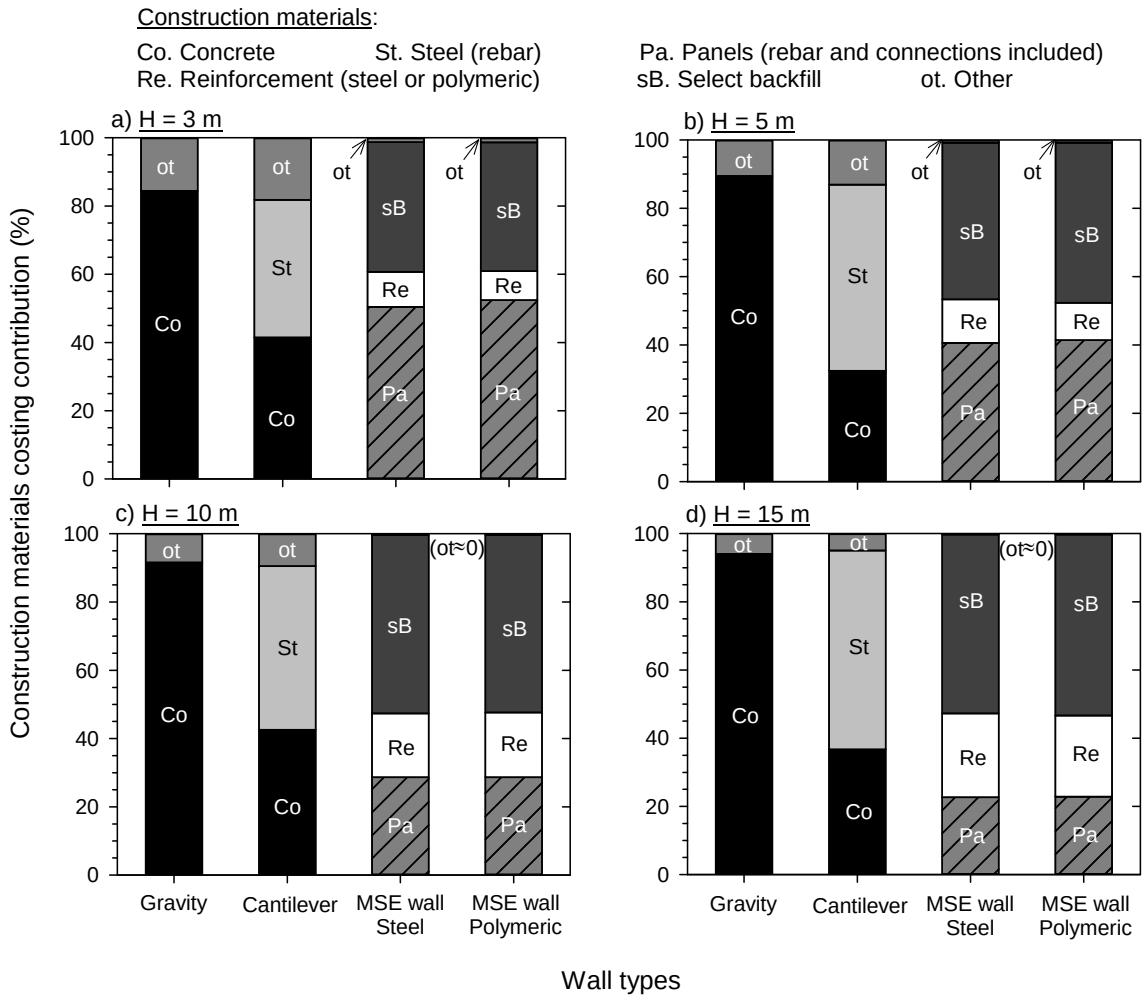

Figure 11.9: Construction material costs for different wall options and different wall heights using component mode prices.

11.4.4. Final MIVES results

The final MIVES scores (V_{final}) in the sequence of calculations shown at the bottom of the flow chart in Figure 11.1 can now be computed using a set of weightings ($W_{requirement}$) taken from Table 11.3. Recall that the weightings reflect possible preferences of different stakeholder groups with respect to the subjective importance of each assessment pillar. The

reference case (A) corresponds to equal weight to each pillar. Cases B, C and D correspond to scenarios where greater importance is assigned to the environmental, economic, and societal/functional levels in that order.

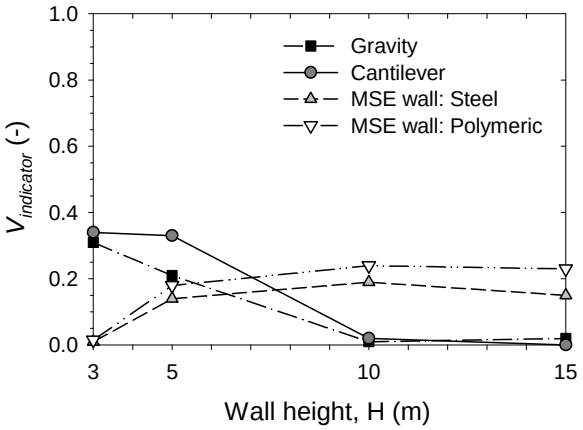

Figure 11.10: Economic value results at requirement level for different wall types and wall height cases.

The final MIVES scores for scenarios A and B are summarized in Figure 11.11 and for scenarios C and D in Figure 11.12. For each wall type and height the contributions of each of the sustainability pillars are identified. Figure 11.11a results correspond to the reference case with no weighting preferences assigned to the three sustainability pillars. The final score outcomes can be seen to be strongly influenced by the final weighting preferences assumed for each of the four scenarios. For example, the MSE wall options are the best solutions at all wall heights when the heaviest weighting preference is applied to the environmental pillar (**Figure 11.11b**). The difference in scores between MSE wall solutions and conventional wall types can be seen to increase with wall height in this figure and are substantially in favour of the MSE wall options for all wall heights. However, when the economic pillar is given the highest weighting, the conventional wall solutions score higher than the MSE wall options for the lowest height walls (H = 3 m in Figure 11.12a). Figure 11.12b shows that when greatest final weight is placed on the societal and functional pillar the influence of wall height on final scores diminishes and the final scores for each wall type remain closer at each height and there is less spread in scores across all options.

11.5. CONCLUSIONS

Sustainability assessment approaches that account for environment impact, cost and societal/functional considerations are becoming an important civil engineering tool for selection of the best option among multiple solutions performing the same function. This study is focused on the example of the sustainability assessment of four different retaining

wall solutions constructed to four different heights. The walls were conventional gravity and cantilever types, and MSE walls constructed with steel and polymeric soil reinforcement materials. The analysis model is based on the MIVES-methodology using value theory and multi-attribute assumptions. The analyses were restricted to "cradle-to-operational" time frames (i.e., up to end of construction) but the general approach can be extended to "cradle-to-grave" corresponding to end of project life.

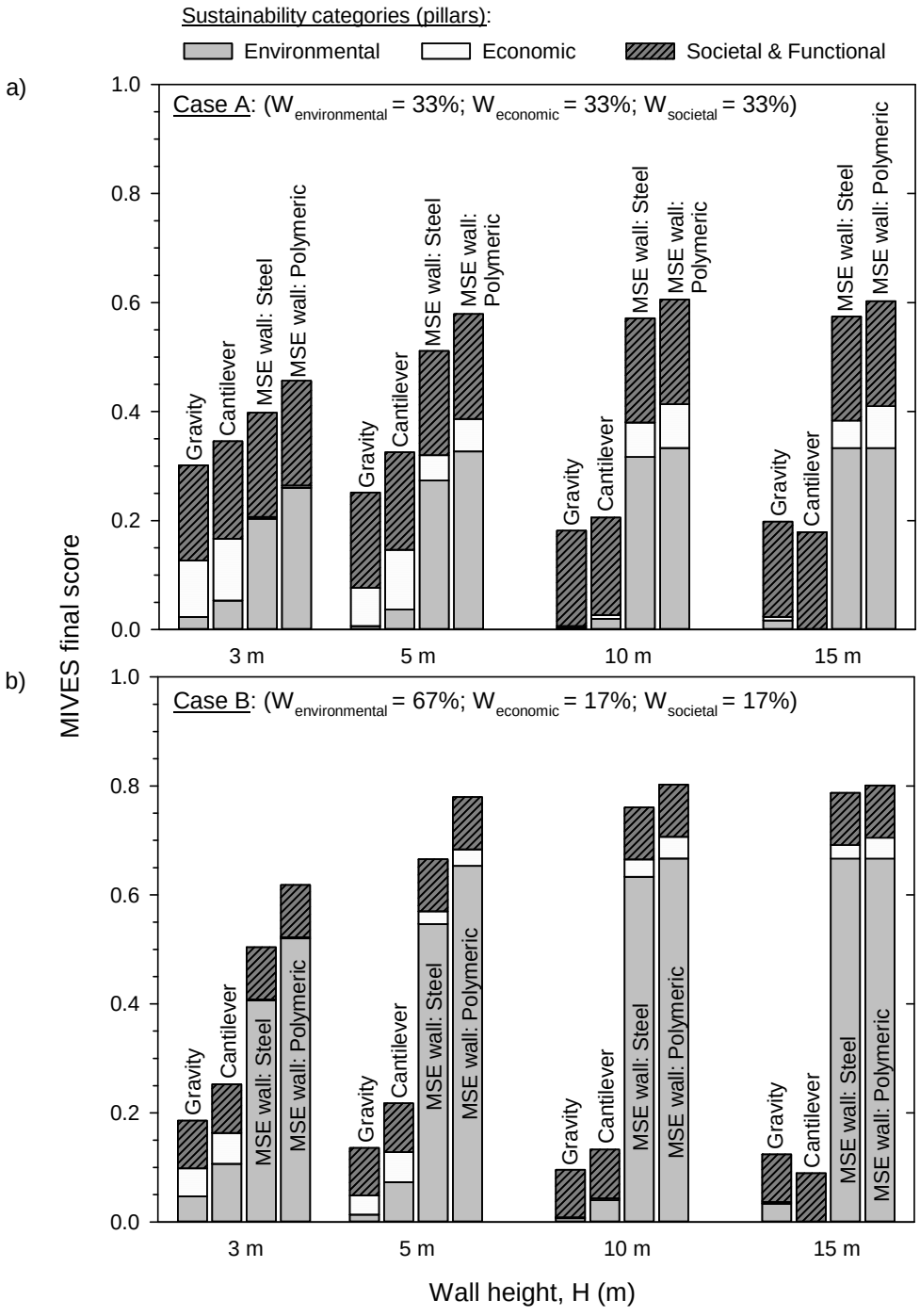

Figure 11.11: Sustainability assessment results using final MIVES scores for A (a) and B (b) weighting scenarios.

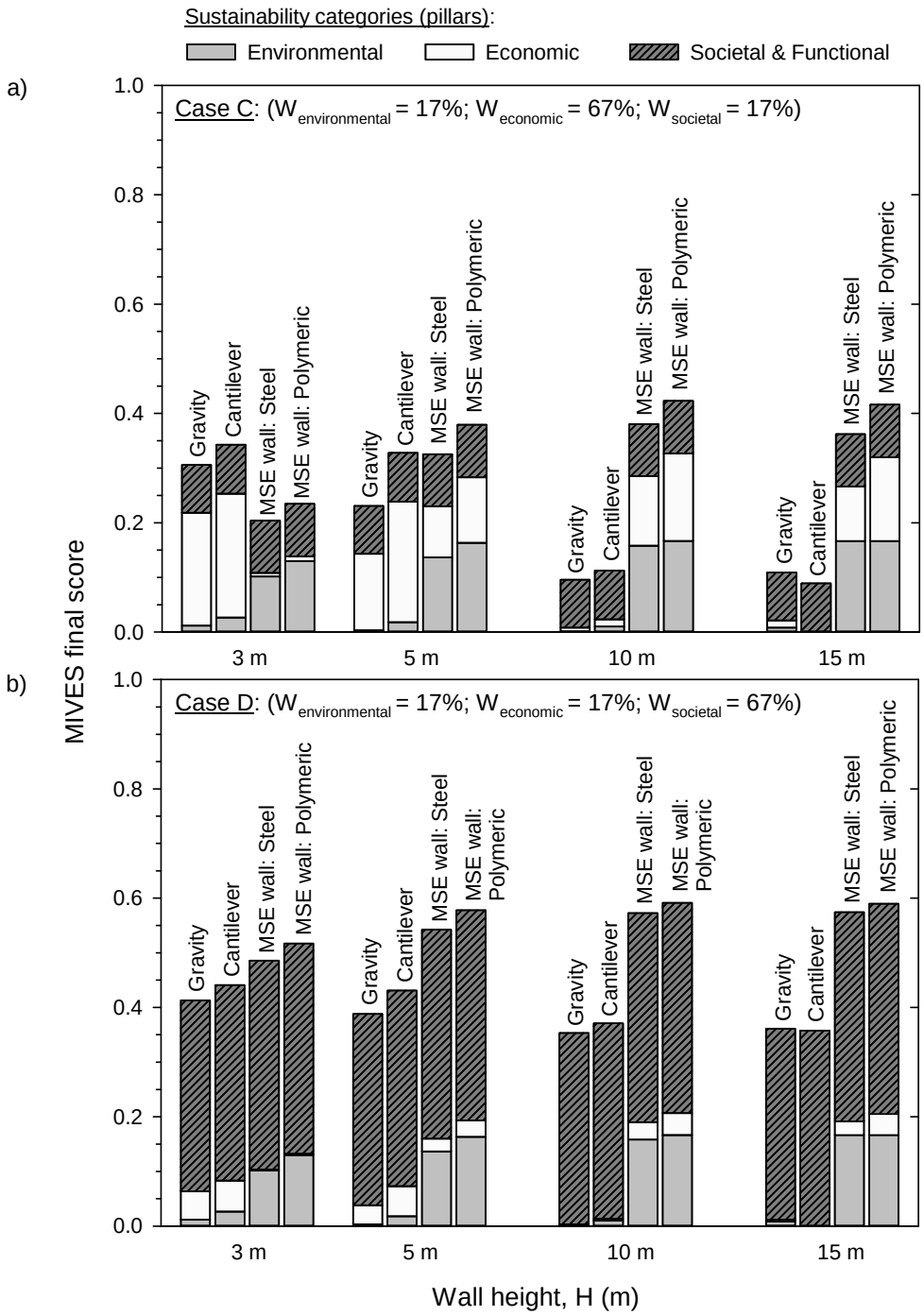

Figure 11.12: Sustainability assessment results using final MIVES scores for C (a) and D (b) weighting scenarios.

The indicator items used in each of the sustainability pillars in the current study appear elsewhere in the literature. Most sustainability assessment protocols are based on a scoring system tied to the list of indicators. Each option is assessed independently with the best solution identified as the option with the best aggregate score. An important feature of the MIVES sustainability assessment model used in the current study is that the strength of each

option is influenced by the strength of the competing options during the scoring calculations for each of the three pillar categories identified above.

The analysis results show that the MSE wall solutions were most often the best option in each sustainability pillar category (environmental, economic and societal/functional) compared to conventional gravity and cantilever wall solutions and thus most often the best final choice when scores from each pillar were aggregated to a final score. Nevertheless, different scenarios are presented with regard to stakeholder preferences for the relative importance of the three sustainability pillars. When cost is weighted most highly of the three pillars, then the conventional wall solutions give the highest (best) MIVES score for walls of 3 m height. If environmental issues are the most important concern of stakeholders then the MSE solutions are the best solution by a substantial margin for all wall heights.

CONCLUSIONS

I. GENERAL

The mechanical behaviour of reinforced soil walls is mechanically complex because of the different component materials, their interactions, wall geometry, foundation condition and method of construction, in addition to the unquantifiable effects of construction method and quality. Most of the investigations described in this Thesis are focused on steel reinforced soil wall systems with precast concrete panels under operational -working stress- conditions. However, walls with polymeric reinforcement are also considered including those with masonry block facings.

For walls under operational (working stress) conditions using current limit equilibrium (strength-based) design methods for the calculation of reinforcement loads, many wall performance features cannot be predicted. Current design methods are typically based on classical notions of soil and reinforcement ultimate strength. Furthermore, internal stability design using conventional analytical solutions assumes rigid foundation conditions so that the compressibility of the foundation soil does not influence reinforcement loads.

The finite element method (FEM) models developed as part of this Thesis have been used to carry out parametric analyses to investigate in a systematic manner the influence of a wide range of input parameters on wall performance (e.g., soil backfill materials, foundation and bearing pad compressibility, reinforcement type and arrangement, soil-structure interactions, and wall heights), and the influence of the choice of constitutive soil model.

Analyses of reinforced soil earth retaining structures within the context of sustainability assessment against other conventional structures that meet the same functionality (such as gravity and cantilever walls) for different structural heights. Using a methodology through a model based on multi-attribute utility theory and value analysis for decision-making utility, the most representative and most impactful processes were identified from a sustainable perspective. The final results included also possible scenario-based decision-making by the relative importance of the three pillars of sustainability (environmental, economic, and social/functional).

The generated models and analysis methodologies developed in this Thesis have provided a deeper understanding of the behaviour of these structures and offered strategies for design improvement and optimization.

II. MECHANICAL PERFORMANCE: 2D NUMERICAL ANALYSIS

II.a. Calibration of full-height MSE wall structures

An important issue to obtain accurate results from a numerical model is the proper calibration of the model using real cases. A comparison between the results from finite element method 2D model simulation with PLAXIS software and measured wall responses from a case study with a wide range of recorded wall performance features was done and presented in the Thesis (Chapter 2), demonstrating a good agreement. Additional calibrations have been also developed following the same methodology and model adjustments with satisfactory results (Chapters 4, 5, 8 and 9).

There were generally satisfactory agreement between numerical and measured results, which give confidence that commercial FEM software packages can be a useful analysis and design tool for steel reinforced soil wall structures. However, important lessons learned in the Thesis that care must be taken in the selection of input parameters.

II.b. Constitutive soil model selection

In real cases, the delivered backfill soil materials may satisfy design specifications but in many cases these materials may not match the properties of the soil assumed in numerical computations at the design stage. Consequently, regardless of the numerical approach to design a wall, numerical predictions can only be expected to be approximate. Design engineers routinely use simple constitutive models in practice even for substantial reinforced steel wall structures. In practical terms and as previously stated, numerical models need only be as accurate as the measurements against which the predictions can be compared.

Linear-elastic constitutive model for the soil together with a Mohr-Coulomb failure criterion is a well-known approach in many geotechnical soil-structure interaction problems. More complex constitutive soil models are available, such as the hyperbolic Hardening and Lade soil models. However, these models require input properties that are seldom available to design engineers. Furthermore, improved accuracy of numerical predictions using more advanced models may not be assured.

While there have been detectable differences in numerical outcomes in most cases using the linear-elastic plastic Mohr-Coulomb soil model and the Hardening soil model in the PLAXIS software, there have been often encouraging satisfactory agreement between physical and numerically predicted results using either soil model. Despite there were detectable higher vertical loads through the concrete facing panels and more gap compression in some cases using the advanced backfill soil model, the differences are small and thus judged not to be of practical concern. Furthermore, at the end of construction (working stress conditions) there was no practical difference between computed toe loads or reinforcement loads using the simpler soil model and the range of measured values.

II.c. Vertical facing loads and panel-joint gap analysis (bearing pads)

Vertical facing loads were determined to be controlled by the panel self-weight plus a combination of mobilized shear forces between the back of the concrete panels and the backfill soil, and down-drag forces generated at the connections between the steel reinforcement elements and the concrete facing panels. Thus, facing walls must carry loads that are greater than the self-weight of the panels. The vertical load carried by the facing will result in compression of the horizontal joints between adjoining panels. Excessive vertical loads and/or excessively compliant bearing pads can lead to panel to panel contact which can cause the concrete panels to crack or spall. The backfill soil stiffness, foundation compressibility, and horizontal joint stiffness influence the magnitude and distribution of vertical load through the height of the wall and bearing pad compression. For example, results show that when the backfill soil is relatively soft, the compressibility of the horizontal joint has relatively little influence on the vertical facing load.

An important contribution of this study is that it provides a strategy for design engineers to investigate the influence of soil stiffness and panel joint stiffness using available commercial finite element model packages together with simple constitutive models. This approach allows the engineer to optimize the selection of bearing pads for similar steel reinforced soil wall structures. Design charts was developed that can be used to select the number and type of bearing pads placed at the horizontal joints between the concrete panels so that gap closure is restricted to tolerable amounts and vertical loads transmitted through the concrete panels are not excessive.

II.d. Backfill and foundation soils compressibility

A wide range of soil stiffness values were used to capture the possible influence of foundation modulus on reinforced soil wall behaviour. The backfill soil stiffness and foundation compressibility were found to influence the magnitude and distribution of vertical load through the height of the wall. There was also a significant variation in reinforcement tensile load results depending on the combination of the backfill and foundation stiffness values. In the Thesis, the contribution of foundation vertical stiffness on reinforced soil wall behaviour was isolated from other parameters. Wall facing deformations, connection loads and axial strains in the reinforcement layers all increased with decreasing foundation stiffness. However, the magnitude of wall displacements, maximum reinforcement loads (or strains) and vertical toe loads for the two different reinforcement materials considered, are influenced more by the relative stiffness of the two reinforcement materials than by the compressibility of the foundation when all other conditions are the same.

II.e. Complementary case studies

The Thesis shows that an appropriately selected number and type of compressible bearing pad can be effective in reducing vertical compression loads in these structures and at the

same time ensure an acceptable vertical gap between concrete panels. In particular, for the precast facing panel steel reinforced soil wall cases analyzed, it was found that the vertical stiffness of the facing (represented by the number of horizontal joints along the facing and/or different thicknesses of the bearing pad elements) produce significantly different effects on the vertical facing load and the reinforcement tensile loads. In cases with polymeric strip reinforcement, the installation procedure (i.e., pre-tension or no-tension load applied to the strips during construction) has a direct effect on the behaviour of this type of reinforced soil wall. The wall performance features at the end of construction can be purposely influenced by using a specified pre-tension load during construction. For example, vertical facing loads, toe settlements and facing displacements can be significantly reduced by applying an appropriate tensioning load at the tail-end of the strip reinforcement layers.

III. MECHANICAL PERFORMANCE: 3D NUMERICAL ANALYSIS

Both PLAXIS and FLAC 2D commercial software programs have been used in the Thesis work. The programs use different numerical approaches, such as finite element (PLAXIS and CODE_BRIGHT programs) and finite difference methods (FLAC program). The magnitudes of predicted wall performance features using these two different numerical approaches in this study are judged to have been in satisfactory agreement from a practical point of view even though there were detectable differences in many data plots. Both programs are used around the world to design complex reinforced soil walls and other types of soil structures. It is assumed that the user has sufficient experience to select appropriate component constitutive model parameters and to correctly judge the reasonableness of all numerical outcomes and mechanical issues.

The interaction between the backfill soil and facing components, and between the backfill and the reinforcement elements, strongly affect the performance of reinforced soil walls. The numerical modelling of earth retaining structures requires the use of interface boundaries between the dissimilar materials to simulate the discontinuity and transfer of normal and shear stresses from the soil to the facing component. Numerical software programs generally have interface models to simulate soil-structure interactions using zero-thickness interface elements (available in PLAXIS) and/or spring interface elements (available in FLAC). However, in some software packages neither zero-thickness interface models nor other similar special interface models are available. Thus, an appropriate methodology using continuum elements (separated material with a real thickness value) at the interfaces between the soil and structural components is an option to numerically examine soil-structure interactions.

In the Thesis, a small earth retaining wall segment was first used to demonstrate how soil-facing interfaces can be modelled using both zero-thickness elements and continuum elements to capture soil-structure interactions. Is has been possible to perform 3D modelling of the soil-structure interactions by using this continuous element (“soft” substitute materials with reduced thickness) implemented within the CODE_BRIGHT program; good agreement

using results from other interface approaches were reported. As demonstrated, once the mesh reached a certain size value, the finite element mesh type had a minor influence on the predicted normal and shear stresses at the interface between the facing panel and backfill soil when using zero-thickness elements. Fluctuations of normal and shear stresses for the interface with continuum elements were observed once the soil within the interface zone reached plasticity (failed) in PLAXIS model cases. However, the total vertical and horizontal loads at the interface from continuum elements generally agreed with those from zero-thickness or spring elements in both PLAXIS and FLAC models. In some modelling cases, it may be very difficult (even impossible) to satisfactorily refine he numerical mesh around these interaction zones, which puts a limit on the accuracy of numerical outcomes. As demonstrated in the Thesis, the actual interface zone using continuum elements with a thickness greater than the interface virtual thickness from zero-thickness or spring elements can be used to generate similar numerical outcomes for finite element models with continuum elements and zero-thickness elements, if the equivalent interface stiffness is kept the same for both methods.

Reinforcement pullout tests are frequently performed to determine the actual soil-reinforcement interaction strength in project-specific soil-reinforcement case studies. Results of several pullout testing series performed with both steel ladders and polymeric strip reinforcement types have been presented. The design of these reinforcement materials is not included or at best is poorly defined in international Codes. From the obtained test results it is has been demonstrated that the strength default values from Codes typically underestimate the real reinforcement strength, particularly for steel ladders at low confining scenarios.

A 3D numerical finite element model has been generated with the CODE_BRIGHT software program. The model has been used to analyze these kinds of pullout tests with special focus on sensitivity of numerical results to typical parameter changes (basically the strength and stiffness of different component materials). The same interface methods described earlier were also assumed for soil-facing interactions in these simulations. The model demonstrates and quantifies, for example, the effect of soil dilatancy with significant increase of the vertical stress around the reinforcement, and how increasing soil and interface strength and stiffness may result in higher reinforcement pullout strength. The resulting approaches and presented methodology may be of interest for designers when results of soil-reinforcement pullout interaction are required for projects where actual test data are not available or are limited.

The Thesis also demonstrates a good agreement between the measured performance values from laboratory pullout tests and the numerical approach using an interface material for soil-reinforcement interaction. The presented results from pullout tests have led to better estimates of the soil-reinforcement pullout interaction factors for steel ladders and polymeric strip reinforcement materials found in some Codes. The numerical approaches allow the modelling of base-case laboratory pullout tests to be extended tor other soil cases, geometry and vertical pressures. The 3D effects identified in the reinforcement pullout tests may not be satiafactory simulated using 2D modelling.

Finally, a simple equivalent 3 m-high model was developed to perform analysis of a 6 m-high structure. The purpose of this model was to achieve more accurate qualitative and quantitative results beyond the scope of the two-dimensional models. The results obtained demonstrated that there is an actual 3D-effect for these structures that cannot be captured using 2D model analyses in some cases. Nevertheless there are some other cases where these 3D effects may not be significant and 2D analyses are sufficiently accurate.

The numerical simulation results demonstrate satisfactory agreement with reported data from a similar instrumented real wall. The methodology presented looks promising to achieve further results for other geometries, structural material data, and even under different boundary conditions.

IV. SUSTAINABILITY ASSESSMENT

Sustainability assessment approaches that account for environment impact, cost and societal/functional considerations are becoming an important civil engineering tool for selection of the best option among multiple solutions performing the same function. A key part of any sustainability assessment is a life cycle assessment (LCA) which is used to quantify the environmental impacts of candidate design solutions.

The principal parts and stages in a LCA and how they apply to the example of environmental impact assessment of typical earth retaining wall solutions have been investigated in the Thesis. Analyses were carried out for four earth retaining wall options that perform the same function over cradle-to-operational time frames (i.e., up to end of construction) constructed up to four different heights (3, 5, 10, and 15 m high). The walls were conventional gravity and cantilever types, and MSE walls constructed with steel and polymeric soil reinforcement options.

From the results of analyses, major conclusions have been obtained; for example, for each wall height, MSE wall solutions resulted in lower environmental impacts than gravity and cantilever wall solutions (in terms of global warming potential, cumulative energy demand, and other complementary midpoint environmental indicators and endpoint damage categories), and these quantitative environmental benefits of MSE walls in all categories over conventional wall options were seen to increase markedly with increasing wall height.

The reason for the better environmental performance of the MSE solutions compared to the gravity wall options was the use of soil backfill as the principle structural component rather than concrete. The better environmental impact performance of the MSE solutions compared to the cantilever wall solutions was again the use of soil as the major structural component, but also because less steel was required. This general approach showed that differences in environmental impacts between MSE walls constructed with steel and polymeric soil reinforcement were detectable in favour of the MSE polymeric options. However, the

differences were small enough not to be of practical significance when compared to conventional solutions.

In practice, the final choice between the earth retaining wall solutions in this study for a given height must also be based on cost as well as societal and functional factors which are part of a larger sustainability assessment. The LCA described in the Thesis has been included as the environmental impact component in a sustainability study, which has been focused on the same four different retaining wall solutions constructed to four different heights. The analysis model is based on the MIVES-methodology using value theory and multi-attribute assumptions. The analyses were restricted to “cradle-to-operational” time frames (i.e., up to end of construction) but the general approach can be extended to “cradle-to-grave” corresponding to end of project life.

From the obtained results the alternative of reinforced soil turned out to be the best choice against the other alternatives (gravity walls and cantilevered), obtaining a higher score in much of the decision making scenarios considered. Nevertheless, in one particular decision-making scenario where the cost becomes more important against social and/or environmental impact, conventional solutions score higher for lower height wall cases. However, in scenarios where environmental issues are given more weight, reinforced soil solutions are markedly better than the other alternatives for wall heights greater than 5 meters.

REFERENCES

Abdelouhab, A, Dias, D. and Freitag, N., 2011. Numerical analysis of the behaviour of mechanically stabilized earth walls reinforced with different types of strips. Geotextiles and Geomembranes 29: 116-129.

Aguado, A. del Caño, A. de la Cruz, MªP. Gómez, D., and Josa, A., 2012. Sustainability assessment of concrete structures within the Spanish structural concrete code. ASCE Journal of Construction Engineering Manage 138(2), 268-276.

Alarcon, B. Aguado, A. Manga, R., and Josa, A., 2011. A Value Function for Assessing Sustainability: Application to Industrial Buildings, Sustainability 3, 35-50.

Allen, T., Christopher, B., Elias, V., and DeMaggio, J., 2001. Development of the Simplified Method for internal stability. Report WA-RD 513.1 July 2001, Washington State Department of Transportation, Olympia, WA, USA.

Allen, T.M., Bathurst, R.J., Walters, D.L., Holtz, R.D., and Lee, W.F., 2003. A new working stress method for prediction of reinforcement loads in geosynthetic walls. Canadian Geotechnical Journal 40(5): 976-994.

Allen, T.M., Bathurst, R.J., Holtz, R.D., Lee, W.F., and Walters, D.L., 2004. A new working stress method for prediction of loads in steel reinforced soil walls. Journal of Geotechnical and Geoenvironmental Engineering, 130(11): 1109-1120.

Allen, T.M. and Bathurst, R.J., 2013a. Performance of an 11m high block-faced geogrid wall designed using the K-stiffness method. Canadian Geotechnical Journal dx.doi.org/10.1139/cgj-2013-0261.

Allen, T.M. and Bathurst, R.J., 2013b. Comparison of working stress and limit equilibrium behavior of reinforced soil walls. ASCE Geotechnical Special Publication No.230, "Sound Geotechnical Research to Practice" Honoring Robert D, Holtz II, pp.500-514.

AASHTO, 2004. The Classification of Soils and Soil Aggregate Mixtures for Highway Construction Purposes (M145). American Association of State Highway and Transportation Officials (AASHTO), 444 N. Capitol St., NW, Suite 249, Washington, DC, USA.

AASHTO, 2010. LRFD Bridge Design Specifications (5th edition). American Association of State Highway and Transportation Officials (AASHTO), Washington, DC, USA.

AASHTO, 2012. LRFD Bridge Design Specifications (6th edition). American Association of State Highway and Transportation Officials (AASHTO), Washington, DC, USA.

AASHTO, 2014. LRFD Bridge Design Specifications (7th edition). American Association of State Highway and Transportation Officials (AASHTO), Washington, DC, USA.

ACI, 2002. Building code requirements for structural concrete (ACI 318-02) and Commentary (318R-02). ACI Committee 318, American Concrete Institute (ACI), Farmington Hills, MI, USA.

ASTM D2487, 2011. Standard Practice for Classification of Soils for Engineering Purposes (Unified Soil Classification System). American Society for Testing Materials (ASTM International), West Conshohocken, PA, USA.

ASTM D5321, 2008. Standard Test Method for Detemining the Coefficient of Soil and Geosynthetic or Geosynthetic and Geosynthetic Friction by Direct Shear Method. American Society for Testing Materials (ASTM International), West Conshohocken, PA, USA.

ASTM D6706-01, 2013. Standard test method for measuring geosynthetic pullout resistance in soil. American Society for Testing Materials (ASTM International), West Conshohocken, PA, USA.

Anderson, P.L. and Brabant, K., 2006. Increased Use of MSE Abutments. International Bridge Conference, IBC-05-10, Pittsburgh, PA, USA.

Bare, J.C., Hofstetter P., Pennington D., and Udo de Hades H.A., 2000. Midpoints versus endpoints: The sacrifices and benefits. The International Journal of Life Cycle Assessment 5(6): 319-326.

Basu, D., Misra, A., and Puppala, A.J., 2014. Sustainability and geotechnical engineering: perspectives and review. Canadian Geotechnical Journal 52(1): 96-113.

Bathurst, R.J. and Benjamin, D.J., 1990. Failure of a geogrid-reinforced soil wall. Transportation Research Board 1288: 109-116.

Bathurst, R.J, Allen. T.M., and Walters, D.L., 2005. Reinforcement loads in geosynthetic walls and the case for a new working stress design method. Geotextiles and Geomembranes 23(4): 287-322.

Bathurst, R.J., Nernheim, A., and Allen, T.M., 2008a. Comparison of measured and predicted loads using the Coherent Gravity Method for steel soil walls. Ground Improvement, 161(3): 113-120.

Bathurst, R.J., Miyata, Y., Nernheim, A., and Allen, T.M., 2008b. Refinement of K-stiffness method for geosynthetic reinforced soil walls, Geosynthetics International, 15(4): 269-295.

Bathurst, R.J., Nernheim, A., and Allen, T.M., 2009. Predicted loads in steel reinforced soil walls using the AASHTO Simplified Method. Journal of Geotechnical and Geoenvironmental Engineering, 135(2): 177-184.

Bathurst, R.J., Huang, B., and Allen, T.M., 2011. Load and resistance factor design (LRFD) calibration for steel grid reinforced soil walls. Georisk, 5(3-4): 218-228.

Bathurst, R.J., Damians, I.P., Josa, A., and Lloret, A., 2012. Influence of foundation compressibility on reinforcement loads in geosynthetic reinforced soil walls, Proceedings of the 5th European Geosynthetics Congress, Valencia, Spain, Vol.5, pp.43-47.

Bathurst, R.J., Allen, T.M., Miyata, Y., and Huang, B., 2013. Lessons learned from LRFD calibration of reinforced soil wall structures. Modern Design Codes of Practice - Development, Calibration, and Experiences. (eds. P. Arnold, M. Hicks, T. Schweckendiek, B. Simpson & G. Fenton). IOS Press. Amsterdam, The Netherlands, pp.261-276.

Bastick, M., Schlosser, F., Segrestin, P., Amar, S., and Canepa, Y., 1993. Experimental reinforced earth structure of Bourron Marlotte: Slender wall and abutment test. Reinforcement Des Sols: Experimentations en Vraie Grandeur des Annees 80, Presses de L'école Nationale des Ponts et Chaussees, Paris, France, pp.201-228.

Basu, D. and Puppala A.J., 2015. Principles of sustainability and their applications in geotechnical engineering. In CD Proceedings of 15th Pan-American Conference on Soil Mechanics and Geotechnical Engineering, Buenos Aires, Argentina, IOS Press, pp.162-183.

Berg, R.R., Christopher, B.R., and Samtani, N.C., 2009. Design and construction of mechanically stabilized earth walls and reinforced soil slopes, Volume I (FHWA NHI-10-024) and Volume II (FHWA NHI-10-025), National Highway Institute, Federal Highway Administration. U.S. Department of Transportation, Washington, DC, USA.

Bergado, D.T. and Teerawattanasuk, C., 2008. 2D and 3D numerical simulations of reinforced embankments on soft ground. Geotextiles and Geomembranes 26: 39-55.

Berthoneet, A., 2003. La Cooperation des Laboratoires des Ponts et Chausses avec les Enterprises Routieres, les Constructeurs de Materiels et les Producteurs de Granulats Français de 1945 a 1980. Comité d'Histoire du Ministère de l'Equipement. Paris, France.

Bloomfield, R.A., 1984. Proposed design modifications - VSL retained earth, VSL Corporation.

Boscardin, M.D., Selig, E.T., Lin, R.S., and Yang, G.R., 1990. Hyperbolic parameters for compacted soils. Journal of Geotechnical Engineering, 116(1): 88-104.

Bowles, J.E., 1996. Foundation Analysis and Design. Fifth edition. McGraw-Hill, New York, NY, USA.

Brinch Hansen, J., 1968. A Theory for Skin Friction on Piles. Geoteknisk Institut, Akademiet for de Tekniske Videnskaber - The Danish Geotechnical Institute. Bulletin No.25, Copenhagen, Denmark.

BSI, 2010. Code of Practice for Strengthened/Reinforced Soil and Other Fills, British Standards Institution (BSI), Milton Keynes, UK.

Brundtland, G., Khalid, M., Agnelli, S., Al-Athel, S., Chidzero, B., et al., 1987. Our Common Future: Report of the 1987 World Commission on Environment and Development (WCED), United Nations Documents, NGO Committee on Education, Oxford University Press, Oxford.

CFEM, 2006. Canadian Foundation Engineering Manual (4th edition). The Canadian Geotechnical Society, BiTech Publishers, Richmond, BC, Canada.

Carter, J.P., Desai, C.S., Potts, D.M., Schweiger, H.F., and Sloan, S.W., 2000. Computing and computer modelling in geotechnical engineering. In proceedings of GeoEng 2000, International Conference on Geotechnical and Geological Engineering, Melbourne, Australia, Technomic, pp.1157-1252.

CEN/TC350, 2012. Technical Committee on Sustainability of Construction Works. (http://portailgroupe.afnor.fr/public_espacenormalisation/CENTC350/index.html).

Chamberlain, B., and Cooper, G., 2009. Paraweb straps for rein-forced soil retaining walls and bridge abutments, Linear Composites Ltd. Roads and Bridges Certificate No 09/R146, Product Sheet 1. British Board of Agrément (BBA), Garston, Watford, UK.

Chen, J.F. and Bathurst, R.J., 2013. Investigation of interface toe sliding of reinforced soil block face walls using FLAC, Proceedings of Continuum and Distinct Element Numerical Modeling in Geomechanics, Shanghi, China, Itasca International Inc., 15p.

Chida, S. and Nakagaki, M., 1979. Test and experiment on a full-scale model of reinforced earth wall. Proceedings of the International Conference on Soil Reinforcement, Paris, France, Vol.2, pp.533-538.

Choufani, C., Wu, P., Gagnon, G., and Macintosh, M., 2011. A precast faced mechanical stabilized earth solution for a 20 metre high mining crusher wall with various technical and site challenges. In CD proceedings of 2011 Pan-Am Canadian Geotechnical Conference, Toronto, Canada, Paper 625, 6p.

Christopher, B.R., Bonczkiewicz, C., and Holtz, R.D., 1994. Design, construction and monitoring of full scale test of reinforced soil walls and slopes. Recent case histories of permanent geosynthetic-reinforced soil retaining walls, F. Tatsuoka & D. Leshchinsky, eds, Balkema, Rotterdam, ISBN 90-5410-358-2, pp.45-60.

Christopher B.R., 2014. Cost savings using geosynthetics in the construction of civil engineering projects. In Proceedings of the 10th International Conference on Geosynthetics, Berlin, Germany. German Geotechnical Society, Essen, Germany.

CYPE, 2014. CYPECAD v.2014. CYPE Ingenieros, S.A., Alicante, Spain. (http://www.cype.com/en/).

Damians, I.P., Bathurst, R.J., Josa, A., Lloret, A., and Albuquerque, P.J.R, 2013a. Vertical facing loads in steel reinforced soil walls. ASCE Journal of Geotechnical and Geoenvironmental Engineering, 139(9): 1419-1432.

Damians, I.P., Lloret, A., Josa, A., and Bathurst, R.J., 2013b. Influence of facing vertical stiffness on reinforced soil wall design, Proceedings of the 18th International Conference on Soil Mechanics and Geotechnical Engineering, Paris, France, 4p.

Damians, I.P., Bathurst, R.J., Josa, A., and Lloret, A., 2014. Numerical study of the influence of foundation compressibility and reinforcement stiffness on the behavior of reinforced soil walls. International Journal of Geotechnical Engineering, 8(3): 247-259.

Damians, I.P., Bathurst, R.J., Josa, A., and Lloret, A., 2015a. Numerical analysis of an instrumented steel-reinforced soil wall. ASCE International Journal of Geomechanics, 15(1): 04014037.

Chapter based on Damians, I.P., Bathurst, R.J., Josa, A. and Lloret, A.; 2015b. Vertical facing panel-joint gap analysis for steel-reinforced soil walls. ASCE International Journal of Geomechanics. 10.1061/(ASCE)GM.1943-5622.0000632, 04015103.

Damians, I.P., Bathurst, R.J Adroguer E., Josa, A., and Lloret, A., 2016. Environmental assessment of earth retaining wall structures. ICE Environmental Geotechnics. 10.1680/jenge.15.00040.

Day R.A. and Potts D.M., 1994. Zero thickness interface elements—numerical stability and application. International Journal for Numerical and Analytical Methods in Geomechanics 18, 689-708.

Desai C.S., Zaman M.M., Lightner J.G., and Siriwardane H.J., 1984. Thin-layer element for interfaces and joints. International Journal for Numerical and Analytical Methods in Geomechanics 8, 19-43.

Ecoinvent, 2014. Ecoinvent database v3.1. Ecoinvent Centre, Swiss Centre for Life Cycle Inventories, Zurich, Switzerland. (http://www.ecoinvent.ch/).

EN 13738, 2004. Geotextiles and geotextile-related products – Determination of pullout resistance in soil. European Committee for Standardisation, Brussels, Belgium.

EN 14475, 2011. Execution of special geotechnical works – Reinforced fill. European Committee for Standardisation, Brussels, Belgium.

EN, 2012. EN 15804: Sustainability of construction works - Environmental product declarations - Core rules for the product category of construction products. European Committee for Standardisation, Brussels, Belgium.

Findlay, T.W., 1978. Performance of a Reinforced Earth Structure at Granton. Ground Engineering, 2(7): 42-44.

Fine, 2010. GEO5 - Geotechnical Engineering Software. Fine – Civil Engineering Software, Praha, Czech Republic. (http://www.finesoftware.eu).

Fraser, I., Elsing, A., Stucki, M., et al., 2012. Comparative life cycle assessment of geosynthetics versus conventional construction materials, a study on behalf of the E.A.G.M., case 4, soil retaining wall. In Proceedings of the 5th European Geosynthetics Congress, Valencia, Spain. International Geosynthetics Society - España, Vol.4, pp.218-222.

Frischknecht, R., Itten, R., Ehrenberg, H., and von Maubeuge, K.P., 2014. Environmental product declarations in civil engineering works. In Proceedings of the 10th International Conference on Geosynthetics, Berlin, Germany. German Geotechnical Society, Essen, Germany.

Frischknecht, R., Jungbluth, N., Althaus, H-J., et al., 2007. Implementation of life cycle impact assessment methods. Swiss Centre for Life Cycle Inventories, Dübendorf, Switzerland, Ecoinvent Report No.3, v2.0. (http://www.ecoinvent.ch/).

Gerber, T.M., 2012. Assessing the Long-Term Performance of Mechanically Stabilized Earth Walls. (National Cooperative Highway Research Program (NCHRP) Synthesis 437). Transportation Research Board, Washington, DC, USA.

Goedkoop, M., Heijungs, R., Huijbregts, M., et al., 2008. ReCiPe 2008. A life cycle impact assessment method which comprises harmonised category indicators at the midpoint and the endpoint level, Report I: Characterisation. Den Haag, The Netherlands. (http://www.lcia-recipe.net/).

Goodman, R., Taylor, R., and Brekke, T., 1968. A model for the mechanics of jointed rock. Journal of Soil Mechanics and Foundations Division 99, 637-659.

Hammond G.P. and Jones C.I., 2011. Inventory of (embodied) carbon & energy v2.0. Department of Mechanical Engineering, University of Bath, UK.

Hatami, K., Bathurst, R.J., and Di Pietro, P., 2001. Static response of reinforced soil retaining walls with non-uniform reinforcement. International Journal of Geomechanics, 1(4): 477-506.

Hatami, K. and Bathurst, R.J., 2005. Development and verification of a numerical model for the analysis of geosynthetic reinforced soil segmental walls under working stress conditions. Canadian Geotechnical Journal, 42(4): 1066-1085.

Hatami, K. and Bathurst, R.J., 2006. Numerical model for reinforced soil segmental walls under surcharge loading. ASCE Journal of Geotechnical and Geoenvironmental Engineering, 132(6): 673-684.

Hammond G.P. and Jones C.I., 2008. Embodied energy and carbon in construction materials, Proceedings of the ICE – Energy 161(2): 87-98.

Heerten G., 2012. Reduction of climate-damaging gases in geotechnical engineering practice using geosynthetics. Geotextiles and Geomembranes 30: 43-49.

Holt, D.G., Jefferson, I., Braithwaite, P.A., and Chapman, D.N., 2010. Embedding sustainability into geotechnics. Part A: methodology. In Proceedings of the ICE-Engineering Sustainability 163(3): 127-135.

Huang, B., Bathurst, R.J., and Hatami, K., 2009. Numerical study of reinforced soil segmental walls using three different constitutive soil models. Journal of Geotechnical and Geoenvironmental Engineering, 135(10): 1486-1498.

Huang, B., Bathurst, R.J., Hatami, K., and Allen, T.M., 2010. Influence of toe restraint on reinforced soil segmental walls. Canadian Geotechnical Journal, Vol.47, No.8, pp.885-904.

Huang, B., Bathurst, R.J., and Allen, T.M., 2012. Load and resistance factor design (LRFD) calibration for steel strip reinforced soil walls. Journal of Geotechnical and Geoenvironmental Engineering, 138(8): 922-933.

Ingold, T.S., 1983. Laboratory pull-out testing of grid reinforcements in sand. Geotechnical Testing Journal (GTJODJ), Vol.6, No.3, pp.101-111.

Inui T., Chau C.Y.K., Soga K., Nicholson D., and O'Riordan N., 2011. Embodied energy and gas emissions of retaining wall structures. Journal of Geotechnical and Geoenvironmental Engineering ASCE 137(10): 958-967.

ISO 14040, 2006. Environmental management - Life cycle assessment - Principles and framework (ISO 14040). International Organisation for Standardisation, Geneva, Switzerland.

ISO 14044, 2006. Environmental management - Life cycle assessment - Requirements and guidelines (ISO 14044). International Organisation for Standardisation, Geneva, Switzerland.

Itasca, 2005. FLAC: Fast Lagrangian Analysis of Continua, User's Guide, Itasca Consulting Group, Inc., Minneapolis, USA.

ITeC, 2014. Banco Estructurado de Datos de Elementos Constructivos (BEDEC), The Foundation Catalonia Institute of Construction Technology (ITeC), Barcelona. (http://www.itec.es/home/index.asp).

Jayawickrama, P.W., Surles, J.G., Wood, T.A., and Lawson, W.D., 2013. Pullout resistance of mechanically stabilized earth reinforcement in backfills typically used in Texas: Volume 1. Report No.0-6493-1, Texas Department of Transportation, Austin, TX, USA.

Jewell, R.A., Milligan, G.W.E., Sarsby, R.W., and Dubois, D., 1984. Interaction between soil and geogrids. Proc., Symp. on Polymer Grid Reinforcement in Civil Engineering, Thomas Telford, London, 18-30.

Jones, C.J.F.P. and Edwards, L.W. 1980. Reinforced earth structures situated on soft foundations. Geotéchnique, 30(2): 207-213.

Jones, C.J.F.P., 1996. Earth Reinforcement and Soil Structures. Thomas Telford, London UK.

Jones, C.J.F.P., 2002. Guide to reinforced fill structure and slope design (Geoguide 6). Geotechnical Engineering Office, Civil Engineering Department, Hong Kong, China.

Josa, A. San José, T., and Cuadrado, J., 2008. El caso de la EHE. Jornada sobre Sostenibilidad en la tecnología del hormigón: MIVES, una herramienta de apoyo a la toma de decisiones, 84-95. Department of Construction Engineering, UPC-BarcelonaTech, Barcelona.

Josa, A. and Alavedra, P., 2006. El concepto de sostenibilidad. La medida de la sostenibilidad en edificación industrial: MIVES (Eds: Losada, R. Rojí, E. & Cuadrado, J.), 59-70. UPV, UPC, Labein-Tecnalia, Bilbao.

Kerisel, J., 1961. Foundations profondes en milieux sableaux: Variation de la force portante limite en fonction de la densité, de la profondeur, du diamètre et de la vitesse d'enfoncement. Proceedings of the 5th International Conference of Soil Mechanics, 2: 73-83. Paris, France.

Khan A.J. and Sikder M., 2004. Design basis and economic aspects of different types of retaining walls. Journal of Civil Engineering 32(1): 17-34.

Kibria, G., Hossain, M., and Khan, M., 2013. Influence of soil reinforcement on horizontal displacement of MSE wall. International Journal of Geomechanics, 10.1061/(ASCE)GM.1943-5622.0000297.

Kim, D. and Salgado, R., 2012. Load and resistance factors for internal stability checks of mechanically stabilized earth walls. ASCE Journal of Geotechnical and Geoenvironmental Engineering, 138(8): 910-921.

Koerner, R.M. and Koerner, G.M., 2011. The importance of drainage control for geosynthetic reinforced mechanically stabilized earth walls. Journal of GeoEngineering 6(1): 3-13

Koerner, J., Soong T-Y., and Koerner R.M., 1998. Earth retaining wall costs in the USA. Geosynthetics Institute, Folsom, PA, USA, GRI Report 20.

Koerner, R.M. and Soong, T.Y., 2001. Geosynthetic reinforced segmental retaining walls. Geotextiles and Geomembranes, 19(6): 359-386.

Kreijger, P.C., 1987. Ecological properties of building materials. Materials and Structures 20(4): 248-254.

Kulhawy, F.H. and Mayne, P.W., 1990. Manual on estimating soil properties for foundation design. Report EL-6800, Electric Power Research Institute (EPRI). Palo Alto, California, 306p.

Lade, P.V., 2005. Overview of constitutive models for soils. Soil constitutive models: evaluation, selection and calibration, ASCE geotechnical special publication No.128, J.A. Yamamuro & V.N. Kaliakin, eds., pp.1-34.

Lawson C.R., 1991. Use of geotextiles in reinforced soil retaining structures. Sydney Technological University, Australia, 44p.

Lee, M. and Basu, D., 2015. Sustainability assessment of mechanically stabilized earth walls. In CD Proceedings of 15th Pan-American Conference on Soil Mechanics and Geotechnical Engineering, Buenos Aires, Argentina, IOS Press, pp.830-837.

Ling, H.I., 2003. Finite element applications to reinforced soil retaining walls–Simplistic versus sophisticated analyses. Proceedings of Geomechanics: Testing, Modeling, and Simulation, 1st Japan-U.S. Workshop on Testing, Modeling, and Simulation, J.A. Yamamuro & J. Koseki, eds., ASCE, Reston, VA, USA, pp.77-94.

Lindquist, D.D., 2008. Seismic modeling of a 135-foot-tall MSE wall. Soil dynamics IV, ASCE, Reston, VA, USA, 10p.

Lo, S.C.R., 1998. Pull-out resistance of polyester straps at low overburden stress, Geosynthetics International 5(4): 361-381.

Luo, Y., Leshchinsky, D., Rimoldi, P., Lugli, G., and Xu, C., 2015. Instrumented mechanically stabilized earth wall reinforced with polyester straps. Journal of the Transportation Research Board, No.2511, Transportation Research Board, Washington, D.C., pp.9-17.

MacAskill, K. and Guthrie, P., 2013. Risk-based approaches to sustainability in civil engineering. Proceedings of the ICE-Engineering Sustainability 166(4): 181-190.

Matsui, T., San, K.C., Nabeshima, Y., and Amin, U.N., 1996. Bearing mechanism of steel grid reinforcement in pullout test. Proc., Int. Symp. on Earth Reinforcement, Vol.1, A.A. Balkema, Rotterdam, The Netherlands, 101-105.

Mitchell, J.K. and Villet, W.C.B., 1987. Reinforcement of earth slopes and embankments. Rep.290, Transportation Research Board, National Research Council, Washington, DC, USA.

Miyata, Y. and Bathurst, R.J., 2012a. Measured and predicted loads in steel strip reinforced c-ϕ soil walls in Japan. Soils and Foundations, 52(1): 1-17.

Miyata, Y. and Bathurst, R.J., 2012b. Analysis and calibration of default steel strip pullout models used in Japan. Soils and Foundations, 52(3): 481-497.

NF P 94-222, 1995. Renforcement des sols - Ouvrages en sols rapportés renforcés par armatures ou nappes peu extensibles et souples - Essai statique d'extraction en place d'inclusion. Norme française, Association Française de Normalisation (AFNOR), La Plaine Saint-Denis, France.

NF P 94-232-1, 2001. Renforcement des sols – Ouvrages en sols rapportés, renforcés par armatures extensibles et souples. Partie 1 : Essai d'extraction en place, par paliers, d'une bande d'armature. Norme française, Association Française de Normalisation (AFNOR), La Plaine Saint-Denis, France.

NF P 94-270, 2009. Calcul géotechnique: Ouvrages de soustènement. Remblais renforcés et massifs en soil cloué. Norme française, Association Française de Normalisation (AFNOR), La Plaine Saint-Denis, France.

NFEC, 1986. DESIGN MANUAL 7.02. Foundations and Earth Structures. Naval Facilities Engineering Command (NFEC), Alexandria, VA, USA

Neely, W.J., 2005. Calculated and measured axial loads on bearing pads in MSE retaining walls. Presented at 2005 Western Bridge Engineer's Seminar, Session, 6C, Portland, Oregon, USA, Sept. 26-28.

Neely, W.J. and Tan, S.L., 2010. Effects of second order design factors on the behaviour of MSE walls. Earth Retention Conference 3. Earth Retaining Structures Committee of the Geo-Institute of ASCE. Geotechnical Special Publications (GSP) n. 208. Proceedings of the 2010 Earth Retention Conference held in Bellevue, Washington, August 1-4, pp.522-530.

Ng P.C.F., Pyrah I.C., and Anderson W.F., 1997. Assessment of three interface elements and modification of the interface element in CRISP90. Computers and Geotechnics 21, 315-339.

Olivella, S., Gens, A., Carrera, J., and Alonso, E.E., 1996. Numerical Formulation for a Simulator (CODE_BRIGHT) for the Coupled Analysis of Saline Media, Engineering Computations, Vol.13, No.7, 87-112.

Palmeira, E.M., and Milligan, G.W.E., 1989. Scale and other factors affecting the results of pull-out tests of grids buried in sand. Geotechnique, 39(3): 511-524.

Palmeira, E.M., 2009. Soil–geosynthetic interaction: Modelling and analysis, Geotextiles and Geomembranes 27: 368–390.

Pennington, D.W., Potting, J., Finnveden, G., Lindeijer, E., Jolliet, O., Rydberg, T., and Rebitzer, G., 2004. Life cycle assessment Part 2: Current impact assessment practice. Environment International 30(5): 721-739.

PLAXIS, 2008. Reference Manual, 2D - Version 9.0. PLAXIS B.V., Delft University of Technology, The Netherlands. (http://www.plaxis.nl/).

PLAXIS, 2012. Material Models Manual. PLAXIS B.V., Delft University of Technology, The Netherlands. (http://www.plaxis.nl/).

Potyondy, J.G., 1961. Skin friction between various soils and construction materials. Géotechnique 11, 339-353.

PRé Consultants B.V., 2010. SimaPro software, v.8.0.2. Amersfoort, Utrecht, The Netherlands. (http://www.pre-sustainability.com).

PWRC, 2003. Design method, construction manual and specifications for steel strip reinforced retaining walls (3rd Edition). Public Works Research Center (PWRC), Tsukuba, Ibaraki, Japan, 302p.

Rafalko, S.D., Sankey, J.E., and Freitag, N., 2010. Sustainability measures for MSE walls and baseline environmental impact evaluations. In Proceedings of the 2010 Earth Retention Conference, Bellevue, Washington, USA (Finno RJ, Hashash YMA and Arduino P (eds)). Geo-Institute of the American Society of Civil Engineers, Reston, VA, USA.

Raja, J., Dixon, N., Fowmes, G., Frost, M., and Assinder, P., 2015. Obtaining reliable embodied carbon values for geosynthetics. Geosynthetics International 22(5): 393-401

Rebitzer, G., Ekvall, T., Frischknecht, R., et al., 2004. Life cycle assessment Part 1: Framework, goal and scope definition, inventory analysis, and applications. Environment International 30, 701-720.

ReCiPe, 2014. ReCiPe. (http://www.lcia-recipe.net/).

RTA QA-R57, 2005. Design of Reinforced Soil Walls (QA Specification R57 - 2nd edition). Roads and Traffic Authority, New South Wales.

Rowe, K.R. and Ho, S.K., 1997. Continuous panel reinforced soil walls on rigid foundations. Journal of Geotechnical and Geoenvironmental Engineering, 123(10): 912–920. doi:10.1061/(ASCE)1090-0241(1997)123:10(912).

Runser, D.J., 1999. Instrumentation and experimental evaluation of a 17 m tall reinforced earth retaining wall, M.S. Thesis, School of Civil Engineering, Purdue University, West Lafayette, Indiana, USA, 289p.

Runser, D.J., Fox, P.J., and Bourdeau, P.L., 2001. Field performance of a 17 m-high reinforced soil retaining wall. Geosynthetics International, 8(5): 367-391.

Saaty, T., 2008. Decision making with the analytic hierarchy process. International Journal of Services Sciences 1, 83-98.

Samtani, N.C., and Nowatzki, E.A., 2006. Soils and Foundations Reference Manual. Report FHWA-NHI-06-088, National Highway Institute, Federal Highway Administration, Washington, DC, USA.

Santos, E.C.G., Palmeira, E.M., and Bathurst, R.J., 2014. Performance of two geosynthetic reinforced walls with recycled construction waste backfill and constructed on collapsible ground. Geosynthetics International 21(4): 256-269.

Santos, E.C.G., Palmeira, E.M., and Bathurst, R.J., 2013. Behaviour of a geogrid reinforced wall built with recycled construction and demolition waste backfill on a collapsible foundation. Geotextiles and Geomembranes 39: 9-19.

Schlosser, F. and Elias, V., 1978. Friction in reinforced earth. Proceedings of ASCE Symposium on Earth Reinforcement, Pittsburgh, PA, USA, pp.735-763.

Schlosser, F., 1978. History, current development and future developments of reinforced earth. In proceedings of the Symposium on Soil Reinforcing and Stabilizing Techniques, sponsored by New South Wales Institute of Technology and the University of Sidney, Australia.

Schlosser, F. and Segrestin, P., 1979. Dimensionnement des ouvrages en terre armée par la méthode de l'équilibre local (Local stability analysis method of design of reinforced earth structures). In proceedings of International Conference on Sol Reinforcement, Paris, France, Vol.1, pp.157-162.

Skejic, A. and Balic, A., 2015. Three-dimensional numerical analysis of reinforced earth walls including transverse ribs. 2nd International Conference on Multi-scale Computational Methods for Solids and Fluids. University of Sarajevo, GF Sarajevo, Bosnia-Herzegovina, June 10-12,

Stuedlein, A.W., Bailey, M.J., Lindquist, D.D., Sankey, J., and Neely, W.J., 2010. Design and performance of a 46-m-high MSE wall. Journal of Geotechnical and Geoenvironmental Engineering, 136(6), 786-796.

Stuedlein, A.W., Allen, T.M., Holtz, R.D., and Christopher, B.R., 2012. Assessment of reinforcement strains in very tall mechanically stabilized earth walls. Journal of Geotechnical and Geoenvironmental Engineering, 138(3), 345-356.

Stucki, M., Büsser, S., Itten, R., Frischknecht, R., and Wallbaum, H., 2011. Comparative Life Cycle Assessment of Geosynthetics versus Conventional Construction Materials. European Association of Geosynthetics Manufacturers, ESU-services, Uster, ETH Zürich, Switzerland.

Tanyu B.F., Sabatini P.J., and Berg R.R., 2008. Earth Retaining Structures (FHWA-NHI-07-071). US Department of Transportation, Federal Highway Administration, Washington, DC. USA.

Tajiri, N., Sasaki, H., Nishimura, J., Ochiai, Y., and Dobashi, K., 1996. Full-scale failure experiments of geotextile-reinforced soil walls with different facings. IS-Kyushu 96, 3rd International Symposium on Earth Reinforcement, Fukuoka, Japan, pp.525-530.

Thome, D.A. and Janke, R.C., 2005. Rehabilitation of an existing mechanically stabilized earth wall using soil nails. Presented at the 30th Annual Conference on Deep Foundations. Deep Foundations Institute, Chicago, Illinois, USA, 6p.

Vidal, H., 1966. La Terre Armée, un Matériau Nouveau Pour les Travaux Publics. Annales de l'I.T.B.T.P., Paris, France, 223/224: 887-936.

Vieira, C.S. and Pereira, P.M., 2015. Interface shear properties of geosynthetics and construction and demolition waste from large-scale direct shear tests. Geosynthetics International (on line: http://dx.doi.org/10.1680/gein.15.00030).

Wallbaum, H., Büsser, S., Itten, R., and Frischknecht, R., 2014. Environmental benefits by using construction methods with geosynthetics. In Proceedings of the 10th International Conference on Geosynthetics, Berlin, Germany. German Geotechnical Society, Essen, Germany.

WRAP, 2010. Sustainable Geosystems in Civil Engineering Applications: Geosystems Report. Waste and Resources Action Programme, Banbury, UK.

Yoo, C. and Kim, S-B., 2008. Performance of a two-tier geosynthetic reinforced segmental retaining wall under a surcharge load: Full-scale load test and 3D finite element analysis. Geotextiles and Geomembranes 26: 460-472.

Yu, Y., Damians, I.P., Bathurst, R.J., Lloret, A., and Josa, A., 2014. Equivalent interface properties for FLAC and PLAXIS models to simulate soil-strucutre interactions in MSE walls. Proceedings of the GeoRegina 2014. 67th Canadian Geotechnical Conference, Regina, Saskatchewan, Canada. September 28 – October 1, 2014, 8p.

Yu, Y. and Bathurst, R.J., 2015. Analysis of soil-steel bar mat pullout models using a statistical approach. ASCE Journal of Geotechnical and Geoenvironmental Engineering 141(5): 04015006.

Yu, Y., Bathurst, R.J., and Miyata, Y., 2015a. Numerical analysis of a mechanically stabilized earth wall reinforced with steel strips. Soils and Foundations 55(3): 536-547.

Yu, Y., Damians, I.P., and Bathurst, R.J., 2015b. Influence of choice of FLAC and PLAXIS interface models on reinforced soil-structure interactions. Computers and Geotechnics, 65:164-174.

Barcelona, June 2016

Universitat Politècnica de Catalunya (UPC-BarcelonaTech)
School of Civil Engineering (ETSECCPB)
Department of Civil Engineering and Environmental Engineering (DECA)